Discrete Dynamics in Nature and Society

Analysis, Control and Applications of Passivity in Complex Networks

Lead Guest Editor: Jinliang Wang
Guest Editors: Jianquan Lu and Hao Shen

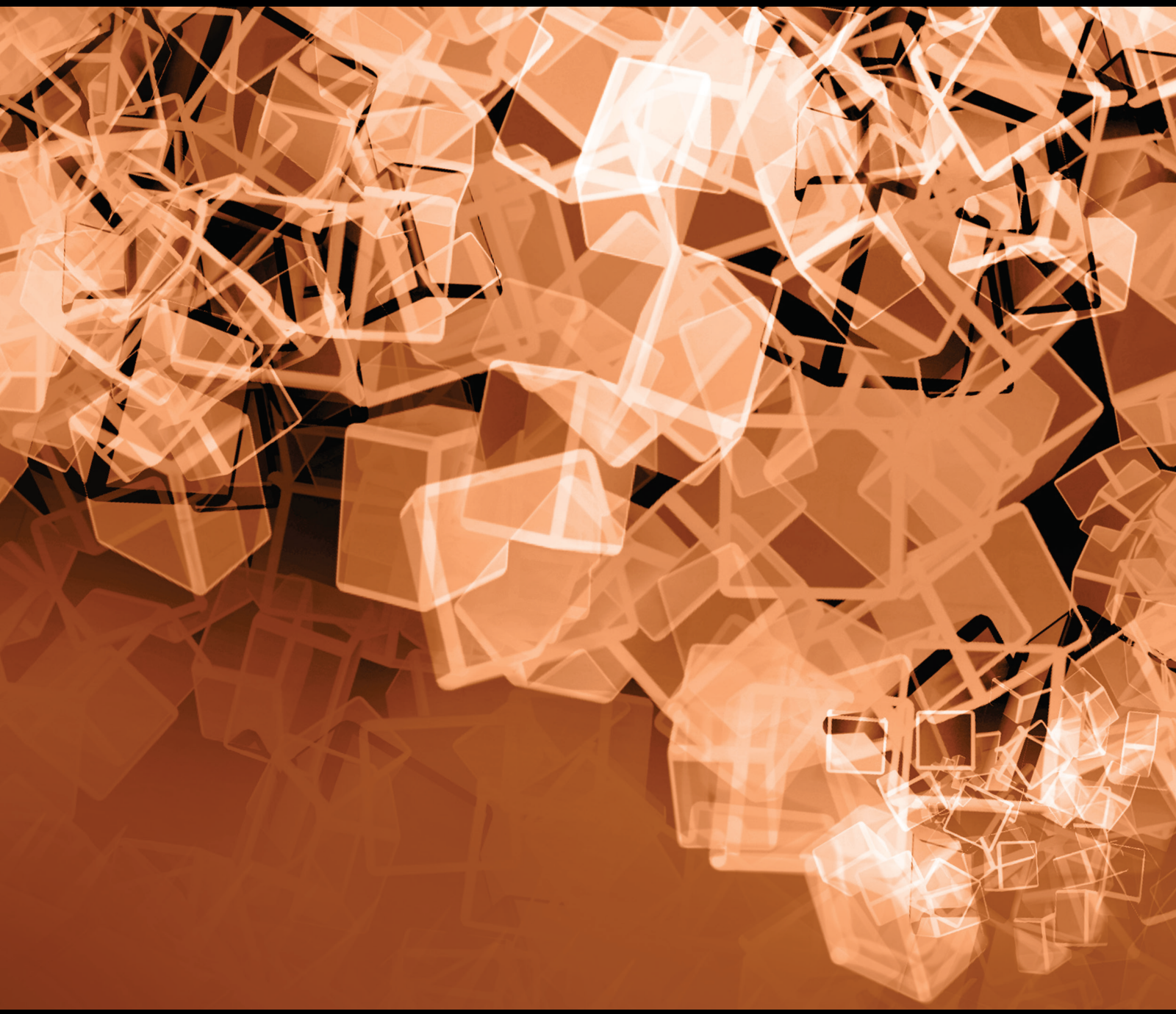

Analysis, Control and Applications of Passivity in Complex Networks

Discrete Dynamics in Nature and Society

Analysis, Control and Applications of Passivity in Complex Networks

Lead Guest Editor: Jinliang Wang
Guest Editors: Jianquan Lu and Hao Shen

Chief Editor

Associate Editors

Academic Editors

Contents

Hindawi
Discrete Dynamics in Nature and Society
Volume 2020, Article ID 5041761, 12 pages
https://doi.org/10.1155/2020/5041761

Research Article

Dynamical Analysis for the Hybrid Network Model of Delayed Predator-Prey Gompertz Systems with Impulsive Diffusion between Two Patches

Li Xiang,[1,2] Yurong Zhang,[2] Dan Zhang,[2] Zhichun Yang ,[2] and Lingzhi Huang[2]

[1]*Computer College, Civil Aviation Flight University of China, Guanghan 618307, China*
[2]*Key Laboratory for Optimization and Control of Ministry of Education, Mathematical College, Chongqing Normal University, Chongqing 401331, China*

Correspondence should be addressed to Zhichun Yang; yangzhch@126.com

Received 10 May 2020; Revised 18 July 2020; Accepted 22 July 2020; Published 28 September 2020

Guest Editor: Jinliang Wang

In this paper, we consider a hybrid network model of delayed predator-prey Gompertz systems with impulsive diffusion between two patches, in which the patches represent nodes of the network such that the prey population interacts locally in each patch and diffusion occurs along the edges connecting the nodes. Using the discrete dynamical system determined by the stroboscopic map which has a globally stable positive fixed point, we obtain the global attractive condition of predator-extinction periodic solution for the network system. Furthermore, by employing the theory of delay functional and impulsive differential equation, we obtain sufficient condition with time delay for the permanence of the network.

1. Introduction

Along with the continuous development of the network science, the mathematical models organized as networks have received considerable attention [1]–[3]. Taking epidemic models for an example, locations such as cities or urban areas can be represented as nodes of a network; individuals can be divided into different states, such as infection, susceptibility, immunity, etc. These individuals interact moving between connecting nodes [2, 3]. Furthermore, in the study of population dynamical systems, due to the universality and importance of the predator-prey relationship, the dynamics of the predator-prey system has been widely concerned. In recent decades, the dynamical behaviors of the predator-prey model defined on the network have enjoyed remarkable progress [4–8]. In [6], each node of the coupled network represents a discrete predator-prey system, and the network dynamics are investigated. In [7], Chang studied instability induced by time delay for a predator-prey model on complex networks and instability conditions were obtained via linear stability analysis of network organized systems.

Since the severe competition, natural enemy, or deterioration of the patch environment, the population dispersal phenomena of biological species can often occur between patches. Therefore, the effect of spatial factors in population dynamics becomes a very hot subject [9, 10]. Concerning qualitative analysis for predator-prey models with diffusion, such as local (or global) stability of equilibria and the existence of periodic solutions, many nice results have been obtained (see also, e.g., [11–13]). Regretfully, in all of the above population dispersion systems, dispersal behavior of the populations is occurring at every time. That is, it is a continuous dispersal. In practice, it is often the case that population diffusion occurs in regular pulses. For example, when winter comes, birds will migrate between patches in search for a better environment, whereas they do not diffuse during other seasons. Thus, impulsive diffusion provides a more natural behavior phenomenon. At present, many scholars have applied the theory of impulsive differential equations to population dynamics, and many important studies have been performed [14–19]. Accordingly, it is an interesting subject to analyze the dynamic behaviors of the

system by extending the predator-prey model with impulsive diffusion to the network version. In addition, in the 1825s, Benjamin Gompertz established the Gompertz function $y = \mathrm{k}e^{-e^{a-bx}}$, which can be translated into a Gompertz differential equation $\mathrm{d}y/\mathrm{d}x = by\ln(k/y)$ (see [20, 21]). Compared with the logistic function, it has been proven to be a simple example to generate an asymmetric S-shaped curve [22]. Since then, many models have been established for biological growth by using the Gompertz function (e.g., [23, 24]). Furthermore, many species usually go through two distinct life stages, immature and mature. Considering that the immature becomes the mature need to spend units of time and the number of deaths in the juvenile period, it is essential to consider time-delay in stage-structured model. Many stage-structured predator-prey models with time delay and impulsive diffusive were investigated [25–28]. Liu [25] studied a delayed predator-prey model with impulsive perturbations and gave the predator-extinction periodic solution of the model, which is globally attractive and permanence. Jiao et al. [26] and Dhar and Jatav [27] investigated a delayed predator-prey model with impulsive diffusion and sufficient conditions of the global attractiveness of the predator-extinction periodic solution and the permanence were derived.

Motivated by the above discussion, in this paper, we shall organize the patches into networks to investigate a delayed stage-structured functional response predator-prey Gompertz model with impulsive diffusion between two predators territories. We also consider the harvesting effort of the two mature predators. By employing the comparison theorem of impulsive differential equations and the global attractivity of the first order time-delay system, we will obtain some sufficient conditions on the global attractiveness of predator-extinction periodic solution and permanence of our model. The results can provide a reliable strategic basis for the protection of biological resources.

The paper is organized as follows. In the next section, introduce model development. In Section 3, some useful preliminaries are given. In Section 4, we give the conditions of the global attractivity for our model. In Section 5, we give the conditions of permanence for our model. Finally, discussion is given in Section 6.

2. Hybrid Network Model-Organized Predator-Prey System

Aiello and Freedman [29] introduced the following stage-structured single species model:

$$\begin{cases} x_1'(t) = \alpha x_2(t) - \gamma_1 x_1(t) - \alpha e^{-\gamma_1 \tau} x_2(t-\tau), \\ x_2'(t) = \alpha e^{-\gamma_1 t} x_2(t-\tau) - \gamma_2 x_2^2(t), \end{cases} \tag{1}$$

where $x_1(t)$ and $x_2(t)$ denote the immature and mature population densities, respectively, $\alpha > 0$ represents the birth rate, $\gamma_1 > 0$ is the immature death rate, $\gamma_2 > 0$ is the mature death and overcrowding rate, and τ represents the mean length of the juvenile period. The term $\alpha e^{-\gamma_1 \tau} x_2(t-\tau)$ represents the immature populations who were born at time $t-\tau$ and survived at time t (with the immature death rate γ_1) and therefore represents the transformation of immature to mature.

Wang et al. [23] considered the following model:

$$\begin{cases} \left.\begin{aligned} x_1'(t) &= r_1 x_1(t) \ln \frac{k_1}{x_1}, \\ x_2'(t) &= r_2 x_2(t) \ln \frac{k_2}{x_2}, \end{aligned}\right\} t \neq n\tau, \\ \left.\begin{aligned} \Delta x_1(t) &= d_1(x_2(t) - x_1(t)), \\ \Delta x_2(t) &= d_2(x_1(t) - x_2(t)), \end{aligned}\right\} t = n\tau, \quad n \in \mathbb{N}, \end{cases} \tag{2}$$

where x_i $(i = 1, 2)$ is the density of species in the ith patch, r_i $(i = 1, 2)$ is the intrinsic rate of natural increase of population in the ith patch, k_i $(i = 1, 2)$ denotes the carrying capacity in the ith patch, and d_i $(i = 1, 2)$ is dispersal rate in the ith patch. It is assumed here that the net exchange from the jth to ith patch is proportional to the difference $x_j - x_i$ of population densities. The pulse diffusion occurs every τ period (τ is a positive constant). Here $\Delta x_i(t) = x_i(n\tau^+) - x_i(n\tau^-)$, where $x_i(n\tau^+)$ represents the density of population in the ith patch immediately after the nth diffusion pulse, and $x_i(n\tau^-)$ represents the density of population in the ith patch before the nth diffusion pulse at time $t = n\tau$. r_i, k_i and d_i $(i = 1, 2)$ are positive constants.

According to the model formulation in the literature [15, 23, 25–27], in the following, we shall extend predator-prey model to the network analogue version. Firstly, we propose in this paper a predator-prey model on the network with the following assumptions:

(A1) The patches are created by predator territories and are represented as nodes of the network.

(A2) The prey population in different nodes has different growth rates. The prey population interacts locally in each patch and impulsively diffuses through connected nodes.

(A3) The predator population is divided into immature and mature. Immature becoming mature requires a constant time.

(A4) Mature predator in different nodes has a different conversion rate.

(A5) Immature predators only feed on mature predators and can not reproduce.

(A6) Mature predators in different nodes have different harvest efforts.

We formulate the following hybrid network model of delayed predator-prey Gompertz system with impulsive diffusion between two patches:

$$\left\{\begin{array}{l} \left.\begin{array}{l} x_1'(t) = r_1 x_1(t)\ln\dfrac{k_1}{x_1(t)} - p_1\left(x_1(t)\right)z_1(t), \\ y_1'(t) = \alpha_1 z_1(t) - \alpha_1 e^{-\omega_1\tau_1} z_1\left(t-\tau_1\right) - \omega_1 y_1(t), \\ z_1'(t) = \alpha_1 e^{-\omega_1\tau_1} z_1\left(t-\tau_1\right) + \beta_1 p_1\left(x_1(t)\right)z_1(t) - E_1 z_1(t) - \gamma_1 z_1^2(t), \\ x_2'(t) = r_2 x_2(t)\ln\dfrac{k_2}{x_2(t)} - p_2\left(x_2(t)\right)z_2(t), \\ y_2'(t) = \alpha_2 z_2(t) - \alpha_2 e^{-\gamma_1\tau_2} z_2\left(t-\tau_2\right) - \gamma_1 y_2(t), \\ z_2'(t) = \alpha_2 e^{-\omega_2\tau_1} z_1\left(t-\tau_1\right) + \beta_2 p_2\left(x_2(t)\right)z_2(t) - E_2 z_2(t) - \gamma_2 z_2^2(t), \end{array}\right\} t \neq n\tau, \\ \left.\begin{array}{l} \Delta x_1(t) = d_1\left(x_2(t) - x_1(t)\right), \\ \Delta x_2(t) = d_2\left(x_1(t) - x_2(t)\right), \\ \Delta y_1(t) = 0, \\ \Delta y_2(t) = 0, \\ \Delta z_1(t) = 0, \\ \Delta z_2(t) = 0, \end{array}\right\} t = n\tau, n \in \mathbb{N}, \end{array}\right. \tag{3}$$

where x_i $(i = 1, 2)$ is the prey population density in the ith patch at time t, $y_1(t)$ and $z_1(t)$ are predator populations density with immature and mature in the first patch at time t, $y_2(t)$ and $z_2(t)$ are predator populations density with immature and mature in the second patch at time t; r_i and k_i are the Gompertz intrinsic growth rates and the carrying capacity in the ith patch, α_i represents the growth rate of immature to mature predators in the ith patch; ω_1 and γ_1 are the immature and mature predator death rates in the first patch, ω_2 and γ_2 are the immature and mature predator death rates in the second patch, E_i $(i = 1, 2)$ is the harvesting effort of the mature population in the ith patch. Further, τ_i, β_i, $d_i \in (0, 1)$ are the constant time to maturity, the conversion rates of predator, and dispersal rates of prey in the ith patch. The pulse diffusion occurs every τ period (τ is a positive constant).

Also, $p_i(\cdot) \in H$; here $H = \{f: R \longrightarrow R | f(0) = 0, f'(x) > 0$ and $f''(x) \leq 0$ for all $x > 0\}$. Examples of functions found in the biological literature that satisfy H are as follows:

$(F1)$ $f_1(x) = ax$, with $a > 0$

$(F2)$ $f_2(x) = ax/(1 + bx)$, with $a, b > 0$

$(F3)$ $f_3(x) = a(1 - e^{-bx})$, with $a, b > 0$

Functions $(F1)$ and $(F2)$ are known as Holling type functional responses. Function $(F3)$ is Ivlev type functional responses. Functions $(F1)$ and $(F2)$ also were regarded as incidence rate function. Function $(F1)$ is a double linear incidence rate function. Function $(F2)$ is saturated incidence rate function.

We only consider system (3) in the biological meaning region: $D = \{(x_1(t)y_1(t), z_1(t), x_1(t), y_2(t)z_2(t)) \mid x_1(t) \geq 0, y_1(t) \geq 0, z_1(t) \geq 0, x_2(t) \geq 0, y_2(t) \geq 0, z_2(t) \geq 0\}$ and assume that solutions of system (3) satisfy the initial conditions:

$$\left(\phi_1(s), \phi_2(s), \phi_3(s), \phi_4(s), \phi_5(s), \phi_6(s)\right) \in C\left([-\tau, 0], \mathbb{R}_+^6\right), \quad \phi_i(0) > 0, \quad i = 1, 2, 3, 4, 5, 6. \tag{4}$$

We can simplify model (3) organized by network and need to restrict our attention to the following model:

$$\left\{\begin{array}{l} x_1'(t) = r_1 x_1(t)\ln\dfrac{k_1}{x_1(t)} - p_1(x_1(t))z_1(t), \\ z_1'(t) = \alpha_1 e^{-\omega_1\tau_1} z_1(t-\tau_1) + \beta_1 p_1(x_1(t))z_1(t) - E_1 z_1(t) - \gamma_1 z_1^2(t), \\ x_2'(t) = r_2 x_2(t)\ln\dfrac{k_2}{x_2(t)} - p_2(x_2(t))z_2(t), \\ z_2'(t) = \alpha_2 e^{-\omega_2\tau_1} z_1(t-\tau_1) + \beta_2 p_2(x_2(t))z_2(t) - E_2 z_2(t) - \gamma_2 z_1^2(t), \end{array}\right\} t \neq n\tau,$$

$$\left\{\begin{array}{l} \Delta x_1(t) = d_1(x_2(t) - x_1(t)), \\ \Delta x_2(t) = d_2(x_1(t) - x_2(t)), \\ \Delta z_1(t) = 0, \\ \Delta z_2(t) = 0, \end{array}\right\} t = n\tau, n \in \mathbb{N}, \tag{5}$$

with the initial condition

$$\begin{aligned} (\phi_1(s), \phi_3(s), \phi_4(s), \phi_6(s)) \in C\left([-\tau, 0], \mathbb{R}_+^4\right), \\ \phi_i(0) > 0, \quad i = 1, 3, 4, 6. \end{aligned} \tag{6}$$

3. Preliminaries

The solution $x(t) = (x_1(t), y_1(t), z_1(t), x_2(t), y_2(t), z_2(t))^T$ of (3) is a piecewise continuous function x: $R_+ \longrightarrow R_+^6$. Thus, $x(t)$ is continuous on $(n\tau, (n+1)\tau]$, for all $n \in Z_+$ and $\lim_{t\longrightarrow n\tau^+} x(t) = x(n\tau^+)$ exists. Obviously, the smoothness properties of x guarantee the global existence and uniqueness of the solution of (3) (see [30]). We assumed that $x_1(t), y_1(t), z_1(t), x_2(t), y_2(t), z_2(t) \geq 0$. If $z_1(t) = 0$, $z_2(t) = 0$, we can obtain the following subsystem of (5):

$$\left\{\begin{array}{l} x_1'(t) = r_1 x_1(t)\ln\dfrac{k_1}{x_1(t)}, \\ x_2'(t) = r_2 x_2(t)\ln\dfrac{k_2}{x_2(t)}, \end{array}\right\} t \neq n\tau,$$

$$\left\{\begin{array}{l} \Delta x_1(t) = d_1(x_2(t) - x_1(t)), \\ \Delta x_2(t) = d_2(x_1(t) - x_2(t)), \end{array}\right\} t = n\tau, n \in \mathbb{N}. \tag{7}$$

For simplicity, let $u_1 = x_1/k_1$, $u_2 = x_2/k_2$, $k = k_2/k_1$, so the system (7) can be written as follows:

$$\left\{\begin{array}{l} u_1'(t) = r_1 u_1(t)\ln\dfrac{1}{u_1(t)}, \\ u_2'(t) = r_2 u_2(t)\ln\dfrac{1}{u_2(t)}, \end{array}\right\} t \neq n\tau,$$

$$\left\{\begin{array}{l} \Delta u_1(t) = d_1(k u_2(t) - u_1(t)), \\ \Delta u_2(t) = d_2\left(\dfrac{1}{k}u_1(t) - u_2(t)\right), \end{array}\right\} t = n\tau, n \in \mathbb{N}. \tag{8}$$

Integrating and solving the first two equations of system (8) between pulses, we have the following:

$$\begin{aligned} u_i(t) = u_i(n\tau^+)^{e^{-r_i(t-n\tau)}}, \\ n\tau < t \leq (n+1)\tau, \quad i = 1, 2. \end{aligned} \tag{9}$$

Then, considering the last two equations of system (8), we get the following stroboscopic map of system (8):

$$\left\{\begin{array}{l} u_{1,(n+1)\tau} = u_{1,n}^{b_1} + d_1\left(k u_{2,n}^{b_2} - u_{1,n}^{b_1}\right), \\ u_{2,(n+1)\tau} = u_{2,n}^{b_2} + d_2\left(\dfrac{1}{k}u_{1,n}^{b_1} - u_{2,n}^{b_2}\right). \end{array}\right. \tag{10}$$

Here, $u_{i,(n+1)\tau} = u_i[(n+1)\tau^+]$, $0 < b_1 = e^{-r_1\tau} < 1$, $0 < b_2 = e^{-r_2\tau} < 1$. Equation (10) is a difference equation. It describes the densities of the population in two patches at a pulse in terms of values at the previous pulse, in other words, stroboscopically sampling at its pulsing period. The dynamical behavior of system (10), coupled with (9), determines the dynamical behavior of system (8). To write system (8) as a map, we can define a map F: $R_+^2 \longrightarrow R_+^2$ such that

$$\begin{cases} F_1(u) = u_1^{b_1} + d_1\left(ku_2^{b_2} - u_1^{b_1}\right), \\ F_2(u) = u_2^{b_2} + d_2\left(\frac{1}{k}u_1^{b_1} - u_2^{b_2}\right). \end{cases} \tag{11}$$

We see that $F_i(n\tau)$ describes the population densities in time $n\tau$, and the sets of all iterations of the map F are equivalent to the set of all density sequence generated by system (10). Furthermore, we have the following.

Lemma 1 (see [23]). There exists a unique positive fixed point $q = (q_1, q_2)$ of F, and for every $u = (u_1, u_2) > 0$, $F^n \longrightarrow q$ as $n \longrightarrow \infty$.

That is, the fixed point $q = (q_1, q_2)$ of F is globally stable. The trajectory of system (8) will trend to the positive periodic solution $(\widetilde{u}_1, \widetilde{u}_2)$ with a period τ, i.e.,

$$\begin{aligned} &\widetilde{u}_i(t) = q_i^{e^{-r_i(t-n\tau)}}, \\ &n\tau < t \le (n+1)\tau, \quad i = 1, 2. \end{aligned} \tag{12}$$

Then, the trajectory of system (7) will trend to the positive periodic solution $(\widetilde{x}_1, \widetilde{x}_2)$ with a period τ, i.e.,

$$\begin{aligned} &\widetilde{x}_i(t) = k_i q_i^{e^{-r_i(t-n\tau)}}, \\ &n\tau < t \le (n+1)\tau, \quad i = 1, 2. \end{aligned} \tag{13}$$

Lemma 2. *There exists a constant $M > 0$ such that $x_1(t) \le M/\beta_1$, $y_1(t) \le M$, $z_1(t) \le M$, $x_2(t) \le M/\beta_2$, $y_2(t) \le M$, $z_2(t) \le M$ for each solution of (3) with all t large enough.*

Proof. First, we define $V(t) = \beta_1 x_1(t) + y_1(t) + z_1(t) + \beta_2 x_2(t) + y_2(t) + z_2(t)$; then, we have $\lambda_0 = \min\{\omega_1, r_1\}$. Then, it is obvious that

$$\begin{aligned} V'(t) = {} & \beta_1 r_1 x_1(t) \ln \frac{k_1}{x_1(t)} + \beta_2 r_2 x_2(t) \ln \frac{k_2}{x_2(t)} \\ & + (\alpha_1 - E_1) z_1(t) + (\alpha_2 - E_2) z_2(t) - \omega_1 y_1(t) \\ & - \omega_2 y_2(t) - \gamma_1 z_1^2(t) - \gamma_2 z_2^2(t). \end{aligned} \tag{14}$$

$$\begin{aligned} \frac{dV(t)}{dt} + \lambda_0 V(t) \le {} & \beta_1 r_1 x_1(t) \ln \frac{k_1 e^{\lambda_0/r_1}}{x_1(t)} + \beta_2 r_2 x_2(t) \ln \frac{k_2 e^{\lambda_0/r_2}}{x_2(t)} \\ & + (\alpha_1 - E_1 + \lambda_0) z_1(t) - \gamma_1 z_1^2(t) \\ & + (\alpha_2 - E_2 + \lambda_0) z_2(t) - \gamma_2 z_2^2(t) \\ \le {} & \beta_1 r_1 k_1 e^{(\lambda_0/r_1)} + \beta_2 r_2 k_2 e^{(\lambda_0/r_2)} \\ & + \frac{(\alpha_1 - E_1 + \lambda_0)^2}{4\gamma_1} + \frac{(\alpha_2 - E_2 + \lambda_0)^2}{4\gamma_2} = M_0. \end{aligned} \tag{15}$$

Then, we can obtain $V(t) \le M_0/\lambda_0 + (V(0^+) - M_0/\lambda_0)e^{-\lambda_0 t}$, when $t \longrightarrow \infty$, $V(t) \le M_0/\lambda_0$. So $V(t)$ is uniformly ultimately bounded. Hence, by the definition of $V(t)$, there exists a constant $M = M_0/\lambda_0$ such that $x_1(t) \le M/\beta_1$, $y_1(t) \le M$, $z_1(t) \le M$, $x_2(t) \le M/\beta_2$, $y_2(t) \le M$, $z_2(t) \le M$ for all t large enough. The proof is completed. □

Lemma 3 (see [31]). Consider the following equation with delay:

$$x'(t) = ax(t-\tau) - bx(t) - cx^2(t). \tag{16}$$

We assumed that a, b, c, and τ are positive constants. $x(t) > 0$ for $t \in [-\tau, 0]$, we have the following:

(i) If $a > b$, then $\lim_{t \longrightarrow +\infty} x(t) = (a-b)/c$

(ii) If $a < b$, then $\lim_{t \longrightarrow +\infty} x(t) = 0$

4. Extinction of the Predator

From the previous section, we know there exists a predator eradicated periodic solution $(\widetilde{x}_1, 0, 0, \widetilde{x}_2, 0, 0)$ of system (3). In this section, we will prove that $(\widetilde{x}_1, 0, 0, \widetilde{x}_2, 0, 0)$ for the network organized system (3) is globally attractive.

Theorem 1. *If*

$$\begin{aligned} &\alpha_1 e^{-\omega_1 \tau_1} + \beta_1 p_1(x_1^*) < E_1, x_1^* = k_1 q_1^{e^{-r_1\tau}}; \\ &\alpha_2 e^{-\omega_2 \tau_2} + \beta_2 p_2(x_2^*) < E_2, x_2^* = k_2 q_2^{e^{-r_2\tau}} \end{aligned} \tag{17}$$

holds, the predator-extinction periodic solution $(\widetilde{x}_1, 0, 0, \widetilde{x}_2, 0, 0)$ of system (3) is globally attractive.

Proof. It is obvious from the global attraction of the periodic solution of $(\widetilde{x}_1, 0, 0, \widetilde{x}_2, 0, 0)$, system (3) is equivalent to the global attraction of the periodic solution $(\widetilde{x}_1, 0, \widetilde{x}_2, 0)$ of system (5). From (17), we can choose $\varepsilon_0 > 0$ sufficiently small such that

$$\alpha_1 e^{-\omega_1 \tau_1} + \beta_1 p_1(x_1^* + \varepsilon_0) < E_1, \alpha_2 e^{-\omega_2 \tau_2} + \beta_2 p_2(x_2^* + \varepsilon_0) < E_2. \tag{18}$$

It follows from that the first and third equations of system (5) that

$$\begin{cases} x_1'(t) \le r_1 x_1(t) \ln \frac{k_1}{x_1(t)}, \\ x_2'(t) \le r_2 x_2(t) \ln \frac{k_2}{x_2(t)}. \end{cases} \tag{19}$$

So we consider the following comparison impulsive differential system:

$$\left\{\begin{array}{l} \left.\begin{array}{l} v_1'(t) = r_1 v_1(t)\ln\dfrac{k_1}{v_1(t)}, \\ \\ v_2'(t) = r_2 v_2(t)\ln\dfrac{k_2}{v_2(t)}, \end{array}\right\} t \neq n\tau, \\ \left.\begin{array}{l} \Delta v_1(t) = d_1\left(v_2(t) - v_1(t)\right), \\ \\ \Delta v_2(t) = d_2\left(v_1(t) - v_2(t)\right), \end{array}\right\} t = n\tau, n \in \mathbb{N}. \end{array}\right. \tag{20}$$

By Lemma 1 and (11), we obtain the boundary periodic solution of system (20):

$$\begin{aligned} &\widetilde{v}_i(t) = k_i q_i^{e^{-r_i(t-n\tau)}}, \\ &n\tau < t \leq (n+1)\tau, \quad i = 1, 2, \end{aligned} \tag{21}$$

which is globally asymptotically stable. In view of the comparison theorem of the impulsive differential equation (see [30]), we have $x_i(t) \leq v_i(t) \longrightarrow \widetilde{x}_i(t)$ as $t \longrightarrow \infty$. Then, there exist n_2 with $n_2 > n_1$ and $t > n_2$ such that

$$\begin{aligned} x_1(t) &\leq v_1(t) < \widetilde{x}_1(t) + \varepsilon_0, \\ x_2(t) &\leq v_2(t) < \widetilde{x}_2(t) + \varepsilon_0, \\ n\tau &< t \leq (n+1)\tau, \\ n &> n_2. \end{aligned} \tag{22}$$

That is,

$$\begin{aligned} x_1(t) &\leq \widetilde{x}_1(t) + \varepsilon_0 \leq x_1^* + \varepsilon_0 \triangleq \delta_1, \\ x_2(t) &\leq \widetilde{x}_2(t) + \varepsilon_0 \\ &\leq x_2^* + \varepsilon_0 \triangleq \delta_2, \\ n\tau &< t \leq (n+1)\tau. \end{aligned} \tag{23}$$

From the second and fourth equations of system (5), we have the following:

$$\left\{\begin{array}{l} z_1'(t) \leq \alpha_1 e^{-\omega_1\tau_1} z_1(t-\tau_1) - \left(E_1 - \beta_1 p_1\left(\delta_1(t)\right)\right) z_1(t) - \gamma_1 z_1^2(t), \quad t > n\tau + \tau_1, n > n_2, \\ z_2'(t) \leq \alpha_2 e^{-\omega_2\tau_2} z_2(t-\tau_2) - \left(E_2 - \beta_2 p_2\left(\delta_2(t)\right)\right) z_2(t) - \gamma_2 z_1^2(t), \quad t > n\tau + \tau_2, n > n_2. \end{array}\right. \tag{24}$$

Now, consider the following comparison differential system:

$$\left\{\begin{array}{l} m_1'(t) = \alpha_1 e^{-\omega_1\tau_1} m_1(t-\tau_1) - \left(E_1 - \beta_1 p_1\left(\delta_1(t)\right)\right) m_1(t) - \gamma_1 m_1^2(t), \quad t > n\tau + \tau_1, n > n_2, \\ m_2'(t) = \alpha_2 e^{-\omega_2\tau_2} m_2(t-\tau_1) - \left(E_2 - \beta_2 p_2\left(\delta_2(t)\right)\right) m_2(t) - \gamma_2 m_1^2(t), \quad t > n\tau + \tau_2, n > n_2. \end{array}\right. \tag{25}$$

From (18), we have $\alpha_1 e^{-\omega_1\tau_1} < E_1 - \beta_1 p_1(x_1^* + \varepsilon_0)$ and $\alpha_2 e^{-\omega_2\tau_2} < E_2 - \beta_2 p_2(x_2^* + \varepsilon_0)$, by Lemma 3, $\lim_{t\longrightarrow\infty} m_1(t) = 0$ and $\lim_{t\longrightarrow\infty} m_2(t) = 0$. By the comparison theorem, we have $\lim_{t\longrightarrow\infty} z_1(t) \leq \lim_{t\longrightarrow\infty} m_1(t) = 0$ and $\lim_{t\longrightarrow\infty} z_2(t) \leq \lim_{t\longrightarrow\infty} m_2(t) = 0$. Because of the positivity of $z_1(t)$ and $z_2(t)$, we know that $\lim_{t\longrightarrow\infty} z_1(t) = 0$ and $\lim_{t\longrightarrow\infty} z_2(t) = 0$. Therefore, for a small $\varepsilon_1 > 0$, there exists a $n_3\,(n_3\tau > n_2\tau + \tau_1, n_3\tau > n_2\tau + \tau_2)$ such that $z_1(t) < \varepsilon_1$, $z_2(t) < \varepsilon_1$ for all $t > n_3\tau$. From system (5), we have the following:

$$\left\{\begin{array}{l} \left.\begin{array}{l} x_1'(t) > r_1 x_1(t)\ln\dfrac{k_1 e^{\left(-p_1'(0)\varepsilon_1/r_1\right)}}{x_1(t)}, \\ \\ x_2'(t) > r_2 x_2(t)\ln\dfrac{k_2 e^{\left(-p_1'(0)\varepsilon_1/r_2\right)}}{x_2(t)}, \end{array}\right\} t \neq n\tau, \\ \left.\begin{array}{l} \Delta x_1(t) = d_1\left(x_2(t) - x_1(t)\right), \\ \\ \Delta x_2(t) = d_2\left(x_1(t) - x_2(t)\right), \end{array}\right\} t = n\tau, n \in \mathbb{N}. \end{array}\right. \tag{26}$$

Here, $p_i(\bullet) \in H$ and we have $p_i(x_i(t)) \leq p_i'(0)x_i(t)$. Consider the following comparison differential system:

$$\left\{\begin{array}{l} \left.\begin{array}{l} s_1'(t) = r_1 s_1(t)\ln\dfrac{k_1 e^{\left(-p_1'(0)\varepsilon_1/r_1\right)}}{s_1(t)}, \\ \\ s_2'(t) = r_2 s_2(t)\ln\dfrac{k_2 e^{\left(-p_1'(0)\varepsilon_1/r_1\right)}}{s_2(t)}, \end{array}\right\} t \neq n\tau, \\ \left.\begin{array}{l} \Delta s_1(t) = d_1\left(s_2(t) - s_1(t)\right), \\ \\ \Delta s_2(t) = d_2\left(s_1(t) - s_2(t)\right), \end{array}\right\} t = n\tau, n \in \mathbb{N}, \end{array}\right. \tag{27}$$

where $\widetilde{s}_1(t) = k_1 e^{-p_1'(0)\varepsilon_1/r_1}\left(q_1'\right)^{e^{-r_1(t-n\tau)}}$ and $\widetilde{s}_2(t) = k_2 e^{-p_2'(0)\varepsilon_1/r_2}\left(q_2'\right)^{e^{-r_2(t-n\tau)}}$, q_1' and q_2' can be confirmed homoplastically as q_1, q_2. Let $\varepsilon_1 \longrightarrow 0$ use the comparison theorem $x_i(t) \geq s_i(t) \longrightarrow \widetilde{x}_i(t)$ as $t \longrightarrow \infty$; there for any $\varepsilon_2 > 0$ and t large enough, there exists a n_4, $n > n_4$ such that

$$\begin{aligned} x_1(t) &> \widetilde{x}_1(t) - \varepsilon_2, \\ x_2(t) &> \widetilde{x}_2(t) - \varepsilon_2. \end{aligned} \tag{28}$$

Thus, from (23) and (28), we get $x_1(t) \longrightarrow \widetilde{x_1}(t)$ and $x_2(t) \longrightarrow \widetilde{x_2}(t)$ as $t \longrightarrow \infty$. The proof is complete. □

5. Permanence

In this section, we will discuss the permanence of the system (3) organized by the network. To facilitate the discussion, we give the following lemma.

Lemma 4. *If* $\alpha_1 e^{-\omega_1\tau_1} + \beta_1 p_1(q_1) > E_1 + \gamma_1 M$ *and* $\alpha_2 e^{-\omega_2\tau_2} + \beta_2 p_2(q_2) > E_2 + \gamma_2 M$, *then there exist two positive constants* g_1 *and* g_2 *such that each positive solution of (5) satisfies* $z_1(t) \geq g_1$ *and* $z_2(t) \geq g_2$ *for* t *large enough.*

Proof. From the second and fourth equations of system (5), it can be rewritten as follows:

$$\begin{cases} z_1'(t) = \left[\alpha_1 e^{-\omega_1\tau_1} + \beta_1 P_1\left(x_1(t)\right) - \left(E_1 + \gamma_1 z_1(t)\right)\right] z_1(t) - \alpha_1 e^{-\omega_1\tau_1} \dfrac{\mathrm{d}}{\mathrm{d}t} \displaystyle\int_{t-\tau_1}^{t} z_1(u)\mathrm{d}u, \\ z_2'(t) = \left[\alpha_2 e^{-\omega_2\tau_2} + \beta_2 P_2\left(x_2(t)\right) - \left(E_2 + \gamma_2 z_2(t)\right)\right] z_2(t) - \alpha_2 e^{-\omega_2\tau_2} \dfrac{\mathrm{d}}{\mathrm{d}t} \displaystyle\int_{t-\tau_2}^{t} z_2(u)\mathrm{d}u. \end{cases} \tag{29}$$

We can define Q_1 and Q_2 as follows:

$$\begin{cases} Q_1(t) = z_1(t) + \alpha_1 e^{-\omega_1\tau_1} \displaystyle\int_{t-\tau_1}^{t} z_1(u)\mathrm{d}u, \\ Q_2(t) = z_2(t) + \alpha_2 e^{-\omega_2\tau_2} \displaystyle\int_{t-\tau_2}^{t} z_2(u)\mathrm{d}u. \end{cases} \tag{30}$$

Calculate the derivative of Q_1 and Q_2 along the solution of (5) as follows:

$$\begin{cases} Q_1'(t) = \left[\alpha_1 e^{-\omega_1\tau_1} + \beta_1 P_1\left(x_1(t)\right) - \left(E_1 + \gamma_1 z_1(t)\right)\right] z_1(t), \\ Q_2'(t) = \left[\alpha_2 e^{-\omega_2\tau_2} + \beta_2 P_2\left(x_2(t)\right) - \left(E_2 + \gamma_2 z_2(t)\right)\right] z_2(t). \end{cases} \tag{31}$$

By using Lemma 2 and combining with (30), we can obtain $Q_1(t) \leq M(1 + \alpha_1\tau_1 e^{-\omega_1\tau_1})$ and $Q_2(t) \leq M(1 + \alpha_2\tau_2 e^{-\omega_2\tau_2})$ as $t \longrightarrow \infty$. Since $\alpha_1 e^{-\omega_1\tau_1} + \beta_1 p_1(q_1) > E_1 + \gamma_1 M$ and $\alpha_2 e^{-\omega_2\tau_2} + \beta_2 p_2(q_2) > E_2 + \gamma_2 M$, we can find a sufficiently small $\varepsilon > 0$ such that $\alpha_1 e^{-\omega_1\tau_1} + \beta_1 p_1(q_1 - \varepsilon) > E_1 + \gamma_1 M$ and $\alpha_2 e^{-\omega_2\tau_2} + \beta_2 p_2(q_2 - \varepsilon) > E_2 + \gamma_2 M$. We suppose $t_0 > 0$, such that $z_1(t) < z_1^*$ and $z_2(t) < z_2^*$ for all $t > t_0$. It follows the first two equations of system (5) that for all $t > t_0$,

$$\begin{cases} x_1'(t) > r_1 x_1(t) \ln \dfrac{k_1 e^{\left(-p_1'(0) z_1^*/r_1\right)}}{x_1(t)}, \\ x_2'(t) > r_2 x_2(t) \ln \dfrac{k_2 e^{\left(-p_1'(0) z_2^*/r_2\right)}}{x_2(t)}. \end{cases} \tag{32}$$

Here, $p_i(\bullet) \in H$, we have $p_i(x_i(t)) \leq p_i'(0) x_i(t)$. For all $t > t_0$, consider the following comparison differential system:

$$\left.\begin{cases} l_1'(t) = r_1 l_1(t) \ln \dfrac{k_1 e^{p_1'(0) z_2^*/r_1}}{l_1(t)} \\ l_2'(t) = r_2 l_2(t) \ln \dfrac{k_2 e^{\left(-p_2'(0) z_2^*/r_2\right)}}{l_2(t)}, \end{cases}\right\} t \neq n\tau, \qquad \left.\begin{cases} \Delta l_1(t) = d_1\left(l_2(t) - l_1(t)\right), \\ \Delta l_2(t) = d_2\left(l_1(t) - l_2(t)\right), \end{cases}\right\} t = n\tau, \quad n \in \mathbb{N}. \tag{33}$$

By Lemma 1, we obtain the following global asymptotically periodic unique positive solution of system (33):

$$\begin{cases} \widetilde{l_1}(t) = k_1 e^{-p_1'(0) z_1^*/r_1} \left(q_1''\right)^{e^{-r_1(t-n\tau)}}, \\ \widetilde{l_2}(t) = k_2 e^{-p_2'(0) z_2^*/r_2} \left(q_2''\right)^{e^{-r_2(t-n\tau)}}, \end{cases} \tag{34}$$

where q_1'' and q_2'' can be confirmed homoplastically as q_1, q_2. By the comparison theorem for an impulsive differential equation, we know there exists a $t_1, t_2 (t_1 \geq t_0 + \tau_1, t_2 > t_0 + \tau_2)$ such that the inequality $x_1(t) > l_1(t) > \widetilde{l_1}(t) - \varepsilon$ holds for all $t \geq t_1$ and $x_2(t) > l_2(t) > \widetilde{l_2}(t) - \varepsilon$ holds for all $t \geq t_2$. Let $z_1^* \longrightarrow 0$ and $z_2^* \longrightarrow 0$, then $x_1(t) > \widetilde{x_1}(t) - \varepsilon$ holds for all $t \geq t_1$ and $x_2(t) > \widetilde{x_2}(t) - \varepsilon$ holds for all $t \geq t_2$. Thus, $x_1(t) > q_1 - \varepsilon$ holds for $t \geq t_1$ and $x_2(t) > q_2 - \varepsilon$ holds for all $t \geq t_2$. We make a notation as $\sigma_1 = q_1 - \varepsilon$ and $\sigma_2 = q_2 - \varepsilon$, for convenience. So we have $\alpha_1 e^{-\omega_1\tau_1} + \beta_1 p_1(\sigma_1) > E_1 + \gamma_1 M$ and $\alpha_2 e^{-\omega_2\tau_2} + \beta_2 p_2(\sigma_2) > E_2 + \gamma_2 M$. Then from (31), we can obtain the following:

$$\begin{cases} Q_1'(t) > \left[\alpha_1 e^{-\omega_1\tau_1} + \beta_1 P_1\left(x_1(t)\right) - \left(E_1 + \gamma_1 z_1(t)\right)\right] z_1(t), \; t \geq t_1, \\ Q_2'(t) > \left[\alpha_2 e^{-\omega_2\tau_2} + \beta_2 P_2\left(x_2(t)\right) - \left(E_2 + \gamma_2 z_2(t)\right)\right] z_2(t), \; t \geq t_2. \end{cases} \tag{35}$$

Let $\overline{z_1} = \min_{t\in[t_1,t_1+\tau_1]} z_1(t)$ and $\overline{z_2} = \min_{t\in[t_2,t_2+\tau_2]} z_2(t)$; we show that $z_1(t) \geq \overline{z_1}$ for all $t \geq t_1$ and $z_2(t) \geq \overline{z_2}$ for all $t \geq t_2$. Suppose the contrary, then there are T_0, $T_1 > 0$ such that $z_1(t) \geq \overline{z_1}$ for $t \in [t_1, t_1 + \tau_1 + T_0]$, $z_1(t_1, t_1 + \tau_1 + T_0) = \overline{z_1}$ and $z_1'(t_1, t_1 + \tau_1 + T_0) \leq 0$ and such that $z_2(t) \geq \overline{z_2}$ for $t \in [t_2, t_2 + \tau_2 + T_1]$, $z_2(t_2, t_2 + \tau_2 + T_1) = \overline{z_1}$, and $z_2'(t_2, t_2 + \tau_2 + T_1) \leq 0$. Thus, from the third and fourth equations of system (5) imply that

$$\begin{aligned} z_1'(t_1+\tau_1+T_0) &= \alpha_1 e^{-\omega_1\tau_1} z_1(t_1+T_0) + \beta_1 p_1(x_1(t_1+\tau_1+T_0)) z_1(t_1+\tau_1+T_0) - E_1 z_1(t_1+\tau_1+T_0) \\ &\quad - \gamma_1 z_1^2(t_1+\tau_1+T_0) \geq [\alpha_1 e^{-\omega_1\tau_1} + \beta_1 P_1(\sigma_1) - (E_1+\gamma_1 M)]\overline{z_1} > 0, \\ z_2'(t_2+\tau_2+T_1) &= \alpha_2 e^{-\omega_2\tau_2} z_2(t_2+T_1) + \beta_2 p_2(x_2(t_2+\tau_2+T_1)) z_2(t_2+\tau_2+T_1) - E_2 z_2(t_2+\tau_2+T_1) \\ &\quad - \gamma_2 z_2^2(t_2+\tau_2+T_1) \geq [\alpha_2 e^{-\omega_2\tau_2} + \beta_2 P_2(\sigma_2) - (E_2+\gamma_2 M)]\overline{z_2} > 0. \end{aligned} \tag{36}$$

This is a contradiction. Thus, $z_1(t) \geq \overline{z_1}$ for all $t \geq t_1$ and $z_2(t) \geq \overline{z_2}$ for all $t \geq t_2$. From (35), we have the following:

$$\begin{aligned} Q_1'(t) &\geq [\alpha_1 e^{-\omega_1\tau_1} + \beta_1 P_1(\sigma_1) - (E_1+\gamma_1 M)]\overline{z_1} > 0, \quad t \geq t_1, \\ Q_2'(t) &\geq [\alpha_2 e^{-\omega_2\tau_2} + \beta_2 P_2(\sigma_2) - (E_2+\gamma_2 M)]\overline{z_2} > 0, \quad t \geq t_2, \end{aligned} \tag{37}$$

which implies $Q_1(t) \longrightarrow \infty$ and $Q_2(t) \longrightarrow \infty$ as $t \longrightarrow \infty$. It is a contradiction to $Q_1(t) \leq M(1 + \alpha_1\tau_1 e^{-\omega_1\tau_1})$ and $Q_2(t) \leq M(1 + \alpha_2\tau_2 e^{-\omega_2\tau_2})$. Therefore, the claim is complete. By the claim, we are left to consider two cases. First, $z_1(t) \geq z_1^*$ and $z_2(t) \geq z_2^*$ for t large enough. Second, $z_1(t)$ and $z_2(t)$ oscillate about z_1^* and z_1^* for t large enough. Define

$$g_1 = \min\left\{\frac{z_1^*}{2}, g_1^*\right\}, g_2 = \min\left\{\frac{z_2^*}{2}, g_2^*\right\}, \tag{38}$$

where $g_1^* = z_1^* e^{-(E_1+\gamma_1 M)\tau_1}$ and $g_2^* = z_2^* e^{-(E_2+\gamma_2 M)\tau_2}$. In the following, we shall show that $z_1(t) \geq g_1$ and $z_2(t) \geq g_2$ for t are large enough; the conclusion is evident in the first case. For the second case, let $t_1^*, t_2^* > 0$ and $\zeta_1, \zeta_2 > 0$ satisfy $z_1(t_1^*) = z_1(t_1^* + \zeta_1) = z_1^*$ and $z_1(t) < z_1^*$ for all $t \in (t_1^*, t_1^* + \zeta_1)$ and $z_2(t_2^*) = z_2(t_2^* + \zeta_2) = z_2^*$ and $z_2(t) < z_2^*$ for all $t \in (t_2^*, t_2^* + \zeta_2)$, where t_1^*, t_2^* are large enough such that $x_1(t) > \sigma_1$ for $t_1^* < t < t_1^* + \zeta_1$ and $x_2(t) > \sigma_2$ for $t_2^* < t < t_2^* + \zeta_2$. Thus, $z_1(t)$ and $z_2(t)$ are uniformly continuous. The positive solutions of (3) are ultimately bounded and not affected by impulses. Hence, there are $T_1', T_2' (0 < T_1' < \tau_1, 0 < T_2' < \tau_2$ and T_1', T_2' are dependent on the choice of t_1^*, t_2^*) such that $z_1(t) > z_1^*/2$ for all $t \in (t_1^*, t_1^* + T_1')$ and $z_2(t) > z_2^*/2$ for all $t \in (t_2^*, t_2^* + T_2')$. If $\zeta_1 < T_1'$, $\zeta_2 < T_2'$, our aim is obtained. Let us consider the case $T_1' < \zeta_1 \leq \tau_1$, $T_2' < \zeta_2 \leq \tau_2$, since $z_1'(t) > -(E_1+\gamma_1 M) z_1(t)$, $z_1(t_1^*) = z_1^*$ and $z_2'(t) > -(E_2+\gamma_2 M) z_2(t)$, $z_2(t_1^*) = z_2^*$, it is clear that $z_1(t) \geq g_1$ for all $t \in (t_1^*, t_1^* + \tau_1)$ and $z_2(t) \geq g_2$ for all $t \in (t_2^*, t_2^* + \tau_2)$. If $\zeta_1 > \tau_1$ and $\zeta_2 > \tau_2$; then we have that $z_1(t) \geq g_1$ for all $t \in (t_1^*, t_1^* + \tau_1)$ and $z_2(t) \geq g_2$ for all $t \in (t_2^*, t_2^* + \tau_2)$. The same arguments can be continued and we can obtain $z_1(t) \geq g_1$ for all $t \in (t_1^* + \tau_1, t_1^* + \zeta_1)$ and $z_2(t) \geq g_2$ and for all $t \in (t_2^* + \tau_2, t_2^* + \zeta_2)$. Since the interval $[t_1^*, t_1^* + \zeta_1]$ and $[t_2^*, t_2^* + \zeta_2]$ are arbitrarily chosen (t_1^*, t_2^* to be enough), we get that $z_1(t) \geq g_1$ and $z_2(t) \geq g_2$ for t are large enough. In view of the above discussion, the choice of g_1, g_2 is independent of the positive solution of system (5), which satisfies $z_1(t) \geq g_1$ and $z_2(t) \geq g_2$ for sufficiently large t. The proof is completed. □

Theorem 2. *If* $\alpha_1 e^{-\omega_1\tau_1} + \beta_1 p_1(q_1) > E_1 + \gamma_1 M$ *and* $\alpha_2 e^{-\omega_2\tau_2} + \beta_2 p_2(q_2) > E_2 + \gamma_2 M$, *then the system (3) is permanent.*

Proof. From system (3) and Lemma 2, we have the following:

$$\begin{cases} \left.\begin{aligned} x_1'(t) &\geq r_1 x_1(t) \ln \frac{k_1 e^{-p_1'(0)M/n}}{x_1(t)}, \\ x_2'(t) &\geq r_2 x_2(t) \ln \frac{k_2 e^{-p_2'(0)M/r_2}}{x_2(t)}, \end{aligned}\right\} t \neq n\tau, \\ \left.\begin{aligned} \Delta x_1(t) &= d_1(x_2(t) - x_1(t)), \\ \Delta x_2(t) &= d_2(x_1(t) - x_2(t)), \end{aligned}\right\} t = n\tau, n \in \mathbb{N}. \end{cases} \tag{39}$$

By the similar argument as those in the proof of Theorem 1, we have that $x_1(t) \geq f_1 - \varepsilon$ and $x_2(t) \geq f_2 - \varepsilon$, and $\varepsilon > 0$ is small enough, where

$$f_i = k_i e^{-p_i'(0)M/r_i} (\overline{q}_i)^{e^{-r_i\tau}}, \quad i = 1, 2. \tag{40}$$

$\overline{q}_1$ and $\overline{q}_2$ can be confirmed homoplastically to be q_1, q_2. Using Lemma 2 and Lemma 4, the second and fifth equations of system (3) become as follows:

$$\begin{cases} y_1'(t) \geq \alpha_1(g_1 - Me^{-\omega_1\tau_1}) - \omega_1 y_1(t), \\ y_2'(t) \geq \alpha_2(g_2 - Me^{-\omega_2\tau_2}) - \omega_2 y_2(t). \end{cases} \tag{41}$$

It is easy to obtain $y_1(t) \geq \rho_1 - \varepsilon$ and $y_2(t) \geq \rho_2 - \varepsilon$, $\varepsilon > 0$ is small enough, where $\rho_1 = \alpha_1(g_1 - Me^{-\omega_1\tau_1})/\omega_1 - e^{-\omega_1\tau_1}/\omega_1$ and $\rho_2 = \alpha_2(g_2 - Me^{-\omega_2\tau_2})/\omega_2 - e^{-\omega_2\tau_2}/\omega_2$. Hence, by Lemma 2, Lemma 4, and the above discussion, we obtain that system (3) is permanent. The proof is completed. □

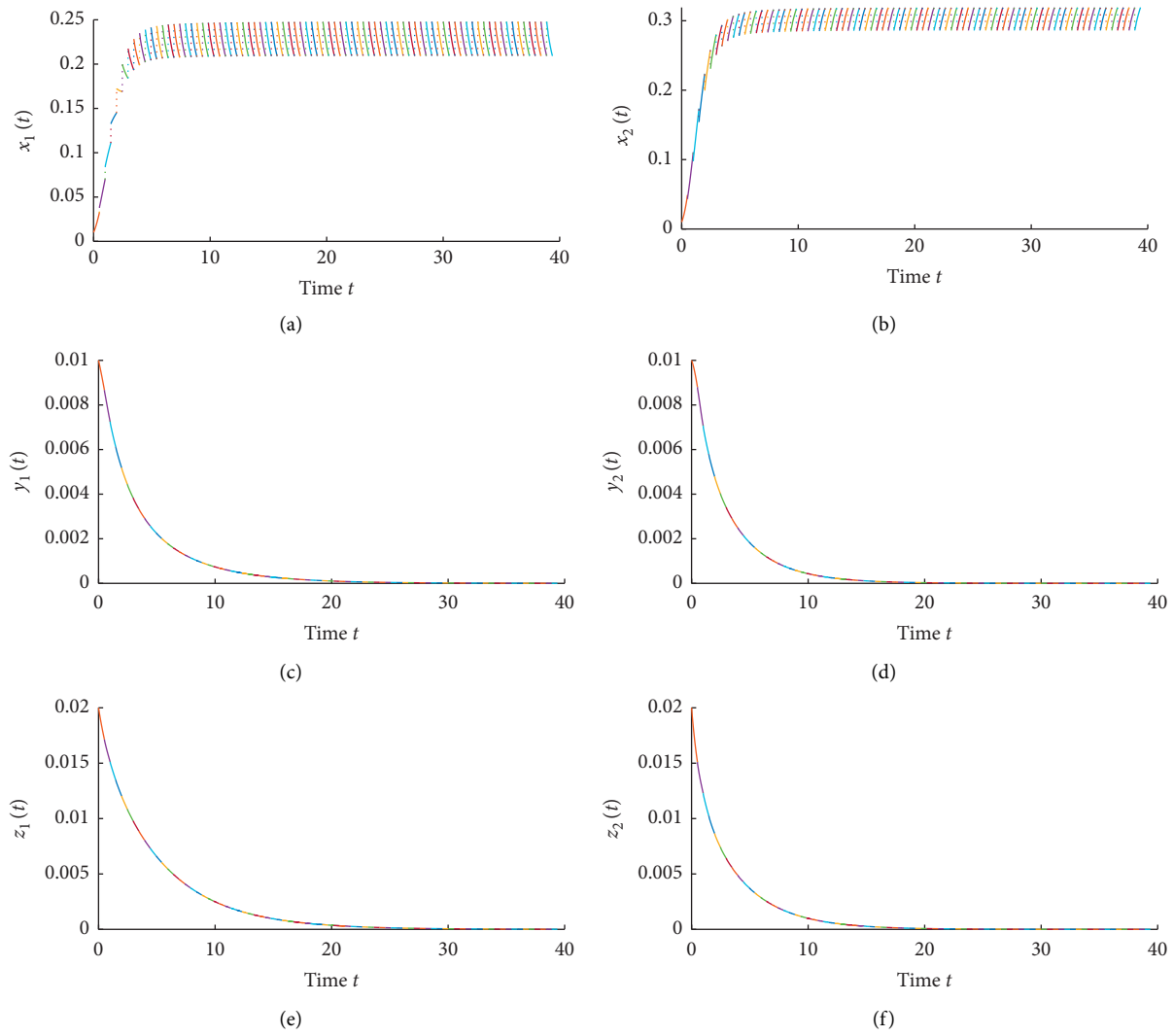

Figure 1: The time response in Case 1.

6. Illustrative Example and Discussion

Example 1. Consider the hybrid network model (3) of delayed predator-prey Gompertz system with impulsive diffusion between two patches, in which $p_1(x_1) = 1.5x_1$, $p_2(x_2) = 5x_2$, $\tau = 0.5$, and

$$\begin{aligned} r_1 &= 1.1, \\ k_1 &= 0.2, \\ \alpha_1 &= 0.4, \\ \omega_1 &= 0.5, \\ \beta_1 &= 0.3, \\ \gamma_1 &= 0.2, \\ \tau_1 &= 0.8, \\ d_1 &= 0.35; \end{aligned}$$

$$\begin{aligned} r_2 &= 1.2, \\ k_2 &= 0.6, \\ \alpha_2 &= 0.5, \\ \omega_2 &= 0.4, \\ \beta_2 &= 0.2, \\ \gamma_2 &= 0.2, \\ \tau_2 &= 0.8, \\ d_2 &= 0.3. \end{aligned} \tag{42}$$

From (11), we compute the fixed point $q = (1.7659, 0.7553)$.

Case 1. $E_1 = 0.6$ and $E_2 = 1$. In Theorem 1, we have $(x_1^*, x_2^*) = (0.2199, 0.5752)$ and

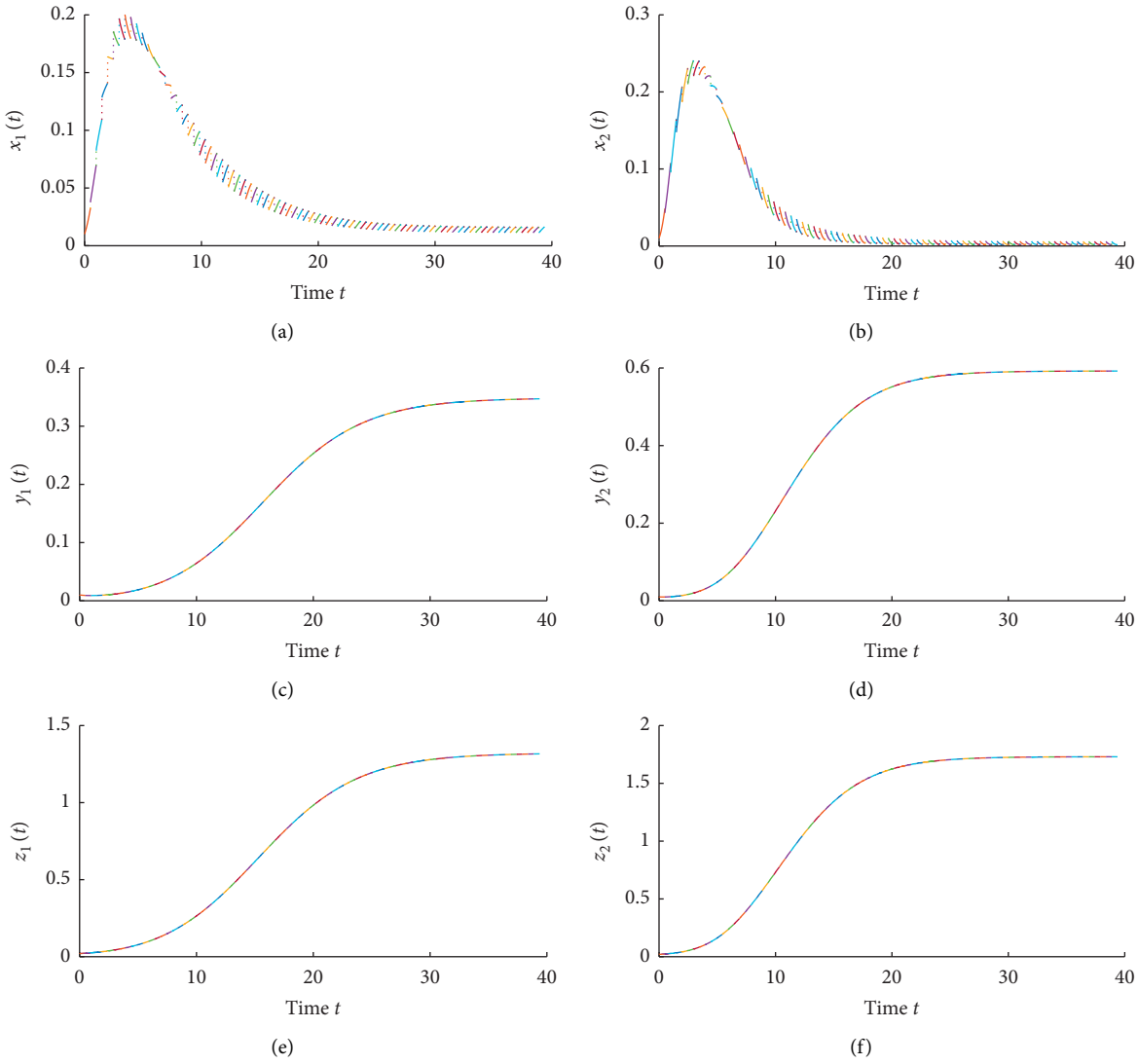

Figure 2: The time response in Case 2.

$$\alpha_1 e^{-\omega_1\tau_1} + \beta_1 p_1(x_1^*) - E_1 = -0.2329 < 0; \alpha_2 e^{-\omega_2\tau_2} + \beta_2 p_2(x_2^*) - E_2 = -0.0618 < 0. \quad (43)$$

It follows from Theorem 1 that the predator-extinction periodic solution $(\tilde{x}_1, 0, 0, \tilde{x}_2, 0, 0)$ of the system (3) is globally attractive. Figure 1 shows the attractivity of the solution with the initial condition $x_1(s) = 0.01, x_2(s) = 0.02$, and $s \in [-0.8, 0]$.

Case 2. $E_1 = 0.01$ and $E_2 = 0.02$. In Theorem 2, we have $M = 5.0261$ and

$$\alpha_1 e^{-\omega_1\tau_1} + \beta_1 p_1(q_1) - E_1 - \gamma_1 M = 0.0476 > 0; \alpha_2 e^{-\omega_2\tau_2} + \beta_2 p_2(q_2) - E_2 - \gamma_2 M = 0.0931 > 0. \quad (44)$$

It follows from Theorem 2 that system (3) is permanent. Figure 2 shows the permanent of the solution with the above initial condition.

In this paper, a delayed functional response predator-prey Gompertz system with impulsive diffusion between two patches defined on the network was investigated. The patches represent nodes of a network such that the prey population interacts locally in each patch and occurs diffusively over links connecting nodes. By extending system (3) to the network version, we analyzed that the predator-extinction solution of system (3) is globally attractive and obtained the permanence condition of system (3). We also observed that constant time delay and the growth rate of the immature predator can bring obvious effects on the dynamics of the system, and the stability and extinction (or prey and predators coexist) of the system are determined by their thresholds. Thus, from Theorems 1 and 2, we can easily guess that there must exist thresholds τ_1^* and τ_2^*. If $\tau_1 > \tau_1^*$ and $\tau_2 > \tau_2^*$, then the immature and mature predator tends to be extinct; if $\tau_1 < \tau_1^*$ and $\tau_2 < \tau_2^*$, then the system will be permanent. If immature predator growth rates are below (or above) their thresholds, then the predators become extinct

(or prey and predators coexist) in all patches. Hence, the immature predator growth rates and the predator's maturation times play an important role in delayed functional response predator-prey Gompertz systems with impulsive diffusion between the two patches. We hope that the results will provide a reliable tactic basis for biological resource protection. In addition, it is meaningful to generalize the results to the case of n-patch case, but it is difficult to discuss the properties of the n-dimension stroboscopic map. One may instigate this problem in the future.

Data Availability

No data or codes were generated or used during this study.

Conflicts of Interest

The authors declare that there are no conflicts of interest regarding the publication of this paper.

Acknowledgments

This work was partially supported by the National Natural Science Foundation of China (NSFC) under Grant no. 11971081, the Fundamental and Frontier Research Project of Chongqing under Grant no. cstc2018jcyjAX0144, the Program of Chongqing Graduate Research and Innovation Project under Grant no. CYS19290, the Science and Technology Research Program of Chongqing Municipal Education Commission under Grant no. KJZD-M202000502, and the Science Foundation of Civil Aviation Flight University of China under Grant no. J2019-063.

References

[1] V. A. A. Jansen and A. L. Lloyd, "Local stability analysis of spatially homogeneous solutions of multi-patch systems," *Journal of Mathematical Biology*, vol. 41, no. 3, pp. 232–252, 2000.

[2] V. Colizza, R. Pastor-Satorras, and A. Vespignani, "Reaction-diffusion processes and metapopulation models in heterogeneous networks," *Nature Physics*, vol. 3, no. 4, pp. 276–282, 2007.

[3] N. Masuda, "Effects of diffusion rates on epidemic spreads in metapopulation networks," *New Journal of Physics*, vol. 9, Article ID 093009, 2010.

[4] C. Liu, L. Chang, Y. huang et al., "Turing patterns in a predator-prey model on complex networks," *Nonlinear Dynamics*, vol. 86, pp. 1–10, 2020.

[5] B. J. Kim and J. Liu, "Instability of defensive alliances in the predator-prey model on complex networks," *Physical Review E*, vol. 4, Article ID 041906, 2005.

[6] T. Huang, H. Zhang, S. Ma et al., "Bifurcations, complex behaviors, and dynamic transition in a coupled network of discrete predator-prey system," *Discrete Dynamics in Nature Society*, vol. 2019, no. 1-2, pp. 1–22, Article ID 2583730, 2019.

[7] L. L. Chang, C. Liu, S. Gui-Quan, and Z. Wang, "Delay-induced patterns in a predator-prey model on complex networks with diffusion," *New Journal of Physics*, vol. 7, Article ID 073035, 2019.

[8] A. Nagurney and L. S. Nagurney, "Dynamics and equilibria of ecological predator-prey networks as nature's supply chains," *Transportation Research Part E: Logistics and Transportation Review*, vol. 48, no. 1, pp. 89–99, 2012.

[9] S. A. Levin, "Dispersion and population interactions," *The American Naturalist*, vol. 108, no. 960, pp. 207–228, 1974.

[10] S. A. Levin, "Spatial patterning and the structure of ecological communities," in *Some Mathematic Questions in Biology*American Mathematical Society, Providence, RI, USA, 1976.

[11] R. Xu and Z. Ma, "The effect of dispersal on the permanence of a predator-prey system with time delay," *Nonlinear Analysis: Real World Applications*, vol. 9, no. 2, pp. 354–369, 2008.

[12] E. Beretta, F. Solimano, and Y. Takeuchi, "Global stability and periodic orbits for two-patch predator-prey diffusion-delay models," *Mathematical Biosciences*, vol. 85, no. 2, pp. 153–183, 1987.

[13] S. Chen, J. Zhang, and T. Young, "Existence of positive periodic solution for nonautonomous predator-prey system with diffusion and time delay," *Journal of Computational and Applied Mathematics*, vol. 159, no. 2, pp. 375–386, 2003.

[14] J. Jiao, X. Yang, S. Cai, and L. Chen, "Dynamical analysis of a delayed predator-prey model with impulsive diffusion between two patches," *Mathematics and Computers in Simulation*, vol. 80, no. 3, pp. 522–532, 2009.

[15] E. Funasaki and M. Kot, "Invasion and chaos in a periodically pulsed mass-action chemostat," *Theoretical Population Biology*, vol. 44, no. 2, pp. 203–224, 1993.

[16] A. Lakmeche and O. Arino, "Bifurcation of nontrivial periodic solution of impulsive differential equations arising chemotherapeutic treatment," *Dynamics of Continuous, Discrete and Impulsive Systems Series*, vol. 7, pp. 265–287, 2000.

[17] X. Liu, "Impulsive stabilization and applications to population growth models," *Rocky Mountain Journal of Mathematics*, vol. 25, no. 1, pp. 381–395, 1995.

[18] L. Zhang, Z. Teng, and Z. Liu, "Survival analysis for a periodic predator-prey model with prey impulsively unilateral diffusion in two patches," *Applied Mathematical Modelling*, vol. 35, no. 9, pp. 4243–4256, 2011.

[19] Y. Shao, "Analysis of a delayed predator-prey system with impulsive diffusion between two patches," *Mathematical and Computer Modelling*, vol. 52, no. 1-2, pp. 120–127, 2010.

[20] B. Gompertz, "On the nature of the function expressive of the law of human mortality and on a new method of determining the value of life contingencies," *Philosophical Transactions of the Royal Society of London*, vol. 115, pp. 513–585, 1825.

[21] C. P. Windson, "The Gompertz curve as a growth curve," *PNAS*, vol. 22, pp. 73–83, 1932.

[22] S. Wright, "Book review," *Journal of the American Statistical Association*, vol. 21, p. 494, 1926.

[23] L. Wang, Z. Liu, J. Jinghui, and L. Chen, "Impulsive diffusion in single species model," *Chaos, Solitons & Fractals*, vol. 33, no. 4, pp. 1213–1219, 2007.

[24] L. Zhang and Z. Teng, "The dynamical behavior of a predator-prey system with Gompertz growth function and impulsive dispersal of prey between two patches," *Mathematical Methods in the Applied Sciences*, vol. 39, no. 13, pp. 3623–3639, 2016.

[25] K. Liu, X. Meng, and L. Chen, "A new stage structured predator-prey Gomportz model with time delay and impulsive perturbations on the prey," *Applied Mathematics and Computation*, vol. 196, no. 2, pp. 705–719, 2008.

[26] J. Jiao, L. Chen, S. Cai, and L. Wang, "Dynamics of a stage-structured predator-prey model with prey impulsively diffusing between two patches," *Nonlinear Analysis: Real World Applications*, vol. 11, no. 4, pp. 2748–2756, 2010.

[27] J. Dhar and K. S. Jatav, "Mathematical analysis of a delayed stage-structured predator-prey model with impulsive diffusion between two predators territories," *Ecological Complexity*, vol. 16, pp. 59–67, 2013.

[28] J. Jiao, "The effect of impulsive diffusion on dynamics of a stage-structured predator-prey system," *Discrete Dynamics in Nature and Society*, vol. 2010, Article ID 716932, 17 pages, 2010.

[29] W. G. Aiello and H. I. Freedman, "A time-delay model of single-species growth with stage structure," *Mathematical Biosciences*, vol. 101, no. 2, pp. 139–153, 1990.

[30] V. Lakshmikantham, D. D. Bainov, and P. Simeonov, *Theory of Impulsive Differential Equation*, World Scientific, Singapore, 1989.

[31] Y. Jinghui, *Delay Differential Equation with Application in Population Dynamics*, Academic Press, San Diego, CA, USA, 1993.

Hindawi
Discrete Dynamics in Nature and Society
Volume 2020, Article ID 9756162, 23 pages
https://doi.org/10.1155/2020/9756162

Research Article

Existence of Positive Solutions and Asymptotic Behavior for Evolutionary $q(x)$-Laplacian Equations

Aboubacar Marcos and Ambroise Soglo

Institut de Mathématiques et de Sciences Physiques, Université d'Abomey-Calavi, Cotonou, Benin

Correspondence should be addressed to Ambroise Soglo; ambroise.soglo@yahoo.fr

Received 21 January 2020; Revised 25 March 2020; Accepted 5 June 2020; Published 25 July 2020

Academic Editor: Jianquan Lu

In this paper, we extend the variational method of M. Agueh to a large class of parabolic equations involving $q(x)$-Laplacian parabolic equation $(\partial\rho(t,x)/zt) = \mathrm{div}_x(\rho(t,x)\,|\,\nabla_x(G'(\rho)+V)\,|^{q(x)-2}\nabla_x(G'(\rho)+V))$. The potential V is not necessarily smooth but belongs to a Sobolev space $W^{1,\infty}(\Omega)$. Given the initial datum ρ_0 as a probability density on Ω, we use a descent algorithm in the probability space to discretize the $q(x)$-Laplacian parabolic equation in time. Then, we use compact embedding $W^{1,q(.)}(\Omega)\hookrightarrow\hookrightarrow L^{q(.)}(\Omega)$ established by Fan and Zhao to study the convergence of our algorithm to a weak solution of the $q(x)$-Laplacian parabolic equation. Finally, we establish the convergence of solutions of the $q(x)$-Laplacian parabolic equation to equilibrium in the $p(.)$-variable exponent Wasserstein space.

1. Introduction and the Main Results

In this paper, we study the existence of positive solutions and the asymptotic behavior for a class of parabolic equations involving parabolic equations governed by the q (x)-Laplacian operator:

$$\frac{\partial\rho(t,x)}{\partial t} = \mathrm{div}_x\Big(\rho(t,x)\,|\,\nabla_x(G'(\rho)+V)\Big|^{q(x)-2}\nabla_x(G'(\rho)+V)\Big), \quad \text{in } [0,+\infty[\times\Omega, \tag{1}$$

where $\Omega\subset\mathbb{R}^d$ is a convex, bounded, and smooth domain of $\mathbb{R}^d$, G: $[0,+\infty[\longrightarrow\mathbb{R}$ is a convex function of class $C^2(]0,\infty[)$, $q(.)$: $\Omega\longrightarrow]1,+\infty]$ is a continuous function, and V: $\Omega\longrightarrow\mathbb{R}$ belongs to a Sobolev space $W^{1,\infty}(\Omega)$.

$q(x)$-Laplacian parabolic equation type is a broad family of parabolic equations including many equations emerging in the mathematical modeling of a variety of phenomena in physics such as the flow of compressible fluids in nonhomogeneous isotropic porous media, the behavior of electrorheological fluids [1, 2], image processing [3], and the curl systems emanating from electromagnetism [4, 5].

Some authors have studied the existence of solutions of the $q(x)$-Laplacian parabolic equation with the variable exponent, when $G(t)=t^2$ and $V\equiv 0$ (see [1, 2, 6]), for a given initial datum ρ_0 and a homogeneous boundary condition. In their works, they use an approximation method to approach the $q(x)$-Laplacian parabolic equation by regularized problems under the following conditions: $\rho_0\in L^\infty(\Omega)$ and $|\nabla_x\rho_0|^{q_+}\in L^1(\Omega)$.

In [7], M. Agueh studied the existence of positive solutions for the $q(x)$-Laplacian parabolic equation when the variable exponent $q(x)\equiv q$ is constant (with $q>1$), and the potential V is a convex function of class $C^1(\Omega)$. Moreover, the author in [7] proved that the parabolic q-Laplacian equation

$$\frac{\partial\rho(t,x)}{\partial t} = \mathrm{div}_x\Big(\rho(t,x)\,|\,\nabla_x(G'(\rho)+V)\Big|^{q-2}\nabla_x(G'(\rho)+V)\Big), \quad \text{in } [0,+\infty[\times\Omega, \tag{2}$$

is a gradient flow of the functional $E(\rho)=\int_\Omega(G(\rho)+\rho V)\mathrm{d}x$ with respect to the p-Wasserstein distance $(p=(q/q-1))$ defined by

$$W_p(\rho_1,\rho_2)=\left(\inf_{S_{\#}\rho_1=\rho_2}\int_\Omega |x-S(x)|^p\rho_1 dx\right)^{(1/p)}, \quad (3)$$

where ρ_1 and ρ_2 are two probability densities on Ω.

In fact, by fixing the time step $h>0$ and a probability density ρ_0 on Ω, the author defines ρ_{k-1} $(k\in\mathbb{N}^*)$ as the solution of (2) at $t=h(k-1)$ and ρ_k as the solution of (2) at $t=hk$ such that ρ_k is the unique solution of the variational problem

$$(P_k):\ \inf_{\rho\in P(\Omega)}\left[E(\rho)+\frac{1}{\mathrm{ph}^{p-1}}W_p^p(\rho,\rho_{k-1})\right]. \quad (4)$$

Then, the author established the convergence of the approximate solutions $(\rho_k)_k$ to a weak solution of the Laplacian parabolic equation . Here, we extend the work of [7] to a general case where $V\neq 0$ may not be smooth but belongs to a Sobolev space $W^{1,\infty}(\Omega)$. Roughly speaking, we use mass the transportation method borrowing ideas from [7, 8] to establish the existence of positive solutions and the long time behavior of solutions of the Laplacian parabolic equation. As in [7], we prove that the Laplacian parabolic equation is a gradient flow of the functional $E(\rho)=\int_\Omega[G(\rho)+\rho V]dx$ with respect to the $p(.)$–Wasserstein distance $W_{p(.)}$ defined by

$$W_{p(.)}(\rho_1,\rho_2)=\inf_{\rho(t,.)}\left\{\|v\|_{L^{p(.)}_{\rho(t,.)}([0,1]\times\Omega)},\quad \frac{\partial\rho(t,x)}{\partial t}+\mathrm{div}_x(\rho(t,x)v(t,x))=0,\quad \text{in }\Omega,\ \rho(0,.)=\rho_1 \text{ and } \rho(1,.)=\rho_2\right\}. \quad (5)$$

Next, we proceed with the discretization of the $q(x)$-Laplacian parabolic equation as follows: fixing the time step $h>0$ and a probability density ρ_0 on Ω, we define ρ_k as the approximate solution of the $q(x)$-Laplacian parabolic equation at $t_k=hk$, which minimizes the variational problem

$$(P_k):\ \inf_{\rho\in P(\Omega)}\left\{\int_\Omega[G(\rho)+\rho V]dx+K^h_{p(.)}(\rho_{k-1},\rho)\right\}, \quad (6)$$

where

$$K^h_{p(.)}(\rho_{k-1},\rho)=\inf_{\gamma\in\Pi(\rho_{k-1},\rho)}\int_{\Omega\times\Omega}\frac{|x-y|^{p(x)}}{p(x)h^{p(x)-1}}d\gamma. \quad (7)$$

Here, $\Pi(\rho_{k-1},\rho)$ is the set of all probability measures on $\Omega\times\Omega$ having ρ_{k-1} and ρ as their marginals, and

$$K^h_{p(.)}(\rho_{k-1},\rho),\quad k\geq 1, \quad (8)$$

is the Monge–Kantorovich work associated to the cost $c_h(x,y)=(|x-y|^{p(x)}/p(x)h^{p(x)-1})$.

The establishment of our result will be derived according to the following steps:

(1) Given ρ_0 as a probability density on Ω such as $N\leq\rho_0\leq M$ and $V\in L^\infty(\Omega)$, we prove that (P_k) admits a unique solution ρ_k which satisfies $N\leq\rho_0\leq M$ (see Lemma 1).

(2) We prove in (28) that the Kantorovich problem

$$(K):\ \inf_{\gamma\in\Pi(\rho_{k-1},\rho_k)}\int_{\Omega\times\Omega}\frac{|x-y|^{p(x)}}{p(x)h^{p(x)-1}}d\gamma, \quad (9)$$

admits a unique solution γ_k in $\Pi(\rho_{k-1},\rho_k)$ and that $\mathrm{supp}\gamma_k$ satisfy

$$\mathrm{supp}\gamma_k\subset\left\{(x,y)\in\Omega\times\Omega,\quad y=x-h\left|\nabla_x(G'(\rho_k)+V)\right|^{q(x)-2}\nabla_x(G'(\rho_k)+V)\right\}, \quad (10)$$

where $q(x)=(p(x)/p(x)-1)$.

Here, $V\in W^{1,\infty}(\Omega)$ being not necessarily smooth, we approximate V by $C^2(\Omega)$-functions, and we use descent algorithm (6), the maximum principle $N\leq\rho_k\leq M$, and compact embedding $W^{1,q(x)}(\Omega)\hookrightarrow\hookrightarrow L^{q(x)}(\Omega)$ to establish (10).

(3) We now use the maximum principle $N\leq\rho_k\leq M$ and (10) to prove that the sequence $(\rho_k)_k$ is a time discretization of the nonlinear $q(x)$-Laplacian parabolic equation, that is, for all test functions, $\phi\in C_c^\infty(\mathbb{R}^d)$,

$$\int_\Omega(\rho_k-\rho_{k-1})\phi dx+h\int_\Omega<\left|\nabla_x(G'(\rho_k)+V)\right|^{q(x)-2}\nabla_x(G'(\rho_k)+V),\quad \nabla_x\phi>\rho_k dx=A^h_k(\phi), \quad (11)$$

where $A_k^h(\phi)$ converges to 0 when h tends to 0.

(4) We define $\rho^h(t,x)$ by

$$\rho^h(t,x) = \rho_k, \quad \text{if } t \in]h(k-1), hk], \ \rho(0,x) = \rho_0. \tag{12}$$

Afterward, we establish the following:

(i) The strong convergence of the sequence $(\rho^h)_h$ to a function $\rho(t,x)$ in $L^{q(x)}([0,T]\times\Omega)$ for $0<T<\infty$

(ii) The weak convergence of nonlinear term $(\mathrm{div}_x(\rho^h|)\nabla_x(G'(\rho^h)+V)|^{q(x)-2}\nabla_x(G'(\rho^h)+V))_h$ to $\mathrm{div}_x(\rho|)\nabla_x(G'(\rho^h)+V)|^{q(x)-2}\nabla_x(G'\rho+V)$ in $[C_c^\infty(\mathbb{R}\times\mathbb{R}^d)]'$

To prove (i), we use descent algorithm (6) and the maximum principle $N \le \rho^h \le M$ to deduce that the sequence $(\rho^h)_h$ is bounded in $W^{1,q(x)}([0,T]\times\Omega)$ for $0<T<\infty$. Then, taking into account the compact embedding $W^{1,q(x)}([0,T]\times\Omega) \hookrightarrow\hookrightarrow L^{q(x)}([0,T]\times\Omega)$ established by Fan and Zhao in [9], we conclude that the sequence $(\rho^h)_h$ converges strongly to $\rho(t,x)$ in $L^{q(x)}([0,T]\times\Omega)$.

We now use (i) and the fact that $v \longmapsto |v|^{q(x)}$ is convex for all $x \in \Omega$ fixed to establish (ii). We combine (i) and (ii) to prove that the sequence $(\rho^h)_h$ converges to a weak solution of the $q(x)$-Laplacian parabolic equation.

Finally, we use the energy method to study the convergence of solutions of the $q(x)$-Laplacian parabolic equation to ρ_∞ when $t \longrightarrow \infty$, where $\rho_\infty \in P(\Omega)$ is the probability density which satisfies $\rho_\infty \nabla_x(G'(\rho_\infty)+V) = 0$.

Note that in [10, 11], the authors proved a convergence of solutions to the equilibrium without specifying the speed of convergence. In [11], the long-time behavior of solutions of the $q(x)$-Laplacian parabolic equation is only established if $2 \le q_- \le q_+$.

In this paper, we extend to the variable exponent $q(.)\colon \Omega \longrightarrow]1,+\infty[$ such that $1<q_-<q_+<\infty$, the results obtained by the previous authors, and we also specify the rates of convergence.

Our results in this work are stated as follows:

Theorem 1. *Assume that* (H_{ρ_0}), (H_G), $(H_{q(.)}^{p(.)})$, *and* (H_V^1) *hold, and define* $\rho^h(t,x)\colon [0,+\infty[\times\Omega \longrightarrow [0,+\infty[$ *by*

$$\rho^h(t,x) = \rho_k(x), \quad \text{if } t \in]h(k-1); \mathrm{hk}], \ \rho(0,x) = \rho_0(x). \tag{13}$$

Then, the sequence $(\rho^h)_h$ converges to a weak solution $\rho(t,x)$ of the $q(x)$-Laplacian parabolic equation.

Theorem 2. *Assume that* (H_{ρ_0}), (H_G), $(H_{q(.)}^{p(.)})$, (H_V^1), *and* (H_V^2) *hold. Let* $\rho(t,x)$ *be a weak solution of the q(x)-Laplacian parabolic equation. Define*

$$I_1 := \left\{ t \in [0,+\infty[, \quad \left\| \left(\nabla_x\left(G'(\rho(t,.))\right)+V\right)\right\|_{L^{q(.)}_{\rho(t,.)}(\Omega)} \ge 1 \right\},$$
$$I_2 := \left\{ t \in [0,+\infty[, \quad \left\| \left(\nabla_x\left(G'(\rho(t,.))\right)+V\right)\right\|_{L^{q(.)}_{\rho(t,.)}(\Omega)} \le 1 \right\}. \tag{14}$$

Then,

$$[E(\rho(t_2,.)) - E(\rho_\infty)] \le \frac{[E(\rho(t,.)) - E(\rho_\infty)]}{\left[1+(\lambda/2)^{p_+ \prime q_+}(q_+ - 1)(E(\rho(t_2,.))) - E(\rho_\infty)^{(q_+-1)}(t-t_2)\right]^{(1/q_+-1)}}, \quad \text{on } I_2,$$

$$W^{p_+}_{p(.)}(\rho(t,.),\rho_\infty(.)) \le \frac{2^{p_+}[E(\rho(t_2,.)) - E(\rho_\infty)]}{\lambda\left[1+(\lambda/2)^{p_+ \prime q_+}(q_+ - 1)(E(\rho(t_2,.))) - E(\rho_\infty)^{(q_+-1)}(t-t_2)\right]^{(1/q_+-1)}}, \quad \text{on } I_2, \tag{15}$$

$$[E(\rho(t,.)) - E(\rho_\infty)] \le e^{-(\lambda/2)^{p_+'}(t-t_1)}[E(\rho_0) - E(\rho_\infty)], \quad \text{on } I_1,$$

$$W^{p_+}_{p(.)}(\rho(t,.),\rho_\infty(.)) \le \frac{2^{p_+}}{\lambda} e^{-(\lambda/2)^{p_+'}(t-t_1)}[E(\rho_0) - E(\rho_\infty)], \quad \text{on } I_1, \tag{16}$$

where $t_1 := \inf I_1$ and $t_2 := \inf I_2$.

2. Preliminaries

2.1. Assumptions. Throughout this work, we will assume the following:

(H_{ρ_0}) ρ_0 is a probability density on Ω, with $N \le \rho_0 \le M$, for some $0<N<M$, and $\int_\Omega G(\rho_0)\mathrm{d}x < \infty$.

$(H_{q(.)}^{p(.)})$: $q(.), p(.)\colon \Omega \longrightarrow]1,+\infty[$ are continuous functions such that $((1/p(x)) + (1/q(x))) = 1$ for all $x \in \Omega$, and $1 < p := \min_\Omega p(x) \le \max_\Omega p(x) := p_+$; $1 < q := \min_\Omega q(x) \le \max_\Omega q(x) := q_+$.

(H_G) $G\colon [0,+\infty[\longrightarrow \mathbb{R}$ is strictly convex, $G \in C^2(]0,+\infty[)$, and $t \longmapsto t^d G(t^{-d})$ is convex.

$$\left(H_V^1\right) V \in W^{1,\infty}(\Omega). \tag{17}$$

(H_V^2) $V\colon \mathbb{R}^d \longrightarrow \mathbb{R}$ is a potential which satisfies $V(0) = 0$, $V \in C^2(\Omega)$, and

$$V(x) - V(y) \geq \nabla V(y).(x-y) + \lambda |x-y|^{p_+}, \quad \text{for all } x, y \in \Omega, \text{ for some } \lambda > 0. \tag{18}$$

2.2. Lebesgue–Sobolev Spaces with Variable Exponents. We recall in this section some definitions and fundamental properties of the Lebesgue and Sobolev space with variable exponents.

Definition 1. Let ρ be a probability measure on Ω and $p(.)\colon \Omega \longrightarrow]1, +\infty[$ be a measurable function. We denote by $L_\rho^{p(.)}(\Omega)$ the Lebesgue space with the variable exponent defined by

$$L_\rho^{p(.)}(\Omega) := \left\{ u\colon \Omega \longrightarrow \mathbb{R}; \int_\Omega \left| \frac{u(x)}{\lambda} \right|^{p(x)} \rho(x)\mathrm{d}x \leq 1, \text{ for some } \lambda > 0 \right\}, \tag{19}$$

with the norm

$$\|u\|_{L_\rho^{p(.)}(\Omega)} = \inf \left\{ \lambda > 0, \int_\Omega \left| \frac{u(x)}{\lambda} \right|^{p(x)} \rho(x)\mathrm{d}x \leq 1 \right\}, \tag{20}$$

for all $u \in L_\rho^{p(.)}(\Omega)$.

We denote by $W_\rho^{1,p(.)}(\Omega)$ the Sobolev space with the variable exponent defined by

$$W_\rho^{1,p(.)}(\Omega) := \left\{ u \in L_\rho^{p(.)}(\Omega), \quad |\nabla u| \in L_\rho^{p(.)}(\Omega) \right\}, \tag{21}$$

equipped with the norm

$$\|u\|_{W_\rho^{1,p(.)}(\Omega)} := \|u\|_{L_\rho^{p(.)}(\Omega)} + \|\nabla u\|_{L_\rho^{p(.)}(\Omega)}. \tag{22}$$

In particular, if $\rho(x) = 1$, then $L_\rho^{p(.)}(\Omega) = L^{p(.)}(\Omega)$ and $W_\rho^{1,p(.)}(\Omega) = W^{1,p(.)}(\Omega)$.

We also define the space $W_0^{1,p(.)}(\Omega)$ as the closure of the space of C^∞-functions with compact support in $\Omega C_c^\infty(\Omega)$ in the space $W^{1,p(.)}(\Omega)$ endowed with the norm

$$\|u\|_{W_0^{1,p(.)}(\Omega)} := \|\nabla u\|_{W^{1,p(.)}(\Omega)}. \tag{23}$$

It is well known (cf. [9]) that $L_\rho^{p(.)}(\Omega)$ and $W_\rho^{1,p(.)}(\Omega)$ are Banach spaces, respectively, with norms (20) and (22).

Proposition 1 (Hölder inequality; see [12]). *Let $\rho \in P(\Omega)$ and $p(.), q(.)\colon \Omega \longrightarrow]1, +\infty[$ be two measurable functions such that $((1/p(x)) + (1/q(x))) = 1$, for all $x \in \Omega$.*

If $u \in L_\rho^{p(.)}(\Omega)$ and $v \in L_\rho^{q(.)}(\Omega)$, then

$$\int_\Omega |u(x)v(x)|\rho(x)\mathrm{d}x \leq \left(\frac{1}{p_-} + \frac{1}{q_-} \right) \|u\|_{L_\rho^{p(.)}(\Omega)} \|v\|_{L_\rho^{q(.)}(\Omega)}. \tag{24}$$

Furthermore, if $p_1(.), p_2(.), p_3(.)\colon \Omega \longrightarrow]1, +\infty[$ are measurable functions such that $(1/p_1(x)) = (1/p_2(x)) + (1/p_3(x))$, for almost all $x \in \Omega$, we have

$$\|uv\|_{L_\rho^{p_1(.)}(\Omega)} \leq 2\|u\|_{L_\rho^{p_2(.)}(\Omega)} \|v\|_{L_\rho^{p_3(.)}(\Omega)}, \tag{25}$$

for $u \in L_\rho^{p_2(.)}(\Omega)$ and $v \in L_\rho^{p_3(.)}(\Omega)$.

Proposition 2 (see [9]). *Let $\rho \in P(\Omega)$ and $p_1(.), p_2(.)\colon \Omega \longrightarrow [1, +\infty[$ be two measurable functions such that $p_1(x) \leq p_2(x)$ on Ω. Then, we have the following continuous injection:*

$$L_\rho^{p_2(.)}(\Omega) \longmapsto L_\rho^{p_1(.)}(\Omega). \tag{26}$$

Furthermore,

$$\|u\|_{L_\rho^{p_1(.)}(\Omega)} \leq 2\|u\|_{L_\rho^{p_2(.)}(\Omega)}, \tag{27}$$

for all $u \in L_\rho^{p_2(.)}(\Omega)$.

Proposition 3 (see [9]). *Assume that $(H_{q(.)}^{p(.)})$ holds. Then, the following statements hold:*

(i) The Banach spaces $W_\rho^{1,p(x)}(\Omega)$ and $L_\rho^{p(.)}(\Omega)$ are separable and reflexive Banach spaces

(ii) The embedding $W^{1,q(x)}(\Omega) \hookrightarrow\hookrightarrow L^{q(x)}(\Omega)$ is continuous and compact

(iii) There is a constant $C(\Omega)$ such that $\|u\|_{W^{1,q(x)}(\Omega)} \leq C(\Omega)\|\nabla u\|_{L^{q(x)}(\Omega)}$ for all $u \in W_0^{1,q(x)}(\Omega)$

3. Existence of Solutions for the Nonlinear $q(x)$-Laplacian Parabolic Equation

In this section, we prove the existence of solutions for the nonlinear $q(x)$-Laplacian parabolic equation.

3.1. Euler–Lagrangian Equation for Variational Problem (37). Here, we show that the sequence $(\rho_k)_k$ defined in (37) is a time discretization of the $q(x)$-Laplacian parabolic equation, i.e., for all test functions, $\phi \in C_c^\infty(\mathbb{R}^d, \mathbb{R})$, we have

$$\int_\Omega (\rho_k - \rho_{k-1})\phi \mathrm{d}x + h \int_\Omega < \left| \nabla_x (G'(\rho_k) + V) \right|^{q(x)-2} \cdot \nabla_x (G'(\rho_k) + V), \quad \nabla_x \phi > \rho_k \mathrm{d}x = A_k^h(\phi), \tag{28}$$

where $A_k^h(\phi)$ converges to 0 when h tends to 0.

Lemma 1. *Assume that (H_{ρ_0}), (H_G), and (H_V^1) hold. Then, the variational problem*

$$(P_1)\colon \inf_{\rho \in P(\Omega)} \left\{ I(\rho) := \int_\Omega (G(\rho) + \rho V)\mathrm{d}x + K_{p(.)}^h(\rho_0, \rho) \right\}, \tag{29}$$

where

$$K_{p(.)}^h(\rho_0, \rho) := \inf_{\gamma \in \Pi(\rho_0, \rho)} \int_{\Omega \times \Omega} \frac{|x-y|^{p(x)}}{p(x) h^{p(x)-1}} \mathrm{d}\gamma, \tag{30}$$

admits a unique solution ρ_1 in $P(\Omega)$ which satisfies $N \leq \rho_1 \leq M$.

Proof 1. Since $N \le \rho_0 \le M$, then the solution ρ_1 of variational problem (P_1) (if there exists) satisfies $N \le \rho_1 \le M$. The proof of the maximum principle is carried out similarly as given in [7].

Since $\int_\Omega G(\rho_0)\mathrm{d}x < \infty$ and $V \in L^\infty(\Omega)$, we have $I(\rho_0) < \infty$.

Let $\rho \in P(\Omega)$; since G is convex and $V \in L^\infty(\Omega)$,

$$I(\rho) \ge \int_\Omega [G(\rho) + \rho V]\mathrm{d}x \ge |\Omega| G\left(\frac{1}{|\Omega|}\right) - \|V\|_{L^\infty(\Omega)}. \quad (31)$$

We conclude that $\inf_{\rho \in P(\Omega)} I(\rho)$ is finite.

Let $(\rho^n)_n$ be a sequence in $P(\Omega)$ such that $N \le \rho^n \le M$ and $I(\rho^n)$ converges to $\inf_{\rho \in P(\Omega)} I(\rho)$. Then, $(\rho^n)_n$ converges weakly$*$ to ρ_1 in $L^\infty(\Omega)$ up to a subsequence.

G being positive and convex, then

$$\begin{aligned}\int_\Omega [G(\rho^n) + \rho^n V]\mathrm{d}x &\ge \int_\Omega [G(\rho_1) + \rho_1 V]\mathrm{d}x \\ &+ \int_\Omega G'(\rho_1)(\rho^n - \rho_1)\mathrm{d}x + \int_\Omega (\rho^n - \rho_1) V \mathrm{d}x.\end{aligned} \quad (32)$$

Next, we use the fact that $G'(\rho_1) \in L^\infty(\Omega)$ and $V \in L^\infty(\Omega)$ to obtain

$$\liminf_{n \longrightarrow \infty} \int_\Omega [G(\rho^n) + \rho^n V]\mathrm{d}x \ge \int_\Omega [G(\rho_1) + \rho_1 V]\mathrm{d}x. \quad (33)$$

Since the variable exponent $p(.)$ is continuous on Ω, the Kantorovich problem

$$(K): \inf_{\gamma \in \Pi(\rho_0, \rho^n)} \int_{\Omega \times \Omega} \frac{|x-y|^{p(x)}}{p(x) h^{p(x)-1}} \mathrm{d}\gamma, \quad (34)$$

admits a solution γ^n. Moreover, since Ω is bounded, the sequence $(\gamma^n)_n$ converges to a measure γ_1 in $P(\Omega \times \Omega)$ narrowly, and $\gamma_1 \in \Pi(\rho_0, \rho_1)$; and then, we derive that

$$\liminf_{n \longrightarrow \infty} K^h_{p(.)}(\rho_0, \rho^n) \ge \int_{\Omega \times \Omega} \frac{|x-y|^{p(x)}}{p(x) h^{p(x)-1}} \mathrm{d}\gamma_1 \ge K^h_{p(.)}(\rho_0, \rho_1). \quad (35)$$

We combine (35) and (33) to obtain

$$\liminf_{n \longrightarrow \infty} I(\rho^n) \ge I(\rho_1). \quad (36)$$

Thus, ρ_1 is a solution of variational problem (P_1). From the strict convexity of G, we deduce that $\rho \longmapsto \int_\Omega (G(\rho) + \rho V)\mathrm{d}x$ is strictly convex and so is $\rho \longmapsto I(\rho)$ on $P(\Omega)$, and consequently, the uniqueness of the solution ρ_1 of (P_1) follows. □

Now, we assume that (H_{ρ_0}), (H_G), and (H^1_V) hold. Then, from Lemma 1, we obtain that the variational problem

$$(P_k): \inf_{\rho \in P(\Omega)} \left\{ I(\rho) := \int_\Omega [G(\rho) + \rho V]\mathrm{d}x + K^h_{p(.)}(\rho_{k-1}, \rho) \right\}, \quad (37)$$

with

$$K^h_{p(.)}(\rho_{k-1}, \rho) := \inf_{\gamma \in \Pi(\rho_{k-1}, \rho)} \int_{\Omega \times \Omega} \frac{|x-y|^{p(x)}}{p(x) h^{p(x)-1}} \mathrm{d}\gamma, \quad (38)$$

admits a unique solution ρ_k for all $k \ge 1$.

Next, we prove that $(\rho_k)_k$ is a time discretization of the nonlinear $q(x)$-Laplacian parabolic equation. In order to achieve this, we use the following lemma.

Lemma 2. *Assume that (H_{ρ_0}), (H_G), and (H^1_V) hold. Then, the Kantorovich problem*

$$(K): \inf_{\gamma \in \Pi(\rho_{k-1}, \rho_k)} \left\{ \int_{\Omega \times \Omega} \frac{|x-y|^{p(x)}}{p(x) h^{p(x)-1}} \mathrm{d}\gamma \right\}, \quad (39)$$

admits a solution γ_k such that

$$\mathrm{supp}\gamma_k \subset \left\{ (x,y) \in \Omega \times \Omega, \quad y = x - h \,|\, \nabla_x (G'(\rho_k) + V) \big|^{q(x)-2} \nabla_x (G'(\rho_k) + V) \right\}, \quad (40)$$

where $q(x) = (p(x)/p(x) - 1)$.

Proof 2. The proof of Lemma 2 is derived following the two steps. □

Step 1. We first assume that $V \in C^2(\Omega)$.

Fix $\psi \in C^\infty_c(\mathbb{R}^d, \mathbb{R}^d)$. Let $(T_\epsilon)_{\epsilon \in \mathbb{R}}$ in $C^\infty(\mathbb{R}^d, \mathbb{R}^d)$ defined by

$$T_\epsilon(x) = x + \epsilon \psi(x). \quad (41)$$

Define the probability density ρ_ϵ as $\rho_\epsilon = T_\epsilon \# \rho_k$ and γ^ϵ as a probability measure on $\Omega \times \Omega$ defined by

$$\int_{\Omega \times \Omega} \phi(x,y)\mathrm{d}\gamma^\epsilon = \int_{\Omega \times \Omega} \phi(x, T_\epsilon(y))\mathrm{d}\gamma_k, \quad (42)$$

for all $\phi \in C^0_b(\Omega \times \Omega)$.

For $\epsilon \ne 0$,

$$\begin{aligned}\frac{I(\rho_\epsilon) - I(\rho_k)}{\epsilon} &= \int_\Omega \frac{G(\rho_\epsilon) - G(\rho_k)}{\epsilon}\mathrm{d}x + \int_\Omega \frac{V(T_\epsilon) - V(x)}{\epsilon}\mathrm{d}x \\ &+ \frac{1}{\epsilon}\left[K^h_{p(.)}(\rho_\epsilon, \rho_{k-1}) - K^h_{p(.)}(\rho_{k-1}, \rho_k)\right].\end{aligned} \quad (43)$$

Since G satisfies (H_G), then

$$\lim_{\epsilon\longrightarrow 0}\int_{\Omega}\frac{G(\rho_\epsilon)-G(\rho_k)}{\epsilon}\mathrm{d}x=\int_{\Omega}\nabla_x G'(\rho_k).\psi\rho_k\mathrm{d}x. \tag{44}$$

Since $V\in C^2(\Omega)$, from the Taylor formula, we have (see [7])

$$\begin{aligned}V(T_\epsilon(x))-V(x)&=\epsilon\nabla_x V(x)\cdot\psi(x)\\&\quad+\epsilon^2(\psi(x))^\tau\nabla_x^2 V(x+\epsilon\theta\psi(x))\\&\quad\cdot\psi(x),\quad\text{with }\theta\in\,]0,1[.\end{aligned} \tag{45}$$

Then, we have after integration,

$$\begin{aligned}\int_{\Omega}\frac{V(T_\epsilon)-V(x)}{\epsilon}\mathrm{d}x&=\int_{\Omega}<\nabla V(x),\psi>\rho_k\mathrm{d}x\\&\quad+\epsilon\int_{\Omega}(\psi(x))^\tau\cdot\nabla^2 V\\&\quad\cdot(x+\epsilon\theta\psi(x))\cdot\psi(x)\rho_k\mathrm{d}x.\end{aligned} \tag{46}$$

By using (41) and the fact that $V\in W^{1,\infty}(\Omega)$, we have

$$\left|(\psi(x))^\tau.\nabla^2 V(x+\epsilon\theta\psi(x)).\psi(x)\right|\le\left\|\nabla^2 V\right\|_{L^\infty(\Omega)}\|\psi\|_{L^\infty(\Omega)}. \tag{47}$$

We now use the dominated convergence theorem to have

$$\lim_{\epsilon\longrightarrow 0}\int_{\Omega}\frac{V(T_\epsilon)-V(x)}{\epsilon}\mathrm{d}x=\int_{\Omega}\nabla V.\psi\rho_k\mathrm{d}x. \tag{48}$$

Note that γ^ϵ defined in (42) belongs to $\Pi(\rho_{k-1},\rho_\epsilon)$, and

$$\begin{aligned}K^h_{p(.)}(\rho_{k-1},\rho_k)&=\int_{\Omega\times\Omega}\frac{|x-y|^{p(x)}}{p(x)h^{p(x)-1}}\mathrm{d}\gamma_k,K^h_{p(.)}(\rho_{k-1},\rho_\epsilon)\\&\le\int_{\Omega\times\Omega}\frac{\left|x-T_\epsilon(y)\right|^{p(x)}}{p(x)h^{p(x)-1}}\mathrm{d}\gamma_k.\end{aligned} \tag{49}$$

So, for $\epsilon>0$, we have

$$\begin{aligned}&\frac{1}{\epsilon}\left[K^h_{p(.)}(\rho_{k-1},\rho_\epsilon)-K^h_{p(.)}(\rho_{k-1},\rho_k)\right]\\&\le\frac{1}{\epsilon}\int_{\Omega\times\Omega}\left[\frac{\left|x-T_\epsilon(y)\right|^{p(x)}-|x-y|^{p(x)}}{p(x)h^{p(x)-1}}\right]\mathrm{d}\gamma_k.\end{aligned} \tag{50}$$

Note that

$$\begin{aligned}&\lim_{\epsilon\longrightarrow 0^+}\frac{1}{\epsilon}\int_{\Omega\times\Omega}\left[\frac{\left|x-T_\epsilon(y)\right|^{p(x)}-|x-y|^{p(x)}}{p(x)h^{p(x)-1}}\right]d\gamma_k\\&=-\int_{\Omega\times\Omega}<\left|\frac{x-y}{h}\right|^{p(x)-2}\left(\frac{x-y}{h}\right),\psi>d\gamma_k.\end{aligned} \tag{51}$$

Indeed,

(i) We have

$$\begin{aligned}&\lim_{\epsilon\longrightarrow 0^+}\frac{1}{\epsilon}\left[\frac{\left|\left|x-T_\epsilon(y)\right|^{p(x)}-|x-y|^{p(x)}\right|}{p(x)h^{p(x)-1}}\right]\\&=-\left|\frac{x-y}{h}\right|^{p(x)-2}\left(\frac{x-y}{h}\right).\psi.\end{aligned} \tag{52}$$

(ii) On the contrary, the Taylor formula with respect to ϵ enables us to write

$$\begin{aligned}\frac{\left|\left|x-T_\epsilon(y)\right|^{p(x)}-|x-y|^{p(x)}\right|}{p(x)h^{p(x)-1}}&=-\epsilon\left|\frac{x-y-\theta\epsilon\psi(y)}{h}\right|^{p(x)-2}\\&\quad\cdot\left(\frac{x-y-\theta\epsilon\psi(y)}{h}\right).\psi(y),\end{aligned} \tag{53}$$

where $\theta\in(0,1)$ and $T_\epsilon(y)=y+\epsilon\psi(y)$. Also, we have

$$\begin{aligned}&\left|\frac{\left|\left|x-T_\epsilon(y)\right|^{p(x)}-|x-y|^{p(x)}\right|}{\epsilon p(x)h^{p(x)-1}}\right|\\&=\left|\frac{x-y-\theta\epsilon\psi(y)}{h}\right|^{p(x)-1}|\psi(y)|\\&\le\left[\left|\frac{x-y-\theta\epsilon\psi(y)}{h}\right|+1\right]^{p(x)-1}|\psi(y)|\\&\le\left[\left|\frac{x-y-\theta\epsilon\psi(y)}{h}\right|+1\right]^{p(x)}|\psi(y)|\\&\le 2^{p_+-1}\left|\frac{x-y}{h}\right|^{p(x)}+2^{p_+-1}\left(\frac{|\psi(y)|}{h}+1\right)^{p_+}|\psi(y)|,\end{aligned} \tag{54}$$

with

$$\begin{aligned}&\int_{\Omega\times\Omega}\left[2^{p_+-1}\left|\frac{x-y}{h}\right|^{p(x)}+2^{p_+-1}\left(\frac{|\psi(y)|}{h}+1\right)^{p_+}|\psi(y)|\right]\mathrm{d}\gamma_k\\&(x,y)<\infty.\end{aligned} \tag{55}$$

We then combine the results given in (i) and (ii) and the dominated convergence theorem to obtain (50).

Since ρ_k minimizes I on $P(\Omega)$, then

$$\lim_{\epsilon\longrightarrow 0}\frac{I(\rho_\epsilon)-I(\rho_k)}{\epsilon}=0. \tag{56}$$

So, we combine (44), (48), and (50) to obtain that

$$\begin{aligned}0=\lim_{\epsilon\longrightarrow 0^+}\frac{I(\rho_\epsilon)-I(\rho_k)}{\epsilon}&\le\int_{\Omega}\nabla_x(G'(\rho_k)+V).\psi\rho_k\mathrm{d}x\\&\quad-\int_{\Omega\times\Omega}<\left|\frac{x-y}{h}\right|^{p(x)-2}\left(\frac{x-y}{h}\right),\\&\quad\psi>\mathrm{d}\gamma_k.\end{aligned} \tag{57}$$

Replacing ψ by $-\psi$ in (56), we get

$$\int_\Omega < \nabla_x (G'(\rho_k) + V), \psi > \rho_k dx - \int_{\Omega\times\Omega} < \left|\frac{x-y}{h}\right|^{p(x)-2}\left(\frac{x-y}{h}\right), \quad \psi > \mathrm{d}\gamma_k \le 0. \tag{58}$$

From (56) and (57), we deduce that

$$\int_\Omega < \nabla_x (G'(\rho_k) + V), \psi > \rho_k \mathrm{d}x + \int_{\Omega\times\Omega} < \left|\frac{y-x}{h}\right|^{p(x)-2}\left(\frac{y-x}{h}\right), \quad \psi > \mathrm{d}\gamma_k = 0. \tag{59}$$

Thus, we obtain (40) when $V \in C^2(\Omega)$.

Now, let us establish the proof of the lemma when $V \in W^{1,\infty}(\Omega)$ and is nonregular.

Step 2. Assume that $V \in W^{1,\infty}(\Omega)$. Let $(V^\delta)_\delta$ be a sequence in $C^2(\Omega)$ such that $\lim_{\delta\longrightarrow 0}\|V^\delta - V\|_{W^{1,\infty}(\Omega)} = 0$.

By fixing $\delta > 0$, we define the sequence $(\rho_k^\delta)_k$ such that $\rho_0^\delta = \rho_0$ with ρ_k^δ (for $k \ge 1$), the solution of the variational problem

$$\left(P_k^\delta\right): \inf_{\rho\in P(\Omega)}\left[\int_\Omega \left(G(\rho) + \rho V^\delta\right)\mathrm{d}x + K^h_{p(.)}\left(\rho_{k-1}^\delta, \rho\right)\right], \tag{60}$$

where $K^h_{p(.)}(\rho_{k-1}^\delta, \rho)$ is defined as in (38). As in Lemma 1, the variational problem (P_k^δ) admits a unique solution ρ_k^δ in $P(\Omega)$, and $N \le \rho_k^\delta \le M$. Hence, the Kantorovich problem

$$K^\delta: \inf_{\gamma\in\Pi\left(\rho_{k-1}^\delta, \rho_k^\delta\right)}\left[\int_{\Omega\times\Omega}\frac{|x-y|^{p(x)}}{p(x)h^{p(x)-1}}\mathrm{d}\gamma\right], \tag{61}$$

admits a solution γ_k^δ such that

$$\mathrm{supp}\gamma_k^\delta \subset \left\{(x,y) \in \Omega\times\Omega,\ y = x - h\left|\nabla_x\left(G'\left(\rho_k^\delta\right) + V^\delta\right)\right|^{q(x)-2}\nabla_x\left(G'\left(\rho_k^\delta\right) + V^\delta\right)\right\}. \tag{62}$$

Let us show that $(\rho_k^\delta)_\delta$ converges to ρ_k and $(\gamma_k^\delta)_\delta$ converges to γ_k up to a subsequence, as well as $\mathrm{supp}\gamma_k$ satisfies (40)

Using (P_k^δ) and (61), we have

$$\int_\Omega\left(G\left(\rho_{k-1}^\delta\right) + \rho_{k-1}^\delta V^\delta\right)\mathrm{d}x - \int_\Omega\left(G\left(\rho_k^\delta\right) + \rho_k^\delta V^\delta\right)\mathrm{d}x \ge h\int_\Omega\frac{\left|\nabla_x\left(G'\left(\rho_k^\delta\right) + V^\delta\right)\right|^{q(x)}}{p(x)}\rho_k^\delta\mathrm{d}x. \tag{63}$$

However, G is convex, and $V \in W^{1,\infty}(\Omega)$; and then,

$$\int_\Omega\left|\nabla_x\left(G'\left(\rho_k^\delta\right) + V^\delta\right)\right|^{q(x)}\rho_k^\delta \le \frac{p_+}{h}\left[\int_\Omega G(\rho_0)\mathrm{d}x - |\Omega|G\left(\frac{1}{|\Omega|}\right) + 2\|V\|_{L^\infty(\Omega)}\right]. \tag{64}$$

Furthermore, recalling (63) and the fact that $N \le \rho_k^\delta \le M$, $\nabla_x(G'(\rho_k^\delta)) = G''(\rho_k^\delta)\nabla_x(\rho_k^\delta)$, and $|\nabla_x(G'(\rho_k^\delta))|^{q(x)} \le 2^{q_+-1}[|\nabla_x(G'(\rho_k^\delta) + V^\delta)|^{q(x)} + |\nabla V^\delta|^{q(x)}]$, we obtain

$$\int_\Omega\left|\nabla_x\rho_k^\delta\right|^{q(x)}\mathrm{d}x \le \frac{2^{q_+-1}}{k_0}\left[\frac{p_+}{\mathrm{Nh}}\left(\int_\Omega G(\rho_0)\mathrm{d}x - |\Omega|G\left(\frac{1}{|\Omega|}\right) + 2\|V\|_{L^\infty(\Omega)}\right) + \|\nabla V\|^{q_+}_{L^\infty(\Omega)}\right], \tag{65}$$

where $k_0 = \inf_{(t,x)\in[N,M]\times\Omega}[G''(t)]^{q(x)}$. We conclude that $(\rho_k^\delta)_\delta$ is bounded on $W^{1,q(x)}(\Omega)$. Since $q(.)$ is continuous and Ω is a bounded set, the injection $W^{1,q(x)}(\Omega)\hookrightarrow\hookrightarrow L^{q(x)}(\Omega)$ is compact (see [9]), and hence, the sequence $(\rho_k^\delta)_\delta$ converges strongly to some u_k in $L^{q(x)}(\Omega)$ up to a subsequence. Moreover, ρ_k^δ minimizes (P_k^δ) for $k \in \mathbb{N}^*$, and then, we have

$$\int_\Omega\left(G(\rho) + \rho V^\delta\right)\mathrm{d}x + K^h_{p(.)}\left(\rho_{k-1}^\delta, \rho\right) \ge \int_\Omega\left(G\left(\rho_k^\delta\right) + \rho_k^\delta V^\delta\right)\mathrm{d}x + K^h_{p(.)}\left(\rho_{k-1}^\delta, \rho_k^\delta\right), \tag{66}$$

for all $\rho \in P(\Omega)$. Also, from the boundedness of Ω, $(\gamma_k^\delta)_\delta$ converges narrowly to a measure Γ_k in $P(\Omega\times\Omega)$, and

$\Gamma_k \in \Pi(u_{k-1}, u_k)$. Then, we use the strong convergence of $(\rho_k^\delta)_\delta$ to u_k and the fact that $\|V^\delta - V\|_{W^{1,\infty}(\Omega)}$ converges to 0 when $\delta \longrightarrow 0$ to obtain that

$$\int_\Omega (G(\rho) + \rho V)\mathrm{d}x + K^h_{p(.)}(u_{k-1}, \rho) \geq \int_\Omega (G(u_k) + u_k V)\mathrm{d}x + K^h_{p(.)}(u_{k-1}, u_k), \tag{67}$$

for all $\rho \in P(\Omega)$. Since $\rho_0^\delta = \rho_0$, we conclude that $u_k = \rho_k$ and $\Gamma_k = \gamma_k$ for all $k \in \mathbb{N}^*$.

By using (63) and $N \leq \rho_k \leq M$, we deduce that $(\nabla_x(G'(\rho_k^\delta) + V^\delta))_\delta$ is bounded in $[L^{q(x)}(\Omega)]^d$. Since $(\rho_k^\delta)_\delta$ converges strongly to ρ_k in $L^{q(x)}(\Omega)$ and G' is continuous, then $(\nabla_x(G'(\rho_k^\delta) + V^\delta))_\delta$ converges weakly to $\nabla_x(G'(\rho_k) + V)$ in $[L^{q(x)}(\Omega)]^d$.

Next, we use (57), and we have

$$\int_\Omega < \nabla_x\left(G'\left(\rho_k^\delta\right) + V^\delta\right), \psi > \rho_k^\delta \mathrm{d}x + \int_{\Omega\times\Omega} < \left|\frac{y-x}{h}\right|^{p(x)-2}\left(\frac{y-x}{h}\right), \quad \psi > d\gamma_k^\delta = 0. \tag{68}$$

Since $(\rho_k^\delta)_\delta$ converges strongly to ρ_k in $L^{q(x)}(\Omega)$, $(\nabla_x(G'(\rho_k^\delta) + V^\delta))_\delta$ converges weakly to $\nabla_x(G'(\rho_k) + V)$ in $[L^{q(x)}(\Omega)]^d$, and $(\gamma_k^\delta)_\delta$ converges narrowly to γ_k in $P(\Omega \times \Omega)$; then, tending δ to 0 in (67), we obtain

$$\int_\Omega < \nabla_x\left(G'(\rho_k) + V^\delta\right), \psi > \rho_k \mathrm{d}x + \int_{\Omega\times\Omega} < \left|\frac{y-x}{h}\right|^{p(x)-2}\left(\frac{y-x}{h}\right), \quad \psi > d\gamma_k = 0, \tag{69}$$

for all test functions, $\psi \in C_c^\infty(\mathbb{R}^d, \mathbb{R}^d)$.

Finally, we obtain the equality

$$y = x - h\left|\nabla_x(G'(\rho_k) + V)\right|^{q(x)-2}\nabla_x(G'(\rho_k) + V)\gamma_k \text{ a.e.} \tag{70}$$

Now, let us prove that $(\rho_k)_k$ is a time discretization of a nonlinear $q(x)$-Laplacian parabolic equation. Let $\psi \in C_c^\infty(\mathbb{R}^d, \mathbb{R})$ be a test function; we have

$$\int_\Omega (\rho_k - \rho_{k-1})\psi \mathrm{d}x = \int_{\Omega\times\Omega} (\psi(y) - \psi(x))\mathrm{d}\gamma_k(x, y). \tag{71}$$

We now use (69) and the Taylor formula to obtain

$$\begin{aligned}\int_\Omega (\rho_k - \rho_{k-1})\psi \mathrm{d}x = &-h\int_\Omega < \left|\nabla_x(G'(\rho_k) + V)\right|^{q(x)-2}\nabla_x(G'(\rho_k) + V), \nabla\psi > \rho_k \mathrm{d}x \\ &+ h^2\int_{\Omega\times\Omega} < \left[\left[\nabla_x(G'(\rho_k) + V)\right]^\tau, \nabla^2\psi(x + \theta(y-x))\left[\nabla_x(G'(\rho_k) + V)\right]\right] > \mathrm{d}\gamma_k(x, y),\end{aligned} \tag{72}$$

where $\theta \in [0, 1]$ and $[\nabla_x(G'(\rho_k) + V)]^\tau$ is the transpose of $[\nabla_x(G'(\rho_k) + V)]^\tau$.

Let us show that

$$A_k^h(\psi) = h^2\int_{\Omega\times\Omega} < \left[\nabla_x(G'(\rho_k) + V)\right]^\tau, \nabla^2\psi(x + \theta(y-x))\left[\nabla_x(G'(\rho_k) + V)\right] > \mathrm{d}\gamma_k(x, y) \tag{73}$$

converge to 0 when h tends to 0. Since $q(x) - 1 = (q(x)/p(x))$, we have

$$\left|A_k^h(\psi)\right| \leq h^2\left\|\nabla^2\psi\right\|_{L^\infty(\Omega)}\int_\Omega \left|\nabla_x(G'(\rho_k) + V)\right|^{(2q(x)/p(x))}\rho_k \mathrm{d}x. \tag{74}$$

Define $\Omega_1 := \{x \in \Omega,\ p(x) \geq 2\}$ and $\Omega_1 := \{x \in \Omega,\ p(x) < 2\}$:

$$\begin{aligned}\int_{\Omega_1} \left|\nabla_x(G'(\rho_k) + V)\right|^{(2q(x)/p(x))}\rho_k \mathrm{d}x &\leq 2^{q_+ - 1}\left[\int_\Omega \left|\nabla_x(G'(\rho_k) + V)\right|^{q(x)}\rho_k \mathrm{d}x + 1\right], \\ \int_{\Omega_2} \left|\nabla_x(G'(\rho_k) + V)\right|^{(2q(x)/p(x))}\rho_k \mathrm{d}x &\leq h^{1-\frac{2}{p_-}}\left[\int_\Omega \left|\nabla_x(G'(\rho_k) + V)\right|^{q(x)}\rho_k \mathrm{d}x\right].\end{aligned} \tag{75}$$

We use (64) and (73) in (72), and we have

$$\left|A_k^h(\psi)\right| \le \frac{2^{p_+-1}}{k_0} h^2 \left\|\nabla_x \psi\right\|_{L^\infty(\Omega)} + p_+\left(h\left\|\nabla_x \psi\right\|_{L^\infty(\Omega)} + h^{(2-2/p_-)}\right) \cdot \left(\int_\Omega G(\rho_0)\mathrm{d}x - |\Omega| G\left(\frac{1}{|\Omega|}\right) + 2\|\nabla\|_{L^\infty(\Omega)}\right). \tag{76}$$

We tend h to 0, and we conclude that $A_k^h(\psi)$ converges to 0. Thus, the sequence $(\rho_k)_k$ is a time discretization of the nonlinear $q(x)$-Laplacian parabolic equation.

Define $\rho^h(t,x)$: $[0,+\infty[\times\Omega \longrightarrow [0,+\infty[$ as follows:

$$\rho^h(t,x) = \rho_k(x) \; if \; t \in](k-1)h, \mathrm{kh}], \text{ and } \rho^h(0,x) = \rho_0(x). \tag{77}$$

We prove in the next section that the sequence $(\rho^h)_h$ converges strongly to a function $\rho(t,x)$ in $L^{q(x)}([0,T]\times\Omega)$ for $0<T<\infty$ and that the nonlinear term sequence $\mathrm{div}_x(\rho^h)|(\nabla_x(G'(\rho^h))+V)|^{q(x)-2}(\nabla_x(G'(\rho^h))+V)_h$ converges weakly to $\mathrm{div}_x(\rho^h)|(\nabla_x(G'(\rho^h))+V)|^{q(x)-2}(\nabla_x(G'(\rho^h))+V)_h$ in $\psi \in C_c^\infty(\mathbb{R}^d,\mathbb{R}^d)$.

3.2. Strong Convergence of $(\rho^h)_h$ and Weak Convergence of the Nonlinear Term Sequence. Here, we denote the nonlinear term sequence by $\mathrm{div}_x(\rho^h\omega^h)_h$, with $\omega^h := ||(\nabla_x(G'(\rho^h))+V)|^{q(x)-2}(\nabla_x(G'(\rho^h))+V)$.

Since $N \le \rho_k \le M$, then $N \le \rho^h \le M$. Thus, we use (64), and we have

$$\int_{[0,T]\times\Omega}\left|\nabla_x \rho^h\right|^{q(x)}\mathrm{d}x \le \frac{2^{q_+-1}}{k_0}\left[\frac{p_+}{N}\left(\int_\Omega G(\rho_0)\mathrm{d}x - |\Omega|G\left(\frac{1}{|\Omega|}\right) + 2\|V\|_{L^\infty(\Omega)}\right) + \|\nabla V\|_{L^\infty(\Omega)}^{q_+}\right], \tag{78}$$

where $0<T<\infty$. We conclude that $(\rho^h(t,.))_h$ is bounded in $W^{1,q(x)}(\Omega)$ for almost all $t \in [0,T]$. By using the compact injection $W^{1,q(x)}(\Omega) \hookrightarrow\hookrightarrow L^{q(x)}(\Omega)$, we deduce that $(\rho^h(t,.))_h$ converges strongly to a function $\rho(t,.)$ in $L^{q(x)}(\Omega)$. Since $N \le \rho^h \le M$ and $[0,T]\times\Omega$ is bounded, we use the dominated convergence theorem to have

$$\lim_{h\longrightarrow 0}\int_0^T\int_\Omega\left|\rho^h(t,x)-\rho(t,x)\right|^{q(x)}\mathrm{d}x\,\mathrm{d}t = 0. \tag{79}$$

Then, up to a subsequence, the sequence $(\rho^h)_h$ converges strongly to $\rho(t,x)$ in $L^{q(x)}([0,T]\times\Omega)$. By using (64) and $N \le \rho^h \le M$, we deduce that $(\nabla_x(G'(\rho^h)+V))_h$ is bounded in $[L^{q(x)}([0,T]\times\Omega)]^d$. Then, since G' is continuous and $(\rho^h)_h$ converges strongly to ρ in $L^{q(x)}([0,T]\times\Omega)$, we conclude that $(\nabla_x(G'(\rho^h)+V))_h$ converges weakly to $\nabla_x(G'(\rho)+V)$ in $[L^{q(x)}([0,T]\times\Omega)]^d$.

Note that $|\omega^h|^{p(x)} = |\nabla_x(G'(\rho^h)+V)|^{q(x)}$. Then, using the fact that $(\nabla_x(G'(\rho^h)+V))_h$ is bounded in $L^{q(x)}([0,T]\times\Omega)$, we conclude that $(\omega^h)_h$ is bounded in $L^{q(x)}([0,T]\times\Omega)$. Thus, the sequence $(\omega^h)_h$ converges weakly to some $\omega \in L^{p(x)}([0,T]\times\Omega)$.

As in [7], we derive easily that $\mathrm{div}_x(\rho^h)|(\nabla_x(G'(\rho^h))+V)|^{q(x)-2}(\nabla_x(G'(\rho^h))+V)_h$ converges weakly to $\mathrm{div}_x(\rho)|(\nabla_x(G'(\rho))+V)|^{q(x)-2}(\nabla_x(G'(\rho))+V)$ in $\psi \in C_c^\infty(\mathbb{R}^d,\mathbb{R}^d)$.

Lemma 3. *Fix $T>0$. Let $u \in C_c^\infty(\mathbb{R})$ be a test function such that $\mathrm{supp}\,u \subset [-T,T]$. We have*

$$\lim_{h\longrightarrow 0}\int_{[0,T]\times\Omega} <\rho^h\omega^h, \nabla_x\left(G'\left(\rho^h\right)+V\right)> u(t)\mathrm{d}t\mathrm{d}x = \int_{[0,T]\times\Omega} <\rho\omega, \nabla_x\left(G'\left(\rho^h\right)+V\right)> u(t)\mathrm{d}t\mathrm{d}x. \tag{80}$$

Proof 3. The proof of this lemma is achieved via the following three claims:

Claim 1:

$$\liminf_{h\longrightarrow 0}\int_{[0,T]\times\Omega}\rho^h <\omega^h, \nabla_x\left(G'\left(\rho^h\right)+V\right)> u(t)\mathrm{d}t\mathrm{d}x \ge \int_{[0,T]\times\Omega}\rho <\omega, \nabla_x\left(G'\left(\rho^h\right)+V\right)> u(t)\mathrm{d}t\mathrm{d}x. \tag{81}$$

□

Proof 4. Since $\rho^h \ge 0$, $u \ge 0$, and $v \longmapsto |v|^{q(x)-2}v$ is monotone for all x fixed in Ω, we have

$$\int_{[0,T]\times\Omega}\rho^h <\omega^h - \left|\nabla_x(G'(\rho)+V)\right|^{q(x))-2}\nabla_x(G'(\rho)+V), \nabla_x\left(G'\left(\rho^h\right)+V\right)-\nabla_x(G'(\rho)+V)> u(t)\mathrm{d}t\mathrm{d}x \ge 0. \tag{82}$$

Using (81), we have

$$\int_{[0,T]\times\Omega} <\rho^h\omega^h, \nabla_x\left(G'\left(\rho^h\right)+V\right)>u(t)\mathrm{d}t\mathrm{d}x \geq \int_{[0,T]\times\Omega} <\rho^h\omega^h, \nabla_x\left(G'(\rho)+V\right)>u(t)\mathrm{d}t\mathrm{d}x + \int_{[0,T]\times\Omega} <\rho^h\left|\nabla_x\left(G'(\rho)+V\right)\right|^{q(x)-2}\nabla_x\left(G'(\rho)+V\right), \nabla_x\left(G'\left(\rho^h\right)+V\right)-\nabla_x\left(G'(\rho)+V\right)>u(t)\mathrm{d}t\mathrm{d}x. \tag{83}$$

Since $(\rho^h)_h$ converges strongly to ρ in $L^{q(x)}([0,T]\times\Omega)$, $(\nabla_x(G'(\rho^h)+V))_h$ converges weakly to $\nabla_x(G'(\rho)+V)$ in $L^{q(x)}([0,T]\times\Omega)$, and $(\omega^h)_h$ converges weakly to ω in $L^{q(x)}([0,T]\times\Omega)$, then

$$\lim\inf_{h\longrightarrow 0}\int_{[0,T]\times\Omega} <\rho^h\omega^h, \nabla_x\left(G'(\rho)+V\right)>u(t)\mathrm{d}t\mathrm{d}x = \int_{[0,T]\times\Omega} <\rho\omega, \nabla_x\left(G'(\rho)+V\right)>u(t)\mathrm{d}t\mathrm{d}x, \tag{84}$$

$$\lim\inf_{h\longrightarrow 0}\int_{[0,T]\times\Omega} <\rho^h\left|\nabla_x\left(G'(\rho)+V\right)\right|^{q(x)-2}\nabla_x\left(G'(\rho)+V\right), \nabla_x\left(G'\left(\rho^h\right)+V\right)-\nabla_x\left(G'(\rho)+V\right)>u(t)\mathrm{d}t\mathrm{d}x = 0. \tag{85}$$

We now use (83) and (84) in (82) to conclude the proof of claim 1.

Claim 2:

$$\lim\sup_{h\longrightarrow 0}\int_{[0,T]\times\Omega} <\rho^h\omega^h, \nabla_x\left(G'\left(\rho^h\right)+V\right)>u(t)\mathrm{d}t\mathrm{d}x \leq \int_\Omega\left[\rho_0 G'(\rho_0)-G^*\left(G'(\rho_0)\right)\right]u(0)\mathrm{d}x + \int_{[0,T]\times\Omega}\left[\rho G'(\rho)-G^*\left(G'\left(\rho^h\right)\right)\right]u'(t)\mathrm{d}t\mathrm{d}x + \int_{[0,T]\times\Omega}\rho V u'(t)\mathrm{d}t\mathrm{d}x + \int_\Omega \rho_0 V u(0)\mathrm{d}x. \tag{86}$$

□

Proof 5. We use the descent algorithm (P_k) and (70) to obtain

$$\int_\Omega\left(G(\rho_{k-1})+\rho_{k-1}V\right)\mathrm{d}x - \int_\Omega\left(G(\rho_k)+\rho_k V\right)\mathrm{d}x \geq h\int_\Omega\frac{\left|\nabla_x\left(G'(\rho_k)+V\right)\right|^{q(x)}}{p(x)}\rho_k\mathrm{d}x. \tag{87}$$

Note that $<\omega_k, \nabla_x(G'(\rho_k)+V)> = |\nabla_x(G'(\rho_k)+V)|^{q(x)}$, with $\omega_k = |\nabla_x(G'(\rho_k)+V)|^{q(x)-2}\nabla_x(G'(\rho_k)+V)$. Then, we obtain after integration over $[0,T]$ that

$$\frac{1}{h}\sum_{k=1}^{(T/h)}\int_{h(k-1)}^{hk}\left[\int_\Omega\left(G(\rho_{k-1})+\rho_{k-1}V\right)\mathrm{d}x - \int_\Omega\left(G(\rho_k)+\rho_k V\right)\mathrm{d}x\right]u(t)\mathrm{d}t \geq \int_0^T\int_\Omega\frac{<\omega_k, \nabla_x\left(G'(\rho_k)+V\right)>}{p(x)}\rho_k u(t)\mathrm{d}t\mathrm{d}x. \tag{88}$$

We use $p(x)\leq p_+$ and $\tau = (h/p_+)$ in (87), and we have

$$\frac{1}{h}\sum_{k=1}^{(T/h)}\int_{h(k-1)}^{hk}\left[\int_\Omega\left(G(\rho_{k-1})+\rho_{k-1}V\right)\mathrm{d}x - \int_\Omega\left(G(\rho_k)+\rho_k V\right)\mathrm{d}x\right]u(t)\mathrm{d}t \geq \int_0^T\int_\Omega <\omega^\tau, \nabla_x\left(G'\left(\rho^\tau\right)+V\right)>\rho^\tau u(t)\mathrm{d}t\mathrm{d}x, \tag{89}$$

where ρ^τ is defined as follows:

$$\rho^\tau(t,x) = \rho_k(x), \quad \text{if } t\in\,]\tau(k-1),\tau k], \ \rho^\tau(0,x) = \rho_0(x), \tag{90}$$

and $\omega^\tau = |\nabla_x (G'(\rho^\tau) + V)|^{q(x)-2} \nabla_x (G'(\rho^\tau) + V)$.

Using the fact that suppu $\subset [-T, T]$, we have

$$\frac{1}{\tau} \sum_{k=1}^{(T/\tau)} \int_{\tau(k-1)}^{\tau k} \left[\int_\Omega (G(\rho_{k-1}) + \rho_{k-1} V) \mathrm{d}x - \int_\Omega (G(\rho_k) + \rho_k V) \mathrm{d}x \right] u(t) \mathrm{d}t = \frac{1}{\tau} \int_0^\tau \int_\Omega (G(\rho_0) + \rho_0 V) u(t) \mathrm{d}t \mathrm{d}x + \int_0^{T-\tau} \left(\frac{u(t+\tau) - u(t)}{\tau} \right) \int_\Omega (G(\rho^\tau) + \rho^\tau V) \mathrm{d}t \mathrm{d}x. \tag{91}$$

Recalling inequalities (88) and (89), we get

$$\int_0^T \int_\Omega < \omega^\tau, \nabla_x (G'(\rho^\tau) + V) > \rho^\tau u(t) \mathrm{d}t \mathrm{d}x \leq \frac{1}{\tau} \int_0^\tau \int_\Omega (G(\rho_0) + \rho_0 V) u(t) \mathrm{d}t \mathrm{d}x + \int_0^{T-\tau} \left(\frac{u(t+\tau) - u(t)}{\tau} \right) \int_\Omega (G'(\rho^\tau) + \rho^\tau V) \mathrm{d}t \mathrm{d}x. \tag{92}$$

We tend τ toward 0, and we obtain

$$\lim \sup_{\tau \longrightarrow 0} \int_{[0,T]\times\Omega} < \rho^\tau \omega^\tau, \nabla_x (G'(\rho^\tau) + V) > u(t) \mathrm{d}t \mathrm{d}x \leq \int_\Omega (G(\rho_0) + \rho_0 V) u(0) \mathrm{d}x + \int_{[0,T]\times\Omega} (G'(\rho^\tau) + \rho V) u'(t) \mathrm{d}t \mathrm{d}x. \tag{93}$$

From the strict convexity of $G \in C^1(]0, \infty[)$, we derive that

$$\begin{aligned} G(\rho_0) &= \rho_0 G'(\rho_0) - G^*(G'(\rho_0)), \text{ and } G(\rho) \\ &= \rho G'(\rho) - G^*(G(\rho)), \end{aligned} \tag{94}$$

where G^* is a Legendre transform of G.

We conclude the proof of claim 2 by using (92) in (93).

Claim 3:

$$\int_{[0,T]\times\Omega} < \rho\omega, \nabla_x (G'(\rho) + V) > u(t) \mathrm{d}t \mathrm{d}x \geq \int_\Omega [\rho_0 G'(\rho_0) - G^*(G'(\rho_0))] u(0) \mathrm{d}x + \int_{[0,T]\times\Omega} [\rho G(\rho) - G^*(G'(\rho))] u'(t) \mathrm{d}t \mathrm{d}x + \int_{[0,T]\times\Omega} \rho V u'(t) \mathrm{d}t \mathrm{d}x + \int_\Omega \rho_0 V u(0) \mathrm{d}x. \tag{95}$$

□

Proof 6. Define $\psi(t, x) = (G'(\rho) + V) u(t)$, for $(t, x) \in [0, T] \times \Omega$.

$\psi \in W^{1,q(x)}([0, T] \times \Omega)$, and then we approximate ψ by $C_c^\infty(\mathbb{R} \times \mathbb{R}^d)$-functions, and (70) becomes

$$\frac{1}{h} \sum_{k=1}^{(T/h)} \int_{h(k-1)}^{hk} \int_\Omega (\rho_{k-1} - \rho_k) \psi(t, x) \mathrm{d}t \mathrm{d}x - \int_{[0,T]\times\Omega} < \rho^h \omega^h, (\nabla_x (G')(\rho) + V) > u(t) \mathrm{d}t \mathrm{d}x = o(h), \tag{96}$$

where $o(h)$ converges to 0 when h tends to 0. As in (89), we have

$$\frac{1}{h}\sum_{k=1}^{(T/h)}\int_{h(k-1)}^{hk}\int_{\Omega}(\rho_{k-1}-\rho_k)\psi(t,x)\mathrm{d}t\mathrm{d}x=\frac{1}{h}\int_0^h\int_{\Omega}\rho_0\psi(t,x)\mathrm{d}t\mathrm{d}x+\int_h^T\int_{\Omega}\rho^h\partial_t^{-h}\psi(t,x)\mathrm{d}t\mathrm{d}x, \tag{97}$$

where $\partial_t^{-h}\psi(t,x)=(\psi(t,x)-\psi(t-h,x)/h)$.

Using (96), (97) becomes

$$\frac{1}{h}\int_0^h\int_{\Omega}\psi(t,x)\rho_0\mathrm{d}t\mathrm{d}x+\int_h^T\int_{\Omega}\rho^h\partial_t^{-h}\psi(t,x)\mathrm{d}t\mathrm{d}x-\int_{[0,T]\times\Omega}<\rho^h\omega^h,\nabla_x\left(\left(G'\right)(\rho)+V\right)>u(t)\mathrm{d}t\mathrm{d}x=o(h). \tag{98}$$

We tend h to 0 in (98) and use the fact that ρ^h converges strongly to ρ in $L^{q(x)}([0,T]\times\Omega)$ and ω^h weakly to ω in $L^{q(x)}([0,T]\times\Omega)$ to get

$$\int_{\Omega}\rho_0\left[G'\left(\rho_0\right)+V\right]u(0)\mathrm{d}x+\lim_{h\longrightarrow 0}\int_0^T\int_{\Omega}\rho\partial_t^{-h}\psi(t,x)\mathrm{d}t\mathrm{d}x-\int_{[0,T]\times\Omega}<\rho\omega,\nabla_x\left(\left(G'\right)(\rho)+V\right)>u(t)\mathrm{d}t\mathrm{d}x=0. \tag{99}$$

By using

$$\rho\partial^{-h}\psi(t,x)=\rho G'(\rho)\partial_t^{-h}u(t)+\rho V\partial_t^{-h}u(t)+\frac{1}{h}\rho u(t-h)\left[G'(\rho)-G'(\rho(t-h,x))\right] \tag{100}$$

$$\rho\left[G'(\rho)-G'(\rho(t-h,x))\right]\geq G^*\left(G'(\rho)\right)-G^*\left(G'(\rho(t-h,x))\right), \tag{101}$$

we have

$$\begin{aligned}\rho\partial^{-h}\psi(t,x)&\geq\rho G'(\rho)\partial_t^{-h}u(t)+\rho V\partial_t^{-h}u(t)+\frac{1}{h}u(t-h)\left[G^*\left(G'(\rho)\right)-G^*\left(G'(\rho(t-h,x))\right)\right]\\&=\left[\rho G'(\rho)-G^*\left(G'(\rho)\right)\right]\partial_t^{-h}u(t)+\rho V\partial_t^{-h}u(t)+\frac{1}{h}\left[G^*\left(G'(\rho)\right)u(t)-G^*\left(G'(\rho(t-h,x))\right)u(t-h)\right].\end{aligned} \tag{102}$$

Next, after integration of the inequality above, we have

$$\begin{aligned}\int_0^T\int_{\Omega}\rho\partial^{-h}\psi(t,x)\mathrm{d}t\mathrm{d}x&\geq\int_0^T\int_{\Omega}\left[\rho G'(\rho)-G^*\left(G'(\rho)\right)\right]\partial_t^{-h}u(t)\mathrm{d}t\mathrm{d}x\\&+\int_0^T\int_{\Omega}\rho V\partial_t^{-h}u(t)\mathrm{d}t\mathrm{d}x+\frac{1}{h}\int_0^T\int_{\Omega}\left[G^*\left(G'(\rho)\right)u(t)-G^*\left(G'(\rho(t-h,x))\right)u(t-h)\right]\mathrm{d}t\mathrm{d}x.\end{aligned} \tag{103}$$

Note that

$$\begin{aligned}&\frac{1}{h}\int_0^T\int_\Omega\left[G^*\left(G'(\rho)\right)u(t)-G^*\left(G'(\rho(t-h,x))\right)u(t-h)\right]\mathrm{d}t\mathrm{d}x\\&=\frac{1}{h}\int_0^T\int_\Omega G^*\left(G'(\rho)\right)u(t)\mathrm{d}t\mathrm{d}x-\frac{1}{h}\int_0^T\int_\Omega\left[G^*\left(G'(\rho(t-h,x))\right)u(t-h)\right]\mathrm{d}t\mathrm{d}x,\end{aligned}\tag{104}$$

$$\frac{1}{h}\int_0^T\int_\Omega\left[G^*\left(G'(\rho(t-h,x))\right)u(t-h)\right]\mathrm{d}t\mathrm{d}x=\frac{1}{h}\sum_{k=1}^{(T/h)}\int_{h(k-1)}^{hk}\int_\Omega\left[G^*\left(G'(\rho(t-h,x))\right)u(t-h)\right]\mathrm{d}t\mathrm{d}x.\tag{105}$$

Using the change of variable $s=t-h$ in (105), we obtain

$$\int_{h(k-1)}^{hk}\int_0^T\int_\Omega\left[G^*\left(G'(\rho(t-h,x))\right)u(t-h)\right]\mathrm{d}t\mathrm{d}x=\int_{h(k-2)}^{h(k-1)}\int_0^T\int_\Omega\left[G^*\left(G'(\rho(t-h,x))\right)u(t-h)\right]\mathrm{d}t\mathrm{d}x,\quad\text{for all } k\geq 2.\tag{106}$$

We combine (106) and (105) to deduce that

$$\begin{aligned}&\frac{1}{h}\int_0^T\int_\Omega G^*\left(G'(\rho(t-h,x))\right)u(t-h)\mathrm{d}t\mathrm{d}x\\&=\frac{1}{h}\int_0^h\int_\Omega\left[G^*\left(G'(\rho(t-h,x))\right)u(t-h)\right]\mathrm{d}t\mathrm{d}x+\frac{1}{h}\sum_{k=2}^{(T/h)}\int_{h(k-2)}^{h(k-1)}\int_\Omega G^*\left(G'(\rho(t-h,x))\right)u(t)\mathrm{d}t\mathrm{d}x\\&=\frac{1}{h}\int_0^h\int_\Omega G^*\left(G'(\rho(t-h,x))\right)u(t-h)\mathrm{d}t\mathrm{d}x+\frac{1}{h}\int_0^{T-h}\int_\Omega G^*\left(G'(\rho(t-h,x))\right)u(t)\mathrm{d}t\mathrm{d}x.\end{aligned}\tag{107}$$

Now, we use (107) in (108) to derive

$$\begin{aligned}&\frac{1}{h}\int_0^T\int_\Omega\left[G^*\left(G'(\rho)\right)u(t)-G^*\left(G'(\rho(t-h,x))\right)u(t-h)\right]\mathrm{d}t\mathrm{d}x\\&=-\frac{1}{h}\int_0^h\int_\Omega\left[G^*\left(G'(\rho(t-h,x))\right)u(t-h)\right]+\frac{1}{h}\int_{T-h}^T\int_\Omega G^*\left(\rho(t,x)\right)u(t)\mathrm{d}t\mathrm{d}x.\end{aligned}\tag{108}$$

So, (103) becomes

$$\begin{aligned}&\int_0^T\int_\Omega\rho\partial^{-h}\psi(t,x)\mathrm{d}t\mathrm{d}x\geq\int_0^T\int_\Omega\left[\rho G'(\rho)-G^*\left(G'(\rho)\right)\right]\partial_t^{-h}u(t)\mathrm{d}t\mathrm{d}x\\&+\int_0^T\int_\Omega\rho V\partial_t^{-h}u(t)\mathrm{d}t\mathrm{d}x-\frac{1}{h}\int_0^h\int_\Omega G^*\left(G'(\rho)\right)u(t-h)\mathrm{d}t\mathrm{d}x+\frac{1}{h}\int_{T-h}^T\int_\Omega G^*\left(G'(\rho(t,x))\right)u(t)\mathrm{d}t\mathrm{d}x.\end{aligned}\tag{109}$$

Since $\mathrm{supp}(u) \subset [-T, T]$, then

$$\lim_{h\longrightarrow 0} \frac{1}{h} \int_{T-h}^{T} \int_{\Omega} G^{*}\left(G'\left(\rho\left(t,x\right)\right)\right) u\left(t\right) \mathrm{d}t\mathrm{d}x = \int_{\Omega} G^{*}\left(G'\left(\rho\left(T,x\right)\right)\right) u\left(T\right) \mathrm{d}x = 0. \tag{110}$$

We deduce that

$$\lim_{h\longrightarrow 0} \int_{0}^{T} \int_{\Omega} \rho \partial^{-h} \psi\left(t,x\right) \mathrm{d}t\mathrm{d}x \geq \int_{0}^{T} \int_{\Omega} \left[\rho G'\left(\rho\right) - G^{*}\left(G'\left(\rho\right)\right)\right] u'\left(t\right) \mathrm{d}t\mathrm{d}x + \int_{0}^{T} \int_{\Omega} \rho V u'\left(t\right) \mathrm{d}t\mathrm{d}x - \int_{\Omega} G^{*}\left(G'\left(\rho_{0}\right)\right) u\left(0\right) \mathrm{d}x. \tag{111}$$

Now, we combine (99) and (111) to obtain

$$\begin{aligned} &\int_{0}^{T} \int_{\Omega} \left[\rho G'\left(\rho\right) - G^{*}\left(G'\left(\rho\right)\right)\right] u'\left(t\right) \mathrm{d}t\mathrm{d}x + \int_{0}^{T} \int_{\Omega} \rho V u'\left(t\right) \mathrm{d}t\mathrm{d}x \\ &\quad - \int_{\Omega} G^{*}\left(G'\left(\rho_{0}\right)\right) u\left(0\right) \mathrm{d}x + \int_{\Omega} \rho_{0} \left[G'\left(\rho_{0}\right) + V\right] u\left(0\right) \mathrm{d}x \\ &\quad - \int_{[0,T]\times\Omega} < \rho\omega, \nabla_{x}\left(\left(G'\right)\left(\rho\right) + V\right) > u\left(t\right) \mathrm{d}t\mathrm{d}x \leq 0. \end{aligned} \tag{112}$$

Finally, we conclude that

$$\begin{aligned} &\int_{0}^{T} \int_{\Omega} \left[\rho G'\left(\rho\right) - G^{*}\left(G'\left(\rho\right)\right)\right] u'\left(t\right) \mathrm{d}t\mathrm{d}x + \int_{0}^{T} \int_{\Omega} \rho V u'\left(t\right) \mathrm{d}t\mathrm{d}x + \int_{\Omega} \rho_{0} V u\left(0\right) \mathrm{d}x \\ &\quad + \int_{\Omega} \left[\rho_{0} G'\left(\rho_{0}\right) - G^{*}\left(G'\left(\rho_{0}\right)\right)\right] u\left(0\right) \mathrm{d}x \\ &\int_{[0,T]\times\Omega} < \rho\omega, \nabla_{x}\left(\left(G'\right)\left(\rho\right) + V\right) > u\left(t\right) \mathrm{d}t\mathrm{d}x. \end{aligned} \tag{113}$$

This completes the proof of claim 3.

Now, we are ready to show that the sequence $(\mathrm{div}_{x}(\rho^{h}\omega^{h}))_{h}$ converges weakly to $\mathrm{div}_{x}(\rho|\nabla_{x}(G'(\rho)+V)|)^{q(x)-2}\nabla_{x}(G'(\rho)+V)$ in $[C_{c}^{\infty}(\mathbb{R}\times\mathbb{R}^{d})]\prime$. Let $\psi \in C_{c}^{\infty}(\mathbb{R}^{d})$ and $u \in C_{c}^{\infty}(\mathbb{R})$ be some positive functions such that $\mathrm{supp}(u) \subset [-T, T]$, with $0 < T < \infty$. For $\epsilon \neq 0$, we define $\psi_{\epsilon}(t,x) = G'(\rho) + V - \epsilon\psi$, and then

$$\int_{[0,T]\times\Omega} \rho^{h} < \omega^{h} - \left|\nabla_{x}\psi_{\epsilon}\right|^{q(x)-2} \nabla_{x}\psi_{\epsilon}, \nabla_{x}\left(G'\left(\rho^{h}\right) + V\right) - \nabla_{x}\psi_{\epsilon} > u\left(t\right) \mathrm{d}t\mathrm{d}x \geq 0. \tag{114}$$

So, we obtain

$$\begin{aligned} &\int_{[0,T]\times\Omega} \rho^{h} < \omega^{h}, \nabla_{x}\left(G'\left(\rho^{h}\right) + V\right) < u\left(t\right) \mathrm{d}t\mathrm{d}x - \int_{[0,T]\times\Omega} \rho^{h} < \omega^{h}, \nabla_{x}\psi_{\epsilon} > u\left(t\right) \mathrm{d}t\mathrm{d}x \\ &\quad + \int_{[0,T]\times\Omega} \rho^{h} < \left|\nabla_{x}\psi_{\epsilon}\right|^{q(x)-2} \nabla_{x}\psi_{\epsilon}, \nabla_{x}\psi_{\epsilon} - \nabla_{x}\left(G'\left(\rho^{h}\right) + V\right) > u\left(t\right) \mathrm{d}t\mathrm{d}x \geq 0. \end{aligned} \tag{115}$$

We use Lemma 3 and we tend h to 0 in (115), and then we get

$$\int_{[0,T]\times\Omega}\rho<\omega^h,\nabla_x\left(G'\left(\rho^h\right)+V\right)<u(t)\mathrm{d}t\mathrm{d}x-\int_{[0,T]\times\Omega}\rho<\omega^h,\nabla_x\psi_\epsilon>u(t)\mathrm{d}t\mathrm{d}x+\int_{[0,T]\times\Omega}\rho<\left|\nabla_x\psi_\epsilon\right|^{q(x)-2}\nabla_x\psi_\epsilon,\nabla_x\psi_\epsilon-\nabla_x\left(G'\left(\rho^h\right)+V\right)>u(t)\mathrm{d}t\mathrm{d}x\geq 0. \tag{116}$$

So,

$$\int_{[0,T]\times\Omega}\rho<\omega-\left|\nabla_x\psi_\epsilon\right|^{q(x)-2}\nabla_x\psi_\epsilon,\epsilon\nabla_x\psi>u(t)\mathrm{d}t\mathrm{d}x\geq 0. \tag{117}$$

Dividing (116) by $\epsilon>0$ and tending ϵ to 0, we reach

$$\int_{[0,T]\times\Omega}\rho<\omega-\left|\nabla_x\left(G'(\rho)V\right)\right|^{q(x)-2}\nabla_x\left(G'(\rho)V\right),\nabla_x\psi>u(t)\mathrm{d}t\mathrm{d}x\geq 0. \tag{118}$$

By replacing ψ by $-\psi$, we have

$$\int_{[0,T]\times\Omega}\rho<\omega-\left|\nabla_x\left(G'(\rho)V\right)\right|^{q(x)-2}\nabla_x\left(G'(\rho)V\right),\nabla_x\psi>u(t)\mathrm{d}t\mathrm{d}x=0, \tag{119}$$

for all test functions $\psi\in C_c^\infty(\mathbb{R}^d)$ and $u\in C_c^\infty(\mathbb{R})$ such that $\mathrm{supp}(u)\subset[-T,T]$.

Thus, we conclude that $(\mathrm{div}_x(\rho^h\omega^h))_h$ converges weakly to $\mathrm{div}_x(\rho|\nabla_x(G'(\rho)V)|^{q(x)-2}\nabla_x(G'(\rho)V))$ in $[C_c^\infty(\mathbb{R}\times\mathbb{R}^d)]\prime$. □

3.3. Proof of the Theorem of the Laplacian Parabolic Equation. Here, we use the strong convergence of the sequence $(\rho^h)_h$ to ρ in $L^{q(x)}([0,T]\times\Omega)$ and the weak convergence of the nonlinear term $(\mathrm{div}_x(\rho^h\omega^h))_h$ to $\mathrm{div}_x(\rho|\nabla_x(G'(\rho)V)|^{q(x)-2}\nabla_x(G'(\rho)V))$ in $[C_c^\infty(\mathbb{R}\times\mathbb{R}^d)]\prime$, and we establish that $\rho(t,x)$ is a weak solution of the $q(x)$-Laplacian parabolic equation. Let $\psi\in C_c^\infty(\mathbb{R}\times\mathbb{R}^d)$ be a test function such that $\mathrm{supp}\psi(.,x)\subset[-T,T]$. By using (71), we obtain

$$\frac{1}{h}\sum_{k=1}^{(T/h)}\int_{[h(k-1),\mathrm{hk}]\times\Omega}\left(\rho_{k-1}-\rho_k\right)\psi(t,x)\mathrm{d}t\mathrm{d}x-\int_{[0,T]\times\Omega}\rho^h<\omega^h,\nabla_x\psi>\mathrm{d}t\mathrm{d}x=0(h), \tag{120}$$

where $o(h)$ tends to 0 when h tends to 0.

Note that

$$\frac{1}{h}\sum_{k=1}^{(T/h)}\int_{[h(k-1),\mathrm{hk}]\times\Omega}\left(\rho_{k-1}-\rho_k\right)\psi(t,x)\mathrm{d}t\mathrm{d}x=\frac{1}{h}\int_0^h\int_\Omega\rho_0\psi(t,x)\mathrm{d}t\mathrm{d}x+\int_h^{T-h}\int_\Omega\rho^h\bar{\partial}_t^{-h}\psi(t,x)\mathrm{d}t\mathrm{d}x. \tag{121}$$

Then, (120) becomes

$$\frac{1}{h}\int_0^h\int_\Omega\rho_0\psi(t,x)\mathrm{d}t\mathrm{d}x+\int_h^{T-h}\int_\Omega\rho^h\bar{\partial}_t^{-h}\psi(t,x)\mathrm{d}t\mathrm{d}x-\int_{[0,T]\times\Omega}\rho^h<\omega^h,\quad\nabla_x\psi>dt\mathrm{d}x=o(h). \tag{122}$$

Finally, we tend h to 0 in (122), and we use the fact that ρ^h converges strongly to ρ and that $(\mathrm{div}_x(\rho^h\omega^h))_h$ converges weakly to $\mathrm{div}_x(\rho|\nabla_x(G'(\rho)V)|^{q(x)-2}\nabla_x(G'(\rho)V))$:

$$\int_\Omega\rho_0\psi(0,x)\mathrm{d}x+\int_{[0,T]\times\Omega}\rho\frac{\partial\psi}{\partial t}\mathrm{d}t\mathrm{d}x-\int_{[0,T]\times\Omega}\rho<\left|\nabla_x\left(G'(\rho)+V\right)\right|^{q(x)-2}\nabla_x\left(G'(\rho)+V\right),\nabla_x\psi>\mathrm{d}t\mathrm{d}x=0. \tag{123}$$

We deduce that

$$\int_{[0,T]\times\Omega}\rho < \frac{\partial\psi}{\partial t} - \left|\nabla_x\left(G'(\rho)+V\right)\right|^{q(x)-2}\nabla_x\left(G'(\rho)+V\right),$$
$$\nabla_x\psi > \mathrm{d}t\mathrm{d}x = -\int_\Omega \rho_0\psi(0,x)\mathrm{d}x. \tag{124}$$

It follows that $\rho(t,x)$ is a weak solution of a nonlinear $q(x)$-Laplacian parabolic equation.

4. Asymptotic Behavior

In this section, we give the proof of Theorem 2 which is derived from the following three lemmas.

Lemma 4. *Let ρ_1 and ρ_2 be two probability densities on Ω. Assume that V satisfies (H_V^2). If $T^+_{\#}\rho_1 = \rho_2$ is the solution of the Monge problem*

$$(M_+):\ \inf_{T^+_{\#}\rho_1=\rho_2}\int_\Omega \left|x - T^+\right|(x)^{p_+}\rho_1\mathrm{d}x, \tag{125}$$

then

$$E(\rho_1) - E(\rho_2) + \frac{\lambda}{2^{p_+}}W^{p_+}_{p(.)}(\rho_1,\rho_2) \le \int_\Omega < x - T^+(x), \nabla_x\left(G'(\rho_1)+V\right) > \rho_1\mathrm{d}x. \tag{126}$$

In particular, if $\rho_\infty \in P(\Omega)$ satisfies $\rho_\infty\nabla_x(G'(\rho_\infty)+V) = 0$, then

$$W^{p_+}_{p(.)}(\rho,\rho_\infty) \le \frac{2^{p_+}}{\lambda}\left[E(\rho) - E(\rho_\infty)\right], \tag{127}$$

for all $\rho \in P(\Omega)$.

Here, $W_{p(.)}$ is the $p(.)$-Wasserstein distance defined in (5).

Proof 7. Let $\rho_1,\rho_2 \in P(\Omega)$. Fix $p_+ = \sup_\Omega p(x) > 1$. It is known from the work in [8] that the Monge problem

$$(M_+):\ \inf_{T^+_{\#}\rho_1=\rho_2}\int_\Omega \left|x - T^+\right|(x)^{p_+}\rho_1\mathrm{d}x, \tag{128}$$

admits a unique solution T^+. Therefore, since G and V satisfy, respectively, (H_G) and (H_V^2), then

$$E(\rho_1) - E(\rho_2) + \lambda W^{p_+}_{p_+}(\rho_1,\rho_2) \le \int_\Omega < x - T^+, \nabla_x\left(G'(\rho_1)+V\right) > \rho_1\mathrm{d}x, \tag{129}$$

where $\int_\Omega |x - T^+|^{p_+}\rho_1\mathrm{d}x = W^{p_+}_{p_+}(\rho_1,\rho_2)$ and W_{p_+} is the p_+-Wasserstein distance.

The continuous injection $L^{p_+}_{\rho_1}(\Omega)\hookrightarrow L^{p(.)}_{\rho_1}(\Omega)$ implies that

$$W_{p(.)}(\rho_1,\rho_2) \le 2W_{p_+}(\rho_1,\rho_2). \tag{130}$$

So, we use (129) and (128) to derive

$$E(\rho_1) - E(\rho_2) + \frac{\lambda}{2^{p_+}}W^{p_+}_{p(.)}(\rho_1,\rho_2) \le \int_\Omega < x - T^+, \nabla_x\left(G'(\rho_1)+V\right) > \rho_1\mathrm{d}x. \tag{131}$$

In particular, if $\rho_1 = \rho_\infty \in P(\Omega)$ satisfies $\rho_\infty\nabla_x(G'(\rho_\infty)+V) = 0$ and $\rho_2 = \rho \in P(\Omega)$, then

$$E(\rho_\infty) - E(\rho) + \frac{\lambda}{2^{p_+}}W^{p_+}_{p(.)}(\rho_\infty,\rho) \le 0. \tag{132}$$

So, we have

$$W^{p_+}_{p(.)}(\rho_\infty,\rho) \le \frac{2^{p_+}}{\lambda}\left[E(\rho) - E(\rho_\infty)\right], \tag{133}$$

for all $\rho \in P(\Omega)$.

Note that ρ_∞ is a stationary solution of the $q(x)$-Laplacian parabolic equation, which minimizes the functional $E(\rho) = \int_\Omega (G(\rho) + \rho V)\mathrm{d}x$ on $P(\Omega)$. □

Lemma 5. *Let $\rho_1,\rho_2 \in P(\Omega)$. Then,*

$$E(\rho_1) - E(\rho_2) \le \frac{2^{p_+\prime}}{\lambda^{p_+\prime}}\left\|\nabla_x\left(G'(\rho_1)+V\right)\right\|^{p_+'}_{L^{q(.)}_{\rho_1}(\Omega)}, \tag{134}$$

with $p_+' = (p_+/(p_+-1))$.

Proof 8. We applied Young's inequality to obtain

$$< x - T_+, \nabla_x\left(G'(\rho_1)+V\right) > \le \mu\left|x - T_+\right|^{p_+} + \frac{1}{\mu^{p_+\prime}}\left|\nabla_x\left(G'(\rho_1)+V\right)\right|^{p_+\prime}, \tag{135}$$

where $\mu > 0$ and $p_+' = (p_+/(p_+-1))$. Then,

$$\int_\Omega < x - T_+, \nabla_x\left(G'(\rho_1)+V\right) > \rho_1\mathrm{d}x \le \mu\int_\Omega\left|x - T_+\right|^{p_+}\rho_1\mathrm{d}x + \frac{1}{\mu^{p_+\prime}}\int_\Omega\left|\nabla_x\left(G'(\rho_1)+V\right)\right|^{p_+\prime}\rho_1\mathrm{d}x, \tag{136}$$

and since $p_+' \le q(x)$, we use the continuous injection $L^{q(.)}_{\rho_1}(\Omega)\hookrightarrow L^{p_+}_{\rho_1}(\Omega)$, and we get

$$\int_\Omega\left|\nabla_x\left(G'(\rho_1)+V\right)\right|^{p_+\prime}\rho_1\mathrm{d}x \le 2^{p_+\prime}\left\|\nabla_x\left(G'(\rho_1)+V\right)\right\|^{p_+'}_{L^{q(.)}_{\rho_1}(\Omega)}. \tag{137}$$

Now, we combine (128), (137), and (136) to obtain

$$E(\rho_1) - E(\rho_2) + (\lambda - \mu) W_{p_+}^{p_+}(\rho_1, \rho_2) \leq \frac{2^{p_+'}}{\mu^{p_+'}} \left\| \nabla_x (G'(\rho_1) + V) \right\|_{L_{\rho_1}^{q(\cdot)}(\Omega)}^{p_+'}. \tag{138}$$

In particular, if $\mu = \lambda$, we obtain (135). □

Lemma 6.

$$\left\| \nabla_x (G'(\rho_1) + V) \right\|_{L_{\rho_1}^{q(\cdot)}(\Omega)}^{p_+'} \leq \mathrm{Max}\left\{ \int_\Omega \left| \nabla_x (G'(\rho_1) + V) \right|^{q(x)} \rho_1 \mathrm{d}x, \left(\int_\Omega \nabla_x (G'(\rho_1) + V)^{q(x)} \rho_1 \mathrm{d}x \right)^{(1/q_+)} \right\}. \tag{139}$$

Proof 9. From [9], we get

$$\left\| \nabla_x (G'(\rho_1) + V) \right\|_{L_{\rho_1}^{q(\cdot)}(\Omega)}^{q_-} \leq \int_\Omega \left| \nabla_x (G'(\rho_1) + V) \right|^{q(x)} \rho_1 \mathrm{d}x, \quad \text{if } \left\| \nabla_x (G'(\rho_1) + V) \right\|_{L_{\rho_1}^{q(\cdot)}(\Omega)} \geq 1, \tag{140}$$

and

$$\left\| \nabla_x (G'(\rho_1) + V) \right\|_{L_{\rho_1}^{q(\cdot)}(\Omega)}^{p_+'} \leq \int_\Omega \left| \nabla_x (G'(\rho_1) + V) \right|^{q(x)} \rho_1 \mathrm{d}x, \quad \text{if } \left\| \nabla_x (G'(\rho_1) + V) \right\|_{L_{\rho_1}^{q(\cdot)}(\Omega)} < 1. \tag{141}$$

Since $1 < p_+' \leq q_-$, we have

$$\left\| \nabla_x (G'(\rho_1) + V) \right\|_{L_{\rho_1}^{q(\cdot)}(\Omega)}^{p_+'} \leq \left| \nabla_x (G'(\rho_1) + V) \right|^{q(x)} \rho_1 \mathrm{d}x, \quad \text{if } \left\| \nabla_x (G'(\rho_1) + V) \right\|_{L_{\rho_1}^{q(\cdot)}(\Omega)} \geq 1, \tag{142}$$

$$\left\| \nabla_x (\dot{G}(\rho_1) + V) \right\|_{L_{\rho_1}^{q(\cdot)}(\Omega)}^{p_+'} \leq \left\| \nabla_x (G'(\rho_1) + V) \right\|_{L_{\rho_1}^{q(\cdot)}(\Omega)}, \quad \text{if } \left\| \nabla_x \left(G\prime(\rho_1) + V \right) \right\|_{L_{\rho_1}^{q(\cdot)}(\Omega)} < 1. \tag{143}$$

By using (141), we derive that

$$\left\| \nabla_x (G'(\rho_1) + V) \right\|_{L_{\rho_1}^{q(\cdot)}(\Omega)} \leq \left(\int_\Omega \left| \nabla_x (G'(\rho_1) + V) \right|^{q(x)} \rho_1 \mathrm{d}x \right)^{(1/q_+)}, \quad \text{if } \left\| \nabla_x (G'(\rho_1) + V) \right\|_{L_{\rho_1}^{q(\cdot)}(\Omega)} < 1. \tag{144}$$

Next, we combine (143) and (144) to derive

$$\left\| \nabla_x (G'(\rho_1) + V) \right\|_{L_{\rho_1}^{q(\cdot)}(\Omega)}^{p_+'} \leq \left(\int_\Omega \left| \nabla_x (G'(\rho_1) + V) \right|^{q(x)} \rho_1 \mathrm{d}x \right)^{(1/q_+)}, \quad \text{if } \left\| \nabla_x (G'(\rho_1) + V) \right\|_{L_{\rho_1}^{q(\cdot)}(\Omega)} < 1. \tag{145}$$

By using (142) and (143), we obtain (140). □

4.1. Proof of Theorem 2. Let $\rho(t, x)$ be a solution of the $q(x)$-Laplacian parabolic equation. We have

$$\frac{d}{dt}\left[E(\rho(t,.)) - E(\rho_\infty)\right] = -\int_\Omega \left|\nabla_x\left(G'(\rho(t,x)) + V\right)\right|^{q(x)}\rho(t,x)\mathrm{d}x. \tag{146}$$

Define

$$I_1 := \left\{t \in [0,+\infty[, \quad \left\|\nabla_x\left(G'(\rho(t,.)) + V\right)\right\|_{L^{q(.)}_{\rho(t,.)}(\Omega)} \geq 1\right\}, \tag{147}$$

$$I_2 := \left\{t \in [0,+\infty[, \quad \left\|\nabla_x\left(G'(\rho(t,.)) + V\right)\right\|_{L^{q(.)}_{\rho(t,.)}(\Omega)} < 1\right\}. \tag{148}$$

We combine (135), (142), and (146) to get

$$\frac{d}{dt}\left[E(\rho(t,.)) - E(\rho_\infty)\right] \leq -\left(\frac{\lambda}{2}\right)^{p_+ + 1}\left[E(\rho(t,.)) - E(\rho_\infty)\right], \tag{149}$$

on I_1, and we combine (135), (145), and (146) to have

$$\frac{d}{dt}\left[E(\rho(t,.)) - E(\rho_\infty)\right] \leq -\left(\frac{\lambda}{2}\right)^{p_+ q_+}\left[E(\rho(t,.)) - E(\rho_\infty)\right]^{q_+}, \tag{150}$$

on I_2.

Next, we have after integration,

$$\left[E(\rho(t,.)) - E(\rho_\infty)\right] \leq \frac{\left[E(\rho(t_2,.)) - E(\rho_\infty)\right]}{\left[1 + (\lambda/2)^{p_+ q_+}(q_+ - 1)\left(E(\rho(t_2,.)) - E(\rho_\infty)\right)^{(q_+ - 1)}(t - t_2)\right]^{(1/q_+ - 1)}}, \tag{151}$$

on I_2, and

$$\left[E(\rho(t,.)) - E(\rho_\infty)\right]\right] \leq e^{-(\lambda/2)^{p_+ 1}}(t - t_1)\left[E(\rho_0) - E(\rho_\infty)\right], \tag{152}$$

on I_1.

To conclude, we use Lemma 4 and expressions (151) and (152), and then, the proof of Theorem 2 is complete.

5. Error Estimate

In this section, we provide in the L^2 norm an estimate of the gap between the approximate solution and the exact solution.

Lemma 7. *Assume that* (H_{ρ_0}), (H_G), $(H^{p(.)}_{q(.)})$, *and* (H^1_V) *hold. Let* $\rho = \rho(t,x)$ *be a weak solution of the q(x)-Laplacian parabolic equation and* $\rho^h = \rho^h(t,x)$ *be an approximate solution of the q(x)-Laplacian parabolic equation defined in (12). Then,*

$$\left\|\rho - \rho^h\right\|^2_{L^2([0,T]\times\Omega)} \leq C(T,N,M,\rho,\Omega,G,p(.),q(.))h, \tag{153}$$

where $C(T,N,M,\rho,\Omega,G,p(.),q(.))$ *is a constant depending on* $T,N,M,\rho,\Omega,G,p(.),q(.)$.

Proof 10. Since $\rho = \rho(t,x)$ is a weak solution of the $q(x)$-Laplacian parabolic equation, then

$$\rho(t,x) = \rho_{k-1}(x) + \int_{h(k-1)}^t \mathrm{div}_x(\rho)\left|\nabla_x\left(G'(\rho) + V\right)\right|^{q(x)-2}\nabla_x\left(G'(\rho) + V\right)\mathrm{d}s, \quad \text{for } t \in h(k-1), \mathrm{hk}. \tag{154}$$

Similarly, the approximate solution ρ^h satisfies

$$\rho^h(t,x) = \rho_{k-1}(x) + \int_{h(k-1)}^t \mathrm{div}_x\left(\rho^h\right)\left|\nabla_x\left(G'\left(\rho^h\right) + V\right)\right|^{q(x)-2}\nabla_x\left(G'\left(\rho^h\right) + V\right)\mathrm{d}s, \quad \text{for } t \in h(k-1), \mathrm{hk}. \tag{155}$$

We combine (154) and (155) to have

$$\rho(t,x) - \rho^h(t,x) = \int_{h(k-1)}^t \left[\left(\mathrm{div}_x\left(\rho\left|\nabla_x\left(G'(\rho) + V\right)\right|^{q(x)-2}\nabla_x\left(G'(\rho) + V\right)\right) - \mathrm{div}_x\left(\rho^h\left|\nabla_x\left(G'\left(\rho^h\right) + V\right)\right|^{q(x)-2}\nabla_x\left(G'\left(\rho^h\right) + V\right)\right)\right)\right]\mathrm{d}s. \tag{156}$$

We multiply (156) by $G'(\rho) - G'(\rho^h)$, and we integrate it on $[0,T]\times\Omega$. Consequently,

$$\int_{[0,T]\times\Omega}\left[\left[\rho(t,x)-\rho^h(t,x)\right]\left[G'(\rho)-G'\left(\rho^h\right)\right]\right]\mathrm{d}t\mathrm{d}x = -\int_{[0,T]\times\Omega}\int_{h(k-1)}^{t} <\rho|\sigma|^{q(x)-2}\sigma-\rho^h\left|\sigma^h\right|^{q(x)-2}\sigma^h, \sigma-\sigma^h> dt\mathrm{d}x\mathrm{d}s, \tag{157}$$

where $\sigma = \nabla_x(G'(\rho)+V)$ and $\sigma^h = \nabla_x(G'(\rho^h)+V)$.

Since $N\le\rho\le M$, $N\le\rho^h\le M$, and G is a convex function of class C^2, then $G''\ge 0$, and

$$\begin{aligned}&\left[\rho(t,x)-\rho^h(t,x)\right]\left[G'(\rho)-G'\left(\rho^h\right)\right]\\ &\quad= G''\left(\rho^h+\theta\left(\rho-\rho^h\right)\right)\left|\rho-\rho^h\right|^2\\ &\quad\ge k_0\left|\rho-\rho^h\right|^2,\end{aligned} \tag{158}$$

where $k_0 = \inf_{t\in[N;M]}G''(t)$ and $\theta\in(0;1)$. Then, we combine (157) and (158) to deduce that

$$\int_{[0,T]\times\Omega}\left|\rho(t,x)-\rho^h(t,x)\right|^2\mathrm{d}t\mathrm{d}x \le -\frac{1}{k_0}\left[\int_{[0,T]\times\Omega}\int_{h(k-1)}^{t} <\rho|\sigma|^{q(x)-2}\sigma-\rho^h\left|\sigma^h\right|^{q(x)-2}\sigma^h, \sigma-\sigma^h> \mathrm{d}t\mathrm{d}x\mathrm{d}s\right]. \tag{159}$$

Since $N\le\rho\le M$ and $N\le\rho^h\le M$, then

$$\begin{aligned}&-\frac{1}{k_0}\left[\int_{[0,T]\times\Omega}\int_{h(k-1)}^{t} <\rho|\sigma|^{q(x)-2}\sigma-\rho^h\left|\sigma^h\right|^{q(x)-2}\sigma^h, \sigma-\sigma^h> \mathrm{d}t\mathrm{d}x\mathrm{d}s\right]\\ &\le\frac{2M}{k_0}h\left[\left\||\sigma|^{q(x)-2}\sigma\right\|_{L^{p(\cdot)}([0,T]\times\Omega)}+\left\|\left|\sigma^h\right|^{q(x)-2}\sigma^h\right\|_{L^{p(\cdot)}([0,T]\times\Omega)}\right]\left[\|\sigma\|_{L^{q(\cdot)}([0,T]\times\Omega)}+\left\|\sigma^h\right\|_{L^{q(\cdot)}([0,T]\times\Omega)}\right].\end{aligned} \tag{160}$$

By using $\sigma = \nabla_x(G'(\rho)+V)$ and $\sigma^h = \nabla_x(G'(\rho^h)+V)$, we obtain

$$\left\|\sigma^h\right\|_{L^{q(\cdot)}([0,T]\times\Omega)} \le \max\left\{\left(\int_{[0,T]\times\Omega}\left|\nabla_x\left(G'\left(\rho^h\right)+V\right)\right|^{q(x)}\mathrm{d}t\mathrm{d}x\right)^{(1/q_+)}, \left(\int_{[0,T]\times\Omega}\left|\nabla_x\left(G'\left(\rho^h\right)+V\right)\right|^{q(x)}\mathrm{d}t\mathrm{d}x\right)^{(1/q_-)}\right\}, \tag{161}$$

$$\left\|\left|\sigma^h\right|^{q(x)-2}\sigma^h\right\|_{L^{p(\cdot)}([0,T]\times\Omega)} \le \max\left\{\left(\int_{[0,T]\times\Omega}\left|\nabla_x\left(G'\left(\rho^h\right)+V\right)\right|^{q(x)}\mathrm{d}x\mathrm{d}t\right)^{(1/p_+)}, \left(\int_{[0,T]\times\Omega}\left|\nabla_x\left(G'\left(\rho^h\right)+V\right)\right|^{q(x)}\mathrm{d}t\mathrm{d}x\right)^{(1/p_-)}\right\}. \tag{162}$$

By using (64), then

$$\int_{[0,T]\times\Omega}\left|\nabla_x\left(G'\left(\rho^h\right)+V\right)\right|^{q(x)}\mathrm{d}t\mathrm{d}x \le \frac{\mathrm{Tp}_+}{N}\left[\int_\Omega G(\rho_0)\mathrm{d}x - |\Omega|G\left(\frac{1}{|\Omega|}\right)+2\|V\|_{L^\infty(\Omega)}\right]. \tag{163}$$

Finally, we combine (159)–(163) to obtain the desired estimate:

$$\int_{[0,T]\times\Omega} \left|\rho(t,x) - \rho^h(t,x)\right|^2 \mathrm{d}t\mathrm{d}x \leq C(T,N,M,\Omega,G,p(.),q(.))h, \tag{164}$$

where $C(T,N,M,\Omega,G,p(.),q(.))$ is a constant depending on $T,N,M,\Omega,G,p(.),q(.)$. □

6. Numerical Example

Here, we give an illustration of our work by testing the algorithm on an example of the $q(x)$-Laplacian parabolic equation in the dimension equal to 1 for determining an approximate solution. We limit ourselves to the first-order approximation just for the sake of simplicity and to avoid cumbersome calculations. An error table is obtained from different values of step h, showing that the error values decrease to zero in the L^2−norm when h tends to zero, in relevance with the similarity between the graphical representations of both the analytical solution and the approximate solution.

$q(x)$-Laplacian parabolic equation is a nonhomogeneous equation and may be considered as a model of response over the time of nonhomogeneous media under the stress of a physical phenomenon. We suppose in our example that the functions p,V, and G in the $q(x)$-Laplacian parabolic equation are as follows:

$$\begin{aligned} V(x) &= \frac{x^2}{2}\chi_{[(1/2),(3/4))}, \quad \text{if } x \in (0,1), \\ q(x) &= \frac{5}{2}\chi_{(0,(1/2))\cup[(3/4),1)} + 2\chi_{[(1/2),(3/4))}, \\ G(x) &= \frac{9}{4}x^{\frac{3}{4}}\chi_{(0,(1/2))\cup[(3/4),1)} + x\ln(x)\chi_{[(1/2),(3/4))}, \quad \text{for } x \in (0,1). \end{aligned} \tag{165}$$

Consequently, the parabolic $q(x)$-Laplacian parabolic equation becomes the following couple of the linear Fokker–Planck equation and the (5/2)-Laplacian parabolic equation:

$$\begin{cases} \dfrac{\partial\rho}{\partial t} = \Delta_x\rho + \mathrm{div}_x(x\rho) \text{ in } [0,+\infty)\times\left[\dfrac{1}{2},\dfrac{3}{4}\right), \\ \dfrac{\partial\rho}{\partial t} = \mathrm{div}_x\left(\left|\nabla_x\rho\right|^{(1/2)}\nabla_x\rho\right) \text{in}[0,+\infty) \\ \quad \times\left(0,\dfrac{1}{2}\right)\cup[0,+\infty[\times\left[\dfrac{3}{4},1\right). \end{cases} \tag{166}$$

One can assimilate the set $(0,1)$ to a nonhomogeneous composite rod of length 1 cast in two distinct materials and made of a main piece $[(1/2),(3/4))$ surrounded at its extremities by two other pieces $(0,(1/2))$ and $[(3/4),1)$. The nonhomogeneity is characterized by the two different constant values taken by the variable exponent $q(x)$ on the distinct pieces of the rod.

Let us express the solution of the linear Fokker–Planck equation

$$\frac{\partial\rho}{\partial t} = \Delta_x\rho + \mathrm{div}_x(x\rho), \tag{167}$$

in the form

$$\begin{aligned} \rho(t,x) &= e^t u(\tau,y), \\ (\tau,y) &= \left(\frac{1}{2}e^{2t}, e^t x\right), \end{aligned} \tag{168}$$

where $u(\tau,y)$ is an unknown function, supposed to be a solution of the heat equation

$$\frac{\partial u}{\partial\tau} = \Delta_y u. \tag{169}$$

Thus, after a simple computation, we have that

$$\begin{aligned} \frac{\partial\rho}{\partial t} &= e^t u(\tau,y) + e^{3t}\frac{\partial u}{\partial\tau} + xe^{2t}\frac{\partial u}{\partial y}, \\ \Delta_x\rho &= e^{3t}\Delta_y u, \\ \mathrm{div}_x(x\rho) &= e^t u(\tau,y) + xe^{2t}\frac{\partial u}{\partial y}. \end{aligned} \tag{170}$$

So, if $u = u(t,x)$ satisfies

$$\frac{\partial u}{\partial\tau} = \Delta_y u, \tag{171}$$

then $\rho(t,x) = e^t u(\tau,y)$ satisfies

$$\frac{\partial\rho}{\partial t} = \Delta_x\rho + \mathrm{div}_x(x\rho). \tag{172}$$

Besides, the function $u(\tau,y) = (1/\sqrt{4\tau+1})e^{(-y^2/4\tau+1)}$ is an exact solution of heat equation (169). Accordingly, the function $\rho(t,x) = e^t u((1/2)e^{2t}, e^t x)$ defined by

$$\rho(t,x) = \frac{e^t}{\sqrt{2e^{2t}+1}}e^{-\left(e^{2t}x^2/2e^{2t}+1\right)}, \tag{173}$$

is an exact solution of equation (167).

Next, let us deal with the parabolic 5/2-Laplacian equation:

$$\frac{\partial\rho}{\partial t} = \mathrm{div}_x\left(\left(\left|\nabla_x\rho\right|\right)^{(1/2)}\nabla_x\rho\right). \tag{174}$$

We obtain an exact solution $\rho = \rho(t,x)$ of (174) in the form

$$\rho(t,x) = \frac{4x^5}{5(30t+1)^2}. \tag{175}$$

Finally, fix the initial datum ρ_0 to be

$$\begin{cases} \rho_0(x) = \dfrac{4}{5}x^5, & \text{if } x \in \left(0,\dfrac{1}{2}\right)\cup\left[\dfrac{3}{4},1\right), \\ \rho_0(x) = \dfrac{1}{\sqrt{3}}e^{-(x^2/3)}, & \text{if } x \in \left[\dfrac{1}{2},\dfrac{3}{4}\right). \end{cases} \tag{176}$$

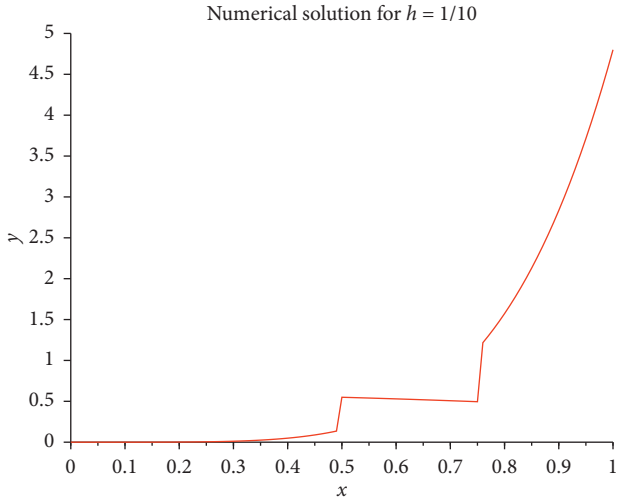

Figure 1: Numerical solution $\rho_1^{(1/10)}(x)$ for $h = (1/10)$.

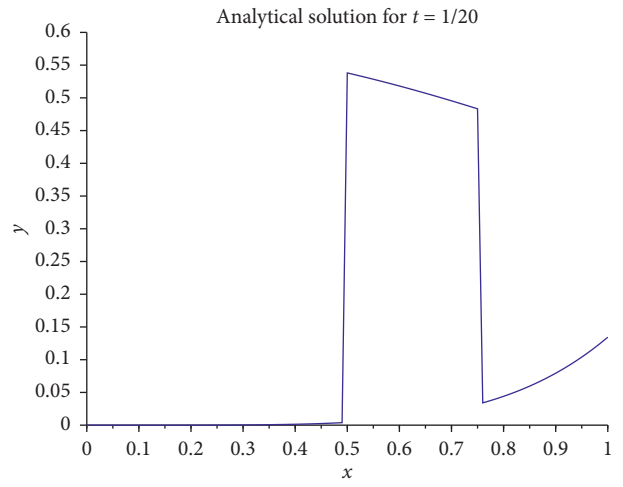

Figure 2: Analytical solution $\rho((1/20), x)$ for $h = (1/10)$ and $t = (1/20) \in (0, (1/10)]$.

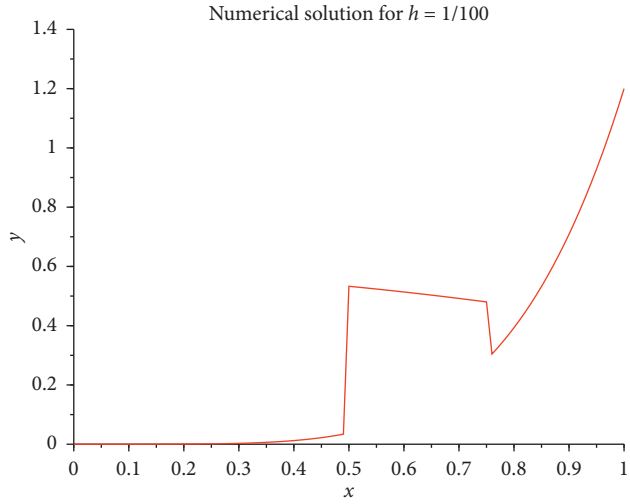

Figure 3: Numerical solution $\rho^{(1/1000)}(x)$ for $h = (1/100)$.

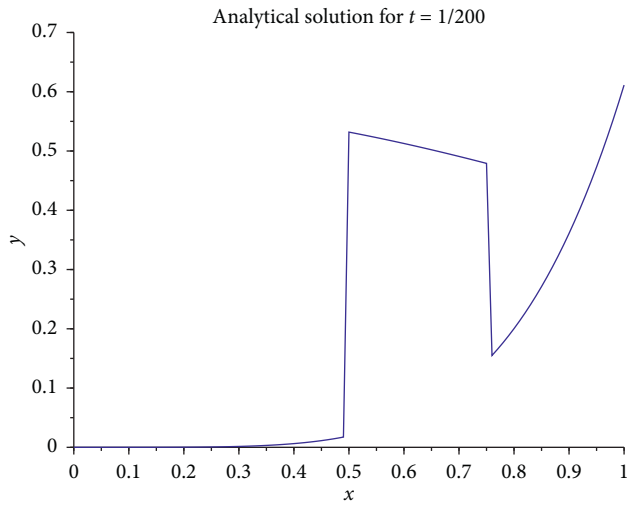

Figure 4: Analytical solution $\rho((1/200), x)$ for $h = (1/100)$ and $t = (1/2000) \in (0, (1/1000)]$.

Then, the exact solution $\rho = \rho(t, x)$ of the $q(x)$-Laplacian parabolic equation is presented as follows:

$$\begin{cases} \rho(t,x) = \dfrac{4x^5}{5(30t+1)^2}, & \text{if } (t,x) \in [0,+\infty) \times \left(0, \dfrac{1}{2}\right) \cup [0,+\infty[\times\left[\dfrac{3}{4}, 1\right), \\ \rho(t,x) = \dfrac{e^t}{\sqrt{2e^{2t}+1}} e^{-\left(e^{2t}x^2/2e^{2t}+1\right)}, & \text{if } (t,x) \in [0,+\infty) \times \left[\dfrac{1}{2}, \dfrac{3}{4}\right). \end{cases} \tag{177}$$

In this part of our work, we are interested in the existence of the stationary solution for our example. With the functions G and V as defined in the above, we deduce that the equation

$$\rho_\infty \nabla_x \left(G'(\rho_\infty) + V\right) = 0 \tag{178}$$

becomes

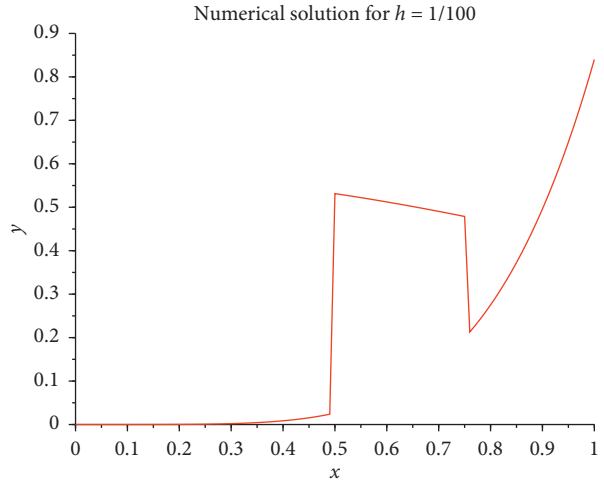

Figure 5: Numerical solution $\rho^{(1/1000)}(x)$ for $h = (1/1000)$.

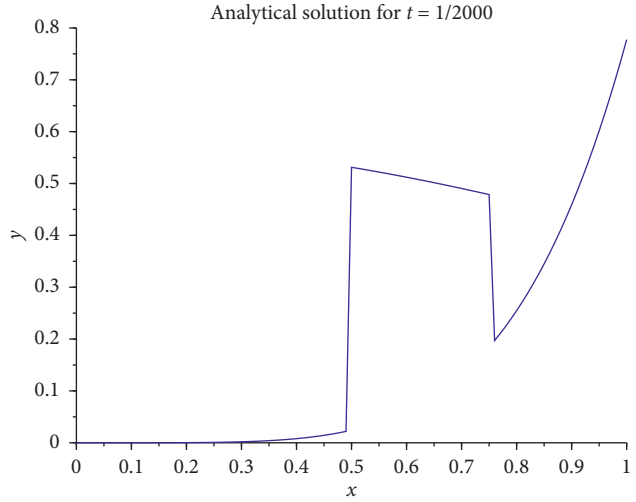

Figure 6: Analytical solution $\rho((1/2000), x)$ for $h = (1/1000)$ and $t = (1/2000) \in (0, (1/1000)]$.

Table 1: Error table.

h	1/10	1/50	1/100	1/500	1/1000	1/5000	1/10000
δt	1/20	1/100	1/200	1/1000	1/2000	1/20000	1/20000
$\|\rho - \rho^h\|_{L^2}$	14.144343	3.3886130	1.7847695	0.3764119	0.1896313	0.0381622	0.0190961

$$\begin{cases} \rho_\infty \nabla_x \left(\rho_\infty^{(1/3)}\right) = 0, & \text{in } \left(0, \frac{1}{2}\right) \cup \left[\frac{3}{4}, 1\right), \\ \rho_\infty \nabla_x \left(1 + \ln\left(\rho_\infty\right) + \frac{x^2}{2}\right) = 0, & \text{in } \left[\frac{1}{2}, \frac{3}{4}\right). \end{cases} \tag{179}$$

Consequently, the function ρ_∞ which is defined by

$$\begin{cases} \rho_\infty(x) = 0, & \text{if } x \in \left(0, \frac{1}{2}\right) \cup \left[\frac{3}{4}, 1\right), \\ \rho_\infty = \frac{1}{\sqrt{2}} e^{-x^2/2}, & \text{if } x \in \left[\frac{1}{2}, \frac{3}{4}\right) \end{cases} \tag{180}$$

solves (179) as the stationary solution of the $q(x)$-Laplacian parabolic equation.

In order to appreciate the effectiveness of our approximation method, we apply descent algorithm (6) to derive the approximate solution ρ^h for comparison with the exact solution, and we get

$$\begin{cases} \rho^h(t,x) = \dfrac{4}{5}(1+50h)x^5, & \text{if } (t,x) \in (0,h] \times \left(0,\dfrac{1}{2}\right) \cup (0,h] \times \left[\dfrac{3}{4},1\right), \\ \rho^h(t,x) = \dfrac{\sqrt{3}}{3-h}e^{-\left(x^2/3\right)}, & \text{if } (t,x) \in (0,h] \times \left[\dfrac{1}{2},\dfrac{3}{4}\right). \end{cases} \tag{181}$$

6.1. The Figures. For some values of h, we have drawn the figures of both analytical and approximate solutions when step $h \in \{(1/10), (1/50), (1/100)\}$, using Scilab software. We mention that Figure 1 represents an approximation of Figure 2 when, Figure 3 represents an approximation of Figure 4 when $h = (1/100)$, and Figure 5 represents an approximation of Figure 6 when $h = (1/1000)$.

6.2. Table of Error Progression. The Table of Error Progression is provide in the Table 1

Data Availability

The data used to support the findings of this study are available from the corresponding author upon request.

Conflicts of Interest

The authors declare that they have no conflicts of interest.

Acknowledgments

This work was supported by IMSP under the CEA-SMA project grant.

References

[1] H. Zhan, "The stability of evolutionary p (x)-Laplacian equation," *Zhan Boundary value Problems*, vol. 13, 2017.

[2] S. Lian, W. Gao, H. Yuan, and C. Cao, "Existence of solutions to an initial Dirichlet problem of evolutional p (x)-Laplace equations," *Annales de l'Institut Henri Poincare (C) Non Linear Analysis*, vol. 29, no. 3, pp. 377–399, 2012.

[3] Y. Chen, S. Levine, and M. Rao, "Variable exponent, linear growth functionals in image restoration," *SIAM Journal on Applied Mathematics*, vol. 66, no. 4, pp. 1383–1406, 2006.

[4] S. Antontsev, F. Miranda, and L. Santos, "Blow-up and finite time extinction for p (x , t)-curl systems arising in electromagnetism," *Journal of Mathematical Analysis and Applications*, vol. 440, no. 1, pp. 300–322, 2016.

[5] A. Bahrouni and D. Repovš, "Existence and nonexistence of solutions for p (x)-curl systems arising in electromagnetism," *Complex Variables and Elliptic Equations*, vol. 63, no. 2, pp. 292–301, 2018.

[6] T. G. Myers, "Thin films with high surface tension," *SiAM Review*, vol. 40, no. 3, pp. 441–462, 1998.

[7] M. Agueh, "Existence of solutions to degenerate parabolic equations via the Monge-Kantorovich theory," *Advances in Difference Equations*, vol. 10, pp. 309–360, 2005.

[8] M. Agueh, *Asymptotic Behavior for Doubly Degenerate Parabolic Equations*, Department of Mathematics, The University of British Columbia, Vancouver, B. C. V6T 1Z2, Canada, 2003.

[9] Z. Fan, *On The Spaces $L^{p(x)}(\Omega)$ and, $W^{m,p(x)}(\Omega)$*. Department of Mathematics, Lanzhou University, Lanzhou, China, 2009.

[10] M. Hamta and B. Salad, *Existence of Positive Solutions and its Asymptotic Behavior of (P (x),q (x))-laplacian Parabolic System*, Licence MDPI, Basel, Switzerland, 2019.

[11] G. Yanchao, "Extinction and asymptotic behavior of solution for nonlinear parabolic equations with variable exponent of nonlinearity," *Boundary Value Problems*, vol. 164, 2013.

[12] L. Diening, P. Harjulehto, P. Hasto, and M. Růžička, "Lebesgue and sobolev spaces with variable exponents," *Lecture Notes in Mathematics*, Springr, Berlin, Germany, 2017.

Hindawi
Discrete Dynamics in Nature and Society
Volume 2020, Article ID 1053283, 10 pages
https://doi.org/10.1155/2020/1053283

Research Article

Complex Behavior Analysis of a Fractional-Order Land Dynamical Model with Holling-II Type Land Reclamation Rate on Time Delay

Li Wu,[1,2] Zhouhong Li,[3] Yuan Zhang,[3] and Binggeng Xie[1]

[1]*College of Resources and Environmental Sciences, Hunan Normal University, Changsha, Hunan 410028, China*
[2]*Department of Geography and Land Engineering, Yuxi Normal University, Yuxi, Yunnan 653100, China*
[3]*Department of Mathematics, Yuxi Normal University, Yuxi, Yunnan 653100, China*

Correspondence should be addressed to Binggeng Xie; xbgyb1961@163.com

Received 14 May 2020; Accepted 25 June 2020; Published 25 July 2020

Guest Editor: Jinliang Wang

In this paper, a fractional-order land model with Holling-II type transformation rate and time delay is investigated. First of all, the variable-order fractional derivative is defined in the Caputo type. Second, by applying time delay as the bifurcation parameter, some criteria to determine the stability and Hopf bifurcation of the model are presented. It turns out that the time delay can drive the model to be oscillatory, even when its steady state is stable. Finally, one numerical example is proposed to justify the validity of theoretical analysis. These results may provide insights to the development of a reasonable strategy to control land-use change.

1. Introduction

Since the 20th century, the global environment has changed at an unprecedented speed, and a series of major global environmental problems pose a serious threat to the survival and development of mankind. From the perspective of earth system science, the generation of global environmental problems can be recognized as the result of the interaction between the earth's atmosphere, hydrosphere, biosphere, lithosphere, and human activities [1, 2]. Land use/land cover change (LUCC) is as a key link connecting the four circles of the earth system, being an ideal entry point for the study of natural and human processes, and has rapidly become the focus of global change research [3, 4]. LUCC dynamic change is to describe, evaluate, interpret, and predict the quantity, quality, spatial distribution, classification, rate, and process of land use/land cover change by accumulating spatiotemporal continuous land use/land cover data and using the mathematical model [5]. The driving forces of land use change are mainly divided into natural and social systems. Notably, hydrology, topography, and geomorphology [6, 7] are the main driving forces in the natural system, while economic development, population growth, and policies are the main driving forces in the social and economic systems [8]. Generally speaking, it is the interwoven factors in these two systems that cause land use changes [9], but compared with the natural factors (such as climate, soil, and topography), human factors (such as regional policy, economic development, and population growth) play a dominant role [10].

Since the key of LUCC research is to understand the driving force and driving mechanism [11], a variety of system analysis and mathematical statistic methods have been well applied in the research of driving force. For example, the internal and human driving force of land use change is studied through the analysis of the multiple linear regression model [12]. The system dynamic model was used to quantitatively diagnose the contribution of each driving factor to land use change [13]. The CLUE comprehensive model was used to establish the interaction between land-use change and its influencing factors, and land change and its spatial distribution were simulated [14–16]. Therefore, the comprehensive mathematical model will be a development trend of LUCC research at present and in the future.

In 1997, Dobson et al. considered the land model with four coupled differential equations [17]:

$$\begin{cases} \dot{F}(t) = -\mathrm{d}P(t)F(t) + sU(t), \\ \dot{A}(t) = \mathrm{d}P(t)F(t) - aA(t) + bU(t), \\ \dot{U}(t) = aA(t) - sU(t) - bU(t), \\ \dot{P}(t) = rP(t)\left[1 - \dfrac{h}{A(t)}P(t)\right], \end{cases} \tag{1}$$

where F stands for an original area of pristine forest habitat, A denotes the agricultural land, unused land is U, and P is the population density with time t, for more detail, one can read [17] and the references cited therein. In [18], Chen et al. studied the dynamical analysis of the land model with Holling-II type land reclamation rate, and they found the positive equilibrium point, the basic reproductive rate R_0, and, furthermore, some sufficient conditions for the global stability of the positive equilibrium and one of the boundary equilibrium.

On the one hand, it is well known that time delays are unavoidable for population modelling. It is therefore important to consider the dynamics for the population models with time delays, and dynamic complex analysis is obviously one of the most important problems. For example, delay differential equations have been applied in the stability of population dynamic systems [19–25], impulsive effects, and control systems [26–28].

On the other hand, there are two types of differential equations, namely, integer-order and fractional-order differential equations. Traditionally, the fractional-order differential equations have enjoyed a preference over integer-order differential equations because of the mathematical tractability of fractional systems. Over the past 30 decades, fractional-order differential equations have been applied in many fields, such as design and control of various ecological systems [29–32], secure communication [33–35], and system control [36–42].

Recently, the existence of Hopf bifurcation of differential equations has been studied as an important qualitative behavior of integer-order differential equations [43]. Moreover, fractional calculus is merged into complicated, dynamical systems which extremely renovate the theory of the design and control performance for complex systems. It has been discovered that physical phenomena in nature can be depicted more accurately by fractional-order models in comparison with classical integer-order ones [44, 45]. Some scholars introduced fractional calculus into population models and constructed fractional population or epidemic models [46–50], fractional dynamic systems, and fractional neural networks [51–53]. However, to the best of our knowledge, there are few studies to investigate the existence of Hopf bifurcation to the fractional-order land model with time delay.

Motived by the above ideas, in this paper, we will consider the following fractional-order land model with Holling-II type response and time delay:

$$\begin{cases} D^{\phi}F(t) = \dfrac{-\mathrm{d}F(t)P(t-\tau)}{1+P(t-\tau)} + sU(t), \\ D^{\phi}R(t) = \dfrac{\mathrm{d}F(t)P(t-\tau)}{1+P(t-\tau)} - aR(t) + bU(t), \\ D^{\phi}U(t) = aR(t) - sU(t) - bU(t), \\ D^{\phi}P(t) = rP(t)\left[1 - \dfrac{h}{R(t)}P(t-\tau)\right], \end{cases} \tag{2}$$

where $\phi \in (0, 1]$ is the fractional order, $F(t), R(t)$, and $U(t)$ represent the land of wood and grass, survival land, and unused land, respectively, and $P(t)$ is the density of the predator population at time t; $R(t)$ (land area of survival) of a period of time $1/a$ becomes unused land (area $U(t)$), which in turn recovers through natural succession or ecological restoration to become a forest after a time interval $1/s$. The unused land may also be restored to survival viable land after a time interval $1/b$. Average clearing ability is described by constant d. r is the growth rate into the population. $\tau > 0$ is the time delay required for the gestation of the mature population.

The main contributions can be summed up in three aspects:

(1) A novel fractional-order land model with Holling-II type land reclamation rate and time delay is formulated

(2) Two primary dynamical properties—stability and oscillation—of the delayed fractional-order land model are investigated

(3) The influences of the order on the Hopf bifurcation are obtained

Throughout this paper, we address the following assumptions.

Assumption 1. $bd + ds - ahs > 0$.

Assumption 2. $abd + ads - ha^2 s > 0$.

Suppose Assumptions 1 and 2 hold, then system (2) has an unique positive equilibrium point $E^* = (F^*, R^*, U^*, P^*)$, which is described by

$$\begin{aligned} F^* &= \frac{as(ah + bh + b + hs + s)}{(b+s)(ad + as + bd + ds)}, \\ R^* &= \frac{bd + ds - ahs}{ad + as + bd + ds}, \\ U^* &= \frac{abd + ads - ha^2 s}{(b+s)(ad + as + bd + ds)}, \\ P^* &= \frac{bd + ds - ahs}{h(ad + as + bd + ds)}. \end{aligned} \tag{3}$$

The remainder of the current paper is organized as follows: In Section 2, some definitions and lemmas of fractional calculus are recalled. In Section 3, the fractional

land model with Holling-II type land reclamation rate and time delay is investigated by using time delay as the bifurcation parameter, and the conditions of Hopf bifurcation are presented. One numerical example is given to illustrate the effectiveness of our main results in Section 4. Finally, conclusions are drawn in the last section.

2. Basic Tools of Fractional Calculus

In this section, we recall some definitions and lemmas of fractional calculus, which can be used in the proofs of the main results in Section 3.

There are several definitions of fractional derivatives. The Grünwald–Letnikov definition, the Riemann–Liouville definition, and the Caputo definition are usually used to deal with fractional-order systems. Since the Caputo derivative only requires the initial conditions which are based on the integer-order derivative and represents well-understood features of physical situation, it is more applicable to real-world problems. Hence, the Caputo fractional-order derivative is adopted in this paper.

Definition 1 (see [44]). The fractional integral of order α for a function $g(t)$ is defined as

$$I^{\alpha} g(t) = \frac{1}{\Gamma(\alpha)} \int_{t_0}^{t} (t-s)^{\alpha-1} g(s) \mathrm{d}s, \tag{4}$$

where $t \geq t_0$, $\alpha > 0$, $\Gamma(\cdot)$ is the gamma function, and $\Gamma(s) = \int_0^{\infty} t^{s-1} e^{-t} \mathrm{d}t$.

Definition 2 (see [44]). The Caputo fractional derivative of order α for a function $g(t) \in C^n([t_0, \infty), R)$ is defined by

$$D^{\alpha} g(t) = \frac{1}{\Gamma(n-\alpha)} \int_{t_0}^{t} \frac{g^{(n)}(s)}{(t-s)^{\alpha-n+1}} \mathrm{d}s, \tag{5}$$

where $t \geq t_0$ and n is a positive integer such that $n-1 \leq \alpha < n$.

Moreover, when $0 < \alpha < 1$,

$$D^{\alpha} g(t) = \frac{1}{\Gamma(1-\alpha)} \int_{t_0}^{t} \frac{g'(s)}{(t-s)^{\alpha}} \mathrm{d}s. \tag{6}$$

Lemma 1 (see [41]). *The following autonomous system*

$$\begin{aligned} D^{\alpha} y &= Jy, \\ y(0) &= y_0, \end{aligned} \tag{7}$$

where $0 < \alpha < 1$, $y \in R^n$, and $A \in R^{n \times n}$, is asymptotically stable if and only if $|\arg(\lambda_i)| > \alpha\pi/2$ $(i = 1, 2, \ldots, n)$. In this case, each component of the states decays towards 0 like $t^{-\alpha}$. Also, this system is stable if and only if $|\arg(\lambda_i)| \geq \alpha\pi/2$, and those critical eigenvalues that satisfy $|\arg(\lambda_i)| = \alpha\pi/2$ have geometric multiplicity one.

3. Main Results

In this section, by applying the previous analytic technique, we shall investigate the stability and bifurcation of system (2) with time delay by taking time delay as the bifurcation parameter. The conditions of delay-induced bifurcation will be derived.

From reference [18], the dynamics of system (2) crucially depend on the basic reproduction number R_0, which is given by

$$R_0 = \frac{b\,d + ds}{ash}. \tag{8}$$

Let $x_1(t) = F(t) - F^*$, $x_2(t) = R(t) - R^*$, $x_3(t) = U(t) - U^*$, and $x_4(t) = P(t) - P^*$, and then we have

$$\begin{cases} D^{\phi} x_1(t) = \dfrac{-d\left(x_1(t) + F^*\right)\left(x_4(t-\tau) + P^*\right)}{1 + \left(x_4(t-\tau) + P^*\right)} + s\left(x_3(t) + U^*\right), \\ D^{\phi} x_2(t) = \dfrac{d\left(x_1(t) + F^*\right)\left(x_4(t-\tau) + P^*\right)}{1 + \left(x_4(t-\tau) + P^*\right)} - a\left(x_2(t) + R^*\right) + b\left(x_3(t) + U^*\right), \\ D^{\phi} x_3(t) = a\left(x_2(t) + R^*\right) - s\left(x_3(t) + U^*\right) - b\left(x_3(t) + U^*\right), \\ D^{\phi} x_4(t) = r\left(x_4(t) + P^*\right)\left[1 - \dfrac{h}{\left(x_2(t) + R^*\right)}\left(x_4(t-\tau) + P^*\right)\right]. \end{cases} \tag{9}$$

Taking advantage of the Taylor expansion formula, the linearized system of system (9) at the zero equilibrium is

$$\begin{cases} D^{\phi} x_1(t) = a_{11} x_1(t) + a_{13} x_3(t) + b_{14} x_4(t-\tau), \\ D^{\phi} x_2(t) = a_{21} x_1(t) + a_{22} x_2(t) + a_{23} x_3(t) + b_{24} x_4(t-\tau), \\ D^{\phi} x_3(t) = a_{32} x_2(t) + a_{33} x_3(t), \\ D^{\phi} x_4(t) = a_{42} x_2(t) + b_{44} x_4(t-\tau), \end{cases} \tag{10}$$

where $a_{11} = (-dP^*/(1+P^*)), a_{13} = s, b_{14} = -(dF^*/((1+P^*)^2)), a_{21} = (dP^*/(1+P^*)), a_{22} = -a, a_{23} = b, b_{24} = (dF^*/((1+P^*)^2)), a_{32} = a, a_{33} = -(b+s), a_{42} = (hrP^{*2}/R^{*2}), a_{44} = r - (hrP^*/R^*)$, and $b_{44} = -(hrP^*/R^*)$.

The associated characteristic equation of system (10) can be obtained as

$$\det\begin{pmatrix} s^\phi - a_{11} & 0 & -a_{13} & -b_{14}e^{-s\tau} \\ -a_{21} & s^\phi - a_{22} & -a_{23} & -b_{24}e^{-s\tau} \\ 0 & -a_{32} & s^\phi - a_{33} & 0 \\ 0 & -a_{42} & 0 & s^\phi - a_{44} - b_{44}e^{-s\tau} \end{pmatrix} = 0, \tag{11}$$

which leads to

$$P_1(s) + P_2(s)e^{-s\tau} = 0, \tag{12}$$

where

$$\begin{aligned} P_1(s) =& \left(-a_{11}s^{2\phi} - a_{22}s^{2\phi} - a_{33}s^{2\phi} + a_{11}a_{22}s^\phi \right. \\ & - a_{23}a_{32}s^\phi + a_{11}a_{33}s^\phi + a_{22}a_{33}s^\phi \\ & \left. -a_{12}a_{21}a_{32} + a_{11}a_{23}a_{32} - a_{11}a_{22}a_{33} + s^{3\phi}\right)\left(s^\phi - a_{44}\right), \\ P_2(s) =& a_{21}\left(a_{12}a_{32}b_{44} - a_{42}b_{14}\left(s^\phi - a_{33}\right)\right) \\ & -\left(s^\phi - a_{11}\right)\left(a_{42}b_{24}\left(s^\phi - a_{33}\right)\right. \\ & \left. + b_{44}\left(-a_{33}s^\phi + a_{22}\left(a_{33} - s^\phi\right) - a_{23}a_{32} + s^{2\phi}\right)\right). \end{aligned} \tag{13}$$

Let $P_1(s) = A_1 + iB_1$ and $P_2(s) = A_2 + iB_2$, and from equation (12), we have

$$\left(A_1 + iB_1\right) + \left(A_2 + iB_2\right)e^{-s\tau} = 0. \tag{14}$$

Assume that $s = iw = w(\cos(\pi/2) + i\sin(\pi/2))$ is a root of equation (12), $\omega > 0$. Substituting s into equation (12) and separating the real and imaginary parts, one can have

$$\begin{cases} A_2\cos w\tau + B_2\sin w\tau = -A_1, \\ B_2\cos w\tau - A_2\sin w\tau = -B_1. \end{cases} \tag{15}$$

Applying equation (15), direct calculation yields

$$\begin{cases} \cos w\tau = -\dfrac{A_1A_2 + B_1B_2}{A_2^2 + B_2^2} = \mathscr{F}(w), \\ \sin w\tau = -\dfrac{-A_2B_1 + A_1B_2}{A_2^2 + B_2^2} = \mathscr{G}(w), \end{cases} \tag{16}$$

where

$$\begin{aligned} A_1 =& \left(-a_{23}a_{32} + a_{22}a_{33} + (a_{22} + a_{33})a_{44} + a_{11}(a_{22} + a_{33} + a_{44})\right)w^{2\phi}\cos(\pi\phi) \\ & -(a_{11} + a_{22} + a_{33} + a_{44})w^{3\phi}\cos\left(\frac{3\pi\phi}{2}\right) + (a_{12}a_{21}a_{32} + (a_{22}a_{33} - a_{23}a_{32})a_{44} \\ & +a_{11}(-a_{23}a_{32} + a_{22}a_{33} + (a_{22} + a_{33})a_{44}))w^\phi\left(-\cos\left(\frac{\pi\phi}{2}\right)\right) + (a_{12}a_{21}a_{32} \\ & +a_{11}(a_{22}a_{33} - a_{23}a_{32}))a_{44} + w^{4\phi}\cos(2\pi\phi), \\ B_1 =& a_{21}\left(a_{12}a_{32}b_{44} - a_{42}b_{14}\left(w^\phi\cos\left(\frac{\pi\phi}{2}\right) - a_{33}\right)\right) + a_{42}b_{24}\left(-\left((a_{11} + a_{33})w^\phi\left(-\cos\left(\frac{\pi\phi}{2}\right)\right)\right.\right. \\ & \left.\left. +a_{11}a_{33} + w^{2\phi}\cos(\pi\phi)\right)\right) + b_{44}\left((a_{11} + a_{22} + a_{33})w^{2\phi}\cos(\pi\phi) + (a_{11}a_{22} - a_{23}a_{32}\right. \\ & \left. +(a_{11} + a_{22})a_{33})w^\phi\left(-\cos\left(\frac{\pi\phi}{2}\right)\right) + a_{11}(a_{22}a_{33} - a_{23}a_{32}) - w^{3\phi}\cos\left(\frac{3\pi\phi}{2}\right)\right), \\ A_2 =& a_{21}\left(a_{12}a_{32}b_{44} - a_{42}b_{14}\left(w^\phi\cos\left(\frac{\pi\phi}{2}\right) - a_{33}\right)\right) + a_{42}b_{24}\left(-\left((a_{11} + a_{33})w^\phi\left(-\cos\left(\frac{\pi\phi}{2}\right)\right)\right.\right. \\ & \left.\left. + a_{11}a_{33} + w^{2\phi}\cos(\pi\phi)\right)\right) + b_{44}\left((a_{11} + a_{22} + a_{33})w^{2\phi}\cos(\pi\phi) + (a_{11}a_{22} - a_{23}a_{32}\right. \\ & \left. + (a_{11} + a_{22})a_{33})w^\phi\left(-\cos\left(\frac{\pi\phi}{2}\right)\right) + a_{11}(a_{22}a_{33} - a_{23}a_{32}) - w^{3\phi}\cos\left(\frac{3\pi\phi}{2}\right)\right), \\ B_2 =& -w^\phi\sin\left(\frac{\pi\phi}{2}\right)\left(a_{42}b_{24}\left(-a_{11} - a_{33} + 2w^\phi\cos\left(\frac{\pi\phi}{2}\right)\right) + b_{44}(-2(a_{11} + a_{22} + a_{33})\right. \\ & \times w^\phi\cos\left(\frac{\pi\phi}{2}\right) + a_{11}a_{22} - a_{23}a_{32} + a_{11}a_{33} + a_{22}a_{33} + w^{2\phi}(2\cos(\pi\phi) + 1)\Big) \\ & \left. + a_{21}a_{42}b_{14}\right). \end{aligned} \tag{17}$$

From (16), we obtain

$$\tau^{(k)} = \frac{1}{w}\left[\arccos\mathscr{F}(w) + 2k\pi\right], \quad k = 0, 1, 2, \ldots. \tag{18}$$

Define

$$\tau_0^* = \min\left\{\tau^{(k)}\right\}, \quad k = 0, 1, 2, \ldots, \tag{19}$$

where $\tau^{(k)}$ is defined by equation (18).

To derive the condition of the occurrence for Hopf bifurcation, we further give the following assumption.

Assumption 3

$$\frac{W_1V_1 + W_2V_2}{V_1^2 + V_2^2} \neq 0, \tag{20}$$

where

$$\begin{aligned} W_1 &= w_0\left(A_2 \sin w_0\tau_0 - B_2 \cos w_0\tau_0\right),\\ W_2 &= w_0\left(A_2 \cos w_0\tau_0 + B_2 \sin w_0\tau_0\right),\\ V_1 &= A_1' + \left(A_2' - \tau_0 A_2\right)\cos w_0\tau_0 + \left(B_2' - \tau_0 B_2\right)\sin w_0\tau_0,\\ V_2 &= B_1' + \left(B_2' - \tau_0 B_2\right)\cos w_0\tau_0 \left(A_2' - \tau_0 A_2\right)\sin w_0\tau_0. \end{aligned} \tag{21}$$

Lemma 2. *Let $s(\tau) = \nu(\tau) + iw(\tau)$ be the root of equation (18) near $\tau = \tau_j$ satisfying $\nu(\tau_j) = 0$, $w(\tau_j) = w_0$, then the following transversality condition holds*

$$\operatorname{Re}\left[\frac{\mathrm{d}s}{\mathrm{d}\tau}\right]\Bigg|_{(w=w_0,\tau=\tau_0)} \neq 0. \tag{22}$$

Proof. By using implicit function theorem and differentiating (12) with respect to τ, we have

$$P_1'(s)\frac{\mathrm{d}s}{\mathrm{d}\tau} + P_2'(s)e^{-s\tau}\frac{\mathrm{d}s}{\mathrm{d}\tau} + P_2(s)e^{-s\tau}\left(-\tau\frac{\mathrm{d}s}{\mathrm{d}\tau} - s\right) = 0, \tag{23}$$

where $P_i'(s)$ are the derivatives of $P_i(s)(i = 1, 2)$.

Thus, we obtain

$$\frac{\mathrm{d}s}{\mathrm{d}\tau} = \frac{W(s)}{V(s)}, \tag{24}$$

where

$$\begin{aligned} W(s) &= sP_2(s)e^{-s\tau},\\ V(s) &= P_1'(s) + P_2'(s)e^{-s\tau} - \tau P_2(s)e^{-s\tau}. \end{aligned} \tag{25}$$

Let P_i^R and P_i^I be the real and imaginary parts of $P_i(s)(i = 1, 2)$, respectively. We further suppose that W_1 and W_2 are the real and imaginary parts of $W(s)$, respectively, and V_1, V_2 are the real and imaginary parts of $V(s)$, respectively.

Hence,

$$\operatorname{Re}\left[\frac{\mathrm{d}s}{\mathrm{d}\tau}\right]\Bigg|_{(\tau=\tau_0,w=w_0)} = \frac{W_1V_1 + W_2V_2}{V_1^2 + V_2^2}. \tag{26}$$

Therefore, based on Assumption 3, the transversality condition is satisfied. This completes the proof of Lemma 2.

Denote

$$\begin{aligned} \beta_1 &= \alpha_1,\\ \beta_2 &= \begin{vmatrix} \alpha_1 & 1\\ \alpha_3 & \alpha_2 \end{vmatrix},\\ \beta_3 &= \begin{vmatrix} \alpha_1 & 1 & 0\\ \alpha_3 & \alpha_2 & \alpha_1\\ 0 & \alpha_4 & \alpha_3 \end{vmatrix},\\ \beta_4 &= \alpha_3\beta_3, \end{aligned} \tag{27}$$

where

$$\begin{aligned} \alpha_1 &= -a_{11} - a_{22} - a_{33} - a_{44} - b_{44},\\ \alpha_2 &= a_{22}b_{44} - a_{42}b_{24} + a_{11}b_{44} + a_{33}b_{44} + a_{11}a_{22} + a_{33}a_{22}\\ &\quad + a_{44}a_{22} - a_{23}a_{32} + a_{11}a_{33} + a_{11}a_{44} + a_{33}a_{44},\\ \alpha_3 &= a_{23}a_{32}b_{44} - a_{21}a_{42}b_{14} + a_{11}a_{42}b_{24} + a_{33}a_{42}b_{24}\\ &\quad - a_{11}a_{22}b_{44} - a_{11}a_{33}b_{44} - a_{22}a_{33}b_{44}\\ &\quad - a_{13}a_{21}a_{32} + a_{11}a_{23}a_{32} + a_{23}a_{44}a_{32} - a_{11}a_{22}a_{33}\\ &\quad - a_{11}a_{22}a_{44} - a_{11}a_{33}a_{44} - a_{22}a_{33}a_{44},\\ \alpha_4 &= a_{21}a_{33}a_{42}b_{14} - a_{11}a_{33}a_{42}b_{24}\\ &\quad + a_{13}a_{21}a_{32}a_{44} - a_{11}a_{23}a_{32}a_{44} + a_{11}a_{22}a_{33}a_{44}\\ &\quad + a_{13}a_{21}a_{32}b_{44} - a_{11}a_{23}a_{32}b_{44} + a_{11}a_{22}a_{33}b_{44}. \end{aligned} \tag{28}$$

□

Lemma 3. *If Assumptions 1 and 2 hold, then the positive equilibrium point (F^*, R^*, U^*, P^*) of the delayed fractional-order land model (2) is asymptotically stable when $\tau = 0$.*

Proof. When $\tau = 0$, system (2) changes into

$$\lambda^4 + \beta_1\lambda^3 + \beta_2\lambda^2 + \beta_3\lambda + \beta_4 = 0. \tag{29}$$

If the conditions of $\beta_i > 0\,(i = 1, 2, 3, 4)$ hold and, furthermore, if Assumptions 1 and 2 are satisfied, it is easy to check from the Routh–Hurwitz criterion that the four eigenvalues of the characteristic equation (29) have negative real parts. Hence, the positive equilibrium point (F^*, R^*, U^*, P^*) of the delayed fractional-order land model (2) is asymptotically stable when $\tau = 0$.

From the above analysis, together with Lemma 3, we will give the following theorem. □

Theorem 1. *For the model (2):*

(i) Under Assumptions 1–3, the equilibrium point $E^* = (F^*, R^*, U^*, P^*)$ is global asymptotically stable for $\tau \in [0, +\infty)$

(ii) Under Assumptions 1–3:

(a) The equilibrium point $E^* = (F^*, R^*, U^*, P^*)$ is locally asymptotically stable for $\tau \in [0, \tau_0)$

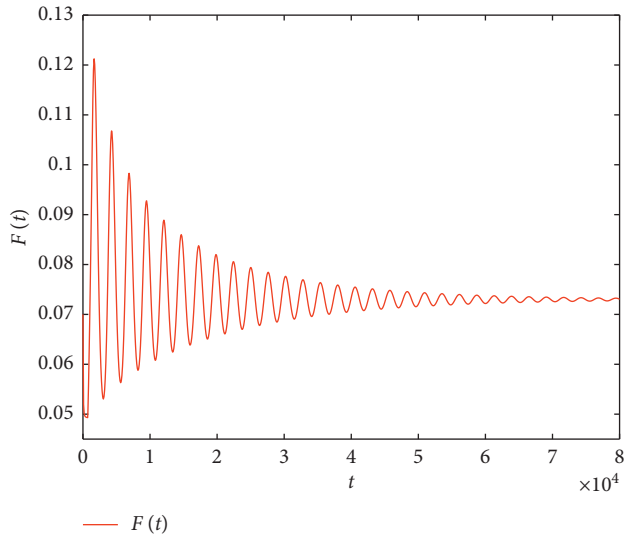

Figure 1: Time series solution of system (30) with $\phi = 0.90$, $\tau = 700 < \tau_0 = 728.403$.

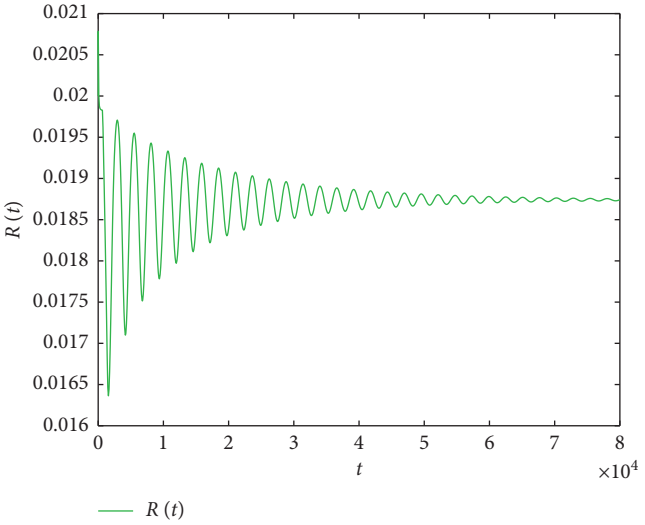

Figure 2: Time series solution of system (30) with $\phi = 0.90$, $\tau = 700 < \tau_0 = 728.403$.

(b) Model (2) undergoes a Hopf bifurcation at the $E^* = (F^*, R^*, U^*, P^*)$ when $\tau = \tau_0$, i.e., it has a branch of periodic solutions bifurcating from the equilibrium near $\tau = \tau_0$

4. Numerical Example and Application

In this section, we give one example to demonstrate the effectiveness of the proposed approach. The simulation results are based on theAdams–Bashforth–Moulton predictor-corrector scheme [54], and step length $\Delta t = 0.01$.

Consider the following fractional-order land dynamical model with time delay:

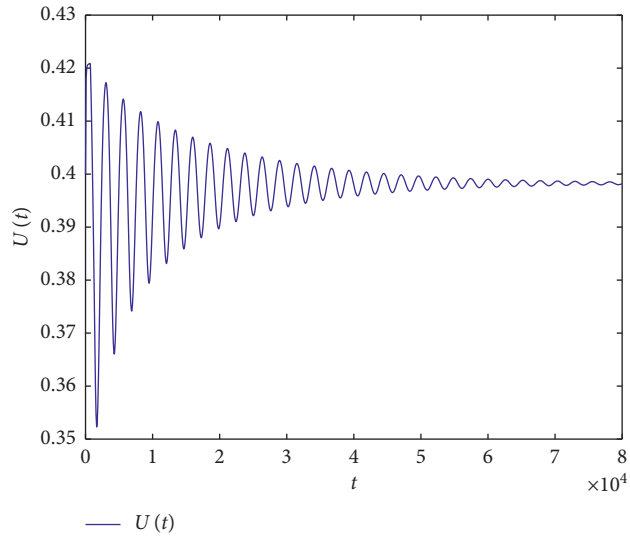

Figure 3: Time series solution of system (30) with $\phi = 0.90$, $\tau = 700 < \tau_0 = 728.403$.

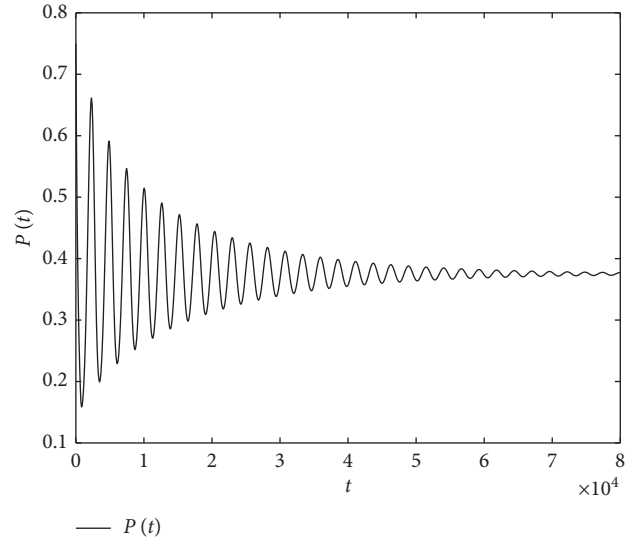

Figure 4: Time series solution of system (30) with $\phi = 0.90$, $\tau = 700 < \tau_0 = 728.403$.

$$\begin{cases} D^{\phi}F(t) = \dfrac{-\mathrm{d}F(t)P(t-\tau)}{1+P(t-\tau)} + sU(t), \\ D^{\phi}R(t) = \dfrac{\mathrm{d}F(t)P(t-\tau)}{1+P(t-\tau)} - aR(t) + bU(t), \\ D^{\phi}U(t) = aR(t) - sU(t) - bU(t), \\ D^{\phi}P(t) = rP(t)\left[1 - \dfrac{h}{R(t)}P(t-\tau)\right], \end{cases} \tag{30}$$

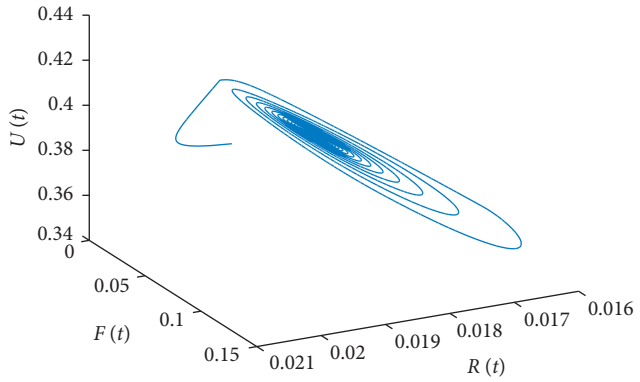

Figure 5: Portrait diagram of land model (30) with $\phi = 0.90$, $\tau = 700 < \tau_0 = 728.403$.

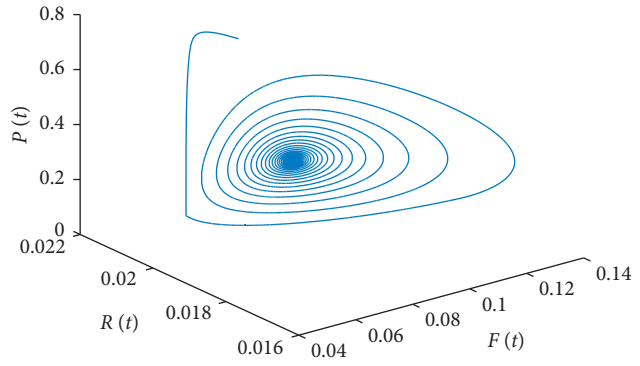

Figure 6: Portrait diagram of land model (30) with $\phi = 0.90$, $\tau = 700 < \tau_0 = 728.403$.

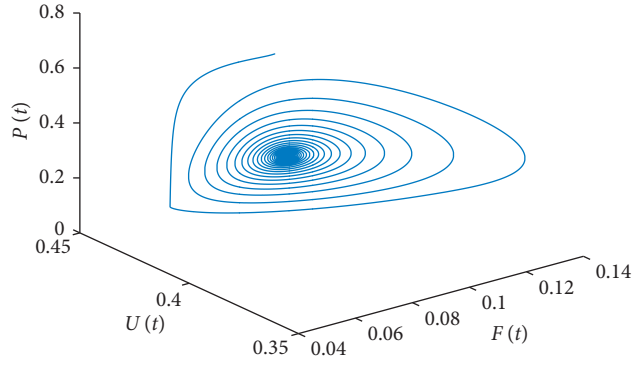

Figure 7: Portrait diagram of land model (30) with $\phi = 0.90$, $\tau = 700 < \tau_0 = 728.403$.

in this case, taking $\phi = 0.9$, and according to Yuxi city land and population data of Yunan Province, China, let $a = 0.34, b = 0.012, r = 0.0048, s = 0.004, h = 0.05$, and $d = 0.08$. By computing, we obtain the positive equilibrium point as $(0.075617, 0.021169, 0.44984, 0.423379)$. Moreover, we have $R_0 = ((bd + ds)/ash) = 18.8235 > 1$, $\omega_0 = 0.002358$, and $\tau_0 = 728.403$. Furthermore, the initial values are selected

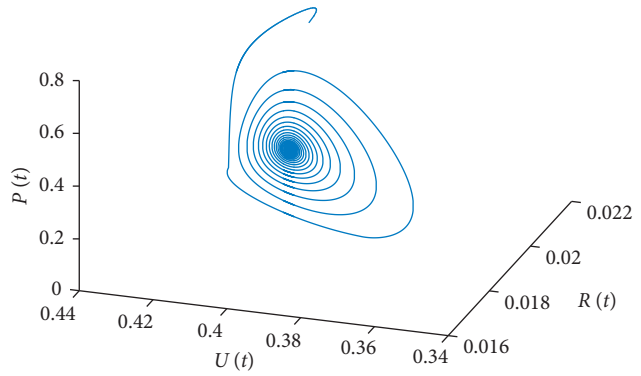

Figure 8: Portrait diagram of land model (30) with $\phi = 0.90$, $\tau = 700 < \tau_0 = 728.403$.

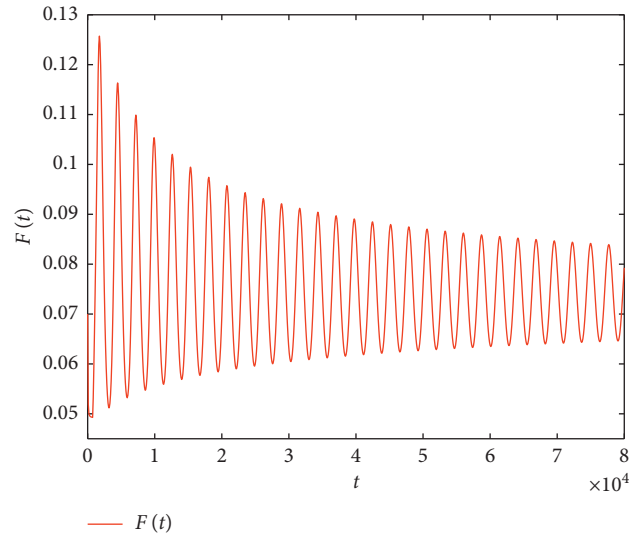

Figure 9: Time series solution of system (30) with $\phi = 0.90$, $\tau = 740 > \tau_0 = 728.403$.

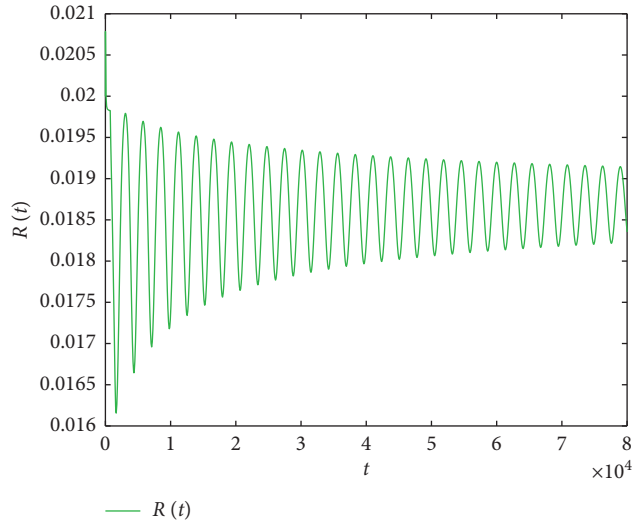

Figure 10: Time series solution of system (30) with $\phi = 0.90$, $\tau = 740 > \tau_0 = 728.403$.

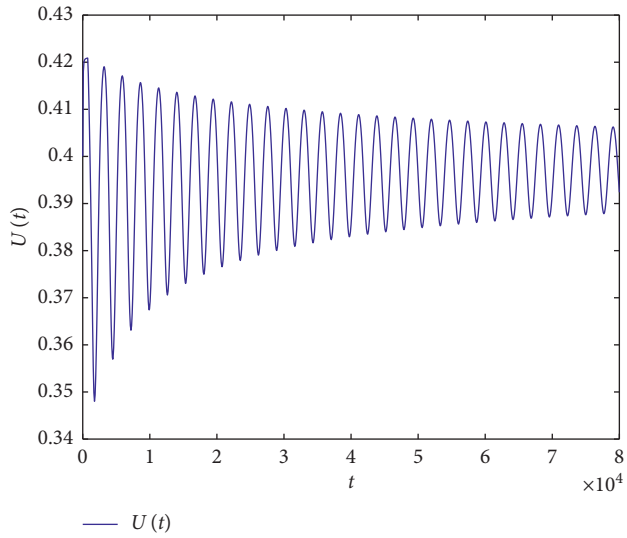

Figure 11: Time series solution of system (30) with $\phi = 0.90$, $\tau = 740 > \tau_0 = 728.403$.

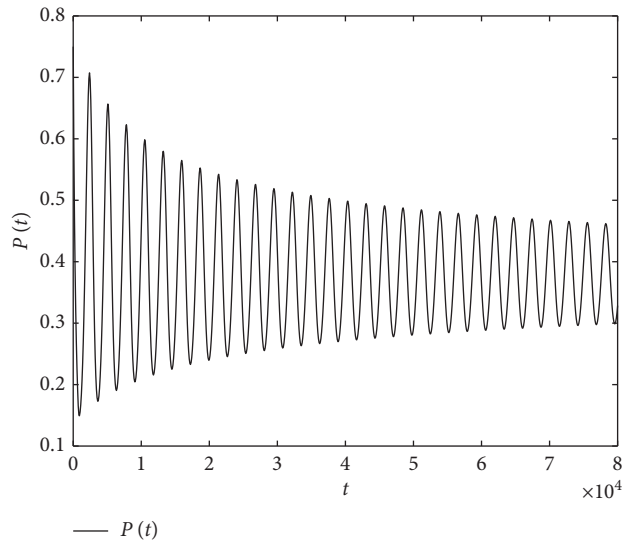

Figure 12: Time series solution of system (30) with $\phi = 0.90$, $\tau = 740 > \tau_0 = 728.403$.

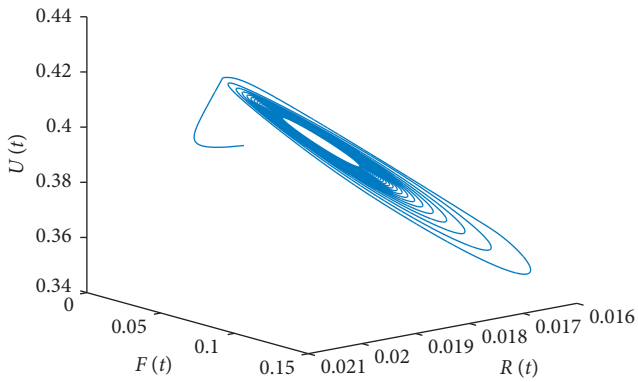

Figure 13: Portrait diagram of land model (30) with $\phi = 0.90$, $\tau = 740 > \tau_0 = 728.403$.

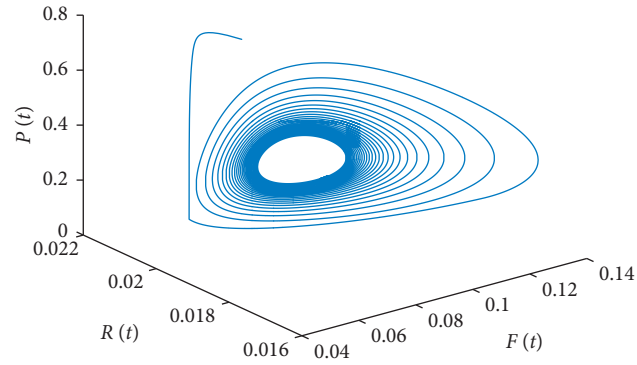

Figure 14: Portrait diagram of land model (30) with $\phi = 0.90$, $\tau = 740 > \tau_0 = 728.403$.

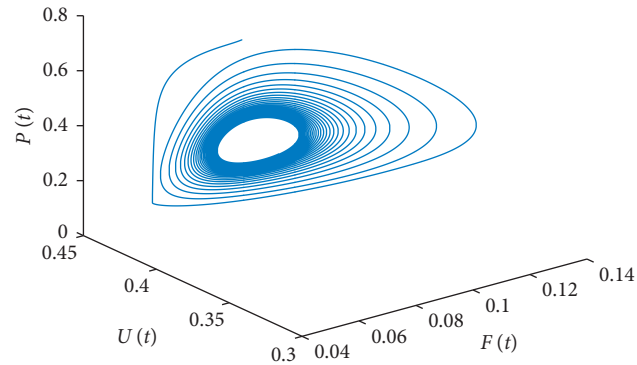

Figure 15: Portrait diagram of land model (30) with $\phi = 0.90$, $\tau = 740 > \tau_0 = 728.403$.

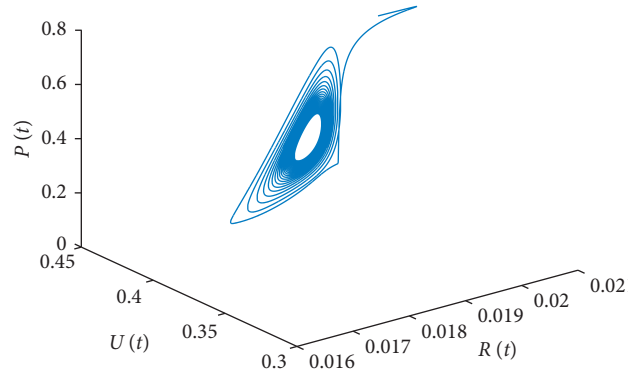

Figure 16: Portrait diagram of land model (30) with $\phi = 0.90$, $\tau = 740 > \tau_0 = 728.403$.

as $(F(0), R(0), U(0), P(0)) = (0.07, 0.02, 0.4, 0.75)$, and it is easy to verify that the conditions of (ii) in Theorem 1 are satisfied. Figures 1–8 depict the equilibrium point $(0.075617, 0.021169, 0.44984, 0.423379)$ which is locally asymptotically stable when $\tau = 700 < \tau_0$, while Figures 9–16 display the equilibrium point $(0.075617, 0.021169, 0.44984, 0.423379)$ that is unstable, and Hopf bifurcation occurs when $\tau = \tau_0$ (see Supplementary Materials (available here)).

5. Conclusion

The problem of bifurcation for a fractional land model with time delay has been studied in this paper. Firstly, by comprehensively analyzing the characteristic equation, the stability criterion and the conditions of existence of Hopf bifurcation are established. It was shown that the presence of delay heavily affects the stability of the model. Finally, according to China, Yunan Province, Yuxi city land data, some simulation examples have been exploited to illustrate the applicability and usefulness of the developed theoretical result.

Data Availability

The labeled dataset used to support the findings of this study is available from the corresponding author upon request.

Conflicts of Interest

The authors declare that there are no conflicts of interest regarding the publication of this paper.

Acknowledgments

This work was supported by the National Natural Science Foundation of China under Grant nos. 61903323 and 11361072, the Natural Scientific Research Fund Project of Yunnan Province under Grant nos. 2017FH001-045 and 2018FH001-012, and the National Key Research and Development Project under Grant no. 2016YFC0502406.

Supplementary Materials

In this paper, in "Section 4," according to Yuxi city land and population data of Yunan Province, China, that is to say, from numerical simulation of data (see attachment of data.txt, basic data), we have $a = 0.34$, $b = 0.012$, $r = 0.0048$, $s = 0.004$, $h = 0.05$, and $d = 0.08$. By computing, we obtain the positive equilibrium point as (0.075617, 0.021169, 0.44984, 0.423379). Moreover, we have $R_0 = ((b\,d + ds)/ash) = 18.8235 > 1$, $\omega_0 = 0.002358$, and $\tau_0 = 728.403$. Furthermore, by using software of mathematics, we obtain fitting results, that is, it is in the attachments data1.txt and data2.txt (data after numerical simulation). As a matter of fact, this shows that numerical simulation is consistent with the actual, see Figures 1–8 and Figures 9–16. (*Supplementary Materials*)

References

[1] B. W. Huang, "On earth system science and sustainable development strategy (I)," *Acta Geographica Sinica*, vol. 51, pp. 350–354, 1996, in Chinese.

[2] W. V. Reid, D. Chen, L. Goldfarb et al., "Earth system science for global sustainability: grand challenges," *Science*, vol. 330, no. 6006, pp. 916-917, 2010.

[3] B. L. Turner II, "Local faces, global flows: the role of land use and land cover in global environmental change," *Land Degradation and Development*, vol. 5, no. 2, pp. 71–78, 1994.

[4] X. B. Li, "A review of the international researches on land use/land cover change," *Acta Geographica Sinica*, vol. 51, pp. 553–557, 1996, in Chinese.

[5] A. M. Dewan and Y. Yamaguchi, "Land use and land cover change in greater Dhaka, Bangladesh: using remote sensing to promote sustainable urbanization," *Applied Geography*, vol. 29, no. 3, pp. 390–401, 2009.

[6] H. J. Geist and E. F. Lambin, "Proximate causes and underlying driving forces of tropical deforestation," *Bioscience*, vol. 52, no. 2, pp. 143–150, 2002.

[7] S. Rost, D. Gerten, A. Bondeau, W. Lucht, J. Rohwer, and S. Schaphoff, "Agricultural green and blue water consumption and its influence on the global water system," *Water Resources Research*, vol. 44, pp. 137–148, 2008.

[8] L. H. Hou and Y. L. Cai, "An essential analysis and review on land use/cover change research," *Progress in Geography*, vol. 23, pp. 96–103, 2004, In Chinese.

[9] E. O'Rourke, "Socio-natural interaction and landscape dynamics in the Burren, Ireland," *Landscape and Urban Planning*, vol. 70, no. 1-2, pp. 69–83, 2005.

[10] J. Ni and J. A. Shao, "The drivers of land use change in the migration area, three gorges project, China: advances and prospects," *Journal of Earth Science*, vol. 24, no. 1, pp. 136–144, 2013.

[11] N. K. Msofe, L. X. Sheng, and J. Lyimo, "Land use change trends and their driving forces in the Kilombero valley floodplain, Southeastern Tanzania," *Sustainability*, vol. 11, no. 2, p. 505, 2019.

[12] J. Kleemann, G. Baysal, H. N. N. Bulley, and C. Frst, "Assessing driving forces of land use and land cover change by a mixed-method approach in north-eastern Ghana, West Africa," *Journal of Environmental Management*, vol. 196, pp. 411–442, 2017.

[13] D. Y. Liu, X. Q. Zheng, and H. B. Wang, "Land-use simulation and decision-support system (landSDS): seamlessly integrating system dynamics, agent-based model, and cellular automata," *Ecological Modelling*, vol. 417, pp. 1–10, 2020.

[14] Y. Q. Chen, H. V. Peter, and B. Xu, "Spatial modeling of land use and its effects in China," *Progress in Geography*, vol. 19, pp. 116–127, 2000, in Chinese.

[15] J. Zhang, W. B. Zhu, S. Y. Wu, and S. C. Li, "Simulation of temporal and special land use changes in Jing-Jin-Ji urban agglomeration using CLUE-S model," *Acta Scientiarum Naturalium Universitatis Pekinensis*, vol. 54, pp. 115–124, 2018, in Chinese.

[16] J. J. Liu, M. Xia, Y. Z. Liu, K. L. Zhang, and Z. H. Zhang, "Driving mechanism of rural land use change based on multi-agent system and cellular automata," *Transactions of the Chinese Society of Agricultural Engineering*, vol. 34, pp. 242–252, 2018, in Chinese.

[17] A. P. Dobson, A. D. Bradshaw, and A. J. M. Baker, "Hopes for the future: restoration ecology and conservation biology," *Science*, vol. 277, no. 5325, pp. 515–522, 1997.

[18] S. S. Chen, J. Hua, F. X. Zhang, and Y. M. Li, "Dynamical analysis of land model with Holling II land reclamation rate," *Journal of Systems Science and Complexity*, vol. 37, pp. 819–827, 2017.

[19] I. Kubiaczyk and S. H. Saker, "Oscillation and stability in nonlinear delay differential equations of population dynamics," *Mathematical and Computer Modelling*, vol. 35, no. 3-4, p. 295, 2002.

[20] K. Gopalsamy and I. Leung, "Delay induced periodicity in a neural netlet of excitation and inhibition," *Physica D*, vol. 89, no. 3-4, pp. 395–426, 1996.

[21] Y. H. Xia and V. G. Romanovski, "Bifurcation analysis of a population dynamics in a critical state," *Bulletin of the Malaysian Mathematical Sciences Society*, vol. 38, no. 2, pp. 499–527, 2015.

[22] Z. Wei, Y. H. Xia, and T. H. Zhang, "Stability and bifurcation analysis of a amensalism model with weak Allee effect," *Qualitative Theory of Dynamical Systems*, vol. 19, no. 1, pp. 19–23, 2020.

[23] X. D. Li, J. H. Shen, and R. Rakkiyappan, "Persistent impulsive effects on stability of functional differential equations with finite or infinite delay," *Applied Mathematics and Computation*, vol. 329, pp. 14–22, 2018.

[24] X. Y. Yang, X. D. Li, X. Li, Q. Xi, and P. Y. Duan, "Review of stability and stabilization for impulsive delayed systems," *Mathematical Biosciences & Engineering*, vol. 15, no. 6, pp. 1495–1515, 2018.

[25] X. D. Li, X. Y. Yang, and T. W. Huang, "Persistence of delayed cooperative models: impulsive control method," *Applied Mathematics and Computation*, vol. 342, pp. 130–146, 2019.

[26] D. Yang, X. D. Li, J. Shen, and Z. J. Zhou, "State-dependent switching control of delayed switched systems with stable and unstable modes," *Mathematical Methods in the Applied Sciences*, vol. 41, no. 16, pp. 6968–6983, 2018.

[27] D. Yang, X. D. Li, and J. L. Qiu, "Output tracking control of delayed switched systems via state-dependent switching and dynamic output feedback," *Nonlinear Analysis: Hybrid Systems*, vol. 32, pp. 294–305, 2019.

[28] Y. Q. Wang, J. Q. Lu, and Y. J. Lou, "Halanay-type inequality with delayed impulses and its applications," *Science China: Information Sciences*, vol. 62, no. 9, Article ID 192206, 2019.

[29] E. Ahmed, A. M. A. El-Sayed, and H. A. A. El-Saka, "Equilibrium points, stability and numerical solutions of fractional-order predator-prey and rabies models," *Journal of Mathematical Analysis and Applications*, vol. 325, no. 1, pp. 542–553, 2007.

[30] C. D. Huang, J. D. Cao, M. Xiao, A. Alsaedi, and F. E. Alsaadi, "Controlling bifurcation in a delayed fractional predator-prey system with incommensurate orders," *Applied Mathematics and Computation*, vol. 293, pp. 293–310, 2017.

[31] S. Das, P. K. Gupta, and Rajeev, "A fractional predator-prey model and its solution," *International Journal of Nonlinear Sciences and Numerical Simulation*, vol. 10, no. 7, pp. 873–876, 2009.

[32] H. A. El-Saka, E. Ahmed, M. I. Shehata, and A. M. A. El-Sayed, "On stability, persistence, and Hopf bifurcation in fractional order dynamical systems," *Nonlinear Dynamics*, vol. 56, no. 1-2, pp. 121–126, 2009.

[33] C. Luo and X. Y. Wang, "Chaos generated from the fractional-order complex chen system and its application to digital secure communication," *International Journal of Modern Physics C*, vol. 24, no. 04, p. 1350025, 2013.

[34] E. Kaslik and S. Sivasundaram, "Nonlinear dynamics and chaos in fractional-order neural networks," *Neural Networks*, vol. 32, no. 1, pp. 245–256, 2012.

[35] Y. Li, H. P. Wang, and Y. Tian, "Fractional-order adaptive controller for chaotic synchronization and application to a dual-channel secure communication system," *Modern Physics Letters B*, vol. 33, no. 24, pp. 1097–1106, 2019.

[36] L. X. Yang, W. S. He, and X. J. Liu, "Synchronization between a fractional-order system and an integer order system," *Computers & Mathematics with Applications*, vol. 62, no. 12, pp. 4708–4716, 2011.

[37] M. Odai and Y. Hori, "Controller design robust to nonlinear elements based on fractional order control system," *IEEE Transactions on Industry Applications*, vol. 120, no. 1, pp. 11–18, 2010.

[38] C. D. Huang, H. Liu, X. P. Chen, M. S. Zhang, J. D. Cao, and A. Alsaedi, "Dynamic optimal control of enhancing feedback treatment for a delayed fractional order predator-prey model," *Physica A: Statistical Mechanics and Its Applications*, vol. 554, Article ID 124136, 2020.

[39] Z. Wang, Y. K. Xie, J. W. Lu, and Y. X. Li, "Stability and bifurcation of a delayed generalized fractional-order prey-predator model with interspecific competition," *Applied Mathematics and Computation*, vol. 347, pp. 360–369, 2019.

[40] C. D. Huang, Z. H. Li, D. W. Ding, and J. D. Cao, "Bifurcation analysis in a delayed fractional neural network involving self-connection," *Neurocomputing*, vol. 314, pp. 186–197, 2018.

[41] D. Matignon, "Stability results for fractional differential equations with applications to control processing," in *Proceedings of the Computational Engineering in Systems and Application Multi-Conference, IMACS*, vol. 2, pp. 963–968, Lille, France, 2016.

[42] X. Li and R. C. Wu, "Hopf bifurcation analysis of a new commensurate fractional-order hyperchaotic system," *Nonlinear Dynamics*, vol. 78, no. 1, pp. 279–288, 2014.

[43] N. Laskin, "Fractional quantum mechanics," *Physical Review E*, vol. 62, no. 3, pp. 3135–3145, 2000.

[44] I. Podlubny, *Fractional Differential Equations*, Academic Press, Cambridge, MA, USA, 1999.

[45] A. A. Kilbas, H. M. Srivastava, and J. J. Trujillo, *Theory and Application of Fractional Differential Equations*, Elsevier, New York, NY, USA, 2006.

[46] T. Zhao, Z. Z. Zhang, and R. K. Upadhyay, "Delay-induced Hopf bifurcation of an SVEIR computer virus model with nonlinear incidence rate," *Advances in Difference Equations*, vol. 2018, no. 1, 2018.

[47] E. Hanert, E. Schumacher, and E. Deleersnijder, "Front dynamics in fractional-order epidemic models," *Journal of Theoretical Biology*, vol. 279, no. 1, pp. 9–16, 2011.

[48] C. Vargas-De-León, "Volterra-type Lyapunov functions for fractional-order epidemic systems," *Communications in Nonlinear Science and Numerical Simulation*, vol. 24, no. 1–3, pp. 75–85, 2015.

[49] H. AbdelhamedAsfour and M. Ibrahim, "On the differential fractional transformation method of MSEIR epidemic model," *International Journal of Computer Applications*, vol. 113, no. 3, pp. 10–16, 2015.

[50] W. Zhu, Y. H. Xia, B. Zhang, and Y. Bai, "Exact traveling wave solutions and bifurcations of the time fractional differential equations with applications," *International Journal of Bifurcation and Chaos*, vol. 29, no. 3, Article ID 1950041, 2019.

[51] A. S. Deshpande, V. Daftardar-Gejji, and Y. V. Sukale, "On Hopf bifurcation in fractional dynamical systems," *Chaos, Solitons & Fractals*, vol. 98, pp. 189–198, 2017.

[52] H. Wang, Y. Yu, G. Wen, and S. Zhang, "Stability analysis of fractional-order neural networks with time delay," *Neural Processing Letters*, vol. 42, no. 2, pp. 479–500, 2015.

[53] M. Xiao, W. X. Zheng, G. Jiang, and J. D. Cao, "Undamped oscillations generated by Hopf bifurcations in fractional-order recurrent neural networks with caputo derivative," *IEEE Transactions on Neural Networks and Learning Systems*, vol. 26, no. 12, pp. 3201–3214, 2015.

[54] S. Bhalekar and D. Varsha, "A predictor-corrector scheme for solving nonlinear delay differential equations of fractional order," *Journal of Fractional Calculus and Applications*, vol. 1, pp. 1–9, 2011.

Hindawi
Discrete Dynamics in Nature and Society
Volume 2020, Article ID 2196893, 10 pages
https://doi.org/10.1155/2020/2196893

Research Article

Speech Separation Using Convolutional Neural Network and Attention Mechanism

Chun-Miao Yuan, Xue-Mei Sun, and Hu Zhao

School of Computer Science and Technology, TianGong University, Tianjin 300387, China

Correspondence should be addressed to Xue-Mei Sun; sunxuemei@tiangong.edu.cn

Received 14 May 2020; Accepted 8 July 2020; Published 25 July 2020

Academic Editor: Jianquan Lu

Speech information is the most important means of human communication, and it is crucial to separate the target voice from the mixed sound signals. This paper proposes a speech separation model based on convolutional neural networks and attention mechanism. The magnitude spectrum of the mixed speech signals, as the input, has its high dimensionality. By analyzing the characteristics of the convolutional neural network and attention mechanism, it can be found that the convolutional neural network can effectively extract low-dimensional features and mine the spatiotemporal structure information in the speech signals, and the attention mechanism can reduce the loss of sequence information. The accuracy of speech separation can be improved effectively by combining two mechanisms. Compared to the typical speech separation model DRNN-2 + discrim, this method achieves 0.27 dB GNSDR gain and 0.51 dB GSIR gain, which illustrates that the speech separation model proposed in this paper has achieved an ideal separation effect.

1. Introduction

Voice information plays an increasingly important role in our lives, and voice communication becomes more and more frequent, such as using chatting software to send voice messages, using voice to control mobile phone applications, making mobile phone calls for voice communication, recognizing the singers from songs [1], and identifying singer's information, lyrics, and song style [2, 3]. The goal of speech separation is to separate the mixed speech into two original speech signals. In signal processing, speech separation is a basic task with a wide range of applications, including mobile communication, speaker recognition, and song separation. There are many potential values for separating mixed speech. Nowadays, speech separation plays a more and more important role in speech processing, and more and more devices need to carry out speech separation task.

Although humans can easily perform speech separation, it is very challenging to build an automatic system that matches the human auditory system. Therefore, speech separation has always been an important research direction of speech processing. The early speech separation method is very limited in the ability of mining nonlinear structure information, and the performance of monaural speech separation has been unsatisfactory. With the development of deep neural networks in recent years [4–6], good results have been achieved in various fields. Compared with traditional speech methods, there are many advantages for deep neural network-based speech separation models. The main contribution of this paper is to apply the convolution neural network to the speech separation tasks, use the multilayer nonlinear processing structure of the convolution neural network to mine the structure information in the speech signals, automatically extract the abstract features, integrate the attention mechanism to reduce the loss of the sequence information, and finally achieve the monaural speech separation.

2. Relative Research

Speech separation problem has been widely studied worldwide. The traditional methods of monaural speech

separation are speech enhancement, which analyze the data of the mixed speech and the noise and then estimate the target speech through the interference estimation of the mixed speech. From the viewpoint of signal processing, many speech enhancement methods propose a power spectrum of estimated noise or an ideal Wiener wave recorder, such as spectral subtraction [7] and Wiener filter [8]. There are many other ways to achieve speech enhancement (e.g., through Bayesian model [9] or time-frequency masking methods [10]). Some researchers tried to use computer auditory scene analysis (CASA) to achieve speech separation, which is the use of computer technology to allow computers to imitate the processing of human auditory signals for modeling, so as to have the ability to perceive sound, process sound, and interpret sound from complex mixed sound sources such as humans. The basic computational goal of auditory scene analysis is to estimate an ideal binary mask to achieve speech separation based on auditory masking of the human ears [11–13]. Speech enhancement technology generally assumes that the interference speech is stable, so its separation performance will be severely degraded when the actual interference noise is nonstationary. Computational auditory scene analysis, with better generalization performance, has no assumptions about noise. Meanwhile, the computational auditory scene analysis heavily relies on speech pitch detection, which is very difficult under the interference of background sounds.

Speech separation is designed to isolate useful signals from disturbed speech signals, a process that can be expressed naturally as a supervised learning problem [14]. A typical supervised speech separation system learns a mapping function from noisy features to separation targets (e.g., ideal masking or magnitude spectrum of speech interested) through supervised learning algorithms such as deep neural networks. Many supervised speech separation methods have been proposed in recent years [15–18]. The learning models for supervised speech separation are mainly divided into two kinds. (1) Traditional methods such as model-based methods and speech enhancement methods. (2) Newer methods using DNNs (Deep Neural Networks). Due to the speech generation mechanism, the input features and output targets of the speech separation show obvious spatiotemporal structure. These characteristics are very suitable for modeling with deep models. Many deep models are widely used in speech separation. Sun et al. [19] proposed two-stage approach with two DNN-based methods to address the problem of the performance of current speech separation methods. New training targets in complement of existing magnitude training targets were trained through neural network methods to compensate for phase of target in order to achieve better separation performance by the authors of [20]. Zhou et al. [21] designed a separation system on Recurrent Neural Network (RNN) with long short-term memory (LSTM), which effectively learns the temporal dynamics of spatial features. Supervised speech separation does not require spatial orientation information of the sound sources, and there are no restrictions on the statistical characteristics of noise. It shows obvious advantages and a fairly bright research prospective under the conditions of monaural, nonstationary noise, and low signal-to-noise ratio [22, 23].

Deep Recurrent Neural Network (DRNN) among them is a representative of deep models and has been widely used in speech separation. DRNN has strong learning ability in speech separation. RNN series of units, such as LSTM [24]/GRU (Gated Recurrent Unit, GRU) [25], all of whose hidden states are calculated according to the Markov model. The previous hidden state will save some previous information, while the magnitude spectrum of the mixed speech is a relatively long sequence, and sequence information will be lost (after all, the capacity of the cell state is limited in practice), which will affect the separation of mixed speech and reduce the accuracy of estimated speech.

Convolutional neural network (CNN) has been widely used in deep learning since it was firstly proposed by Yann Lecun et al. [26] in 1998. CNN has its natural advantages in two-dimensional signal processing, and its powerful modeling capabilities have been verified in tasks such as image recognition. CNN at present has been applied to speech separation [27, 28] and has achieved the best separation performance under the same conditions, which has exceeded the DNN-based speech separation systems. Luo et al. [29] proposed Conv-TasNet, which was a fully convolutional time-domain audio separation network to solve the problems of time-frequency masking. Wang et al. [30] applied CNN and modified its loss function to solve the imbalance between classification accuracy, hit rate, and error rate.

Both the traditional and DNN-based separation models have achieved good results, but they all have corresponding shortcomings. Convolutional neural network can make use of the spatial connection of input data so that each element can learn local features without learning global features, and then at a higher-level these local features will be combined together to get global features. Weight sharing can reduce the parameters between different neurons, reduce the calculation time, and improve the speed of the model. By using a variety of convolution filters, multiple feature maps can be obtained, which can detect the same type of features in different positions and ensure the invariance of displacement and deformation to a certain extent. Therefore, this paper proposes a method based on convolutional neural network to solve the problem of the loss of long sequence information of mixed speech. Combined with the attention mechanism, our model can better focus on the timing sequence step, which contributes the most, and solve the problem of insufficient memory of the temporal model to a certain extent, so as to improve the speech separation effect.

3. System Modeling

The purpose of the speech separation is to separate the target voice from the background sound. The overall structure of the speech separation system is shown in Figure 1. The first process of speech separation is to obtain the magnitude spectrum and phase information of mixed speech through STFT (Short-time Fourier Transform) [31]. The estimated targets using speech magnitude spectrum have been shown to suppress noise significantly and improve the speech

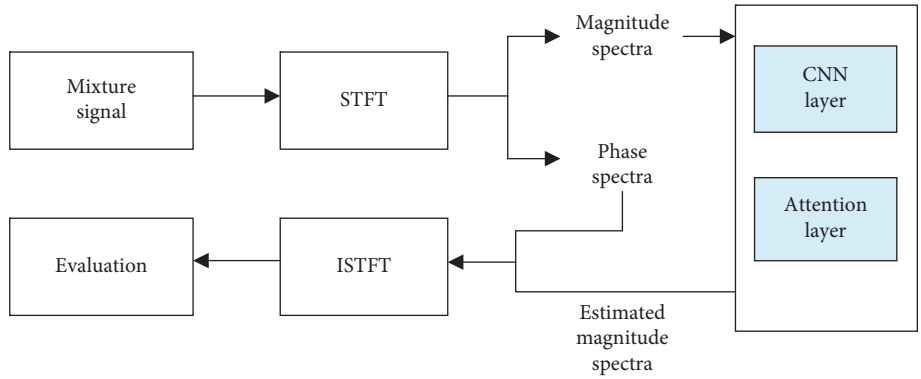

Figure 1: The modeling of speech separation.

intelligibility and its perceived quality. Then, the magnitude spectrum information is used as the input of the speech separation model. The magnitude spectrum is trained by convolutional neural network, and the region of interest of speech is extracted by the attention module. Finally, through the overlap-add method [32], the target speech is obtained by the combination of the magnitude spectrum information estimated by the separation model and the previous phase information. The speech separation ability of the model is evaluated based on the comparison between the estimated speech and the pure speech.

4. Proposed Methods

Deep models, with multilevel nonlinear structures, good at mining structural information in data, which can automatically extract abstract feature representations, have been widely used in image, video, and speech processing. This paper presents a monaural speech separation model based on the convolutional neural network and attention mechanism; we name it CASSM. There are two main modules in this model: convolutional neural network module and attention mechanism, both of which are jointly optimized to complete the task of speech separation. In the convolutional neural network module, it can extract features from the magnitude spectrum of the mixed speech, reduce the dimension of the magnitude spectrum, and model the current and contextual information effectively. Although convolutional neural networks can extract the magnitude spectrum features of mixed speech signals effectively, they cannot model sequence information in the same way. The attention mechanism RNN is good at processing sequence information; however, there are shortcomings in extracting information features versus convolutional neural networks. After the training of neural network, it can recognize the difference of different signal sources at different frame levels effectively; the attention mechanism-based neural network can recognize the importance of each part of the magnitude spectrum with the help of context information [33], thus considerably improving the effect of speech separation.

4.1. Network Structure. The network structure of the model is shown in Figure 2. The magnitude spectrum of the mixed speech is used as the input of the neural network, the estimated magnitude spectrum is obtained by training the neural network, and the original phase is combined to get the estimated speech by ISTFT (inverse short-time Fourier transform).

The amplitude spectrum of mixed speech has high dimensionality when it acts as the input of neural network. CNN is good at mining the spatiotemporal structure information of the input signal and can extract the local feature information of the magnitude spectrum, which can improve the performance of speech separation.

The magnitude spectrum of the mixed speech is used as the network input and then forward propagates along two paths, one of which is used as the input of the convolutional layer, while the other forms the combination sequence of the input layer with the low-dimensional sequence that has been processed by the convolution. The input information transmits through two convolutional filters with different sizes and important information about the mixed speech magnitude spectrum is able to be extracted.

We use relu as an activation function. The output of the two convolutions is superimposed and processed by the maximum pooling layer, which provides strong robustness, increases the invariance of the current information, speeds up the calculation speed, and prevents overfitting. The sequence continues through several convolutional layers that can be effectively modeled for current as well as contextual information to obtain a low-dimensional embedding sequence. The low-dimensional and high-dimensional embedded sequences are superimposed into a combined one, which passes through two-tier high-speed networks to extract higher-level features.

Still, there are many shortcomings in processing serialized information for speech separation although convolutional neural networks can extract features from the magnitude spectrum of mixed speech, reduce the dimension of the magnitude spectrum, and model the current and contextual information effectively. Comparatively, the attention mechanism RNN is much skilled in processing serialized information, helpful in strengthening the dependence between the magnitude spectrum, and can jointly fulfill the task of speech separation with the convolutional neural network module.

The attention mechanism is used for the input of the mixed speech magnitude spectrum so that the model pays different attention to the information features from different

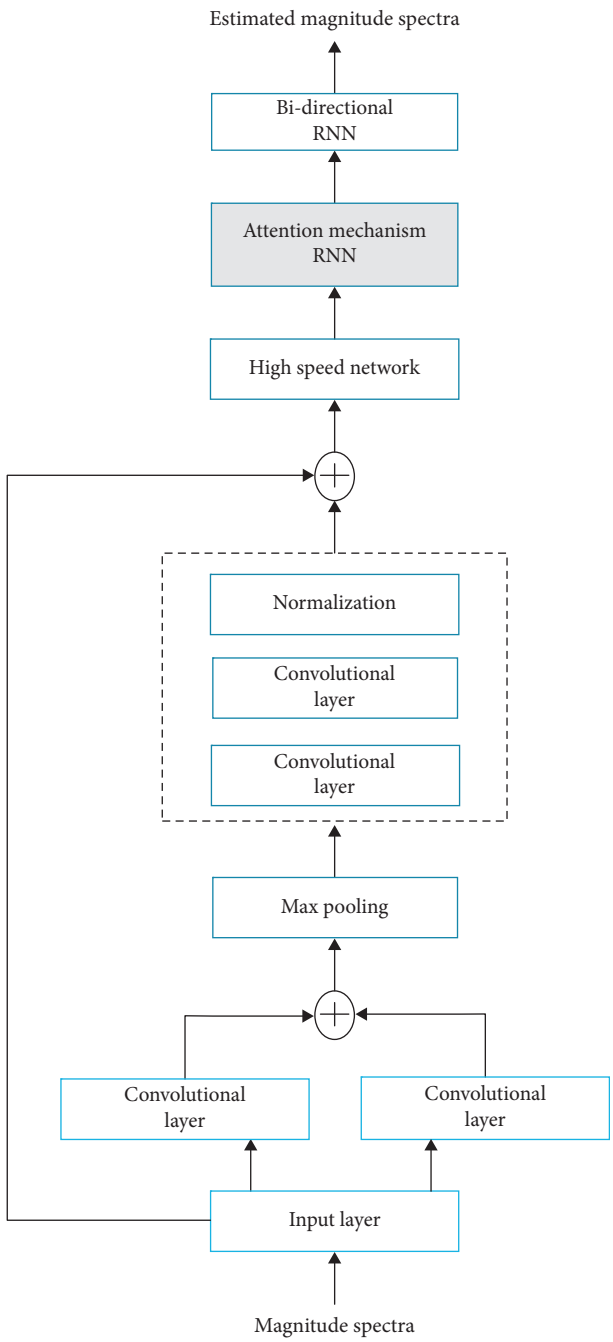

Figure 2: Network architecture of proposed CASSM.

moments. The traditional recurrent neural network uses only the information of state [t−1] when calculating the state [t] at the t moment. Since the magnitude spectrum is a long sequence, there will be a loss of information although the previous state [t−1] contains some previous information. The attention mechanism uses the previous information to calculate the state information at the current moment. The attention mechanism used in this paper is based on a layer of RNN (LSTM unit) with an attention length of 32.

Long Short-Term Memory (LSTM) is a specific recurrent neural network (RNN) architecture that was designed to model temporal sequences and their long-range dependencies more accurately than conventional RNNs. LSTM RNNs are more effective than DNNs and conventional RNNs for acoustic modeling, considering moderately sized models trained on a single machine [34]. LSTM RNN makes more effective use of model parameters than the others considered, converges quickly, and outperforms a deep feedforward neural network having an order of magnitude more parameters.

A bidirectional recurrent neural network and two feedforward layers are used to form a separation module after the attention mechanism RNN.

4.2. Short-Term Fourier Transform. The spectrum of speech signals has its significant role in speech, through which, some nontrivial speech features can be obtained. Stationary signals refer to the signals that the distribution law does not change over time, while nonstationary signals are signals that change over time. The mixed speech signals belong to the nonstationary signals, and the speech signals have the characteristics of nonstationary one.

The Fourier transform (FT) is ubiquitous in science and engineering. For example, it finds application in the solution of equations for the flow of heat, for the diffraction of electromagnetic radiation, and for the analysis of electrical circuits. The concept of the FT lies at the core of modern electrical engineering and is a unifying concept that connects seemingly different fields. The STFT is a fine resolution to the problem of determining the frequency spectrum of signals with time-varying frequency spectra. Fourier transform is the process of conversion between time domain and frequency. The Fourier transform is in its essence, a reversible transform that can transform the original signals and the transformed signals into each other. The characteristics of the Fourier transform are not suitable for analyzing nonstationary signals, which cannot directly represent speech signals. The speech signals change slowly with the change of time, which even can be regarded as unchanged in a short period of time. Analysis of the frequency domain information in a short time is the short-time Fourier transform.

Short-time Fourier transform (STFT) is a commonly used tool for processing speech signals. There is only one difference between the Fourier transform and the short-time Fourier transform. The short-time Fourier transform is to divide the speech signals into sufficiently small fragments so that the speech signals can be seen as a stable one. The short-time Fourier transform formula is defined as

$$\mathrm{STFT}(t,\omega) = \int_{-\infty}^{\infty} s(x)\gamma(x-t)e^{-j\omega x}dx. \quad (1)$$

In which, $\gamma(t)$ is the length M window function, $s(x)$ denotes an input signal at time x to be transformed, and STFT (t, ω) is a two-dimensional complex function, which represents the magnitude and phase that change over time and frequency.

In supervised speech separation, feature extraction is an indispensable process, and the selection of features will affect the speech separation model training. From the point of the extracted basic units, the features of speech separation are mainly divided into time-frequency unit-level features and frame-level

ones. Frame-level features are extracted from a frame of signals. This level of features has a larger granularity and can capture the spatiotemporal structure of speech, especially the frequency band correlation of speech. It is more general and holistic and has clear characteristics of speech perception.

The feature extraction in this paper is based on the frame level. The short-time Fourier transform is used to frame and window the speech signals. In each frame, the magnitude spectrum and phase in this paper are obtained by 1024-point STFT. The speech separation model can better display the information of speech by using frame-level features and can mine the space-time structure of speech in all directions during training. The magnitude spectrum obtained by using the short-time Fourier transform in this paper can make model training easier and accelerate the model convergence.

4.3. Attention Mechanisms. In recent years, the attention mechanism has been widely used by many scholars in deep learning models in different fields, such as speech recognition and image recognition. Due to the limitations of information processing, when much information is processed, people usually choose some of the important parts for processing, while ignoring other parts of the information. This idea is the origin of the attention mechanism. When people are reading, they will pay more attention to and deal with some important vocabulary and ignore some less important parts, which will speed up the reading and improve reading efficiency. Attention mechanism now has become a widely used tool; thus, attention mechanism is one of the crucial important algorithms in deep learning algorithms that need the most attention and understanding. However, attention mechanism is currently not widely used in speech separation; therefore, this paper attempts to introduce attention mechanism into the process of speech separation, focusing on the region of interest in speech feature information, so as to improve the accuracy of speech separation.

Strictly speaking, attention mechanism is an idea rather than an implementation of some models, which can be implemented in a variety of ways. Due to the bottleneck of information processing, attention mechanism requires to decide which part may be the focus, allocate the limited information processing resources to more important parts, and specially focus on the key information.

There are many variants of the attention mechanism, and the attention mechanism used in this paper is AttentionCellWrapper in TensorFlow [35], which is a general attention mechanism. This attention structure can be used through a one-way recurrent neural network. While processing the input of each step, it will consider the output of the previous N steps and add the previous historical information to the prediction of the current input through a mapping weighting method:

$$\begin{aligned} \mathscr{U}_i^t &= \mathscr{V}^T \tan h\left(W_\alpha h_t + W_\beta o_i\right), \\ a_i^t &= \text{soft}\max\left(\mathscr{U}_i^t\right), \\ h_t' &= \sum_{i=1}^{t-1} a_i^t o_i. \end{aligned} \tag{2}$$

In which, the vector $\mathscr{V}$ and matrix W_α, W_β are the learnable parameters of the model in the formula, h_t is the matrix of the current hidden-layer state of the LSTM and the LSTM unit connection, and o_i is the output of the ith LSTM unit. The attention weights a_i^t of each moment are normalized calculated by the softmax function. Finally, connecting h_t with h_t' becomes the predicted new hidden state and is also fed back to the next step of the model.

It becomes possible for the simple timing model to use the attention mechanism by using this general attention structure designed by TensorFlow, which can make the entire model more focus on the timing step that contributes the most, and solve the timing model with memory problems to some extent.

4.4. Time-Frequency Masking Calculation Layer. Considering the constraints of TF (time-frequency) masking between the forced input mixed speech signals and the estimated speech signals as well as the benefits of smooth separation, a time-frequency masking calculation layer is used in the speech separation model to jointly optimize the TF model with the entire deep learning model. The time-frequency masking calculation layer is defined as

$$\begin{aligned} \widetilde{y}_1 &= \frac{\left|\widehat{y}_1\right|}{\left|\widehat{y}_1\right| + \left|\widehat{y}_2\right|} \odot z, \\ \widetilde{y}_2 &= \frac{\left|\widehat{y}_2\right|}{\left|\widehat{y}_1\right| + \left|\widehat{y}_2\right|} \odot z, \end{aligned} \tag{3}$$

where $\widetilde{y}_1$ and $\widetilde{y}_2$ are the magnitude spectrums of the estimated speech signals; $\widehat{y}_1$ and $\widehat{y}_2$ are the output magnitude spectrums of the two feedforward networks of the speech separation module; and z is the magnitude spectrum of the input mixed speech signals.

The masking effect is a phenomenon that occurs when the human ears perceive speech. A louder sound will mask a lower one. If the difference between the two sound frequencies is small, the effect of the masking effect becomes more obvious. The masking effect is of great significance in speech processing.

4.5. Loss Function. The loss function is used to describe the difference between the predicted value and the target value. The loss function is generally positive, and the size of the loss function reflects the quality of the model. When the model performs speech separation, the value of the loss function is relatively small if the model speech separation works well. The size of the loss function directly reflects the speech separation effect of the model. The loss function of the training network model in this paper is defined as [36]

$$\begin{aligned} J_{\text{DIS}} = &\left\|y_1 - \widetilde{y}_1^2\right\| + \left\|y_2 - \widetilde{y}_2^2\right\| \\ &- \gamma\left\|y_1 - \widetilde{y}_1^2\right\| - \gamma\left\|y_2 - \widetilde{y}_2^2\right\|, \quad \gamma > 0, \end{aligned} \tag{4}$$

where y_1 and y_2 are the ground truth of magnitude spectrum, $\widetilde{y}_1$ and $\widetilde{y}_2$ are the estimated magnitude spectrum of speech, and $0 \le \gamma \le 1$ is a regularization parameter.

5. Simulation Experiments and Analysis

In this paper, experiments were performed on a Windows 10 Professional 64-bit computer with hardware configuration of i5, 8GB RAM, and GT1060X 6G graphics card. The program was written in PyCharm software using Python.

The MIR-1K dataset [37] was used to evaluate the model. The dataset has 1,000 mixed music clips encoded at a 16 KHz sampling rate, with a duration from 4 to 13 seconds. The clips were extracted from 110 Chinese karaoke songs performed by both male and female amateurs. The singing voice and background music were mixed into a music fragment with a signal-to-noise ratio of 0 dB. In this dataset, 175 clips were used for the training sets, and 825 were used for the testing sets.

Speech separation usually uses three parameters of BSS-EVAL [38] to verify the performance of the model: SDR (Signal to Distortion Ratio), SIR (Signal to Interference Ratio), and SAR (Signal to Artifact Ratio). SDR is the ratio between the power of mixed speech signals and the difference value of the mixed speech signals and the target speech signals. SIR is the total power ratio between the target speech signals and the interference signals. SAR stands for artifacts introduced by processing speech signals. SDR calculates how much total distortion exists in the separated sound. A higher SDR value indicates a smaller overall distortion of the speech separation system. SIR directly compares the degree of speech separation between nontarget sound and target sound. A higher SAR value indicates a smaller introduced error of the speech separation system. A higher value of the three parameters indicates a better effect of the speech separation model.

In this experiment, in order to evaluate the effect of the speech separation model, the global NSDR (GNSDR), global SIR (GSIR), and global SAR (GSAR) were used to evaluate the overall effect, all of which were the mean value of the tested fragments based on their lengths calculated. The normalized SDR (NSDR) [39] is defined as

$$\mathrm{NSDR}(\hat{o}, o, m) = \mathrm{SDR}(\hat{o}, o) - \mathrm{SDR}(m, o). \tag{5}$$

In which, o is the original pure signal, $\hat{o}$ is the estimated speech signal, and m is the mixed speech signals. NSDR is used to estimate the SDR improvement of mixed speech signal m and speech signal $\hat{o}$.

We conducted multiple comparative experiments to comprehensively evaluate the validity and reliability of the proposed model. Firstly, we tested the influence of LSTM and GRU gating units on the effect of speech separation. Secondly, we verified the improvement of the separation effect of the traditional speech separation models by the attention mechanism. Then, we compared the separation effect between DRNN-2 + discrim proposed by Huang et al. and CASSM proposed in this paper. Finally, we explored the effect of attention length on the effect of speech separation.

5.1. The Influence of LSTM and GRU on Speech Separation Model. The recurrent neural network has the function of short-term memory, but if the training sequence is long enough, it is difficult for the network to transmit the more important information from the previous to the later process. Therefore, if the speech problem is processed, the recurrent neural network will miss some important information, resulting in a reduction in processing power and a negative impact on speech processing results. Another problem is that, in the later backpropagation phase, the recurrent neural network will encounter the problem of gradient disappearance, which is the weight value of updating each layer in the network. Gradient disappearance means that the gradient value will continue to decrease as the training proceeds, and when the gradient drops to a very small amount, the neural network will not continue to learn, and the training process will stop, which may affect the training results.

In order to solve these problems, two methods, LSTM unit (Long Short-Term Memory unit) [24] and GRU (Gated Recurrent Unit) [25], have been proposed through the efforts of many researchers. Both types of units have internal mechanisms, gates, which can regulate the flow of information to achieve the function of memory. These two gating units have different characteristics. In our experiments, the effect from the two types of gating units, LSTM and GRU, on the results of the speech separation model was evaluated.

Firstly, the effect on the separation model was reflected by using the different gating units of the three-layer unidirectional recurrent neural network layer, RSSM (RNN-based Speech Separation Model). The speech separation results of each model were described by three parameters: GNSDR, GSIR, and GSAR. The experimental results of the two gating units are shown in Figure 3.

The effect of different gating units was analyzed from the experimental results in the Figure 3. The speech separation model using LSTM gating units obtained a gain of 0.07 dB on the GNSDR, a gain of 0.39 dB on the GSIR and a gain of −0.09 dB on the GSAR relative to the GRU.

The ASSM (Attention-based Speech Separation Model) was mainly used to analyze the effect of attention mechanism on speech separation and to verify the effectiveness of attention mechanism in speech separation. Next, the ASSM was used to evaluate the effect from the two gated units, LSTM and GRU, on the results of the speech separation model in the attention mechanism. The ASSM was mainly used to analyze the effect of attention mechanism on speech separation and verify the effectiveness of attention mechanism in speech separation. ASSM was composed of fully connected layer, attention mechanism RNN, and bidirectional RNN.

The experimental results in Figure 4 showed three indicators of speech separation. In the experiment, the ASSM using the LSTM unit was 0.05 dB higher in GNSDR and 0.37 dB in GSIR than that of using GRU unit. From the experimental results of the two groups, it can be concluded that LSTM is superior to GRU on GNSDR and GSIR. Therefore, LSTM was employed in our proposed model in terms of the attention mechanism.

5.2. CASSM Performance Verification Experiment. This experiment mainly aimed to verify the effect of the speech separation model proposed in this paper. Since the results of

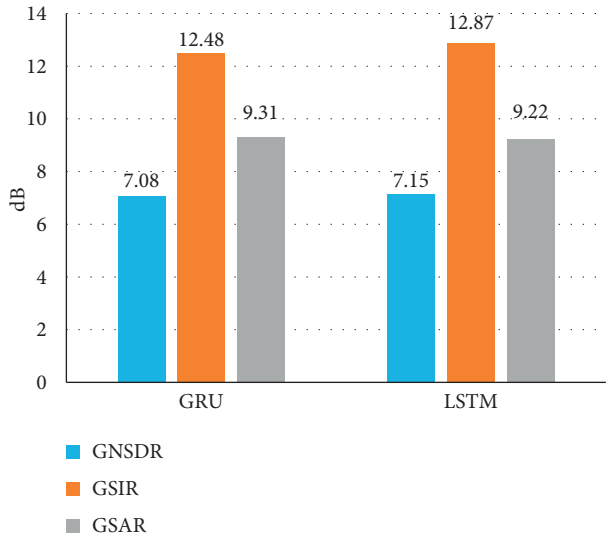

Figure 3: The comparison for the effect of GRU and LSTM in RSSM.

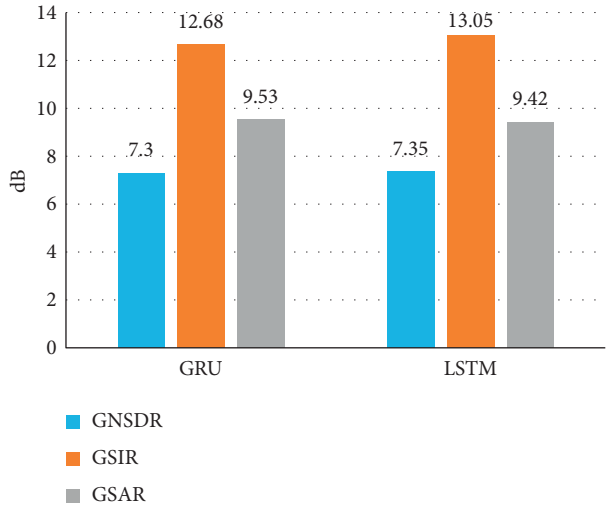

Figure 4: The comparison for the effect of GRU and LSTM in ASSM.

the speech separation model based on recurrent neural network were not very satisfactory, inspired by attention mechanism and convolutional neural network, this paper proposed a speech separation model based on attention mechanism and convolutional neural network, CASSM, and the effectiveness of the model would be verified through the following experiments.

Huang et al. [36] applied the recurrent neural network to speech separation and proposed a speech separation variant model based on deep recurrent neural network. The speech separation effect varies from different models employed. In previous research, masking of monochannel signal separation and the joint optimization of deep recurrent neural network have achieved better speech separation performance. In our experiment, a comparison was made among these models: CASSM, the DRNN-2 + discrim model with the best separation effect achieved by Huang et al. [36], RNMF (Robust Low-Rank Nonnegative Matrix Factorization), and MLRR (Multiple Low-Rank Representation).

The attention mechanism used was LSTM unit with an attention length of 32. The experimental results are shown in Figure 5. Compared with MLRR and RNMF, the value of CASSM was 3.87 dB and 2.75 dB higher in GNSDR, 7.96 dB and 5.93 dB higher in GSIR, and −1.06 dB and -0.39 dB lower in GSAR. Experiments demonstrated that convolutional neural network plus attention mechanism had greater advantages over traditional speech separation models. Convolutional neural network can more fully extract sound spectrum features. Attention mechanism can strengthen the dependence between magnitude spectrum features and improve the speech separation performance. Compared with DRNN-2 + discrim, the improvement of CASSM was 0.27 dB higher in GNSDR and 0.51 dB higher in GSIR. Experiments illustrated that there was still a gap between DRNN-2 + discrim and CASSM in terms of processing amplitude spectra. In DRNN-2 + discrim, the original magnitude spectrum of the mixed speech was directly used as the input features, while the CNN module of CASSM used the combined sequence formed by the high-dimensional magnitude spectrum of the mixed speech as the input features. Meanwhile, a better speech separation effect in the experiment was achieved since the attention mechanism module of CASSM had reduced the loss of sequence information.

The "discrim" denotes the models with discriminative training

5.3. Ablation Experiment. In this section, we conducted ablation experiments to verify the effectiveness of our proposed model. Firstly, we removed the convolutional neural network module in our model and observed the speech separation results of only attention module; then, we continued to remove the attention module and observed the speech separation result of the model with only recurrent neural network.

In our experiment, the attention mechanism used was LSTM unit with an attention length of 32, and RNN was a unidirectional RNN with 1000 hidden layers. The effect of each model was analyzed from the experimental results. After removing the CNN module, the GNSDR, GSIR, and GSAR of the model decreased by 0.37 dB, 0.66 dB, and 0.18 dB, respectively, while the attention module was removed, the GNSDR, GSIR, and GSAR of the model declined by 0.57 dB, 0.72 dB, and 0.42 DB, respectively. On the whole, the speech separation performance was substantially decreased.

The results of ablation experiments show that, after removing CNN and attention mechanism, respectively, the speech separation ability of the model has decreased to varying degrees (Figure 6).

5.4. Effect of Attention Length on Speech Separation. This simulation experiment explored the effect of attention length on speech separation through a speech separation model

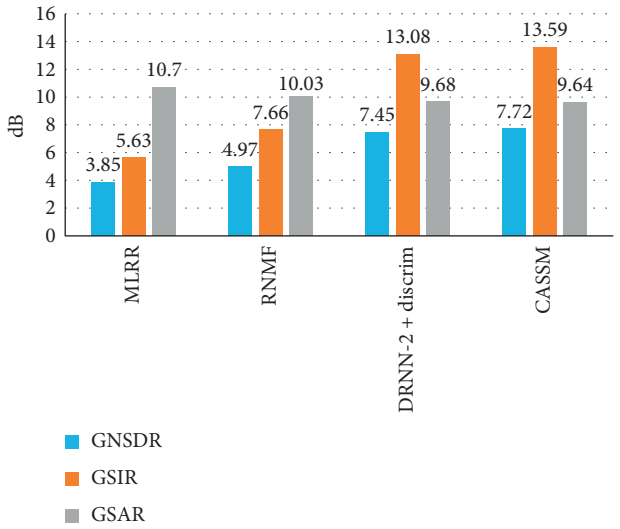

Figure 5: The comparison for the effect of MLRR, RNF, DRNN-2 + discrim, and CASSM.

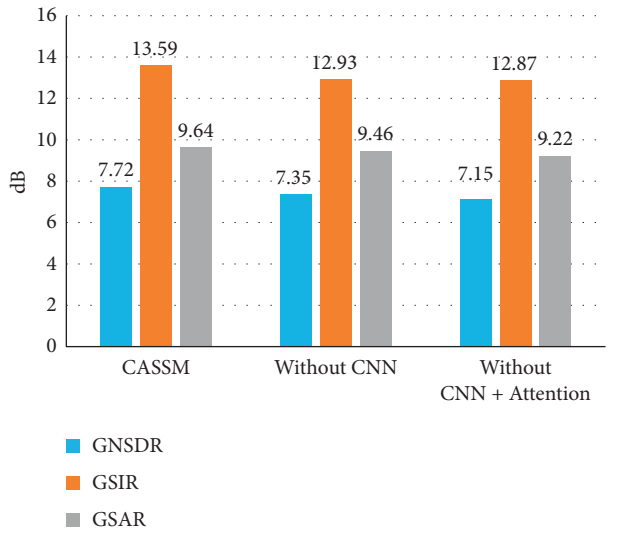

Figure 6: The comparison for the effect of ablation experiments.

based on convolutional neural network and attention mechanism. In this experiment, the attention mechanism used in this paper was based on a one-way RNN (hidden layers are 1000 layers, LSTM units); the length of attention was 8, 16, and 32, respectively.

The experimental results in Figure 7 showed that the speech separation model with attention length of 16 was 0.09 dB higher in GNSDR, 0.2 dB in GSIR, and 0.03 dB higher in GSAR than the speech separation model with attention length of 8. Compared with the speech separation model with attention length of 16, the speech separation model with attention length of 32 was 0.06 dB higher in GNSDR, 0.37 dB higher in GSIR, and 0.1 dB lower in GSAR.

The experimental results indicated that the attention length of the attention mechanism had taken a relatively large effect on speech separation. The effect of speech

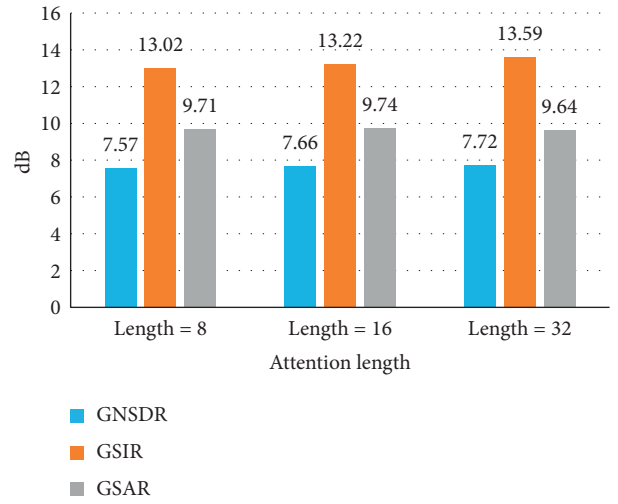

Figure 7: The comparison for the effect of different attention lengths.

separation is getting better and better with the increase of attention length. It can be concluded from the simulation experiment that the increase of attention length could improve the effect of speech separation.

The simulation results also illustrated that the training time would increase with the increase of attention length and the demand for video memory would relatively increase; therefore, a reasonable choice of attention length is highly recommended. There are still some limitations and shortcomings in the experiment. Due to the limitation of equipment, the attention length of the speech separation model could only be adjusted to 32. If it continues to increase, the device may report an insufficient memory. Therefore, research and discussion on this indicator in future experiments can be carried out.

6. Conclusion

This paper proposed and implemented a speech separation model based on convolutional neural network and attention mechanism. Convolutional neural network can effectively extract low-dimensional features and mine the spatiotemporal structure information in speech signals. Attention mechanism can reduce the loss of sequence information. The accuracy of speech separation can be effectively improved by combining two mechanisms. The simulation experiments illustrated that the model had greater advantages over the speech separation model based on recurrent neural network, and the effect of speech separation can be improved through joint optimization of convolutional neural network and attention mechanism.

Data Availability

All data have been included in this article.

Conflicts of Interest

The authors declare that they have no conflicts of interest.

Acknowledgments

This work was supported by the Program for the Science and Technology Plans of Tianjin, China, under Grant no. 19JCTPJC49200.

References

[1] T. L. Nwe and H. Li, "Exploring vibrato-motivated acoustic features for singer identification," *IEEE Transactions on Audio, Speech and Language Processing*, vol. 15, no. 2, pp. 519–530, 2007.

[2] W. H. Tsai and C. H. Ma, "Triangulation-based singer identification for duet music data indexing," in *Proceedings of the IEEE International Congress on Big Data*, Anchorage, AK, USA, July 2014.

[3] M. I. Mandel, G. E. Poliner, and D. P. W. Ellis, "Support vector machine active learning for music retrieval," *Multimedia Systems*, vol. 12, no. 1, pp. 3–13, 2006.

[4] M. Hermans and B. Schrauwen, "Training and analyzing deep recurrent neural networks," in *Proceedings of the International Conference on Neural Information Processing Systems*, Curran Associates Inc., Daegu, South Korea, November 2013.

[5] A. Krizhevsky, I. Sutskever, and G. Hinton, *ImageNet Classification with Deep Convolutional Neural Networks*, Curran Associates Inc., Red Hook, NY, USA, 2012.

[6] D. Bahdanau, K. Cho, and Y. Bengio, "Neural machine translation by jointly learning to align and translate," https://arxiv.org/abs/1409.0473.

[7] S. Boll, "Suppression of acoustic noise in speech using spectral subtraction," *IEEE Transactions on Acoustics, Speech, and Signal Processing*, vol. 27, no. 2, pp. 113–120, 1979.

[8] J. Chen, J. Benesty, Y. Huang et al., "New insights into the noise reduction Wiener filter," *IEEE Transactions on Audio Speech & Language Processing*, vol. 14, no. 4, pp. 1218–1234, 2006.

[9] Y. Laufer and S. Gannot, "A bayesian hierarchical model for speech enhancement with time-varying audio channel," *IEEE/ACM Transactions on Audio, Speech, and Language Processing*, vol. 27, no. 1, pp. 225–239, 2019.

[10] S. Samui, I. Chakrabarti, and S. K. Ghosh, "Time-frequency masking based supervised speech enhancement framework using fuzzy deep belief network," *Applied Soft Computing*, vol. 74, pp. 583–602, 2019.

[11] R. Cusack, J. Decks, G. Aikman, and R. P. Carlyon, "Effects of location, frequency region, and time course of selective attention on auditory scene analysis," *Journal of Experimental Psychology: Human Perception and Performance*, vol. 30, no. 4, pp. 643–656, 2004.

[12] Y. Chen, "Single channel blind source separation based on NMF and its application to speech enhancement," in *Proceedings of the 2017. IEEE 9th International Conference on Communication Software and Networks (ICCSN)*, pp. 1066–1069, Guangzhou, China, May 2017.

[13] Z. Li, Y. Song, L. Dai, and I. McLoughlin, "Listening and grouping: an online autoregressive approach for monaural speech separation," *IEEE/ACM Transactions on Audio, Speech, and Language Processing*, vol. 27, no. 4, pp. 692–703, 2019.

[14] Y. X. Wang, A. Narayanan, and D. L. Wang, "On training targets for supervised speech separation," *IEEE/ACM Transactions on Audio, Speech, and Language Processing*, vol. 22, no. 12, pp. 1849–1858, 2014.

[15] L. I. U. Wen-Ju, S. NIE, S. Liang et al., "Deep learning based speech separation technology and its developments," *Acta Automatica Sinica*, vol. 42, no. 6, pp. 819–833, 2016.

[16] D. Wang and J. Chen, "Supervised speech separation based on deep learning: an overview," *IEEE/ACM Transactions on Audio, Speech, and Language Processing*, vol. 26, no. 10, pp. 1702–1726, 2018.

[17] J. Zhou, H. Zhao, J. Chen, and X. Pan, "Research on speech separation technology based on deep learning," *Cluster Computing*, vol. 22, no. S4, pp. 8887–8897, 2019.

[18] L. Hui, M. Cai, C. Guo, L. He, W. Zhang, and J. Liu, "Convolutional maxout neural networks for speech separation," in *Proceedings of the IEEE International Symposium on Signal Processing and Information Technology (ISSPIT)*, IEEE, Abu Dhabi, UAE, December 2015.

[19] Y. Sun, W. Wang, J. Chambers, and S. M. Naqvi, "Two-stage monaural source separation in reverberant room environments using deep neural networks," *IEEE/ACM Transactions on Audio, Speech, and Language Processing*, vol. 27, no. 1, pp. 125–139, 2019.

[20] C. P. Wang and T. Zhu, "Neural network based phase compensation methods on monaural speech separation," in *Proceedings of the IEEE International Conference on Multimedia and Expo (ICME)*, pp. 1384–1389, Shanghai, China, July 2019.

[21] L. Zhou, S. Lu, Q. Zhong, Y. Chen, Y. Tang, and Y. Zhou, "Binaural speech separation algorithm based on long and short time memory networks," *Computers, Materials & Continua*, vol. 63, no. 3, pp. 1373–1386, 2020.

[22] P. Haffner, L. Bottou, and Y. Bengio, "Gradient-based learning applied to document recognition," *Proceedings of the IEEE*, vol. 86, no. 11, pp. 2278–2324, 1998.

[23] F. Weninger, J. R. Hershey, J. Le Roux, and B. Schuller, "Discriminatively trained recurrent neural networks for single-channel speech separation," in *Proceedings of the 2014 IEEE Global Conference on Signal and Information Processing*, pp. 577–581, IEEE, Atlanta, GA, USA, December 2014.

[24] J. Schmidhuber and J. Schmidhuber, "Long short-term memory," *Neural Computation*, vol. 9, no. 8, pp. 1735–1780, 1997.

[25] K. Cho, B. Van Merrienboer, C. Gulcehre et al., "Learning phrase representations using RNN encoder-decoder for statistical machine translation," in *Proceedings of the 2014 Conference on Empirical Methods in Natural Language Processing (EMNLP)*, pp. 1724–1734, Doha, Qatar, October 2014.

[26] Y. Wang and D. Wang, "A deep neural network for time-domain signal reconstruction," in *Proceedings of the 2015 IEEE International Conference on Acoustics, Speech, and Signal Processing (ICASSP)*, pp. 4390–4394, IEEE, South Brisbane, Australia, April 2015.

[27] Z. Shi, H. Lin, L. Liu et al., "Furcax: end-to-end monaural speech separation based on deep gated (de) convolutional neural networks with adversarial example training," in *ICASSP 2019 - 2019 IEEE International Conference on Acoustics, Speech and Signal Processing (ICASSP)*, IEEE, Brighton, UK, May 2019.

[28] A. J. R. Simpson, G. Roma, and M. D. Plumbley, "Deep karaoke: extracting vocals from musical mixtures using a convolutional deep neural network," in *Proceedings of the 12th International Conference on Latent Variable Analysis and Signal Separation (LVA/ICA 2015)*, Springer-Verlag, New York, NY, USA, August 2015.

[29] Y. Luo and N. Mesgarani, "Conv-TasNet: surpassing ideal time-frequency magnitude masking for speech separation," *IEEE/ACM Transactions on Audio, Speech, and Language Processing*, vol. 27, no. 8, pp. 1256–1266, 2019.

[30] J. X. Wang, S. B. Li, H. M. Jiang, and X. X. Bian, "Speech separation based on CHF-CNN," *Computer Simulation*, vol. 36, no. 5, pp. 279–283, 2019.

[31] D. Gabor, "Theory of communication. Part 1: the analysis of information," *Journal of the Institution of Electrical Engineers—Part III: Radio and Communication Engineering*, vol. 93, no. 26, pp. 429–441, 1946.

[32] J. Allen, "Short term spectral analysis, synthesis, and modification by discrete Fourier transform," *IEEE Transactions on Acoustics, Speech, and Signal Processing*, vol. 25, no. 3, pp. 235–238, 1977.

[33] Z. Yang, D. Yang, C. Dyer et al., "Hierarchical attention networks for document classification," in *Proceedings of the 2016 Conference of the North American Chapter of the Association for Computational Linguistics: Human Language Technologies*, pp. 1480–1489, San Diego, CA, USA, June 2016.

[34] M. Delfarah and D. Wang, "Deep learning for talker-dependent reverberant speaker separation: an Empirical Study," *IEEE/ACM Transactions on Audio, Speech, and Language Processing*, vol. 27, no. 11, pp. 1839–1848, 2019.

[35] J. Cheng, L. Dong, and M. Lapata, "Long short-term memory-networks for machine reading," in *Proceedings of the 2016 Conference on Empirical Methods in Natural Language Processing*, Austin, TX, USA, November 2016.

[36] P. S. Huang, M. Kim, M. Hasegawa-Johnson, and P. Smaragdis, "Joint optimization of masks and deep recurrent neural networks for monaural source separation," *IEEE/ACM Transactions on Audio, Speech, and Language Processing*, vol. 23, no. 12, pp. 2136–2147, 2015.

[37] C. L. Hsu and J. S. Jang, "On the improvement of singing voice separation for monaural recordings using the MIR-1K dataset," *IEEE Transactions on Audio, Speech, and Language Processing*, vol. 18, no. 2, pp. 310–319, 2010.

[38] C. Vincent, R. Gribonval, and C. Fevotte, "Performance measurement in blind audio source separation," *IEEE Transactions on Audio, Speech and Language Processing*, vol. 14, no. 4, pp. 1462–1469, 2006.

[39] R. Gribonval, P. Philippe, and F. Bimbot, "Adaptation of bayesian models for single-channel source separation and its application to voice/music separation in popular songs," *IEEE Transactions on Audio, Speech and Language Processing*, vol. 15, no. 5, pp. 1564–1578, 2007.

Hindawi
Discrete Dynamics in Nature and Society
Volume 2020, Article ID 6021687, 11 pages
https://doi.org/10.1155/2020/6021687

Research Article

Passivity and Synchronization of Multiple Multi-Delayed Neural Networks via Impulsive Control

Yong Wang,[1] Zhichun Yang,[2,3] Tonglai Liu,[1] and Hong-An Tang[2,4,5]

[1]*School of Computers, Guangdong University of Technology, Guangzhou 510006, China*
[2]*Chongqing Key Lab on IFBDA, School of Mathematical Sciences, Chongqing Normal University, Chongqing 400047, China*
[3]*School of Mathematical Sciences, Chongqing Normal University, Chongqing 400047, China*
[4]*School of Computer Science and Technology, Tiangong University, Tianjin 300387, China*
[5]*School of Artificial Intelligence, Chongqing University of Technology, Chongqing 401135, China*

Correspondence should be addressed to Hong-An Tang; tanghongan163@163.com

Received 12 May 2020; Accepted 26 June 2020; Published 18 July 2020

Guest Editor: Hao Shen

This paper is concerned with the passivity and synchronization for multiple multi-delayed neural networks (MMDNNs) under impulsive control. To ensure the passivity, input strict passivity, and output strict passivity in MMDNNs, a suitable impulsive controller is designed. Moreover, an impulsive time-dependent Lyapunov functional is exploited to obtain the synchronization criterion of MMDNNs, where the criterion is formulated by linear matrix inequalities. Numerical examples are given to verify the validity of the theoretical results.

1. Introduction

Neural networks (NNs) have received extensive attention due to their successful applications in vision system [1], associative memory [2], pattern recognition [3], and image compression [4]. NNs always require stability, which is a prerequisite for many applications. Therefore, the stability of NNs has become a hot issue in recent years [5–11]. Zhang et al. [7] considered some asymptotic stability criteria of NNs with distributed delays based on Lyapunov–Krasovskii functionals. By improving the auxiliary polynomial-based functions, Li et al. [9] solved the stability problem in delayed NNs. Since the main property of passivity is to keep the system internally stable, some researchers have focused on the passivity for NNs [12–17]. Lian et al. [14] proposed a kind of switched NNs with time-varying delays and stochastic disturbances, and the passivity of networks was analyzed by designing a state-dependent switching law and a hysteresis switching law. Cao et al. [17] addressed the robust passivity issue of uncertain NNs with additive time-varying delays and leakage delay, and a general activation function was utilized to ensure that the proposed network model was passive.

In addition, multi-weighted network models [18–21] can be used to describe many real-world networks including public transportation road networks, communication networks, social networks, and so forth. Recently, some researchers have investigated the dynamical behaviors of complex networks with multiple weights [20, 21]. Wang et al. [20] concentrated on two types of multi-weighted complex networks with several different weights between two nodes, and sufficient conditions ensuring the synchronization were developed by utilizing the pinning control method. Under the help of pinning adaptive control techniques, the passivity of multi-weighted complex networks with different dimensions of input and output was discussed in [21]. However, a few authors have considered the stability and passivity of NNs with multiple delays.

Compared with continuous control, there are many advantages of impulsive control strategies, which include low maintenance costs, high reliability, ease of installation, and high efficiency [22]. So far, a series of investigations in regard to the stability [23–28] and passivity [29–31] for impulsive NNs have been reported. Zhu and Cao [25] dealt with the stability problem of impulsive stochastic BAM NNs

with mixed time delays and Markovian jump parameters by exploiting Itô's formula and stochastic analysis theory. According to the comparison principle and compression mapping theorem, the global exponential stability of periodic solution was considered in an array of Cohen–Grossberg NNs with time-varying delays and periodic coefficients via impulsive control in [26]. Zhou [31] took into account the passivity of recurrent NNs with multiproportional delays and impulse. But very few authors have discussed the stability and passivity problems of multi-delayed NNs under impulsive control.

At present, most of the literatures with respect to identifying network structures from the observation and control of dynamical behavior are concentrated in a single neural network [5, 7, 12, 13]. In practical applications, some tasks are difficult to complete by a single neural network; even if the network can accomplish these tasks, it may result in high costs. But multiple NNs can solve some difficult problems through cooperation with each other so that the cost can be reduced. Recently, some cooperative control problems [32–35] involving passivity and synchronization [36–38] have been concerned in multiple NNs. Unfortunately, as far as we know, the passivity and synchronization of multiple multi-delayed NNs (MMDNNs) via impulsive control have never been considered. Inspired by the above discussion, this paper aims to further study the passivity and global exponential synchronization of MMDNNs by using impulsive control techniques. The contributions of this paper are as follows. First, compared with the traditional impulse-time-independent Lyapunov functional, the impulse-time-dependent feature of the Lyapunov functional in this paper can capture more dynamical behaviors of MMDNNs. Second, with the help of some piecewise linear functions and inequality techniques, the passivity problems of MMDNNs are addressed via impulsive control. Third, a newly designed impulsive controller is applied to synchronize the proposed networks.

2. Preliminaries

2.1. Notations. Let $\mathcal{N} = \{1, 2, \ldots, N\}$, $\mathbb{N} = \{0, 1, 2, \ldots\}$. The fixed moments t_k satisfy $0 = t_0 < t_1 < t_2 < \cdots < t_k < \cdots$ and $\lim_{k\longrightarrow+\infty} t_k = +\infty, k \in \mathbb{N}$. $\lambda_{\min}(\cdot)(\lambda_{\max}(\cdot))$ denotes the smallest (largest) eigenvalue of a matrix. For any $\xi(t) = (\xi_1(t), \xi_2(t), \ldots, \xi_N(t))^T \in \mathbb{R}^N$, $\|\xi(t)\| = (\sum_{i=1}^N \xi_i^2(t))^{1/2}$, $\|\xi(t)\|_\tau = \sup_{-\tau\le\epsilon\le0}\|\xi(t+\epsilon)\|$.

The notation $\mathbb{S}(\nu_1, \nu_2)$ represents the set of impulse time sequences $\{t_k\}$ satisfying $\nu_2 \ge t_{k+1} - t_k \ge \nu_1 > 0$ for all $k \in \mathbb{N}$, in which $\nu_1, \nu_2 \in \mathbb{R}$. For a given impulse time sequence $\{t_k\} \in \mathbb{S}(\nu_1, \nu_2)$, some piecewise linear functions can be defined as follows:

$$\phi(t) = \frac{1}{t_{k+1} - t_k}, \quad t \in [t_k, t_{k+1}), k \in \mathbb{N},$$
$$\phi_1(t) = \begin{cases} (t - t_k)\phi(t), & t \in [t_k, t_{k+1}), k \in \mathbb{N}, \\ 1, & t_0 > t. \end{cases} \tag{1}$$

Let $\phi_2(t) = 1 - \phi_1(t)$. It is obvious to see that $[0,1] \ni \phi_1(t)$, $[0,1] \ni \phi_2(t)$, for $\mathbb{R} \ni t$, and $\phi_1(t_k) = \phi_2(t_k^-) = 0$, $\phi_1(t_k^-) = \phi_2(t_k) = 1, \mathbb{N} \ni k$.

For $\{t_k\} \in \mathbb{S}(\nu_1, \nu_2)$, $\phi(t)$ can be written as

$$\phi(t) = \frac{\psi_1(t)}{\nu_1} + \frac{\psi_2(t)}{\nu_2}, \tag{2}$$

where

$$\psi_1(t) = 1 - \psi_2(t),$$
$$\psi_2(t) = \begin{cases} \dfrac{\phi(t) - (1/\nu_2)}{(1/\nu_1) - (1/\nu_2)}, & \text{if } \nu_1 \ne \nu_2, \\ 1, & \text{if } \nu_1 = \nu_2. \end{cases} \tag{3}$$

Definition 1 (see [21]). A system is said to be passive with output $y(t) \in \mathbb{R}^{\epsilon N}$ and input $v(t) \in \mathbb{R}^{nN}$, if there is a storage function S: $[0, +\infty) \longrightarrow [0, +\infty)$ and a matrix $A \in \mathbb{R}^{\epsilon N \times nN}$ satisfying

$$S(t_\varrho) - S(t_0) \le \int_{t_0}^{t_\varrho} y^T(t) A v(t) \mathrm{d}t, \tag{4}$$

for any $t_\varrho, t_0 \in [0, +\infty)$ and $t_0 \le t_\varrho$.

Definition 2 (see [21]). A system is said to be strictly passive with output $y(t) \in \mathbb{R}^{\epsilon N}$ and input $v(t) \in \mathbb{R}^{nN}$, if there is a storage function S: $[0, +\infty) \longrightarrow [0, +\infty)$, matrices $A \in \mathbb{R}^{\epsilon N \times nN}$, $0 \le A_1 \in \mathbb{R}^{nN \times nN}$, $0 \le A_2 \in \mathbb{R}^{\epsilon N \times \epsilon N}$, and eigenvalues $\lambda_m(A_1) + \lambda_m(A_2) > 0$ satisfying

$$S(t_\varrho) - S(t_0) \le \int_{t_0}^{t_\varrho} \left[y^T(t) A v(t) - v^T(t) A_1 v(t) - y^T(t) A_2 y(t) \right] \mathrm{d}t, \tag{5}$$

for any $t_\varrho, t_0 \in [0, +\infty)$ and $t_0 \le t_\varrho$.

The system is input-strictly passive if $0 < A_1$ and output-strictly passive if $0 < A_2$.

3. Passivity of MMDNNs via Impulsive Control

3.1. Network Model. The MMDNNs are considered as follows:

$$\dot{z}_i(t) = -D z_i(t) + \sum_{\iota=1}^{p} W_\iota g^\iota(z_i(t - \tau_\iota)) + J + \nu_i(t), \tag{6}$$

in which $i \in \mathcal{N}$; $z_i(t) = (z_{i1}(t), z_{i2}(t), \ldots, z_{in}(t))^T \in \mathbb{R}^n$ is the state vector of node i; $D = \mathrm{diag}(d_1, d_2, \ldots, d_n) > 0$; $W_\iota \in \mathbb{R}^{n\times n}$; $g^\iota(z_i(t-\tau_\iota)) = (g_1^\iota(z_{i1}(t-\tau_\iota)), g_2^\iota(z_{i2}(t-\tau_\iota)), \ldots, g_n^\iota(z_{in}(t-\tau_\iota)))^T \in \mathbb{R}^n$; $J = (J_1, J_2, \ldots, J_n)^T \in \mathbb{R}^n$; $\nu_i(t) \in \mathbb{R}^n$ means the input vector of node i; and τ_ι is the transmission delay and $0 \le \tau_\iota \le \tau$.

In this paper, there is $\mathbb{R} \ni \rho_\varsigma > 0 (\varsigma = 1, 2, \ldots, n)$ such that

$$\left| g_\varsigma^\iota(\theta_1) - g_\varsigma^\iota(\theta_2) \right| \le \rho_\varsigma^\iota |\theta_1 - \theta_2|. \tag{7}$$

for any $\theta_1, \theta_2 \in \mathbb{R}$. Let $\Lambda_\iota = \mathrm{diag}((\rho_1^\iota)^2, (\rho_2^\iota)^2, \ldots, (\rho_n^\iota)^2)$.

Suppose that $z^* = (z_1^*, z_2^*, \ldots, z_n^*)^T \in \mathbb{R}^n$ is an equilibrium solution of an isolated node of the MMDNNs (6). Then, one gets

$$-Dz^* + J + \sum_{\iota=1}^{p} W_\iota g^\iota(z^*) = 0. \tag{8}$$

For the MMDNNs (6), construct the following impulsive controller:

$$u_i(t_k) = \sum_{j=1}^{N} B_{ij}\Phi z_j(t_k^-), \quad k \in \mathbb{N}, i \in \mathcal{N}, \tag{9}$$

in which $0 < \Phi \in \mathbb{R}^{n\times n}$; $z_i(t_k^-) = \lim_{t\longrightarrow t_k^-} z_i(t)$; $B = (B_{ij})_{N\times N}$ means the impulsive coupling matrix, where B_{ij} is described as follows: if there is a link from node i to node j, then ; otherwise, $B_{ij} = 0\,(i \neq j)$; and

$$B_{ii} = -\sum_{\substack{j=1\\ j\neq i}}^{N} B_{ij}, \quad i \in \mathcal{N}. \tag{10}$$

It is derived from (6) and (9) that

$$\begin{cases} \dot{z}_i(t) = -Dz_i(t) + \sum_{\iota=1}^{p} W_\iota g^\iota(z_i(t-\tau_\iota)) + J + v_i(t), & t \neq t_k, \\ I_k(z_i(t)) = \sum_{j=1}^{N} B_{ij}\Phi z_j(t_k^-), & k \in \mathbb{N}, i \in \mathcal{N}, \end{cases} \tag{11}$$

where $I_k(z_i(t)) = z_i(t_k^+) - z_i(t_k^-)$, $z_i(t_k^+) = \lim_{t\longrightarrow t_k^+} z_i(t)$. Suppose $z_i(t_k) = z_i(t_k^+)$.

Let $\zeta_i(t) = z_i(t) - z^*$. Then, by (8) and (11), we acquire

$$\begin{cases} \dot{\zeta}_i(t) = -D\zeta_i(t) + \sum_{\iota=1}^{p} W_\iota[g^\iota(z_i(t-\tau_\iota)) - g^\iota(z^*)] + v_i(t), & t \neq t_k, \\ I_k(\zeta_i(t)) = \sum_{j=1}^{N} B_{ij}\Phi\zeta_j(t_k^-), & k \in \mathbb{N}, i \in \mathcal{N}. \end{cases} \tag{12}$$

The output vector $y_i(t) \in \mathbb{R}^\epsilon$ of the MMDNNs (12) is chosen as

$$y_i(t) = C_1\zeta_i(t) + C_2 v_i(t), \tag{13}$$

in which $C_1 \in \mathbb{R}^{\epsilon\times n}$ and $C_2 \in \mathbb{R}^{\epsilon\times n}$ are known matrices.

3.2. Passivity Criteria

Theorem 1. *Under the impulsive controller (9), the MMDNNs (12) are passive over $\mathbb{S}(\nu_1, \nu_2)$ if there exist matrices $0 < F_1 \in \mathbb{R}^{nN\times nN}$, $0 < F_2 \in \mathbb{R}^{nN\times nN}$, and $A \in \mathbb{R}^{\epsilon N\times nN}$ and a scalar $\gamma \in (0, 1]$ such that*

$$\Gamma_{1rh} = \begin{pmatrix} \Omega_{1rh} & \Omega_{2r} \\ \Omega_{2r}^T & \Omega_3 \end{pmatrix} \leq 0, \tag{14}$$

$$\begin{pmatrix} -\gamma F_1 & (I_{nN} + B\otimes\Phi)^T F_2 \\ F_2(I_{nN} + B\otimes\Phi) & -F_2 \end{pmatrix} \leq 0, \tag{15}$$

in which $r = 1, 2, h = 1, 2$, $\Omega_{1rh} = 1/\nu_h(F_1 - F_2) - F_r(I_N\otimes D) - (I_N\otimes D)F_r + \sum_{\iota=1}^{p}\{F_r[I_N\otimes(W_\iota W_\iota^T)]F_r + I_N\otimes\Lambda_\iota\}$, $\Omega_{2r} = F_r - (I_N\otimes C_1^T)A$, and $\Omega_3 = -A^T(I_N\otimes C_2) - (I_N\otimes C_2^T)A$.

Proof. Let $F(t) = \sum_{r=1}^{2}\phi_r(t)F_r, \Omega_1(t) = \phi(t)(F_1 - F_2) - (I_N\otimes D)F(t) - F(t)(I_N\otimes D) + \sum_{\iota=1}^{p}\{F(t)[I_N\otimes(W_\iota W_\iota^T)]F(t) + I_N\otimes\Lambda_\iota\}, \Omega_2(t) = F(t) - (I_N\otimes C_1^T)A$.

Then, by (14), we have

$$\Gamma_1(t) \triangleq \sum_{r,h=1}^{2}\phi_r(t)\psi_h(t)\Gamma_{1rh} = \begin{pmatrix} \Omega_1(t) & \Omega_2(t) \\ \Omega_2^T(t) & \Omega_3 \end{pmatrix} \leq 0. \tag{16}$$

The impulse-time-dependent Lyapunov functional for the MMDNNs (12) is considered as follows:

$$V_1(t) = \zeta^T(t)F(t)\zeta(t) + \sum_{\iota=1}^{p}\int_{t-\tau_\iota}^{t}\zeta^T(s)(I_N\otimes\Lambda_\iota)\zeta(s)\mathrm{d}s, \tag{17}$$

where $\zeta(t) = (\zeta_1^T(t), \zeta_2^T(t), \ldots, \zeta_N^T(t))^T$.

Then,

$$\begin{aligned} \dot{V}_1(t) = {} & \zeta^T(t)[\phi(t)(F_1 - F_2) - (I_N\otimes D)F(t) \\ & - F(t)(I_N\otimes D)]\zeta(t) + 2\zeta^T(t)F(t) \\ & \cdot\left\{\sum_{\iota=1}^{p}(I_N\otimes W_\iota)\times[\widehat{g}^\iota(z(t-\tau_\iota)) - \widehat{g}^\iota(\widehat{z}^*)] + v(t)\right\} \\ & - \sum_{\iota=1}^{p}\zeta^T(t-\tau_\iota)(I_N\otimes\Lambda_\iota)\zeta(t-\tau_\iota) \\ & + \sum_{\iota=1}^{p}\zeta^T(t)(I_N\otimes\Lambda_\iota)\zeta(t), \end{aligned} \tag{18}$$

where $\widehat{z}^* = ((z^*)^T, (z^*)^T, \ldots, (z^*)^T)^T$, $\widehat{g}^\iota(z(t-\tau_\iota)) = ((g^\iota(z_1(t-\tau_\iota)))^T, (g^\iota(z_2(t-\tau_\iota)))^T, \ldots, (g^\iota(z_N(t-\tau_\iota)))^T)^T$, $\widehat{g}^\iota(\widehat{z}^*) = ((g^\iota(z^*))^T, (g^\iota(z^*))^T, \ldots, (g^\iota(z^*))^T)^T$, $v(t) = (v_1^T(t), v_2^T(t), \ldots, v_N^T(t))^T$.

Obviously,

$$\begin{aligned} & 2\zeta^T(t)F(t)(I_N\otimes W_\iota)[\widehat{g}^\iota(z(t-\tau_\iota)) - \widehat{g}^\iota(\widehat{z}^*)] \\ & \quad \leq \zeta^T(t)F(t)\left[I_N\otimes\left(W_\iota W_\iota^T\right)\right]F(t)\zeta(t) \\ & \quad + \zeta^T(t-\tau_\iota)(I_N\otimes\Lambda_\iota)\zeta(t-\tau_\iota). \end{aligned} \tag{19}$$

Substituting (19) into (18) yields

$$\begin{aligned} \dot{V}_1(t) \leq {} & \zeta^T(t)\left\{\phi(t)(F_1 - F_2) - (I_N\otimes D)F(t) - F(t)\times(I_N\otimes D) + \sum_{\iota=1}^{p}F(t)\left[I_N\otimes\left(W_\iota W_\iota^T\right)\right]F(t) + \sum_{\iota=1}^{p}I_N\otimes\Lambda_\iota\right\}\zeta(t) \\ & + 2\zeta^T(t)F(t)v(t). \end{aligned} \tag{20}$$

From (13), (16), and (20), one obtains

$$\begin{aligned}
&\dot{V}_1(t) - 2y^T(t)Av(t)\\
&\quad\le \zeta^T(t)\{\phi(t)(F_1 - F_2) - (I_N \otimes D)F(t) - F(t)(I_N \otimes D)\\
&\quad + \sum_{\iota=1}^{p} \left\{F(t)\left[I_N \otimes \left(W_\iota W_\iota^T\right)\right]F(t) + I_N \otimes \Lambda_\iota\right\}\zeta(t)\\
&\quad + v^T(t)\left[-A^T(I_N \otimes C_2) - \left(I_N \otimes C_2^T\right)A\right]v(t)\\
&\quad + 2\zeta^T(t)\left[F(t) - \left(I_N \otimes C_1^T\right)A\right]v(t)\\
&\quad = \varpi_1^T(t)\begin{pmatrix} \Omega_1(t) & \Omega_2(t) \\ \Omega_2^T(t) & \Omega_3 \end{pmatrix}\varpi_1(t)\\
&\quad \le 0, t \in (t_k, t_{k+1}), \mathbb{N} \ni k,
\end{aligned} \tag{21}$$

in which $\varpi_1(t) = (\zeta^T(t), v^T(t))^T$.

Integrating (21) with respect to t from t_0 to t_ϱ ($t_\eta \le t_\varrho < t_{\eta+1}, \eta = 0, 1, \ldots$), we acquire

$$\begin{aligned}
&\int_{t_0}^{t_\varrho}\left[\dot{V}_1(t) - 2y^T(t)Av(t)\right]\mathrm{d}t\\
&\quad = \int_{t_\eta}^{t_\varrho}\dot{V}_1(t)\mathrm{d}t + \sum_{\sigma=1}^{\eta}\int_{t_{\sigma-1}}^{t_\sigma}\dot{V}_1(t)\mathrm{d}t - 2\int_{t_0}^{t_\varrho}y^T(t)Av(t)\mathrm{d}t\\
&\quad = \left[V_1(t_\varrho) - V_1(t_\eta)\right] + \sum_{\sigma=1}^{\eta}\left[V_1(t_\sigma^-) - V_1(t_{\sigma-1})\right]\\
&\qquad - 2\int_{t_0}^{t_\varrho}y^T(t)Av(t)\mathrm{d}t\\
&\quad = \left[V_1(t_\varrho) - V_1(t_0)\right] + \sum_{\sigma=1}^{\eta}\left[V_1(t_\sigma^-) - V_1(t_\sigma)\right]\\
&\qquad - 2\int_{t_0}^{t_\varrho}y^T(t)Av(t)\mathrm{d}t,
\end{aligned} \tag{22}$$

in which $t_\varrho, t_0 \in [0, +\infty)$ and $t_0 \le t_\varrho$.

At the impulse time $t_k, k \in \mathbb{N}$, according to the definition of $F(t)$, one gets

$$\begin{aligned}
F(t_k^-) &= F_1,\\
F(t_k) &= F_2.
\end{aligned} \tag{23}$$

It is found from (12), (15), and (17) that

$$\begin{aligned}
V_1(t_k) &= \zeta^T(t_k)F(t_k)\zeta(t_k) + \sum_{\iota=1}^{p}\int_{t_k-\tau_\iota}^{t_k}\zeta^T(s)(I_N \otimes \Lambda_\iota)\zeta(s)\mathrm{d}s\\
&= \zeta^T(t_k^-)(I_{nN} + B \otimes \Phi)^T F_2(I_{nN} + B \otimes \Phi)\zeta(t_k^-)\\
&\quad + \sum_{\iota=1}^{p}\int_{t_k-\tau_\iota}^{t_k}\zeta^T(s)(I_N \otimes \Lambda_\iota)\zeta(s)\mathrm{d}s\\
&\le \gamma\zeta^T(t_k^-)F_1\zeta(t_k^-) + \sum_{\iota=1}^{p}\int_{t_k-\tau_\iota}^{t_k}\zeta^T(s)(I_N \otimes \Lambda_\iota)\zeta(s)\mathrm{d}s\\
&\le \zeta^T(t_k^-)F(t_k^-)\zeta(t_k^-) + \sum_{\iota=1}^{p}\int_{t_k-\tau_\iota}^{t_k}\zeta^T(s)(I_N \otimes \Lambda_\iota)\zeta(s)\mathrm{d}s\\
&= V_1(t_k^-), \mathbb{N} \ni k.
\end{aligned} \tag{24}$$

By (21)–(24), we have

$$V_1(t_\varrho) - V_1(t_0) \le 2\int_{t_0}^{t_\varrho}y^T(t)Av(t)\mathrm{d}t. \tag{25}$$

Hence,

$$S(t_\varrho) - S(t_0) \le \int_{t_0}^{t_\varrho}y^T(t)Av(t)\mathrm{d}t, \tag{26}$$

for any $t_\varrho, t_0 \in [0, +\infty)$ and $t_0 \le t_\varrho$, in which $S(t) = V_1(t)/2$. □ □

Theorem 2. *Under the impulsive controller (9), the MMDNNs (12) are input-strictly passive over $\mathbb{S}(\nu_1, \nu_2)$ if there exist matrices $0 < F_1 \in \mathbb{R}^{nN\times nN}$, $0 < F_2 \in \mathbb{R}^{nN\times nN}$, $A \in \mathbb{R}^{\epsilon N\times nN}$, and $0 < A_1 \in \mathbb{R}^{nN\times nN}$ and a scalar $\gamma \in (0, 1]$ such that*

$$\Gamma_{2rh} = \begin{pmatrix} \Omega_{1rh} & \Omega_{2r} \\ \Omega_{2r}^T & \Omega_4 \end{pmatrix} \le 0, \tag{27}$$

$$\begin{pmatrix} -\gamma F_1 & (I_{nN} + B \otimes \Phi)^T F_2 \\ F_2(I_{nN} + B \otimes \Phi) & -F_2 \end{pmatrix} \le 0, \tag{28}$$

in which $r = 1, 2, h = 1, 2$, $\Omega_{1rh} = 1/\nu_h(F_1 - F_2) - F_r(I_N \otimes D) - (I_N \otimes D)F_r + \sum_{\iota=1}^{p}\{F_r[I_N \otimes (W_\iota W_\iota^T)]F_r + I_N \otimes \Lambda_\iota\}$, $\Omega_{2r} = F_r - (I_N \otimes C_1^T)A$, $\Omega_4 = 2A_1 - A^T(I_N \otimes C_2) - (I_N \otimes C_2^T)A$.

Proof. Let $F(t) = \sum_{r=1}^{2}\phi_r(t)F_r, \Omega_1(t) = \phi(t)(F_1 - F_2) - (I_N \otimes D)F(t) - F(t)(I_N \otimes D) + \sum_{\iota=1}^{p}\{F(t)[I_N \otimes (W_\iota W_\iota^T)]\ F(t) + I_N \otimes \Lambda_\iota\}, \Omega_2(t) = F(t) - (I_N \otimes C_1^T)A$.

Then, from (27), one obtains

$$\Gamma_2(t) \triangleq \sum_{r,h=1}^{2}\phi_r(t)\psi_h(t)\Gamma_{2rh} = \begin{pmatrix} \Omega_1(t) & \Omega_2(t) \\ \Omega_2^T(t) & \Omega_4 \end{pmatrix} \le 0. \tag{29}$$

Selecting the same V_1 as (17) for the networks (12) and using (29), one has

$$\begin{aligned}
&\dot{V}_1(t) - 2y^T(t)Av(t) + 2v^T(t)A_1v(t)\\
&\quad \le \zeta^T(t)\{\phi(t)(F_1 - F_2) - (I_N \otimes D)F(t) - F(t)(I_N \otimes D)\\
&\qquad + \sum_{\iota=1}^{p}\left\{F(t)\left[I_N \otimes \left(W_\iota W_\iota^T\right)\right]F(t) + I_N \otimes \Lambda_\iota\right\}\zeta(t)\\
&\qquad + v^T(t)\left[2A_1 - A^T(I_N \otimes C_2) - \left(I_N \otimes C_2^T\right)A\right]v(t)\\
&\qquad + 2\zeta^T(t)\left[F(t) - \left(I_N \otimes C_1^T\right)A\right]v(t)\\
&\quad = \varpi_1^T(t)\begin{pmatrix} \Omega_1(t) & \Omega_2(t) \\ \Omega_2^T(t) & \Omega_4 \end{pmatrix}\varpi_1(t)\\
&\quad \le 0, t \in (t_k, t_{k+1}), \mathbb{N} \ni k,
\end{aligned} \tag{30}$$

in which $\varpi_1(t) = (\zeta^T(t), v^T(t))^T$.

Integrating (30) with respect to t from t_0 to t_ϱ ($t_\eta \le t_\varrho < t_{\eta+1}, \eta = 0, 1, \ldots$), we acquire

$$\begin{aligned}&\int_{t_0}^{t_\varrho}\left[\dot{V}_1(t)-2y^T(t)A\nu(t)+2\nu^T(t)A_1\nu(t)\right]\mathrm{d}t\\&=\left[V_1\left(t_\varrho\right)-V_1\left(t_0\right)\right]+\sum_{\sigma=1}^{\eta}\left[V_1\left(t_\sigma^-\right)-V_1\left(t_\sigma\right)\right]\\&\quad-2\int_{t_0}^{t_\varrho}\left[y^T(t)A\nu(t)\mathrm{d}t-\nu^T(t)A_1\nu(t)\right]\mathrm{d}t,\end{aligned}\tag{31}$$

in which $t_\varrho, t_0 \in [0,+\infty)$ and $t_0 \le t_\varrho$.

At the impulse time $t_k, k \in \mathbb{N}$, according to the definition of $F(t)$, one acquires

$$\begin{aligned}F\left(t_k^-\right)&=F_1,\\F\left(t_k\right)&=F_2.\end{aligned}\tag{32}$$

On the basis of (12), (17), and (28), we get

$$V_1\left(t_k\right)\le V_1\left(t_k^-\right),\quad \mathbb{N}\ni k.\tag{33}$$

Considering (30)–(33), it is obtained that

$$V_1\left(t_\varrho\right)-V_1\left(t_0\right)\le 2\int_{t_0}^{t_\varrho}\left[y^T(t)A\nu(t)-\nu^T(t)A_1\nu(t)\right]\mathrm{d}t.\tag{34}$$

Thus,

$$S\left(t_\varrho\right)-S\left(t_0\right)\le\int_{t_0}^{t_\varrho}y^T(t)A\nu(t)\mathrm{d}t-\int_{t_0}^{t_\varrho}\nu^T(t)A_1\nu(t)\mathrm{d}t,\tag{35}$$

for any $t_\varrho, t_0 \in [0,+\infty)$ and $t_0 \le t_\varrho$, in which $S(t)=V_1(t)/2$. □

Theorem 3. *Under the impulsive controller (9), the MMDNNs (12) are output-strictly passive over $\mathbb{S}(\nu_1,\nu_2)$ if there exist matrices $0<F_1\in\mathbb{R}^{nN\times nN}$, $0<F_2\in\mathbb{R}^{nN\times nN}$, $A\in\mathbb{R}^{\epsilon N\times nN}$, and $0<A_2\in\mathbb{R}^{\epsilon N\times\epsilon N}$ and a scalar $\gamma\in(0,1]$ such that*

$$\Gamma_{3rh}=\begin{pmatrix}\Omega_{5rh}&\Omega_{6r}\\\Omega_{6r}^T&\Omega_7\end{pmatrix}\le 0,\tag{36}$$

$$\begin{pmatrix}-\gamma F_1&\left(I_{nN}+B\otimes\Phi\right)^TF_2\\F_2\left(I_{nN}+B\otimes\Phi\right)&-F_2\end{pmatrix}\le 0,\tag{37}$$

in which $r=1,2,h=1,2$, $\Omega_{5rh}=1/\nu_h(F_1-F_2)-F_r(I_N\otimes D)-(I_N\otimes D)F_r+\sum_{\iota=1}^{p}\{F_r[I_N\otimes(W_\iota W_\iota^T)]F_r+(I_N\otimes\Lambda_\iota)\}+2(I_N\otimes C_1^T)A_2(I_N\otimes C_1)$, $\Omega_{6r}=2(I_N\otimes C_1^T)\ A_2(I_N\otimes C_2)+F_r-(I_N\otimes C_1^T)A$, and $\Omega_7=-A^T(I_N\otimes C_2)-(I_N\otimes C_2^T)A+2(I_N\otimes C_2^T)A_2(I_N\otimes C_2)$.

Proof. Let $F(t)=\sum_{r=1}^{2}\phi_r(t)F_r$, $\Omega_5(t)=-(I_N\otimes D)F(t)+\phi(t)(F_1-F_2)+\sum_{\iota=1}^{p}\{F(t)[I_N\otimes(W_\iota W_\iota^T)]F(t)+I_N\otimes\Lambda_\iota\}+2(I_N\otimes C_1^T)A_2(I_N\otimes C_1)-F(t)(I_N\otimes D)$, $\Omega_6(t)=2(I_N\otimes C_1^T)A_2(I_N\otimes C_2)+F(t)-(I_N\otimes C_1^T)A$.

Then, it is derived from (36) that

$$\Gamma_3(t)\triangleq\sum_{r,h=1}^{2}\phi_r(t)\psi_h(t)\Gamma_{3rh}=\begin{pmatrix}\Omega_5(t)&\Omega_6(t)\\\Omega_6^T(t)&\Omega_7\end{pmatrix}\le 0.\tag{38}$$

Selecting the same V_1 as (17) for the networks (12) and utilizing (38), we get

$$\begin{aligned}&\dot{V}_1(t)-2y^T(t)A\nu(t)+2y^T(t)A_2y(t)\\&\le\zeta^T(t)\left\{\phi(t)(F_1-F_2)-(I_N\otimes D)F(t)-F(t)(I_N\otimes D)+2\left(I_N\otimes C_1^T\right)A_2(I_N\otimes C_1)+\sum_{\iota=1}^{p}\left\{I_N\otimes\Lambda_\iota+F(t)\times\left[I_N\otimes\left(W_\iota W_\iota^T\right)\right]F(t)\right\}\right\}\zeta(t)\\&\quad+2\zeta^T(t)\left[2\left(\left(I_N\otimes C_1^T\right)\right)\left(A_2(I_N\otimes C_2)+F(t)-\left(I_N\otimes C_1^T\right)A\right]\nu(t)\right]\\&\quad+\nu^T(t)\left[-A^T(I_N\otimes C_2)-\left(I_N\otimes C_2^T\right)A+2\left(I_N\otimes C_2^T\right)A_2(I_N\otimes C_2)\right]\nu(t)\\&=\varpi_1^T(t)\begin{pmatrix}\Omega_5(t)&\Omega_6(t)\\\Omega_6^T(t)&\Omega_7\end{pmatrix}\varpi_1(t)\\&\le 0,t\in\left(t_k,t_{k+1}\right),\quad\mathbb{N}\ni k,\end{aligned}\tag{39}$$

in which $\varpi_1(t)=(\zeta^T(t),\nu^T(t))^T$.

Integrating (39) with respect to t from t_0 to t_ϱ ($t_\eta\le t_\varrho<t_{\eta+1},\eta=0,1,\ldots$), one has

$$\begin{aligned}&\int_{t_0}^{t_\varrho}\left[\dot{V}_1(t)-2y^T(t)A\nu(t)+2y^T(t)A_2y(t)\right]\mathrm{d}t\\&=\left[V_1\left(t_\varrho\right)-V_1\left(t_0\right)\right]+\sum_{\sigma=1}^{\eta}\left[V_1\left(t_\sigma^-\right)-V_1\left(t_\sigma\right)\right]\\&\quad-2\int_{t_0}^{t_\varrho}\left[y^T(t)A\nu(t)-y^T(t)A_2y(t)\right]\mathrm{d}t,\end{aligned}\tag{40}$$

in which $t_\varrho, t_0 \in [0,+\infty)$ and $t_0 \le t_\varrho$.

At the impulse time $t_k, k \in \mathbb{N}$, according to the definition of $F(t)$, we derive

$$\begin{aligned}F\left(t_k^-\right)&=F_1,\\F\left(t_k\right)&=F_2.\end{aligned}\tag{41}$$

It is obtained from (12), (17), and (37) that

$$V_1\left(t_k\right)\le V_1\left(t_k^-\right),\quad\mathbb{N}\ni k.\tag{42}$$

Using (39)–(42), we can acquire

$$V_1(t_\varrho) - V_1(t_0) \le 2\int_{t_0}^{t_\varrho} \left[y^T(t)Av(t) - y^T(t)A_2y(t)\right]dt. \tag{43}$$

Therefore,

$$S(t_\varrho) - S(t_0) \le \int_{t_0}^{t_\varrho} y^T(t)Av(t)dt - \int_{t_0}^{t_\varrho} y^T(t)A_2y(t)dt, \tag{44}$$

for any $t_\varrho, t_0 \in [0, +\infty)$ and $t_0 \le t_\varrho$, in which $S(t) = V_1(t)/2$. □

Remark 1. In recent years, as an effective method to study synchronization, the passivity of NNs has been investigated by some researchers [12–17]. Impulsive control is a popular control method among control methods due to its reliability, low cost, and flexibility [22]. Using impulsive control strategies, some authors have focused on the passivity and synchronization of NNs. However, the passivity and synchronization of MMDNNs have not been considered under impulsive control.

4. Synchronization of MMDNNs via Impulsive Control

Setting $v_i(t) = 0$ in the MMDNNs (6), we obtain

$$\dot{z}_i(t) = -Dz_i(t) + \sum_{\iota=1}^{p} W_\iota g^\iota(z_i(t-\tau_\iota)) + J, \quad i \in \mathcal{N}. \tag{45}$$

The initial value of (45) is given by

$$z_i(t) = \chi_i(t), t \in [-\tau, 0], \quad i \in \mathcal{N}, \tag{46}$$

where $\chi_i(t) \in C([-\tau, 0], \mathbb{R}^n)$ is the set of continuous functions from $[-\tau, 0]$ to $\mathbb{R}^n, \chi(t) = (\chi_1^T(t), \chi_2^T(t), \ldots, \chi_N^T(t))^T$.

Suppose that $z^* = (z_1^*, z_2^*, \ldots, z_n^*)^T \in \mathbb{R}^n$ is an equilibrium solution of an isolated node of the MMDNNs (45). Then, one has

$$-Dz^* + J + \sum_{\iota=1}^{p} W_\iota g^\iota(z^*) = 0. \tag{47}$$

For the MMDNNs (45), select the following impulsive controller:

$$u_i(t_k) = \sum_{j=1}^{N} B_{ij}\Phi z_j(t_k^-), \quad k \in \mathbb{N}, i \in \mathcal{N}, \tag{48}$$

in which B_{ij} and Φ have the same meanings as in the third section. Assume $z_i(t_k^-) = \lim_{t \longrightarrow t_k^-} z_i(t)$.

It is obtained from (45) and (48) that

$$\begin{cases} \dot{z}_i(t) = -Dz_i(t) + \sum_{\iota=1}^{p} W_\iota g^\iota(z_i(t-\tau_\iota)) + J, & t \ne t_k, \\ I_k(z_i(t)) = \sum_{j=1}^{N} B_{ij}\Phi z_j(t_k^-), & k \in \mathbb{N}, i \in \mathcal{N}, \end{cases} \tag{49}$$

where $I_k(z_i(t)) = z_i(t_k^+) - z_i(t_k^-)$, $z_i(t_k^+) = \lim_{t \longrightarrow t_k^+} z_i(t)$. Suppose $z_i(t_k) = z_i(t_k^+)$.

Let $\zeta_i(t) = z_i(t) - z^*$. Then, it is found from (47) and (49) that

$$\begin{cases} \dot{\zeta}_i(t) = -D\zeta_i(t) + \sum_{\iota=1}^{p} W_\iota[g^\iota(z_i(t-\tau_\iota)) - g^\iota(z^*)], & t \ne t_k, \\ I_k(\zeta_i(t)) = \sum_{j=1}^{N} B_{ij}\Phi\zeta_j(t_k^-), & k \in \mathbb{N}, i \in \mathcal{N}. \end{cases} \tag{50}$$

Definition 3 (see [20]). The MMDNNs (45) achieve synchronization if

$$\lim_{t \longrightarrow +\infty} \|z_i(t) - z^*\| = 0, \quad i \in \mathcal{N}. \tag{51}$$

Theorem 4. *If there exist matrices* $0 < M_1 \in \mathbb{R}^{n\times n}$ *and* $0 < M_2 \in \mathbb{R}^{n\times n}$ *and scalars* $\beta \in (0, 1], \xi > 0$ *such that*

$$\Gamma_{4rh} = \begin{pmatrix} \Omega_{8rh} & \Psi_{r1} & \Psi_{r2} & \cdots & \Psi_{rp} \\ \Psi_{r1}^T & -I_n & 0 & \cdots & 0 \\ \Psi_{r2}^T & 0 & -I_n & \cdots & 0 \\ \vdots & \vdots & \vdots & \ddots & \vdots \\ \Psi_{rp}^T & 0 & 0 & \cdots & -I_n \end{pmatrix} \le 0, \tag{52}$$

$$\begin{pmatrix} -\beta(I_N \otimes M_1) & Y_1 \\ Y_1^T & -(I_N \otimes M_2) \end{pmatrix} \le 0, \tag{53}$$

where $r = 1, 2, h = 1, 2, \Omega_{8rh} = (\xi + (ln\beta/\nu_h))M_r - M_r D - DM_r + 1/\nu_h(M_1 - M_2) + \sum_{\iota=1}^{p} e^{\xi\tau}\Lambda_\iota$, $\Psi_{r1} = \beta^{-(1/2)}M_rW_1$, $\Psi_{r2} = \beta^{-(1/2)}M_rW_2, \ldots, \Psi_{rp} = \beta^{-(1/2)}M_rW_p$, *and* $Y_1 = (I_{nN} + B \otimes \Phi)^T(I_N \otimes M_2), i \in \mathcal{N}$, *then under the impulsive controller (48), the MMDNNs (45) achieve global exponential synchronization over* $\mathbb{S}(\nu_1, \nu_2)$ *with convergence rate* $\xi/2$.

Proof. Let $M(t) = \sum_{r=1}^{2}\phi_r(t)M_r, \Psi_1(t) = \beta^{-(1/2)}M(t)W_1$, $\Psi_2(t) = \beta^{-(1/2)}M(t)W_2, \ldots, \Psi_p(t) = \beta^{-(1/2)}M(t)W_p, \Omega_8(t) = -M(t)D - DM(t) + [\xi + \phi(t)\ln\beta]M(t) + \sum_{\iota=1}^{p} e^{\xi\tau}\Lambda_\iota + \phi(t)(M_1 - M_2)$.

Then, by (52), we have

$$\Gamma_4(t) \triangleq \sum_{r,h=1}^{2} \phi_r(t)\psi_h(t)\Gamma_{4rh} = \begin{pmatrix} \Omega_8(t) & \Psi_1(t) & \Psi_2(t) & \cdots & \Psi_p(t) \\ \Psi_1^T(t) & -I_n & 0 & \cdots & 0 \\ \Psi_2^T(t) & 0 & -I_n & \cdots & 0 \\ \vdots & \vdots & \vdots & \ddots & \vdots \\ \Psi_p^T(t) & 0 & 0 & \cdots & -I_n \end{pmatrix} \le 0. \tag{54}$$

The impulse-time-dependent Lyapunov functional for the MMDNNs (50) is considered as follows:

$$V_2(t) = \sum_{\iota=1}^{p}\sum_{i=1}^{N}\int_{t-\tau_\iota}^{t} e^{\xi(s+\tau-t_0)}\varphi(s)\zeta_i^T(s)\Lambda_\iota\zeta_i(s)\mathrm{d}s + \sum_{i=1}^{N} e^{\xi(t-t_0)}\varphi(t)\zeta_i^T(t)M(t)\zeta_i(t), \tag{55}$$

in which $\varphi(t) = \beta^{\phi_1(t)}$.

For $(t_k, t_{k+1}) \ni t$, $\mathbb{N} \ni k$, differentiating $V_2(t)$ along the solution of the MMDNNs (50) and applying the fact that $\varphi(t-s)/\varphi(t) \geq \beta$, for all $0 \leq s$ and $t_0 < t$, one gets

$$\begin{aligned}
\dot{V}_2(t) &= \sum_{i=1}^{N} e^{\xi(t-t_0)}\varphi(t)\Big\{\zeta_i^T(t)\left[(\xi+\phi(t)\ln\beta)M(t) + \phi(t)(M_1-M_2) - M(t)D - DM(t)\right]\zeta_i(t) \\
&\quad + 2\sum_{\iota=1}^{p} M(t)W_\iota\left[g^\iota(z_i(t-\tau_\iota)) - g^\iota(\widehat{z}^*)\right]\Big\} \\
&\quad + \sum_{\iota=1}^{p}\sum_{i=1}^{N} e^{\xi(t+\tau-t_0)}\varphi(t)\zeta_i^T(t)\Lambda_\iota\zeta_i(t) - \sum_{\iota=1}^{p}\sum_{i=1}^{N} e^{\xi(t-\tau_\iota+\tau-t_0)}\varphi(t-\tau_\iota)\times\zeta_i^T(t-\tau_\iota)\Lambda_\iota\zeta_i(t-\tau_\iota) \\
&\leq \sum_{i=1}^{N} e^{\xi(t-t_0)}\varphi(t)\Big\{\zeta_i^T(t)\Big[(\xi+\phi(t)\ln\beta)M(t) + \phi(t)(M_1-M_2) + \sum_{\iota=1}^{p} e^{\xi\tau}\Lambda_\iota - M(t)D - DM(t)\Big]\zeta_i(t) \\
&\quad - \beta\sum_{\iota=1}^{p}\zeta_i^T(t-\tau_\iota)\Lambda_\iota\zeta_i(t-\tau_\iota) + 2\sum_{\iota=1}^{p} M(t)W_\iota\left[g^\iota(z_i(t-\tau_\iota)) - g^\iota(\widehat{z}^*)\right]\Big\}.
\end{aligned} \tag{56}$$

Moreover,

$$\begin{aligned}
&2\zeta_i^T(t)M(t)W_\iota\left[g^\iota(z_i(t-\tau_\iota)) - g^\iota(\widehat{z}^*)\right] \\
&\leq \beta^{-1}\zeta_i^T(t)M(t)W_\iota W_\iota^T M(t)\zeta_i(t) \\
&\quad + \beta\zeta_i^T(t-\tau_\iota)\Lambda_\iota\zeta_i(t-\tau_\iota).
\end{aligned} \tag{57}$$

It is obtained from (54), (56), and (57) that

$$\begin{aligned}
\dot{V}_2(t) &\leq \sum_{i=1}^{N} e^{\xi(t-t_0)}\varphi(t)\zeta_i^T(t)\Big\{(\xi+\phi(t)\ln\beta)M(t) + \phi(t)(M_1-M_2) \\
&\quad - DM(t) - M(t)D + \sum_{\iota=1}^{p}\left[e^{\xi\tau}\Lambda_\iota + \beta^{-1}M(t)W_\iota W_\iota^T M(t)\right]\Big\}\zeta_i(t) \\
&\leq 0, t \in (t_k, t_{k+1}), \quad \mathbb{N} \ni k.
\end{aligned} \tag{58}$$

Therefore,

$$V_2(t) \leq V_2(t_k), \forall t \in (t_k, t_{k+1}), \quad \mathbb{N} \ni k. \tag{59}$$

At the impulse time $t_k, k \in \mathbb{N}$, on the basis of the definitions of $M(t)$ and $\varphi(t)$, one has

$$\begin{aligned}
\varphi(t_k^-) &= \beta, \\
\varphi(t_k) &= 1, \\
M(t_k^-) &= M_1, \\
M(t_k) &= M_2.
\end{aligned} \tag{60}$$

Combining (50), (53), and (55) together, we derive that

$$
\begin{aligned}
V_2(t_k) &= \sum_{i=1}^{N} e^{\xi(t_k-t_0)}\varphi(t_k)\zeta_i^T(t_k)M(t_k)\zeta_i(t_k) \\
&\quad + \sum_{\iota=1}^{p}\sum_{i=1}^{N}\int_{t_k-\tau_\iota}^{t_k} e^{\xi(s+\tau-t_0)}\varphi(s)\zeta_i^T(s)\Lambda_\iota\zeta_i(s)\mathrm{d}s \\
&= e^{\xi(t_k-t_0)}\varphi(t_k)\zeta^T(t_k)\left(I_N\otimes M(t_k)\right)\zeta(t_k) \\
&\quad + \sum_{\iota=1}^{p}\sum_{i=1}^{N}\int_{t_k-\tau_\iota}^{t_k} e^{\xi(s+\tau-t_0)}\varphi(s)\zeta_i^T(s)\Lambda_\iota\zeta_i(s)\mathrm{d}s \\
&= e^{\xi(t_k-t_0)}\zeta^T(t_k^-)\left(I_{nN}+B\otimes\Phi\right)^T\left(I_N\otimes M_2\right) \\
&\quad \left(I_{nN}+B\otimes\Phi\right)\zeta(t_k^-) \\
&\quad + \sum_{\iota=1}^{p}\sum_{i=1}^{N}\int_{t_k-\tau_\iota}^{t_k} e^{\xi(s+\tau-t_0)}\varphi(s)\zeta_i^T(s)\Lambda_\iota\zeta_i(s)\mathrm{d}s \\
&\le e^{\xi(t_k-t_0)}\beta\zeta^T(t_k^-)\left(I_N\otimes M_1\right)\zeta(t_k^-) \\
&\quad + \sum_{\iota=1}^{p}\sum_{i=1}^{N}\int_{t_k-\tau_\iota}^{t_k} e^{\xi(s+\tau-t_0)}\varphi(s)\zeta_i^T(s)\Lambda_\iota\zeta_i(s)ds \\
&= \sum_{i=1}^{N} e^{\xi(t_k-t_0)}\varphi(t_k^-)\zeta_i^T(t_k^-)M(t_k^-)\zeta_i(t_k^-) \\
&\quad + \sum_{\iota=1}^{p}\sum_{i=1}^{N}\int_{t_k-\tau_\iota}^{t_k} e^{\xi(s+\tau-t_0)}\varphi(s)\zeta_i^T(s)\Lambda_\iota\zeta_i(s)\mathrm{d}s \\
&= V_2(t_k^-), \quad \mathbb{N}\ni k.
\end{aligned}
\tag{61}
$$

By (59) and (61), one obtains $V_2(t_0)\ge V_2(t), \forall t_0\le t$. Hence, we acquire

$$
\begin{aligned}
\|\zeta(t)\| &\le \sqrt{\frac{\bar{\lambda}_M+\sum_{\iota=1}^{p}\lambda_{\max}(\Lambda_\iota)\left(e^{\xi\tau}-1\right)/\xi}{\beta\underline{\lambda}_M}} \\
&\quad\cdot\left\|\chi(t_0)-\hat{z}^*\right\|_\tau e^{-(\xi/2)(t-t_0)}, \quad t_0\le t,
\end{aligned}
\tag{62}
$$

in which $\bar{\lambda}_M=\max\{\lambda_{\max}(M_1),\lambda_{\max}(M_2)\}$, $\underline{\lambda}_M=\min\{\lambda_{\min}(M_1),\lambda_{\min}(M_2)\}$. Thus, the MMDNNs (45) reach global exponential synchronization over $\mathbb{S}(\nu_1,\nu_2)$ with convergence rate $\xi/2$. □ □

Remark 2. Compared with [37], the sufficient condition for the synchronization of MMDNNs depends on the length of impulsive intervals, and the time-varying Lyapunov function in Theorem 4 can capture the dynamical characteristics of MMDNNs.

5. Numerical Examples

Example 1. The MMDNNs are given by

$$
\dot{z}_i(t) = -Dz_i(t)+\sum_{\iota=1}^{3}W_\iota g^\iota\left(z_i(t-\tau_\iota)\right)+J+\nu_i(t), \tag{63}
$$

in which $i=1,2,\ldots,5$, $g_\varsigma^1(\theta)=(1/8)(|\theta+1|-|\theta-1|)$, $g_\varsigma^2(\theta)=(1/16)(|\theta+1|-|\theta-1|)$, $g_\varsigma^3(\theta)=(1/32)(|\theta+1|-|\theta-1|)$, $\varsigma=1,2,3$, $J=(0,0,0)^T$, $D=\mathrm{diag}(0.9,0.8,0.9)$, $\tau_1=0.3,\tau_2=0.5$, $\tau=\tau_3=0.7$,

$$
\begin{aligned}
W_1 &= \begin{pmatrix} 0.1 & 0.2 & 0.1 \\ 0.3 & 0.1 & 0.3 \\ 0.4 & 0.2 & 0.4 \end{pmatrix}, \\
W_2 &= \begin{pmatrix} 0.2 & 0.3 & 0.4 \\ 0.1 & 0.4 & 0.5 \\ 0.3 & 0.5 & 0.1 \end{pmatrix}, \\
W_3 &= \begin{pmatrix} 0.2 & 0.5 & 0.5 \\ 0.4 & 0.3 & 0.3 \\ 0.1 & 0.6 & 0.3 \end{pmatrix}.
\end{aligned}
\tag{64}
$$

Apparently, $g_\varsigma^1(\cdot)$, $g_\varsigma^2(\cdot)$, and g_ς^3, $(\cdot)$, $(\varsigma=1,2,3)$, respectively, satisfy the Lipschitz condition with $\rho_\varsigma^1=0.25,\rho_\varsigma^2=0.125$, and $\rho_\varsigma^3=0.0625$. $z^*=(0,0,0)^T\in\mathbb{R}^3$ is an equilibrium solution of the MMDNNs (63).

Take $t_k=k,\Phi=\mathrm{diag}(0.2,0.3,0.1),\nu_1=1.12,\ \nu_2=2.12$, $\gamma=0.6$,

$$
\begin{aligned}
C_1 &= \begin{pmatrix} 0.4 & 0.3 & 0.2 \\ 0.3 & 0.5 & 0.3 \\ 0.2 & 0.1 & 0.1 \\ 0.6 & 0.3 & 0.1 \end{pmatrix}, \\
C_2 &= \begin{pmatrix} 0.2 & 0.5 & 0.3 \\ 0.4 & 0.1 & 0.4 \\ 0.1 & 0.5 & 0.4 \\ 0.2 & 0.1 & 0.3 \end{pmatrix}, \\
B &= \begin{pmatrix} -0.7 & 0.2 & 0 & 0.2 & 0.3 \\ 0.1 & -0.4 & 0.1 & 0 & 0.2 \\ 0 & 0.1 & -0.7 & 0.1 & 0.5 \\ 0.1 & 0 & 0.2 & -0.4 & 0.1 \\ 0.1 & 0.2 & 0.1 & 0.2 & -0.6 \end{pmatrix}.
\end{aligned}
\tag{65}
$$

Case 1. Utilizing MATLAB YALMIP Toolbox, one obtains

$$
\begin{aligned}
F_1 &= I_5\otimes\begin{pmatrix} 0.3631 & -0.4413 & 0.4421 \\ -0.4413 & 2.1340 & -1.3911 \\ 0.4421 & -1.3911 & 1.4273 \end{pmatrix}>0, \\
F_2 &= I_5\otimes\begin{pmatrix} 0.2043 & -0.2327 & 0.2396 \\ -0.2327 & 1.1282 & -0.7170 \\ 0.2396 & -0.7170 & 0.7490 \end{pmatrix}>0, \\
A &= I_5\otimes\begin{pmatrix} -17.7983 & 82.4589 & -36.1229 \\ 5.1034 & -28.0123 & 7.4528 \\ 16.4980 & -40.5024 & 56.8256 \\ 4.0410 & -26.6311 & 1.9003 \end{pmatrix},
\end{aligned}
\tag{66}
$$

satisfying (14) and (15). From Theorem 1, the MMDNNs (12) under the impulsive controller (9) are passive.

Case 2. Utilizing MATLAB YALMIP Toolbox, one gets

$$F_1 = I_5 \otimes \begin{pmatrix} 0.3501 & -0.4108 & 0.4248 \\ -0.4108 & 2.0450 & -1.3180 \\ 0.4248 & -1.3180 & 1.3634 \end{pmatrix} > 0,$$

$$F_2 = I_5 \otimes \begin{pmatrix} 0.1991 & -0.2203 & 0.2343 \\ -0.2203 & 1.0979 & -0.6921 \\ 0.2343 & -0.6921 & 0.7281 \end{pmatrix} > 0,$$

$$A = I_5 \otimes \begin{pmatrix} -37.2329 & 83.8487 & -129.0016 \\ 10.8454 & -29.4624 & 34.1967 \\ 33.2126 & -33.9720 & 141.5292 \\ 8.5271 & -28.8543 & 22.1856 \end{pmatrix}, \quad (67)$$

$$A_1 = I_5 \otimes \begin{pmatrix} 1.1069 & -0.3548 & 5.0976 \\ -0.3548 & 4.8449 & 1.3080 \\ 5.0976 & 1.3080 & 25.3992 \end{pmatrix},$$

satisfying (27) and (28). From Theorem 2, the MMDNNs (12) under the impulsive controller (9) are input-strictly passive.

Case 3. Utilizing MATLAB YALMIP Toolbox, one derives

$$F_1 = I_5 \otimes \begin{pmatrix} 0.3936 & -0.4735 & 0.4538 \\ -0.4735 & 2.2493 & -1.4582 \\ 0.4538 & -1.4582 & 1.4735 \end{pmatrix} > 0,$$

$$F_2 = I_5 \otimes \begin{pmatrix} 0.2258 & -0.2531 & 0.2484 \\ -0.2531 & 1.2036 & -0.7613 \\ 0.2484 & -0.7613 & 0.7839 \end{pmatrix} > 0,$$

$$A = I_5 \otimes \begin{pmatrix} 17.2060 & 97.5401 & -23.8482 \\ 4.7611 & -33.8467 & 2.1733 \\ 17.1505 & -43.0380 & 58.5388 \\ 3.6457 & -32.6881 & -3.9551 \end{pmatrix},$$

$$A_2 = I_5 \otimes \begin{pmatrix} 20.6353 & -7.8392 & -4.8377 & -7.9339 \\ -7.8392 & 3.4784 & -1.4360 & 3.7580 \\ -4.8377 & -1.4360 & 25.2331 & -4.0463 \\ -7.9339 & 3.7580 & -4.0463 & 4.5656 \end{pmatrix} > 0, \quad (68)$$

satisfying (36) and (37). According to Theorem 3, the MMDNNs (12) under the impulsive controller (9) are output-strictly passive. Figure 1 shows the results of simulation.

Example 2. The MMDNNs are given by

$$\dot{z}_i(t) = -Dz_i(t) + \sum_{\iota=1}^{3} W_\iota g^\iota(z_i(t-\tau_\iota)) + J, \quad (69)$$

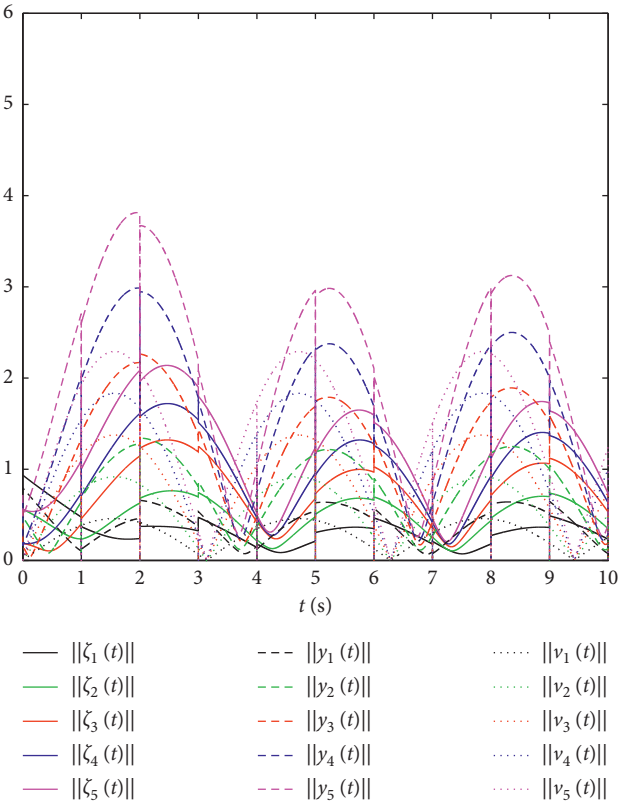

Figure 1: $\|\zeta_i(t)\|, \|y_i(t)\|, \|v_i(t)\|, i = 1, 2, \ldots, 5$.

in which $i = 1, 2, \ldots, 5$, $g_\varsigma^1(\theta) = (1/8)(|\theta+1| - |\theta-1|)$, $g_\varsigma^2(\theta) = (1/16)(|\theta+1| - |\theta-1|)$, $g_\varsigma^3(\theta) = (1/32)(|\theta+1| - |\theta-1|)$, $\varsigma = 1, 2, 3$, $D = \mathrm{diag}(0.7, 0.9, 0.8)$, $J = (0, 0, 0)^T$, $\tau_1 = 0.2$, $\tau_2 = 0.3$, $\tau = \tau_3 = 0.4$,

$$W_1 = \begin{pmatrix} 0.3 & 0.4 & 0.5 \\ 0.5 & 0.6 & 0.1 \\ 0.2 & 0.3 & 0.2 \end{pmatrix},$$

$$W_2 = \begin{pmatrix} 0.5 & 0.6 & 0.2 \\ 0.2 & 0.3 & 0.3 \\ 0.1 & 0.2 & 0.5 \end{pmatrix}, \quad (70)$$

$$W_3 = \begin{pmatrix} 0.2 & 0.1 & 0.3 \\ 0.3 & 0.4 & 0.4 \\ 0.4 & 0.5 & 0.6 \end{pmatrix}.$$

Apparently, $g_\varsigma^1(\cdot), g_\varsigma^2(\cdot)$, and $g_\varsigma^3, (\cdot)$, $(\varsigma = 1, 2, 3)$, respectively, satisfy the Lipschitz condition with $\rho_\varsigma^1 = 0.25, \rho_\varsigma^2 = 0.125$, and $\rho_\varsigma^3 = 0.0625$. $z^* = (0, 0, 0)^T \in \mathbb{R}^3$ is an equilibrium solution of the MMDNNs (69).

Let $t_k = 1.8k, \nu_1 = 1.3, \quad \nu_2 = 3.1, \beta = 0.8, \xi = 0.2$, $\Phi = \mathrm{diag}(0.5, 0.4, 0.2)$,

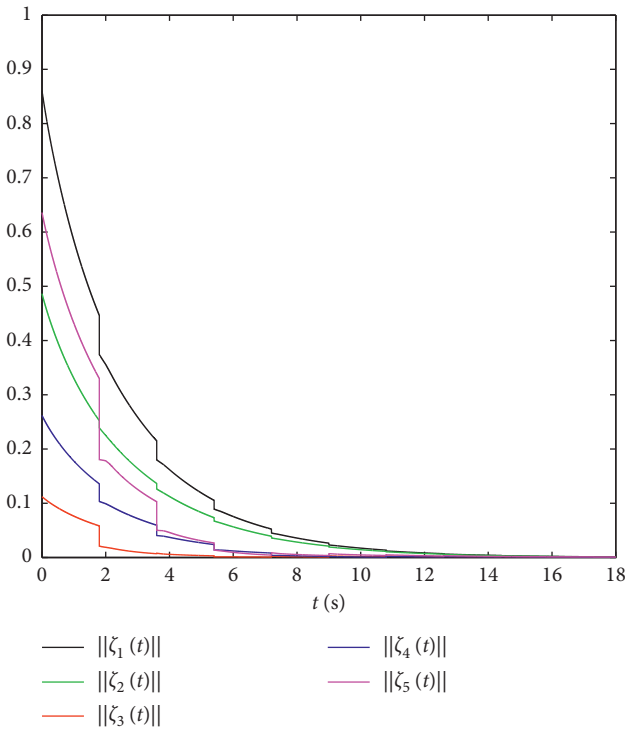

FIGURE 2: $\|\zeta_i(t)\|, i = 1, 2, \ldots, 5$.

$$B = \begin{pmatrix} -0.4 & 0.1 & 0 & 0.2 & 0.1 \\ 0.3 & -0.6 & 0.2 & 0 & 0.1 \\ 0 & 0.2 & -0.8 & 0.2 & 0.4 \\ 0.2 & 0 & 0.1 & -0.5 & 0.2 \\ 0.2 & 0.3 & 0.3 & 0.1 & -0.9 \end{pmatrix}. \tag{71}$$

By using MATLAB YALMIP Toolbox, we derive

$$\begin{aligned} M_1 &= \begin{pmatrix} 1.1830 & -0.8947 & -0.2582 \\ -0.8947 & 2.9926 & -1.5950 \\ -0.2582 & -1.5950 & 2.0166 \end{pmatrix} > 0, \\ M_2 &= \begin{pmatrix} 0.7928 & -0.5673 & -0.1779 \\ -0.5673 & 1.6871 & -0.7982 \\ -0.1779 & -0.7982 & 1.1134 \end{pmatrix} > 0, \end{aligned} \tag{72}$$

satisfying (52) and (53). According to Theorem 4, the MMDNNs (45) under the impulsive controller (48) are globally exponentially synchronized. Figure 2 shows the results of simulation.

6. Conclusion

In this paper, a class of multiple multi-delayed neural network models has been introduced, and the model can describe the dynamics of neurons more accurately. On the one hand, several passivity criteria for MMDNNs have been established by means of inequality techniques. On the other hand, the synchronization of the proposed model has also been researched based on stability theory. Finally, the correctness of the synchronization and passivity criteria has been verified by two numerical examples. In future work, we will design a suitable impulsive controller to further study the passivity and synchronization of multiple reaction-diffusion neural networks.

Data Availability

No data were used to support this study.

Conflicts of Interest

The authors declare that there are no conflicts of interest regarding the publication of this paper.

Acknowledgments

This study was supported in part by the Open Project Funded by the Chongqing Key Lab on IFBDA, School of Mathematical Sciences, Chongqing Normal University (CSSXKFKTQ201811), and in part by the National Natural Science Foundation of China under grant no. 11971081.

References

[1] J. Shin, K. Kwak, S. Kim, and H. J. Kim, "Adaptive range estimation in perspective vision system using neural networks," *IEEE/ASME Transactions on Mechatronics*, vol. 23, no. 2, pp. 972–977, 2018.

[2] J. Sun, G. Han, Z. Zeng, and Y. Wang, "Memristor-based neural network circuit of full-function pavlov associative memory with time delay and variable learning rate," *IEEE Transactions on Cybernetics*, vol. 50, no. 7, pp. 1–11, 2019.

[3] W.-R. Yang, C.-S. Wang, and C.-P. Chen, "Motion-pattern recognition system using a wavelet-neural network," *IEEE Transactions on Consumer Electronics*, vol. 65, no. 2, pp. 170–178, 2019.

[4] T. Dumas, A. Roumy, and C. Guillemot, "Context-adaptive neural network-based prediction for image compression," *IEEE Transactions on Image Processing*, vol. 29, pp. 679–693, 2020.

[5] X. M. Zhang and Q. L. Han, "Global asymptotic stability for a class of generalized neural networks with interval time-varying delays," *IEEE Transactions on Neural Networks*, vol. 22, no. 8, pp. 1180–1192, 2011.

[6] Z. Wang, H. Zhang, and B. Jiang, "LMI-based approach for global asymptotic stability analysis of recurrent neural networks with various delays and structures," *IEEE Transactions on Neural Networks*, vol. 22, no. 7, pp. 1032–1045, 2011.

[7] B. Zhang, J. Lam, and S. Xu, "Stability analysis of distributed delay neural networks based on relaxed Lyapunov-Krasovskii functionals," *IEEE Transactions on Neural Networks and Learning Systems*, vol. 26, no. 7, pp. 1480–1492, 2015.

[8] R. Samli, S. Senan, E. Yucel, and Z. Orman, "Some generalized global stability criteria for delayed Cohen-Grossberg neural networks of neutral-type," *Neural Networks*, vol. 116, pp. 198–207, 2019.

[9] Z. Li, H. Yan, H. Zhang, X. Zhan, and C. Huang, "Stability analysis for delayed neural networks via improved auxiliary polynomial-based functions," *IEEE Transactions on Neural Networks and Learning Systems*, vol. 30, no. 8, pp. 2562–2568, 2019.

[10] R. Zhang, D. Zeng, J. H. Park, Y. Liu, and S. Zhong, "A new approach to stochastic stability of Markovian neural networks with generalized transition rates," *IEEE Transactions on Neural Networks and Learning Systems*, vol. 30, no. 2, pp. 499–510, 2019.

[11] C. Hu, H. He, and H. Jiang, "Fixed/preassigned-time synchronization of complex networks via improving fixed-time stability," *IEEE Transactions on Cybernetics*, pp. 1–11, 2020.

[12] C. Li and X. Liao, "Passivity analysis of neural networks with time delay," *IEEE Transactions on Circuits and Systems–II: Express Briefs*, vol. 52, no. 8, pp. 471–475, 2005.

[13] S. Xu, W. Zheng, and Y. Zou, "Passivity analysis of neural networks with time-varying delays," *IEEE Transactions on Circuits and Systems–II: Express Briefs*, vol. 56, no. 4, pp. 325–329, 2009.

[14] J. Lian and J. Wang, "Passivity of switched recurrent neural networks with time-varying delays," *IEEE Transactions on Neural Networks and Learning Systems*, vol. 26, no. 2, pp. 357–366, 2015.

[15] Y. Chen, Z. Fu, Y. Liu, and F. E. Alsaadi, "Further results on passivity analysis of delayed neural networks with leakage delay," *Neurocomputing*, vol. 224, pp. 135–141, 2017.

[16] S. Saravanan, V. Umesha, M. Syed Ali, and S. Padmanabhan, "Exponential passivity for uncertain neural networks with time-varying delays based on weighted integral inequalities," *Neurocomputing*, vol. 314, pp. 429–436, 2018.

[17] Y. Cao, R. Samidurai, and R. Sriraman, "Robust passivity analysis for uncertain neural networks with leakage delay and additive time-varying delays by using general activation function," *Mathematics and Computers in Simulation*, vol. 155, pp. 57–77, 2019.

[18] X.-L. An, L. Zhang, Y.-Z. Li, and J.-G. Zhang, "Synchronization analysis of complex networks with multi-weights and its application in public traffic network," *Physica A: Statistical Mechanics and its Applications*, vol. 412, pp. 149–156, 2014.

[19] X.-L. An, L. Zhang, and J.-G. Zhang, "Research on urban public traffic network with multi-weights based on single bus transfer junction," *Physica A: Statistical Mechanics and its Applications*, vol. 436, pp. 748–755, 2015.

[20] J.-L. Wang, P.-C. Wei, H.-N. Wu, T. Huang, and M. Xu, "Pinning synchronization of complex dynamical networks with multiweights," *IEEE Transactions on Systems, Man, and Cybernetics: Systems*, vol. 49, no. 7, pp. 1357–1370, 2019.

[21] J.-L. Wang, M. Xu, H.-N. Wu, and T. Huang, "Passivity analysis and pinning control of multi-weighted complex dynamical networks," *IEEE Transactions on Network Science and Engineering*, vol. 6, no. 1, pp. 60–73, 2019.

[22] G. Wen, X. Zhai, Z. Peng, and A. Rahmani, "Fault-tolerant secure consensus tracking of delayed nonlinear multi-agent systems with deception attacks and uncertain parameters via impulsive control," *Communications in Nonlinear Science and Numerical Simulation*, vol. 82, Article ID 105043, 2020.

[23] C. Hu, H. Jiang, and Z. Teng, "Globally exponential stability for delayed neural networks under impulsive control," *Neural Processing Letters*, vol. 31, no. 2, pp. 105–127, 2010.

[24] X.-A. Li and J.-Z. Zou, "Globally exponential stability for stochastic delayed neural networks under impulsive control," *Procedia Engineering*, vol. 15, pp. 386–391, 2011.

[25] Q. Zhu and J. Cao, "Stability analysis of Markovian jump stochastic BAM neural networks with impulse control and mixed time delays," *IEEE Transactions on Network Science and Engineering*, vol. 23, no. 3, pp. 467–479, 2012.

[26] J. Qi, C. Li, and T. Huang, "Existence and exponential stability of periodic solution of delayed Cohen-Grossberg neural networks via impulsive control," *Neural Computing and Applications*, vol. 26, no. 6, pp. 1369–1377, 2015.

[27] H. Li, C. Li, and T. Huang, "Periodicity and stability for variable-time impulsive neural networks," *Neural Networks*, vol. 94, pp. 24–33, 2017.

[28] D. Li, P. Cheng, M. Hua, and F. Yao, "Robust exponential stability of uncertain impulsive stochastic neural networks with delayed impulses," *Journal of the Franklin Institute*, vol. 355, no. 17, pp. 8597–8618, 2018.

[29] L. Li and J. Jian, "Delay-dependent passivity analysis of impulsive neural networks with time-varying delays," *Neurocomputing*, vol. 168, pp. 276–282, 2015.

[30] R. Samidurai and R. Manivannan, "Robust passivity analysis for stochastic impulsive neural networks with leakage and additive time-varying delay components," *Applied Mathematics and Computation*, vol. 268, pp. 743–762, 2015.

[31] L. Zhou, "Delay-dependent and delay-independent passivity of a class of recurrent neural networks with impulse and multi-proportional delays," *Neurocomputing*, vol. 308, pp. 235–244, 2018.

[32] W. Jiang, G. Wen, Z. Peng, T. Huang, and A. Rahmani, "Fully distributed formation-containment control of heterogeneous linear multiagent systems," *IEEE Transactions on Automatic Control*, vol. 64, no. 9, pp. 3889–3896, 2019.

[33] J. Wang, L. Shen, J. Xia, Z. Wang, and X. Chen, "Asynchronous dissipative filtering for nonlinear jumping systems subject to fading channels," *Journal of the Franklin Institute*, vol. 357, no. 1, pp. 589–605, 2020.

[34] J. Wang, C. Yang, H. Shen, J. Cao, and L. Rutkowski, "Sliding-mode control for slow-sampling singularly perturbed systems subject to Markov jump parameters," *IEEE Transactions on Systems, Man, and Cybernetics: Systems*, pp. 1–8, 2020.

[35] Y. Gong, G. Wen, Z. Peng, T. Huang, and Y. Chen, "Observer-based time-varying formation control of fractional-order multi-agent systems with general linear dynamics," *IEEE Transactions on Circuits and Systems II: Express Briefs*, vol. 67, no. 1, pp. 82–86, 2020.

[36] Y. Lv, C. Hu, J. Yu, H. Jiang, and T. Huang, "Edge-based fractional-order adaptive strategies for synchronization of fractional-order coupled networks with reaction-diffusion terms," *IEEE Transactions on Cybernetics*, vol. 50, no. 4, pp. 1582–1594, 2020.

[37] T. Wu, X. Huang, X. Chen, and J. Wang, "Sampled-data H∞ exponential synchronization for delayed semi-Markov jump CDNs: a looped-functional approach," *Applied Mathematics and Computation*, vol. 377, Article ID 125156, 2020.

[38] C. Hu, H. He, and H. Jiang, "Synchronization of complex-valued dynamic networks with intermittently adaptive coupling: a direct error method," *Automatica*, vol. 112, Article ID 108675, 2020.

Hindawi
Discrete Dynamics in Nature and Society
Volume 2020, Article ID 9369813, 12 pages
https://doi.org/10.1155/2020/9369813

Research Article

Passivity Analysis of Markov Jumping Delayed Reaction-Diffusion Neural Networks under Different Boundary Conditions

Ziwei Li, Xuelian Wang, Qingkai Kong, and Jing Wang

School of Electrical and Information Engineering, Anhui University of Technology, Ma'anshan 243002, China

Correspondence should be addressed to Qingkai Kong; kqk1234@163.com and Jing Wang; jingwang08@126.com

Received 20 April 2020; Accepted 8 June 2020; Published 6 July 2020

Guest Editor: Jinliang Wang

This work analyzes the passivity for a set of Markov jumping reaction-diffusion neural networks limited by time-varying delays under Dirichlet and Neumann boundary conditions, respectively, in which Markov jumping is used to describe the variations among system parameters. To overcome some difficulties originated from partial differential terms, the Lyapunov–Krasovskii functional that introduces a new integral term is proposed and some inequality techniques are also adopted to obtain the delay-dependent stability conditions in terms of linear matrix inequalities, which ensures that the designed neural networks satisfy the specified performance of passivity. Finally, the advantages and effectiveness of the obtained results are verified via displaying two illustrated examples.

1. Introduction

In the last few decades, the research of neural networks (NNs) has received widespread attention, and abundant works have been obtained. NNs have been successfully used in all kinds of areas, such as signal processing, voiceprint recognition, nonlinear dynamics, and image compression [1–3]. Additionally, time-varying delays (TVDs) are omnipresent in reality such that their effects on the NNs cannot be ignored, and mainly in that the existence of time delays (TDs) may cause instability and poor performance of systems in practical situations [4–10]. Correspondingly, not introducing TDs will cause the inaccuracy of values when NNs are mathematically modeled. Therefore, much research attention has been concentrated on the issue of stability analysis for the NNs with TDs, and accordingly a great number of works have been published in the literature (see, e.g., [11] and the references therein).

It should be remarkable that the behavior of the networks depends not only on time but also on the spatial position from the perspective of engineering, such as liquid flow and diffusion processes. In reality, reaction-diffusions exist in many systems, such as chemical systems and NNs [12]. It should be remarkable that the node states of such systems should consider the variables of space and time, which can be described by partial differential equations with reaction-diffusion terms (RDTs). Thus, it is of great essential to introduce the RDT into NNs to achieve a better approximation effect of the spatiotemporal actions. To name a few, for the complex spatiotemporal networks, the synchronization problem of space-varying coefficients was concerned in [13]. For the coupled partial differential systems, the synchronization issue with space-independent coefficients was discussed in [14]. However, finding a suitable method to deal with the RDT of neural networks is a difficult challenge. Although it is very tricky, this challenge has driven the development of RDNNs. Up to now, a mass of outstanding works on the stability analysis of NNs with RDT have been published [15, 16]. For example, the synchronization issue of hybrid-coupled RDNNs with TDs was discussed in [17]. In [18], the passivity of coupled RDNNs with nonlinear coupling was considered. Via detailed understanding, it is found that most of the existing methods are used to handle the RDT under the framework of Friedrichs inequality. In this case, there is a certain degree of conservatism, which is difficult to be extended to the general

matrix form. To tackle this problem, using appropriate matrix inequalities to better reduce the conservatism was investigated. Based on the abovementioned analysis, it prompts us to take the stability problem of RDNNs into consideration by using proper matrix inequality.

On the contrary, NNs often show a special switching characteristic of the network mode, and this case will make that the RDNNs cannot be handily modeled [19, 20]. Fortunately, the Markov process has been proved to be able to depict the switching (or jumping) cases effectively [16, 21–25]. Hence, taking the Markov jumping model applied into RDNNs with TVDs is practical and reasonable, in which each state represents a jumping mode. Recently, lots of works for RDNNs with the Markov jumping parameters have been published [26–28]. For instance, the stochastic delayed NNs with RDT and Markov jumping parameters were studied in [29]. In [30], the state estimation of Markov jump delayed NNs with RDT was discussed. In this case, the study of RDNNs with TVDs and Markov jumping is of significance. Besides, passivity theory is recognized as a powerful tool and plays a critical role in diverse areas such as energy management and flow control [31–35]. In early days, the passivity was widely used in a system where the variables of input and output merely depend on time and rarely in a system with RDT. Thereby, it is extremely necessary to explore the passivity of RDNNs with TVDs. As far as we know, only a small number of investigators have studied the passivity analysis of Markov jumping RDNNs, which powerfully motivates the present study.

Based on the above discussions, this paper concentrates on the stability and passivity analysis of Markov jumping RDNNs with TVDs. In addition, the main contributions include the following three sides:

(1) Compared with some existing literature [11, 36], in this paper, Jensen's inequality and the Wirtinger-type integral inequality, a new inequality dealing with the reaction-diffusion terms and the reciprocally convex method, are introduced to derive criteria based on linear matrix inequalities (LMIs), which is beneficial for reducing the conservativeness of the results.

(2) Furthermore, by using some inequality techniques, several passive criteria for RDNNs with TVDs and Markov jumping parameters are obtained, and the passivity of Markov jumping RDNNs with TVDs is analyzed.

(3) The Markov jumping model is employed to the research of RDNNs, and the passivity of Markov jumping RDNNs is investigated under the different boundary conditions (BCs), which determines the common internal stability of Markov jumping RDNNs.

2. Preliminaries

Consider the RDNNs with Markov jumping parameters and TVDs as follows:

$$\begin{aligned}\frac{\partial \eta_i(t,x)}{\partial t} &= \sum_{k=1}^{r}\frac{\partial}{\partial x_k}\left(a_{ik}\frac{\partial \eta_i(t,x)}{\partial x_k}\right) - b_i(\alpha_t)\eta_i(t,x)\\ &\quad + \sum_{j=1}^{\varrho} c_{ij}(\alpha_t) f_j(\eta_i(t,x))\\ &\quad + \sum_{j=1}^{\varrho} d_{ij}(\alpha_t) g_j(\eta_i(t-\tau(t),x)) + \nu_i(t,x),\end{aligned} \tag{1}$$

$$\eta_i(0,x) = \varepsilon_i(x), \quad (t,x) \in [-\tau_2, 0] \times \Omega,$$

where $x = (x_1, x_2, \ldots, x_r)^T \in \mathbb{R}^r$, $i = 1, 2, \ldots, \rho$; $\eta_i(t,x)$ denotes the state variable at time t and in space s; $a_{ik} > 0$ means the transmission diffusion coefficient of the ith neuron; $b_i(\alpha_t) > 0$ is the neuron charging time constants; $c_{ij}(\alpha_t)$ and $d_{ij}(\alpha_t)$ denote the connection weight coefficients of the jth neuron on the ith neuron; $f_j(\cdot)$ and $g_j(\cdot)$ represent the neuron activation functions of the jth neuron at time t; $\nu_i(t,x)$ is the control input; $\varepsilon_i(s,x)$ is bounded and continuous on $[-\tau_2, 0) \times \Omega$, $i = 1, 2, \ldots, \rho$; $\tau(t)$ indicates the transmission delay and satisfies $0 < \tau(t) \le \tau_2$ and $\dot{\tau}(t) \le \sigma < 1$, in which τ_2 and σ are some given constants; $\{\alpha_t\}$ $(t \in \mathbb{Z}^+)$ is a right-continuous Markov process taking values in a finite state space $\mathscr{M} = \{1, 2, \ldots, \rho\}$ with the transition probability matrix $\Phi \triangleq \{\pi_{\upsilon\kappa}\}$ given by

$$\Pr\{\alpha_{t+\triangle} = \kappa \mid \alpha_t = \upsilon\} = \begin{cases} \pi_{\upsilon\kappa}\triangle + o(\triangle), & \pi\upsilon \ne \kappa, \\ 1 + \pi_{\upsilon\upsilon}\triangle + o(\triangle), & \upsilon = \kappa, \end{cases} \tag{2}$$

where $\lim_{\triangle \longrightarrow 0}(o(\triangle)/\triangle) = 0$, $(\triangle > 0)$, and $\pi_{\upsilon\kappa} \ge 0$ for $\upsilon \ne \kappa$ is the transition rate from mode υ at time t to mode κ at time $t + \triangle$.

In our paper, two kinds of BCs are introduced:

(1) Dirichlet BCs:

$$\eta_i(t,x) = 0, \quad (t,x) \in [-\tau_2, +\infty) \times \partial\Omega. \tag{3}$$

(2) Neumann BCs:

$$\frac{\partial \eta_i(t,x)}{\partial \overline{n}} = \left(\frac{\partial \eta_i(t,x)}{\partial x_1}, \frac{\partial \eta_i(t,x)}{\partial x_2}, \ldots, \frac{\partial \eta_i(t,x)}{\partial x_r}\right)^T = 0, \quad (t,x) \in [-\tau_2, +\infty) \times \partial\Omega. \tag{4}$$

Besides, f_i and g_i are defined as the activation functions, which are assumed to meet the listed condition as below.

Assumption 1 (see [30]). The activation functions f_i and g_i satisfy the bounded conditions and there exist positive matrices $\mathsf{F}_0 = \mathrm{diag}\{\mathsf{F}_{01}, \mathsf{F}_{02}, \ldots, \mathsf{F}_{0\rho}\}$ and $\mathsf{F}_1 = \mathrm{diag}\{\mathsf{F}_{11}, \mathsf{F}_{12}, \ldots, \mathsf{F}_{1\rho}\}$ such that

$$0 \le \frac{f_i(a_1) - f_i(a_2)}{a_1 - a_2} \le \mathsf{F}_{0i}, \qquad 0 \le \frac{g_i(a_1) - g_i(a_2)}{a_1 - a_2} \le \mathsf{F}_{1i}, \tag{5}$$

where $i = 1, 2, \ldots, \rho$, $f_i(0) = 0$, and $g_i(0) = 0$, for any a_1, $a_2 \in \mathbb{R}^l$ and $a\_\{\_1\} \neq a\_\{\_2\}$.

In this paper, for each $\alpha_t = \alpha \in \mathscr{M}$, system (1) can be rewritten as the vector matrix form as follows:

$$\begin{aligned}\frac{\partial \eta(t,x)}{\partial t} &= A_k \circ \nabla^2 \eta(t,x) - B_\alpha \eta(t,x) + C_\alpha f(\eta(t,x)) \\ &\quad + D_\alpha g(\eta(t-\tau(t),x)) + \nu(t,x), \\ \eta(0,x) &= \varepsilon(x), \quad (t,x) \in [-\tau_2, 0] \times \Omega,\end{aligned} \tag{6}$$

where

$$\begin{aligned}A_k &\triangleq diag\{a_{1k}, a_{2k}, \ldots, a_{\rho k}\}, \\ B_\alpha &\triangleq diag\{b_1(\alpha), b_2(\alpha), \ldots, b_\rho(\alpha)\}, \quad j = 1, 2, \ldots, \rho, \\ C_\alpha &\triangleq \{c_{ij}(\alpha)\}_{\rho\times\rho}, \\ D_\alpha &\triangleq \{d_{ij}(\alpha)\}_{\rho\times\rho}, \\ \varepsilon(x) &= [\, \varepsilon_1(x) \ \cdots \ \varepsilon_2(x) \,]^T, \\ g(\eta(\cdot)) &\triangleq [\, g_1(\eta_1(\cdot)) \ \cdots \ g_\rho(\eta_\rho(\cdot)) \,]^T, \\ \nu(t,x) &\triangleq [\, \nu_1(t,x) \ \cdots \ \nu_\rho(t,x) \,]^T, \\ \eta(t,x) &\triangleq [\, \eta_1(t,x) \ \cdots \ \eta_\rho(t,x) \,]^T, \\ f(\eta(\cdot)) &\triangleq [\, f_1(\eta_1(\cdot)) \ \cdots \ f_\rho(\eta_\rho(\cdot)) \,]^T,\end{aligned} \tag{7}$$

with

$$A_k \circ \nabla^2 \eta(t,x) \triangleq \left[\sum_{k=1}^{r} \frac{\partial}{\partial x_k} \left(a_{1k} \frac{\partial \eta_1(t,x)}{\partial x_k} \right) \cdots \sum_{k=1}^{r} \frac{\partial}{\partial x_k} \left(a_{\rho k} \frac{\partial \eta_\rho(t,x)}{\partial x_k} \right) \right]^T. \tag{8}$$

The output vector $y(t,x) \in \mathbb{R}^\rho$ of system (6) is chosen as

$$y(t,x) = E\eta(t,x) + H\nu(t,x), \tag{9}$$

where E, $F \in \mathbb{R}^{\rho\times\rho}$ are known constant matrices.

Definition 1 (see [37]). For $(t,x) \in [0, +\infty) \times \Omega$, if the input $\nu(t,x)$ and the output $y(t,x)$ satisfy the following inequality:

$$\begin{aligned}&\int_{t_1}^{t_2} \int_\Omega \left(y^T(t,x) M \nu(t,x) - \nu^T(t,x) W \nu(t,x) \right) dx dt \\ &\quad \geq \mathscr{S}(t_2) - \mathscr{S}(t_1),\end{aligned} \tag{10}$$

in which M, $W \in \mathbb{R}^{\rho\times\rho}$, $W > 0$, and $\lambda_m(M) + \lambda_m(W) > 0$, $\forall t_2, t_1 \in [0, +\infty)$ and $t_2 > t_1$, where $\mathscr{S}(t)$: $[0, +\infty) \longrightarrow [0, +\infty)$ is the storage function, then network (6) is said to be input-strictly passive.

Lemma 1 (see [38]). *For the compact set Ω and system (6), if $\eta_i(t,x) = \eta_i(t, x_1, x_2, \ldots, x_r) \in C^1(\Omega)$ satisfies $\eta_i(t,x)|_{\partial\Omega=0}$, that is, it vanishes on the boundary $\partial\Omega$ of Ω, then*

$$\int_\Omega \eta_i(t,x) \frac{\partial^2 \eta_i(t,x)}{\partial x_k^2} dx \leq -\left(\frac{\pi}{2l_k} \right)^2 \int_\Omega \eta_i^2(t,x) dx. \tag{11}$$

Remark 1. It is worth noting that compared to other methods of coping with RDT, such as Lemma 1 in [39], in our paper, it is validated that utilizing (11) can better reduce conservativeness, with regards to deriving of our main results which is very significant. The proof is omitted therein but can be found in the literature [38].

3. Main Results

In this section, we consider dynamical NNs, which includes r identical with spatial diffusion, and each node is a ρ-dimensional for Markov jumping RDNNs. Additionally, sufficient condition for assuring the asymptotic stability of Markov jumping RDNNs is acquired. Besides, the passivity criteria for RDNNs (6) under the different BCs are achieved.

Theorem 1. *Given scalars $\tau_2 > 0$ and $1 > \sigma > 0$, the solution of RDNNs (6) is input-strictly passive under the Dirichlet boundary condition if there exist some diagonal matrices $P_\alpha > 0$, $\Gamma_0 > 0$, $\Gamma_1 > 0$, and $X > 0$, real positive matrices Q_1, Q_2, Z, U, R, and W, and matrix Y of appropriate dimensions, such that $\forall \tau \in \{0, \tau_2\}$, the following inequalities hold:*

$$\begin{bmatrix} \check{R} & \Upsilon \\ \Upsilon^T & \check{R} \end{bmatrix} \geq 0, \tag{12}$$

$$\begin{aligned}\Pi &\triangleq \Pi_0 + \sum_{i=1}^{4} \Pi_i + \Pi_5(\tau) + \Pi_6 - 2\omega_1^T E^T M \omega_{11} \\ &\quad - 2\omega_{11}^T H^T M \omega_{11} - \omega_{11}^T W \omega_{11} < 0,\end{aligned} \tag{13}$$

where

$$\begin{aligned}\Pi_1 &\triangleq 2\left[\omega_1^T \left(-\frac{\pi^2}{4} P_\alpha K A_k K^T - P_\alpha B_\alpha \right) \omega_1 + \omega_1^T \sum_{\kappa=1}^{\rho} \pi_{\upsilon\kappa} P_\kappa \omega_1 + \omega_1^T P_\alpha C_\alpha \omega_4 + \omega_1^T P_\alpha D_\alpha \omega_5 + \omega_1^T P_\alpha H_\alpha \omega_{11} \right. \\ &\quad \left. - \omega_1^T B_\alpha^T X \omega_6 + \omega_4^T C_\alpha^T X \omega_6 + \omega_5^T D_\alpha^T X \omega_6 + \omega_6^T X \omega_{11} - \omega_6^T X \omega_6 \right], \\ \Pi_0 &\triangleq \omega_1^T \Gamma_0 \mathsf{F}_0 \omega_4 - 2\omega_4^T \Gamma_0 \omega_4, \\ \Pi_2 &\triangleq \omega_1^T Q_1 \omega_1 - (1-\sigma) \omega_3^T Q_1 \omega_3,\end{aligned}$$

$$\Pi_3 \triangleq \omega_1^T Q_2 \omega_1 - \omega_2^T Q_2 \omega_2,$$

$$\Pi_4 \triangleq \omega_1^T \mathsf{F}_1^T Z \mathsf{F}_1 \omega_1 - (1-\sigma)\omega_5^T Z \omega_5,$$

$$\Pi_{51} \triangleq -\tau_2(\tau_2 - \tau)\omega_7^T U \omega_7 - \tau_2 \tau \omega_9^T U \omega_9,$$

$$\omega_i \triangleq \left[\, 0_{\rho\times(i-1)\rho} \;\; I_n \;\; 0_{\rho\times(\rho-i)\rho} \,\right], \quad i = 1, 2, \ldots, 11,$$

$$\Pi_5 \triangleq \tau_2^2 \omega_1^T U \omega_1 + \Pi_{51},$$

$$K \triangleq \left[\frac{\eta_1}{l_1} \;\cdots\; \frac{\eta_1}{l_r} \;\cdots\; \frac{\eta_\rho}{l_1} \;\cdots\; \frac{\eta_\rho}{l_r} \right]_{\rho\times\rho r},$$

$$\check{R} \triangleq \mathrm{diag}\{R, 3R, 5R\},$$

$$\check{\tau} \triangleq \tau_2 - \tau(t),$$

$$\Lambda_2 \triangleq \left[\, \omega_1^T - \omega_3^T \;\; \omega_1^T + \omega_3^T - 2\omega_9^T \;\; \omega_1^T - \omega_3^T + 6\omega_9^T - 12\omega_{10}^T \,\right],$$

$$\Lambda_1 \triangleq \left[\, \omega_3^T - \omega_2^T \;\; \omega_3^T + \omega_2^T - 2\omega_7^T \;\; \omega_3^T - \omega_2^T + 6\omega_7^T - 12\omega_8^T \,\right],$$

$$\Pi_6 \triangleq \tau_2^2 \omega_6^T R \omega_6 - \left[\, \Lambda_1 \;\; \Lambda_2 \,\right] \begin{bmatrix} \check{R} & \Upsilon \\ \Upsilon^T & \check{R} \end{bmatrix} \left[\, \Lambda_1 \;\; \Lambda_2 \,\right]^T,$$

$$\xi(t,x) \triangleq \Bigg[\eta^T(t,x)\eta^T(t-\tau_2,x)\eta^T(t-\tau(t),x) f^T(\eta(t,x)) g^T(\eta(t-\tau(t),x)) \frac{\partial \eta^T(t,x)}{\partial t} \frac{1}{\check{\tau}} \int_{t-\tau_2}^{t-\tau(t)} \eta^T(s,x)\mathrm{d}s$$
$$\cdot \frac{1}{(\check{\tau})^2} \int_{t-\tau_2}^{t-\tau(t)} \int_{\delta}^{t-\tau(t)} \eta^T(s,x)\mathrm{d}s\,\mathrm{d}\delta \frac{1}{\tau(t)} \int_{t-\tau(t)}^{t} \eta^T(s,x)\mathrm{d}s \frac{1}{\tau^2(t)} \int_{t-\tau(t)}^{t} \int_{\delta}^{t} \eta^T(s,x)\mathrm{d}s\,\mathrm{d}\delta \nu^T(t,x) \Bigg]^T. \tag{14}$$

Proof. We firstly choose the following Lyapunov–Krasovskii functional:

$$V(k) = \sum_{i=1}^{6} V_i(\eta(t,x), \alpha, t), \tag{15}$$

where

$$\begin{aligned}
V_1(\eta(t,x),\alpha,t) &= \int_\Omega \eta^T(t,x) P_\alpha \eta(t,x)\mathrm{d}x + \sum_{k=1}^{r} \int_\Omega \frac{\partial \eta^T(t,x)}{\partial x_k} X A_k \frac{\partial \eta(t,x)}{\partial x_k}\mathrm{d}x,\\
V_2(\eta(t,x),\alpha,t) &= \int_\Omega \int_{t-\tau(t)}^{t} \eta^T(s,x) Q_1 \eta(s,x)\mathrm{d}s\,\mathrm{d}x,\\
V_3(\eta(t,x),\alpha,t) &= \int_\Omega \int_{t-\tau_2}^{t} \eta^T(s,x) Q_2 \eta(s,x)\mathrm{d}s\,\mathrm{d}x,\\
V_4(\eta(t,x),\alpha,t) &= \int_\Omega \int_{t-\tau(t)}^{t} g^T(\eta(s,x)) Z g(\eta(s,x))\mathrm{d}s\,\mathrm{d}x,\\
V_5(\eta(t,x),\alpha,t) &= \tau_2 \int_\Omega \int_{-\tau_2}^{0} \int_{t+w}^{t} \eta^T(s,x) U \eta(s,x)\mathrm{d}s\,\mathrm{d}w\,\mathrm{d}x,\\
V_6(\eta(t,x),\alpha,t) &= \tau_2 \int_\Omega \int_{-\tau_2}^{0} \int_{t+w}^{t} \frac{\partial \eta^T(s,x)}{\partial s} R \frac{\partial \eta(s,x)}{\partial s}\mathrm{d}s\,\mathrm{d}w\,\mathrm{d}x.
\end{aligned} \tag{16}$$

Then, calculating time derivatives of $V_i(\eta(t,x),\alpha,t)$, one has

$$\begin{aligned}\frac{\partial}{\partial t}V_1(\eta(t,x),\alpha,t) &= 2\int_\Omega \xi^T(t,x)\omega_1^T P_\alpha\left[A\circ\nabla^2\eta(t,x) - B_\alpha\omega_1 + C_\alpha\omega_4 + D_\alpha\omega_5 + \omega_{11}\right]\xi(t,x)\mathrm{d}x \\ &\quad + \sum_{\kappa=1}^{\rho}\pi_{\upsilon\kappa}\int_\Omega \xi^T(t,x)\omega_1^T P_\kappa\omega_1\xi(t,x)\mathrm{d}x + 2\sum_{k=1}^{r}\int_\Omega \frac{\partial\eta^T(t,x)}{\partial x_k}XA_k\frac{\partial}{\partial x_k}\left(\frac{\partial\eta(t,x)}{\partial t}\right)\mathrm{d}x,\end{aligned} \tag{17}$$

$$\frac{\partial}{\partial t}V_2(\eta(t,x),\alpha,t) \le \int_\Omega \xi^T(t,x)\left\{\omega_1^T Q_1\omega_1 - (1-\sigma)\omega_3^T Q_1\omega_3\right\}\xi(t,x)\mathrm{d}x = \int_\Omega \xi^T(t,x)\Pi_2\xi(t,x)\mathrm{d}x, \tag{18}$$

$$\frac{\partial}{\partial t}V_3(\eta(t,x),\alpha,t) = \int_\Omega \xi^T(t,x)\left\{\omega_1^T Q_2\omega_1 - \omega_2^T Q_2\omega_2\right\}\xi(t,x)\mathrm{d}x = \int_\Omega \xi^T(t,x)\Pi_3\xi(t,x)\mathrm{d}x, \tag{19}$$

$$\begin{aligned}\frac{\partial}{\partial t}V_4(\eta(t,x),\alpha,t) &\le \int_\Omega\left\{g^T(\eta(t,x))Zg(\eta(t,x)) - (1-\sigma)\xi^T(t,x)\omega_5^T Z\omega_5\xi(t,x)\right\}\mathrm{d}x, \\ &\le \int_\Omega \xi^T(t,x)\Pi_4\xi(t,x)\mathrm{d}x,\end{aligned} \tag{20}$$

$$\frac{\partial}{\partial t}V_5(\eta(t,x),\alpha,t) = \tau_2^2\int_\Omega \xi^T(t,x)\omega_1^T U\omega_1\xi(t,x)\mathrm{d}x - \tau_2\int_\Omega\int_{t-\tau_2}^{t}\eta^T(s,x)U\eta(s,x)\mathrm{d}s\,\mathrm{d}x, \tag{21}$$

$$\frac{\partial}{\partial t}V_6(\eta(t,x),\alpha,t) = \tau_2^2\int_\Omega \xi^T(t,x)\omega_6^T R\omega_6\xi(t,x)dx - \tau_2\int_\Omega\int_{t-\tau_2}^{t}\frac{\partial\eta^T(s,x)}{\partial s}R\frac{\partial\eta(s,x)}{\partial s}\mathrm{d}s\,\mathrm{d}x. \tag{22}$$

From (11), we can obtain

$$2\int_\Omega \eta^T(t,x)P_\alpha\left[A\circ\nabla^2\eta(t,x)\right]\mathrm{d}x \le 2\int_\Omega \eta^T(t,x)\left(-\frac{\pi^2}{4}P_\alpha KAK^T\right)\eta(t,x)\mathrm{d}x. \tag{23}$$

For diagonal matrices $X>0$, from (6), we can find that

$$0 = 2\int_\Omega \frac{\partial\eta^T(t,x)}{\partial t}X\left[A_k\circ\nabla^2\eta(t,x) - B_\alpha\eta(t,x) + C_\alpha g(\eta(t,x)) + D_\alpha g((\eta(t-\tau(t),x)) + \nu(t,x) - \frac{\partial\eta(t,x)}{\partial t}\right]\mathrm{d}x. \tag{24}$$

On the basis of Lemma 3 in [37], we obtain

$$2\int_\Omega \frac{\partial\eta^T(t,x)}{\partial t}XA_k\circ\nabla^2\eta(t,x)\mathrm{d}x = -2\sum_{k=1}^{r}\int_\Omega \frac{\partial\eta^T(t,x)}{\partial x_k}XA_k\frac{\partial}{\partial x_k}\left(\frac{\partial\eta(t,x)}{\partial t}\right)\mathrm{d}x. \tag{25}$$

From (24) and (25), one has

$$\begin{aligned}\frac{\partial}{\partial t}V_1(\eta(t,x),\alpha,t) &\le 2\int_\Omega \xi^T(t,x)\omega_1^T P_\alpha\left[-\frac{\pi^2}{4}KAK^T\omega_1 - B_\alpha\omega_1 + C_\alpha\omega_4 + D_\alpha\omega_5 + \omega_{11}\right]\xi(t,x)\mathrm{d}x \\ &\quad - 2\int_\Omega \xi^T(t,x)\omega_6^T X\left[B_\alpha\omega_1 - C_\alpha\omega_4 - D_\alpha\omega_5 - \omega_{11} + \omega_6\right]\xi(t,x)\mathrm{d}x + \sum_{\kappa=1}^{\rho}\pi_{\upsilon\kappa}\int_\Omega \xi^T(t,x)\omega_1^T P_\kappa\omega_1\xi(t,x)\mathrm{d}x \\ &\le \int_\Omega \xi^T(t,x)\Pi_1\xi(t,x)\mathrm{d}x.\end{aligned} \tag{26}$$

By Jensen's inequality, we can obtain

$$\begin{aligned}-\tau_2\int_\Omega\int_{t-\tau_2}^{t}\eta^T(s,x)U\eta(s,x)\mathrm{d}s\mathrm{d}x &\le -\frac{\tau_2}{\check{\tau}}\int_\Omega\int_{t-\tau_2}^{t-\tau(t)}\eta^T(s,x)\mathrm{d}sU\int_{t-\tau_2}^{t-\tau(t)}\eta(s,x)\mathrm{d}s\,\mathrm{d}x \\ &\quad -\frac{\tau_2}{\tau(t)}\int_\Omega\int_{t-\tau(t)}^{t}\eta^T(s,x)\mathrm{d}sU\int_{t-\tau(t)}^{t}\eta(s,x)\mathrm{d}s\,\mathrm{d}x \\ &\le \int_\Omega \xi^T(t,x)\Pi_{51}\xi(t,x)\mathrm{d}x.\end{aligned} \tag{27}$$

From conditions (21) and (27), it can be obtained that

$$\begin{aligned}\frac{\partial}{\partial t}V_5(\eta(t,x),\alpha,t) &\le \int_\Omega \xi^T(t,x)\left\{\tau_2^2\omega_1^T U\omega_1 + \Pi_{51}\right\}\xi(t,x)\mathrm{d}x \\ &= \int_\Omega \xi^T(t,x)\Pi_5\xi(t,x)\mathrm{d}x.\end{aligned} \tag{28}$$

According to the Wirtinger-type integral inequality in [40] and Lemma 5 of [41], we have

$$\begin{aligned}&-\tau_2\int_\Omega\int_{t-\tau_2}^{t}\frac{\partial\eta^T(s,x)}{\partial s}R\frac{\partial\eta(s,x)}{\partial s}\mathrm{d}s\,\mathrm{d}x \\ &\le -\int_\Omega \xi^T(t,x)\begin{bmatrix}\Lambda_1 & \Lambda_2\end{bmatrix}\begin{bmatrix}\check{R} & \Upsilon \\ \Upsilon^T & \check{R}\end{bmatrix}\begin{bmatrix}\Lambda_1^T \\ \Lambda_2^T\end{bmatrix}\xi(t,x)\mathrm{d}x.\end{aligned} \tag{29}$$

By (23) and (29), one has

$$\frac{\partial}{\partial_t}V_6(\eta(t,x),\alpha,t) \le \int_\Omega \xi^T(t,x)\Pi_6\xi(t,x)\mathrm{d}x. \tag{30}$$

Furthermore, for positive diagonal matrices Γ_0 and Γ_1, from (5), one obtains

$$\begin{aligned}&2\eta^T(t,x)\Gamma_0\mathsf{F}_0 f(\eta(t,x)) - 2f^T(\eta(t,x))\Gamma_0 f(\eta(t,x)) \ge 0, \\ &\eta^T(t,x)\mathsf{F}_1^T Z\mathsf{F}_1\eta(t,x) - g^T(\eta(t,x))Zg(\eta(t,x)) \ge 0.\end{aligned} \tag{31}$$

By (15)-(31), for each $\alpha \in \mathscr{M}$, we can get

$$\begin{aligned}&\sum_{i=1}^{6}\frac{\partial V_i(\eta(t,x),\alpha,t)}{\partial t} - \int_\Omega 2y^T(t,x)M\nu(t,x)\mathrm{d}x \\ &\quad + \int_\Omega \nu^T(t,x)W\nu(t,x)\mathrm{d}x \le \int_\Omega \xi^T(t,x)\Pi\xi(t,x)\mathrm{d}x,\end{aligned} \tag{32}$$

which combining with (13) means

$$\int_\Omega y^T(t,x)M\nu(t,x)\mathrm{d}x - \frac{1}{2}\int_\Omega \nu^T(t,x)W\nu(t,x)\mathrm{d}x \ge \dot{\mathscr{S}}(t), \tag{33}$$

in which $\mathscr{S}(t) = (V(\eta(t,x),\alpha,t)/2)$.

From (33), one can see that

$$\begin{aligned}&\int_{t_1}^{t_2}\int_\Omega y^T(t,x)M\nu(t,x)\mathrm{d}x\mathrm{d}t \\ &\quad -\int_{t_1}^{t_2}\int_\Omega \nu^T(t,x)\frac{W}{2}\nu(t,x)\mathrm{d}x\mathrm{d}t \ge \mathscr{S}(t_2) - \mathscr{S}(t_1),\end{aligned} \tag{34}$$

$\forall t_2, t_1 \in [0,+\infty)$ and $t_2 > t_1$. This completes the proof. □

Remark 2. It is noted that the method of Lemma 2 in [42] to deal with the integrals to a certain degree has reduced the conservatism of the system, compared to the general Jensen's inequalities. Therefore, in our paper, this technique is adopted to estimate the integral:

$$\tau_2 \int_\Omega \int_{-\tau_2}^{0} \int_{t+w}^{t} \frac{\partial \eta^T(s,x)}{\partial s} R \frac{\partial \eta(s,x)}{\partial s} \mathrm{d}s\, \mathrm{d}w\, \mathrm{d}x. \tag{35}$$

Remark 3. Compared with the traditional Wirtinger-based integral inequality in [42], Lemma 2 used in [40] is an improved method of the Wirtinger-based integral inequality that can better reduce conservativeness. Then, some delay-dependent stability criteria are obtained by applying the abovementioned inequalities and computed by using standard LMI techniques.

Theorem 2. *Given scalars $\tau_2 > 0$ and $1 > \sigma > 0$, the solution of RDNNs (6) is input-strictly passive under the Neumann boundary conditions if there exist some diagonal matrices $P_\alpha > 0$, $\Gamma_0 > 0$, $\Gamma_1 > 0$, and $X > 0$, real positive matrices Q_1, Q_2, Z, U, R, and W, and matrix Υ of appropriate size, such that $\forall \tau \in \{0, \tau_2\}$, the following inequalities hold:*

$$\begin{bmatrix} \check{R} & \Upsilon \\ \Upsilon^T & \check{R} \end{bmatrix} \geq 0, \tag{36}$$

$$\begin{aligned} \Pi = \Pi_0 + \overline{\Pi}_1 + \sum_{i=2}^{4} \Pi_i + \Pi_5(\tau) + \Pi_6 - 2\omega_1^T E^T M \omega_{11} \\ - 2\omega_{11}^T H^T M \omega_{11} - \omega_{11}^T W \omega_{11} < 0, \end{aligned} \tag{37}$$

where

$$\begin{aligned} \overline{\Pi}_1 \triangleq 2\Bigg[& -\omega_1^T P_\alpha B_\alpha \omega_1 + \omega_1^T \sum_{\kappa=1}^{\rho} \pi_{\upsilon\kappa} P_q \omega_1 + \omega_1^T P_\alpha C_\alpha \omega_4 + \omega_1^T P_\alpha D_\alpha \omega_5 + \omega_1^T P_\alpha \omega_{11} \\ & - \omega_1^T B_\alpha^T X \omega_6 + \omega_4^T C_\alpha^T X \omega_6 + \omega_5^T D_\alpha^T X \omega_6 + \omega_6^T X \omega_{11} - \omega_6^T X \omega_6 \Bigg], \end{aligned} \tag{38}$$

and Π_0, Π_2, Π_3, Π_4, $\Pi_5(\tau)$, and Π_6 are defined the same as in Theorem 1.

Proof. Considering the same Lyapunov–Krasovskii functional given in (15), afterwards, and calculating the derivative along the trajectory of (6) under the Neumann BCs (4), we can obtain that

$$\begin{aligned} 2\int_\Omega \eta(t,x) P_\alpha A_k \circ \nabla^2 \eta(t,x) \mathrm{d}x &= 2\int_{\partial\Omega} \sum_{i=1}^{\rho} \left(\eta_i(t,x) P_\alpha A_{ik} \frac{\partial \eta_i(t,x)}{\partial x_k} \right)_{k=1}^{r} \cdot \overline{n} \mathrm{d}S - \int_\Omega \sum_{i=1}^{\rho} P_\alpha \sum_{k=1}^{r} A_{ik} \left(\frac{\partial \eta_i(t,x)}{\partial x_k} \right)^2 \mathrm{d}x \\ &= -2\int_\Omega \sum_{i=1}^{\rho} \sum_{k=1}^{r} P_\alpha A_{ik} \left(\frac{\partial \eta_i(t,x)}{\partial x_k} \right)^2 \mathrm{d}x, \\ &\leq 0. \end{aligned} \tag{39}$$

Then, following the same procedure as in Theorem 1, we can obtain the craved results immediately. □

4. Numerical Examples

In this section, two numerical examples are provided to expound the effectiveness of the main results derived above.

Example 1. Consider continuous-time Markov jump RDNNs with TVDs under the Dirichlet BCs as follows:

$$\begin{aligned} \frac{\partial \eta(t,x)}{\partial t} &= A_k \circ \nabla^2 \eta(t,x) - B_\alpha \eta(t,x) + C_\alpha f(\eta(t,x)) \\ &\quad + D_\alpha g(\eta(t-\tau(t),x)) + \nu(t,x), \\ \eta(0,x) &= \begin{bmatrix} 0.5\cos(\pi x) & 0.3\cos(\pi x) \end{bmatrix}^T, \\ (t,x) &\in [-0.4, 0] \times \Omega, \end{aligned} \tag{40}$$

in which $r = 1, 2, \Omega = \{x \mid -0.5 < x < 0.5\}$, and some system matrices in system (6) containing two modes can be given as follows:

Mode1:

$$\begin{aligned} A &= \mathrm{diag}\{1.2, 0.9\}, \\ B_1 &= \mathrm{diag}\{0.9, 0.8\}, \\ C_1 &= \begin{bmatrix} 0.2 & 0.13 \\ -0.5 & -2.8 \end{bmatrix}, \\ D_1 &= \begin{bmatrix} 0.1 & 0.4 \\ -0.3 & 0.5 \end{bmatrix}. \end{aligned} \tag{41}$$

Mode2:

$$B_2 = \mathrm{diag}\{0.8, 1.6\},$$
$$E = \mathrm{diag}\{0.8, 0.9\},$$
$$C_2 = \begin{bmatrix} 0.2 & 0.3 \\ -1.1 & -0.8 \end{bmatrix},$$
$$D_2 = \begin{bmatrix} 0.1 & 0.2 \\ -0.1 & 0.8 \end{bmatrix}, \quad (42)$$
$$H = \begin{bmatrix} 0.8 & 0.3 \\ 0.5 & 1.1 \end{bmatrix},$$

where $f_j(\eta) = 0.5(|\eta + 1| - |\eta - 1|)$ and $g_j(\eta) = \arctan(\eta)$, both satisfy assumption 1. Moreover, we set that $\sigma = 0.8$, $\tau_2 = 0.4$, $\mathsf{F}_0 = I$, and $\mathsf{F}_1 = 2I$. The transition probability matrix of Markov process α_t is taken as

$$\Phi = \begin{bmatrix} -0.5 & 0.5 \\ 0.24 & -0.24 \end{bmatrix}. \quad (43)$$

By solving the LMIs (12) and (13) in Theorem 1, it is obvious that there is a feasible solution. For the sake of simplicity, only partial solution matrices are listed:

$$P_1 = \mathrm{diag}\{0.9878, 0.7383\},$$
$$P_2 = \mathrm{diag}\{0.9587, 0.8063\},$$
$$Q_1 = \begin{bmatrix} 0.9888 & -0.0434 \\ -0.0434 & 0.0081 \end{bmatrix},$$
$$Q_2 = \begin{bmatrix} 0.5843 & -0.0273 \\ -0.0273 & 0.0247 \end{bmatrix}, \quad (44)$$
$$U = \begin{bmatrix} 2.2454 & -0.1032 \\ -0.1032 & 0.0814 \end{bmatrix},$$
$$Z = \begin{bmatrix} 0.6341 & -0.1211 \\ -0.1211 & 0.7005 \end{bmatrix}.$$

Therefore, one can conclude that the Markov jump RDNNs (6) with TVDs under Dirichlet BCs is input-strictly passive according to Definition 1. Here, we assume that the input function $\nu_1(t,x) = 0.15t\cos(\pi x)$ and $\nu_2(t,x) = 0.1t\cos(\pi x)$. Then, the state trajectories of variables $\eta_1(t,x)$ and $\eta_2(t,x)$ are plotted in Figures 1 and 2, respectively. On the other hand, Figures 3 and 4, respectively, describe the state trajectories of variables $\eta_1(t,x)$ and $\eta_2(t,x)$, in which we choose $\nu_1(t,x) = 0$ and $\nu_2(t,x) = 0$, which means system (40) is globally stable under the zero input.

Example 2. Consider the RDNNs with Markov jumping parameters and TVDs under Neumann BCs in the following:

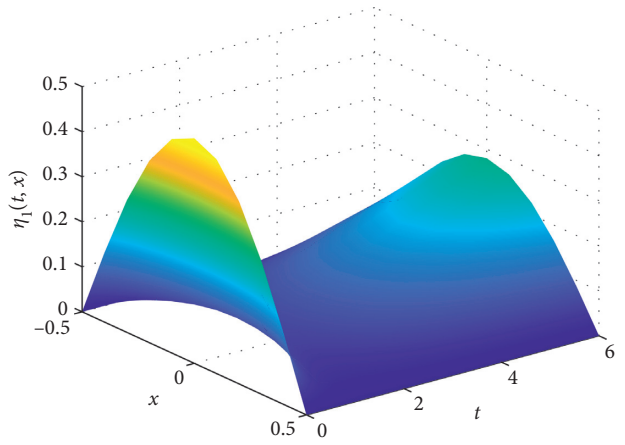

Figure 1: State trajectories of variables $\eta_1(t,x)$ with $\nu_1(t,x) = 0.15t\cos(\pi x)$ in example 1.

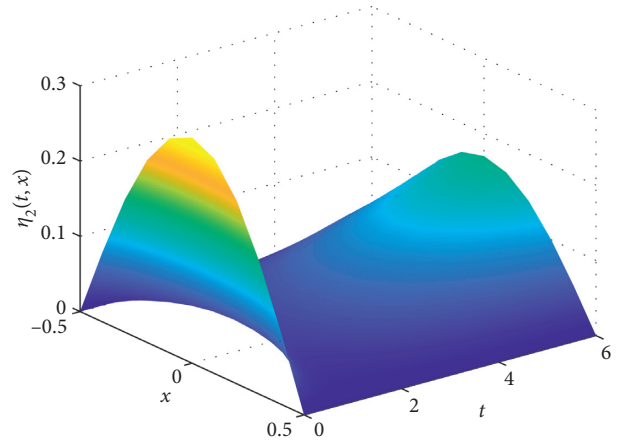

Figure 2: State trajectories of variables $\eta_2(t,x)$ with $\nu_2(t,x) = 0.1t\cos(\pi x)$ in example 1.

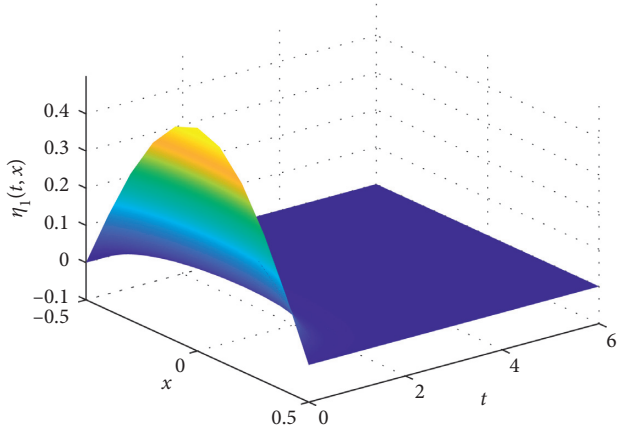

Figure 3: State trajectories of variables $\eta_1(t,x)$ with $\nu_1(t,x) = 0$ in example 1.

$$\frac{\partial \eta(t,x)}{\partial t} = A_k \circ \nabla^2 \eta(t,x) - B_\alpha \eta(t,x) + C_\alpha f(\eta(t,x)) + D_\alpha g(\eta(t-\tau(t),x)) + \nu(t,x),$$
$$\eta(0,x) = \left[\, -0.4\cos(\pi x) \;\; -0.8\cos(\pi x) \,\right]^T, \quad (45)$$
$$(t,x) \in [-0.4, 0] \times \Omega,$$

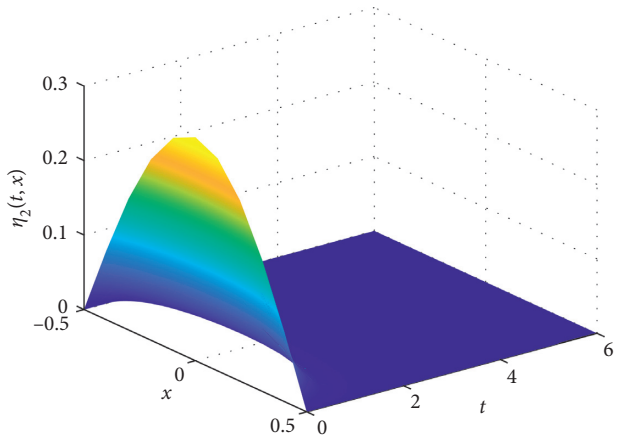

Figure 4: State trajectories of variables $\eta_2(t,x)$ with $\nu_2(t,x) = 0$ in example 1.

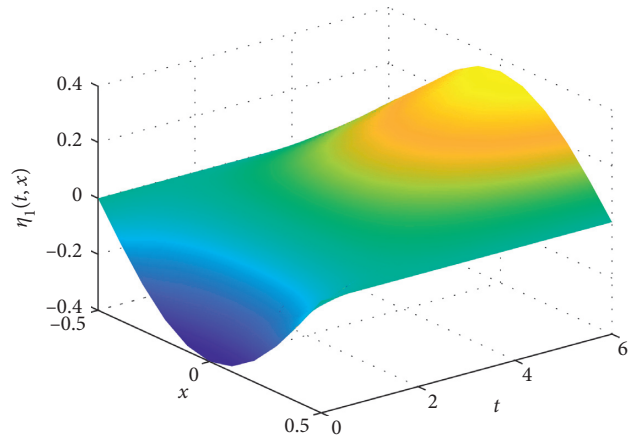

Figure 5: State trajectories of variables $\eta_1(t,x)$ with $\nu_1(t,x) = 0.15t\cos(\pi x)$ in example 2.

in which the rest of the values are the same as in example 1, and some system matrices containing two modes are given as follows:

Mode1:

$$A = \mathrm{diag}\{1.2, 0.9\},$$
$$B_1 = \mathrm{diag}\{0.9, 0.8\},$$
$$C_1 = \begin{bmatrix} 0.2 & 0.13 \\ -0.5 & -2.8 \end{bmatrix}, \quad (46)$$
$$D_1 = \begin{bmatrix} 0.7 & 0.4 \\ -0.3 & 0.5 \end{bmatrix}.$$

Mode2:

$$B_2 = \mathrm{diag}\{0.8, 0.6\},$$
$$E = \mathrm{diag}\{0.8, 0.9\},$$
$$C_2 = \begin{bmatrix} 0.2 & 0.3 \\ -1.1 & -0.8 \end{bmatrix}, \quad (47)$$
$$D_2 = \begin{bmatrix} 0.9 & 0.6 \\ -0.1 & 0.8 \end{bmatrix},$$
$$H = \begin{bmatrix} 0.8 & 0.3 \\ 0.5 & 1.1 \end{bmatrix}.$$

In this case, we set $\sigma = 0.7$ and $\tau_2 = 0.2$. Afterwards, the maximum allowable upper bound value $\tau(t)$ is obtained via solving the LMIs of (36) and (37) in Theorem 2. Then, we can get the NNs (6) of RDT with Markov jumping parameters under Neumann BCs which are also input-strictly passive. Here, only some of the feasible solutions are shown in the following:

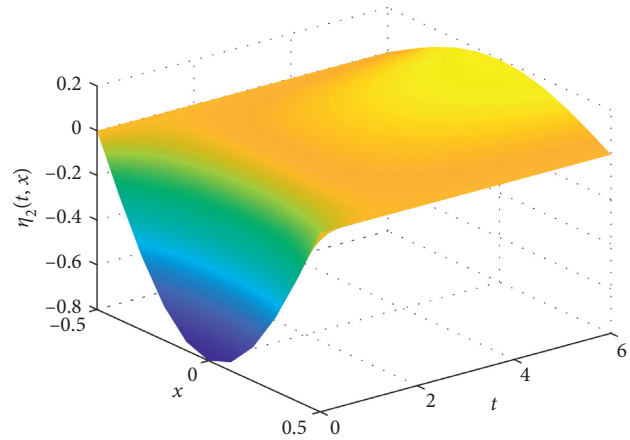

Figure 6: State trajectories of variables $\eta_2(t,x)$ with $\nu_2(t,x) = 0.1t\cos(\pi x)$ in example 2.

$$P_1 = 10^{-2} * \mathrm{diag}\{0.7, 1.6\},$$
$$P_2 = 10^{-2} * \mathrm{diag}\{0.39, 0.39\},$$
$$Q_1 = 10^{-3} * \begin{bmatrix} 2.0 & -0.5 \\ -0.5 & 2.2 \end{bmatrix},$$
$$Q_2 = 10^{-3} * \begin{bmatrix} 2.2 & -0.6 \\ -0.6 & 2.4 \end{bmatrix}, \quad (48)$$
$$U = 10^{-2} * \begin{bmatrix} 5.88 & -1.45 \\ -1.45 & 6.53 \end{bmatrix},$$
$$Z = 10^{-2} * \begin{bmatrix} 1.36 & 0.43 \\ 0.43 & 1.87 \end{bmatrix}.$$

Here, Figures 5 and 6, separately, depict the state trajectories of variables $\eta_1(t,x)$ and $\eta_2(t,x)$ under Neumann BCs, in which the input function is regarded as $\nu_1(t,x) = 0.15t\cos(\pi x)$ and $\nu_2(t,x) = 0.1t\cos(\pi x)$. In the other case, consider the input function $\nu_1(t,x) = \nu_2(t,x) = 0$, and the numerical simulations of system (45) are presented in Figures 7 and 8, respectively.

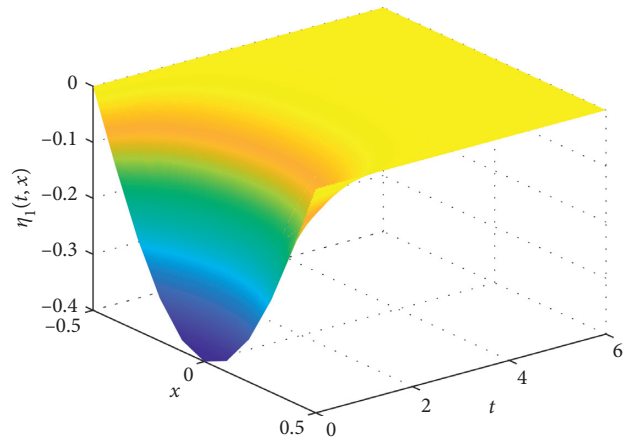

Figure 7: State trajectories of variables $\eta_1(t,x)$ with $\nu_1(t,x) = 0$ in example 2.

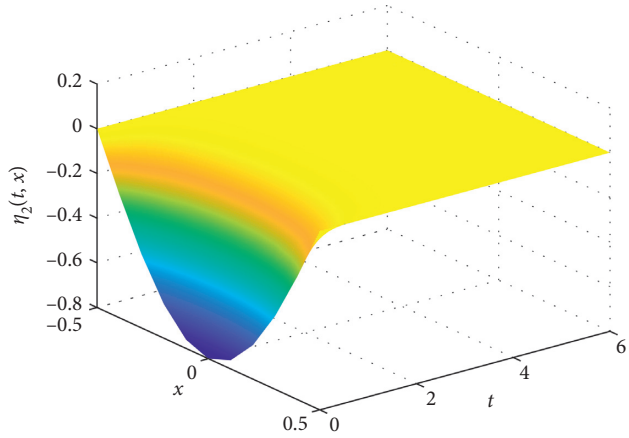

Figure 8: State trajectories of variables $\eta_2(t,x)$ with $\nu_2(t,x) = 0$ in example 2.

Furthermore, from Tables 1 and 2, we can find that the upper bound of τ_2 decreases with the value of σ increasing in the interval $(0,1)$ from the Dirichlet BCs or the Neumann BCs, which means the increasing of σ has a negative impact on τ_2. Moreover, from Table 3, compared with the different cases with obtained results, it is easy to discover that the maximum allowed value of time-varying delays in Theorem 1 is larger than the delay upper bound in Theorem 2, and one can get two observations:

(i) We can find that the assumptions about the BCs are limited to the Neumann zero-boundary condition. The main reason is that the results are obtained without consideration of the influence of RDT on the NNs, which increases the conservatism of the system.

(ii) Correspondingly, in order to avoid this problem, a RDNNs model with Dirichlet BCs introduces a new inequality, and the results consider the influence of the diffusion terms. Thus, the conservatism of the results obtained in this paper is reduced.

Table 1: Upper bound of τ_2 under the Dirichlet BCs with different σ.

σ	0.82	0.84	0.86	0.88
τ_2	0.4181	0.3551	0.3077	0.2688

Table 2: Upper bound of τ_2 under the Neumann BCs with different σ.

σ	0.70	0.75	0.80	0.85
τ_2	0.3267	0.2982	0.2668	0.2531

Table 3: Upper bound of τ_2 under different cases of boundary conditions with different σ.

σ	0.7	0.75	0.82	0.84	0.86
Theorem 1	∞	∞	0.4181	0.3551	0.3077
Theorem 2	0.3267	0.2982	0.2531	0.2387	0.2311

5. Conclusions

In this paper, we have analyzed the passivity problem for Markov jumping reaction-diffusion neural networks, in which the time-varying delay phenomenon and reaction-diffusion terms have been taken into consideration. By introducing several novel Lyapunov–Krasovskii functionals and employing a new inequality, some sufficient conditions expressed as linear matrix inequalities have been established, which guarantees the passive stability of the considered reaction-diffusion neural networks. Two numerical examples have been provided to exhibit the effectiveness of the offered approaches. Finally, we will try to apply the above results to other practical systems in future works.

The notations used throughout this paper are standard, which are presented in the following.

Notations

diag{·}:	Diagonal matrix
Z^T:	Transpose of the matrix Z
$\mathbb{Z}^+$:	Set of the nonnegative integer
$\mathbb{R}^{m_1 \times m_2}$:	Set of the $m_1 \times m_2$ dimensional real matrix
$*$:	Symmmetric block of a symmetric matrix
I:	Identity matrix with appropriate dimensions
$L_2[0,\infty)$:	Space of the square summable infinite sequence
$P > 0\ (\geq 0)$:	Positive (positive semi) definite matrix P
Ω:	A compact set in the vector space $\mathbb{R}^r$ with smooth boundary $\partial\Omega$.

Data Availability

All data sets used in this study are hypothetical.

Conflicts of Interest

The authors declare that there are no conflicts of interest regarding the publication of this paper.

Acknowledgments

This work was supported by the Key University Science Research Project of Anhui Province (Grant no. KJ2017A064), National Innovation and Entrepreneurship Training Program for College Students, China.

References

[1] X. Jin, X. Zhao, J. Yu, X. Wu, and J. Chi, "Adaptive fault-tolerant consensus for a class of leader-following systems using neural network learning strategy," *Neural Networks*, vol. 121, pp. 474–483, 2020.

[2] H. Shen, Z. Huang, J. Cao, and J. H. Park, "Exponential H∞ filtering for continuous-time switched neural networks under persistent dwell-time switching regularity," *IEEE Transactions on Cybernetics*, vol. 50, no. 6, pp. 2440–2449, 2020.

[3] H. Shen, Y. Zhu, L. Zhang, and J. H. Park, "Extended dissipative state estimation for Markov jump neural networks with unreliable links," *IEEE Transactions on Neural Networks and Learning Systems*, vol. 28, no. 2, pp. 346–358, 2017.

[4] X. Lin, W. Zhang, Z. Yang, and Y. Zou, "Finite-time boundedness of switched systems with time-varying delays via sampled-data control," *International Journal of Robust and Nonlinear Control*, vol. 30, no. 7, pp. 2953–2976, 2020, In press.

[5] X. Lin, X. Li, and J. H. Park, "Output-feedback stabilization for planar output-constrained switched nonlinear systems," *International Journal of Robust and Nonlinear Control*, vol. 30, no. 5, pp. 1819–1830, 2020, In press.

[6] M. Dai, Z. Huang, J. Xia, B. Meng, J. Wang, and H. Shen, "Non-fragile extended dissipativity-based state feedback control for 2-D Markov jump delayed systems," *Applied Mathematics and Computation*, vol. 362, Article ID 124571, 2019.

[7] L. Fang, L. Ma, S. Ding, and D. Zhao, "Finite-time stabilization for a class of high-order stochastic nonlinear systems with an output constraint," *Applied Mathematics and Computation*, vol. 358, pp. 63–79, 2019.

[8] S. Ding, W.-H. Chen, K. Mei, and D. Murray-smith, "Disturbance observer design for nonlinear systems represented by input-output models," *IEEE Transactions on Industrial Electronics*, vol. 67, no. 2, pp. 1222–1232. In press, 2019.

[9] X. Wang, J. Xia, J. Wang, Z. Wang, and J. Wang, "Reachable set estimation for Markov jump LPV systems with time delays," *Applied Mathematics and Computation*, vol. 376, Article ID 125117, 2020.

[10] Y. Xia, J. Wang, B. Meng, and X. Chen, "Further results on fuzzy sampled-data stabilization of chaotic nonlinear systems," *Applied Mathematics and Computation*, vol. 379, Article ID 125225, 2020.

[11] J.-L. Wang, H.-N. Wu, T. Huang, S.-Y. Ren, and J. Wu, "Pinning control for synchronization of coupled reaction-diffusion neural networks with directed topologies," *IEEE Transactions on Systems, Man, and Cybernetics: Systems*, vol. 46, no. 8, pp. 1109–1120, 2015.

[12] Y. Cao, Y. Cao, S. Wen, T. Huang, and Z. Zeng, "Passivity analysis of delayed reaction-diffusion memristor-based neural networks," *Neural Networks*, vol. 109, pp. 159–167, 2019.

[13] C. Yang, J. Qiu, and H. He, "Exponential synchronization for a class of complex spatio-temporal networks with space-varying coefficients," *Neurocomputing*, vol. 151, pp. 401–407, 2015.

[14] K. Wu and B.-S. Chen, "Synchronization of partial differential systems via diffusion coupling," *IEEE Transactions on Circuits and Systems I: Regular Papers*, vol. 59, no. 11, pp. 2655–2668, 2012.

[15] J.-L. Wang, Z. Qin, H.-N. Wu, and T. Huang, "Passivity and synchronization of coupled uncertain reaction-diffusion neural networks with multiple time delays," *IEEE Transactions on Neural Networks and Learning Systems*, vol. 30, no. 8, pp. 2434–2448, 2019.

[16] J.-L. Wang, X.-X. Zhang, H.-N. Wu, T. Huang, and Q. Wang, "Finite-time passivity and synchronization of coupled reaction–diffusion neural networks with multiple weights," *IEEE Transactions on Cybernetics*, vol. 49, no. 9, pp. 3385–3397, 2019.

[17] B. Lu, H. Jiang, C. Hu, and A. Abdurahman, "Synchronization of hybrid coupled reaction-diffusion neural networks with time delays via generalized intermittent control with spacial sampled-data," *Neural Networks*, vol. 105, pp. 75–87, 2018.

[18] Y.-L. Huang, B.-B. Xu, and S.-Y. Ren, "Analysis and pinning control for passivity of coupled reaction-diffusion neural networks with nonlinear coupling," *Neurocomputing*, vol. 272, pp. 334–342, 2018.

[19] H. Shen, S. Jiao, J. Xia, J. H. Park, and X. Huang, "Generalised state estimation of Markov jump neural networks based on the Bessel-Legendre inequality," *IET Control Theory & Applications*, vol. 13, no. 9, pp. 1284–1290, 2019.

[20] J. Wang, C. Yang, H. Shen, J. Cao, and L. Rutkowski, "Sliding mode control for slow-sampling singularly perturbed systems subject to Markov jump parameters," *IEEE Transactions on Systems, Man, and Cybernetics: Systems*, 2020, In press.

[21] M. Xing, J. Xia, J. Wang, B. Meng, and H. Shen, "Asynchronous H_∞ filtering for nonlinear persistent dwell-time switched singular systems with measurement quantization," *Applied Mathematics and Computation*, vol. 362, Article ID 124578, 2019.

[22] J. Li, K. Pan, D. Zhang, and Q. Su, "Robust fault detection and estimation observer design for switched systems," *Nonlinear Analysis: Hybrid Systems*, vol. 34, pp. 30–42, 2019.

[23] Q. Su, Z. Fan, T. Lu, Y. Long, and J. Li, "Fault detection for switched systems with all modes unstable based on interval observer," *Information Sciences*, vol. 517, pp. 167–182, 2020.

[24] H. Shen, Y. Men, J. Cao, and J. H. Park, "H_∞ filtering for fuzzy jumping genetic regulatory networks with round-robin protocol: a hidden-markov-model-based approach," *IEEE Transactions on Fuzzy Systems*, vol. 28, no. 1, pp. 112–121, 2020.

[25] Y. Wang, J. Xia, Z. Wang, and H. Shen, "Design of a fault-tolerant output-feedback controller for thickness control in cold rolling mills," *Applied Mathematics and Computation*, vol. 369, Article ID 124841, 2020.

[26] X. Hu, J. Xia, Z. Wang, X. Song, and H. Shen, "Robust distributed state estimation for Markov coupled neural networks under imperfect measurements," *Journal of the Franklin Institute*, vol. 357, no. 4, pp. 2420–2436, 2020.

[27] T. Ru, J. Xia, X. Huang, X. Chen, and J. Wang, "Reachable set estimation of delayed fuzzy inertial neural networks with Markov jumping parameters," *Journal of the Franklin Institute*, 2020, In press.

[28] T. Wu, X. Huang, X. Chen, and J. Wang, "Sampled-data H_∞ exponential synchronization for delayed semi-Markov jump CDNs: a looped-functional approach," *Applied Mathematics and Computation*, vol. 377, Article ID 125156, 2020.

[29] T. Wei, Y. Wang, and L. Wang, "Robust exponential synchronization for stochastic delayed neural networks with reaction-diffusion terms and Markovian jumping

parameters," *Neural Processing Letters*, vol. 48, no. 2, pp. 979–994, 2018.

[30] X. Song, J. Man, Z. Fu, M. Wang, and J. Lu, "Memory-based state estimation of T-S fuzzy Markov jump delayed neural networks with reaction-diffusion terms," *Neural Processing Letters*, vol. 50, no. 3, pp. 1–18, 2019.

[31] X. Wang, J. Xia, J. Wang, J. Wang, and Z. Wang, "Passive state estimation for fuzzy jumping neural networks with fading channels based on the hidden Markov model," *Physica A: Statistical Mechanics and Its Applications*, vol. 535, Article ID 122437, 2019.

[32] L. Shen, X. Yang, J. Wang, and J. Xia, "Passive gain-scheduling filtering for jumping linear parameter varying systems with fading channels based on the hidden Markov model," *Proceedings of the Institution of Mechanical Engineers, Part I: Journal of Systems and Control Engineering*, vol. 233, no. 1, pp. 67–79, 2019.

[33] J. Wang, S. Huo, J. Xia, J. H. Park, X. Huang, and H. Shen, "Generalised dissipative asynchronous output feedback control for Markov jump repeated scalar non-linear systems with time-varying delay," *IET Control Theory & Applications*, vol. 13, no. 13, pp. 2114–2121, 2019.

[34] J. Wang, L. Shen, J. Xia, Z. Wang, and X. Chen, "Asynchronous dissipative filtering for nonlinear jumping systems subject to fading channels," *Journal of the Franklin Institute*, vol. 357, no. 1, pp. 589–605, 2020.

[35] H. Shen, S. Huo, H. Yan, J. H. Park, and V. Sreeram, "Distributed dissipative state estimation for Markov jump genetic regulatory networks subject to round-robin scheduling," *IEEE Transactions on Neural Networks and Learning Systems*, vol. 31, no. 3, pp. 762–771, 2020.

[36] X. Yang, Q. Song, J. Cao, and J. Lu, "Synchronization of coupled Markovian reaction-diffusion neural networks with proportional delays via quantized control," *IEEE Transactions on Neural Networks and Learning Systems*, vol. 30, no. 3, pp. 951–958, 2019.

[37] J.-L. Wang, H.-N. Wu, T. Huang, S.-Y. Ren, and J. Wu, "Passivity analysis of coupled reaction-diffusion neural networks with Dirichlet boundary conditions," *IEEE Transactions on Systems, Man, and Cybernetics: Systems*, vol. 47, no. 8, pp. 2148–2159, 2017.

[38] H. Shen, X. Huang, J. Zhou, and Z. Wang, "Global exponential estimates for uncertain Markovian jump neural networks with reaction-diffusion terms," *Nonlinear Dynamics*, vol. 69, no. 1-2, pp. 473–486, 2012.

[39] J. G. Lu, "Global exponential stability and periodicity of reaction-diffusion delayed recurrent neural networks with Dirichlet boundary conditions," *Chaos, Solitons & Fractals*, vol. 35, no. 1, pp. 116–125, 2008.

[40] X. Fan, X. Zhang, L. Wu, and M. Shi, "Finite-time stability analysis of reaction-diffusion genetic regulatory networks with time-varying delays," *IEEE/ACM Transactions on Computational Biology and Bioinformatics*, vol. 14, no. 4, pp. 868–879, 2017.

[41] T. H. Lee, S. Lakshmanan, J. H. Park, and P. Balasubramaniam, "State estimation for genetic regulatory networks with mode-dependent leakage delays, time-varying delays, and Markovian jumping parameters," *IEEE Transactions on NanoBioscience*, vol. 12, no. 4, pp. 363–375, 2013.

[42] Y. Han, X. Zhang, L. Wu, and Y. Wang, "State estimation for genetic regulatory networks with time-varying delays and reaction-diffusion terms," *Environmental Science & Technology*, vol. 45, no. 1, pp. 161–167, 2015.

Hindawi
Discrete Dynamics in Nature and Society
Volume 2020, Article ID 2683981, 8 pages
https://doi.org/10.1155/2020/2683981

Research Article

The User Participation Incentive Mechanism of Mobile Crowdsensing Network Based on User Threshold

Hua Su, Qianqian Wu, Xuemei Sun, and Ning Zhang

School of Computer Science & Technology, Tiangong University, Tianjin 300387, China

Correspondence should be addressed to Hua Su; hua_207@126.com

Received 7 May 2020; Accepted 26 May 2020; Published 20 June 2020

Academic Editor: Jianquan Lu

Mobile crowdsensing (MCS) network means completing large-scale and complex sensing tasks in virtue of the mobile devices of ordinary users. Therefore, sufficient user participation plays a basic role in MCS. On the basis of studying and analyzing the strategy of user participation incentive mechanism, this paper proposes the user threshold-based cognition incentive strategy against the shortcomings of existing incentive strategies, such as task processing efficiency and budget control. The user threshold and the budget of processing subtasks are set at the very beginning. The platform selects the user set with the lowest threshold, and the best user for processing tasks according to users' budget. The incentive cost of the corresponding users is calculated based on the user threshold at last. In conclusion, through the experiment validation and comparison with the existing user participation incentive mechanism, it was found that the user threshold-based incentive strategy is advantageous in improving the proportion of task completion and reducing the platform's budget cost.

1. Introduction

With the development of wireless communication and sensor technology, the communication functions of smart devices (smart phones, iPhone, Huawei, etc.), wearable devices (Google glasses, Apple watch, etc.), and vehicle electronic devices (GPS, OBD-II, etc.) are becoming more powerful than ever. All these smart devices, which are equipped with a variety of powerful built-in sensors, become an important information interface between users and the sensing environment and make it possible to design MCS. As a new cognitive method, MCS can accomplish many large-scale and complex sensing tasks by using various mobile terminal devices held by users through working with ordinary users and can be applied to many different fields through cooperating with users.

MCS system is composed of task publishers, MCS platform, and many users using mobile sensors. It enables ubiquitous mobile devices to collect and share local information through enhanced cognitive ability, so as to achieve a common goal [1]. In general, as a medium between ordinary users and task publishers, the cognitive platform selects interested users to make paid cognition of tasks published by task publishers. A sensing task with reasonable budget is released to the crowdsourcing cognitive platform by a task publisher. Then, participants will be selected from the users who want to complete the sensing task. Upon receiving the cognition information provided by the recruited participants, the platform will reward them according to the cognition quality. For example, Chen et al. [2] used taxi and crowdsourcing platform for transporting the goods to be returned. Some startups have also been established and attracted millions of investments, such as Roadie; Cheng et al. [3] studied the application of crowdsourcing public transportation system in package distribution and proposed the adaptive limited delivery (ALD) method; Chen et al. [4] proposed to outsource the whole transportation task and described it as an integer linear programming issue which includes the maximum detour of drivers, capacity restriction, and options for passing packages between drivers, etc.

Incentive mechanism [5] aims to encourage users to participate in cognition activities and improve data

quality. Research on incentive mechanism of MCS network is gradually launched for the purpose of obtaining high-quality sensing data at a low cost. In view of various factors (sensor quality, noise, etc.), however, the sensing data quality contributed by a single user varies greatly. In [6], the individual quality determined by the cognition platform was included into the design of incentive mechanism, so as to maximize the benefits of MCS. In [7], a bid revision reverse auction (BRRA) was designed, in which participants were informed of the winning opportunities related to their bids and allowed to revise their bids repeatedly to find their most profitable bids. Restuccia et al. [8] proposed a participant selection method under the realistic situation that the task is effective in a limited time and the mobility of participants is uncertain. For example, when participants are vehicles, their movement tends to cover a specific area but they may not feel in time due to some unexpected reasons, such as traffic or severe weather conditions. Luo et al. [9] proposed a cross validation method where the data quality sensed by participants is evaluated by another group of people who are called validation population and the validation results are used for data improvement. In [10], a new multitask assignment plan, MTasker, was proposed, which uses the minimum cognitive quality threshold to achieve the optimal overall utility. The minimum perceptual quality threshold of a specific task is introduced to redefine the multitask assignment to assign each worker an appropriate set of tasks to maximize the effectiveness of the entire system. Liang et al. [11] studied the situation of spatial crowdsourcing under limited task probability coverage and budget, proposed a prediction model of workers' mobile behavior, and obtained the optimal solution of task allocation. In [12], a mathematical model of data quality evaluation was proposed, followed by a participant selection method of quality perception to improve data quality. Abououf et al. [13] assigned multiple staff to multiple tasks according to tasks and staff preferences so as to maximize their satisfaction and service quality and task completion confidence. Hui et al. [14] proposed two real auction mechanisms, i.e., OT-OFMCS and NOT-ONMCS, to select a group of optimal low-cost bid winning plans for the offline and online situation sensed by the mobile population, so as to maximize social welfare. Yui et al. [15] proposed a context cognitive C-MAB incentive mechanism to facilitate quality-based worker selection in MCS. It is an algorithm to evaluate the service quality and cost of employees through context (i.e., environment) and improve Thompson sampling worker selection (MTS-WS) to select workers by intensifying learning. In [16], the task allocation and path planning in MCS were studied with a view to maximizing the total task quality with limited user travel distance budget. The paper proposed a service computing framework for time constrained-task allocation in location-based crowdsensing systems. The proposed framework maximized the aggregated quality of information, reduced the budget and the response time to perform a task, and increased the average recommenders' reputation and their payment [17]. The paper presented a comprehensive framework model that fully integrated human behavior factors for modeling task profile, worker arrival, and work ability and then introduced a service quality concept to indicate the expected service gain that a requester could enjoy when she had recruited an arrival worker by jointly taking into account work ability of workers as well as timeliness and reward of tasks [18]. The paper considered such a dynamic participant recruitment problem with heterogeneous sensing tasks which aimed to minimize the sensing cost while maintaining certain level of probabilistic coverage. Both offline and online algorithms were proposed to solve the challenging problem. Extensive simulations over a real-life mobile dataset confirmed the efficiency of the proposed algorithms [19].

The MCS network system still has some problems in user selection, task completion ratio, and budget cost, regardless of its broad application in many different fields. In this paper, a user threshold-based user incentive mechanism is proposed on the basis of system characteristic incentive mechanism. With the mechanism, the corresponding participation threshold and a budget for task cognition will be generated when the user receives a subtask and reported to the cognitive platform. Then, the cognitive platform selects the corresponding user set from all mobile users as participants according to a certain user selection method and calculates the reward that should be obtained when completing the subtask. The user finally decides whether to participate in the processing of the subtask in a specific way. The user threshold-based incentive mechanism can not only improve the task completion ratio but also reduce the user cost and save the total budget [20].

The structure of this paper is as follows: Part 1 introduces the mobile MCS network system; Part 2 expounds the threshold sensing model; Part 3 verifies the threshold-based cognition model and analyzes the results; and Part 4 is the summary of this paper.

2. MCS Network

The MCS network refers to the collaboration, either consciously or unconsciously, through the mobile Internet by taking the mobile devices of ordinary users as the basic cognitive units so as to distribute sensing tasks, collect sensing data, and finally complete large-scale and complex social sensing tasks. It mainly consists of three parts: sensing task, cognitive platform, and mobile users. To be specific, the sensing tasks are the total tasks held by task publishers who hope to collect data through users' participation and cooperation; cognitive platform, which is composed of multiple cloud cognitive servers, is the platform and medium for interaction between task publishers and mobile users [21]; mobile users are those who have mobile terminal devices in the region of interest and are willing to participate in task processing. They can collect data through various sensors embedded in the mobile device and connect with the cognitive platform through wireless network, so as to upload the sensing data to the server. As shown in Figure 1, in MCS

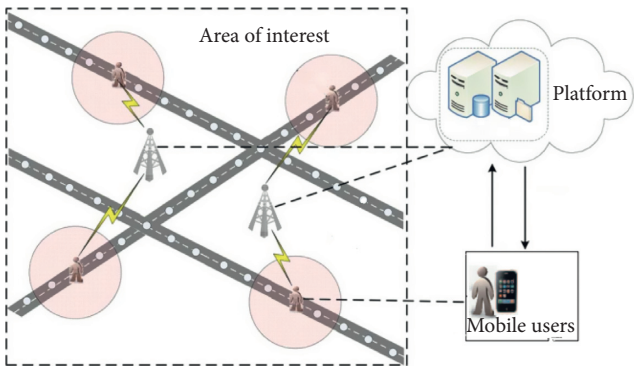

Figure 1: MCS network system.

network system, the cognitive platform publishes tasks in the region of interest and mobile users use various sensors in the mobile phone to sense tasks and submit them to the server, which pays the user remuneration.

2.1. Sensing Task. The task holder first determines a specific set of sensing tasks and then divides the group of tasks into several task subsets through the cognitive platform. In this paper, tasks are divided into task subsets of equal size and with no overlapping, which certainly simplifies the process of task allocation. The sensing task subset is published to the interested users in a certain area through the servers on the mobile platform and the selected mobile users execute the task subset and report to the server.

2.2. Cognitive Platform. The cognitive platform is composed of a group of servers located in the cloud. As a medium for task publishers and mobile users, it should, on the one hand, divide a certain sensing task into multiple sensing task subsets of equal size and with no overlapping and publish them to mobile users. On the other hand, it should take effective incentive mechanism to attract the participation of more users. The cognitive platform also needs to process and analyze the sensing data uploaded by mobile users and pays the corresponding rewards to cognitive users according to the incentive mechanism.

2.3. Mobile Users. Mobile users refer to a collection of users who hold mobile terminal devices in a region of interest and use various kinds of sensors embedded in the mobile devices, such as accelerometer, compass, gyroscope, GPS, microphone, and camera, to carry out the corresponding data sensing and connects server through various wireless networks, such as using mobile cellular network and short-range wireless communication, so as to upload the sensing data to the mobile platform and get paid.

3. Threshold Cognitive Model

MCS network mainly consists of three parts: user set U, task set T, and platform S. Task set T includes several subtasks, each of which is processed in turn (that is, before each subtask is processed, platform S will issue the subtask processing request to the user). Each user will decide whether to accept the request to process the task and get the reward. This process is repeated until all tasks are processed or budget B is used up. Table 1 describes the symbols in the threshold cognitive model.

4. Task Type Classification

For any tasks to be processed, platform S first divides the task set T into several subtasks k: $k \subset \{1, 2, 3, \ldots, K\}$ and publishes these subtasks in a certain region. At the same time, the platform sets a utility value represented by u_k for each subtask in order to facilitate subtask evaluation. According to different task types, utility value u_k is divided into three different types; that is, utility is directly proportional to subtask size、the utility is directly proportional to the task completion ratio and the utility is inversely proportional to the task completion ratio.

4.1. The Utility is Directly Proportional to Subtask Size. The utility obtained by task publishers is directly proportional to the subtasks size to be executed. This task type only considers the subtask size, which means the larger the subtasks are, the higher the weight of the corresponding total sensing tasks is and the higher the utility value will be. The formula is shown as follows:

$$u_k = \frac{\lambda_k}{\lambda}. \tag{1}$$

For example, in the application of environmental monitoring, when the cognitive platform needs to monitor the environmental background noise in a region, the subtask size corresponds to the length of time when the mobile user provides noise monitoring. The longer the time, the larger the corresponding subtask size and the more the background noise information the server collects. In this paper, we only consider the case of equal size and with no overlapping so the utility value of each subtask is fixed. Considering that the subtask λ_k in this paper is equal in size and with no overlapping, it is a fixed value. The total task λ is fixed, so is the utility U_K of subtask.

4.2. The Utility is Directly Proportional to the Task Completion Ratio. The utility obtained by the task publisher is directly proportional to the overall sensing task progress, that is, the utility value of the subtask is directly proportional to the task progress. For this task type, consideration should be taken for the completion ratio of the total task at this stage. With the increase of the completion ratio of the total task, the utility value of the corresponding subtask will increase, as follows:

$$u_k = \frac{(\lambda(t) + \lambda_k)^{\delta}}{\lambda}, \tag{2}$$

where δ is a random variable in the range of (0, 1). For example, in a video rendering application, if a subtask is not completed, the whole sensing task will fail. That is to say, with the execution of the task, the utility value of the

Table 1: Main symbols.

A_i	The i^{th} participant
N	Total number of participants
$N(t)$	The percentage of participants at time t
Mi	Number of subtasks completed by the i^{th} user
thres_i	Participation threshold for user i
C_i	Forecast effort for the i^{th} user
B	Budget for the i^{th} user
$B(t)$	Percentage of budget reserve at time t
U_i	The utility of the k^{th} subtask
I_k	The bid calculated by server for subtask k
λ	Total task size
λ_k	Size of each subtask
T	General tasks
K	Number of subtasks
$\lambda(t)$	Proportion of tasks completed at time t

remaining subtasks will gradually increase for the task publisher, which means the utility is directly proportional to the task progress.

4.3. The Utility is Inversely Proportional to the Task Completion Ratio. The utility obtained by the task publisher is inversely proportional to the overall sensing task progress; that is, the utility value of the subtask is inversely proportional to the task progress. For this task type, consideration shall be taken for the completion ratio of the total task at this stage. With the increase of the completion ratio of the total task, the utility value of the corresponding subtask will gradually decrease, as follows:

$$u_k = \frac{\lambda_k}{\lambda(t) + d}, \tag{3}$$

where d is a normal quantity in it. For example, in a target tracking application, the accuracy of target tracking will increase rapidly with the participation of the first mobile user A_1, so the utility of the first subtask is the highest for task publishers. With the involvement of more users, the accuracy of target tracking will no longer increase, which means, with the execution of the task, the utility value of cognitive information provided by participating users decreases for task publishers; that is, the utility value is inversely proportional to task progress.

5. Users Effort and Incentive Strategy

After receiving the subtask, users in the task publishing area will generate the corresponding threshold $thres_i$ and a predicted effort C for sensing the task, which will be reported to the cognitive platform. The platform selects a user set U which then is divided into U_i: $i \subset \{1, 2, \ldots, N\}$, and threshold $thres_i$ of each subuser is confidential to other users. In this paper, where a subtask k is given, C_i is used to express the cost function; that is to say, the user's effort is affected by the size of the allocated subtask and is directly proportional to the subtask size, as shown in the following:

$$C_i = \alpha_i \lambda_k^{\beta_i}, \tag{4}$$

where α and β are two divisors in it.

According to the threshold cognitive incentive mechanism, the cognitive platform designs a threshold-based incentive mechanism in virtue of the residual $B(t)$ of the total budget, the utility value U_k of the subtask to be executed, and the threshold $thres_i$ of the selected user. The formula used is shown as follows:

$$I_k = \frac{k}{\text{thres}_i} u_k B(t). \tag{5}$$

By selecting the appropriate parameter k, the incentive cost I_k of the server can be reduced and the budget reservation ratio can be increased.

6. User Participation Strategy

User A_i can decide whether to accept the processing request of the subtask finally according to the cost C_i required for processing subtask k and the reward I_k paid by platform S for k. In this paper, it is represented by the function P_i and the formula is shown as follows:

$$P_i = \begin{cases} 1, & if \dfrac{\mathrm{I_k}}{c_i} \triangleright \text{thres}_i, \\ 0, & \text{otherwise.} \end{cases} \tag{6}$$

As shown in Algorithm 1, select the user with the lowest threshold in Line 4, apply formulas (1)–(3) to calculate the utility value of subtasks according to different task types in Line 5, and apply formulas (4) and (5) to calculate the user's effort and reward after processing subtasks in Lines 6–8. User accepts subtask requests according to the relationship of cost, reward, and threshold. This not only improves the user's participation rate and reduces effort but also speeds up subtask processing and reduces the total budget, as shown in Lines 9–12. Upon accepting the subtask, the user will compete for the next subtask, as shown in Lines 16–17.

7. Experimental Results and Analysis

7.1. Simulation Experiment Environment. In this paper, we set the total number of users $N = 100$ and then divide the users into three groups according to their thresholds, i.e., high-threshold users, low-threshold users, and intermediate-threshold users. We also set the participation threshold $thres_i$ for each user and the number of subtasks $K = 1{,}000$ and the initial budget to $B = 1{,}000$. The experiment is simulated in MATLAB R2014a.

7.2. Task Completion Proportion. The platform divides the task set into several subtasks and ensures that each subtask can be processed smoothly in turn. The goal of this paper is to finish the subtasks as soon as possible, which means, under the given budget limit, a higher task completion ratio can be achieved within a shorter time. Figure 2 shows the comparison chart between the two incentive mechanisms under the task type where the utility is directly proportional to subtask size. The x coordinate represents time while the y coordinate represents task completion ratio. In the simple

Input: Tasks number K, set of users N, budget B
Output: remaining budget $B(t)$, task percentage completed $T(t)$
(1) initial the tasks and users, set credit values *thres*
(2) **while** $!k||B$
(3) **for** $k = 1:1:K$
(4) Min $thres_i \longleftarrow$ find the user of the max credit value
(5) $U_k \longleftarrow$ calculate the utility of segment k
(6) $C_i \longleftarrow$ calculate the cost of segment k
(7) $P_k \longleftarrow$ calculate incentives for user
(8) According to C_i, P_k, *thres* to determine whether accept segment or not
(9) **if** accept segment
(10) $N(t) \longleftarrow$ calculate proportion of user participation
(11) $B(t) \longleftarrow B - P_k$
(12) **else**
(13) constant values
(14) **end if**
(15) **end for**
(16) calculate $T(t)$
(17) Next loop
(18) **end while**
(19) **return** $B(t)$, $T(t)$

Algorithm 1: Threshold cognition model.

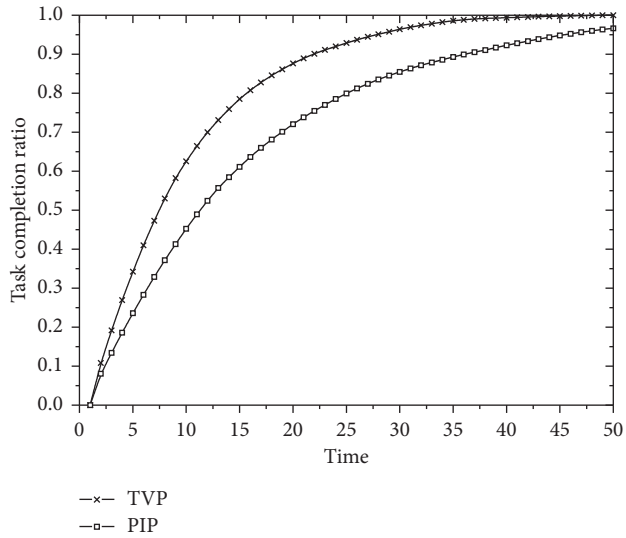

Figure 2: Task type where utility is directly proportional to subtask size.

participation mode, the threshold cognitive incentive mechanism (TVP) can complete the task faster and the completion speed of the participation cognition incentive mechanism (PIP) is relatively average at the beginning of task publishing. In this task type, both of the incentive mechanisms can better complete the tasks published by the server. By contrast, the threshold cognitive incentive mechanism (TVP) has a higher task completion ratio.

Figure 3 shows the comparison chart of the two incentive mechanisms under the task type where the utility is inversely proportional to task progress. The x coordinate represents time while y coordinate represents task completion ratio. The threshold cognitive incentive mechanism (TVP) can complete tasks faster and the completion speed of participating in the cognitive incentive mechanism (PIP) is relatively average at the beginning of task publishing. In this task type, both of the two incentive mechanisms can better complete the tasks published by the server. By contrast, the threshold perception incentive mechanism (TVP) has a higher task completion ratio.

Figure 4 shows the comparison chart of the two incentive mechanisms in the task type where utility is directly proportional to task progress. The threshold cognitive incentive mechanism (TVP) can complete the task faster at the

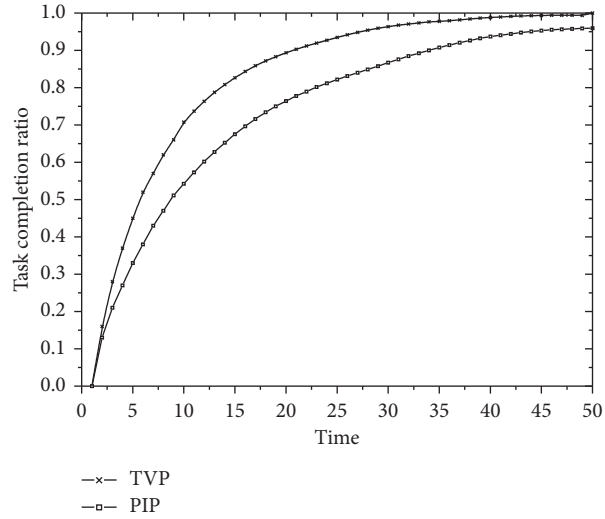

Figure 3: Task type where utility is inversely proportional to task progress.

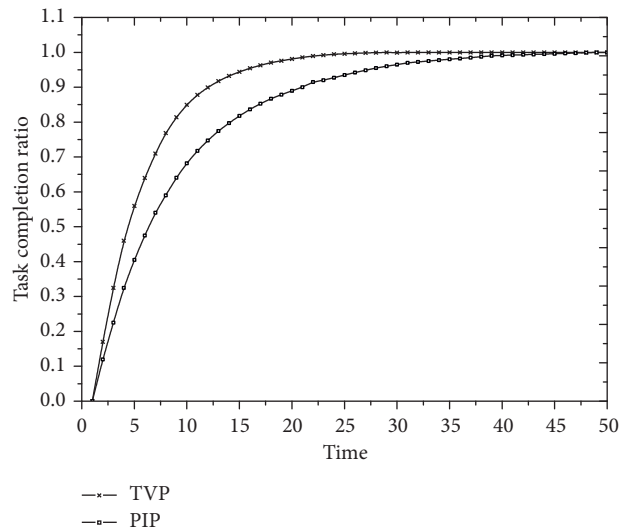

Figure 4: Task type where utility is directly proportional to task progress.

beginning of task publishing but both incentive mechanisms can complete the task published by the server in this task type well.

7.3. Budget Surplus Ratio. The platform pays the user according to the subtasks processed by them. One of the goals of this paper is to minimize the budget on the basis of ensuring smooth subtask treatment. Selecting users with high reputation to process subtasks can reduce the cost of processing subtasks C_i. Figure 5 shows the comparison chart of the two incentive mechanisms under the task type where utility is directly proportional to subtask size. The x coordinate represents time while the y coordinate represents budget reservation proportion. The chart represents the budget reserve ratio along with time. For the task type where utility is directly proportional to subtask size, both incentive mechanisms perform well in the budget reservation proportion of the server, which can save the task publisher's budget dramatically.

Figure 6 shows the budget chart of the two incentive mechanisms under the task type where utility is inversely proportional to task progress. The x coordinate represents time while the y coordinate represents budget reservation proportion. This chart represents the budget reservation proportion along with time. The two incentive mechanisms spend budget at a faster speed at the beginning and then tend to be stable. By contrast, the budget reserve ratio of threshold cognitive incentive mechanism (TVP) is higher.

Figure 7 shows the budget comparison chart of the two incentive mechanisms under the task type with where utility is directly proportional to task progress. The x coordinate represents time while the y coordinate represents budget reservation proportion. This chart represents the budget

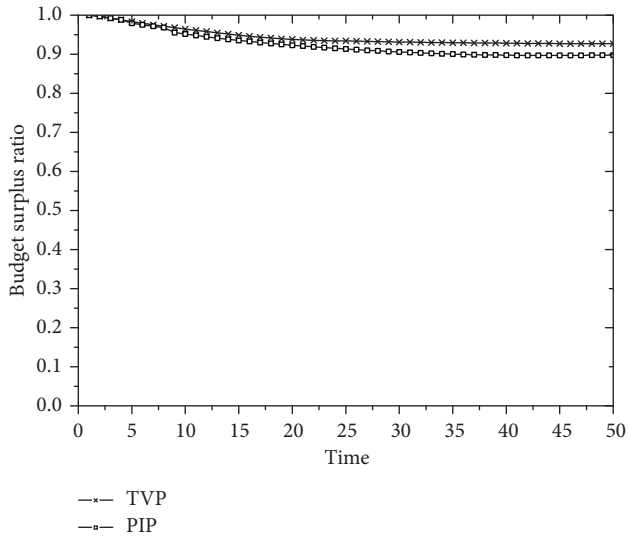

Figure 5: Task type where utility is directly proportional to subtask size.

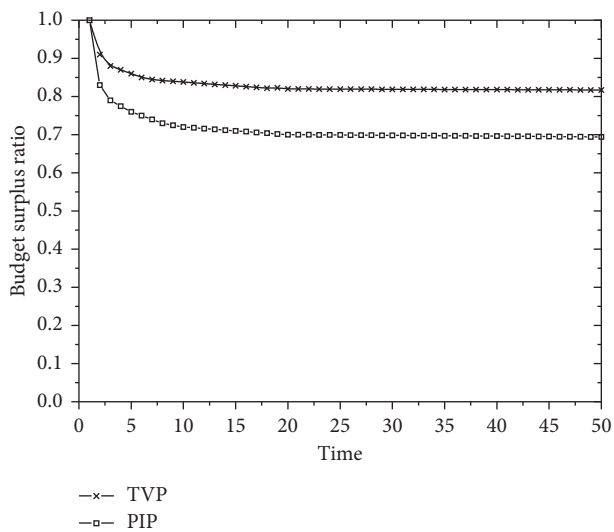

Figure 6: Task type where utility is inversely proportional to task progress.

reservation proportion along with time. In this type, both incentive mechanisms spend budget at a faster speed and the budget expenses are high because the server will allocate budget as much as possible to complete the reserved subtasks in order to finish all tasks.

8. Conclusion

This paper proposes the settings of the threshold of user participation based on the incentive mechanism of user participation cognition and selects the users with low threshold each time to process subtask set in turn. The utility value of subtask is affected by threshold, which further influences the platform's payment mechanism for users. A new selection function is introduced to determine whether users

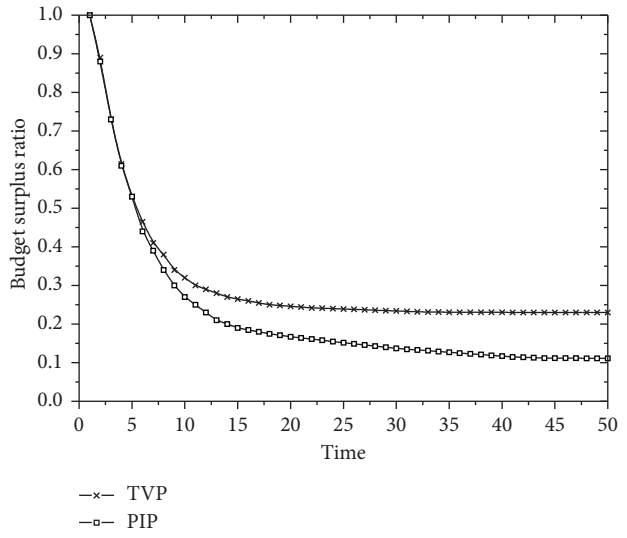

Figure 7: Task type where utility is directly proportional to task progress.

finally accept the processing request of subtask. Compared with the incentive mechanism of user participation awareness, this mechanism model is much advantageous in improving task completion speed and reducing budget.

General incentive mechanism methods, such as unequal division of subtasks and overlapping of processing time, will be taken into consideration in the future work on the basis of further improving the model. Other models can also be introduced at the same time to optimize model performance further.

Data Availability

The dataset supporting the conclusions of this article is included within the article.

Conflicts of Interest

The authors declare that they have no conflicts of interest.

References

[1] D. Peng, F. Wu, and G. Chen, "Data quality guided incentive mechanism design for crowdsensing," *IEEE Transactions on Mobile Computing*, vol. 17, no. 2, pp. 307–319, 2018.

[2] C. Chen, S. Pan, Z. Wang, and R. Y. Zhong, "Using taxis to collect citywide E-commerce reverse flows: a crowdsourcing solution," *International Journal of Production Research*, vol. 55, no. 7, pp. 1833–1844, 2017.

[3] G. Cheng, D. Guo, J. Shi, and Y. Qin, "Planning city-wide package distribution schemes using crowdsourced public transportation systems," *IEEE Access*, vol. 7, pp. 1234–1246, 2018.

[4] W. Chen, M. Mes, M. Schutten, and J. Quint, "A ride-sharing problem with meeting points and return restrictions," *Transportation Science*, vol. 53, no. 2, pp. 401–426, 2019.

[5] K. Han, H. Huang, and J. Luo, "Quality-aware pricing for mobile crowdsensing," *IEEE/ACM Transactions on Networking*, vol. 26, no. 4, pp. 1728–1741, 2018.

[6] Z. Yufeng, X. Yuanqing, and Z. Jinhui, "Quality-aware incentive mechanism based on payoff maximization for mobile crowdsensing," *Ad Hoc Networks*, vol. 72, pp. 44–55, 2018.

[7] S. Saadatmand and S. Kanhere, "BRRA: a bid-revisable reverse auction based framework for incentive mechanisms in mobile crowdsensing systems," in *Proceedings of the 21st ACM International Conference on Modeling, Analysis and Simulation of Wireless and Mobile Systems*, pp. 61–70, ACM, Montreal, Canada, October 2018.

[8] F. Restuccia, P. Ferraro, S. Silvestri, S. K. Das, and G. L. Re, "IncentMe: effective mechanism design to stimulate crowdsensing participants with uncertain mobility," *IEEE Transactions on Mobile Computing*, vol. 18, no. 7, pp. 1571–1584, 2018.

[9] T. Luo, J. Huang, S. S. Kanhere, J. Zhang, and S. K. Das, "Improving IoT data quality in mobile crowd crowdsensing: a cross validation approach," *IEEE Internet of Things Journal*, vol. 6, no. 3, pp. 5651–5664, 2019.

[10] W. Jiang Tao, W. Yasha, Z. Daqing et al., "Multi-task allocation in mobile crowd crowdsensing with individual task quality assurance," *IEEE Transactions on Mobile Computing*, vol. 17, no. 9, pp. 2101–2113, 2018.

[11] W. Liang, Y. Zhiwen, H. Qi, B. Guo, and H. Xiong, "Multi objective optimization based allocation of heterogeneous spatial crowdsensing tasks," *IEEE Transactions on Mobile Computing*, vol. 17, no. 7, pp. 1637–1650, 2018.

[12] H. Gao, C. H. Liu, J. Tang et al., "Online quality-aware incentive mechanism for mobile crowd crowdsensing with extra bonus," *IEEE Transactions on Mobile Computing*, vol. 18, no. 11, pp. 2589–2603, 2018.

[13] M. Abououf, S. Singh, H. Otrok, R. Mizouni, and A. Ouali, "Gale-shapley matching game selection-a framework for user satisfaction," *IEEE Access*, vol. 7, pp. 3694–3703, 2018.

[14] C. Hui, Z. Yanmin, Z. Feng et al., "Truthful incentive mechanisms for mobile crowd crowdsensing with dynamic smartphones," *Computer Networks*, vol. 141, pp. 1–16, 2018.

[15] W. Yue, F. Li, M. Liran, Y. Xie, T. Li, and Y. Wang, "A context-aware multi-armed bandit incentive mechanism for mobile crowdsensing systems," *IEEE Internet Things Journal*, vol. 6, no. 5, pp. 7648–7658, 2019.

[16] G. Wei, Z. Baoxian, and L. Cheng, "Location-based online task assignment and path planning for mobile crowdsensing," *IEEE Transactions on Vehicular Technology*, vol. 68, no. 2, pp. 1772–1783, 2018.

[17] R. Estrada, R. Mizouni, H. Otrok, A. Ouali, and J. Bentahar, "A crowd-sensing framework for allocation of time-constrained and location-based tasks," *IEEE Transactions on Services Computing*, vol. 1, 2017.

[18] L. Pu, X. Chen, J. Xu, and X. Fu, "Crowd foraging: a qos-oriented self-organized mobile crowdsourcing framework over opportunistic networks," *IEEE Journal on Selected Areas in Communications*, vol. 35, no. 4, pp. 848–862, 2017.

[19] H. Li, T. Li, and Y. Wang, "Dynamic participant recruitment of mobile crowd sensing for heterogeneous sensing tasks," in *Proceedings of the 2015 IEEE 12th International Conference on Mobile Ad Hoc and Sensor Systems*, pp. 136–144, IEEE, Dallas, TX, USA, October 2015.

[20] C. M. Angelopoulos, S. Nikoletseas, T. P. Raptis, and J. Rolim, "Design and evaluation of characteristic incentive mechanisms in mobile crowdsensing systems," *Simulation Modelling Practice and Theory*, vol. 55, no. 6, pp. 95–106, 2015.

[21] G. Yang, S. He, Z. Shi, and J. Chen, "Promoting cooperation by the social incentive mechanism in mobile crowdsensing," *IEEE Communications Magazine*, vol. 55, no. 3, pp. 86–92, 2017.

Hindawi
Discrete Dynamics in Nature and Society
Volume 2020, Article ID 4540302, 6 pages
https://doi.org/10.1155/2020/4540302

Research Article

An Improved Spectral Clustering Community Detection Algorithm Based on Probability Matrix

Shuxia Ren, Shubo Zhang, and Tao Wu

Department of Computer Science and Technology, Tianjin Polytechnic University, Tianjin 300387, China

Correspondence should be addressed to Shuxia Ren; t_rsx@126.com

Received 21 March 2020; Accepted 28 April 2020; Published 4 June 2020

Academic Editor: Jianquan Lu

The similarity graphs of most spectral clustering algorithms carry lots of wrong community information. In this paper, we propose a probability matrix and a novel improved spectral clustering algorithm based on the probability matrix for community detection. First, the Markov chain is used to calculate the transition probability between nodes, and the probability matrix is constructed by the transition probability. Then, the similarity graph is constructed with the mean probability matrix. Finally, community detection is achieved by optimizing the NCut objective function. The proposed algorithm is compared with SC, WT, FG, FluidC, and SCRW on artificial networks and real networks. Experimental results show that the proposed algorithm can detect communities more accurately and has better clustering performance.

1. Introduction

With the development of information technology, the interactions among the complex systems of biology, sociology, and other fields are getting closer and closer. It is of great theoretical significance and practical value to obtain relevant information from real complex systems. According to graph theory, most real complex systems where their internal entities have rich associations can be abstracted into complex networks, such as neural networks, power networks, and social networks. In addition to the small-world and scale-free properties, complex networks have an extremely important community structure [1]. Community is a mesoscopic structure in which nodes from the same community are closely connected to each other, but nodes from different communities are sparsely connected. It is playing an important role in revealing the topological structure and functional features of complex networks. In recent years, community detection has been a popular research field for searching information, analysing function, and forecasting behaviour.

Community detection is a process of dividing a network into many clusters according to certain relationships among nodes. Moreover, community detection can classify nodes based on the topological structure of the network. It can reveal the hidden hierarchical structure of the real network and improve the performance and efficiency of storing, processing, and analysing network data. So far, there are many methods for community detection, such as spectral bisection algorithm [2], graph segmentation algorithm [3], heuristic algorithm [4], and objective optimization algorithm [5].

2. Related Work

Community detection is an important branch of complex networks. Among the traditional community detection algorithms, the most famous algorithm is the spectral analysis algorithm based on network topology, which is referred to as spectral clustering [2] in the following. Its main idea is eigendecomposing the similarity matrix of the network to obtain the main eigenvectors for finding communities. Not only is the spectral clustering algorithm applicable for a variety of data structures but also it utilizes dimensionality reduction to reduce computational complexity. Consequently, scholars began to research spectral clustering and optimize and expand on it.

Qin et al. [6] proposed a multisimilarity spectral method for clustering dynamic networks. It detects communities by

bootstrapping the clustering of different similarity measures. Ulzii and Sanggil [7] designed an agglomerative spectral clustering method with conductance and edge weights. The most similar nodes are agglomerated based on eigenvector space and edge weights. Ding et al. [8] explored the equivalence relation between the nonnegative matrix factorization and spectral clustering and developed a semi-supervised spectral clustering algorithm.

Spectral clustering typically constructs a similarity matrix with Euclidean distance between nodes. However, the Euclidean distance may lose the hidden relationship among nodes. As a result, the similarity matrices cannot contain complete community information. Clustering performance is not satisfied. If the constructed similarity matrix can approach the ideal matrix, the spectral clustering algorithm will have better clustering performance. Hence, constructing an excellent similarity matrix is the key to the spectral clustering community detection algorithm.

Nataliani and Yang [9] proposed a new affinity matrix generation method by using neighbour relation propagation principle. The method can increase the similarity of point pairs that should be in the same cluster. But the distance threshold is easily affected by outside points or noise points. Beauchemin [10] presented a method to build affinity matrices from a density estimator relying on K-means with subbagging procedure. However, this method would not work well when manifold proximity exists. Zhang and You [11] developed an approach based on a random walk to process the similarity matrix. The pairwise similarity is not only related to the two points but also related to their neighbours. However, the threshold of neighbouring nodes is set manually, and the stability of clustering is bad.

Although many community detection algorithms based on optimizing a similarity graph have been proposed, how to construct the similarity graph that can correctly reflect the community structure has not been solved. Consequently, this paper focuses on the transition probability between nodes to calculate the similarity, presents the concept of probability matrix, and proposes an improved spectral clustering community detection algorithm based on the probability matrix.

3. Improved Spectral Clustering Algorithm

3.1. Constructing a Similarity Graph by Probability Matrix. The similarity graph of spectral clustering is constructed by calculating the similarity between nodes. In this section, the similarity between nodes is calculated by the transition probability among nodes. And the related concepts of probability matrix and mean probability matrix are introduced. Then, the similarity graph is constructed based on the mean probability matrix.

3.1.1. Transition Probability. A Markov chain is a stochastic process of variables with Markov property, describing a sequence of states. The state changes over time, and the next state of the sequence depends on the current state [12]. The possibility of transition between states is called the transition probability.

Given a network N, the number of nodes is n, the adjacency matrix of N is W. The probability that node i reaches to node j after one step is the 1st transition probability, which can be defined as

$$pr_{ij} = \frac{w_{ij}}{\sum_{j=0}^{n-1} w_{ij}}. \quad (1)$$

The 1st transition matrix Pr is a matrix composed of entry pr_{ij}, then $Pr = D_W^{-1} \cdot W$, where $D_W = diag(d_{W0}, d_{W1}, \ldots, dW_{n-1})$, $d_{Wi} = \sum_{j=0}^{n-1} w_{ij}$.

The probability that node i reaches to node j after l steps is the l-th transition probability. And the matrix formed by l-th transition probability is called the l-th transition matrix Pr_l. According to the properties of the Markov chain, we can get

$$Pr_l = Pr^l. \quad (2)$$

Pr^l denotes that Pr is multiplied by l times.

3.1.2. Probability Matrix

Definition 1. Given a network $N(V, E)$, considering that the transition probability from node i to node j is p_{ij}, then the probability matrix of N is a $V \times V$ matrix composed of p_{ij}. The probability matrix can be referred to as P, $P = (p_{ij})$.

The probability matrix describes the transition probability between nodes in the network. The 1st transition probability can reflect the most direct relationship between the node and its adjacent nodes, but there is a lack of hidden relationship with the nonadjacent nodes. The multistep transition probability can include more neighbour nodes, reflecting the multiple complex associations among nodes. However, the multistep walk may fail to reach the adjacent nodes, which could weaken the relationship with the adjacency nodes. Consequently, we propose a method for constructing the probability matrix based on the accumulation of weighted multiorder transition matrices, and P can be defined as

$$P = \sum_{i=1}^{t} w_i Pr_i, \quad (3)$$

where i denotes that the current state of the Markov chain is at time i, t refers to the size of the Markov chain, called time scale, Pr_i is the i-th transition matrix, and w_i represents the weight of Pr_i, $i \in [2, t]$, $w_i \in [0, 1]$, $\sum_{i=0}^{t} w_i = 1$.

3.1.3. Mean Probability Matrix. The time scale is the key to calculating the similarity of nodes. But the optimal time scale of different networks is not necessarily the same. There will be mistakes in using a fixed time scale. In order to reduce the influence of parameters t and w, the mean probability matrix obtained from the mean values of P with different time scales is proposed.

Definition 2. Given a network $N(V, E)$, considering that its probability matrix is P and the time scale is t, then the mean probability matrix is a $V \times V$ matrix composed of the average of $P_1, P_2, \ldots, P_t$. According to equations (2) and (3), the mean probability matrix can be referred to as P_M:

$$P_M = \frac{\sum_{i=1}^{t} P_i}{t} = \frac{\sum_{i=1}^{t} \sum_{j=1}^{i} Pr^j}{t}. \tag{4}$$

Not only does the time scale t of P_M provide the size of time scale for each P, but more importantly, it specifies the number of summing probability matrices. It could take different P to average the error caused by t and w. The mean would reduce mistakes, and the different value of t does not cause a great error. As a result, the value of t can be randomly chosen, but in order to reduce the computational complexity, we set t to be [5, 13].

The weight w_j also represents the weight of the j-th transition matrix. According to Definition 2, we can get that i gradually changes, and the number of corresponding weights w_j also gradually changes. To satisfy the constraint, w_j is defined as

$$w_j = \frac{ws_j}{\sum_{h=1}^{t} ws_h}, \tag{5}$$

where ws is a set of weights of size t, and it is artificially set, satisfying $ws_1 > ws_2 \geq \ldots \geq ws_t$.

3.2. Improved Spectral Clustering Algorithm Based on Mean Probability Matrix

3.2.1. Constructing the New Similarity Graph. The similarity matrix W_P is constructed by the mean probability matrix P_M. Given a network N, the mean probability matrix of N is P_M; then, the similarity between node i and j can be defined as

$$w_{P_{ij}} = \begin{cases} p_{M_{ij}} & for\ i \neq j, \\ 0 & for\ i = j, \end{cases} \tag{6}$$

where w_{Pij} denotes the i, j-th entry of W_P, and p_{Mij} refers to the i, j-th entry of P_M.

The similarity matrix of the traditional spectral clustering is a symmetric matrix, which is beneficial to calculate the Laplacian matrix L. Although W_P is not a symmetric matrix, W_P has special properties and can also construct L. The properties of W_P are as follows:

$L_W = D - W_P$, where D is a diagonal matrix, $D_{ii} = \sum_{j=1}^{n} w_{Pij}$, the entries on the diagonal are positive, W_P is a matrix with nonnegative entries, its diagonal entries are all 0, and each row of entries is not all 0. To sum up, it turns out that L_W is a matrix where all the diagonal elements are positive, and the other elements are negative. Then, we obtain that L_W is invertible.

For any vector f, L_W can satisfy

$$\begin{aligned} f^T L_W f &= f^T D f - f^T W_P f = \sum_{i=1}^{n} d_i f_i^2 - \sum_{i,j=1}^{n} w_{Pij} f_i f_j, \\ &= \frac{1}{2}\left(\sum_{i=1}^{n} d_i f_i^2 - 2 \sum_{i,j=1}^{n} w_{Pij} f_i f_j + \sum_{j=1}^{n} d_j f_j^2 \right), = \frac{1}{2} \sum_{i,j=1}^{n} w_{Pij} \left(f_i - f_j \right)^2. \end{aligned} \tag{7}$$

As a result, L_W is a Laplacian matrix, and W_P can construct a similar graph of spectral clustering.

3.2.2. NCut Objective Function. Spectral clustering has many different objective functions. The purpose of the objective functions is to find a partition of the network such that the edges between different communities have lower weight and the edges within the same community have a higher weight. In other words, nodes in different clusters are dissimilar from each other, and nodes within the same cluster are similar to each other.

The more popular functions are RatioCut [13] and NCut [14]. RatioCut focuses on maximizing the number of nodes in the community, while NCut pays attention to maximizing the weights in the community. Given a network $N(V,E)$, they can be defined as

$$\begin{aligned} \mathrm{RatioCut}\left(C_1, C_2, \ldots, C_K\right) &= \frac{1}{2} \sum_{k=1}^{K} \frac{W\left(C_k, \overline{C}_k\right)}{|C_k|}, \\ \mathrm{NCut}\left(C_1, C_2, \ldots, C_K\right) &= \frac{1}{2} \sum_{k=1}^{K} \frac{W\left(C_k, \overline{C}_k\right)}{\mathrm{vol}\left(C_k\right)}, \end{aligned} \tag{8}$$

where C_k denotes the set of nodes in the community k, $C_a \cap C_b = \varnothing, C_1 \cup C_2 \ldots \cup C_K = V, a \neq b, a, b \in \{1, 2, \ldots, K\}$, K represents the number of communities, $\overline{C}_k$ refers to the complement of C_k, $\overline{C}_k = V - C_k$, $W(C_k, \overline{C}_k) = \sum_{i \in C_k, j \notin C_k} W_{Pij}$, $|C_k|$ is the number of nodes in C_k, and $\mathrm{vol}(C_k)$ is the sum of the weights of edges in C_k, $\mathrm{vol}(C_k) = \sum_{i \in C_k} \sum_{j=1}^{|V|} w_{Pij}$.

The number of nodes in the community does not mean that the weight in the community is high. In comparison, NCut is more consistent with the clustering strategy of spectral clustering. Therefore, we choose NCut as the objective function of the proposed algorithm. Combined with equation (6), the objective function can be optimized as

$$\underbrace{\arg\min}_{F}\ tr\left(F^T D^{-1/2} L_W D^{-1/2} F\right) s.t.\ F^T F = I. \tag{9}$$

F is a matrix composed of vectors f, and I is the identity matrix. F can be obtained by solving the first K smallest eigenvectors of $D^{-1/2} \cdot L_W \cdot D^{-1/2}$. However, a little information is missing due to dimension reduction, resulting in the fact that F cannot fully indicate the attributes of nodes. Therefore, taking a traditional clustering on F, such as K-means, can divide the network into K communities more accurately in the end.

Input network N, adjacency matrix W, community number K, time scale t, and a set of weights ws
Output K communities
(1) Compute the 1st transition matrix Pr according to equation (1)
(2) Compute the mean probability matrix P according to equation (4)
(3) Construct the similarity matrix W_P according to equation (6)
(4) Construct the unnormalised Laplacian matrix L_W according to the property 1 of W_P in Section 3.2.1
(5) Construct the normalized Laplacian matrix L_n with $L_n = D^{-1/2} \cdot L_W \cdot D^{-1/2}$
(6) Compute the first K eigenvectors of L_n, referred to as U
(7) Consider the rows of U as nodes, and use K-means to cluster them into K communities

Algorithm 1: Improved spectral clustering algorithm based on the probability matrix.

Table 1: The hyperparameters of the LFR benchmark.

Parameter	Description	Value
β	Power-law index of the degree distribution	3
γ	Power-law index of community size	1.5
ave_deg	Average degree of each node	10
min_com	Minimum number of nodes in any community	30
seed	Seed number of random number generator	10

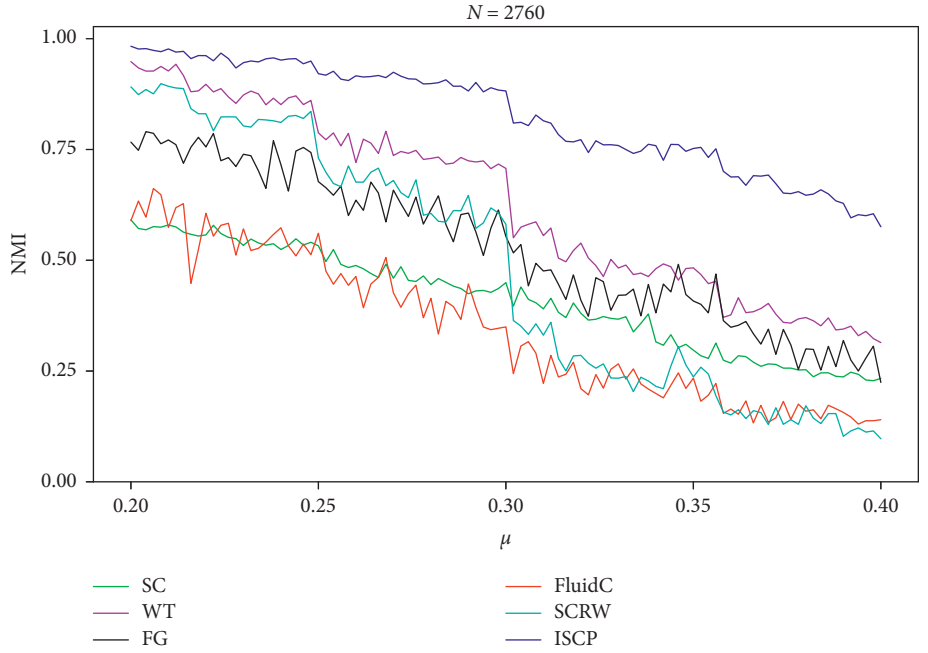

Figure 1: Performance in NMI of six algorithms with various μ. In the experiments, the network size is 2760, the initial value of μ is 0.2, the step length of μ is 0.002, and the number of iterations is 101.

3.2.3. The Main Steps of the Algorithm. The main steps of the improved spectral clustering algorithm is given in Algorithm 1.

4. Experiments and Analyses

The experimental data includes artificially generated networks and real networks. On the one hand, we use the LFR benchmark network [15] to generate the networks and evaluate the quality of community detection by normalized mutual information (NMI) [16]. On the other hand, we adopt several real networks and take the modularity (Q) [17] as the evaluation index.

In order to show the performance of the improved spectral clustering algorithm (ISCP), ISCP is compared with SC [2], WT [18], FG [19], FluidC [20], and SCRW [11]. The experimental environment includes Intel 2.5 Hz i7-4710MQ CPU and 8 G RAM. The software platform is PyCharm 2018.1.2 (Community Edition) in Windows 10 × 64.

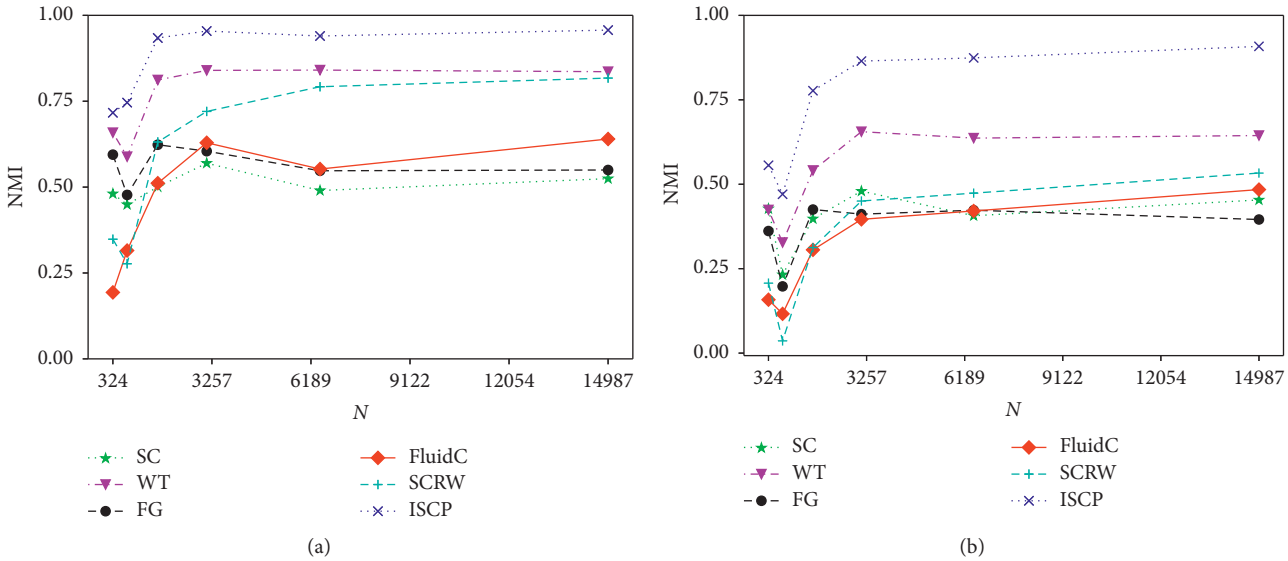

Figure 2: Performance in NMI of the six algorithms with different network sizes N. The network sizes are 324, 736, 1654, 3102, 6458, and 14987, respectively. In (a), the six algorithms are evaluated with $\mu = 0.3$. Already in (b) μ is set to 0.35.

4.1. LFR Benchmark Networks. The LFR benchmark networks are computer-generated networks, and they can produce different features of networks by adjusting some parameters. The experiments mainly use mixing parameter μ (μ denotes the average rate of edges connected with other communities, $0 \le \mu \le 1$) and network size N to evaluate performance. To guarantee consistency, the detailed descriptions and values of other parameters are shown in Table 1.

Figure 1 shows the performance of the six algorithms on μ. From Figure 1, we can get that the NMI trend of ISCP is smoother than other algorithms, and the NMI of ISCP is significantly higher than the other five algorithms. In [16], we can obtain that the larger the NMI is, the better the quality of community detection is. Overall, the clustering effect of ISCP is significantly better than the other five algorithms. In general, ISCP is more stable, and its convergence speed is faster.

Figure 2 demonstrates that the performance of the six algorithms on different network sizes N. As seen in Figure 2, the NMI of ISCP is higher than the other five algorithms. And as network size increases, its NMI increases. When the network size reaches 5000 or more, its NMI tends to be stable and stays around 0.9. Therefore, whether the order of magnitude of the network size is 1000 or 10,000, the clustering performance of ISCP is better than the other five algorithms.

4.2. Real-World Networks. The real-world networks have different topologies from the benchmark networks. To further evaluate the performance of the algorithms, 8 real-world networks are taken to do experiments. Moreover, it is necessary to normalize some real-world networks, such as eliminating self-loops and constructing a connected network. The detailed information of these networks is shown in Table 2.

Table 2: The hyperparameters of the LFR benchmark.

No.	Networks	Nodes	Edges
1	US airlines	332	2126
2	Erdos991	454	1421
3	Roget	1010	3656
4	Science	1461	3009
5	SCiNet	2729	10419
6	US power grid	4941	6594
7	Erdos992	6094	9949
8	PGP	10680	24316

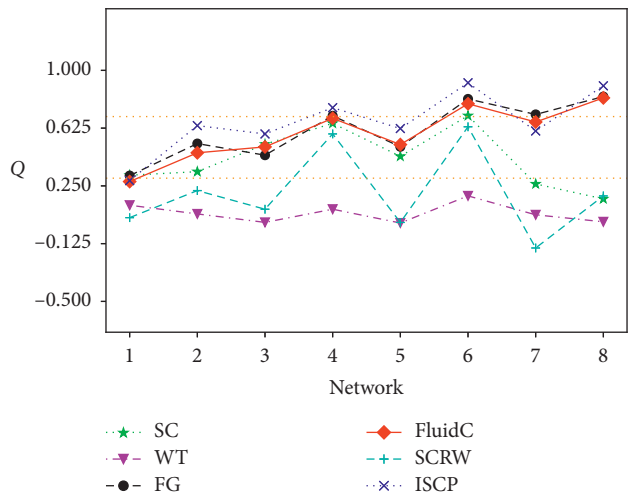

Figure 3: Performance in Q of the six algorithms with eight real-world networks. For each network, Q is the mean value obtained by clustering the same network for different community numbers K. K is from 20 to 100, the step length of K is 10, and the number of iterations is 9. (The two yellow reference lines are 0.3 and 0.7 respectively.)

The experiments take modularity Q to evaluate the clustering performance of the six algorithms. The range of Q is from −0.5 to 1. The larger Q is, the better the community detection performance will be. Q generally falls in about 0.3 to 0.7 in practice [17].

Figure 3 shows the performance of the six algorithms for clustering real-world networks. As shown in Figure 3, Q of ISCP is almost all above 0.3 and is larger than Q of the other algorithms. Although ISCP is not the best community detection algorithm for network 1 and network 7, its performance is very close to the best algorithm. Generally speaking, ISCP has excellent clustering performance and can cluster real-world networks more accurately.

5. Conclusions

Spectral clustering plays an important role in the field of community detection. It is an excellent community detection algorithm, but the traditional similarity graphs contain lots of incorrect information about the community structure. As a result, the performance of community detection is bad. Hence, this paper presents the probability matrix and proposes an improved spectral clustering community detection algorithm ISCP. A large number of experiments on benchmark networks and real-world networks show that ISCP is better than most traditional community detection algorithms and can more accurately cluster complex networks.

However, the ISCP will cost lots of time and space. Given a network N, the number of nodes is n, and the time scale is t. ISCP needs to multiply the transition probability matrix by t times to construct the similarity matrix. Even with the Fast Power algorithm, the time complexity of the algorithm will reach $O(n^3 \mathrm{lb} t)$. As the size of the network is larger, computing the similarity matrix will take more time and space. Moreover, ISCP is only applied to nonoverlapping complex networks. So the next step is to research how to optimize the computational complexity of the algorithm and how to cluster overlapping networks.

Data Availability

The data cannot be released for the time being. When the relevant research is finished, we will release detailed research results.

Conflicts of Interest

The authors declare that there are no conflicts of interest regarding the publication of this paper.

References

[1] M. Girvan and M. E. J. Newman, "Community structure in social and biological networks," *Proceedings of the National Academy of Sciences*, vol. 99, no. 12, pp. 7821–7826, 2002.

[2] A. Y. Ng, M. I. Jordan, and Y. Weiss, "On spectral clustering: analysis and an algorithm," *Advances in Neural Information Processing Systems*, vol. 14, pp. 849–856, 2002.

[3] B. W. Kernighan and S. Lin, "An efficient heuristic procedure for partitioning graphs," *Bell System Technical Journal*, vol. 49, no. 2, pp. 291–307, 1970.

[4] M. Rosvall and C. T. Bergstrom, "Maps of random walks on complex networks reveal community structure," *Proceedings of the National Academy of Sciences*, vol. 105, no. 4, pp. 1118–1123, 2008.

[5] D. He, J. Liu, D. Liu, D. Jin, and Z. Jia, "Ant colony optimization for community detection in large-scale complex networks," in *Proceedings of the Seventh International Conference on Natural Computation*, pp. 1151–1155, Shanghai, China, July 2011.

[6] X. Qin, W. Dai, P. Jiao, W. Wang, and N. Yuan, "A multi-similarity spectral clustering method for community detection in dynamic networks," *Scientific Reports*, vol. 6, no. 1, pp. 31454–31465, 2016.

[7] N. Ulzii and K. Sanggil, "Social network community detection using agglomerative spectral clustering," *Complexity*, vol. 2017, Article ID 3719428, 10 pages, 2017.

[8] S. Ding, H. Jia, M. Du, and Y. Xue, "A semi-supervised approximate spectral clustering algorithm based on HMRF model," *Information Sciences*, vol. 429, pp. 215–228, 2018.

[9] Y. Nataliani and M. S. Yang, "Powered Gaussian kernel spectral clustering," *Neural Computing and Applications*, vol. 31, no. 1, pp. 557–572, 2019.

[10] M. Beauchemin, "A density-based similarity matrix construction for spectral clustering," *Neurocomputing*, vol. 151, pp. 835–844, 2015.

[11] X. Zhang and Q. You, "An improved spectral clustering algorithm based on random walk," *Frontiers of Computer Science in China*, vol. 5, no. 3, pp. 268–278, 2011.

[12] J. Rhodes and A. Schilling, "Unified theory for finite Markov chains," *Advances in Mathematics*, vol. 347, pp. 739–779, 2019.

[13] L. Hagen and A. B. Kahng, "New spectral methods for ratio cut partitioning and clustering," *IEEE Transactions on Computer-Aided Design of Integrated Circuits and Systems*, vol. 11, no. 9, pp. 1074–1085, 1992.

[14] J. Shi and J. Malik, "Normalized cuts and image segmentation," *IEEE Transactions on Pattern Analysis and Machine Intelligence*, vol. 22, no. 8, pp. 888–905, 2000.

[15] A. Lancichinetti, S. Fortunato, and F. Radicchi, "Benchmark graphs for testing community detection algorithms," *Physical Review E*, vol. 78, no. 4, pp. 46110–46115.

[16] P. Zhang, "Evaluating accuracy of community detection using the relative normalized mutual information," *Journal of Statistical Mechanics: Theory and Experiment*, vol. 2015, no. 11, pp. 11006–11013, 2015.

[17] M. E. J. Newman, "Modularity and community structure in networks," *Proceedings of the National Academy of Sciences*, vol. 103, no. 23, pp. 8577–8582, 2006.

[18] P. Pons and M. Latapy, "Computing communities in large networks using random walks," *Journal of Graph Algorithms and Applications*, vol. 10, no. 2, pp. 191–218, 2006.

[19] M. E. J. Newman, "Fast algorithm for detecting community structure in networks," *Physical Review E*, vol. 69, no. 6, pp. 133–138, 2004.

[20] F. Parés, D. Garcia Gasulla, A. Vilalta et al., "Fluid communities: a competitive, scalable and diverse community detection algorithm," in *Proceedings of the Complex Networks & Their Applications*, pp. 229–240, Cham, Switzerland, November 2017.

Hindawi
Discrete Dynamics in Nature and Society
Volume 2020, Article ID 2815073, 13 pages
https://doi.org/10.1155/2020/2815073

Research Article

A Novel User Selection Strategy with Incentive Mechanism Based on Time Window in Mobile Crowdsensing

Xuemei Sun,[1,2] **Xiaorong Yang**,[1,2] **Caiyun Wang**,[1,2] **and Jiaxin Wang**[1,2]

[1]*School of Computer Science and Technology, Tiangong University, Tianjin 300387, China*
[2]*Tianjin Key Laboratory of Autonomous Intelligence Technology and Systems, Tianjin, China*

Correspondence should be addressed to Xuemei Sun; sunxuemei@tiangong.edu.cn

Received 25 March 2020; Revised 8 May 2020; Accepted 13 May 2020; Published 1 June 2020

Academic Editor: Jianquan Lu

With the rapid development of smart phones and wireless communication, mobile sensing has become an efficient environmental data acquisition method capable of accomplishing large-scale and highly complex sensing tasks. Currently, participants want to collect continuous data over a period of time. However, the number of participants varies widely in some periods. In view of this application background, this paper proposes a new incentive mechanism of extra rewards: premium and jackpot incentive mechanism (PJIM), and a new participant selection method based on time window: participant selection for time window dependent tasks (PS-TWDT). In the PJIM, the platform divides the time period of sensing tasks according to the time distribution of task participants and adopts different incentive strategies in different situations; at the same time, it introduces the prize pool mechanism to attract more participants to participate in the sensing task with fewer participants. In the PS-TWDT, we design a participant selection method based on dynamic programming algorithm. The goal is to maximize the data benefit while the sensing time of the selected participants covers the task time period. In addition, the updating strategy of participants' credit value is added, and the credit value of participants is updated according to their willingness to participate in the task and data quality. Finally, simulation experiment verifies that the incentive mechanism and participant selection method proposed in this paper have good performance.

1. Introduction

With the development of wireless network and the progress of embedded sensors technology, there are many sensors embedded in people's smart devices, such as microphone, camera, temperature sensor, light sensor, and positioning sensor. In addition, the popularity of smart phones has given birth to a new kind of sensing network model—mobile crowdsensing. In the mobile crowdsensing network, people with smart devices can use the popular smart phones to collect data to complete various sensing tasks. As shown in Figure 1, we consider a mobile crowdsensing network consisting of task publishers, task platform, and task participants with smart devices. Task publishers publish their own tasks on the task platform and pay a certain fee to the platform. The task platform selects qualified personnel to participate in the sensing task and gives certain reward to motivate the participants. Finally, the task platform transmits the collected data to the task publisher, and the sensing task ends. Compared with the traditional sensor networks, mobile crowdsensing network has prominent advantages due to its wide coverage and low sensing cost [1]. Therefore, it has great potential in completing large-scale and complex sensing tasks as a new sensing mode and also has great advantages in social networking [2–4], medical treatment, environmental monitoring of a certain area, and transportation [5–9].

Although, compared with traditional sensing networks, mobile crowdsensing networks can save the cost of purchasing professional sensors and deploying professionals, it takes time and energy for smart phone participants to participate in sensing tasks. At the same time, smart phone participants sharing their sensing data may reveal their privacy, including location, interests, and identity.

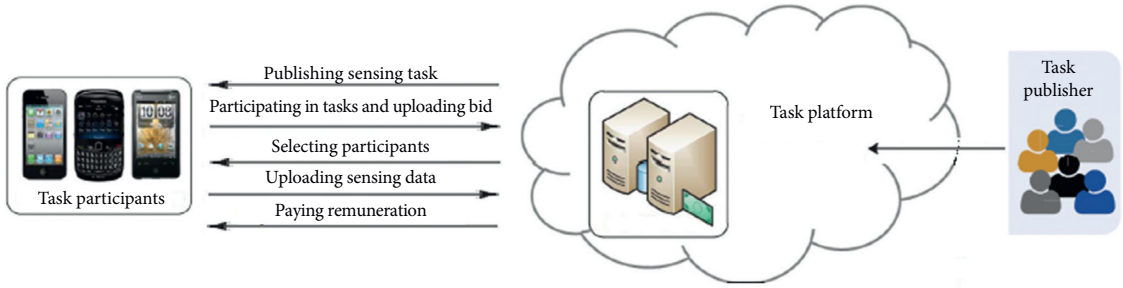

Figure 1: Mobile crowdsensing network model.

Therefore, how to motivate participants to actively participate in the task, complete the task, and successfully submit sensing data is essential. The task platform must have better compensation measures to compensate the participants and drive the crowdsensing task.

In the practical application of mobile crowdsensing, many sensing tasks have certain requirements for the continuity of sensing data, for example, pollution monitoring, traffic monitoring, and noise monitoring in a certain area in recent days or weeks. This kind of sensing tasks needs a long time of continuous monitoring; it cannot be completed by a single participant alone, so it needs multiple participants to cooperate. At the same time, it involves participation in different time periods of the day. Since most participants in a certain region have the same living habits and rest rules, the time periods for participants to participate in the task are relatively concentrated. Some time periods have more participants and some time periods have fewer participants. For example, in a continuous day of sensing tasks, the number of participants at daytime is redundant, and the number of participants at night is insufficient. However, the existing incentive mechanism research does not specifically analyze the participation time period. In order to solve this problem, the platform needs a reasonable incentive strategy to ensure that sufficient participants are involved in the task over a continuous period of time. At the same time, in the practical application of mobile crowdsensing, after ensuring that enough participants engage in the sensing task, the task platform puts forward certain value requirements for the collected data. And these tasks require participants to collect continuous sensing data for a period of time. This task related to the time window puts forward higher requirements for the participant selection method.

The key contributions of our work are summarized as follows:

(1) In this paper, the specific task sensing time is divided, and a prize pool mechanism is proposed to attract participants by offering high rewards to those who have less time to participate. In the task, an optimization algorithm based on dynamic programming is proposed to select participants, and then an extra reward mechanism is proposed. It is based on the participation time of each participant to carry out different incentive strategies.

(2) A time window related participant selection strategy is proposed. This mechanism mainly includes designing a participant selection method based on dynamic programming algorithm. The goal is to maximize the data benefit while the sensing time of the selected participants covers the task time period. In addition, the updating strategy of participants' credit value is added, and the credit value of participants is updated according to their willingness to participate in the task and the data quality.

(3) The proposed incentive mechanism ensures that there will be enough participants to participate in the sensing task, and the participant selection strategy is to select the appropriate participants to meet the task requirements from enough participants. These two parts of work provide a complete working mode for the task platform.

2. Related Work

Research on incentive mechanism in crowdsensing: In [10], Zhao et al., in order to preserve the privacy of task participants and not to ignore the data quality of task participants, propose a privacy-preserving and data quality-aware incentive scheme, called PACE. In particular, data quality consists of the reliability and deviation of data. In [11], Nie et al. apply a two-stage Stackelberg game to analyze the participation level of the mobile users and the optimal incentive mechanism of the crowdsensing service provider using backward induction. In order to motivate the participants, the incentive mechanism is designed by taking into account the social network effects from the underlying mobile social domain. In [12], an incentive mechanism (RTM) based on reputation and trust is proposed for the negative impact of selfish nodes in mobile crowdsensing. This paper analyzes the reputation incentive mechanism and trust incentive mechanism and constructs an incentive model, which is divided into user selection model and reward incentive model. In [13], Zhong et al. study the stage incentive mechanism of mobile crowdsensing and divide the incentive process into two stages: recruitment stage and sensing stage. In [14], Chen et al. proposed an incentive mechanism based on stochastic game for the existing incentive mechanism without considering the uncertainty and probability of user behavior. In [15], two incentive mechanisms are designed from two aspects of participants and

Table 1: Common parameters.

S	Set of selected winners
S_n	Set of participants at night
S_d	Set of participants in the daytime
S_g	Night backup assembly
m_i	The median of the time period reported by the participant i
s	Start time of participating in sensing task
e	End time of participating in sensing task
W	A unit time period of sensing task
T_s	The start time of a unit time period
T_e	The end time of a unit time period
$\|T\|$	The length of a time window
s_i	Start time reported by participant i
e_i	End time reported by participant i
Weight	The ratio of participants in the reported daytime period to all participants
D	Price pool reward
p_i	Rewards received by participant i
b_i	Bid price of participant i
a_i	Extra rewards received by participant i
d_i	Price pool reward received by participant i
U, u_i	Set of participants, participant i
t_i^k	Represents the sensing time of participant i in the k-th time window
b_i^k	Bid price of participant i in the k-th time window
R_i^k	Reliability of participant i in the k-th time window
r_i	Credit value of participant i
d_i^k	Sensing data volume of participant i in the k-th time window
E_i^k	Device battery of participant i in the k-th time window
V^k	Data benefit of the k-th time window
r_i^k	Trust status feedback value of participant i in the k-th time window
w_i^k	Degree of willingness to participate of participant i in the k-th time window
q_i^k	Data quality uploaded by participant i in the k-th time window
p_i	Rewards received by participant i in the k-th time window
$\varepsilon, \eta, \omega, \lambda$	Timeliness, completeness, accuracy, value

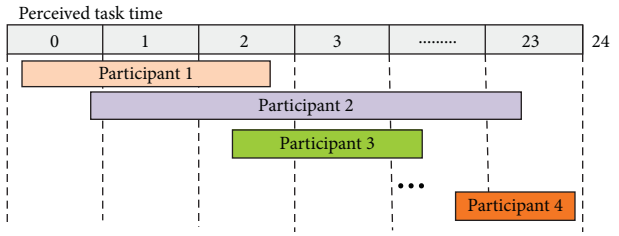

Figure 2: Task time model.

task release platform by using bidding game method, and two different system models are used to achieve the effect of user incentive. The paper [16] aims to design an incentive mechanism to maximize the utility of the platform under certain budget conditions. In [17], Feng et al. propose an incentive mechanism called TRAC, which focuses on the position of participants when assigning tasks. In [18], Li et al. design two incentive mechanisms, QUAC-F and QUAC-I, based on the difference in the sensing information level of participants under the condition of ensuring the maximization of platform utility. In [19], Zhan et al., considering the time characteristics of data collection, proposed an incentive mechanism based on reputation to maximize the reward for data collectors. In [20], two kinds of auction incentive mechanism framework based on privacy protection are designed to achieve the approximate minimization of social cost.

Research on participant selection in crowdsensing: In [21], Li et al. study dynamic (real-time) and heterogeneous (with different time and space coverage requirements) sensing tasks and propose offline and online algorithms for dynamic participant selection of heterogeneous sensing tasks. According to the model proposed in [22], a group based method is adopted for selection, and the participants in the group complete the sensing task by using the combination function of smart phones. Literature [23] proposes a data collection mechanism for participants' reputation perception and divides it into two types of participants: direct sending and indirect sending, dynamically updating participants' reputation to select task participants reasonably. Literature [24] aims to optimize the number of participants and reduce the cost of tasks on the basis of meeting the requirements of task coverage. In [25], Guo et al. propose a visual group intelligence perception framework called UtiPay, which selects participants and data from both macro and micro aspects. In [26], Liu et al., based on the historical activity track data of participants, select the appropriate participants in the sensing area to complete the sensing task. In [27], Li et al. study the privacy of bidding on the basis of time and space and propose a privacy protection participant selection scheme with scalable grouping. In [28], aimed at completing the sensing task with the minimum execution time, a participant selection scheme based on location

information in urban area is proposed by using vehicle ad hoc network.

The above literature has done a lot of research and discussion on incentive mechanism and participants' selection, but this work is only based on the premise that participants are not affected by the time when they perform tasks. For the incentive mechanism, the above work does not consider that participants' work and rest conditions have an impact on the completion time of tasks, not considering also the incentive for the insufficient time period of participants. For the participants' selection, this paper requires participants to collect continuous sensing data for a period of time, but the above work cannot be effectively applied to the tasks related to the time window. In order to solve the above problems, in this paper, the specific task sensing time is divided, and an incentive mechanism based on time window is proposed, which can attract participants to cover the task time by high reward for the task time period with insufficient participants. Due to the differences in the credibility of different participants, this paper proposes a time window related participant selection strategy. The goal is to maximize the platform data benefit based on covering the task time window.

3. System Model and Problem Formulation

In this scenario, there is a task publishing platform and many participants. The task publishing platform wants to collect sensing data in a continuous period of time. This paper assumes that the task publishing platform releases a sensing task, which requires continuous monitoring for several days. After the platform publishes the tasks, all participants report their sensing time period and bid price in the first day. According to the sensing time period and bid price of participants, the platform selects appropriate participants to participate in the sensing tasks. It is not difficult to understand that most participants are more willing to participate in sensing tasks during the day, and only a few are willing to participate in sensing tasks at night. This requires an incentive mechanism to stimulate more people to participate in the nighttime data collection. In this paper, an incentive mechanism is proposed to reward the night participants. Through continuous bonus accumulation and iteration, more and more people are gradually stimulated to participate in the night sensing data. Table 1 shows common parameters.

In this paper, the sensing time period of tasks is defined as 24 hours a day, expressed in $W = [T_s, T_e]$.W is a unit time period of sensing task. T_s refers to the start time of a unit time period, and T_e refers to the end time of a unit time period. Suppose that a certain number of participants $U = \{1, 2, 3, \ldots, n\}$ are interested in the sensing task, and each participant as a two-tuple $B_i = (T_i, b_i), \forall i \in U$. $T_i = [s_i, e_i]$ is the time when participants u_i participate in sensing tasks, where s_i is the start time and e_i is the end time. b_i refers to the bid price of participant u_i participating in sensing task. As shown in Figure 2, when collecting continuous sensing data in N time windows, $|T|$ represents the length of a time window. Suppose that there are enough participants in the platform after the incentive; each participant i is represented as $u_i = \{[t_i^1, b_i^1], [t_i^2, b_i^2], \ldots [t_i^k, b_i^k]\}$, where $t_i^k = \{t_s^k, t_e^k\}$ represents the sensing time of participant u_i in the k-th time window, t_s^k is the start time, and t_e^k is the end time. b_i^k is the bid price of participant u_i in the k-th time window.

3.1. Task Publisher. Task publishers put forward requirements for sensing tasks, for example, to collect sensing data of a certain aspect within a certain range, then send the requirements for sensing tasks to the mobile task platform, and upload the reward to the platform.

3.2. Sensing Participants. After the participants get the task information in the task area, they can decide whether to accept these subtasks according to their own situation. When the sensing participant receives the sensing task, the sensing data is collected and processed by the smart device, and then the sensing data is uploaded to the mobile task platform.

3.3. Mobile Task Platform. According to the requirements of sensing tasks, the mobile task platform divides the tasks reasonably and selects the appropriate participants to send them the sensing tasks. At the same time, the data collected by the participants are processed, analyzed, and integrated; then the sensing data is returned to the task publisher; and the participants who participate in the sensing task are rewarded.

Considering the regularity of participants' work and rest, a unit time period of the task is divided into daytime time period and nighttime period. This paper designs an incentive mechanism and sets the amount to be paid to participants according to different time periods and participants' participation. In order to compensate participants for participating in tasks and attract more participants during nighttime, this paper not only pays participants according to their bid price, but also gives them extra rewards. If the nighttime participants are not enough to cover the night sensing time period of the task, this paper will issue the price pool reward before the participants report the perception time period next time, and pay the price pool reward to the nighttime participants after the task is successfully executed.

The goal of this paper is to minimize the sum of rewards paid to participants on the premise that the task is successfully performed, which can be described as an optimization problem as shown in the following formulas:

$$\min \sum_{i \in S} P = p_i + a_i + d_i, \tag{1}$$

$$s.t. \quad W \subseteq \cup_{i \in S} [s_i, e_i]. \tag{2}$$

In the objective function, p_i represents the reward paid to u_i according to the bid price. a_i is the additional reward paid to participants in the nighttime period of the task. d_i is the price pool rewards paid to participants in the nighttime period of the task. Participants participating in the daytime period of the task have no additional rewards and price pool

rewards, so the rewards and price pool rewards values of those participating in the daytime period of the task are 0. The constraints are shown in (2), where W represents the selected participants to participate in the period of time to cover the whole task.

When there are enough participants to participate in the perception task, it is necessary to select the participants of the sensing task. Task publishers require collecting continuous sensing data in N time windows, so the sensing time of participants selected by the platform in each time window must continuously covers the time window; otherwise, it does not meet the task requirements. In order to get more accurate sensing data, the platform needs to select appropriate participants for each time window, maximize the reliability of the selected participants, and minimize the sensing cost on the premise that the task requirements are met, that is, to maximize the data benefits of the platform. Each time window objective can be described as an optimization problem as shown in the following formulas:

$$\max V^k = \frac{\sum p_i^k}{\sum b_i^k}, \tag{3}$$

$$\text{s.t.} \quad T^k \subseteq \cup_{i \in S} \left[t_s^k, t_e^k\right]. \tag{4}$$

In the objective function (3), p_i^k is the sensing data reliability of participant u_i in the *k-th* time window of the task, and b_i^k is the bid price of participant u_i in the *k-th* time window of the task. In this paper, the ratio of the total data reliability of the selected participant and the total bid price in a time window is defined as the data benefits of the time window. In (3), V^k represents the data benefits in the *k-th* time window. The constraint (4) indicates that the time window participated by the selected participant can cover the time window of the whole task.

4. PJIM and PS-TWDT Algorithm Design

4.1. PJIM Incentive Mechanism Design. In the process of participant selection, most participants tend to participate in sensing tasks at daytime, so this paper assumes that there are enough participants to participate in sensing tasks at daytime. At night, most of the participants will give up participating in the sensing task and choose to rest. Therefore, there may not be enough participants in the sensing task at night. For the convenience of understanding, this paper changes one unit time period of the task from 0 to 24 to 0 to 12. To sum up, a unit time period of the task is divided into daytime and nighttime. In this paper, the nighttime period is 0 to 6 o'clock, and the daytime period is 6 to 12 o'clock.

4.1.1. Extra Reward Mechanism. Because the nighttime of sensing task is not consistent with the working time of most participants, there are not enough nighttime participants in the sensing task. In order to encourage more participants to participate in the nighttime period of the task, this paper sets up extra rewards as shown in (5) to reward participants who complete the nighttime period of the task.

$$a_i = f_i * \left|e_i - s_i\right| * \text{weight}, \tag{5}$$

where a_i is the extra reward paid to participant u_i. f_i represents the lowest single value of participants in the daytime period of the task. The single value is the ratio of the participants' bid price to the sensing task duration. $|e_i - s_i|$ is the participation time length of participant u_i in the sensing task at night. *Weight* represents the proportion of the number of participants at the daytime of the task to the total number of participants. The extra reward at the nighttime of the task is directly proportional to the number of participants at the daytime of the task. The more the participants at the daytime of the task, the higher the extra reward paid to participants at the nighttime of the task.

4.1.2. Price Pool Reward Mechanism. If there are not enough participants in the nighttime period of the task within the first unit time period of the task, the task of this unit time period will not be completed. When selecting participants, the participation time period should be reported in advance. The goal is that the selected participants should cover the whole time period. In order to promote enough participants to complete the task in the unit time period of the next task, this paper sets a price pool mechanism to encourage participants to participate in the nighttime period of the task and issues the price pool reward amount before participants report the next sensing time period. The reward amount of the price pool is calculated by the following formula:

$$\text{pond} = f_i * \left|T_e - T_s\right| * \text{weight}, \tag{6}$$

where pond is the price pool reward amount. f_i represents the lowest single value of participants in the daytime period of the task. $|T_e - T_s|$ indicates the duration of the task nighttime period. Weight represents the proportion of the number of participants at the daytime of the task to the total number of participants. If the second unit time period of the task is still not completed, that is, participants in the nighttime period of the task are still insufficient, and the price pool reward amount is overlapped until the task can be completed, the price pool reward will be paid to participants in the nighttime period of the task.

This paper introduces an important parameter, the private target threshold G_i of participant u_i, $\forall i \in U$. The paper assumes that when the published prize pool amount is greater than the private target threshold of the participant, the participant is satisfied and will be willing to participate in the task night sensing period in the next unit period of the task. Since most participants are not greedy in real life, this assumption is reasonable [29]. In this paper, all sets of participants whose private target threshold is less than the price pool amount are represented by a night backup set S_g.

According to the work and rest rules of the participants, the unit time of the task is divided into daytime and nighttime, and the incentive mechanism is set up, including extra reward and price pool reward to attract enough participants to participate in the nighttime tasks, so as to ensure the successful implementation of the task. The goal of this paper is to minimize the compensation paid to participants

Input: participant set U, participation time period L, participant bid price B, price pool initial reward D, Participant private target threshold G
Output: the selected participant set S, the paid reward P or price pool amount D

$S \longleftarrow \emptyset$, $S_n \longleftarrow \emptyset$, $S_d \longleftarrow \emptyset$, $S_g \longleftarrow \emptyset$
The participants are ranked and judged by the incrementing start time of the report
if $T_s \in [s_1, e_1]$
  for $i = 1$ to n do
    $m_i = |e_i - s_i|/2$
  if $m_i \in [0, 6]$
    $S_n \longleftarrow m_i$
  else if $m_i \in [6, 12]$
    $S_d \longleftarrow m_i$
    end for
Calculate whether participants in the S_n set can cover the night time period of the task
  if the participation time of S_n can't cover the night task
    $D \longleftarrow$ Calculate the prize pool amount
    $S_g \longleftarrow$ Calculate satisfied participants set U
    Return (D, S_g)
  else
  The dynamic programming algorithm is used to select the participant set S and calculate the cost
  for all $i \in U$ do
    $p_i \longleftarrow 0$
  end for
  for all $i \in S \cap S_d$ do
    $p_i \longleftarrow \text{cost}(U \backslash \{i\}) - (\text{cost}(U) - b_i)$
  end for
  for all $i \in S \cap S_n$ do
    $p_i \longleftarrow b_i$
    $a_i \longleftarrow$ Calculate extra rewards
    $d_i \longleftarrow$ Calculate the prize pool amount
  end for
  Return(S, P)
else
  $D \longleftarrow$ Calculate the prize pool amount
  $S_g \longleftarrow$ Calculate satisfied participants set U
  Return(D, S_g)

Algorithm 1: PJIM incentive mechanism algorithm.

on the premise that tasks are successfully executed. First, it is determined whether the nighttime period can be covered by the participation time period of participants. If so, the MST algorithm in literature [30] is used to select the set of participants with the minimum sum of payment and calculate the extra reward amount for nighttime participants. If the nighttime participants are not enough to complete the sensing task, the price pool reward amount will be calculated and announced before the next participant reports the sensing time period. The price pool reward amount is gradually accumulated until there are enough participants in the nighttime period, and then MST Algorithm 1 is used to select the appropriate participants and pay the extra rewards and price pool rewards to the nighttime period participants:

(1) Initialize the participant set U, the corresponding participation time period is L, the bid price is B, and set the price pool reward is pond = 0.

(2) Rank participants in ascending order of sensing start time reported.

(3) Judge whether the start time of the first participant covers the start time T_s of the task. If so, perform the next step. Otherwise, calculate the price pool reward, end the algorithm, and return the price pool reward pond of the day.

(4) Determine the task duration of each participant u in the participant set.

(5) Judge whether the reported time period of the night participant can continuously cover the night task time period. If so, perform the next step. Otherwise, calculate the price pool reward and the algorithm ends and return the price pool reward *pond* of the day.

(6) Use the MST algorithm to select the participant set S with the lowest total bid price.

(7) Calculate the extra reward a_i of the selected participants in the nighttime period, and then give different rewards to the selected participants who participate in the task in different time periods.

Input: set of participants U, set of initial mobile phone battery E, set of initial credit value R, task duration T
Output: Selected participants S, Data benefit V

(1) for $i = 1$ to N do
(2) $e_i \leftarrow$ Calculate the amount of sensing data
(3) $p_i \leftarrow$ Calculate sensing data reliability
(4) end for
(5) Sort participants by end time incrementally
(6) for $i = 1$ to N do
(7) if $T_s \in [t_{si}, t_{ei}]$ then
(8) $pre(i) \leftarrow (-1)$, $P(i) = p_i$, $B(i) = b_i$;
(9) else
(10) $pre(i) \leftarrow arg\ max\ t_{ei} \geq t_{si}, j < i\ (P(j) + pi/B(j) + b_i)$
(11) $P(i) \leftarrow P(pre(i)) + p_i$, $B(i) \leftarrow B(pre(i)) + b_i$
(12) end if
(13) end for
(14) $i \leftarrow \arg\max T_e \in [t_{si}, t_{ei}], j \in U\ (P(j) + p_i/B(j) + b_i)$
(15) $V \leftarrow P(i)/B(i)$
(16) while $i \neq -1$
(17) $S \leftarrow S \cup \{i\}$, $i \leftarrow pre(i)$
(18) for all $i \in U$ do
(19) $c_i \leftarrow 0$
(20) end for
(21) for all $i \in S$ do
(22) $c_i \leftarrow b_i$
(23) end for
(24) Return(S, V)
(25) for all $i \in S$ do
(26) Calculate the degree of willingness to participate
(27) Calculated data quality
(28) Calculate the trust state feedback value
(29) $r_i \leftarrow$ Update participant credit value
(30) end for

Algorithm 2: PS-TWDT participant selection algorithm.

(8) The algorithm ends, and return the selected participant set S and the paid reward P.

4.2. PS-TWDT Participant Selection. When the participants at night meet our requirements, we need to select the participants based on the differences in their credit, participation time, and other aspects. Therefore, this paper proposes two aspects: One is the participant selection method based on dynamic programming algorithm, which aims to maximize the data benefit on the basis of covering the task time window. The second is that the credit value updating mechanism of participants updates the credit value of participants according to the willingness of participants to perform tasks and the quality of data collected.

4.2.1. Data Reliability Definition. Because the sensor nodes in the mobile crowdsensing network are no longer sensor devices deployed by professionals, but ordinary people carrying smart devices, the accuracy of the sensing data provided by participants is low and there are individual differences. The accuracy of sensing data directly affects the results of sensing tasks, so the platform should select participants reasonably in order to meet the task requirements and obtain more reliable sensing data. The reliability of participants is mainly related to two factors. The first is the credibility of participants themselves, that is, the credit value of participants. The higher the credit value of the participants, the higher the reliability of the perceived data. The second is the amount of sensing data that participants can provide. The larger the amount of data, the more the high-quality data, and the higher the data reliability. According to the above two points, the reliability of participants defined in this paper is shown in the following formula:

$$\mathbf{R}_i^k = \mathbf{r}_i * \frac{\mathbf{d}_i^k}{\left|\mathbf{t}_e^k - \mathbf{t}_s^k\right|}, \tag{7}$$

where R_i^k represents the reliability of participant u_i in the k-th time window; r_i represents the credit value of the participant, which reflects the past performance of the task; $d_i^k/|t_e^k - t_s^k|$ represents the amount of data perceived by participants in a unit time; and d_i^k represents the amount of sensing data that the participant u_i can provide in the k-th time window and d_i^k is mainly determined by the power of the smart device that the participant carries [26]. The specific relationship is shown in formula (8), where E_i^k is the initial power of the device when the participant u_i participates in the k-th time window of the

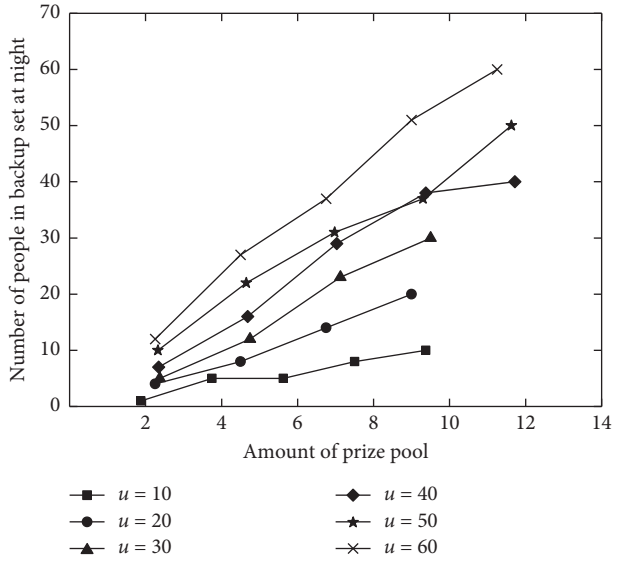

Figure 3: Number of people in backup set at night.

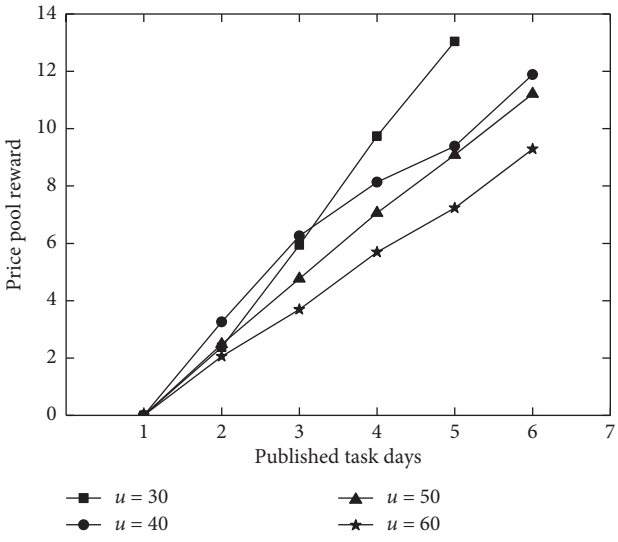

Figure 4: Price pool reward.

task, α and β are parameters in the functional relationship, α is 8.179, and β is 0.4633.

$$\mathbf{d}_i^k = \alpha * \left(\mathbf{E}_i^k\right)^{\beta}. \tag{8}$$

4.2.2. Credit Value Update Mechanism. In this paper, the credit value of participants is defined as r_i, which is quantified as a value within the range [0, 1]. A credit value of 0 indicates complete untrustworthiness, 0.5 indicates uncertainty, and 1 indicates complete credibility. The initial credit value of participants involved in the sensing task for the first time is set to 0.5, which indicates the uncertainty of credit at the initial time. In order to make the credit value of participants more accurately reflect the credibility of participants, this paper designs a credit value update mechanism, which

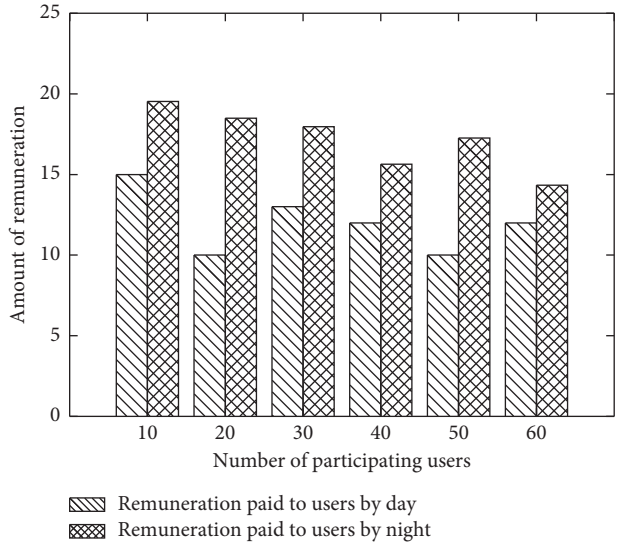

Figure 5: Amount of remuneration.

updates the credit value of participants according to the performance of participants after each task time window. Before introducing the mechanism of updating reputation value, we first introduce the trust state feedback value. The definition of trust state feedback value is divided into two parts: degree of willingness to participate and data quality.

(1) Degree of Willingness to Participate. The degree of willingness to participate is shown in (9), indicating the degree of participation in sensing tasks, where $|t_e^k - t_s^k/T|$represents the time proportion of perception task participants in the *k-th* time window. The larger the time proportion is, the higher the enthusiasm of task participants is. In order to avoid the one-sided influence brought by single factor measurement of willingness to participate, this paper adds the current power E_i^k of mobile devices when participants engage in the *k-th* time window; the more the power is, the more active they are in the sensing task.

$$\mathbf{w}_{\mathrm{i}}^k = \mathbf{E}_i^k * \left|\frac{\mathbf{t}_e^k - \mathbf{t}_s^k}{T}\right|. \tag{9}$$

(2) Data Quality. The data quality is shown in (10). q_i^krepresents the data quality provided by the *k-th* time window of participant u_i, including timeliness ε_i^k, completeness η_i^k, accuracy ω_i^k, and value λ_i^k. In this paper, these four factors are simply quantified as values in [0, 1]. 0 represents poor timeliness, incompleteness, inaccuracy, and no value of the data collected by participants; the data quality is totally unreliable. 1 means the collected data is timely, complete, accurate, and valuable; the data quality is completely reliable.

$$\mathbf{q}_{\mathrm{i}}^k = \boldsymbol{\varepsilon}_i^k * \boldsymbol{\eta}_i^k * \boldsymbol{\omega}_i^k * \boldsymbol{\lambda}_i^k. \tag{10}$$

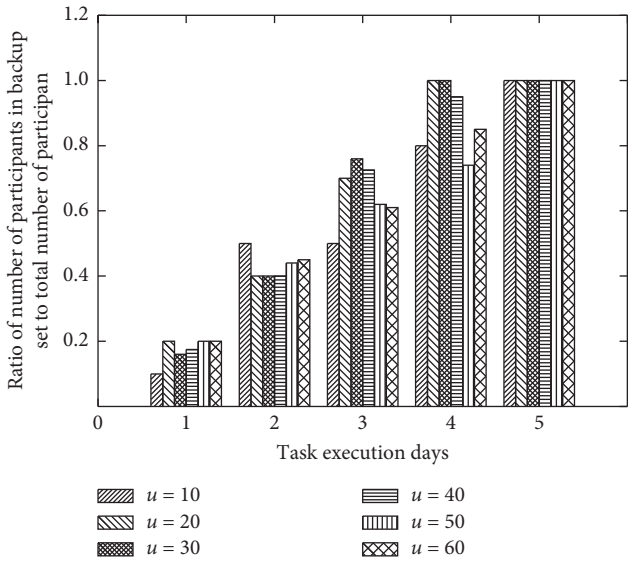

Figure 6: Ratio of number of participants in backup set to total number of participants.

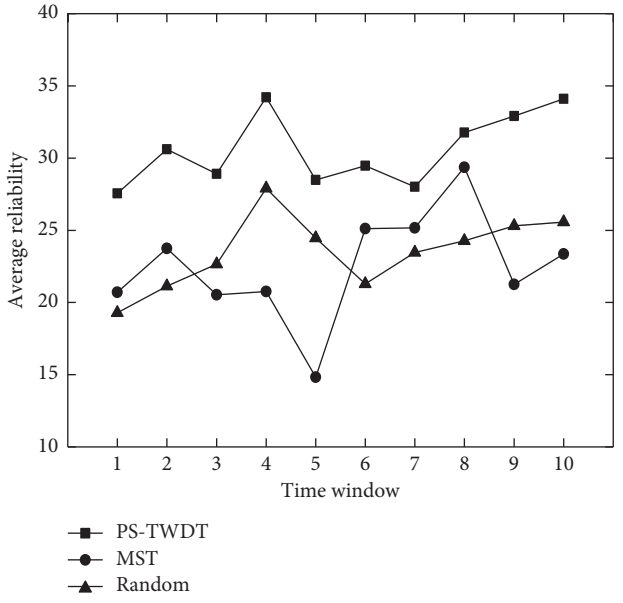

Figure 7: Average data reliability.

(3) Trust State Feedback Value. The calculation method of the trust state feedback value is obtained by comparing the trust status of participants in the task with the average trust status of other selected participants in the task, as shown in (11). r_i^k represents the trust state feedback value obtained after the participant u_i participated in the *k-th* time window. The higher the willingness and data quality of participant u_i are, the more accurate and reliable the perception task is, and the higher the feedback value of trust state is. In addition, the trust state is inversely proportional to the reward received by the participants. The higher the reward received by the participants, the higher the cost of data collection by the platform, which is not conducive to the completion of perception tasks. At this time, the trust state is lower.

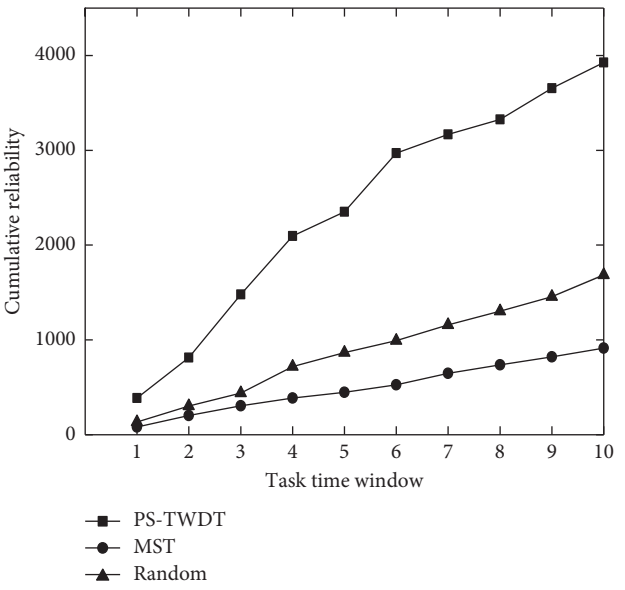

Figure 8: Cumulative data reliability.

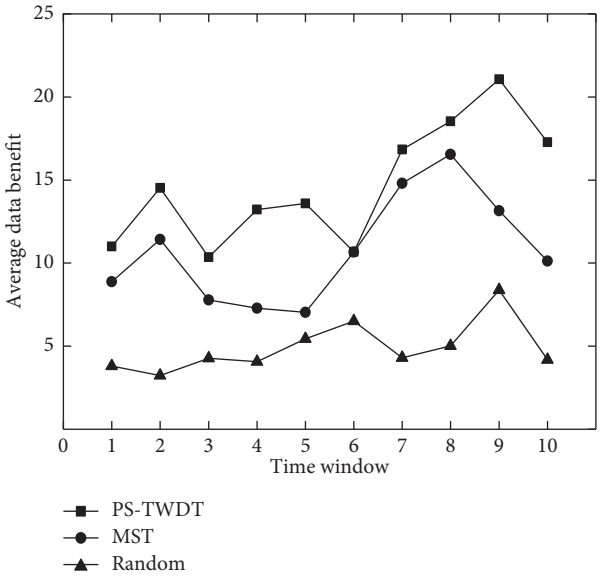

Figure 9: Average data benefit.

$$r_i^k = \log_2\left(\frac{w_i^k + q_i^k}{c_i^k} + 1\right) - \log_2\left(\sum \frac{w_i^k + q_i^k}{c_i^k} + 1\right). \quad (11)$$

(4) Credit Value Update. At the end of each task time window, the platform updates the current credit value of the participant according to the trust status feedback value of the participant in this time window, as shown in (12) [31], and the updated credit value will be the credit value of the participant participating in the next time window.

$$r_i = \frac{1}{\pi}\arctan\left(r_i + r_i^k\right) + \frac{1}{2}. \quad (12)$$

In this paper, data reliability parameters are defined according to the sensing data quantity and credit value of

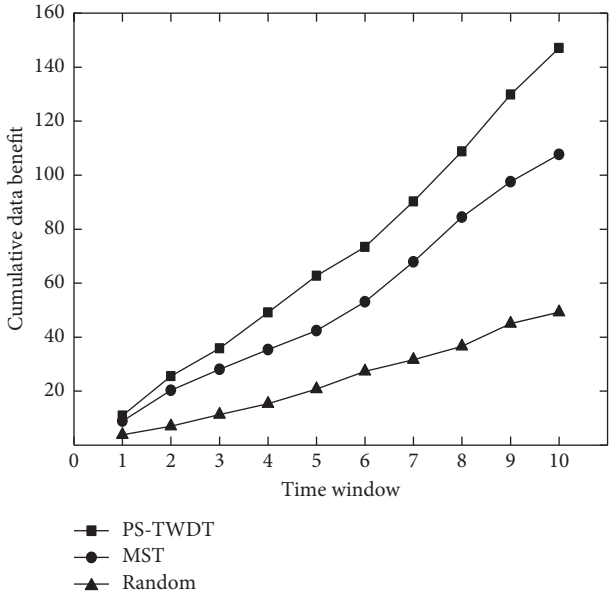

Figure 10: Cumulative data benefit.

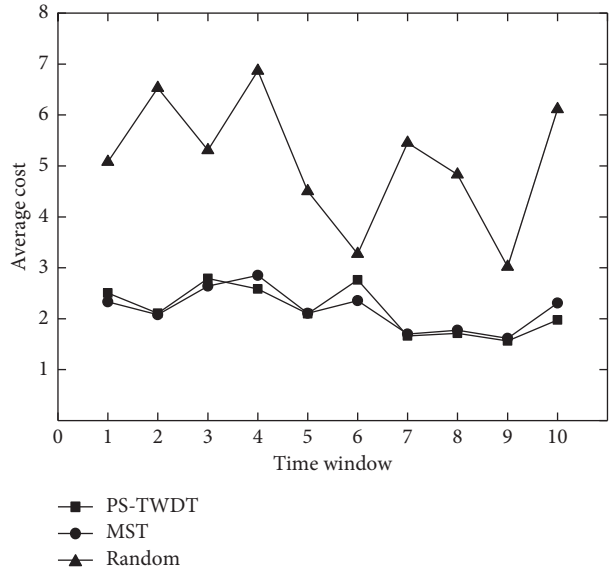

Figure 11: Average data cost.

participants when they participate in tasks. The goal of this paper is to ensure that the sensing time of the selected participants in each task time window continuously covers the time window, and maximize the data benefit in each time window. Finally, the compensation is paid according to the bid price of the selected participants. The pseudocode selected by the participants is shown in Algorithm 2, and the detailed description is as follows:

(1) Initialize participant set U, corresponding to participation time window, bid price, battery of the mobile phone, and credit value.

(2) Calculate the sensing data quantity and sensing data reliability of participants.

(3) Sort all participants incrementally by end time.

(4) Use dynamic programming algorithm to select the participant set S with the greatest data benefit.

(5) Calculate data benefit V.

(6) Reward participants according to their bid price

(7) End of the algorithm, and return to the selected participant set S and data benefit V.

5. Performance Evaluation

5.1. PJIM and PS-TWDT Experimental Settings. In this paper, we propose an incentive mechanism based on the specific division of the time period of the sensing task. Considering the time period reported by the mobile participants, we use the dynamic programming algorithm to select the participants, and carry out different incentive mechanisms for the participants in different time periods. In order to verify the effectiveness of the mechanism proposed in this paper, simulation experiments are carried out in MATLAB R2016a experimental environment, and the results are compared and analyzed. At the same time, in order to verify the effectiveness of the participant selection mechanism proposed in this paper, the experimental results are compared with MST [30] and random participant selection (Random) in terms of data reliability, data benefit, and sensing cost.

Here is the random participant selection method. In this paper, the length of a time window of the task is set to 12 hours. There are 100 participants in each time window of the task. For example, if the task is from 0 o'clock to 12 o'clock, then the selected participants need to cover this time when performing the task. Thus, the random selection method will sort all the participants by their starting time incrementally. Then select the participants from 0 o'clock. For the sake of understanding, let us assume that there are three participants. The first participant reported that the task was performed from 0 o'clock to 2 o'clock. The second participant reported that the task was performed from 1 o'clock to 3 o'clock. The third participant reported that the task was performed from 2 o'clock to 4 o'clock. When choosing one of the three participants at random, you must cover the time point of 0 o'clock. Suppose you pick the first person at random. Thus, the end time for the first person is 2 o'clock. Next, when you select participants, you need to include 2 o'clock and so on, covering directly up to 12 o'clock, until the selection process is complete.

In order to verify the effectiveness of PJIM mechanism, m participants were simulated in MATLAB experimental environment. Because the participants in the crowdsensing are nonprofessionals, the process of sensing data is very random. In order to simulate the actual sensing task, this paper assumes that the bid price of participants is a random value obtained from the uniform distribution of [1, 10], and the private target threshold of each participant is also a random value obtained from the uniform distribution of [1, 10]. Then verify the effectiveness of PS-TWDT. Suppose that the task publisher requires collecting the data of the air quality in a region from 6:00 to 18:00 for ten consecutive

days. In order to simulate the actual sensing task, this paper sets a time window of 12 hours and executes 10 time windows continuously. The candidate number of participants is 100. Randomly set the sensing time reported by the participants, and the bid price of the participants is subject to the uniform distribution on the interval [1, 10]. The electric power of participants' equipment is subject to the uniform distribution on [1, 100], and the timeliness, completeness, accuracy, and value of participants are subject to the uniform distribution on [0, 1].

5.2. Experimental Results

5.2.1. Number of People in Backup Set at Night. Set task time $T = 12$ and task quantity as 1. When the number of mobile participants u and task price pool change, this will affect the number of backup participants at night. As the number of mobile participants increases from 10 to 60, the number of corresponding night backup sets increases. This is because when the number of mobile participants increases, the private target threshold of mobile participants will also increase. For the same price pool, more participants will participate in the sensing task. At the same time, when the number of participants remains the same, the price pool increases, and the corresponding number of night backup sets increases. This is because when the number of participants remains the same, the price pool amount increases cumulatively, which gradually meets the private target threshold of participants, so the number of nighttime backup sets increases as shown in Figure 3.

5.2.2. Price Pool Reward. Set task time $T = 12$ and task quantity as 1. When the number of mobile participants u and sensing task days change, the price pool amount will be affected. As the number of days of unfinished tasks increases, the price pool amount increases. This is because the initial amount of the price pool is small at the beginning of the task release. With the increase of time, the amount of the price pool gradually accumulates. When the number of unfinished tasks increases gradually, the price pool amount will meet the private target threshold of all participants. As the number of participants in the sensing task increases from 30 to 60, the price pool amount generally decreases as shown in Figure 4.

5.2.3. Night Participants' Compensation and Day Participants' Compensation. Figure 5 shows the change in rewards given to night and day participants as the number of mobile participants increases. It can be seen from the figure that the payment for night participants is significantly higher than that for day participants. This is because participants are compensated for participating in tasks during the nighttime period to attract more participants. The average payment for night participants is 17.2067, while the average payment for day participants is 12.

5.2.4. Ratio of the Number of People in the Backup Set at Night to the Total Number of People. Figure 6 shows the change in the ratio of the number of night backup participants to the total number of participants as the number of days of unfinished tasks increases. It can be seen from the figure that, with the increase of the number of days of unfinished tasks, the price pool reward will increase, which will meet the private target threshold of more people. Finally, the ratio of the number of people in the nighttime backup set to the total number of people will reach 1.

5.2.5. Data Reliability. In terms of verifying data reliability, two trend charts of data reliability in Figures 7 and 8 are obtained as the number of task time windows increases. In Figure 7, the ordinate is the average data reliability of the selected participants in a single time window. In the figure, it can be clearly seen that as the number of time windows for task execution increases from 1 to 10, the proposed PS-TWDT selection method is superior to MST and Random in terms of average data reliability in each time window. This is because the data reliability of participants should be fully considered in the selection process of the proposed algorithm. In each time window, participants with high data reliability are selected based on dynamic programming algorithm. In Figure 8, the ordinate is the cumulative data reliability of the selected participants in a single time window. As the number of time windows for task execution increases from 1 to 10, the cumulative increase speed of the PS-TWDT selection method proposed in this paper is significantly faster than the other two selection methods in terms of the total data reliability.

5.2.6. Data Benefit. In terms of data benefits, two trend charts of data benefits in Figures 9 and 10 were obtained as the number of task time windows increased. In Figure 9, the ordinate is the average data benefit of the selected participants in a single time window. As the number of time windows for task execution increases from 1 to 10, although the average data benefit of PS-TWDT selection method proposed in this paper fluctuates greatly, the average data benefit in each time window is better than MST and Random. Because the trust state update mechanism is added to PS-TWDT, each participant selected in the continuous execution task has a high credit value and high data reliability. And due to the dynamic programming algorithm adopted, the ratio between the total reliability selected in each time window and the sum of bid price is the largest, so the data benefit of the last selected participant is the highest. In Figure 10, the ordinate is the cumulative data benefit of the selected participants in a single time window. As the number of task execution time windows increases from 1 to 10, the cumulative growth rate of the PS-TWDT selection method proposed in this paper is significantly faster than the other two selection methods in terms of data benefit, and the gap is gradually increasing.

5.2.7. The Average Cost. In terms of the average data cost, the change trend chart of the average data cost with the increase of the number of task time windows is obtained in Figure 11, in which the ordinate is the average cost of the selected participants in a single time window. As the number of time windows for task execution increases from 1 to 10, we can see that the average data cost of PS-TWDT and MST proposed in this paper is not much different and much lower than that of Random method. This is because, in the process of selecting participants, both the participant selection mechanism and MST proposed in this paper adopt the dynamic programming algorithms, which take the bid price into account when selecting participants, while the Random method does not take the bid price into account; its average data cost is higher than the other two methods, and its fluctuation range is the largest.

6. Conclusions

In the crowdsensing problem that the sensing task depends on the time period, this paper divides the specific time and then proposes an incentive mechanism, PJIM, which gives different rewards to participants in different time periods, setting additional rewards and price pools to attract participants to participate in a smaller number of sensing time periods. Finally, the simulation results show that the incentive mechanism has a higher reward for the time period with a small number of participants and can attract more participants to participate in the sensing task. When selecting participants, this paper proposes a participant selection mechanism, PS-TWDT, to solve the time window related participant selection problem in mobile crowdsensing. Some of the participants' own factors are taken into consideration in the selection, and, at the same time, the credit value updating mechanism is introduced, which can dynamically update the credit value of the participants after each task is performed, thus improving the reliability and data efficiency of the collected data.

Data Availability

No data were used to support this study.

Conflicts of Interest

The authors declare that they have no conflicts of interest.

Acknowledgments

This work was supported by the Natural Science Foundation of Tianjin under Grant no. 19JCYBJC15400, the Program for the Science and Technology Plans of Tianjin, China, under Grant 19JCTPJC48300, and the National Natural Science Foundation of China under Grant 61702366.

References

[1] W. Z. Khan, Y. Xiang, M. Y. Aalsalem, and Q. Arshad, "Mobile phone sensing systems: a survey," *IEEE Communications Surveys & Tutorials*, vol. 15, no. 1, pp. 402–427, 2013.

[2] Z. Wang, C. Xia, Z. Chen et al., "Epidemic propagation with positive and negative preventive information in multiplex networks," *IEEE Transactions on Cybernetics*, vol. 23, pp. 1–9.

[3] C. Xia, Z. Wang, C. Zheng et al., "A new coupled disease-awareness spreading model with mass media on multiplex networks," *Information Sciences*, vol. 34, pp. 185–200, 2019.

[4] Z. Wang, Q. Guo, S. Sun, and C. Xia, "The impact of awareness diffusion on SIR-like epidemics in multiplex networks," *Applied Mathematics and Computation*, vol. 349, pp. 134–147, 2019.

[5] N. Lane, E. Miluzzo, H. Lu, D. Peebles, T. Choudhury, and A. Campbell, "A survey of mobile phone sensing," *IEEE Communications Magazine*, vol. 48, no. 9, pp. 140–150, 2010.

[6] Z. Duan, W. Li, and Z. Cai, "Distributed auctions for task assignment and scheduling in mobile crowdsensing systems," in *Proceedings of the IEEE International Conference on Distributed Computing Systems*, pp. 635–644, Atlanta, GA, USA, June 2017.

[7] Y. Wang, Z. Cai, G. Yin, Y. Gao, X. Tong, and G. Wu, "An incentive mechanism with privacy protection in mobile crowdsourcing systems," *Computer Networks*, vol. 102, pp. 157–171, 2016.

[8] Z. Duan, M. Yan, Z. Cai, X. Wang, M. Han, and Y. Li, "Truthful incentive mechanisms for social cost minimization in mobile crowdsourcing systems," *Sensors*, vol. 16, no. 4, p. 481, 2016.

[9] L. Zhang, X. Wang, J. Lu, P. Li, and Z. Cai, "An efficient privacy preserving data aggregation approach for mobile sensing," *Security and Communication Networks*, vol. 9, no. 16, pp. 3844–3853, Jul.2016.

[10] B. Zhao, S. Tang, X. Liu et al., "PACE: privacy-preserving and quality-aware incentive mechanism for mobile crowdsensing," *IEEE Transactions on Mobile Computing*, vol. 34, 2020.

[11] J. Nie, J. Luo, Z. Xiong, D. Niyato, and P. Wang, "A Stackelberg game approach toward socially-aware incentive mechanisms for mobile crowdsensing," *IEEE Transactions on Wireless Communications*, vol. 18, no. 1, pp. 724–738, 2019.

[12] H. Wang, C. Liu, Y. Wang, and D. Sun, "A novel incentive mechanism based on reputation and trust for mobile crowd sensing network," in *Proceedings of the International Conference on Control, Automation and Information Sciences*, pp. 526–530, Hangzhou, China, 2018.

[13] S. Zhong, D. Tao, H. Luo, M. S. Obaidat, and T. Wu, "Staged incentive mechanism for mobile crowd sensing," in *Proceedings of the IEEE International Conference on Communications (ICC)*, pp. 1–5, Kansas City, MO, USA, March 2018.

[14] X. Chen, Y. Zhao, Z. Li, and Y. Chen, "Incentive mechanism design based on stochastic game for multi-modality crowd sensing," in *Proceedings of the IEEE International Conference on Smart Internet of Things (IEEE SmartIoT 2018)*, pp. 222–228, Xi'an, China, August 2018.

[15] D. Yang, G. Xue, X. Fang, and J. Tang, "Incentive mechanisms for crowdsensing: crowdsourcing with smartphones," *IEEE/ACM Transactions on Networking*, vol. 24, no. 3, pp. 1732–1744, Jun.2016.

[16] X. Zhang, Z. Yang, Z. Zhou, H. Cai, L. Chen, and X. Li, "Free market of crowdsourcing: incentive mechanism design for mobile sensing," *IEEE Transactions on Parallel and Distributed Systems*, vol. 25, no. 12, pp. 3190–3200, 2014.

[17] Z. Feng, Y. Zhu, Q. Zhang, L. M. Ni, and A. V. Vasilakos, "TRAC: truthful auction for location-aware collaborative sensing in mobile crowdsourcing," in *Proceedings of the IEEE INFOCOM 2019 - IEEE Conference on Computer Communications*, pp. 1231–1239, Toronto, ON, USA, 2014.

[18] M. Li, J. Lin, D. Yang, D. Xue, and J. Tang, "QUAC: quality-aware contract-based incentive mechanisms for crowdsensing," in *Proceedings of the 14th IEEE International Conference on Mobile Ad hoc and Sensor Systems (MASS)*, pp. 72–80, Orlando, FL, USA, October 2017.

[19] Y. Zhan, Y. Xia, J. Zhang, and Y. Wang, "Incentive mechanism design in mobile opportunistic data collection with time sensitivity," *IEEE Internet of Things Journal*, vol. 5, no. 1, pp. 246–256, Feb.2018.

[20] J. Lin, D. Yang, M. Li, J. Xu, and G. Xue, "Frameworks for privacy-preserving mobile crowdsensing incentive mechanisms," *IEEE Transactions on Mobile Computing*, vol. 17, no. 8, pp. 1851–1864, 2018.

[21] H. Li, T. Li, W. Wang, and Y. Wang, "Dynamic participant selection for large-scale mobile crowd sensing," *IEEE Transactions on Mobile Computing*, vol. 18, no. 12, pp. 2842–2855, 2019.

[22] M. E. Barachi, A. Lo, S. S. Mathew, and K. Afsari, "A novel quality and reliability-based approach for participants' selection in mobile crowdsensing," *IEEE Access*, vol. 7, pp. 30768–30791, 2019.

[23] J. Yang, P. Li, and J. Yan, "MCS data collection mechanism for participants'reputation awareness," *Chinese Journal of Engineering*, vol. 39, no. 12, pp. 1922–1934, 2017.

[24] H. Xiong, D. Zhang, L. Wang et al., "CrowdRecruiter: selecting participants for piggyback crowdsensing under probabilistic coverage constraint," in *Proceedings of the 2014 ACM International Joint Conference on Pervasive and Ubiquitous Computing*, pp. 703–714, Berlin, Germany, 2014.

[25] B. Guo, H. Chen, Q. Han, Z. Yu, D. Zhang, and Y. Wang, "Worker-contributed data utility measurement for visual crowdsensing systems," *IEEE Transactions on Mobile Computing*, vol. 16, no. 8, pp. 2379–2391, 2017.

[26] C. H. Liu, B. Zhang, X. Su, J. Ma, W. Wang, and K. K. Leung, "Energy-aware participant selection for smartphone-enabled mobile crowd sensing," *IEEE Systems Journal*, vol. 11, no. 3, pp. 1435–1446, 2017.

[27] T. Li, T. Jung, H. Li et al., "Scalable privacy-preserving participant selection in mobile crowd sensing," in *Proceedings of the 2019 IEEE International Conference on Pervasive Computing and Communications (PerCom)*, Kyoto, Japan, March 2019.

[28] Y. Xu, J. Tao, Y. Gao, and L. Zeng, "Location-aware worker selection for mobile opportunistic crowdsensing in VANETs," in *Proceedings of the IEEE Global Communications Conference (GLOBECOM)*, Abu Dhabi, UAE, December 2017.

[29] Y. Sun, "Game theory based strategic decision making of participants in participatory sensing systems," 2015.

[30] J. Xu, J. Xiang, and D. Yang, "Incentive mechanisms for time window dependent tasks in mobile crowdsensing," *IEEE Transactions on Wireless Communications*, vol. 14, no. 11, pp. 6353–6364, 2015.

[31] J. Champaign, R. Cohen, J. Zhang et al., "The validation of an annotations approach to peer tutoring through simulation incorporating the modeling of reputation," 2011.

Hindawi
Discrete Dynamics in Nature and Society
Volume 2020, Article ID 7498605, 8 pages
https://doi.org/10.1155/2020/7498605

Research Article

Complex Network Filtering and Compression Algorithm Based on Triangle-Subgraph

Shuxia Ren, Tao Wu, and Shubo Zhang

Department of Computer Science and Software Engineering, Tianjin Polytechnic University, Tianjin 300387, China

Correspondence should be addressed to Shuxia Ren; t_rsx@126.com

Received 21 March 2020; Accepted 9 May 2020; Published 1 June 2020

Guest Editor: Hao Shen

Compressing the data of a complex network is important for visualization. Based on the triangle-subgraph structure in complex networks, complex network filtering compression algorithm based on the triangle-subgraph is proposed. The algorithm starts from the edge, lists nodes of the edge and their common node sets to form a triangle-subgraph set, parses the triangle-subgraph set, and constructs new complex network to complete compression. Before calculating the set of triangle-subgraph, node importance ranking algorithm is proposed to extract high- and low-importance nodes and filter them to reduce computational scale of complex networks. Experimental results show that filtering compression algorithm can not only improve the compression rate but also retain information of the original network at the same time; sorting result analysis and SIR model analysis show that the sorting result of node importance sorting algorithm has accuracy and rationality.

1. Introduction

Some networks contain millions or even billions of nodes and edges bringing new challenges to understand and analyse complex networks. Without compression, points and edges presented will be very dense, and it is difficult for people to obtain useful information from the network.

Scholars began to pay attention to the compression field of complex networks [1] and designed many methods to compress complex networks. Gilbert [2] proposed an algorithm for node compression based on the node importance evaluation index, which achieves the purpose of compressing the network by deleting noncritical nodes and edges. The disadvantage is the use of keep-one and keep-all strategies to supplement important nodes and edges, which costs much time. Yan and Zhang[3] and others are inspired by centrality that can stress important nodes. Five compression schemes are proposed from five aspects: random centrality, degree centrality, relative node importance, PageRank, and intermediate centrality. The disadvantage is that node and edge are deleted and new network is not considered to supplement, resulting in the loss of network information. Zhang et al. [4] proposed a bound_tri algorithm based on the triangle structure. The algorithm starts from nodes and compresses the network by constructing triangle set. The disadvantage is that the need to access the adjacency matrix and adjacency list at same time leads to high-time complexity, and bound_tri algorithm takes degree as the selection criterion, which does not conform to the actual situation of the network.

The abovementioned algorithm mainly starts from node and uses ways of deleting and merging nodes to realize the compression of a complex network. Based on edge, the paper proposes complex network filtering and compression algorithm based on the triangle-subgraph. In order to shorten compression time and improve compression efficiency, before calculating the triangle-subgraph set, the paper proposes node influence as a global importance measure and proposes node importance sorting algorithm NRSA (Node Rank Select) based on LeaderRank algorithm [5] to extract high- and low-importance nodes and filter them to reduce size of complex networks that need to be calculated. The experimental results show that important node ranking results of NRSA algorithm are better than other sorting algorithms, and compression algorithm improves compression efficiency, and retains most of the information of the original network.

2. NRSA Algorithm

In LeaderRank algorithm, the probability of jumping to an adjacent node is calculated by the degree of each node. The way of calculation only considers partial importance of the node, ignoring global importance in the entire network.

It can be seen from Figure 1 that node 4 has more neighboring nodes than node 7, and the LR value assigned to node 4 with each of the iterations by LeaderRank algorithm is more than node 7. Therefore, the result of the LeaderRank algorithm is that node 4 is more important than node 7. However, from the structure of the network, node 7 acts as an intermediate node connecting three different node groups, which should be the most important in the entire network structure. In order to comprehensively consider partial importance and global importance of nodes, adjacent-degree is used to construct influence of nodes as the global importance.

Definition 1. Adjacent-degree: v_i is the node in the network G; adjacent-degree is the sum of the degrees of all adjacent nodes, recorded as AdjDe.

$$\mathrm{AdjDe}(v_i) = \sum \mathrm{De}(v_j). \tag{1}$$

Definition 2. Node influence: the node influence of v_i is sum of the adjacent-degree of v_i and degree of v_i. It is recorded as Node_In (v_i).

$$\mathrm{Node\_In}(v_i) = \mathrm{AdjDe}(v_i) + \mathrm{De}(v_i). \tag{2}$$

Definition 3. Node rank: the formula for calculating the NR_i of node v_i is as follows:

$$\mathrm{NR}_i = \mathrm{LR}_i \sum_{j \in a_i} \frac{\mathrm{Node\_In}(v_j)}{\mathrm{Node\_In}(v_i)} \mathrm{LR}_j. \tag{3}$$

Equation 3 shows (1) a_i is the adjacent node connected to node v_i. The more the number of adjacent nodes, the higher the NR value of node v_i, which satisfies intuitive judgment. (2) The greater the node influence of node v_j, the more the LR value of v_j obtained by $v_i.v_i$ is more important in the network structure.

The steps of NRSA algorithm are as follows:

(1) The LR value of the complex network's node is calculated using LeaderRank algorithm

(2) The adjacent-degree of node v_i is calculated using equations (1) and (2), and the node influence Node_Ef (v_i) is obtained

(3) Using equation (3), the LR_i value and Node_Ef (v_i) are calculated to obtain NR_i, and the result is mapped to the [0, 1] interval using deviation standardization

3. Complex Network Filtering and Compression Algorithm Based on Triangle-Subgraph

3.1. Triangle-Subgraph. Triangle-subgraph [6] is a special 3-connected subgraph in a graph data-connected subgraph. In a complex network G = (V, E), $T_\triangle = (v_\triangle, e_\triangle)$ can represent a triangle-subgraph with three nodes and three edges:

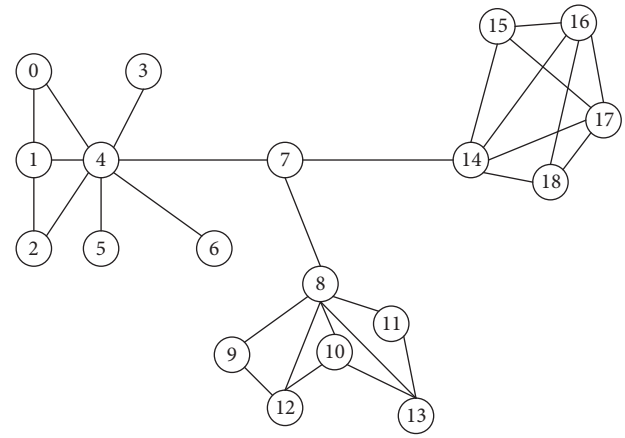

Figure 1: Simple undirected network.

$$\begin{aligned} T_\triangle &= (v_\triangle, e_\triangle) = T_\triangle < a, b, c \geq \{v_\triangle = \{a, b, c\} \subset v, \\ e_\triangle &= \{(a, b), (a, c), (b, c) \subset e\}\}. \end{aligned} \tag{4}$$

For G with e edges, time required to calculate the triangle-subgraph is $o(e^{3/2})$ [7], indicating that the triangle-subgraph can be calculated within certain time.

3.2. List Triangle-Subgraph. The traditional method of listing a triangle-subgraph is node compression algorithm [8]. The algorithm proposed in paper is an edge compression algorithm. First, an edge is randomly selected from the complex network, and then the adjacency list of two nodes connected to the edge is searched to check whether they have a common adjacent node, and finally they are combined with a common adjacent node to form a triangle-subgraph set. For example, the selected edge is (a, b), and the adjacency list of nodes connected to the edge is $\mathrm{Adj}(a) = \{w, h, m, n\}$ and $\mathrm{Adj}(b) = \{w, h, m, n, l, d\}$. The common adjacent nodes of node a and b are $\mathrm{Adj}(a) \cap \mathrm{Adj}(b) = \{w, h, m, n\}$. The set of all triangle-subgraphs for edges (a, b) is $< \mathrm{a, w, b} >$, $< a, h, b >$, $< a, m, b >$, $< a, n, b >$.

3.3. Triangle-Subgraph Compression Algorithm with Filtering Property. From the complex network real dataset Polblogs and Youtube's node importance value statistics chart, Figure 2 shows that two graphs have an important feature, that is, the value distribution of node importance in complex network is very uneven. Moreover, there are very few common adjacent nodes that can be contained between high-importance and low-importance nodes. But, looking for a triangle-subgraph between high-importance and low-importance nodes consumes much computing resources. Therefore, before calculating the triangle-subgraph, the method of filtering out high- and low-importance nodes is used to reduce the data size in the complex network.

We propose and define the triangle-subgraph compression algorithm with filtering properties as the NIIET (node importance in edge triangle) algorithm. NIIET

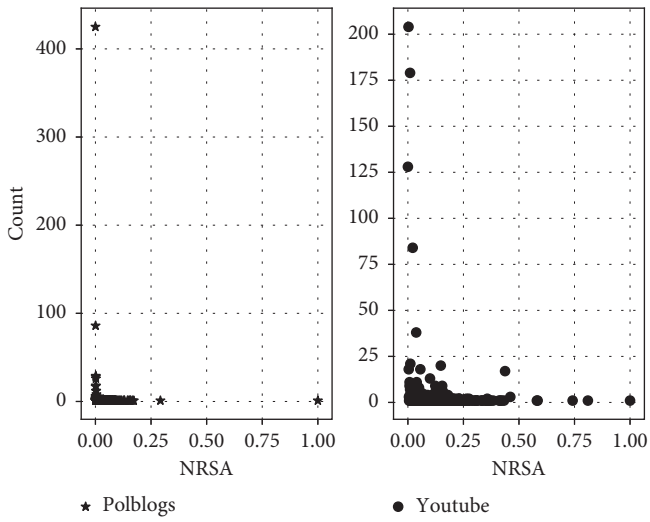

Figure 2: Node importance statistics of real dataset.

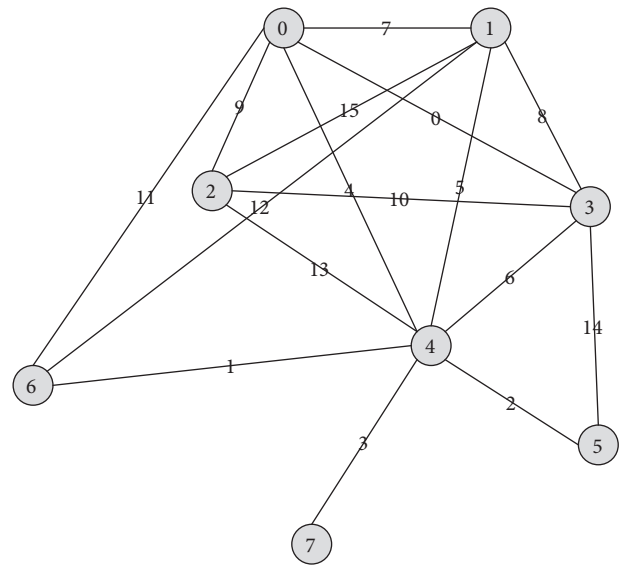

Figure 3: The original network.

algorithm only needs to access the adjacency list of the complex network when compressing complex networks. The adjacency list contains the directionality of edge, so it can be applied to compression of a directed graph and undirected graph.

Figure 3 is a simple undirected network diagram containing 16 edges and 8 nodes. The results obtained by the edge compression algorithm are shown in Table 1. It can get a triangle-subgraph set with 42 triangles, which will result in 27 edge redundancy. If storing edge of triangle-subgraph requires 2 units, then 54 units of redundancy will store. Therefore, by filtering out high- and low-importance nodes, redundancy of the triangle subgraph set and compression efficiency are reduced.

First, the importance of the nodes calculated by the NRSA algorithm is shown in Table 2. Next, set the low importance node standard low_percent = 15% and the high importance node standard high_percent = 85%. The low importance node is node 7, and the high importance node is node 4. Finally, when listing a triangle-subgraph, the information containing node 7 and node 4 is filtered from the adjacency list of other nodes. The network after filtering the high- and low-importance nodes is shown in Figure 4. The calculation results are shown in Table 3. There are only 15 triangle-subgraphs, and the triangle subgraph set contains only 7 redundant edges. The results show that a complex network with a high compression rate can be obtained by filtering the low- and high-importance nodes.

Table 1: Number of triangle-subgraph sets in the original network.

E	Num	E	Num	E	Num	E	Num
0	3	4	4	8	3	12	2
1	2	5	4	9	3	13	3
2	1	6	4	10	3	14	1
3	0	7	4	11	2	15	3

Table 2: Node importance table of the original network.

Node	NRSA	Node	NRSA
4	1.0	2	0.63003303870
0	0.77232674038	6	0.42442432758
1	0.77232674038	5	0.19582840067
3	0.76363255124	7	0.0

3.4. The Steps of NIIET Algorithm

Input: Complex network $G(V, E)$, Adjacency list AdjG.

Output: Complex network $G'(V', E')$, triangle-subgraph set *trangle_list*.

(1) Input complex network $G(V, E)$, and calculate value of node by using NRSA algorithm;

(2) Set percentage of low_percent and high_percent;

(3) According to percentage, the low importance node set low_nodelist and the high importance node set high_nodelist are obtained;

(4) Traversing the edge E. If node v_i and v_j at both ends of the edge are located in low_nodelist or high_nodelist, the information of two nodes is filtered out from the adjacency list of v_i and v_j connected nodes;

(5) Traversing edge E. If $\mathrm{AdjG}(v_i)$ and $\mathrm{AdjG}(v_i)$ intersect, triangle-subgraph set trangle_list consists of nodes v_i and v_j and their common node set;

(6) Parse the triangle-subgraph set trangle_list, construct new complex network $G'(V', E')$;

(7) Output $G'(V', E')$, triangle-subgraph set trangle_list.

4. Experimental Analysis

The paper analyses the node importance experiment and the compression experiment, respectively, and selects Zachary

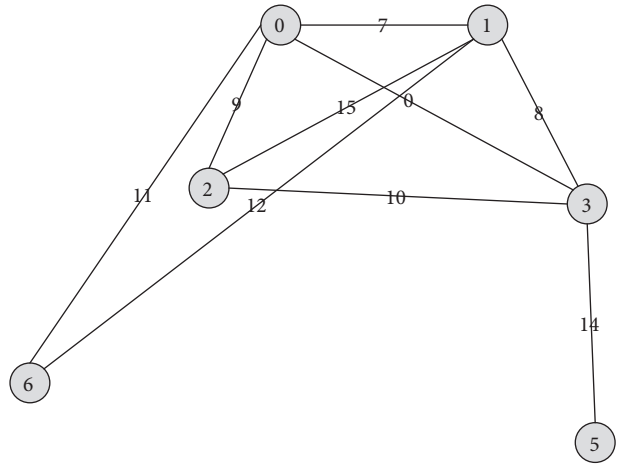

Figure 4: Filter network after high- and low-importance nodes.

Table 3: Number of triangle-subgraph sets of the complex network after filtering.

E	Num	E	Num	E	Num	E	Num
0	2	4	0	8	2	12	1
1	0	5	0	9	2	13	0
2	0	6	0	10	2	14	0
3	0	7	3	11	1	15	2

[9], Football [10], Neural [10], Netscience [11], Polblogs [12], and Youtube [13] to conduct experiments.

4.1. Node Importance Analysis. To further prove the rationality of the NRSA algorithm, the SIR model [14] is used to propagate the node importance ranking results of PageRank, LeaderRank, and NRSA algorithms in the neural network. The change of lin was mainly observed as the ratio of the number of nodes in the I(infected) state in the SIR model to the total number of nodes in the network. Top 10% nodes and top 20% of NRSA algorithm, LeaderRank, and PageRank algorithm are selected as infected nodes for propagation. The results of infection experiments of the neural network are shown in Figure 5.

As can be seen from Figures 5(a)~5(b), the highest value of lin of NRSA algorithm exceeds the LeaderRank algorithm, and both are close to 0.8. It is indicated that the node selected by the NRSA algorithm propagates in the same time step to higher depth than LeaderRank. From the time step mentioned above, the lin value of the two algorithms does not differ much between the 5 and 40 time steps. However, it can be seen from the 5–10 period that the slope of the NRSA algorithm is higher than that of the latter, indicating that the node selected by the NRSA algorithm has faster propagation speed than the LeaderRank algorithm. In general, the nodes selected by the NRSA algorithm are more reasonable than those selected by LeaderRank. Similarly, from the comparison of NRSA and PageRank algorithms in Figures 5(c)~5(d), the NRSA algorithm is better than the PageRank algorithm.

4.2. Compression Experiment Analysis. The compression experiment analysis is mainly carried out from the two parts of node selection and compression. Since NIIET algorithm uses filtering to reduce the computational scale, the selection of nodes with low and high importance will affect compression results of complex networks. Therefore, it is necessary to analyse the influence of high- and low-importance node selection criteria on compression results. At the same time, NIIET algorithm and bound_tri [4], edge_iterator_hash [15], and node_iterator [8] are used to analyse compression efficiency from the aspects of compression rate [16], compression time, and rate of information retention [17].

4.2.1. Analysis of Influence of Node Selection Criteria on Compression Results

(1) Low-Importance Node Selection Criteria Impact. Equation (5) is used in experiment to represent the node compression ratio. The specific formula is as follows:

$$\text{Rate\_}V = 1 - \frac{|v'|}{|v|}. \tag{5}$$

In the abovementioned formula, $|v|$ and $|v'|$ indicate the number of nodes before and after compression.

In this experiment, the range of low importance node selection criterion is set to low_percent = [10%, 30%], and the relationship between the point compression ratio and low-importance node selection criterion is shown in Figure 6. It can be seen that the influence of the criterion on

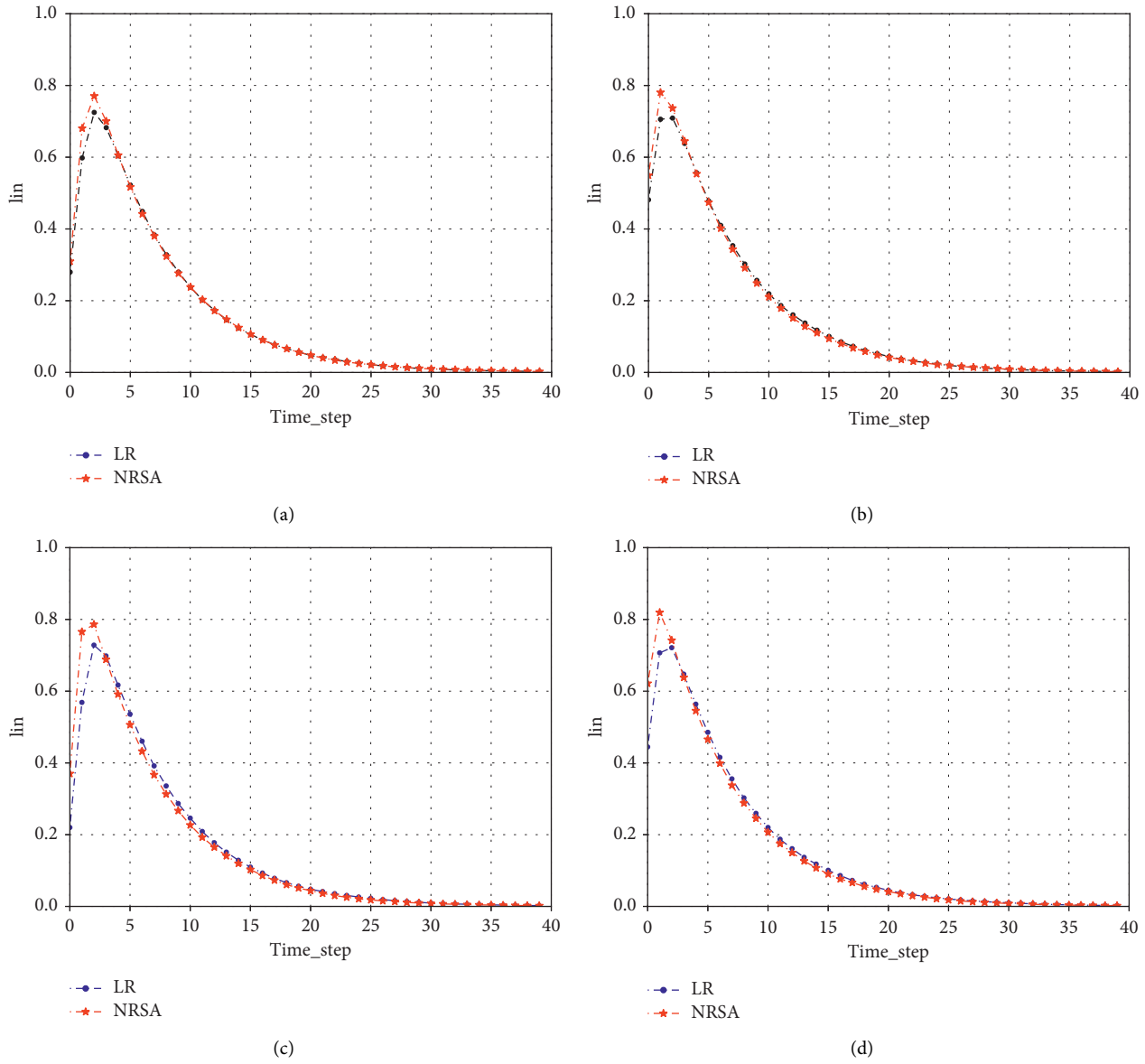

Figure 5: Comparison of neural network propagation results. (a) Top 10% comparison, (b) top 20% comparison, (c) top 10% comparison, and (d) top 20% comparison.

the point set compression rate is very small because the node of the low importance node's connection relationship with other nodes is small and cannot participate in the calculation of the triangle-subgraph. Therefore, the influence of low-importance node selection criteria on the compression ratio of complex networks can be neglected.

(2) High-Importance Node Selection Criteria Impact. As shown in Figure 7(b), the number of triangle-subgraph calculated by a complex network is also increased. However, the more the nodes and edges that need to be calculated for too many triangle-subgraphs, the longer the compression time will be. We will consider setting the filtering criterion to improve the compression efficiency and time of complex networks. Figures 7(a) and 7(b) show that the range of filter criteria is not very large when the range of the filter criteria is [75%, 85%]. At the same time, the range corresponding to Figure 7(a) is [1, 2], the compression ratios in the range are not much different, and the compression ratio is relatively stable, so that the balanced set of triangle-subgraph can be obtained.

4.2.2. Compression Efficiency Comparison Result Analysis. For the quantitative estimation of the compressed complex network, the paper uses the retention rate of the network information as the evaluation standard. At the same time, the high-importance node selection criterion of the experiment is set to high_percent = 85% and low-importance node selection criterion is low_percent = 10%. The compression effect comparison chart is shown in Figure 8.

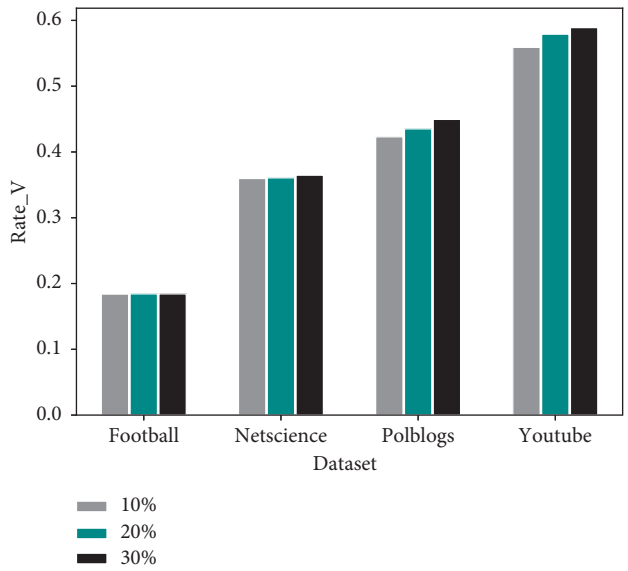

Figure 6: Different dataset points set compression ratio.

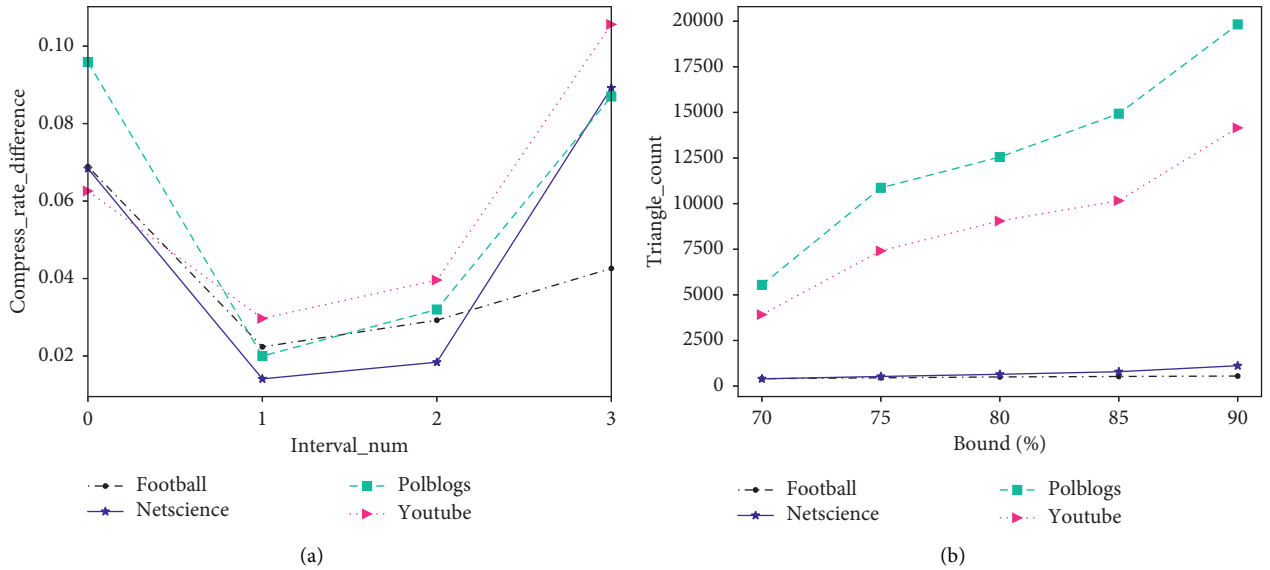

Figure 7: High-importance node selection criteria impact. (a) The difference of compression rate. (b) Number of triangle-subgraphs.

By observing Figure 8(a), from the perspective of compression ratio, as the two compression algorithms node_iterator and edge_iterator_hash require all nodes and edges in a complex network to participate in the calculation of the triangle-subgraph, compared with the first two compression algorithms, they can obtain more triangle-subgraphs, but the compression ratio is the lowest.

At the same time, NIIET algorithm is superior to the bound_tri algorithm in the compression ratio. Since bound_tri algorithm needs to access adjacency matrix of the complex network before compression to determine the edge relationship between nodes and then access and modify the adjacency list, the compression method greatly increases time complexity. Moreover, the adjacency matrix repeatedly confirms the two connected nodes, resulting in a repeated triangle-subgraph in the calculated triangle-subgraph set, which reduces the compression ratio of bound_tri algorithm.

Finally, it can be seen from Figure 8(b) that NIIET algorithm filters high- and low-importance nodes to reduce compression time and increases the compression rate, but the compressed network can still maintain 50%–70% of the network information. The quantity indicates that NIIET algorithm maintains a good effect on the amount of network information, and the compression result is reasonable and credible.

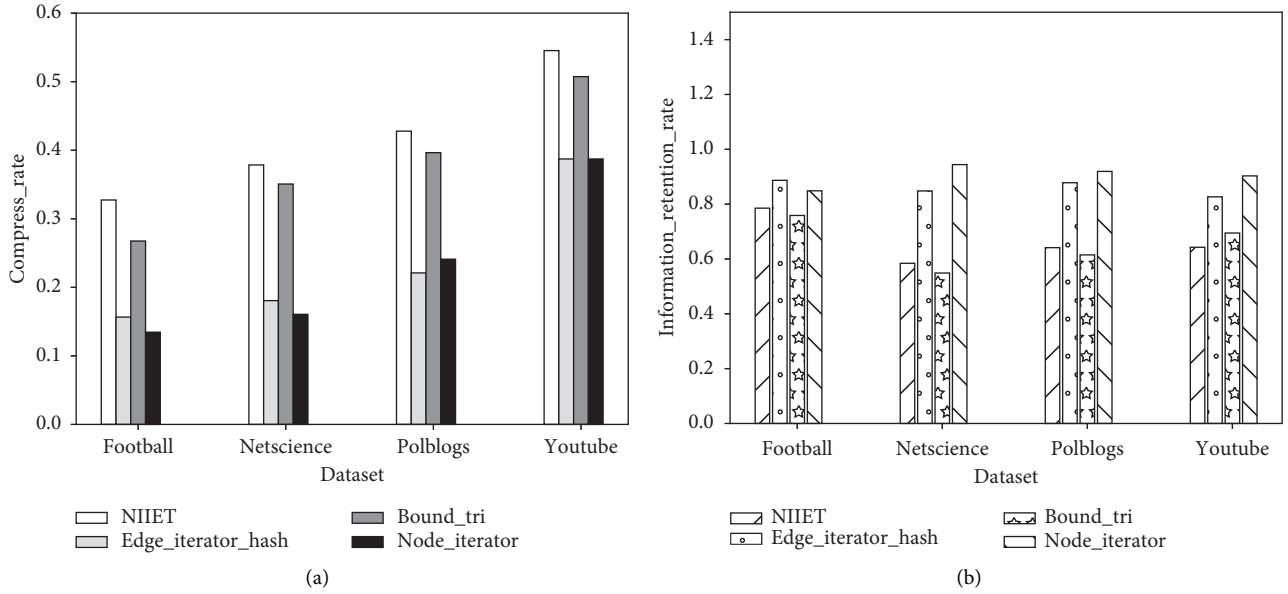

Figure 8: Comparison of the compression effect. (a) Compression rate. (b) Rate of information retention.

5. Conclusion

The paper proposes NIIET algorithm, which uses edges as iteration objects to compress complex networks by listing the triangle-subgraph. Before calculating the triangle-subgraph set, the paper proposes NRSA algorithm to calculate high- and low-importance nodes. The size of the adjacency list is reduced by filtering high-importance and low-importance nodes. The experimental results show that NRSA algorithm is reasonable. NIIET algorithm outperforms other algorithms in terms of compression rate, and the compressed network can still maintain a high amount of information, which is enough to show that compressed network retains most of structure of complex network.

In next stage of work, the paper will proceed from two aspects: (1) from the perspective of the location of the node, the influence of the node on the network function [18] to explore a new ordering method of node importance. (2) Based on the triangle-subgraph structure and other properties of complex networks, new complex network compression algorithm will proposed.

Data Availability

Data will be provided by the corresponding author upon request.

Conflicts of Interest

The authors declare that they have no conflicts of interest.

References

[1] Yu Zhang, Y.-B. Liu, G. Xiong et al., "Survey on succinct representation of graph data," *Journal of Software*, vol. 9, pp. 1937–1952, 2014.

[2] A. C. Gilbert and K. Levchenko, "Compressing network graphs," in *Proceedings of the LinkKDD Workshop at the 10th ACM Conference on KDD*, Suzhou, China, 2004.

[3] J. Yan and Z. Zhang, "Compressing big graph data: a relative node importance approach," in *Proceedings of the 2017 9th International Conference on Wireless Communications and Signal Processing (WCSP)*, pp. 1–6, Nanjing, China, October 2017.

[4] L. Zhang, C. Xu, W. Qian, and A. Zhou, "Common neighbor query-friendly triangulation-based large-scale graph compression," in *Web Information Systems Engineering—WISE 2014*, pp. 234–243, Springer, Berlin, Germany, 2014.

[5] L. Wang and R. Rao, "Multi-label propagation algorithm for overlapping community detection based on LeaderRank and node similarity," *Computer Systems Applications*, vol. 27, no. 6, pp. 146–150, 2018.

[6] Z.-M. Han, C. Yan, Li Meng-Qi, L. Wen, and W.-J. Yang, "An efficient node influence metric based on triangle in complex networks," *Acta Physica Sinica*, vol. 65, no. 16, 2016.

[7] M. Latapy, "Main-memory triangle computations for very large (sparse (power-law)) graphs," *Theoretical Computer Science*, vol. 407, no. 1-3, pp. 458–473, 2008.

[8] A. Itai and M. Rodeh, "Finding a minimum circuit in a graph," *SIAM Journal on Computing*, vol. 7, no. 4, pp. 413–423, 1978.

[9] Z. Zhu, S. Lin, and K. Cui, "Network topology layout algorithm based on community detection of complex networks," *Journal of Computer-Aided Design & Computer Graphics*, vol. 23, no. 11, pp. 1808–1815, 2011.

[10] X. Zhou, L. Xiao, and H. Tinglei, "Time-varying complex network layout algorithm based on node centrality," *Systems Engineering and Electronics*, vol. 39, no. 10, pp. 2346–2352, 2017.

[11] X. Zhu, X. Zhao, and M. Liu, "Analysis of influential node based on community structure," *Application Research of Computers*, vol. 34, no. 9, pp. 2582–2585, 2017.

[12] A. Lada and G. Natalie, "The political blogosphere and the 2004 US Election," in *Proceedings of the 3rd International Workshop on Link Discovery*, pp. 36–43, New York, NY, USA, 2005.

[13] L. Tang and H. Liu, "Uncovering cross-dimension group structures in multi-dimensional networks," in *SDM Workshop on Analysis Of Dynamic Networks*, pp. 568–575, Sparks, NV, USA, 2009.

[14] Lu Wang, Q. Guo, and J. Liu, "Measuring node importance based on weighted nonlinear method," *Application Research of Computers*, vol. 5, 2018.

[15] T. Schank and D. Wagner, "Finding, counting and listing all triangles in large graphs, an experimental study," *Experimental and Efficient Algorithms*, vol. 3503, pp. 606–609, 2005.

[16] H. Li, J. Zhang, J. Yang, J. Bai, Y. Chu, and L. Zhang, "Social network compression based on the importance of the community nodes," *Acta Scientiarum Naturalium Universitatis Pekinensis*, vol. 49, no. 1, pp. 117–125, 2013.

[17] H. Chou, *Research on Complex Network Visualization Technology Based on Compression and Cluster Analysis*, Jiangsu University, Zhenjiang, China, pp. 23-24, 2017.

[18] R. Xiaolong and L. Linyuan, "Review of ranking nodes in complex networks," *Chinese Science Bulletin*, vol. 59, no. 13, p. 1175, 2014.

Hindawi
Discrete Dynamics in Nature and Society
Volume 2020, Article ID 9534392, 7 pages
https://doi.org/10.1155/2020/9534392

Research Article

Segmentation of the Fabric Pattern Based on Improved Fruit Fly Optimization Algorithm

Gang Ding,[1,2] **Xiaoyuan Pei**,[1,3] **Yang Yang**,[4] **and Boxiang Huang**[2]

[1]*School of Textiles Science and Engineering, Tian Gong University, Tianjin 300387, China*
[2]*Faculty of Technology, Tianjin Radio & TV University, Tianjin 300350, China*
[3]*Composites Research Institute, Tian Gong University, Tianjin 300387, China*
[4]*Resource R & D Center, Tianjin Radio & TV University, Tianjin 300350, China*

Correspondence should be addressed to Gang Ding; dinggang@tiangong.edu.cn

Received 14 March 2020; Accepted 27 April 2020; Published 18 May 2020

Guest Editor: Hao Shen

In order to improve the segmentation performance of the printed fabric pattern, a segmentation criterion based on the 3D maximum entropy which is optimized by an improved fruit fly optimization algorithm is designed. The triple is composed of the gray value of the pixel, the average gray values of the diagonal, and the nondiagonal pixels in the neighbourhood. According to the joint probability of the triple, the 3D entropy of the object and the background areas could be designed. The optimal segmentation threshold is resolved by maximizing the 3D entropy. A hybrid fruit fly optimization algorithm is designed to optimize the 3D entropy function. Chaos search is used to enhance the ergodicity of the fruit fly search, and the crowding degree is introduced to enhance the global searching ability. Experiment results show that the segmentation method based on maximizing the 3D entropy could improve the segmentation performance of the printed fabric pattern and the pattern information could be reserved well. The improved fruit fly algorithm has a higher optimization efficiency, and the optimization time could be reduced to 30 percent of the original algorithm.

1. Introduction

Printed fabric pattern segmentation is one of the key technologies in printing and dyeing process [1–3]. It has a direct impact on the accuracy of drawing, hemming, and cloth printing [4]. In actual production, new patterns can be formed by colouring the split pattern, so as to enrich the variety of fabric products [5–8]. At present, there are many common image segmentation methods, for example, segmentation methods based on the edge-extraction operators of Canny and Sobel and segmentation methods based on the clustering analysis of mean shift [9–12]. These methods have been widely used in practical industrial production. However, due to the complex texture structure of the fabric itself, many common image segmentation methods are not ideal in the application of printed fabric pattern segmentation [13]. For example, texture noise will lead to a large number of false edges in segmentation results based on edge extraction, leading to inaccurate segmentation. In addition, due to the spatial distribution of pixels is not fully utilized, the segmentation method based on clustering will lead to wrong segmentation in the case of lack of prior knowledge. The image segmentation method which based on maximum entropy has the advantages of simple implementation and relatively stable segmentation performance. It has been effectively applied in various image-processing fields [14–16]. However, due to the insufficient description of pixel distribution information by one-dimensional entropy, the antinoise performance is poor. Especially, in printed fabric pattern segmentation, it is easy to produce false segmentation because of it is sensitive to texture noise.

The performance of image segmentation can be improved by constructing 2D entropy which introduces the average gray value of neighbouring pixels [17, 18]. However, with the increase of information entropy dimension, the calculation of maximum entropy also increases rapidly. It

causes the calculation time of segmentation threshold to be too long. It can improve the operation speed by combining intelligent optimization algorithm to solve the maximum entropy. Intelligent optimization algorithms, such as genetic algorithm [19], ant colony algorithm [20], and fish swarm algorithm [21] can be used to solve complex functions. However, the implementation of this kind of optimization method is slightly complex, and there are many parameters to be set in the algorithm, which reduces the convenience of the algorithm. In contrast, the fruit fly algorithm has been widely used in many optimization problems because of its low complexity and small computation. However, the fruit fly algorithm is easy to be precocious and fall into local minima because of its optimization mechanism is too simple. In addition, although the 2D entropy considers the distribution information of pixels and their neighbours, the use of more detailed direction information in neighbourhood pixels is insufficient, which reduces the accuracy of feature description of target and background pixels [22]. The texture noise of the image has some influence on the segmentation result.

Compared with the 2D maximum entropy method, the 3D maximum entropy method has better segmentation quality, but the complexity of the algorithm is greatly increased. However, the calculation of entropy still uses the logarithm operation with low efficiency, so the efficiency of the algorithm still has room to rise. In order to improve the segmentation performance of the printed fabric pattern. Based on the 2D entropy of the image, 3D entropy is constructed by integrating the direction information of neighbouring pixels. Fabric pattern segmentation based on maximizing the 3D entropy criterion could improve the segmentation performance of the printed fabric pattern. An improved fruit fly optimization algorithm is designed to optimize the 3D entropy function. This method reduces the computation and increases the image edge. The optimal energy function of the entropy penalty factor is adopted to reduce the loss of effective information. With the help of image segmentation technology of the improved Drosophila optimization algorithm, fabric pattern information can be quickly extracted from the fabric image, which improves the calculation speed and design efficiency of fabric pattern segmentation. Compared with other similar algorithms, this algorithm improves the accuracy of image retrieval and preserves the fabric pattern information more completely.

2. Pattern Segmentation of 3D Maximum Entropy

The Gray binary group (i, j) is composed of the gray level of the pixel itself and the average gray level of its neighbourhood, and its frequency is expressed as f_{ij}. Thus, the 2D entropy can be calculated. According to the principle of maximum entropy, the segmentation threshold can be determined. However, the average gray value of the neighbourhood only reflects the basic spatial distribution information of the pixels, it lacks accurate direction information. Especially, the information description of image edge points is not accurate enough. Texture information mostly has the attributes of edge information. The segmentation criteria based on the 2D maximum entropy have limited ability to suppress texture noise of the fabric pattern. Therefore, considering the neighbourhood direction information, the 3D entropy is designed to realize the automatic segmentation of the fabric pattern.

Taking the 3×3 neighbourhood as an example, the gray value of the pixel point (x, y) and its neighbourhood gray value can be expressed as shown in Table 1.

According to the pixel distribution shown in Figure 1, the average gray value in the diagonal direction of the neighbourhood of the pixel (x, y) is defined as

$$g'(x, y) = \frac{1}{4}[g(x-1, y-1) + g(x+1, y+1) + g(x-1, y+1) + g(x+1, y-1)]. \tag{1}$$

The average gray value of the nondiagonal neighbourhood of a pixel (x, y) is defined as

$$g''(x, y) = \frac{1}{4}[g(x-1, y) + g(x+1, y) + g(x, y-1) + g(x, y+1)]. \tag{2}$$

Set the gray level of the image is L and the gray level of g' and g'' is L too. The gray value of each pixel, the neighbourhood diagonal average gray value, and the neighbourhood nondiagonal average gray value form a gray triple group $(i, j, \text{and } k)$. The frequency of its occurrence is recorded as f_{ijk}. Define the joint probability p_{ijk} as

$$p_{ijk} = \frac{f_{ijk}}{N}, \tag{3}$$

where N is the total number of pixels in the image. p_{ijk} can be regarded as the normalized 3D histogram in 3D space of pixel gray, neighbourhood diagonal average gray, and neighbourhood nondiagonal average gray which are composed of three-dimensional variables of i j, and k. Let the 3D variable's value of i j, and k be s, t, and r, respectively, and the 3D space schematic diagram of the triple is shown in Figure 1.

The 3D space shown in Figure 1 is divided into eight regions. There are two areas on the main diagonal which are A_{11} and A_{22}. The space range corresponding to the area A_{11} is $0 \le i < s$, $0 \le j < t$, and $0 \le k < r$. The space range corresponding to the area A_{22} is $s \le i < L$, $t \le j < L$, and $r \le k < L$. Therefore, areas A_{11} and A_{22} can be regarded as the target (or background) area and background (or target) area, respectively.

For segmentation thresholds $(s, t, \text{and } r)$, the probability of areas A_{11} and A_{22} can be expressed as

$$P_{11} = \sum_{i=0}^{s-1} \sum_{j=0}^{t-1} \sum_{k=0}^{r-1} p_{ijk},$$
$$P_{22} = \sum_{i=s}^{L-1} \sum_{j=t}^{L-1} \sum_{k=r}^{L-1} p_{ijk}. \tag{4}$$

Table 1: Pixel distribution.

$g(x-1, y-1)$	$g(x, y-1)$	$g(x+1, y-1)$
$g(x-1, y)$	$g(x, y)$	$g(x+1, y)$
$g(x-1, y+1)$	$g(x, y+1)$	$g(x+1, y+1)$

Note. $g(x, y)$ represents the gray value of the pixel point (x, y).

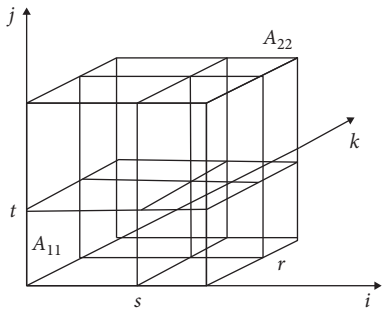

Figure 1: 3D space schematic diagram of the triple.

The entropy of A_{11} and A_{22} can be defined as

$$H_{11} = \sum_{i=0}^{s-1}\sum_{j=0}^{t-1}\sum_{k=0}^{r-1}\left(\frac{p_{ijk}}{P_{11}}\right)\ln\left(\frac{p_{ijk}}{P_{11}}\right),$$
$$H_{22} = \sum_{i=s}^{L-1}\sum_{j=t}^{L-1}\sum_{k=r}^{L-1}\left(\frac{p_{ijk}}{P_{22}}\right)\ln\left(\frac{p_{ijk}}{P_{22}}\right). \quad (5)$$

Therefore, the 3D entropy can be defined as

$$H(s, t, r) = H_{11} + H_{22}. \quad (6)$$

The threshold segmentation method based on the maximum 3D entropy is used to get the best segmentation threshold s^*, t^*, and r^*. In this way, the 3D entropy H of the target and background region of the image can be maximized.

With the increase of dimension, the computational complexity of solving the 3D entropy of image increases. In order to meet the needs of fast solution, this paper proposes an improved fruit fly algorithm to solve the 3D entropy function of the above image.

3. Improved Fruit fly Algorithm

At present, the optimization calculation method develops rapidly, including genetic algorithm, ant colony algorithm, fish swarm algorithm, and fruit fly algorithm. All of these algorithms belong to the population optimization algorithm and have strong optimization computing ability. The difference is that the heuristic search mechanism used by various methods is different. For example, the genetic algorithm is used to use genetic operations such as "copy, select, cross, and mutation" in the genetic process to achieve optimal calculation. The ant colony algorithm is based on the principle of pheromone positive feedback in the process of ant foraging. The fish swarm algorithm is based on the behaviour of "foraging, tail chasing, and clustering" in the process of fish foraging. The algorithm of fruit fly is based on the heuristic mechanism of foraging.

Although the heuristic mechanism of different optimization algorithms is different, there is a common problem that the algorithm is prone to the premature phenomenon. That is to say, the algorithm is easy to fall into local minima, resulting in the decline of global optimization ability. In order to improve the global optimization performance, a hybrid optimization method with combining the optimization methods of different mechanisms to construct the complementary optimization mechanism is proposed in this paper.

In the algorithm of fruit fly, fruit fly individuals can quickly gather to the optimal individual through visual search. The random search near the optimal individual is realized by using olfactory search. The two search methods can be used alternately, and finally the fruit fly can gather to the food source. The concentration evaluation function in the algorithm is the function to be optimized, that is, the 3D entropy corresponding to formula (6). The location of the optimized individual in the ant colony algorithm and fish swarm algorithm is the optimal solution. However, the position of fruit fly does not directly correspond to the optimization solution in the fruit fly algorithm. Its concentration value corresponds to the optimization solution of the optimization function.

The fruit fly algorithm is simple in mechanism, small in calculation, and easy to realize. In addition, the population can approach the optimal individual quickly, so as to ensure the algorithm has fast convergence. However, due to the fruit fly individuals concentrated in the vicinity of the optimal individuals for random search, it will lead to the premature phenomenon of the algorithm, thus reducing the global optimization ability of the algorithm. In this paper, an improved fruit fly hybrid optimization algorithm is designed based on the fruit fly algorithm and combined with chaos search and the optimization mechanism of the fish swarm algorithm.

In the fruit fly algorithm, the fruit fly individual searches randomly near the optimal individual, and the search direction and position are generated by the random number generator. Random search is easy to produce the phenomenon of repeated search, which will reduce the search efficiency. Chaos search has the characteristics of ergodic search [18], which can directly overcome the shortcomings of random search. Therefore, this paper proposes an improved strategy of chaos search instead of individual random search of fruit fly.

In addition, all the fruit flies in the algorithm have the same behaviour criterion and gather near the food source, which reduces the global optimization performance of the algorithm. In the fish swarm algorithm, artificial fish has similar behaviour in the process of foraging. However, the concept of crowding degree is set in the fish swarm algorithm, that is, the artificial fish cannot gather in the same place too much to prevent the algorithm from converging too fast. In this paper, the concept of crowding degree in the artificial fish swarm algorithm is introduced into the fruit fly algorithm which makes fruit fly no longer have a single

behaviour criterion, but choose to search near the optimal individual with a large probability, and search globally with a small probability, so as to improve the global optimization performance of the algorithm.

The above improved algorithm is described as follows:

Step 1: Initialize parameters.

Initialize the parameters involved in the fruit fly optimization algorithm, including maximum number of iterations MaxGen, population size of fruit fly Size, and initial optimal position of fruit fly x_best and y_best, and set the initial congestion probability value p.

Step 2: Set up the mechanism of chaos.

There are many kinds of chaos-generating functions; among which, the logistic map is one of the most commonly used functions, which is simple in form and easy to realize. In this paper, the logistic map is chosen as the mechanism of chaos sequence:

$$z_x(n+1) = \mu \cdot z_x(n) \cdot (1 - z_x(n)), \tag{7}$$

$$z_y(n+1) = \mu \cdot z_y(n) \cdot \left(1 - z_y(n)\right). \tag{8}$$

When $\mu = 4$, the above mapping is a chaotic full mapping. After the initial value is selected, the value after 2000 iterations of formula (7) and formula (8) is obtained as the initial value of chaos in the fruit fly algorithm so that the effect of the initial value of chaos generation mechanism on search process can be eliminated.

Step 3: Set the random search direction of fruit fly.

The i^{th} fruit fly in the population has two search directions. The random number r between $(0, 1)$ is generated by the random number generator.

If $r < p$, then initialize x_axis and y_axis randomly and set the chaos search direction of the i^{th} fruit fly near the (x_axis and y_axis) position; that is,

$$\begin{aligned} x(i) &= x\text{\_axis} + \gamma(z_x - 0.5), \\ y(i) &= y\text{\_axis} + \gamma\left(z_y - 0.5\right), \end{aligned} \tag{9}$$

where z_x and z_y are chaotic variables generated by formula (7) and formula (8) and γ is the coefficient of search range.

If $r \geq p$, set the random search direction of the i^{th} fruit fly near the (x_best and y_best) position; that is,

$$\begin{aligned} x(i) &= x\text{\_best} + \gamma(z_x - 0.5), \\ y(i) &= y\text{\_best} + \gamma\left(z_y - 0.5\right). \end{aligned} \tag{10}$$

Step 4: Calculate the concentration judgment value. The distance Dist_i between the position of i^{th} fruit fly and the origin is calculated:

$$\text{Dist}_i = \sqrt{(x(i))^2 + (y(i))^2}. \tag{11}$$

Calculate the concentration judgment value S_i according to the distance:

$$S_i = \frac{1}{\text{Dist}_i}. \tag{12}$$

Step 5: Calculate concentration $\text{Smell}(i)$ of the i^{th} fruit fly. The concentration function fit is the optimization function, so the concentration value of the i^{th} fruit fly is

$$\text{Smell}(i) = \text{fit}(S_i). \tag{13}$$

Step 6: Keep the current optimal individual. Keep the fruit fly with the highest odor concentration as the current optimal individual:

$$[\text{bestSmell}, \text{bestindex}] = \min(\text{Smell}(i)), \tag{14}$$

where bestindex is the index number of the optimal individual and bestSmell is the concentration value of the optimal individual.

Step 7: Save the optimal concentration and coordinates. Save the concentration value bestSmell of the optimal individual and its location coordinate. Command the fruit flies to fly to this position quickly by visual perception:

$$\begin{cases} \text{Smell\_best} = \text{bestSmell}, \\ x\text{\_best} = x(\text{bestindex}), \\ y\text{\_best} = y(\text{bestindex}). \end{cases} \tag{15}$$

(x_best and y_best) is considered as the optimal initial position for the next optimization. And reduce the probability of congestion:

$$p = \lambda \cdot p, \tag{16}$$

where λ is the probability attenuation coefficient of crowding degree $(0 < \lambda < 1)$.

Step 8: Iterative optimization. Repeat steps 3 to 6 and determine whether the current optimal concentration has been updated.

If yes, perform step 7; if no, repeat steps 3 to 6 directly until the specified number of iterations is reached or the algorithm converges.

The improved fruit fly algorithm proposed in this paper combines chaos ergodic search and the concept of crowding degree of the fish swarm algorithm. It can overcome the shortcomings of the traditional fruit fly algorithm, such as low efficiency of random search, the fruit fly individuals are all concentrated in the optimal individuals, and it is easy to fall into local minima, which is conducive to improving the global optimization performance of the algorithm. In the improved algorithm, the initial stage of crowding probability can be set to a larger probability value, so as to ensure that individual fruit flies can conduct sufficient random search, try to find the best position in the global range,

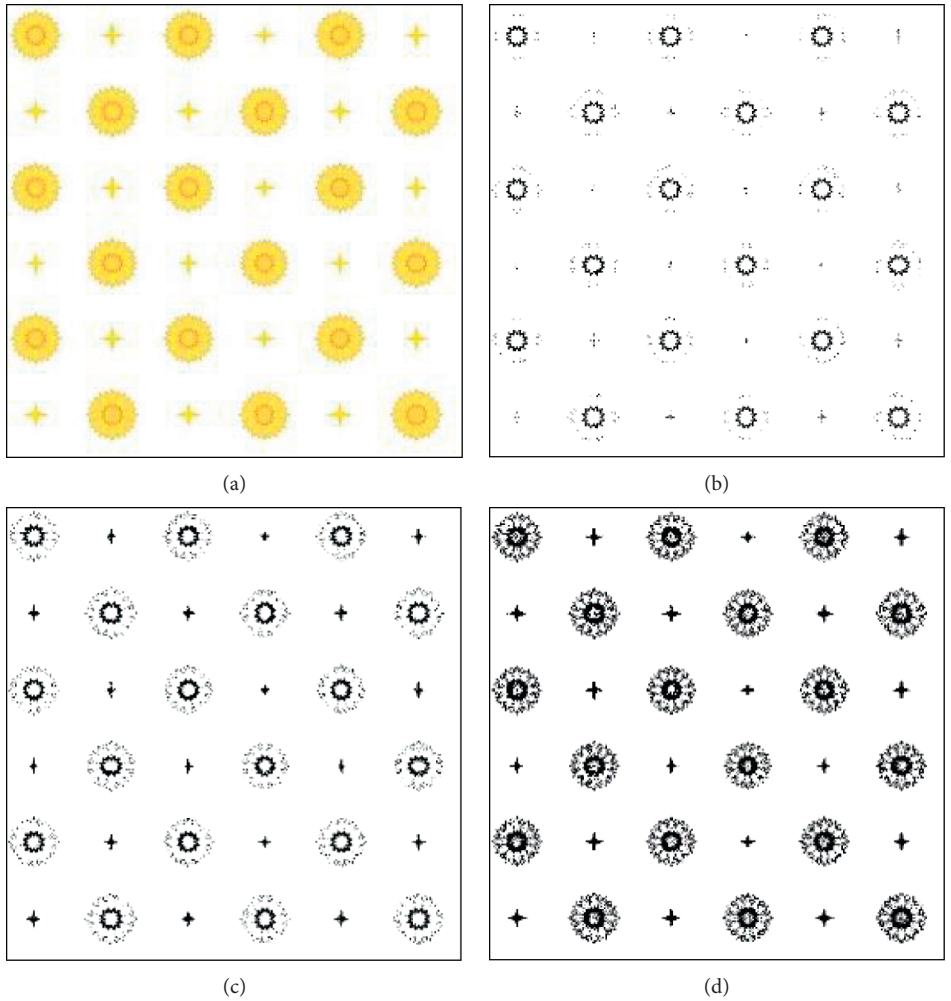

Figure 2: Segmentation result of a single pattern. (a) Original image; (b) 1D maximum entropy; (c) 2D maximum entropy $t_2 = 175$; (d) 3D maximum entropy $t_3 = 183$.

increase the dispersion of individual flies, and help to overcome the premature phenomenon of the population. At the same time, chaos search mechanism can improve the ergodicity of algorithm search, reduce the number of repeated searches, and improve the search efficiency. With the progress of the search process, the probability of crowding degree decreases gradually, the probability of fruit fly individual swarm to the optimal location increases, and the number of searches near the optimal location increases, which can ensure that the algorithm has good convergence characteristics and stability.

When the fruit fly algorithm is used to determine the threshold value of image segmentation, the three threshold variables of s, t, and r are encoded to determine the corresponding concentration value. The 3D entropy of formula (6) is used as the evaluation function of the concentration. After iterative calculation, the optimal solution of the maximum entropy can be completed.

4. Experimental Results and Analysis

The maximum 3D entropy proposed in this paper is used to segment the printed fabric pattern and is compared with the maximum 1D and 2D entropy. The segmentation result of a single pattern is shown in Figure 2.

Figure 2(a) shows the original image, the segmentation threshold $t_1 = 166$ is obtained by maximum 1D entropy. The segmentation result is shown in Figure 2(b). The outline of pattern segmentation is incomplete, and a lot of basic information of the pattern is lost. The maximum 2D entropy is used to obtain the segmentation threshold $t_2 = 175$, and the segmentation result is shown in Figure 2(c). Although the basic contour of the pattern can be preserved in the segmentation result, the contour is not complete. Especially, the segmentation result of the small cross in the figure has a large distortion. The maximum 3D entropy is used to obtain the segmentation threshold $t_3 = 183$, and the segmentation result is shown in Figure 2(d). The result of pattern segmentation has been improved obviously, the contour

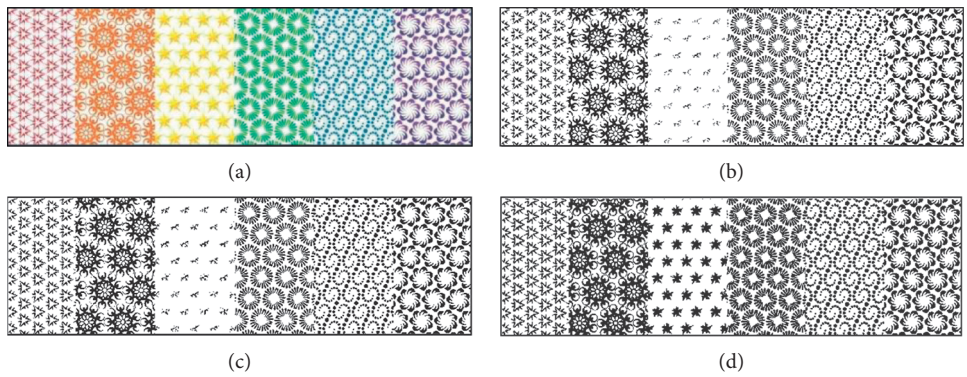

Figure 3: Segmentation result of the combination pattern. (a) Original image; (b) 1D maximum entropy $t_1 = 164$; (c) 2D maximum entropy $t_2 = 168$; (d) 3D maximum entropy $t_3 = 204$.

Table 2: Time comparison of various optimization algorithms.

Fabric pattern	Chaos optimization (s)	Fish swarm algorithm (s)	Fruit fly algorithm (s)	Improved algorithm (s)
Single pattern	5.231	4.212	3.013	0.966
Combination pattern	5.692	5.028	3.742	1.023

information is complete, and the information of each part of the pattern can be displayed clearly.

It can be seen that by expanding the dimension of image entropy and considering the direction information of pixel neighbourhood, the accuracy of feature description of target and background pixels can be improved, and the segmentation effect of printed fabric pattern can also be improved.

The segmentation result of the combination pattern is shown in Figure 3.

Figure 3(a) shows the original image, which is composed of six patterns, it makes the composition of the printed fabric pattern complex and increases the difficulty of threshold segmentation. Figure 3(b) shows the segmentation result obtained by using the maximum 1D entropy, and the segmentation threshold is $t_1 = 164$. In the segmentation result, the segmentation effect of the second and third patterns is not ideal. The external edge information of the second pattern is lost to some extent, and the third pattern has obvious error segmentation. Figure 3(c) is the segmentation result obtained by using the maximum 2D entropy, and its segmentation threshold is $t_2 = 168$. It can be seen from the segmentation results that the segmentation results of fabric patterns are improved when the distribution information of neighbouring pixels is taken into account. For example, the edge segmentation effect of the second pattern is improved, but the segmentation result of the third pattern is not obviously improved, and the main shape of the pattern cannot be segmented. Figure 3(d) shows the segmentation result obtained by using the maximum 3D entropy, and the segmentation threshold is $t_3 = 204$. It can be seen from the segmentation results that the segmentation results of fabric patterns can be further improved when considering the direction distribution information of neighbouring pixels. The second pattern has a complete edge segmentation, while the third pattern can also segment the basic shape, and the overall pattern segmentation performance has been significantly improved.

These algorithms, including the chaos optimization algorithm, fish swarm algorithm, fruit fly algorithm, and improved fruit fly algorithm, proposed in this paper can be used to optimize the threshold value of fabric pattern segmentation. The time comparison of various optimization algorithms is shown in Table 2.

It can be seen from Table 2 that since the chaos optimization algorithm belongs to the serial optimization algorithm, only one solution of optimization space can be searched in each iteration. Compared with the parallel population optimization algorithm, the efficiency is lower. Compared with the fruit fly algorithm, the fish swarm algorithm has more rules and less efficiency. On the basis of keeping the simple rules and high efficiency of the original algorithm, combined with chaos search mechanism, the improved fruit fly algorithm improves the ergodicity of individual search, combined with crowding degree restriction mechanism of fish swarm, improves the global search ability of fruit fly, so it has faster optimization efficiency, less than 30% of the original fruit fly algorithm.

5. Conclusions

Considering the direction information of the neighbourhood of the fabric image pixel, the 3D entropy is designed for the segmentation of the printed fabric pattern, and the threshold segmentation of the fabric pattern based on the maximum 3D entropy is realized. In order to improve the optimization efficiency of the maximum 3D entropy, combining the chaos search mechanism and the crowding degree strategy of the fish swarm algorithm, an improved fruit fly optimization algorithm is proposed, which improves the ergodicity and global optimization performance of the

algorithm. The experimental results show that the improved optimization algorithm has higher search efficiency and can complete the threshold optimization of 3D maximum entropy. The result of the printed fabric pattern segmentation based on the maximum 3D entropy can realize the complete segmentation of the fabric pattern and can effectively suppress the influence of texture noise on the segmentation result.

Data Availability

The data used to support the findings of this study are available from the corresponding author upon request.

Conflicts of Interest

There are no conflicts of interest regarding the publication of this paper.

Acknowledgments

The study was supported by the Science & Technology Development Fund of Tianjin Education Commission for Higher Education (grant no. 2018KJ194), Tianjin Science and Technology Commission Natural Science Foundation (grant no. 18JCYBJC86600), and Science and Technology Guidance Project of China Textile Industry Federation (grant no. 2018051).

References

[1] H. Mo, B. Xu, W. Ouyang, and J. Wang, "Color segmentation of multi-colored fabrics using self-organizing-map based clustering algorithm," *Textile Research Journal*, vol. 87, no. 3, pp. 369–380, 2017.

[2] L. Jia and J. Liang, "Fabric defect inspection based on isotropic lattice segmentation," *Journal of the Franklin Institute*, vol. 354, no. 13, pp. 5694–5738, 2017.

[3] Z. C. Li, H. C. Yan, H. Zhang et al., "Improved inequality-based functions approach for stability analysis of time delay system," *Automatica*, vol. 108, Article ID 108416, 2019.

[4] S. Vargas, M. E. Stivanello, M. L. Roloff et al., "Evaluation of segmentation techniques for automated inspection of defects in fabrics," in *Proceedings of the 2016 12th IEEE/IAS International Conference on Industry Applications (INDUSCON)*, Curitiba, Brazil, November 2016.

[5] Q. W. Li, Z. H. Wei, and W. Shen, "Selective feature fusion based adaptive image segmentation algorithm," *Advances in Multimedia*, vol. 2018, Article ID 4724078, 10 pages, 2018.

[6] Y. Han, C. Xu, G. Baciu, M. Li, and M. R. Islam, "Cartoon and texture decomposition-based color transfer for fabric images," *IEEE Transactions on Multimedia*, vol. 19, no. 1, pp. 80–92, 2017.

[7] L. Liu, J. Zhang, X. Fu, L. Liu, and Q. Huang, "Unsupervised segmentation and elm for fabric defect image classification," *Multimedia Tools and Applications*, vol. 78, no. 9, pp. 12421–12449, 2019.

[8] C. Xu, Y. Han, G. Baciu, and M. Li, "Fabric image recolorization based on intrinsic image decomposition," *Textile Research Journal*, vol. 89, no. 17, pp. 3617–3631, 2019.

[9] G. Beck, T. Duong, M. Lebbah, H. Azzag, and C. Cérin, "A distributed approximate nearest neighbors algorithm for efficient large scale mean shift clustering," *Journal of Parallel and Distributed Computing*, vol. 134, pp. 128–139, 2019.

[10] K. Zhang, Y. Yan, P. Li, J. Jing, X. Liu, and Z. Wang, "Fabric defect detection using salience metric for color dissimilarity and positional aggregation," *IEEE Access*, vol. 6, pp. 49170–49181, 2018.

[11] Y. C. Tong and Y. Zhang, "Automatic pattern separation of jacquard warpknitted fabric by supervised multiscale Markov model," *Indian Journal of Fiber & Textile Research*, vol. 43, no. 2, pp. 257–261, 2018.

[12] Z. C. Li, H. C. Yan, H. Zhang et al., "Stability analysis of linear systems with time-varying delay via intermediate polynomial-based functions," *Automatica*, vol. 113, Article ID 108756, 2020.

[13] A. Van Opbroek, H. C. Achterberg, M. W. Vernooij, and M. De Bruijne, "Transfer learning for image segmentation by combining image weighting and kernel learning," *IEEE Transactions on Medical Imaging*, vol. 38, no. 1, pp. 213–224, 2019.

[14] J. Z. Ma, S. Li, H. Qin et al., "Adaptive appearance modeling via hierarchical entropy analysis over multi-type features," *Pattern Recognition*, vol. 98, 2019.

[15] L. Liu, H. Wang, L. Zhao et al., "In situ characterization of surface-layer structure evolution in γ-irradiated carbon fibers by X-ray photoelectron spectroscopy combined with argon-ion sputtering," *Polymer Composites*, vol. 40, no. S1, pp. E832–E834, 2019.

[16] H. Yan, C. Hu, H. Zhang, H. R. Karimi, X. Jiang, and M. Liu, "H-infinity output tracking control for networked systems with adaptively adjusted event-triggered scheme," *IEEE Transactions on Systems, Man, and Cybernetics: Systems*, vol. 49, no. 10, pp. 2050–2058, 2019.

[17] Z. J. Li, S. Meng, L. Wang et al., "Intelligent recognition of the patterns of yarndyed fabric based on LSRT images," *Journal of Engineered Fibers and Fabrics*, vol. 14, pp. 1–13, 2019.

[18] H. Yan, H. Zhang, F. Yang, C. Huang, and S. Chen, "Distributed H infinity filtering for switched repeated scalar nonlinear systems with randomly occurred sensor nonlinearities and asynchronous switching," *IEEE Transactions on Systems, Man, and Cybernetics: Systems*, vol. 48, no. 12, pp. 2263–2270, 2018.

[19] D. Corus and P. S. Oliveto, "Standard steady state genetic algorithms can hillclimb faster than mutation-only evolutionary algorithms," *IEEE Transactions on Evolutionary Computation*, vol. 22, no. 5, pp. 720–732, 2018.

[20] X. S. Dong, W. Y. Dong, and Y. L. Call, "Ant colony optimisation for coloured travelling salesman problem by multi-task learning," *IET Intelligent Transport Systems*, vol. 12, no. 8, pp. 774–782, 2018.

[21] X. Y. Zhou, Z. M. Wang, D. Li et al., "Guidance systematic error separation for mobile launch vehicles using artificial fish swarm algorithm," *IEEE Access*, vol. 7, pp. 31422–31434, 2019.

[22] Y. J. Hu, F. F. Zhu, L. Zhang, and Y. K. Lui, "Scheduling of manufacturers based on chaos optimization algorithm in cloud manufacturing," *Robotics and Computer Integrated Manufacturing*, vol. 58, pp. 13–20, 2019.

Hindawi
Discrete Dynamics in Nature and Society
Volume 2020, Article ID 3639508, 8 pages
https://doi.org/10.1155/2020/3639508

Research Article

Discrete Dynamics-Based Parameter Analysis and Optimization of Fuzzy Controller for Inverted Pendulum Systems Based on Chaos Algorithm

Xingguo Xia,[1] Jianwei Xia,[2] Mingyi Gang,[1] Qingfeng Zhang,[1] and Jing Wang[3]

[1]*Department of Electrical Engineering, Maanshan Technical College, Ma'anshan 243031, China*
[2]*School of Mathematical Sciences, Liaocheng University, Liaocheng 252059, China*
[3]*School of Electrical and Information Engineering, Anhui University of Technology, Ma'anshan 243002, China*

Correspondence should be addressed to Jing Wang; jingwang08@126.com

Received 21 March 2020; Accepted 30 April 2020; Published 18 May 2020

Guest Editor: Jinliang Wang

In order to reduce the difficulty in the selection of the quantization factor and the proportion factor in the general fuzzy controller, a controller with the novel algorithm based on the Logistic chaotic variable is proposed in this paper. By introducing the chaotic variable factor into the global search, the suboptimal solution can be obtained and the optimization interval reduced. The global optimal solution is obtained in the vicinity of the suboptimal solution under an integrated performance index. Finally, the control scheme is applied to the control of a double inverted pendulum model. The simulated results show the effectiveness of the proposed method.

1. Introduction

The inverted pendulum is a class of systems, which are a common platform and can be used to test the correctness and feasibility of control methods. Control objects in many actual fields, such as aircrafts and intelligent balancing vehicles, are related to the balance control problem of the inverted pendulum. Therefore, research studies on the controller design of the inverted pendulum have particularly important engineering significance [1–3].

It is noted that, in the previous research of control techniques, the precise mathematical model of nonlinear systems should be provided, which is hard to realize in practice [4–6]. However, as an important branch of intelligent control strategies, the fuzzy control can perform well in the nonlinear systems as well as the unstable control objects with the guidance of fuzzy rules and fuzzy membership functions [7–10], and this motivates our study in fuzzy control. Dynamic performances of the fuzzy controller, including the fuzzy rule, membership function, and proportion factor, are important indexes to evaluate the quality of the fuzzy controller [11]. However, the effective design and adjustment methods for the parameters of the fuzzy controller (quantification factor, ratio factor, etc.) are limited. In practice, the tuning work relies on the experience and repeated debugging of operators. It takes a lot of energy and time, and obtaining their optimal values is still a difficult issue. In [12], the genetic algorithm was used to optimize the parameters of the fuzzy controller, but it can only optimize the shape and position of the membership function. However, fuzzy sets that directly affect the completeness of the fuzzy rules cannot be chosen. As the number of variable increases, the system will be paralyzed. With the numerical analysis, we propose a method to optimize the scaling factor, but the optimization of the quantification factor and proportion factor cannot be achieved simultaneously. In [13], a random optimization method based on the simulated annealing algorithm was proposed, which can avoid the local minimum problem. The rate of the convergence is still too slow. Based on the nonlinear dynamic characteristics of chaos, such as ergodicity, randomness, and regularity, the developed chaos optimization algorithm has been widely concerned by many scholars [14, 15].

In this paper, the issues of discrete dynamics-based parameter analysis and optimization of the fuzzy controller for inverted pendulum systems based on a chaos algorithm are investigated. The main contributions can be concluded as follows. (1) Taking the fuzzy control scheme into the implementation of the control for the two-stage inverted pendulum system. Moreover, different chaotic sequences generated by logistic mapping are introduced into the parameter domain of the fuzzy controller in this work. (2) Through using chaotic variables to construct the global rough search method, the optimal solution is obtained. Based on this, the local fine search is proposed in the minimal range near the suboptimal solution to optimize the parameters of the fuzzy controller automatically via optimizing the global search technique by reducing the search space and coefficient. (3) A robust control scheme is used to control an inverted pendulum experiment system model under stochastic disturbance, which shows that the controller with optimized parameters can make the double pendulum rod staying in the straight position and has a fast dynamic response.

1.1. Model Description. To simplify the modeling, it is necessary to ignore the air and the external friction of the inverted pendulum system. The system can be abstracted into a model consisting of a small cart and two uniform pendulum rods. The double inverted pendulum is a typical rigid body motion system to facilitate the modeling of the system. The structure of the double inverted pendulum system is shown in Figure 1 [16]. Moreover, its specific parameters are shown in Table 1.

Select $x, \theta_1, \theta_2, \dot{x}, \dot{\theta}_1$, and $\dot{\theta}_2$ as the system state variables. Based on the Lagrange equation in analytical mechanics, the mathematical model of the double inverted pendulum system is derived, and the linear treatment is finished near the unstable equilibrium point [18], which is replaced by the known parameters in Table 1. The equation of the state for a linear double inverted pendulum system can be obtained as follows:

$$\begin{cases} \dot{X} = AX + Bu, \\ Y = CX, \end{cases} \tag{1}$$

where

$$A = \begin{bmatrix} 0 & 0 & 0 & 1 & 0 & 0 \\ 0 & 0 & 0 & 0 & 1 & 0 \\ 0 & 0 & 0 & 0 & 0 & 1 \\ 0 & 0 & 0 & 0 & 0 & 0 \\ 0 & 86.69 & -21.62 & 0 & 0 & 0 \\ 0 & -40.31 & 39.45 & 0 & 0 & 0 \end{bmatrix},$$
$$B = \begin{bmatrix} 0 & 0 & 0 & 1 & 6.64 & -0.088 \end{bmatrix}^T, \tag{2}$$
$$C = \begin{bmatrix} 1 & 0 & 0 & 0 & 0 & 0 \\ 0 & 1 & 0 & 0 & 0 & 0 \\ 0 & 0 & 1 & 0 & 0 & 0 \end{bmatrix}.$$

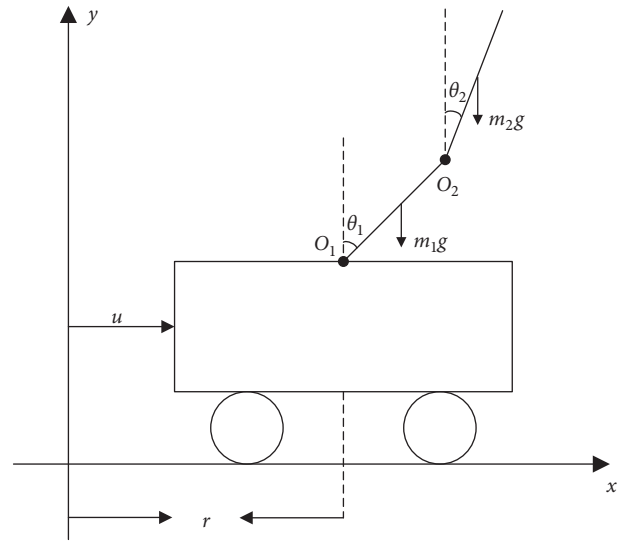

Figure 1: Motion analysis sketch of two-stage inverted pendulum.

1.2. Fuzzy Control Design. In view of the linear model of (1), the Lyapunov theory is applied to analyze its stability [19]. The characteristic root of the system is solved according to matrix A as $\begin{bmatrix} 10.0438 & 5.0262 & -10.0438 & -5.0262 & 0 & 0 \end{bmatrix}$.

It is obvious that the system has two poles located on the right half plane of S. Based on the stability criterion, the double inverted pendulum system is a naturally unstable system.

According to the controllability criterion [20, 21], N-order linear continuous system is $\dot{X} = Ax + Bu$. The condition that the state is fully controllable is if and only if the energy criterion of the system is full $\text{rank}(S) = \begin{bmatrix} B & AB & A^2B & \cdots & A^{n-1}B \end{bmatrix}$, that is, $\text{rank}(S) = n$.

After calculating, one has

$$\text{rank}(ctrb(A, B)) = \text{rank}\begin{bmatrix} B & AB & A^2B & A^3B & A^4B & A^5B \end{bmatrix} = 6. \tag{3}$$

It can be seen that the system is controllable near the equilibrium point, which means it is possible to design a controller maintaining the stability of the system.

1.2.1. The Input and Output Variables of a Fuzzy Controller. For a typical double inverted pendulum system with multiple inputs, if the six state variables are used as input variables of the fuzzy controller, the fuzzy rule explosion will inevitably lead to the difficulty in the optimization of fuzzy parameters [22–24]. The output information of the linear system can be fused directly, and six state variables are weighted into two input variables; thus, the problem of fuzzy rule explosion is solved to simplify the design of the fuzzy controller.

(1) Design State Feedback Matrix. According to the strategy based on the linear quadratic optimal theory, a state feedback matrix K is designed for system (1):

$$K = \begin{bmatrix} K_x & K_{\theta_1} & K_{\theta_2} & K_{\dot{x}} & K_{\dot{\theta}_1} & K_{\dot{\theta}_2} \end{bmatrix}. \tag{4}$$

Table 1: Introduction of symbols used in the double inverted pendulum system [17].

Parameters	Values	Significance
x	$[-1, 1]$ m	Displacements of a cart
θ_1	$[-0.25, 0.25]$ rad	The angle between the inverted pendulum 1 and the vertical direction
θ_2	$[-0.15, 0.15]$ rad	The angle between the inverted pendulum 2 and the vertical direction
m_0	1.096 kg	Equivalent mass of the cart
m_1	0.13 kg	The quality of the inverted pendulum 1
m_2	0.05 kg	The quality of the inverted pendulum 2
J_1	0.0002 kg·m·m	The moment of inertia of an inverted pendulum 1
J_2	0.0034 kg·m·m	The moment of inertia of an inverted pendulum 2
l_1	0.0775 m	The half length of the inverted pendulum 1
l_2	0.25 m	The half length of the inverted pendulum 2
L_1	0.155 m	The length of the inverted pendulum 1
f_0	10.1403 N·m/s	Friction coefficient of the cart
f_1	0.003415 N·m/s	Friction coefficient of the inverted pendulum 1
f_2	0.003224 N·m/s	Friction coefficient of the inverted pendulum 2
g	9.8 m/s^2	Gravitational acceleration

Using state feedback matrix K to construct fusion function $f_1(\cdot)$,

$$f_1(\cdot) = \begin{pmatrix} \frac{K_x}{\|K\|_2} & \frac{K_{\theta_1}}{\|K\|_2} & \frac{K_{\theta_2}}{\|K\|_2} & 0 & 0 & 0 \\ 0 & 0 & 0 & \frac{K_{\dot{x}}}{\|K\|_2} & \frac{K_{\dot{\theta}_1}}{\|K\|_2} & \frac{K_{\dot{\theta}_2}}{\|K\|_2} \end{pmatrix}, \quad (5)$$

$$\|K\|_2 = \sqrt{K_x^2 + K_{\theta_1}^2 + K_{\theta_2}^2 + K_{\dot{x}}^2 + K_{\dot{\theta}_1}^2 + K_{\dot{\theta}_2}^2}.$$

After calculation, take

$$K = [\,17.3312 \;\; 116.5826 \;\; -194.6134 \;\; 18.5759 \;\; 3.5457 \;\; -31.4390\,]. \quad (6)$$

(2) Dimensionality Reduction. Two input variables are obtained by dimensionality reduction: the synthesis error E is synthesized by weighting the position state variables and the comprehensive error rate EC is synthesized by weighting the speed state variables:

$$\begin{bmatrix} E \\ \mathrm{EC} \end{bmatrix} = f_1(\cdot)\begin{bmatrix} x & \theta_1 & \theta_2 & \dot{x} & \dot{\theta}_1 & \dot{\theta}_2 \end{bmatrix}. \quad (7)$$

In view of the abovementioned statement, a two-dimensional Mamdani-type fuzzy controller with two inputs and one output is designed, and the system structure diagram is shown in Figure 2.

In Figure 2, K_e and K_{ec} are the quantitative factors of the system error and the rate of error change, respectively. The input variables are converted from the basic domain to the corresponding fuzzy set theory domain, and K_u is the output proportional factor, which converts the fuzzy set domain of the input variable into the exact value.

1.3. Controller Design

1.3.1. Fuzzy Control Rules. In the process of design, E, EC, and U all define with seven fuzzy subsets: NB, NM, NS, Z, PS, PM, and PB. After dividing the fuzzy linguistic variables into the input and output domains, the total number of fuzzy control rules designed is 49. Rule 1: if E is NB and EC is NB, then U is NB; Rule 2: if E is NB and EC is NM, then U is NB; . . .; Rule 49: if E is PB and EC is PB, then U is PB. The fuzzy control rule is set up, as shown in Table 2.

1.3.2. Membership Function. In fuzzy systems and control, the membership functions are commonly selected as triangle membership function, trapezoid membership function, and Gauss type membership function. In this paper, the input and output variables of the fuzzy controller are designed by the triangular membership function, and the center of gravity method is used for defuzzification.

1.4. Chaos Optimization. The fuzzy controller parameters (quantification factors K_e and K_{ec} and proportion factor $K - u$) play an important role in the fuzzy control of the double inverted pendulum system [25]. Selection is usually achieved by means of experience and trials, which contains subjectivity and seriously affects the effectiveness of the control. Therefore, we combine the fuzzy control with the chaos optimization algorithm, which makes full use of the chaos algorithm to optimize the quantitative factor and proportion factor of the fuzzy controller. The optimized parameters will improve the effectiveness of the fuzzy control.

1.4.1. Selection of Performance Index. For the double inverted pendulum system with nonlinearity and multiple inputs, it is necessary to select a performance index to measure the control effect. The index can reflect not only the dynamic characteristics of the control system but also its steady-state characteristics. Therefore, select the performance index function (8); r, θ_1, and θ_2 are unified by expression, and its performance index functions with different parameters are

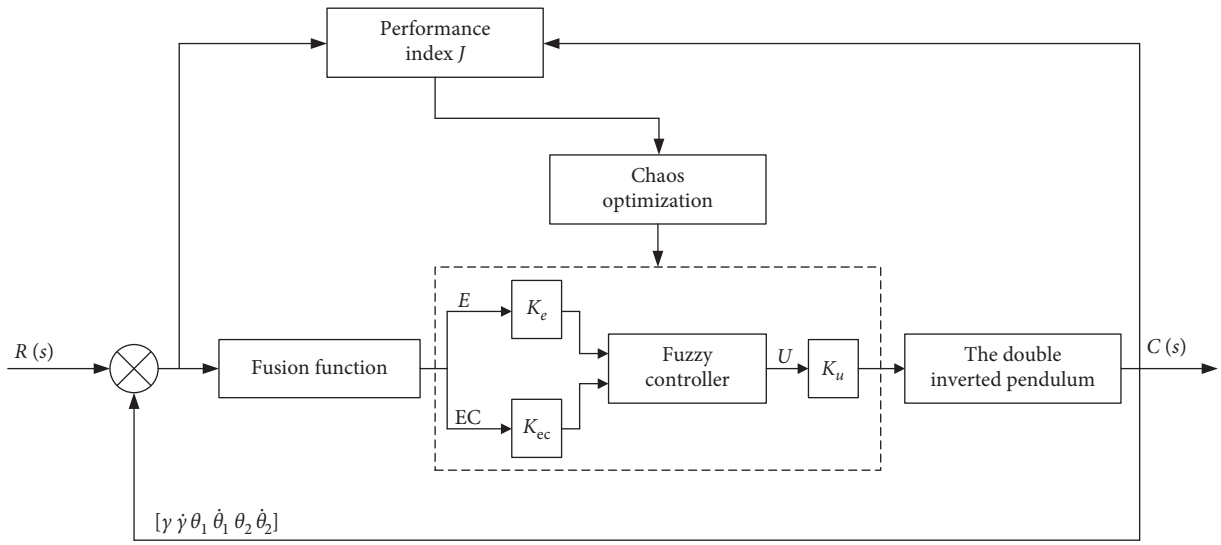

Figure 2: The structure chart of fuzzy control.

Table 2: Fuzzy rules list.

E	EC / U						
	NB	NM	NS	Z	PS	PM	PB
NB	NB	NB	NB	NM	NM	NS	Z
NM	NB	NB	NM	NM	NS	Z	PS
NS	NB	NM	NM	NS	Z	PS	PM
Z	NM	NM	NS	Z	PS	PM	PM
PS	NM	NS	Z	PS	PM	PM	PB
PM	NS	Z	PS	PM	PM	PB	PB
PB	Z	PS	PM	PM	PB	PB	PB

$$J_i = \min\left[w_{i,1}\sum_{k=0}^{i}|e(k)|\,k/|\max(e(k))| + w_{i,2}\delta\right] \quad (i = 1, 2, 3), \tag{8}$$

where δ represents the percentage of overshoot, $w_{i,1}$ and $w_{i,2}$ are selected as the user according to the actual situation, and l represents the number of cycles to be set.

In the control of the double inverted pendulum system, the key is that the two pendulums cannot be reversed, and the cart can move back and forth within a certain range. A comprehensive performance index is introduced in the paper as follows:

$$\begin{cases} J = aJ_1 + bJ_2 + cJ_3, \\ \text{s.t.}0 < c < b < a < 1, \\ a + b + c = 1, \end{cases} \tag{9}$$

where the performance of the cart and the double inverted pendulum bars are expressed by J_i $(i = 1, 2, 3)$; the weight coefficients are expressed as a, b, and c, and the selection is made according to the actual situations. The priority of the control for the cart and two inverted pendulum bars is considered comprehensively, the requirements for the dynamic characteristics and stability performance of the system are satisfied. Combined with the algorithm of prechaotic optimization, the parameters of the fuzzy controller K_e, K_{ec}, and K_u are adjusted and the minimum performance index J is finally obtained.

1.4.2. The Steps of Chaos Optimization. In the paper, the logistic mapping is selected as follows:

$$x_{n+1} = \mu x_n(1 - x_n), \quad n = 0, 1, \ldots, N, \tag{10}$$

where μ is the control variable which satisfies $\mu = 4$, and when $0 < x_n < 1$, formula (11) is completed in chaos. Since the chaotic state is very sensitive to the initial value, we choose different initial values of small differences to get chaotic variables of different trajectories. The N-order fixed formula (10) can not be selected here; otherwise, chaos cannot be generated.

Considering the parameter domain of the fuzzy control, the following set of iterative equations can be considered:

$$\begin{aligned} &x_{n+1} = 4x_n(1 - x_n), \quad \left(x_n = \left(x_{1,n}, x_{2,n}, x_{3,n}\right)\right), \\ &n = 0, 1, \ldots, N, \quad (0 < x_0 < 1), \end{aligned} \tag{11}$$

$$k^*_{e,n} = k^*_p \times x_{1,n}, \tag{12}$$

$$k^*_{ec,n} = k^*_p \times x_{2,n}, \tag{13}$$

$$k^*_{u,n} = k^*_p \times x_{3,n}. \tag{14}$$

The k^*_p in formulas (12)–(14) can be properly amplified and converted. In the interval (0-1), three different initial values are taken into the Logistic mapping; then, three different chaotic variable trajectories can be generated. They are also used in the parameters of the fuzzy controller to calculate the target function J according to formula (9), and then the optimal value is selected.

The steps of the chaos optimization algorithm are as follows:

Step 1 (initialization): in the random interval (0-1), three initial values of different small differences are selected and replaced into the Logistic mapping, and different chaotic locus variables can be obtained as the search space of the fuzzy controller parameters k_e^*, k_{ec}^*, and k_u^*. Then, formula (8) is used to calculate the system performance index of the trolley and the two swing lever $J_i\,(i = 1, 2, 3)$.

Step 2: in formula (9), select appropriate values for parameters a, b, and c. Using formula (10) to calculate the comprehensive performance index J, the minimum of the target function in the N comprehensive performance index J is found as $J_{\min}$. The corresponding fuzzy control parameter value is the approximate optimal solutions k_e^*, k_{ec}^*, and k_u^* of the chaotic rough search method.

Step 3: let $n = 1$.

Step 4: in order to make the system find the global optimal value quickly, the chaotic local fine search is introduced to reduce the range of the variables so as to improve the precision of the control system. The approximate optimal solutions k_e^*, k_{ec}^*, and k_u^* obtained in Step 2 are substituted in the following expressions (15)–(17), respectively:

$$\widehat{k}_{e,n}^{*} = k_e^{*} \times z(t)x_n, \quad (n = 0, 1, \ldots, N), \tag{15}$$

$$\widehat{k}_{ec,n}^{*} = k_{ec}^{*} \times z(t)x_n, \quad (n = 0, 1, \ldots, N), \tag{16}$$

$$k_u^{*} \times z(t)x_n, \quad (n = 0, 1, \ldots, N). \tag{17}$$

Three new chaotic trajectory variables $\widehat{k}_{e,n}^{*}$, $\widehat{k}_{ec,n}^{*}$, and $\widehat{k}_{u,n}^{*}$ are generated, which are used for local fine search of chaos. According to formula (9), the corresponding system performance index $J_i\,(i = 1, 2, 3)$ is calculated.

Step 5: calculate the comprehensive performance J based on formula (9).

Step 6: chaotic search is carried out in the left and right neighborhood of the approximate optimal solution obtained from the chaotic rough search. The time-varying factor $z(t)$ is calculated according to the formula as follows:

$$z(t + 1) = (1 - \lambda)z(t), \quad (0 < \lambda < 1), \tag{18}$$

where λ is the attenuation factor of $z(t)$.

Step 7: $t = t + 1$. Again, the chaotic search space is reduced as in Step 4.

Step 8: compare the value of comprehensive performance index function in the search process, and find $J_{\min}$. Terminate the search. The global optimal solutions $\widehat{k}_{e,n}^{*}$, $\widehat{k}_{ec,n}^{*}$, and $\widehat{k}_{u,n}^{*}$ are the fuzzy controller parameters corresponding to $J_{\min}$.

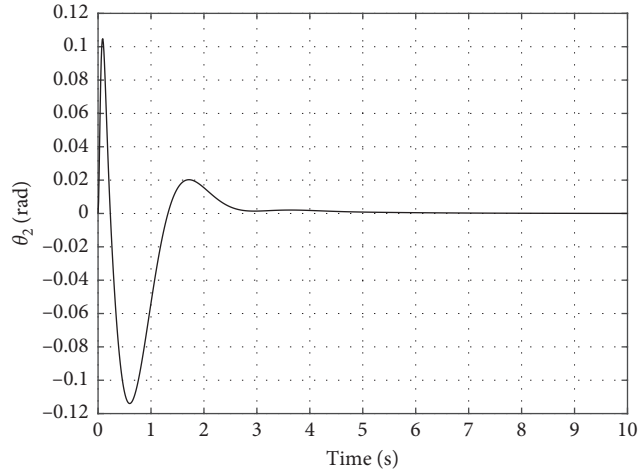

Figure 3: 2 angle simulation curves of the pendulum rod.

In the Matlab software, the module of the double inverted pendulum control system is built, and the sampling time is selected as 5 ms. The parameters of the fuzzy controller after the chaos optimization are applied to the simulation control of the system. The simulation result of the experiment is shown in Figure 3.

Figure 3 shows the curves of θ_2 with the initial states $x(0) = 0$, $\theta_1(0) = \theta_2(0) = 0.1$ rad. From the curves, we can see that the system responds quickly and returns to the equilibrium position within 3-4 seconds. The simulation result also shows the effectiveness of the designed fuzzy controller.

2. Robust Control of the Double Inverted Pendulum

To further verify the robustness, for the inverted pendulum system in the basic Simulink simulation block diagram, as shown in Figure 4, the −80 dBW white Gaussian noise is applied, and the required signal is generated by wgn function in the simulation.

For the considered two-stage inverted cycloidal model system with parameters shown in Table 1 [17], the initial value is given as $[0, 0, 0, 0.02, 0, 0]$. By employing the Matlab software, the corresponding simulation results are shown in Figures 5–7. The sampling period is taken as 0.001 s. In formula (18), the initial value of chaos rough search is $z_0 = 0.002$. Termination conditions are $z_n \leq 10^{-3}$ and $\beta = 0.001$. In formula (9), $a = 0.2$, $b = 0.3$, and $c = 0.5$. It has gone through 692 steps of chaotic fine search, and the global optimal solution of fuzzy controller parameters is in the 357th step. Fuzzy controller parameters are $K_c = 9.00005$, $K_{ec} = 9.00131$, and $K_u = 18.00026$.

Figures 5–7 are the robust control curves of the car displacement, and the angle of the pendulum rod 1 and the angle of the pendulum rod 2 of the two inverted pendulums, respectively. The model is shown as Figure 1. The results show that the controller designed by the chaotic optimization method in this paper can effectively control the two-stage inverted pendulum. The displacement of the car and

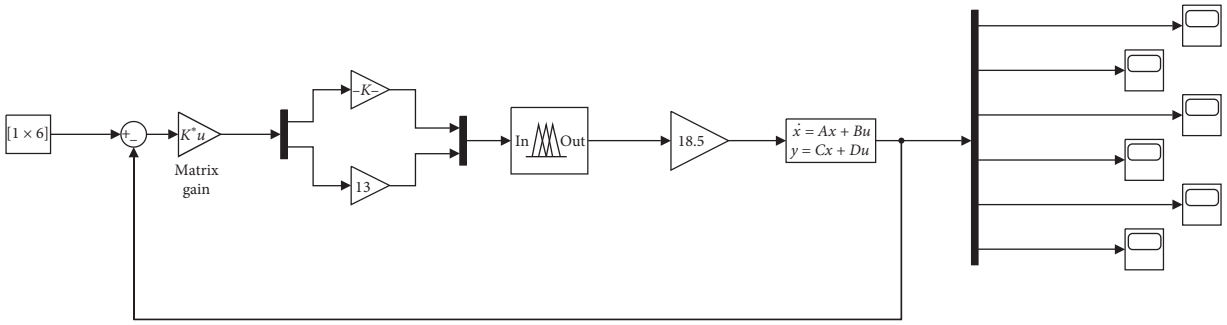

Figure 4: Control block diagram of the double inverted pendulum.

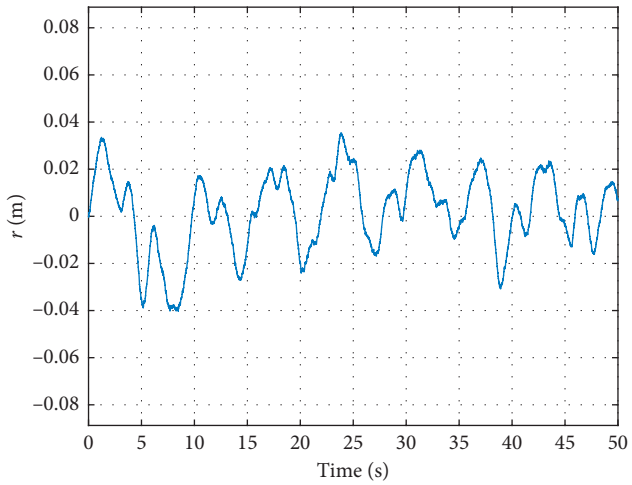

Figure 5: Car displacement.

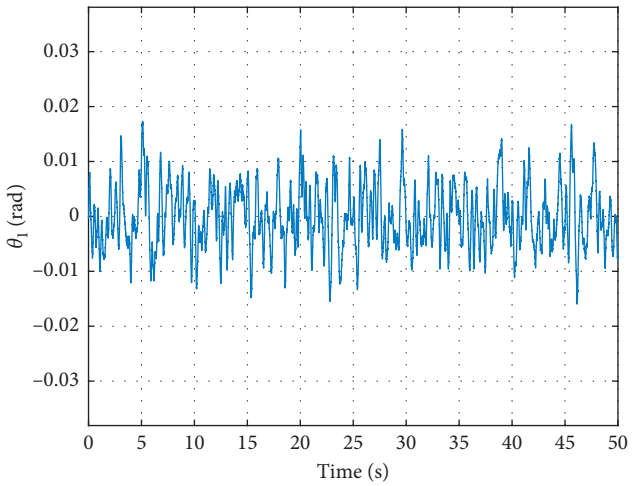

Figure 6: Swing rod 1 angle.

the angle of the pendulum rod are basically stable in the balanced position, and the control is effective.

Remark 1. It is worth noticing that the networked control system has been a high-profile topic during the past few decades. Correspondingly, the control issues of the networked control system subject to various network-induced phenomena, such as communication delays, packet dropouts, and fading channels, have obtained great research interest of scholars and abundant literature studies have been reported on these topics. Aiming at the network control system, the observer-based dissipative control and passivity-based H_∞ control have been proposed in [26, 27], respectively. Nonetheless, the proposed parameter analysis and optimization of the fuzzy control method in this paper can also be employed in the networked control system to further optimize the conservativeness with respect to the aforementioned mechanisms, which is one of the directions of our future work.

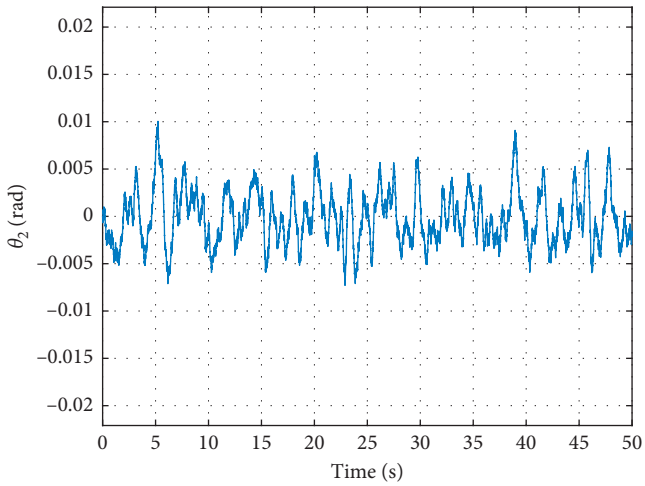

Figure 7: Swing rod 2 angle.

3. Conclusion

In the paper, the optimal control theory has been used to design the fusion function to reduce the dimension of the input variables of the fuzzy controller for a double inverted pendulum system. Then, the chaotic sequence variables have been introduced into the fuzzy control system. The chaotic global rough search and the chaotic fine search technique have been used to optimize the parameters of the fuzzy controller. After optimization, the time of adjusting the parameters has been reduced, and the performance of the double inverted pendulum system has been improved.

Finally, the proposed method has been tested through an example. The effectiveness and capability of our approach have been proved by the simulation results. To further improve the practical application of the proposed parameter analysis and optimization of the fuzzy control technique, our future works will concentrate on other actual systems, such as stochastic switching systems, and this will be an interesting and challenging area.

Data Availability

All datasets used in this study are available from the corresponding author upon request.

Conflicts of Interest

The authors declare that there are no conflicts of interest regarding the publication of this paper.

Acknowledgments

This work was supported by the Key Program in the Youth Elite Support Plan in Universities of Anhui Province (Grant no. gxyqZD2018105), National Natural Science Foundation of Anhui Province (Grant no. 1808085QA18), and Key University Science Research Project of Anhui Province (Grant no. KJ2018A0946).

References

[1] R. Xiaogan, "The research on balancing control of two wheel self-balance robot," *Science Technology and Engineering*, vol. 14, no. 2, pp. 84–88, 2014.

[2] C. Min and W. Si-Ming, "Attitude control of six-rotor helicopter based on anti-delay linear active disturbance rejection control," *Science Technology and Engineering*, vol. 17, no. 6, pp. 77–82, 2017.

[3] A. Mayra, H. Victor Manuel, and S. Ramon, "Limit cycle elimination in inverted pendulums: furuta pendulum and pendubot," *IEEE Access*, vol. 6, pp. 30317–30332, 2018.

[4] T. Wu, X. Huang, X. Chen, and J. Wang, "Sampled-data H_∞ exponential synchronization for delayed semi-Markov jump CDNs: a looped-functional approach," *Applied Mathematics and Computation*, vol. 377, Article ID 125156, 2020.

[5] X. Hu, J. Xia, Z. Wang, X. Song, and H. Shen, "Robust distributed state estimation for Markov coupled neural networks under imperfect measurements," *Journal of the Franklin Institute*, vol. 357, no. 4, pp. 2420–2436, 2020.

[6] Z. Wang, L. Shen, J. Xia, H. Shen, and J. Wang, "Finite-time non-fragile $L_2 - L_\infty$ control for jumping stochastic systems subject to input constraints via an event-triggered mechanism," *Journal of the Franklin Institute*, vol. 355, no. 14, pp. 6371–6389, 2018.

[7] J. Wang, L. Shen, J. Xia, Z. Wang, X. Chen, and X. Chen, "Asynchronous dissipative filtering for nonlinear jumping systems subject to fading channels," *Journal of the Franklin Institute*, vol. 357, no. 1, pp. 589–605, 2020.

[8] H. Shen, Y. Men, J. Cao, and J. H. Park, ".H_∞ filtering for fuzzy jumping genetic regulatory networks with round-robin protocol: a hidden-Markov-model-based approach," *IEEE Transactions on Fuzzy Systems*, vol. 28, no. 1, pp. 112–121, 2020.

[9] L. Fang, L. Ma, S. Ding, and D. Zhao, "Finite-time stabilization for a class of high-order stochastic nonlinear systems with an output constraint," *Applied Mathematics and Computation*, vol. 358, pp. 63–79, 2019.

[10] S. Ding, J. Park, and C. Chen, "Second-order sliding mode controller design with output constraint," *Automatica*, vol. 112, Article ID 108704, 2020.

[11] Y. Xia, J. Xia, Z. Wang, and H. Shen, "Extended non-fragile dissipative estimation for nonlinear semi-Markov jump systems," *Journal of the Franklin Institute*, vol. 357, no. 1, pp. 457–472, 2020.

[12] H. Wang, C. Liu, X. Song, Z. Song, and K. Li, "Parameters optimization of fuzzy controller based on genetic algorithm," *HeBei University of Science and Technology*, vol. 28, no. 4, pp. 276–280, 2007.

[13] L. P. Shi, "Research on simulated annealing algorithm and improvement," *Information Technology*, vol. 2, pp. 176–178, 2013.

[14] X. Li, E. Zou, and T. Zhang, "Optimization design of feedforward neural network structure based on chaos variables," *Control and Decision*, vol. 18, no. 6, pp. 703–707, 2003.

[15] Y. Pan, Q. Xu, and H. Gao, "The research of the fuzzy control algorithm optimization based on chaos," *Control Theory and Application*, vol. 17, no. 5, pp. 702–706, 2000.

[16] D. Qiu, M. Rao, Q. Huo, and Q. Wang, "Dynamical modeling and sliding mode control of inverted pendulum systems," *Control Engineering of China*, vol. 45, no. 15, pp. 325–333, 2013.

[17] G Technology Ltd., *Experiment of Inverted Pendulum and Automatic Control Principle*, G Technology Ltd., Shenzhen, China, 2005.

[18] J. Song, J. Xiao, and X. Xu, "Modeling and control method of the inverted pendulum system," *Journal of Northeastern University*, vol. 23, no. 4, pp. 333–337, 2002.

[19] S. Hu, *The Principle of Automatic Control*, Science Press, Beijing, China, 6th edition, 2013.

[20] W. L. Brogan, *Modern Control Theory*, Prentice Hall, Upper Saddle River, NJ, USA, 1991.

[21] C. Huifeng, "*Research on automatic swing up control of inverted pendulum system*," M.S. thesis, Department of Electronic Engineering, Dalian University of Technology, Dalian, China, 2009.

[22] M. Xing, J. Xia, J. Wang, B. Meng, and H. Shen, "Asynchronous H_∞ filtering for nonlinear persistent dwell-time switched singular systems with measurement quantization," *Applied Mathematics and Computation*, vol. 362, Article ID 124578, 2019.

[23] Y. Xia, J. Wang, B. Meng, and X. Chen, "Further results on fuzzy sampled-data stabilization of chaotic nonlinear systems," *Applied Mathematics and Computation*, vol. 379, no. 15, Article ID 125225, 2020.

[24] S. U. Wang, "The control arithmetic for the double inverted pendulum based on the fuzzy control theory," *Journal of Xidian University*, vol. 33, no. 1, pp. 111–115, 2006.

[25] C. Liu, Q. Wu, X. Zou, and S. Hu, "Scale factors' influence on the performance of a fuzzy logic controller for a double inverted pendulum," *Pattern Recognition and Artificial Intelligence*, vol. 13, no. 4, pp. 404–406, 2000.

[26] K. Mathiyalagan, J. H. Park, and R. Sakthivel, "New results on passivity-based $\mathscr{H}_\infty$ control for networked cascade control systems with application to power plant boiler turbine system," *Nonlinear Analysis: Hybrid Systems*, vol. 17, pp. 56–69, 2015.

[27] K. Mathiyalagan, J. Park, and R. Sakthivel, "Observer-based dissipative control for networked control systems: a switched system approach," *Complexity*, vol. 21, no. 2, pp. 297–308, 2015.

Hindawi
Discrete Dynamics in Nature and Society
Volume 2020, Article ID 7360765, 11 pages
https://doi.org/10.1155/2020/7360765

Research Article

Study on the Home Health Caregiver Scheduling Problem under a Resource Sharing Mode considering Differences in Working Time and Customer Satisfaction

Heping Wang, Yuke He, Yan Li, and Fuyu Wang

School of Management Science and Engineering, Anhui University of Technology, Maanshan 243032, China

Correspondence should be addressed to Yan Li; liyan4@ahut.edu.cn

Received 3 February 2020; Accepted 18 March 2020; Published 11 May 2020

Guest Editor: Jinliang Wang

The stage of social aging and further deepening of population aging has been witnessed in China. The demand for home care is increasingly growing; meanwhile, medical human resources are insufficient. In this context, a home health caregiver scheduling problem under the resource sharing mode is studied in this paper. Under such mode, two types of caregivers, i.e., full-time caregiver and part-time caregiver, are regarded as the main labor force by HHC institutions. In HHC planning, different working times for the two kinds of caregivers will need to be considered. Consequently, in this paper, a corresponding mathematical model is established and a hybrid algorithm that combines the whale optimization algorithm (WOA) with the particle swarm optimization (PSO) algorithm is proposed to solve the model. The proposed algorithm is compared with the existing algorithms to verify its effectiveness through three example tests of different scales and Solomon example. Finally, the resource sharing model is compared with the traditional model through a case, and the rationality of home health caregiver scheduling in the resource sharing model is discussed in terms of cost structure and customer satisfaction.

1. Introduction

The stage of social aging and further deepening of population aging has been witnessed in China. The problem of old-age care is getting more and more serious. The existing traditional pension model has not been able to meet the needs of the elderly well. A novel home health care (HHC) model has been developed and extensively applied in both Europe and North America [1]. This model has been gradually accepted and recognized by an increasing number of people with the growth of the Chinese economy, the advance of science and technology, and the improvement of both the living standard and lifestyle of people in China. Home health care in China is mainly implemented by two entities: community-based well-known local hospitals and home-based medical care companies. According to the *China Health Statistics Yearbook 2018*, only 1.8 medical technicians care for every 1000 people; consequently, there is a significant shortage in medical resources [2]. For the newly emerging home health care industry in China, nursing staff has become the most scarce resource. The hospital has a large number of health caregivers, and the health caregivers have some spare time under the scheduling system of hospital. The home health care industry can use the resource sharing model to solve the resource shortage under the background of the decentralization of idle resources, which can effectively develop the family medical care industry and activate the flexibility of employment in the medical industry. Under the resource sharing mode, HHC institutions employ part-time health caregivers to support daily home health caregiver scheduling. After accepting employment by a well-known community-based local hospital and a home-based medical care company, medical health caregivers must balance both jobs according to their respective working schedules. Given that medical institutions have different schedules, HHC medical health caregivers have different working times. Thus, when designing routing and scheduling plans, HHC

centers must consider the different working times of health caregivers.

Scholars have conducted a series of studies on home health caregiver scheduling. Redjem et al. [3] proposed two integer programming models; each model corresponded to a specific home health caregiver scheduling strategy. They conducted experiments that identified a restrictive relationship between customer waiting time and health caregiver travel time. Rasmussen et al. [4] introduced a constrained set partitioning model to summarize the travel time for visiting different customers and the visit time window. This problem was solved using the B&P algorithm. Numerical simulation indicated that the result was very close to the optimal solution. Larsen et al. [5] modeled HCSP as a multistage (multilevel) combinatorial optimization problem. They developed a modified version for practical problem solving using a tabu search-based heuristic algorithm. Braekers et al. [6] proposed a metaheuristic algorithm, with a large neighborhood search algorithm added to a multiple local search box forward. Tricoire et al. [7] emphasized the need to estimate health caregiver travel time when solving a scheduling problem using the two-stage method. They estimated the travel time using a kernel regression algorithm based on health caregiver travel times observed during previous periods. The numerical calculation on the basis of the examples practical problems shows that the estimation effect of this method is better than that of the classical mean value method.

Liu et al. [8] considered the lunch time of health caregivers in home health caregiver scheduling and built a three-index mathematical model to solve the problem. They decomposed the problem into one master problem and several pricing subproblems and used the branch-and-price algorithm to find the optimal solution. Zhuo et al. [9] proposed a tabu search algorithm based on insertion algorithm and saving algorithm to solve the management problem of home-based medical and health care resources with cyclical service demands. To solve the home health caregiver scheduling problem of simultaneous services, Yang-yi et al. [10] designed an adaptive large neighborhood search algorithm in which multiple removing and insertion algorithms were used for a neighborhood search in feasible and infeasible solution spaces. It adopted a relation matrix and time adjustment strategies to accelerate problem solving and applied a simulated annealing method to accept neighborhood solutions. Finally, numerical experiments and algorithm comparison were carried out to verify the effectiveness of algorithm. Yuan et al. [11] proposed a mathematical model with constraints of multiple types of caregivers and converted it into a major problem based on set partitioning and several pricing subproblems based on the shortest path with resource constraints. Each of these paths corresponds to one type of health caregiver. A column generation algorithm and a B&P algorithm were designed to solve the model. Fang et al. [12] considered the problem of finite-time stabilization in probability for a class of high-order stochastic nonlinear systems with output constraints in which the fractional powers are only required to be positive rather than not less than one. Zhao et al. [13] considered the second-order sliding mode controller design subject to an output constraint. By constructing a new barrier Lyapunov function and applying the technique of adding a power integrator, a novel second-order sliding mode control algorithm, which can be used to deal with the output constraint problem, has been developed. Liang et al. [14] proposed the problem of dissipativity analysis and nonfragile sampled-data control which is investigated for fuzzy Markovian jump systems, and based on the mode-dependent Lyapunov function consisting of a two-sided closed-loop function, the stochastically stable criteria, and strictly dissipative criteria, a truck-trailer model is given to demonstrate the efficiency of the presented method. Xia et al. [15] proposed a command filtered-based adaptive fuzzy tracking control scheme for nonlinear systems with unknown control directions. Combining fuzzy logic system and command filter with Nussbaum gain function, adaptive fuzzy controller constructed in this paper guarantees that error signals converge into bounded compact sets around the origin and all closed-loop signals are bounded. The effectiveness of the presented scheme is verified by a simulation result.

Due to the flexibility of the resource sharing model, many scholars have solved many industrial problems by using the resource sharing model. Yan-ning et al. [16] designed the optimization problem of vehicle logistics path under the resource sharing mode and constructed the mathematical model of path optimization. AlQahtani [17] proposed a resource sharing scheme to solve the data traffic congestion and overload in 5G network. Wu et al. [18] proposed a model of sharing manufacturing resources to solve the decentralization, complexity, and heterogeneity of manufacturing resources. Wu et al. [19] studied the green resource sharing problem of mobile device-to-device (D2D) based on cellular network and established an energy efficiency analysis model.

From the above literatures, many scholars have studied models and algorithms of home health care resources scheduling and have obtained some achievements. There have been many complex models that approximate a real problem. Also, some effective intelligent optimization algorithms and exact solution algorithm have been presented. However, these existing studies have focused on full-time health caregiver scheduling. Few scholars consider both full-time and part-time health caregivers' scheduling. Actually due to shortages in Chinese medical resources, many home health care centers need to hire part-time health caregivers to meet nursing demand of older customers. This problem is becoming increasingly widespread and persistent. To resolve the supply-demand contradiction in health care resources based on the above studies, this paper studies the home health care scheduling problem in resource sharing mode.

The main contributions of the paper include the following points: (1) we propose a home health care scheduling model considering customer satisfaction under a resource sharing mode; (2) in the model, the different working time windows of health caregivers are considered; (3) a hybrid algorithm of whale optimization algorithm (WOA) and particle swarm optimization (PSO) (i.e., WOA-PSO) is designed.

The paper is organized as follows. A mathematical model of home health caregiver scheduling problem is presented in Section 2. A hybrid intelligent optimization algorithm is designed in Section 3. Numerical experiments are conducted in Section 4. Conclusion is given in Section 5.

2. Modeling

2.1. Problem Description. This paper studies the home health care scheduling in resource sharing mode. In this mode, if the full-time health caregivers cannot meet the needs of the elderly customers, home health care center will dispatch part-time staff to serve the elderly customers. The difference between the new service route network and the traditional one is shown in Figure 1.

The problem posed in this paper can be described on a directed graph $G(V, A)$, where V denotes a set of nodes $V = \{0, 1, 2, ..., N\}$, node 0 represents the HHC center, and nodes $1, 2, ..., N$ signify customers. A signifies a set of edges; $A = \{(i, j) \mid i, j \in V, i \neq j\}$. Each customer has a definite request and service time. The service time of node 0 is 0. There are many health caregivers in HHC center. Each customer has an expected time window and a tolerable time window. Each health caregiver has a working time window. When the working time window is open, the health caregiver leaves the health care center to provide customer service. The home caregiver has to wait until the time window opens if the health caregiver arrives at the customer before the start of the time window. If the health caregiver arrives later than the tolerable time window, the customer will refuse his or her service. The arrival time of health caregiver is their starting service time. The health caregivers will continue to serve the next customer when their service time exceeds the working time window, which will result in service cost and overtime penalty cost. The health caregiver does not have to return to the health care center.

In order to formulate the home health caregiver scheduling problem, all symbols for the model are as shown in the following:

i, j: HHC center if $i, j = 0$ and customer if $i, j \neq 0$

k: health caregiver

V: a set of customers and the HHC center

H: a set of health caregivers

S_{ik}: service time of customer i by health caregiver k

$[E_i, L_i]$: an expected time window of customer i

$[EE_i, LL_i]$: a tolerable time window of customer i

t_{ij}: the travel time between customer i and customer j

c_1: the unit travel cost of each health caregiver

c_2: the unit service cost of each health caregiver

c_3: the unit overtime cost of each health caregiver

c_4: the unit waiting time cost of each health caregiver

$[WS_k.WE_k]$: working time window for health caregiver k

AT_{ik}: the starting time of health caregiver k serving customer i

t_k: the off-duty time of health caregiver k

M: big positive real number

x_{ijk}: 0-1 binary variable, 1 if health caregiver k travels from i to j for providing service, 0 otherwise.

2.2. Satisfaction Function. Customers have different tolerances time windows and expected time windows, so the starting time of health care directly influences customer satisfaction. A shorter interval between the starting time of health care and the expected time window leads to higher customer satisfaction. If the starting time is within the expected time window, the customer is most satisfied and satisfaction value is 1. Considering that different customers have different perceptions of time, a time sensitivity coefficient δ is established in this paper. The satisfaction function is as follows:

$$F(AT_{iK}) = \begin{cases} \left(\dfrac{AT_{ik} - EE_i}{E_i - EE_i}\right)^{\delta}, & E_i > AT_{ik} > EE_i \\ 1, & L_i \geq AT_{ik} \geq E_i, \\ \left(\dfrac{AT_{ik} - L_i}{LL_i - L_i}\right)^{\delta}, & LL_i > AT_{ik} > L_i, \\ 0, & \text{others.} \end{cases} \tag{1}$$

2.3. Home Health Caregiver Scheduling Model. The optimization objective of dispatching health caregivers is to minimize the health care center's total serving cost and maximize customer satisfaction.

Based on the above description and mathematical symbols, the mathematical model for the problem is

$$\max f_1 = \sum_{i \in V} \sum_{k \in H} F(AT_{ik}), \tag{2}$$

$$\begin{aligned} \min f_2 = {} & \sum_{i \in V} \sum_{j \in V} \sum_{k \in H} x_{ij} t_{ij} c_1 + \sum_{k \in H} \sum_{i \in V} c_2 S_{ik} \\ & + \sum_{k \in H} c_3 \max(t_k - WE_k, 0) \\ & + \sum_{k \in H} \sum_{i \in V} \sum_{j \in V} c_4 \max(EE_i - AT_{ij}, 0) x_{ijk}, \end{aligned} \tag{3}$$

subject to

$$\sum_{k \in H} \sum_{i \in V} x_{ijk} = 1, \quad \forall j \in V, \tag{4}$$

$$\sum_{j \in V} \sum_{k \in H} x_{ijk} = 1, \quad \forall i \in V, \tag{5}$$

$$\sum_{j \in V} x_{0jk} = 1, \quad \forall k \in H, \tag{6}$$

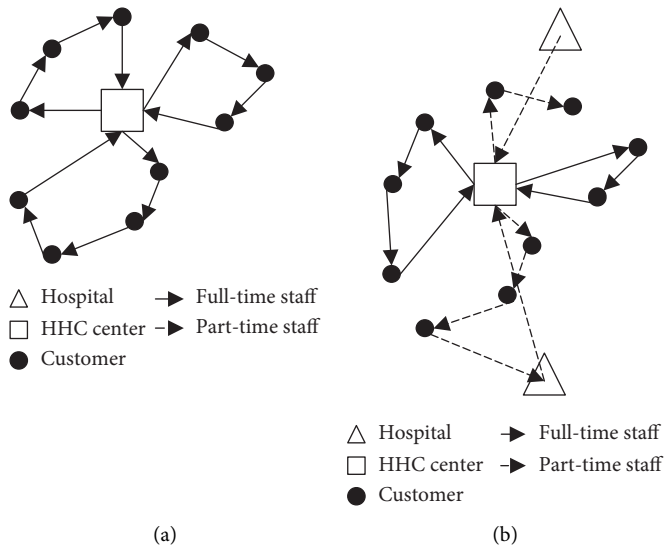

Figure 1: Schematic diagram of (a) traditional mode and (b) resource sharing mode.

$$\sum_{i \in V} x_{iok} = 1, \quad \forall k \in H, \tag{7}$$

$$\sum_{i \in V} x_{ijk} = \sum_{i \in V} x_{jik}, \quad \forall k \in H, \forall j \in V, \tag{8}$$

$$AT_{jk} + M\left(1 - x_{ijk}\right) \geq AT_{ik} + S_{ik} + t_{ij}, \quad \forall i \in V, \forall j \in V, \forall k \in H, \tag{9}$$

$$EE_i \leq AT_{ik} \leq LL_i, \quad \forall \mathrm{i} \in V, \forall k \in H. \tag{10}$$

Objective function formula (2) represents the maximization of customer satisfaction; objective function formula (3) represents the minimization of health care center's total serving cost, including traveling cost, service cost, overtime cost, and waiting cost; constraint equations (4) and (5) ensure that each customer is served by only one health caregiver; constraint equations (6) and (7) ensure that each service route is serviced by only one health caregiver; constraint equation (8) ensures continuity of service; constraint equation (9) ensures the time sequence of service; constraint equation (10) ensures that the starting time of the service cannot exceed the customer's latest tolerable time window.

2.4. Model Processing. The proposed HHC scheduling optimization model in this study includes two objectives: maximizing customer satisfaction and minimizing health care center's serving total cost. This model is a multiobjective optimization model. Available methods to solve multiobjective optimization models include the weight coefficient method and the Pareto optimality method. The weight coefficient method has higher feasibility and lower time complexity. Thus, in this study, it is adopted for model processing. However, it cannot be weighted directly because the model has the dual objectives of maximizing customer satisfaction and minimizing HHC costs. Therefore, the following measures are taken:

(1) By taking the reciprocal of customer satisfaction, the maximum of the customer satisfaction is converted into the minimum of the reciprocal of customer satisfaction. Then, it is weighted with the health care center's total serving cost.

(2) The conversion of customer satisfaction into its reciprocal will yield a difference of several orders of magnitude between cost and the value of the satisfaction function. Thus, the reciprocal of customer satisfaction is multiplied by an equivalence factor to support the equalization and dimensionless of the two objectives.

Based on the above processing, the objective function of this model is

$$\min \frac{f_2 = \rho_1 \beta}{\sum_{i \in N} \sum_{k \in K} F\left(AT_{ik}\right)} + \rho_2 \left[\sum_{i \in V} \sum_{j \in V} \sum_{k \in H} x_{ij} t_{ij} c_1 + \sum_{i \in V} \sum_{k \in H} c_2 S_{ik} + \sum_{k \in H} \max\left(t_k - WE_k, 0\right) c_3 + \sum_{i \in V} \sum_{j \in V} \sum_{k \in H} \max\left(EE_j - AT_{ij}, 0\right) x_{ijk} c_4 \right]. \tag{11}$$

3. A Hybrid WOA-PSO Algorithm

3.1. Standard WOA. WOA was first proposed by Mirjalili [20] in 2016. It is a novel metaheuristic algorithm that is derived by simulating the behavior that the individual whales communicate with each other through ultrasound when whale swarms hunt for prey or conduct other group activities. When a whale discovers prey, it sends ultrasonic signals to inform its companions about the prey. When hunting, each individual in a whale swarm receives

considerable information from other individuals through ultrasound and approaches the prey based on this information.

The search mode in the WOA is divided into a local development stage and a global search stage.

During the global search stage, a stochastic search agent is selected and defined as the current optimal candidate solution. Other search agents are considered to be far from this optimal candidate solution. The mathematical description is as follows:

$$D = \left| \vec{C} \cdot t\vec{X}^{*} n(t) q - h\vec{X}(t) \right|, \tag{12}$$

$$\vec{X}(t+1) = \vec{X}^{*}(t) - \vec{A} \cdot \vec{D}, \tag{13}$$

where t denotes the current number of iterations; $\vec{A}$ and $\vec{C}$ denote coefficient vectors; $\vec{X}^{*}(t)$ is the current optimal position vector, which requires updates for each generation; $\vec{X}(t)$ is the position vector; is the absolute value; and $\cdot$ is an element-by-element multiplication. $\vec{X}^{*}(t)$ will be updated in each iteration if there is a better solution.

The vectors $\vec{A}$ and $\vec{C}$ are calculated as follows:

$$\vec{A} = 2\vec{\alpha} \cdot \vec{r} - \vec{\alpha}, \tag{14}$$

$$\vec{C} = 2 \cdot \vec{r}, \tag{15}$$

$$\vec{\alpha} = 2 - \frac{2t}{I_{\text{gen max}}}, \tag{16}$$

where $\vec{r}$ is a stochastic vector in [0, 1] and $I_{\text{gen max}}$ is the set maximum number of iterations; $\vec{\alpha}$ is linearly decreased from 2 to 0 over the course of iterations. When a "subswarm" approaches the optimal candidate position in the whale swarm, $\vec{A}$ is stochastically selected within the range $[-2, -1] \cup [1, 2]$ to keep other "subswarms" away from the optimal candidate position and avoid being caught in local optimization.

During the local development stage, WOA describes the bubble-net behavior through shrinking encircling and spiral updating position. The spiral updating position is a logarithm spiral curve between the current position and the optimal position. Its mathematical expression is as follows:

$$\vec{X}(t+1) = \vec{D}_1 \cdot e^{hl} \cdot \cos(2\pi l) + \vec{X}^{*}(t), \tag{17}$$

where $D = X * t - Xt$; h is a constant for defining the spiral shape; and l is a stochastic number within the range of $[-1, 1]$.

The modes of shrinking encircling and spiral updating position proceed simultaneously. The probability factor ρ determines the mode used by an agent for local development, where ρ denotes a stochastic number within the range of $[0, 1]$.

$$\vec{X}(t+1) = \begin{cases} \vec{X}^{*}(t) - \vec{A} \cdot \vec{D}, & \rho < 0.5, \\ \vec{D}_1 \cdot e^{hl} \cdot \cos(2\pi l) + \vec{X}^{*}(t), & \rho \geq 0.5. \end{cases} \tag{18}$$

Random numbers such as $\vec{\alpha}$, $\vec{A}$, $\vec{r}$, and ρ make the algorithm more accidental during search. More importantly, $\vec{\alpha}$ makes the algorithm transition to local search slowly as the number of iterations increases, which results in the second half of the algorithm falling into local optimum. Considering the excellent performance of the WOA to solve multiobjective nonlinear optimization problems, a hybrid mechanism is introduced to overcome the defect of the algorithm and to further effectively optimize the solutions in this paper.

3.2. Hybrid Algorithm Based on WOA and PSO

3.2.1. Algorithm Principles. WOA is used for global optimization in the hybrid algorithm so that solution spaces gather in the area of the global optimal solution. Based on WOA, the fitness values of individuals can be calculated and a historically optimal value is recorded. Then, the learning mechanism of PSO algorithm is introduced to learn from historically optimal individuals and conduct screening. The learning mechanism enhances the local search ability of "subswarms" far away from the optimal candidate solution. During the later stage of the algorithm, when the swarm has been caught in the local optimization, individuals trace the current optimal solution through the learning mechanism and search the local new solutions, which make the algorithm jump out of the local optimization more easily. The mathematical expression of the learning mechanism of PSO is

$$L_{n+1} = L_n + M_1 * \text{rand}(0, 1) * (L_n - L_{\text{best}}), \tag{19}$$

where the greater the difference between an individual and the historic optimized value, the bigger the learning factor M_1.

A league competition mechanism is also introduced into the algorithm to enhance the global search ability. The league competition mechanism replaces the stochastic selection in the standard WOA. First, a specific number of individuals are selected from the population with equal probability. Then, the best individual is selected among them and implanted into the progeny population until the new population scale reaches the original population scale.

The specific steps are as follows:

(1) Determine the number of individuals to be selected

(2) Calculate the fitness value of each individual and select the individual with the best fitness value for direct admission into the next generation

(3) Repeat step (2) until the new population scale reaches the original population scale

3.2.2. Problem-Based Coding Scheme. The WOA-PSO algorithm is used to solve multiobjective combinatorial optimization problems. An individual in each search space represents a solution to the space. The home health caregiver scheduling problem is a NP-hard problem that requires solving both the service sequence and routing of health caregivers. Thus, service selection and route sequence should

be mapped onto each individual. The position vector of each individual is an N-dimensional real vector. The integral part in the vector denotes the serial number for the health caregiver who should serve the ith customer, while the decimal part denotes the route of the health caregiver. Assuming that eight customers and three health caregivers work in an area, Figure 2 shows the position vector of an individual.

When $[X]$ denotes the integer part of each gene locus for an individual, the same integer value indicates that the customer is served by the same health caregiver. When $\{X\}$ denotes the decimal part, a greater decimal value means a more forward position in the route sequence (see decoding steps in Figure 3). Thus, the scheme of the individual can be described as follows: customers 2, 4, and 5 are served by health caregiver #1; customers 3, 6, and 8 are served by health caregiver #2; customers 1 and 7 are served by health caregiver #3; the route sequence of health caregiver #1 is 0-4-2-5; the route sequence of health caregiver #2 is 0-6-8-3; and the route sequence of health caregiver #3 is 0-1-7.

3.2.3. Algorithm Steps. The basic steps of the hybrid WOA-PSO algorithm are as follows:

Step 1: initialize the basic parameters of the algorithm by setting the population number P, the league competition mechanism selection proportion g, the learning factor M_1, and the number of iterations *Genmax*.

Step 2: calculate the objective function value of each search agent, and the optimal search agent is denoted by $X^*(t)$, whose function value is the smallest.

Step 3: select the search mode and update the agent position using formula (16).

Step 4: assume each agent approaches the optimal search agent using formula (17) and recalculate the optimal search agent.

Step 5: assess search agents, stochastically select g% agents, and select the optimal agent for admission into the next generation until the new population scale reaches the original population scale.

Step 6: proceed to Step 7 when the maximum number of iterations or the threshold is reached; otherwise, return to Step 3 for the next search.

Step 7: terminate the algorithm and generate the objective function value of the optimal individual.

4. Experimental Simulation and Analysis

All algorithms are programmed using MATLAB 2018 and are tested on an Intel i7-4800MQ (2.7 GHz and 4 GB) computer with a WIN7 operating system.

4.1. Example Description. To test the performance of the proposed algorithm, 10 examples are generated in each of three scales: 25 customers, 45 customers, and 60 customers. N points are randomly generated within the Cartesian coordinate plane $[0, 100]^2$, and the distance between two points is the Euclidean distance. Service time is the integer of uniformly distributed $[10, 15]$. The coordinate of the health care center is $[0, 0]$.The longest working time L is 250. The midpoint LK_i and width LL_i of the stochastic number time window are used to determine the customer time window. The midpoint LK_i is the stochastic integer of uniformly distributed $[0, 250]$; the width LL_i is the stochastic integer of uniformly distributed $[10, 15]$; and the tolerable time window width TL_i is the stochastic integer of the uniformly distributed $[LL_i + 30, LL_i + 50]$. The unit travel cost, unit service cost, unit overtime cost, and waiting cost are 3, 20, 15, and 10, respectively.

Customer number	1	2	3	4	5	6	7	8
Position vector	3.6	1.7	2.1	1.9	1.1	2.6	3.1	2.4

Figure 2: Coding scheme of the hybrid algorithm.

Step 1: perform $[X]$ operation for each dimension of an individual.
Step 2: group customers according to $[X]$.
Step 3: perform $\{X\}$ operation in each group.
Step 4: rank according to $\{X\}$ value to obtain the route sequence.

Figure 3: Decoding process of the hybrid algorithm.

4.2. Algorithm Performance Analysis. To verify the superiority of the proposed WOA-PSO algorithm for solving the scheduling problem of home health caregiver considering working time, a large number of simulation experiments are conducted on the proposed algorithm. The simulation experiment results are compared with those of WOA and PSO. The simulation results in Figure 4 show that WOA-PSO algorithm has a higher convergence rate than WOA and a stronger local search compared to PSO.

Three different scale cases are used to test the hybrid algorithm. They are Scale 1 (25 customers), Scale 2 (40 customers), and Scale 3 (60 customers). From Figures 5–7, the algorithm converges in the 12th generation in a 25-scale example, in the 39th generation in a 40-scale example, and in the 36th generation in a 60-scale example. It can be seen that the algorithm achieves a high convergence rate and stability in these examples of different scales.

From Tables 1 and 2, in Scale 1 example, compared with the PSO algorithm and the WOA, the obtained objective function value by WOA-PSO algorithm is decreased by 10.30% and 6.64% and the calculation time of the WOA-PSO algorithm is reduced by 33.33% and 45.71%. In Scale 2 example, the obtained objective function value by WOA-PSO algorithm is decreased by 4.47% and 0.81% and the calculation time of the WOA-PSO algorithm is reduced by 9.81% and 49.91%. In Scale 3 example, the obtained objective function value by WOA-PSO algorithm is decreased by 2.80% and 0.40% and the calculation time of the WOA-PSO algorithm is reduced by 1.11% and 48.45%. It can be seen

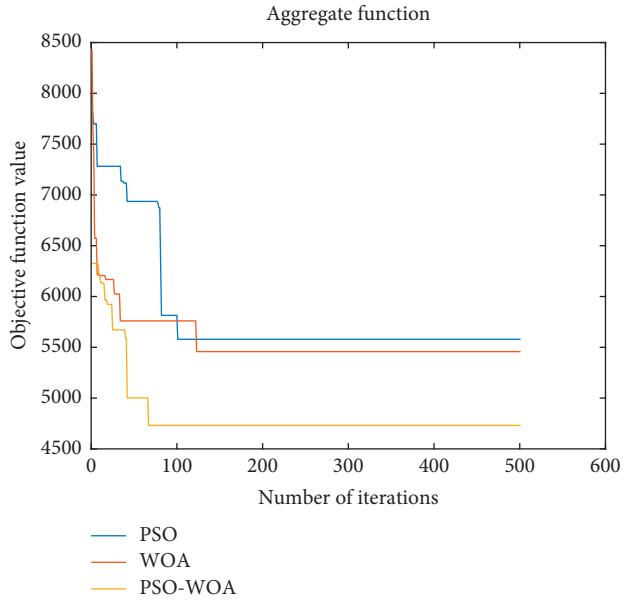

Figure 4: Algorithm comparisons.

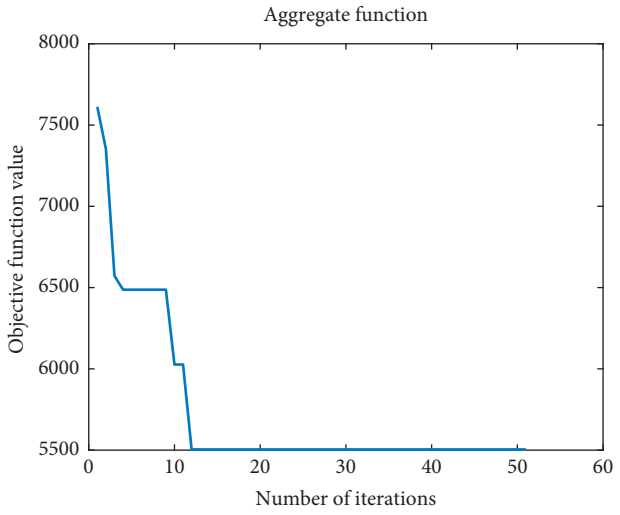

Figure 5: Scale 1 (25 customers).

that the optimization speed and optimization result of the hybrid optimization algorithm in this paper are superior to the single algorithm in the case of the same simulation environment and parameters. The results show that the hybrid algorithm is more feasible and suitable for solving such optimization problems.

4.3. Benchmark Test. To further test the performance of the WOA-PSO algorithm for solving VRPTW, the Solomon example is applied (http://web.cba.neu.edu/~msolomon/problem.htm) as a benchmark, calculating each example 20 times. Table 3 provides the experimental results, expressed as the mean value of the optimal solution and the relative deviation between the mean value and the known optimal value for each example after 20 repeated calculations.

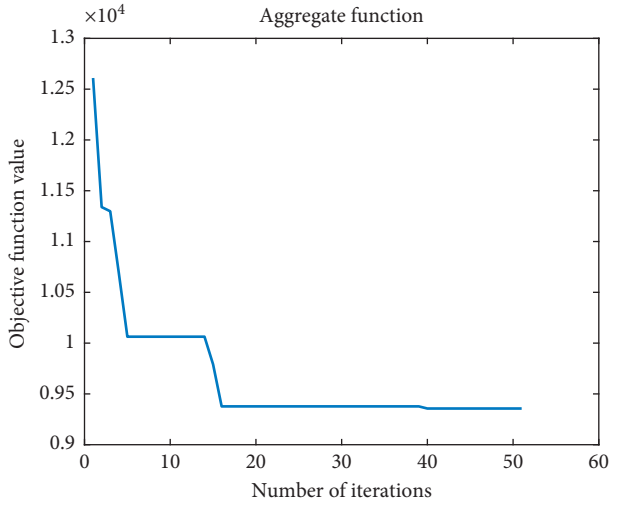

Figure 6: Scale 2 (40 customers).

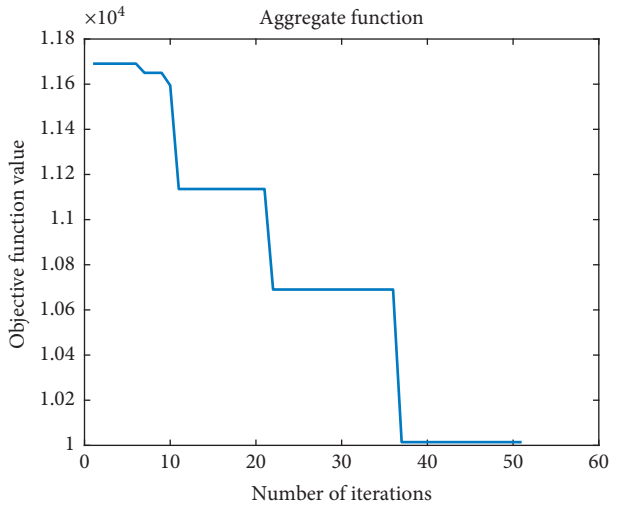

Figure 7: Scale 3 (60 customers).

Table 1: Optimization time comparison among different algorithms.

	Optimization time (s)		
	WOA	PSO	WOA-PSO
Scale 1	4.31	3.51	2.34
Scale 2	10.64	5.91	5.33
Scale 3	25.84	13.47	13.32

Table 2: Optimization result comparison among different algorithms.

	Results of 20 times of optimization		
	WOA	PSO	WOA-PSO
Scale 1	5033.46	5239.18	4699.33
Scale 2	9648.94	10017.98	9569.94
Scale 3	11736.09	12025.90	11689.15

Table 3: Solving the Solomon example with the WOA-PSO algorithm.

Example	Scale	Known optimal solution	Results obtained by WOA-PSO	
			Mean value	Relative deviation (%)
C104	25	186.9	189.1	1.18
C201	25	214.7	216.1	0.65
R103	25	454.6	460.7	1.34
R201	25	463.3	463.9	0.13
RC101	25	461.1	469.1	1.73
RC208	25	269.1	272.1	1.11
C103	50	361.4	365.5	1.13
C201	50	360.2	363.4	0.89
R101	50	1044	1051	0.67
R201	50	791.9	800.3	1.06
RC101	50	944	957.2	1.40
RC204	50	444.2	468.6	4.49
C101	100	827.3	830.5	0.39
RC201	100	589.1	597.1	1.36
R103	100	1201.7	1261.3	4.27
R201	100	1143.2	1188.2	3.94
RC101	100	1619.8	1703.8	4.44
RC205	100	1154	1205.3	4.45

Table 3 shows that the relative deviation between the mean value of the WOA-PSO algorithm and the current optimal value is less than 4.5%. The relative deviation between the mean value of all examples compared to the mean value of the known optimal solution is 2.34%. The WOA-PSO algorithm achieves excellent performance for solving VRPTW and is equivalent to the known optimal solution in each case.

The experimental results of the WOA-PSO algorithm are compared with the optimal solution obtained by the WOA-TS algorithm proposed in the literature [16] and the known optimal solution, as detailed in Table 4. The last column lists the relative deviation between the optimal solution obtained by the proposed algorithm and the known optimal solution.

Table 4 shows that, compared to the WOA-TS algorithm, the maximum optimal value of the WOA-PSO algorithm increases by 6.31% given the same number of vehicles. The relative deviation between the optimal value and the value of the known optimal solution does not exceed 2.3%. Thus, the WOA-PSO algorithm fully uses the global search ability of PSO. It also relies on a competitive mechanism and dual-domain structure to effectively enhance local search ability, avoid being caught in local optimization too early, and improve solution quality.

4.4. Experimental Analysis of Large-Scale Examples. As the demand for pension increases, the number of customers served by home care medical enterprises will increase, so large-scale examples are used to verify the WOA-PSO algorithm proposed in this paper. Ten cases of 100 customers and ten cases of 200 customers are generated randomly. Each case is run 10 times, and the average value is recorded. For large-scale examples, the running time of the heuristic algorithm is long, so all algorithms are run in the same running time to ensure the validity of the experiments. The experimental results are shown in Table 5.

The running results are shown in Table 5. For all the scale 100 examples, 90% cases' running results with WOA-PSO are better than comparison algorithm, and the optimization range is between 9% and 13%. For all the scale 200 examples, 70% cases' running results with WOA-PSO are better than comparison algorithm, but the optimization range is between 7% and 9%. The main reason for the phenomenon is that the running speed of the algorithm slows down with the increase of the example size. Therefore, WOA-PSO cannot fully find a better solution in the case of the same running time for the scale 200 example.

4.5. Cost Analysis. The research on the home health caregiver scheduling in the resource sharing mode can resolve the contradiction between scarce care worker resources and huge demand, improve customer satisfaction, and reduce the cost of home care center. Therefore, the cost structure and customer satisfaction of health care centers are selected as indicators in the experimental section. Taking E25-3 as an example, the resource sharing mode and the traditional mode are compared from five aspects: waiting cost, overtime cost, travel cost, service cost, and customer satisfaction, as shown in Figure 8 and Table 6.

Figure 8 shows that the resource sharing mode reduces the total cost by 9.5% and lowers both the service cost and waiting cost by 25.16% and 26.35%, respectively, compared to the traditional mode, while travel cost is increased by 4.35% and overtime cost is increased by 34.25%. There are two explanations for this: first, in order to match the working time with the customer's expected time, health caregivers must choose customers who are located far away, increasing travel cost; second, given the limitations in working time,

Table 4: Comparison between the WOA-PSO algorithm and existing algorithms.

Example	Scale	WOA-TS Optimal route	WOA-PSO Optimal route	Known optimal solution Optimal route	Relative deviation (%)
C104	25	187.5	187.5	186.9	0.32
C201	25	214.1	214.1	214.7	−0.28
R103	25	455.7	455.7	454.6	0.24
R201	25	467.7	464.4	463.3	0.24
RC101	25	466.7	462.2	461.1	0.24
RC208	25	271.5	271.5	269.1	0.89
C103	50	439.9	362.2	361.4	0.22
C201	50	373.8	361.2	360.2	0.28
R101	50	1081.2	1046.7	1044	0.26
R201	50	831.6	794.3	791.9	0.30
RC101	50	988.4	951.6	944	0.51
RC204	50	459.4	449.2	444.2	1.13
C101	100	1273.6	828.9	827.3	0.19
C201	100	719.3	597.9	589.1	0.47
R103	100	1284	1235.5	1208.7	2.22
RC101	100	1698	1631.8	1619.8	0.74
RC205	100	1221.6	1162.1	1154	0.70

Table 5: Test results of large-scale examples.

Case no.	WOA-PSO	PSO	WOA	Case no.	WOA-PAO	PSO	WOA
100_1	9521.66	9710.41	9637.42	200_1	11503.26	11720.96	11590.73
100_2	8495.22	8601.37	8556.79	200_2	14724.42	14637.68	14534.98
100_3	11034.71	11160.63	10978.62	200_3	15800.42	15724.22	15547.39
100_4	15314.49	15683.85	15366.38	200_4	16468.44	16754.65	16539.50
100_5	13457.68	13067.32	12877.72	200_5	15826.45	16163.20	16037.51
100_6	19865.48	20122.66	19958.18	200_6	16681.47	16944.54	16781.46
100_7	16503.37	16711.56	16491.84	200_7	24236.40	24349.94	24138.60
100_8	12112.59	12467.36	12239.09	200_8	26984.36	27338.86	27121.38
100_9	11163.22	10932.61	111336.78	200_9	17721.60	17503.46	17829.37
100_10	12946.97	13168.34	13011.28	200_10	17406.58	17221.50	17104.00

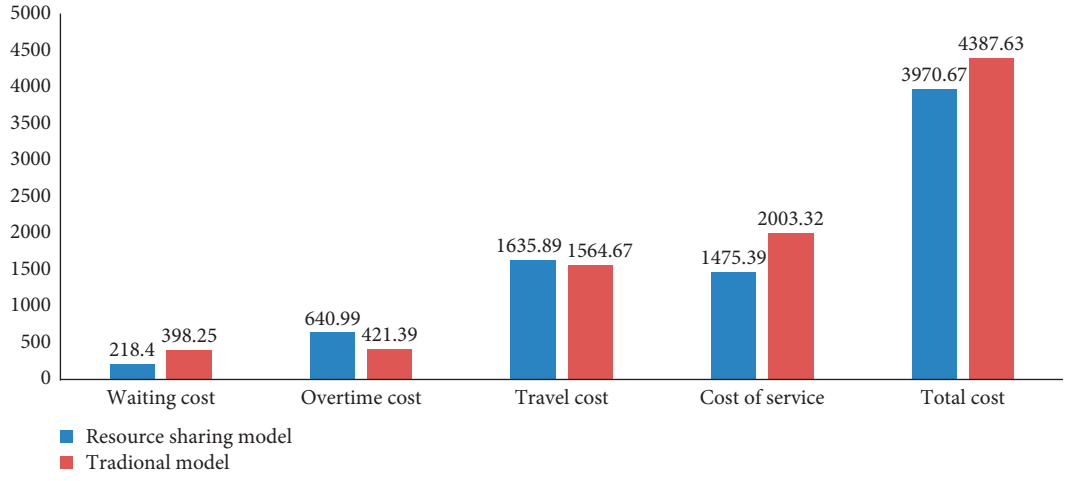

Figure 8: Cost comparison.

they must work overtime to meet the requirements of all customers in the area, increasing overtime cost. Table 6 shows that the customer satisfaction on the three scale examples is increased by 14.03%, 15.25%, and 18.6% in the resource sharing model, respectively. This may be because health caregivers usually choose customers whose schedules can be met in the first place. Thus, adopting the resource sharing model for home health caregiver scheduling can

Table 6: Customer satisfaction comparison.

	Customer satisfaction	
	Resource sharing mode	Traditional mode
Scale 1	14.67	12.19
Scale 2	20.84	17.66
Scale 3	26.44	21.52

reduce the operational cost of health caregivers, save human resources, and improve service quality.

5. Conclusions

This paper investigates the home health caregiver scheduling problem under a resource sharing model. A corresponding mathematical model is established and the WOA-PSO hybrid algorithm is proposed to solve it. The basic WOA has poor convergence performance and is prone to fall into a local optimum. Therefore, the league competition mechanism and the PSO learning mechanism in the WOA are embedded to deal with the subswarms, which make the hybrid algorithm identify an optimization scheme efficiently and effectively. The hybrid WOA-PSO algorithm proposed in this paper can quickly solve the examples on three scales (i.e., 25, 40, and 60 customers). A benchmark test on the Solomon example verifies its effectiveness. Moreover, the comparison results between the resource sharing model and the traditional model from cost structure and customer satisfaction highlight the superiority of the resource sharing model. The resource sharing model can satisfactorily resolve the contradiction between insufficient medical resources and serious social aging in China and can better allocate human resources and can effectively reduce social costs. However, the scheduling problem of domestic home health resources is a complex system. Therefore, how to use the multiagent systems [21] to describe the model will be our future research interest.

Data Availability

The data used to support the findings of this study are included within the article. Part of the data is generated randomly according to the problem and part of the data is from Solomon example.

Conflicts of Interest

The authors declare that they have no conflicts of interest.

Acknowledgments

This study was supported by the National Natural Science Foundation of China (71872002), Humanities and Social Sciences Research Project of Ministry of Education of China (Funding No. 19YJCZH091), and Humanities and Social Sciences Research Project for University in Anhui (Funding No. SK2017A0077).

References

[1] D. S. Mankowska, F. Meisel, and C. Bierwirth, "The home health care routing and scheduling problem with interdependent services," *Health Care Management Science*, vol. 17, no. 1, pp. 15–30, 2014.

[2] National Bureau of Statistics, *China Health Statistics Yearbook 2018*, China Statistics Publishing House, Beijing, China, 2018.

[3] R. Redjem, S. Kharraja, X. Xie et al., "Coordinated multicriteria scheduling of caregivers in home health care services," in *Proceedings of the IEEE Conference on Automation Science and Engineering, CASE 2011*, Trieste, Italy, August 2011.

[4] M. S. Rasmussen, T. Justesen, A. Dohn, and J. Larsen, "The home care crew scheduling problem: preference-based visit clustering and temporal dependencies," *European Journal of Operational Research*, vol. 219, no. 3, pp. 598–610, 2012.

[5] J. Larsen, M. Chaieb, and K. Mellouli, "The home care scheduling problem: a modeling and solving issue," in *Proceedings of the International Conference on Modeling*, Berkeley, CA, USA, August 2013.

[6] K. Braekers, R. F. Hartl, S. N. Parragh, and F. Tricoire, "A bi-objective home care scheduling problem: analyzing the trade-off between costs and client inconvenience," *European Journal of Operational Research*, vol. 248, no. 2, pp. 428–443, 2016.

[7] S. Tricoire, A. Matta, E. Sahin et al., "A two-stage approach for solving assignment and routing problems in home health care services," in *Proceedings of the International Conference on Health Care Systems Engineering*, pp. 66–79, Copenhagen, Denmark, May 2013.

[8] R. Liu, B. Yuan, and Z. Jiang, "Mathematical model and exact algorithm for the home care worker scheduling and routing problem with lunch break requirements," *International Journal of Production Research*, vol. 55, no. 2, pp. 558–575, 2016.

[9] Y. Zhuo, R. Liu, and Y. Hua, "Taboo solving algorithms for periodic home-based medical nursing problems," *Chinese Science and Technology Paper*, vol. 10, no. 14, pp. 1714–1720, 2015.

[10] T. Yang-yi, R. Liu, and Z. Jiang, "Scheduling of family nurses with simultaneous service demand," *Industrial Engineering and Management*, vol. 22, no. 3, 2017.

[11] B. Yuan, R. Liu, and Z. Jiang, "Study on scheduling problems of multi-type family nursing staff," *Journal of Systems Engineering*, vol. 32, no. 1, pp. 57–64, 2017.

[12] L. Fang, L. Ma, S. Ding, and D. Zhao, "Finite-time stabilization for a class of high-order stochastic nonlinear systems with an output constraint," *Applied Mathematics and Computation*, vol. 358, pp. 63–79, 2019.

[13] S. H. Zhao, J. H. Park, and C. C. Chen, "Second-order sliding mode controller design with output constraint," *Automatica*, vol. 112, Article ID 108704, 2020.

[14] X. Liang, J. Xia, G. Chen et al., "Dissipativity-based non-fragile sampled-data control for fuzzy Markovian jump systems," *International Journal of Fuzzy Systems*, vol. 21, no. 12, 2019.

[15] J. Xia, J. Zhang, J. Feng, Z. Wang, and G. Zhuang, "Command filter-based adaptive fuzzy control for nonlinear systems with unknown control directions," *IEEE Transactions on Systems, Man, and Cybernetics: Systems*, vol. 29, pp. 1–9, 2019.

[16] J. Yan-ning, X. Qi, H. Ren et al., "Automobile logistics routing problem optimization under resource sharing mode," *Journal of Highway and Transportation Research and Development*, vol. 34, no. 6, pp. 114–121, 2017.

[17] S. A. AlQahtani, "An efficient resource allocation to improve QoS of 5G slicing networks using general processor sharing-based scheduling algorithm," *International Journal of Communication Systems*, vol. 33, no. 4, 2019.

[18] L. Wu, X. Meng, S. Liu et al., "A trading supported manufacturing resource sharing model for manufacturing grid," in *Proceedings of the Ninth International Conference on Computer Supported Cooperative Work in Design*, Coventry, UK, May 2005.

[19] D. Wu, J. Wang, R. Q. Hu, Y. Cai, and L. Zhou, "Energy-efficient resource sharing for mobile device-to-device multimedia communications," *IEEE Transactions on Vehicular Technology*, vol. 63, no. 5, pp. 2093–2103, 2014.

[20] S. Mirjalili and A. Lewis, "The whale optimization algorithm," *Advances in Engineering Software*, vol. 95, pp. 51–67, 2016.

[21] S. Huo and Y. Zhang, "H_∞ consensus of Markovian jump multi-agent systems under multi-channel transmission via output feedback control strategy," *ISA Transactions*, vol. 99, pp. 28–36, 2020.

Hindawi
Discrete Dynamics in Nature and Society
Volume 2020, Article ID 4820351, 9 pages
https://doi.org/10.1155/2020/4820351

Research Article

Stability Analysis of a Class of Neural Networks with State-Dependent State Delay

Yue Chen and Jin-E Zhang

Hubei Normal University, Huangshi 435002, China

Correspondence should be addressed to Jin-E Zhang; zhang86021205@163.com

Received 13 February 2020; Accepted 2 April 2020; Published 1 May 2020

Academic Editor: Jianquan Lu

The differential equations with state-dependent delay are very important equations because they can describe some problems in the real world more accurately. Due to the complexity of state-dependent delay, it also brings challenges to the research. The value of delay varying with the state is the difference between state-dependent delay and time-dependent delay. It is impossible to know exactly in advance how far historical state information is needed, and then the problem of state-dependent delay is more complicated compared with time-dependent delay. The dominating work of this paper is to solve the stability problem of neural networks equipped with state-dependent state delay. We use the purely analytical method to deduce the sufficient conditions for local exponential stability of the zero solution. Finally, a few numerical examples are presented to prove the availability of our results.

1. Introduction

Neural network is an information processing system to simulate the structures and functions of the human brain. As far as we know, the functions and structures of the individual neuron are simple, but the dynamic behavior of the neural network is very rich and intricate [1, 2]. In the neural network, several simple processing units are connected to each other in a certain way. Neural network system is highly complex, which not only has the common characteristics of general nonlinear systems but also has its own unique features [3–6]. For example, it is proved that the neural network has the ability to approximate nonlinear mapping, and any continuous nonlinear function mapping can be approximated by the multilayer neural network with arbitrary precision. It shows that the neural network has a good application prospect in the challenging nonlinear control field [3]. Also, the parallel distributed integrated optimization processing of information makes the neural network very suitable for solving large-scale real-time computing problems in system control [4]. At the same time, some neural network models have the trait of automatically searching the extremum of energy function, which is very useful in adaptive control design [5]. In addition, the neural network also has the peculiarity of high fault-tolerant ability, generalization ability, and adaptive ability for learning behavior [6].

Over that seventy years, neural networks have been involved in combinatorial optimization, pattern recognition, image processing, robot control, signal processing, and other scientific fields and achieved extensive success [7–10]. In the application of the neural network, on the one hand, information transmission between neurons needs time. On the other hand, due to the influence of hardware implementation in reality (such as limited switching speed), the time delay phenomenon is inevitable [11]. The existence of time delay may induce instability, oscillation, and poor performance, but we can also overcome the unfavorable effect about some types of time delays by developed control frameworks, such as based on the Halanay inequality framework [1, 2, 11, 12]. At present, many different delays have been applied to the neural network [2, 12–18], for instance, time-varying delay [12, 14], distributed delay [13, 15, 16], discrete constant delay [2, 13], proportional delay [17], and unbounded delay [18].

State-dependent delay (SDD) is all around us [19–22]. With limited natural resources, Antarctic whales and seals tend to mature longer if their populations are large [19]. In the problem of car following, it is inevitable to encounter the phenomenon that the time delay changes with the state, which contains physiological time delay, mechanical time delay, and motion time delay [20, 21]. In addition, in the blood circulation system, the concentration of nutrients regulates the mitotic cycle of hematopoietic stem cells; thus, the mitotic cycle of stem cells is affected by the concentration of cells in the region [22]. In these cases, in order to describe change and evolution of things more accurately and make the research results more realistic and modest with nuanced understanding, we must adopt differential equations with SDD.

Neurodynamics help to identify the highly complex and precise multilevel nonlinear brain system. The processing of neural information involves the coupling and cooperation of multiple levels and regions. In this way, the nerve activity about the structural neural network is worthy of study and discussion from the perspective of models and evolution, and then to some extent, the cognitive function of the specific functional neural network is realized by evolutive neurodynamics [13]. The work about evolutive neurodynamics will be helpful to understand the information processing mechanism and the neural energy coding rule in the nervous system and also provides the basis for the research of the potential mechanism of cognitive function.

In this paper, the local evolution characteristics of neural networks with state-dependent state delay (SDSD) will be discussed. The topic introduced here may interest researchers in engaging the theory and application of the new neural network model having kinematics and dynamics feature. Prior to this, there have been many studies on the stability of nonlinear systems with SDSD. Hartung [23] described a type of nonlinear functional differential equation with SDSD and analyzed the stability conditions of periodic solutions based on the linearization method. Exponential stability conditions of nonlinear systems with SDSD were reported via comparing with time-dependent delay systems in [24]. Fiter and Fridman [25] developed the Lyapunov–Krasovskii functional method to discuss asymptotic stability about some particular linear systems with SDSD. Li and Wu [26] considered a class of nonlinear differential systems with SDD pulses. By pulse control theory, uniformly stable, uniformly asymptotically stable, and exponentially stable results were presented. To derive stability criteria of nonlinear systems with SDSD, Li and Yang [27] initially created purely analytical frame structure. To the best of the authors' knowledge, although the neural networks are widely used and the theoretical results are abundant, the research on stability of the neural network with SDSD is still blank. Moreover, since time delay is an inevitable factor in neural networks, it is of great significance to study the problem of neural networks with SDSD. Then, the primary contributions of this paper are generalized as follows: (1) A general neural network model with SDSD is established. Neural network model with SDSD may interest all those professionals and academics in processing operations who would desire to utilize the capabilities of control systems about capturing rich history information for cost effective and yet robust events to be portrayed. Such research also contributes to reveal influences of neurodynamics evoked by SDSD characteristics. (2) Locally exponentially stable sufficient conditions of the neural networks with SDSD are obtained. The purely analytical method employed by us demonstrates that it is possible to analyze computational neurodynamics without a few additional restrictions. The purely analytical method itself intents to address the universality of analysis framework. Definitely, it may be extended to a more general class of nonlinear systems with SDSD.

The rest of this paper is arranged as follows. In Section 2, we will present a specific neural network model. The results of our work are described in Section 3. In Section 4, two numerical examples and simulation results are given to verify the validity of our results. Finally, in Section 5, the thesis is summarized, and the future work is prospected.

2. Preliminaries and Model Description

2.1. Notations. Let $\mathscr{R}$ and $\mathscr{R}^+$ represent the sets of real numbers and nonnegative real numbers, respectively. $\mathscr{R}^n$ denotes the n-dimension Euclidean space. For a matrix E, $\lambda_{\max}(E)$ is used to denote its maximum eigenvalue. $\mathscr{P}(E)$ stands for the minimum value of all elements of matrix E. The vector 1-norm and 2-norm are severally expressed by $\|\cdot\|_1$ and $\|\cdot\|_2$.

2.2. Some Preliminaries and Problem Formulation. Based on the work of Li and Yang [27], we put forward the following neural network model with SDSD, which is described by

$$\dot{x}_i(t) = -a_i x_i(t) + \sum_{j=1}^{n} b_{ij} g_j\left(x_j(t)\right) + \sum_{j=1}^{n} d_{ij} f_j\left(x_j(t-\tau(t,\mathscr{X}))\right), \quad i = 1,2,\ldots,n, t \geq t_0, \tag{1}$$

for the sake of presentation; we also give the compact form of system (1) as follows:

$$\dot{\mathscr{X}}(t) = -A\mathscr{X}(t) + Bg(\mathscr{X}(t)) + Df(\mathscr{X}(t-\tau(t,\mathscr{X}))), \tag{2}$$

where n stands for the number of neurons in the network, $\dot{\mathscr{X}}(t)$ denotes the upper right derivative of $\mathscr{X}(t)$, $\mathscr{X} = \mathscr{X}(t) = (x_1(t), x_2(t), \ldots, x_n(t))^T$, and $x_i(t)$ represents the state of the ith neuron. A is a diagonal matrix, for $i = 1,2,\ldots,n$, $a_i > 0$, and B and D are constant matrices with corresponding dimensions. $g(\mathscr{X}(t)) = (g_1(x_1)(t), g_2(x_2(t)), \ldots, g_n(x_n(t)))^T$ and $f(\mathscr{X}(t-\tau(t,\mathscr{X}))) = (f_1(x_1(t-\tau(t,\mathscr{X}))), f_2(x_2(t-\tau(t,\mathscr{X}))), \ldots, f_n(x_n(t-\tau(t,\mathscr{X}))))^T$ are the excitation functions of the ith neuron at time t and $t-\tau(t,\mathscr{X})$, respectively.

Furthermore, we use $\mathscr{X}(s) = \Psi(s), s \in [t_0 - \eta, t_0]$ to denote the initial value of system (2), where $\Psi = \Psi(s) = (\psi_1(s), \psi_2(s), \ldots, \psi_n(s))^T \in \mathscr{C}([t_0 - \eta, t_0], \mathscr{R}^n)$. $\mathscr{C}([t_0 - \eta, t_0], \mathscr{R}^n)$ is a Banach space whose elements are continuous vector-valued functions. These continuous functions map the interval $[t_0 - \eta, t_0]$ into $\mathscr{R}^n$. Let $\|\Psi\|_\alpha = \sup_{t_0-\eta\le s\le t_0}\|\Psi(s)\|$ stand for the norm of a function $\Psi(\cdot) \in \mathscr{C}([t_0 - \eta, t_0], \mathscr{R}^n)$, where $\|\cdot\|$ is the vector norm matching with the content of the paper.

Remark 1. $\mathscr{X}(t)$ is right-upper derivable, which implies that the solution of system (2) can be continuous but not smooth. The state delay $\tau(t, \mathscr{X})$ is related to the state of each neuron.

For subsequent analysis, we need the following assumptions for system (1) and (2).

Assumption 1. Functions $g(\cdot), f(\cdot) \in \mathscr{R}^n$ satisfy $f(0) = 0$, $g(0) = 0$.

Through Assumption 1, this ensures that $\mathscr{X} = 0$ is a constant solution of systems (1) and (2).

Assumption 2. $g(\cdot), f(\cdot) \in \mathscr{R}^n$ are locally Lipschitz continuous; in other words, $\forall \beta_1, \beta_2 \in \mathscr{R}$, and we have

$$\begin{aligned} &|g_i(\beta_1) - g_i(\beta_2)| \le \ell_i|\beta_1 - \beta_2|, \quad \forall i \in \{1, 2, \ldots, n\}, \\ &|f_i(\beta_1) - f_i(\beta_2)| \le \widetilde{\ell}_i|\beta_1 - \beta_2|, \quad \forall i \in \{1, 2, \ldots, n\}, \end{aligned} \tag{3}$$

where $\ell_i > 0$ and $\widetilde{\ell}_i > 0$.

According to Assumption 2, we can get two constant sets $\{\ell_1, \ell_2, \ldots, \ell_n\}$ and $\{\widetilde{\ell}_1, \widetilde{\ell}_2, \ldots, \widetilde{\ell}_n\}$. Let $\{\ell_1, \ell_2, \ldots, \ell_n\}$ and $l_f = \max\{\widetilde{\ell}_1, \widetilde{\ell}_2, \ldots, \widetilde{\ell}_n\}$.

Assumption 3. The state delay $\tau(t, \mathscr{X}) \in C(\mathscr{R}^+ \times \mathscr{R}^n, [0, \eta])$ is locally Lipschitz continuous, namely, for any $\Gamma_1, \Gamma_2 \in \mathscr{R}^n$, there always exists a constant $\ell_\tau > 0$ such that

$$|\tau(t, \Gamma_1) - \tau(t, \Gamma_2)| \le \ell_\tau\|\Gamma_1 - \Gamma_2\|. \tag{4}$$

Assumption 4. When $\mathscr{X} = 0$, $\tau(t, \mathscr{X})$ has supremum equipped with $\tau_0 (\le \eta)$, $\sup\{\tau(t, 0),\ t \ge t_0\} = \tau_0$.

For ease of expression, let

$$\begin{aligned} \pi_1 &= \max_{1\le i\le n}\left(-a_i + \sum_{j=1}^{n}|b_{ji}|\ell_i\right), \\ \pi_2 &= \max_{1\le i\le n}\sum_{j=1}^{n}|d_{ji}|\widetilde{\ell}_i. \end{aligned} \tag{5}$$

Definition 1 (see [28]). The zero solution of system (2) is said to be locally exponentially stable (LES) in region $\mathscr{M}$; if there exist constants $\gamma > 0$ and Lyapunov exponent $\zeta > 0$, for any $t \ge t_0$, we have

$$\|\mathscr{X}(t; t_0, \Psi)\| \le \gamma\|\Psi\|_\alpha e^{-\zeta(t-t_0)}, \tag{6}$$

where $\mathscr{X}(t; t_0, \Psi)$ is a solution of system (2) with the initial condition $\Psi \in \mathscr{C}([t_0 - \eta, t_0], \mathscr{M})$, $\mathscr{M} \subset \mathscr{R}^n$, and $\mathscr{M}$ is called a local exponential attraction set of the zero solution.

Lemma 1 (see [29]). *Let $\Gamma_1, \Gamma_2 \in \mathscr{R}^n$, and we have*

$$\Gamma_1^T\Gamma_2 + \Gamma_2^T\Gamma_1 \le \varpi\Gamma_1^T\Gamma_1 + \varpi^{-1}\Gamma_2^T\Gamma_2, \tag{7}$$

for any $\varpi > 0$.

3. Main Results

Theorem 1. *Under Assumptions 1–4, the zero equilibrium of system (2) is LES if*

$$\pi_1 + \pi_2 < 0, \tag{8}$$

and Lyapunov exponent $\zeta > 0$ satisfies

$$\zeta + \pi_1 + \pi_2 e^{\zeta(\ell_\tau\|\Psi\|_\alpha + \tau_0)} \le 0. \tag{9}$$

Proof. We assume that $\mathscr{X}(t; t_0, \Psi)$ is a trajectory of system (2) with initial value (t_0, Ψ), where $\Psi \in \mathscr{C}([t_0 - \eta, t_0], \mathscr{R}^n)$ and $\Psi \ne 0$. For the sake of convenience, let $V(t) = V(t, \mathscr{X}) = \|\mathscr{X}(t)\|_1 = \sum_{i=1}^n |x_i(t)|$ and $V_0 = \{\sup V(s), s \in [t_0 - \eta, t_0]\}$. Then, for any $\epsilon \in (0, \zeta)$, we claim that

$$e^{(\zeta-\epsilon)(t-t_0)}V(t) \le V_0, \quad \forall t \ge t_0. \tag{10}$$

Firstly, when $t = t_0$, (10) holds. Next, we prove that (10) holds on $(t_0, +\infty)$. In contrast to (10), there are some instants on $(t_0, +\infty)$ to make (10) untenable, and then we can find an instant $t_q \ge t_0$; the following three events will happen:

(1) $e^{(\zeta-\epsilon)(t_q-t_0)}V(t_q) = V_0$.

(2) $e^{(\zeta-\epsilon)(t-t_0)}V(t) \le V_0$, for $\forall t \in [t_0 - \eta, t_q]$.

(3) There exists a right neighbor of t_q ($U_+^0(t_q, \xi)$) such that $\forall t^\xi \in U_+^0(t_q, \xi)$ and $e^{(\zeta-\epsilon)(t^\xi-t_0)}V(t^\xi) > V_0$.

On the contrary, by Assumptions 1–4 and combining (2), the derivative of $e^{(\zeta-\epsilon)(t-t_0)}V(t)$ at time t_q is as follows:

$$
\begin{aligned}
&\frac{\mathrm{d}}{\mathrm{d}t}\left(e^{(\zeta-\epsilon)(t-t_0)}V(t)\right)\Big|_{t=t_q}\\
&=(\zeta-\epsilon)e^{(\zeta-\epsilon)(t_q-t_0)}V(t_q)+\left[e^{(\zeta-\epsilon)(t-t_0)}\dot{V}(t)\right]\Big|_{t=t_q}\\
&\le(\zeta-\epsilon)V_0+e^{(\zeta-\epsilon)(t_q-t_0)}\left(\sum_{i=1}^{n}sgn\left(x_i(t_q)\right)\left(\dot{x}_i(t_q)\right)\right)\\
&=(\zeta-\epsilon)V_0+e^{(\zeta-\epsilon)(t_q-t_0)}\left(\sum_{i=1}^{n}sgn\left(x_i(t_q)\right)\left[-a_ix_i(t_q)\right.\right.\\
&\quad\left.\left.+\sum_{j=1}^{n}b_{ij}g_j\left(x_j(t_q)\right)+\sum_{j=1}^{n}d_{ij}f_j\left(x_j\left(t_q-\tau\left(t_q,\mathscr{X}(t_q)\right)\right)\right)\right]\right)\\
&\le(\zeta-\epsilon)V_0+e^{(\zeta-\epsilon)(t_q-t_0)}\left(\sum_{i=1}^{n}-a_i\left|x_i(t_q)\right|\right)\\
&\quad+e^{(\zeta-\epsilon)(t_q-t_0)}\sum_{i=1}^{n}\sum_{j=1}^{n}\left|b_{ij}\right|\ell_j\left|x_j(t_q)\right|\\
&\quad+e^{(\zeta-\epsilon)(t_q-t_0)}\left(\sum_{i=1}^{n}\sum_{j=1}^{n}\left|d_{ij}\right|\widetilde{\ell}_j\left|x_j\left(t_q-\tau\left(t_q,\mathscr{X}(t_q)\right)\right)\right|\right)\\
&\le(\zeta-\epsilon)V_0\\
&\quad+e^{(\zeta-\epsilon)(t_q-t_0)}\max_{1\le i\le n}\left(-a_i+\sum_{j=1}^{n}\left|b_{ji}\right|\ell_i\right)\left\|\mathscr{X}(t_q)\right\|\\
&\quad+e^{(\zeta-\epsilon)(t_q-t_0)}\max_{1\le i\le n}\left(\sum_{j=1}^{n}\left|d_{ji}\right|\widetilde{\ell}_i\right)\left\|\mathscr{X}\left(t_q-\tau\left(t_q,\mathscr{X}\right)\right)\right\|\\
&=(\zeta-\epsilon+\pi_1)V_0+e^{(\zeta-\epsilon)\left(t_q-\tau\left(t_q,\mathscr{X}\right)-t_0\right)}\left\|\mathscr{X}\left(t_q-\tau\left(t_q,\mathscr{X}\right)\right)\right\|\\
&\quad\times\pi_2e^{(\zeta-\epsilon)\tau\left(t_q,\mathscr{X}\right)}\\
&\le\left(\zeta-\epsilon+\pi_1+\pi_2e^{(\zeta-\epsilon)\tau\left(t_q,\mathscr{X}\right)}\right)V_0\\
&=\left(\zeta-\epsilon+\pi_1+\pi_2e^{(\zeta-\epsilon)\left[\tau\left(t_q,\mathscr{X}\right)-\tau\left(t_q,0\right)\right]}e^{(\zeta-\epsilon)\tau\left(t_q,0\right)}\right)V_0\\
&\le\left(\zeta-\epsilon+\pi_1+\pi_2e^{(\zeta-\epsilon)\ell_\tau\left\|\mathscr{X}\left(t_q\right)\right\|_1}e^{(\zeta-\epsilon)\tau\left(t_q,0\right)}\right)V_0\\
&\le\left(\zeta-\epsilon+\pi_1+\pi_2e^{(\zeta-\epsilon)\left(\ell_\tau\left\|\mathscr{X}\left(t_q\right)\right\|_1+\tau_0\right)}\right)V_0.
\end{aligned}
\tag{11}
$$

Together with the definition of $V_0, V(t), t_q$ and condition (1), we have

$$
\left\|\mathscr{X}(t_q)\right\|_1=V(t_q)\le V_0=\|\Psi\|_\alpha,
\tag{12}
$$

and then from (9) and (11), we obtain

$$
\begin{aligned}
&\frac{\mathrm{d}}{\mathrm{d}t}\left(e^{(\zeta-\epsilon)(t-t_0)}V(t)\right)\Big|_{t=t_q}\\
&\quad\le\left(\zeta-\epsilon+\pi_1+\pi_2e^{(\zeta-\epsilon)\left(\ell_\tau\|\Psi\|_\alpha+\tau_0\right)}\right)\|\Psi\|_\alpha<0,
\end{aligned}
\tag{13}
$$

which is a contradiction with condition (9), and thus, (10) holds.

Consider the arbitrariness of ϵ, let $\epsilon\longrightarrow 0$, and then we obtain

$$
e^{\zeta(t-t_0)}V(t)\le V_0,\quad\forall t\ge t_0,
\tag{14}
$$

i.e.,

$$
\|\mathscr{X}(t)\|_1=V(t)\le\|\Psi\|_\alpha e^{-\zeta(t-t_0)},\quad\forall t\ge t_0.
\tag{15}
$$

The reasoning process of Theorem 1 is completed. □

Theorem 2. *B and D are symmetric matrices; then, under Assumptions 1–4, the zero equilibrium of system (2) is LES if*

$$
-2\mathscr{P}(A)+\lambda_{\max}\left(B^2\right)+l_g^2+\lambda_{\max}\left(D^2\right)+l_f^2<0,
\tag{16}
$$

and $\mu=2\zeta>0$ satisfies

$$
\begin{aligned}
&\mu-2\mathscr{P}(A)+\lambda_{\max}\left(B^2\right)+l_g^2+\lambda_{\max}\left(D^2\right)\\
&\quad+l_f^2e^{\mu\left(\ell_\tau\|\Psi\|_\alpha+\tau_0\right)}\le 0,
\end{aligned}
\tag{17}
$$

where ζ is the Lyapunov exponent.

Proof. Suppose $\mathscr{X}(t;t_0,\Psi)$ is a solution of system (2) with initial state (t_0,Ψ), where $\Psi\in\mathscr{C}([t_0-\eta,t_0],\mathscr{R}^n)$ and $\Psi\ne 0$. Let $V(t,\mathscr{X})=(\|\mathscr{X}(t)\|_2)^2=\mathscr{X}^T(t)\mathscr{X}(t)$. For convenience, set $V(t)=V(t,\mathscr{X})$ and $V_0=\{\sup V(s),s\in[t_0-\eta,t_0]\}$. Then, for any $\epsilon\in(0,\mu)$, we claim that

$$
e^{(\mu-\epsilon)(t-t_0)}V(t)\le V_0,\quad\forall t\ge t_0.
\tag{18}
$$

Firstly, when $t=t_0$, (18) holds. Next, we prove that (18) holds on $(t_0,+\infty)$. In contrast to (18), there are some instants on $(t_0,+\infty)$ to make (18) untenable, and then we can find an instant $t_q\ge t_0$ to satisfy the following three conditions:

(1) $e^{(\mu-\epsilon)(t_q-t_0)}V(t_q)=V_0$.

(2) $e^{(\mu-\epsilon)(t-t_0)}V(t)\le V_0$, for $\forall t\in[t_0-\eta,t_q]$.

(3) There exists a right neighbor of $t_q(U_+^0(t_q,\xi))$ such that $\forall t^\xi\in U_+^0(t_q,\xi), e^{(\mu-\epsilon)(t^\xi-t_0)}V(t^\xi)>V_0$.

On the contrary, by Assumptions 1–4 and Lemma 1, we compute the derivative of $e^{(\mu-\epsilon)(t-t_0)}V(t)$ at time t_q:

$$
\begin{aligned}
&\frac{\mathrm{d}}{\mathrm{d}t}\Big(e^{(\mu-\epsilon)(t-t_0)}V(t)\Big)\Big|_{t=t_q}\\
&\quad=(\mu-\epsilon)e^{(\mu-\epsilon)(t_q-t_0)}V(t_q)+\Big[e^{(\mu-\epsilon)(t-t_0)}\dot{V}(t)\Big]\Big|_{t=t_q}\\
&\quad\le(\mu-\epsilon)V_0+e^{(\mu-\epsilon)(t_q-t_0)}\big(2\mathscr{X}^T(t_q)\dot{\mathscr{X}}(t_q)\big)\\
&\quad=(\mu-\epsilon)V_0+e^{(\mu-\epsilon)(t_q-t_0)}\times 2\mathscr{X}^T(t_q)\\
&\qquad\times\big[\big(-A\mathscr{X}(t_q)+Bg(\mathscr{X}(t_q))+Df(\mathscr{X}(t_q-\tau(t_q,\mathscr{X})))\big)\big]\\
&\quad=(\mu-\epsilon)V_0+e^{(\mu-\epsilon)(t_q-t_0)}\big(-2\mathscr{X}^T(t_q)A\mathscr{X}(t_q)\big)\\
&\qquad+e^{(\mu-\epsilon)(t_q-t_0)}\big(2\mathscr{X}^T(t_q)Bg(\mathscr{X}(t_q))\big)\\
&\qquad+e^{(\mu-\epsilon)(t_q-t_0)}\big(2\mathscr{X}^T(t_q)Df(\mathscr{X}(t_q-\tau(t_q,\mathscr{X})))\big)\\
&\quad\le(\mu-\epsilon)V_0+e^{(\mu-\epsilon)(t_q-t_0)}(-2\mathscr{P}(A))\mathscr{X}^T(t_q)\mathscr{X}(t_q)\\
&\qquad+e^{(\mu-\epsilon)(t_q-t_0)}\big(\lambda_{\max}(B^2)+l_g^2\big)\mathscr{X}^T(t_q)\mathscr{X}(t_q)\\
&\qquad+e^{(\mu-\epsilon)(t_q-t_0)}\lambda_{\max}(D^2)\mathscr{X}^T(t_q)\mathscr{X}(t_q)\\
&\qquad+e^{(\mu-\epsilon)(t_q-t_0)}l_f^2\mathscr{X}^T(t_q-\tau(t_q,\mathscr{X}))\mathscr{X}(t_q-\tau(t_q,\mathscr{X}))\\
&\quad=\big(\mu-\epsilon-2\mathscr{P}(A)+\lambda_{\max}(B^2)+l_g^2+\lambda_{\max}(D^2)\big)V_0\\
&\qquad+e^{(\mu-\epsilon)(t_q-\tau(t_q,\mathscr{X})-t_0)}l_f^2\mathscr{X}^T(t_q-\tau(t_q,\mathscr{X}))\mathscr{X}(t_q-\tau(t_q,\mathscr{X}))\\
&\qquad\times e^{(\mu-\epsilon)\tau(t_q,\mathscr{X})}\\
&\quad\le\big(\mu-\epsilon-2\mathscr{P}(A)+\lambda_{\max}(B^2)+l_g^2+\lambda_{\max}(D^2)\big)V_0\\
&\qquad+l_f^2e^{(\mu-\epsilon)\tau(t_q,\mathscr{X})}V_0\\
&\quad=\big(\mu-\epsilon-2\mathscr{P}(A)+\lambda_{\max}(B^2)+l_g^2+\lambda_{\max}(D^2)\big)V_0\\
&\qquad+l_f^2e^{(\mu-\epsilon)[\tau(t_q,\mathscr{X})-\tau(t_q,0)]}e^{(\mu-\epsilon)\tau(t_q,0)}V_0\\
&\quad\le\big(\mu-\epsilon-2\mathscr{P}(A)+\lambda_{\max}(B^2)+l_g^2+\lambda_{\max}(D^2)\\
&\qquad+l_f^2e^{(\mu-\epsilon)\left(\ell_\tau\|\mathscr{X}(t_q)\|_2+\tau_0\right)}\Big)V_0.
\end{aligned}
\tag{19}
$$

Combining the definition of $V_0, V(t), t_q$ and condition (1), we have

$$
\|\mathscr{X}(t_q)\|_2=\big(V(t_q)\big)^{1/2}\le(V_0)^{1/2}=\|\Psi\|_\alpha,
\tag{20}
$$

and then from (17) and (19), we obtain

$$
\begin{aligned}
&\frac{\mathrm{d}}{\mathrm{d}t}\Big(e^{(\mu-\epsilon)(t-t_0)}V(t)\Big)\Big|_{t=t_q}\\
&\quad\le\big(\mu-\epsilon-2\mathscr{P}(A)+\lambda_{\max}(B^2)+l_g^2+\lambda_{\max}(D^2)\\
&\qquad+l_f^2e^{(\mu-\epsilon)\left(\ell_\tau\|\Psi\|_\alpha+\tau_0\right)}\Big)(\|\Psi\|_\alpha)^2<0.
\end{aligned}
\tag{21}
$$

This is in contradiction with (9), so (18) holds.

Consider the arbitrariness of ϵ, let $\epsilon\longrightarrow 0$, and then we could be capable of getting

$$
e^{\mu(t-t_0)}V(t)\le V_0,\quad\forall t\ge t_0,
\tag{22}
$$

i.e.,

$$
\|\mathscr{X}(t)\|_2=(V(t))^{1/2}\le\|\Psi\|_\alpha e^{-(\mu/2)(t-t_0)},\quad\forall t\ge t_0.
\tag{23}
$$

The reasoning process of Theorem 2 is completed. □

Remark 2. In Theorem 2, by taking the value of ϖ in Lemma 1 to be 1, we can get the following inequality:

$$
\begin{aligned}
2\mathscr{X}^T(t_q)Bg(\mathscr{X}(t_q))&=\mathscr{X}^T(t_q)Bg(\mathscr{X}(t_q))+\mathscr{X}^T(t_q)Bg(\mathscr{X}(t_q))\\
&=\mathscr{X}^T(t_q)B^Tg(\mathscr{X}(t_q))+g^T(\mathscr{X}(t_q))B\mathscr{X}(t_q)\\
&=\big(B\mathscr{X}(t_q)\big)^Tg(\mathscr{X}(t_q))+g^T(\mathscr{X}(t_q))\big(B\mathscr{X}(t_q)\big)\\
&\le\big(B\mathscr{X}(t_q)\big)^T\big(B\mathscr{X}(t_q)\big)+g^T(\mathscr{X}(t_q))g(\mathscr{X}(t_q))\\
&=\mathscr{X}^T(t_q)B^TB\mathscr{X}(t_q)+g^T(\mathscr{X}(t_q))g(\mathscr{X}(t_q))\\
&=\mathscr{X}^T(t_q)B^2\mathscr{X}(t_q)+g^T(\mathscr{X}(t_q))g(\mathscr{X}(t_q))\\
&\le\lambda_{\max}(B^2)\mathscr{X}^T(t_q)\mathscr{X}(t_q)+l_g^2\mathscr{X}^T(t_q)\mathscr{X}(t_q)\\
&=\big(\lambda_{\max}(B^2)+l_g^2\big)\mathscr{X}^T(t_q)\mathscr{X}(t_q).
\end{aligned}
\tag{24}
$$

We give a particular case of system (2), considering the following one-dimensional system:

$$
\begin{aligned}
&\dot{x}(t)=ax(t)+bg(x(t))+df(x(t-\tau(t,x))),t\ge 0,\\
&\tau(t,x)=\delta+\lambda x(t),
\end{aligned}
\tag{25}
$$

where $a,b,d,\delta,\lambda\in\mathscr{R}$.

Corollary 1. *If system (25) satisfies the following conditions,*

(1) $f(0)=0, g(0)=0$. $g(\cdot), f(\cdot)$ *are locally Lipschitz continuous functions whose Lipschitz constants are* l_1, l_2, *respectively,*

(2) $a<0$ *and* $a+|b|l_1+|d|l_2<0$,

(3) $\delta>0$, *and the initial condition of system (25) satisfies* $|\psi(\cdot)|\le M<(\delta/|\lambda|)$, *where* $|\psi(\cdot)|=\max_{-\eta\le t\le 0}|\psi(\cdot)|$,

then we can obtain

$$
|x(t)|\le Me^{-\zeta t},\quad t\ge 0,
\tag{26}
$$

where $x(t) = x(t; 0, \psi)$ represents the trajectory of system (25) with initial state $(0, \psi)$, and Lyapunov exponent $\zeta > 0$ satisfies

$$\zeta + a + |b| l_1 + |d| l_2 e^{\zeta(|\lambda| M + \delta)} \leq 0. \tag{27}$$

Proof. To prove Corollary 1, we only need to prove that Corollary 1 satisfies Assumptions 1–4. Obviously, from condition (1), we can know that system (25) satisfies Assumptions 1 and 2. Next, we prove that system (25) satisfies Assumptions 3 and 4.

We assume that $x(t; 0, \psi)$ is a trajectory of system (25) with initial value $(0, \psi)$, where $\psi \neq 0$. From $\tau(t, x) = \delta + \lambda x(t)$, we could know that $\tau(t, x)$ is continuous about t. Owing to $|\psi| \leq M$ and $M < (\delta/|\lambda|)$, there exists $\rho > 0$ such that $\forall t \in [0, \rho]$ and $\tau(t, x) \geq 0$. In the circumstances, set $V(t) = |x(t)|$. Next, under conditions (1)–(3) and by Theorem 1, we get $|x(t)| \leq M e^{-\zeta t}$, for $\forall t \in [0, \rho]$, where Lyapunov exponent ζ satisfies (27).

Then, for $\forall t \in [0, +\infty)$, we declare that $\tau(t, x) \geq 0$. In contrast to the claim, there must be some instant on $(\rho, +\infty)$ to make $\tau(t, x(t)) < 0$. Then, we could find an instant $t_q \in [\rho, +\infty)$ to meet the following three conditions:

(1) $\tau(t_q, x(t_q)) = \delta + \lambda x(t_q) = 0$.

(2) $\forall t \in [0, t_q]$, $\tau(t, x(t)) \geq 0$.

(3) There exists a right neighbor of $t_q (U_+^0(t_q, \xi))$ such that $\tau(t^\xi, x(t^\xi)) < 0$, for any $t^\xi \in U_+^0(t_q, \xi)$.

It follows from Theorem 1, for any $t \in [0, t_q]$, we have $|x(t)| \leq M e^{-\zeta t}$, which indicates that $|x(t_q)| \leq M e^{-\zeta t_q} < (\delta/|\lambda|)$. On the basis of the continuity of $x(t)$, there exists $\xi^0 > 0$ such that $|x(t)| < (\delta/|\lambda|)$, for any $t \in [t_q, t_q + \xi^0)$. It means that $\forall t \in [t_q, t_q + \xi^0)$, and $\tau(t, x(t)) = \delta + \lambda x(t) > 0$holds, which contradicts with (9); therefore, $\forall t \in [0, +\infty)$ and $\tau(t, x(t)) \geq 0$. It ulteriorly indicates that Assumptions 3 and 4 are all satisfied. Therefore, it can be known from Theorem 1 that Corollary 1 is valid. The proof is completed. □

Remark 3. Actually, in Theorem 1, when $\pi_1 + \pi_2 < 0$, we can definitely get $\zeta + \pi_1 + \pi_2 e^{\zeta(\ell_\tau \|\Psi\| + \tau_0)} \leq 0$ as long as ζ is small enough. Theorem 2 has a similar conclusion.

Remark 4. In Theorem 1, by taking $t_q - \tau(t_q, \mathcal{X})$ as a whole and then from condition (2), we are able to get $e^{(\zeta - \epsilon)(t_q - \tau(t_q, \mathcal{X}) - t_0)} \|\mathcal{X}(t_q - \tau(t_q, \mathcal{X}))\| \leq V_0$. Theorem 2 has a similar conclusion.

Remark 5. The proofs of Theorems 1 and 2 also provide an estimate of the locally exponentially convergent rate ζ which could be obtained by solving transcendental equation (9) or (17).

Remark 6. Remarkably, the Lyapunov exponent in Theorems 1 and 2 is state-dependent, so only when the initial value is bounded can we find common ζ to make $e^{(\zeta - \epsilon)} V(t) \leq V(0)$. Furthermore, due to the effect of SDSD, the results in our paper are local features, not global features.

4. Illustrative Examples

To prove the effectiveness of our results, two numerical examples will be given in this section.

Example 1. Consider a 2-dimensional neural network with SDSD, which is described by

$$\begin{aligned}
\begin{pmatrix} \dot{x}_1(t) \\ \dot{x}_2(t) \end{pmatrix} &= -\begin{pmatrix} 1 & 0 \\ 0 & 1 \end{pmatrix} \begin{pmatrix} x_1(t) \\ x_2(t) \end{pmatrix} \\
&\quad + \begin{pmatrix} 0.25 & 0.25 \\ 0.02 & 0.01 \end{pmatrix} \begin{pmatrix} g_1(x_1(t)) \\ g_2(x_2(t)) \end{pmatrix} \\
&\quad + \begin{pmatrix} 0.3 & 0.2 \\ 0.01 & 0.02 \end{pmatrix} \begin{pmatrix} f_1(x_1(t - \tau(t, \mathcal{X}))) \\ f_2(x_2(t - \tau(t, \mathcal{X}))) \end{pmatrix},
\end{aligned} \tag{28}$$

where $t_0 = 0$ and

$$\begin{aligned}
g_i(\cdot) &= |x_i(t) + 1| + |x_i(t) - 1|, \quad i = 1, 2, \\
f_i(\cdot) &= \sin\left(x_i\left(t - \left|\sin\left(x_1(t) + x_2(t)\right)\right|\right)\right), \quad i = 1, 2, \\
\tau(t, \mathcal{X}) &= \left|\sin\left(x_1(t) + x_2(t)\right)\right|.
\end{aligned} \tag{29}$$

Evidently, $\ell_1 = \ell_2 = 2, \widetilde{\ell}_1 = \widetilde{\ell}_2 = 1, \ell_\tau = 1, \tau(t, 0) = 0, \tau(t, \mathcal{X}) \in [0, 1]$. By calculating,

$$\begin{aligned}
\pi_1 &= \max_{1 \leq i \leq n} \left(-a_i + \sum_{j=1}^{n} |b_{ji}| \ell_i \right) = -0.46, \\
\pi_2 &= \max_{1 \leq i \leq n} \sum_{j=1}^{n} |d_{ji}| \widetilde{\ell}_i = 0.31.
\end{aligned} \tag{30}$$

Then, from Theorem 1, system (28) is LES. The trajectories of the solution from a random initial value are shown in Figure 1. As shown in Figure 1, $x_1(t)$ and $x_2(t)$ in neural network model (28) are convergent. Figure 2 shows the phase diagram of system (28) evolving with time.

Example 2. Consider another 2-dimensional neural network with SDSD, which is depicted by

$$\begin{aligned}
\begin{pmatrix} \dot{x}_1(t) \\ \dot{x}_2(t) \end{pmatrix} &= -\begin{pmatrix} 2 & 0 \\ 0 & 2 \end{pmatrix} \begin{pmatrix} x_1(t) \\ x_2(t) \end{pmatrix} \\
&\quad + \begin{pmatrix} 0.5 & 0.2 \\ 0.2 & 0.5 \end{pmatrix} \begin{pmatrix} g_1(x_1(t)) \\ g_2(x_2(t)) \end{pmatrix} \\
&\quad + \begin{pmatrix} 0.3 & 0.2 \\ 0.2 & 0.3 \end{pmatrix} \begin{pmatrix} f_1(x_1(t - (t, \mathcal{X}))) \\ f_2(x_2(t - (t, \mathcal{X}))) \end{pmatrix},
\end{aligned} \tag{31}$$

where $t_0 = 0$ and

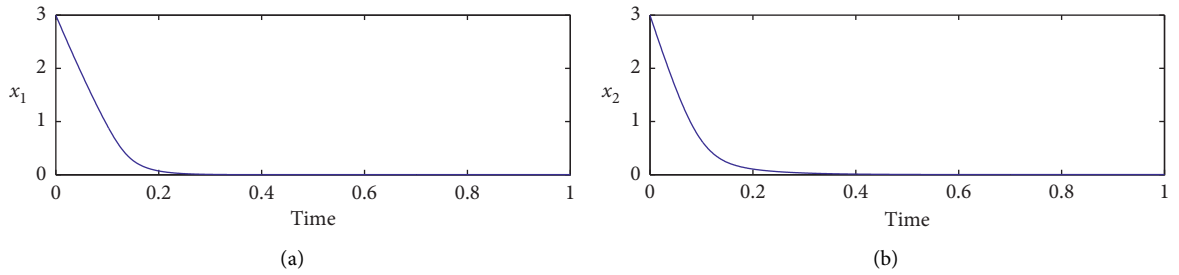

Figure 1: Transient behavior of (a) $x_1(t)$ and (b) $x_2(t)$ in system (28).

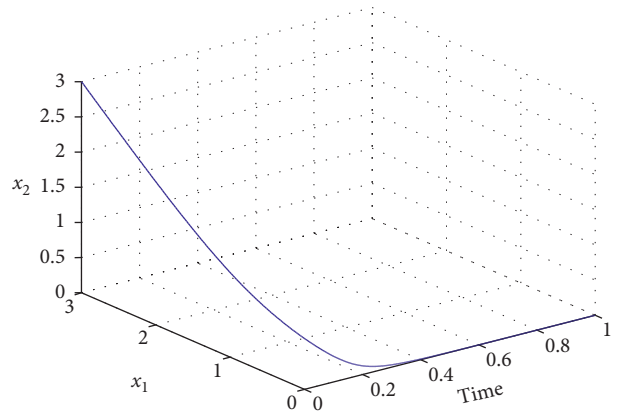

Figure 2: Transient behavior of $(x_1(t), x_2(t))$ in system (28).

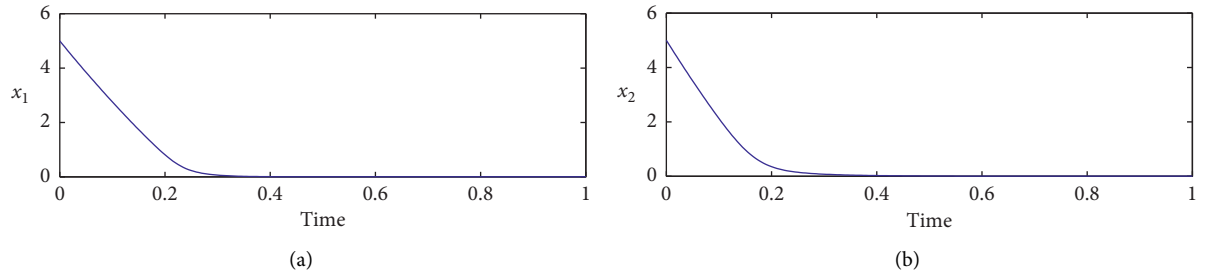

Figure 3: Transient behavior of (a) $x_1(t)$ and (b) $x_2(t)$ in system (31).

$$g_i(\cdot) = \frac{\cos\left(x_i(t) + (\pi/2)\right)}{2}, \quad i = 1, 2,$$

$$f_i(\cdot) = \tanh\left(x_i\left(t - \left|\sin\left(x_1(t) + x_2(t)\right)\right|\right)\right), \quad i = 1, 2,$$

$$\tau(t, \mathcal{X}) = \left|\sin\left(x_1(t) + x_2(t)\right)\right|. \tag{32}$$

Obviously, $l_g = 1/2, l_f = 1, \ell_\tau = 1, \tau(t, 0) = 0, (t, \mathcal{X}) \in [0, 1], \mathcal{P}(A) = 2$. By computing, $\lambda_{\max}(B^2) = 0.49, \lambda_{\max}(C^2) = 0.25$, and $-2\mathcal{P}(A) + l_g^2 + l_f^2 + \lambda(B^2) + \lambda(C^2) = -4 + (1/4) + 1 + 0.49 + 0.25 = -2.01 < 0$. Then, from Theorem 2, system (31) is LES. The trajectories of the solution from a random initial value are shown in Figure 3. As shown in Figure 3, $x_1(t)$ and $x_2(t)$ in neural network model (31) are

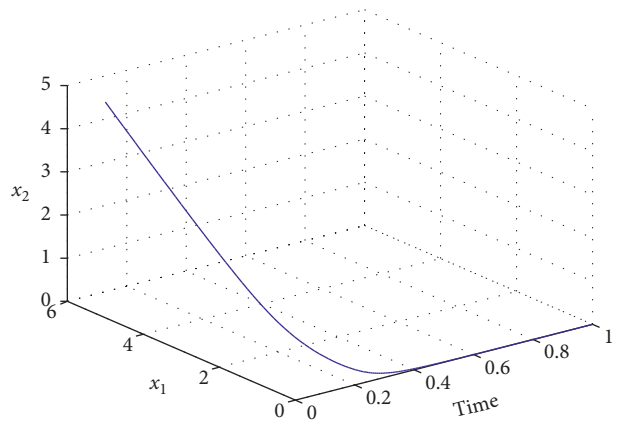

Figure 4: Transient behavior of $(x_1(t), x_2(t))$ in system (31).

convergent. Figure 4 shows the phase diagram of system (31) evolving with time.

5. Concluding Remarks

We devote to resolve the problem of local dynamic property for neural networks with SDSD in this paper. Through pure analysis method and technique of reduction to absurdity, we obtain a certain number of sufficient conditions for local exponential stability of neural networks with SDSD. Based on our results, we know that the Lyapunov exponent relies on the state on account of the effect of SDSD. It also indicates that the exponential stability results derived are local rather than global. Consequently, we can take the global dynamics as a topic in the prospective research. In addition, we can also develop SDSD system methods, for instance, event-triggered control.

Data Availability

No data were used to support this study.

Conflicts of Interest

The authors declare that there are no conflicts of interest regarding the publication of this paper.

Acknowledgments

The work of the first author for master student Yue Chen was done under the direction of Assistant Professor Jin-E Zhang. This work was supported by the Natural Science Foundation of China under Grants 61976084 and 61773152.

References

[1] L. Teng and D. Xu, "Global attracting set for non-autonomous neutral type neural networks with distributed delays," *Neurocomputing*, vol. 94, pp. 64–67, 2012.

[2] J. Cao and J. Wang, "Global exponential stability and periodicity of recurrent neural networks with time delays," *IEEE Transactions on Circuits and Systems I: Regular Papers*, vol. 52, no. 5, pp. 920–931, 2005.

[3] Z. Yang, J. Peng, and Y. Liu, "Adaptive neural network force tracking impedance control for uncertain robotic manipulator based on nonlinear velocity observer," *Neurocomputing*, vol. 331, pp. 263–280, 2019.

[4] H.-G. Han, Y. Li, Y.-N. Guo, and J.-F. Qiao, "A soft computing method to predict sludge volume index based on a recurrent self-organizing neural network," *Applied Soft Computing*, vol. 38, pp. 477–486, 2016.

[5] W. S. Chen and J. M. Li, "Adaptive neural network tracking control for a class of unknown nonlinear time-delay systems," *Journal of Systems Engineering and Electronics*, vol. 17, no. 3, pp. 611–618, 2006.

[6] T. Zan, Z. Liu, H. Wang, M. Wang, and X. Gao, "Control chart pattern recognition using the convolutional neural network," *Journal of Intelligent Manufacturing*, vol. 31, no. 3, pp. 703–716, 2020.

[7] V. Narayanan, S. Jagannathan, and K. Ramkumar, "Event-sampled output feedback control of robot manipulators using neural networks," *IEEE Transactions on Neural Networks and Learning Systems*, vol. 30, no. 6, pp. 1651–1658, 2019.

[8] B. L. Chen, H. D. Li, W. Q. Luo, and J. W. Huang, "Image processing operations identification via convolutional neural network," *Science China Information Sciences*, vol. 63, no. 3, p. 139109, 2020.

[9] M. M. Van Hulle and J. Larsen, "Neural networks in signal processing," *Neurocomputing*, vol. 69, no. 1–3, pp. 1-2, 2005.

[10] Y. Hayakawa and K. Nakajima, "Design of the inverse function delayed neural network for solving combinatorial optimization problems," *IEEE Transactions on Neural Networks*, vol. 21, no. 2, pp. 224–237, 2010.

[11] Z. Zeng and J. Wang, "Analysis and design of associative memories based on recurrent neural networks with linear saturation activation functions and time-varying delays," *Neural Computation*, vol. 19, no. 8, pp. 2149–2182, 2007.

[12] Z. Li, L. Liu, and Q. Zhu, "Mean-square exponential input-to-state stability of delayed Cohen-Grossberg neural networks with Markovian switching based on vector Lyapunov functions," *Neural Networks*, vol. 84, pp. 39–46, 2016.

[13] A. Wu and Z. Zeng, "Lagrange stability of memristive neural networks with discrete and distributed delays," *IEEE Transactions on Neural Networks and Learning Systems*, vol. 25, no. 4, pp. 690–703, 2014.

[14] T. Ensari and S. Arik, "Global stability of a class of neural networks with time-varying delay," *IEEE Transactions on Circuits and Systems II: Express Briefs*, vol. 52, no. 3, pp. 126–130, 2005.

[15] L. Li, Y. Yang, and F. Wang, "The sampled-data exponential stability of BAM with distributed leakage delays," *Neural Processing Letters*, vol. 46, no. 2, pp. 537–547, 2017.

[16] H. Liu, L. Zhao, Z. Zhang, and Y. Ou, "Stochastic stability of markovian jumping Hopfield neural networks with constant and distributed delays," *Neurocomputing*, vol. 72, no. 16–18, pp. 3669–3674, 2009.

[17] C. Zheng, N. Li, and J. Cao, "Matrix measure based stability criteria for high-order neural networks with proportional delay," *Neurocomputing*, vol. 149, pp. 1149–1154, 2015.

[18] J. Y. Zhang, "Global stability analysis in cellular neural networks with unbounded time delays," *Applied Mathematics and Mechanics*, vol. 25, no. 6, pp. 686–693, 2004.

[19] R. Gambell, "Birds and Mammals-Antarctic whales," Edited by W. Bonner and D. Walton, Eds., pp. 223–241, Pergamon Press, New York, NY, USA, 1985.

[20] L. Liu, L. Zhu, and D. Yang, "Modeling and simulation of the car-truck heterogeneous traffic flow based on a nonlinear car-following model," *Applied Mathematics and Computation*, vol. 273, pp. 706–717, 2016.

[21] S. Yu and Z. Shi, "An improved car-following model considering relative velocity fluctuation," *Communications in Nonlinear Science and Numerical Simulation*, vol. 36, pp. 319–326, 2016.

[22] P. Getto and M. Waurick, "A differential equation with state-dependent delay from cell population biology," *Journal of Differential Equations*, vol. 260, no. 7, pp. 6176–6200, 2016.

[23] F. Hartung, "Linearized stability in periodic functional differential equations with state-dependent delays," *Journal of Computational and Applied Mathematics*, vol. 174, no. 2, pp. 201–211, 2005.

[24] I. Györi and F. Hartung, "Exponential stability of a state-dependent delay system," *Discrete & Continuous Dynamical Systems-A*, vol. 18, no. 4, pp. 773–791, 2007.

[25] C. Fiter and E. Fridman, "Stability of piecewise affine systems with state-dependent delay, and application to congestion control," in

Proceedings of the 52nd IEEE Annual Conference on Decision and Control, pp. 1572–1577, Florence, Italy, December 2013.

[26] X. Li and J. Wu, "Stability of nonlinear differential systems with state-dependent delayed impulses," *Automatica*, vol. 64, pp. 63–69, 2016.

[27] X. Li and X. Yang, "Lyapunov stability analysis for nonlinear systems with state-dependent state delay," *Automatica*, vol. 112, p. 108674, 2020.

[28] C. Zhou, X. Zeng, J. Yu, and H. Jiang, "A unified associative memory model based on external inputs of continuous recurrent neural networks," *Neurocomputing*, vol. 186, pp. 44–53, 2016.

[29] L. Liu, X. Ding, W. Zhou, and X. Li, "Global mean square exponential stability and stabilization of uncertain switched delay systems with Lévy noise and flexible switching signals," *Journal of the Franklin Institute*, vol. 356, no. 18, pp. 11520–11545, 2019.

Hindawi
Discrete Dynamics in Nature and Society
Volume 2020, Article ID 4171585, 7 pages
https://doi.org/10.1155/2020/4171585

Research Article

Finite-Time Synchronization of Complex Dynamical Networks with Nondelayed and Delayed Coupling by Continuous Function Controller

Xie Chengrong,[1] **Xing Yu**,[2] **Xia Qing**,[3] **Dongbing Tong**,[4] **and Yuhua Xu**[2]

[1]*School of Statistics and Mathematics, Nanjing Audit University, Nanjing, Jiangsu 211815, China*
[2]*School of Finance, Nanjing Audit University, Nanjing, Jiangsu 211815, China*
[3]*School of Economics, Wuhan Donghu University, Wuhan 430212, China*
[4]*College of Electronic and Electrical Engineering, Shanghai University of Engineering Science, Shanghai 201620, China*

Correspondence should be addressed to Xia Qing; 77218434@qq.com

Received 15 January 2020; Accepted 22 February 2020; Published 27 April 2020

Guest Editor: Hao Shen

This paper investigates the finite-time synchronization of complex dynamical networks with nondelayed and delayed coupling. By designing a simple continuous function controller, sufficient criteria for finite-time synchronization of dynamical networks with nondelayed and delayed coupling are obtained. As a special case, the continuous function controller designed in this paper may be the simplest and easy to implement for the finite-time synchronization of dynamical networks without delay. Finally, numerical simulations are given to verify the effectiveness of the conclusions presented in this paper.

1. Introduction

As synchronization behavior of complex systems is a common phenomenon in the field of nature and engineering technology, synchronization control of complex systems has been attracted people to study [1–8]. However, in many fields, people begin to realize that finite-time control of complex systems may be more practical than infinite-time control of complex systems [9–14]. For example, when the brain is stimulated by external signals, the brain's nervous system will respond accordingly, and the response output signals of the central nervous system and the sensory nervous system should be consistent. That is to say, the driving neural network and the response neural network move under different starting conditions. By properly controlling the neural network, the trajectories of the two neural networks will coincide in a finite-time, which is the finite-time control of the neural dynamic network. Since finite-time of system control mainly depends on the initial state of complex systems, the initial state of complex systems may be random, which is not conducive to solving practical problems. Subsequently, Polyakov proposed a finite-time control method independent of the initial state of complex systems, that is, so-called fixed-time control of complex systems, which compensated for the limitation of the finite-time control method [15, 16]. Therefore, studying the finite-time control problem of complex networks, on the one hand, it expands synchronization control theory of complex networks; on the other hand, the finite-time control method may save the control cost better and may have greater practical value in the stability control application of complex systems.

At present, based on the research of finite-time control in complex networks, the authors have obtained some interesting results, such as finite-time control via optimal method [17], finite-time control via intermittent

feedback [18], finite-time control via linear and nonlinear control method [19], finite-time control with nonlinear dynamics and uncertainties [20], finite-time control with switched discontinuous systems, and so on [21]. However, in these discussions, the designed controller usually contains symbolic functions. As the designed controller contains symbolic function, which is a discontinuous function, a flutter phenomenon may occur during the control process. The occurrence of the flutter phenomenon will obviously affect the finite-time control effect of complex networks. In order to eliminate the flutter phenomenon, some authors have proposed finite-time controller with continuous functions. For example, in [22], the authors effectively synchronize two complex networks by designing continuous function controllers, eliminating the adverse effects caused by symbolic function controllers, that is, the controller is $r_i = -l_i w_i(t) - k_1 w_i^{m_1/m_2}(t) - k_2 w_i^{m_3/m_4}(t)$, where $l_i > 0$, $k_1 > 0$, $k_2 > 0$, m_1, m_2, m_3, and m_4 are positive odd integers satisfying, $m_1 > m_2, m_3 < m_4$, and w_i means the error. In [23], a simpler continuous function controller for fixed-time synchronization of complex networks with nondelayed coupling was proposed, that is, the controller is $r_i = -k_1 w_i^{m_1/m_2}(t) - k_2 w_i^{m_3/m_4}(t)$. Therefore, designing simple and effective finite-time controllers is still an interesting topic.

In addition, in the network, time-delay is inevitable. For example, in the process of transmission and response, the physical limitations of propagation speed and the existence of network congestion often lead to delay in complex networks. The generation of time-delay may affect the stability of the whole network, such as the oscillation and instability of the system. Therefore, it is undoubtedly of great application value and theoretical significance to study the synchronization control of the time-delay coupled network. Although the finite-time synchronization of time-delay complex networks has been discussed in the existing literatures [24, 25], finite-time controllers designed in their papers were generally complex and contained symbolic functions, which may cause chattering during network synchronization. In general, an important criterion for studying finite-time control of complex systems is that the controller is as simple as possible and easy to implement. As far as we know, finite-time synchronization of dynamical networks with delayed coupling was less considered by using a simple continuous function controller. In this paper, we attempt to design a continuous finite-time controller to realize finite-time control of complex systems with delayed, and we also make the effort to propose the simplest finite-time continuous function controller for complex networks with nondelayed coupling.

This paper is organized as follows: Section 2 gives the model and preliminaries. Section 3 puts forward some finite-time synchronization criteria for networks. Section 4 gives an illustrative example. The conclusions are given in Section 5.

2. Model and Preliminaries

Consider the following dynamical network with delay coupling:

$$\dot{\mu}_i(t) = g(\mu_i(t)) + \sum_{j=1}^{N} b_{ij}\mu_j(t) + \sum_{j=1}^{N} c_{ij}\mu_j(t-\tau), \tag{1}$$

where $\mu_i(t) = (\mu_{i1}(t), \mu_{i2}(t), \ldots, \mu_{in}(t))^T \in R^n$ is the state vector, $i = 1, 2, \ldots, N$, N denotes natural number, and $g(\cdot)$ is the activation function. $B = (b_{ij})_{n\times n}$ and $C = (c_{ij})_{n\times n}$ denote connection weight matrix. τ means time-delay.

The controlled dynamic network with delay coupling is represented as follows:

$$\dot{\vartheta}_i(t) = g(\vartheta_i(t)) + \sum_{j=1}^{N} b_{ij}\vartheta_j(t) + \sum_{j=1}^{N} c_{ij}\vartheta_j(t-\tau) + r_i, \tag{2}$$

where $\vartheta_i(t) = (\vartheta_{i1}(t), \vartheta_{i2}(t), \ldots, \vartheta_{in}(t))^T \in R^n$ is the state vector and $i = 1, 2, \ldots, N$, r_i means the controller.

Assumed the errors are expressed as $w_i = \vartheta_i - \mu_i$, then

$$\dot{w}_i(t) = g(\vartheta_i(t)) - g(\mu_i(t)) + \sum_{j=1}^{N} b_{ij}w_j(t) + \sum_{j=1}^{N} c_{ij}w_j(t-\tau) + r_i. \tag{3}$$

Assumption 1. Assume the function $g(\cdot)$ satisfies the following condition:

$$|g(\vartheta_i(t)) - g(\mu_i(t))| \le \gamma|\vartheta_i(t) - \mu_i(t)|, \quad \gamma \in R^+. \tag{4}$$

Lemma 1 (see [22]). *For any vectors $\mu, \vartheta \in R^m$ and positive definite matrix $\Omega \in R^{m\times m}$, the following matrix inequality holds:*

$$2\mu^T\vartheta \le \mu^T\Omega\mu + \vartheta^T\Omega^{-1}\vartheta. \tag{5}$$

Lemma 2 (see [24]). *Consider the dynamical system as follows:*

$$\begin{gathered}\dot{\mu} = g(\mu(t)),\\ g(0) = 0,\\ \mu \in R^n,\\ \mu(0) = \mu_0.\end{gathered} \tag{6}$$

Suppose a continuous and positive definite $V(\mu)$ satisfies

$$\dot{v}(\mu) \le l_1 v(\mu) - l_2 v^{\xi}(\mu),$$

$$v^{1-\xi}(\mu) < \frac{l_2}{l_1}, \tag{7}$$

$$l_1 > 0,\ l_2 > 0,\ 0 < \zeta < 1.$$

Then, the origin of the dynamical system (6) is finite-time stable, and

$$T_{\mu}(\mu_0) \le \frac{1}{l_1(\xi - 1)} \ln\left(1 - \frac{l_1}{l_2} v^{1-\xi}(\mu_0)\right). \tag{8}$$

Lemma 3 (see [26]). *For $\Theta_i \ge 0$, $i = 1, 2, \ldots, n$, $0 < \lambda \le 1$, $\kappa > 1$, then*

$$\sum_{i=1}^{n} \Theta_i^{\lambda} \ge \left(\sum_{i=1}^{n} \Theta_i\right)^{\lambda},$$

$$\sum_{i=1}^{n} \Theta_i^{\kappa} \ge n^{1-\kappa} \left(\sum_{i=1}^{n} \Theta_i\right)^{\kappa}. \tag{9}$$

3. Main Results

Based on the preparation of the second section, the section will discuss the finite-time synchronization of two complex networks.

Theorem 1. *If Assumption 1 holds, two complex dynamical networks (1) and (2) can be synchronized by the following simpler finite-time controller:*

$$r_i = -\frac{k w_i^T(t-\tau) w_i(t-\tau)}{\|w_i(t)\|^2} w_i(t) - h_i w_i^{\xi}(t), \tag{10}$$

and

$$T \le \frac{1}{l(\xi - 1)} \ln\left(1 - \frac{2^{(1-\xi)/2} l}{\lambda_{\min}(H \otimes I)} v^{(1-\xi)/2}(w(0))\right), \tag{11}$$

where $k = (N/2)\lambda_{\max}(\Omega^{-1})$, $l = \gamma + \lambda_{\max}(B \otimes I) + (N\delta^2/2)$ $\lambda_{\max}(\Omega \otimes I)$, $H = diag\{h_1, \ldots, h_N\}$, $h_i > 0$, $\xi = n_1/n_2$, n_1 and n_2 are positive odd integers, $n_1 < n_2$, and Ω is the positive definite matrix.

Proof. Consider the following function:

$$v(t) = \frac{1}{2} w^T(t) w(t), \tag{12}$$

where $w = (w_1^T, w_2^T, \ldots, w_n^T)^T$.

So,

$$\begin{aligned}
\dot{v}(t) &= \sum_{i=1}^{N} w_i^T(t) \left(g(\vartheta_i(t)) - g(\mu_i(t)) + \sum_{j=1}^{N} b_{ij} w_j(t) + \sum_{j=1}^{N} c_{ij} w_j(t-\tau) + r_i\right) \\
&\le \sum_{i=1}^{N} \gamma w_i^T(t) w_i(t) + \sum_{i=1}^{N} w_i^T(t) \sum_{j=1}^{N} b_{ij} w_j(t) + \sum_{i=1}^{N} w_i^T(t) \sum_{j=1}^{N} c_{ij} w_j(t-\tau) - \sum_{i=1}^{N} w_i^T(t) \frac{k w_i^T(t-\tau) w_i(t-\tau)}{\|w_i(t)\|^2} w_i(t) \\
&\quad - \lambda_{\min}(H \otimes I) w^T(t) w^{\xi}(t).
\end{aligned} \tag{13}$$

In equation (13), obviously,

$$\begin{aligned}
w^T(t) w^{\xi}(t) &= \sum_{i=1}^{N} \sum_{j=1}^{n} \left(w_{ij}^2(t)\right)^{(1+\xi)/2} \ge \sum_{i=1}^{N} \left(\sum_{j=1}^{n} w_{ij}^2(t)\right)^{(1+\xi)/2} \ge \left(w^T(t) w(t)\right)^{(1+\xi)/2} = (2)^{(1+\xi)/2} (v(t))^{(1+\xi)/2} \\
\sum_{i=1}^{N} w_i^T(t) \sum_{j=1}^{N} c_{ij} w_j(t-\tau) &\le \frac{N\delta^2}{2} \sum_{i=1}^{N} [w_i(t)]^T \Omega w_i(t) + \frac{N}{2} \sum_{j=1}^{N} \left(w_j(t-\tau)\right)^T \Omega^{-1} w_j(t-\tau)),
\end{aligned} \tag{14}$$

where $|c_{ij}| \le \delta \in R^+$.

So,

$$\begin{aligned}
\dot{v}(t) &\le \sum_{i=1}^{N} \gamma w_i^T(t) w_i(t) + \sum_{i=1}^{N} w_i^T(t) \sum_{j=1}^{N} b_{ij} w_j(t) + \frac{N\delta^2}{2} \sum_{i=1}^{N} [w_i(t)]^T \Omega w_i(t) + \frac{N}{2} \sum_{j=1}^{N} \left(w_j(t-\tau)\right)^T \Omega^{-1} w_j(t-\tau)) \\
&\quad - \sum_{i=1}^{N} \frac{k w_i^T(t-\tau) w_i(t-\tau)}{\|w_i(t)\|^2} w_i^T(t) w_i(t) - \lambda_{\min}(H \otimes I)(2)^{(1+\xi)/2} (v(t))^{(1+\xi)/2} \\
&\le \sum_{i=1}^{N} \gamma w_i^T(t) w_i(t) + \sum_{i=1}^{N} w_i^T(t) \sum_{j=1}^{N} b_{ij} w_j(t) + \frac{N\delta^2}{2} \sum_{i=1}^{N} [w_i(t)]^T \Omega w_i(t) + \frac{N}{2} \lambda_{\max}\left(\Omega^{-1}\right) \sum_{j=1}^{N} \left(w_j(t-\tau)\right)^T w_j(t-\tau)) \\
&\quad - k \sum_{i=1}^{N} w_i^T(t-\tau)) w_i(t-\tau) - \lambda_{\min}(H \otimes I)(2)^{(1+\xi)/2} (v(t))^{(1+\xi)/2} \\
&\le \sum_{i=1}^{N} \gamma w_i^T(t) w_i(t) + \sum_{i=1}^{N} w_i^T(t) \sum_{j=1}^{N} b_{ij} w_j(t) + \frac{N\delta^2}{2} \sum_{i=1}^{N} [w_i(t)]^T \Omega w_i(t) + \left(\frac{N}{2} \lambda_{\max}\left(\Omega^{-1}\right) - k\right) \sum_{j=1}^{N} \left(w_j(t-\tau)\right)^T w_j(t-\tau)) \\
&\quad - \sum_{i=1}^{N} l w_i^T(t) w_i(t) + \sum_{i=1}^{N} l w_i^T(t) w_i(t) - \lambda_{\min}(H \otimes I)(2)^{(1+\xi)/2} (v(t))^{(1+\xi)/2}.
\end{aligned} \tag{15}$$

When $k = (N/2)\lambda_{\max}(\Omega^{-1})$, $l = \gamma + \lambda_{\max}(B \otimes I) + (N\delta^2)/2\lambda_{\max}(\Omega \otimes I)$, we have

$$\begin{aligned}
\dot{v}(t) &\le \sum_{i=1}^{N} l w_i^T(t) w_i(t) - \lambda_{\min}(H \otimes I)(2)^{(1+\xi)/2} (v(t))^{(1+\xi)/2} \\
&= 2lv(t) - \lambda_{\min}(H \otimes I)(2)^{(1+\xi)/2} (v(t))^{(1+\xi)/2}.
\end{aligned} \tag{16}$$

Then, the origin of the error systems (3) is finite-time stable, and T satisfies

$$T \le \frac{1}{l(\xi-1)} \ln\left(1 - \frac{2^{(1-\xi)/2} l}{\lambda_{\min}(H \otimes I)} v^{(1-\xi)/2}(w(0))\right). \tag{17}$$

The proof is completed. □

Remark 1. At present, few continuous function controllers are designed for finite-time synchronization of delay dynamical networks. Therefore, the continuous function finite-time controller in this paper may be more practical.

Remark 2. From the proof of Theorem 1, when the delay is time-varying, Theorem 1 still holds.

Remark 3. If $c_{ij} = 0$, the coupled dynamical networks (1)-(2) can reduce to complex dynamical networks with the nondelayed coupling dynamical network. In this case, the finite-time controller (10) is not available. In this case, since the network does not contain delay, and the following Corollary 1 can be obtained.

Remark 4. The matrix Ω is a positive definite matrix given arbitrarily. To guarantee the optimality of result, the matrix Ω should have minimum eigenvalue. As the convergence time is related to the matrix Ω, the control strength k is also related to the matrix Ω. From their expressions, we can see that the smaller the eigenvalue of the matrix Ω, the shorter the convergence time, but the greater the control strength k, and how to choose the matrix Ω to guarantee the optimality of result will be the topic for further consideration in the future.

When $C = 0$, the complex networks (1)-(2) changed into the following complex dynamical networks with nondelayed coupling:

$$\dot{\mu}_i(t) = g(\mu_i(t)) + \sum_{j=1}^{N} b_{ij} \mu_j(t), \tag{18}$$

$$\dot{\vartheta}_i(t) = g(\vartheta_i(t)) + \sum_{j=1}^{N} b_{ij} \vartheta_j(t) + r_i. \tag{19}$$

Corollary 1. *If Assumption 1 holds, two complex dynamical networks with nondelayed coupling (18) and (19) can be synchronized by the simplest finite-time controller:*

$$r_i = -h_i w_i^{\xi}(t), \tag{20}$$

and the time is bounded as

$$T \le \frac{1}{l(\xi-1)} \ln\left(1 - \frac{2^{(1-\xi)/2} l}{\lambda_{\min}(H \otimes I)} v^{(1-\xi)/2}(w(0))\right), \tag{21}$$

where $l = \gamma + \lambda_{\max}(B \otimes I)$, $\xi = n_1/n_2$, *and* n_1 *and* n_2 *are positive odd integers,* $n_1 < n_2$.

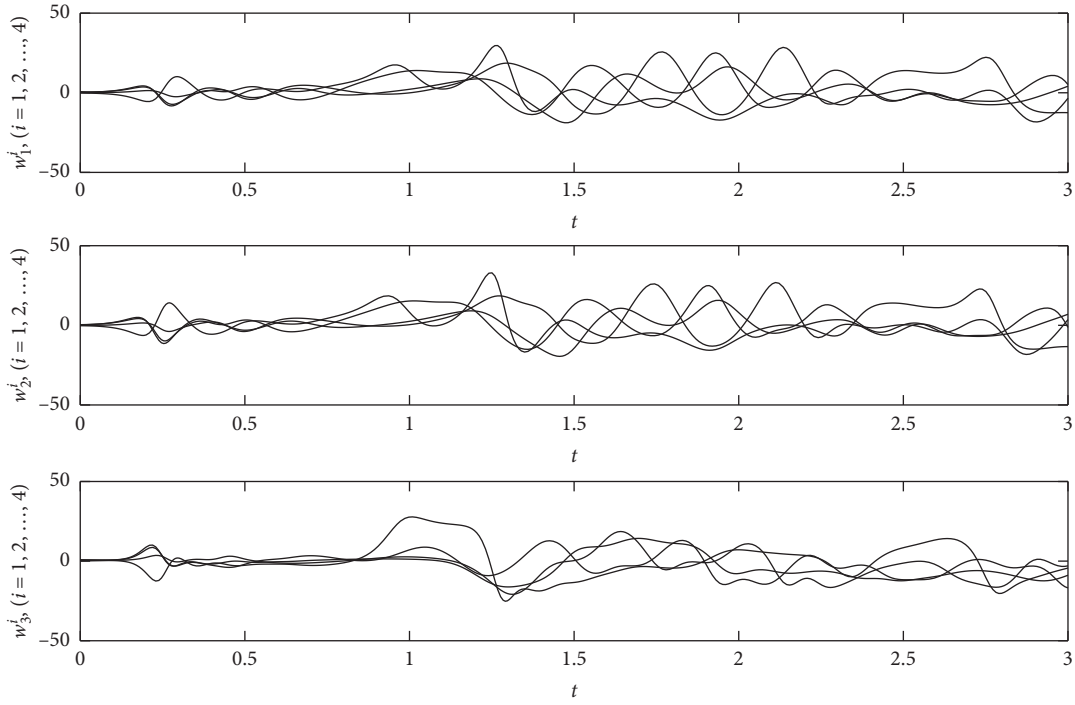

Figure 1: Error evolution of two networks.

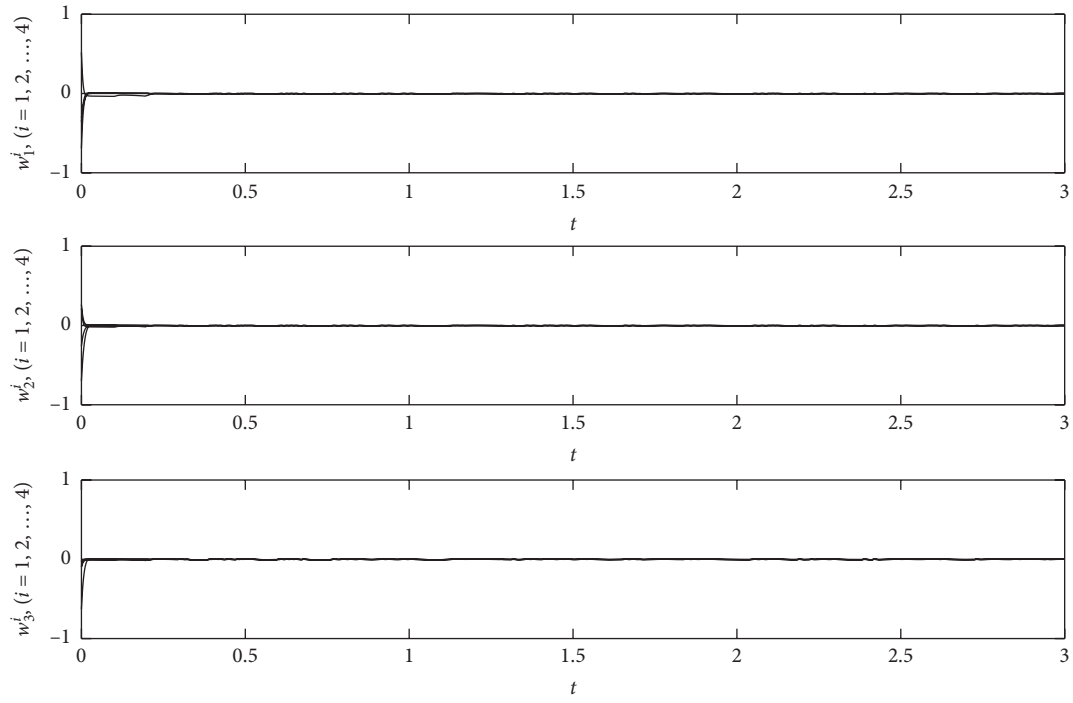

Figure 2: Synchronization evolution of two networks.

The proof of Corollary 1 is similar to that of Theorem 1, so we omit their reasoning process here.

Remark 5. Compared with the existing literature [15–18] on finite-time synchronization of complex networks without delay, the controller (20) designed in this paper may be the simplest one. Generally speaking, simple controllers may have better application in practical engineering.

Remark 6. From (11) and (21), synchronization time of complex networks is the same, that is to say, the delay term

of complex networks does not affect the synchronization time of complex networks.

Remark 7. In [9, 10, 15, 24, 25], the authors proposed continuous function controllers without symbolic functions, but the synchronization of delay networks was not discussed in their paper.

4. Numerical Simulation Example

Considering the following chaos system [27],

$$\dot{\vartheta}_i = \begin{pmatrix} -10 & 10 & 0 \\ 28 & -1 & 0 \\ 0 & 0 & -8/3 \end{pmatrix} \begin{pmatrix} \vartheta_{i1} \\ \vartheta_{i2} \\ \vartheta_{i3} \end{pmatrix} + \begin{pmatrix} 0 \\ -\vartheta_{i1}\vartheta_{i3} \\ \vartheta_{i1}\vartheta_{i2} \end{pmatrix}. \tag{22}$$

It is well known that the chaos system is bounded, and our analyses show

$$\left\| g(\vartheta_i) - g(\mu_i) \right\|_2 \leq 100.5571 \left\| w_i \right\|_2. \tag{23}$$

If we use four nodes to describe the coupled complex network, then

$$\dot{\mu}_i(t) = g(\mu_i(t)) + \sum_{j=1}^{4} b_{ij}\mu_j(t),$$
$$\left(b_{ij}\right)_{4\times 4} = \begin{pmatrix} -4 & 1 & 2 & 1 \\ 1 & -6 & 3 & 2 \\ 2 & 3 & -6 & 1 \\ 1 & 2 & 1 & -4 \end{pmatrix}. \tag{24}$$

Let initial values of the state variable are rand [0, 1] and $\gamma = 115$, $\xi = 0.8$, and $h_i = 200$. Figure 1 shows that the driver network and the response network cannot be synchronized without a controller. Figure 2 shows finite-time synchronization of two networks under the controller. Numerical simulations illustrate the validity of Corollary 1.

5. Conclusion

The paper has studied synchronization of two complex dynamical networks with nondelayed and delayed coupling by the finite-time controller. The designed finite-time controller was continuous function. Especially, the continuous function controller designed might be the simplest for finite-time synchronization of complex dynamical networks without delay. Finally, the numerical simulation verified the validity of the theoretical results. As the results are sufficient conditions in this paper, which implies that there is still room for further improvement, which will be our next research topic.

Data Availability

No data were used to support this study.

Conflicts of Interest

The authors declare that there are no conflicts of interest regarding the publication of this paper.

Acknowledgments

This work was supported by the National Natural Science Foundation of China (61673221); Natural Science Foundation of Jiangsu Province (BK20181418); "Qing-Lan Engineering" Foundation of Jiangsu Higher Education Institutions; Six Talent Peaks Project in Jiangsu Province (DZXX-019); the Natural Science Foundation of Jiangsu Higher Education Institutions (19KJB120007); and Natural Science Foundation For Youths of Jiangsu Province (BK20171072).

References

[1] J. Lu, L. Sun, Y. Liu, D. W. C. Ho, and J. Cao, "Stabilization of Boolean control networks under aperiodic sampled-data control," *SIAM Journal on Control and Optimization*, vol. 56, no. 6, pp. 4385–4404, 2018.

[2] B. Li, J. Lu, J. Zhong, and Y. Liu, "Fast-time stability of temporal Boolean networks," *IEEE Transactions on Neural Networks and Learning Systems*, vol. 30, no. 8, pp. 2285–2294, 2019.

[3] Y. Wang, Y. Wei, X. Liu, N. Zhou, and C. Cassandras, "Optimal persistent monitoring using second-order agents with physical constraints," *IEEE Transactions on Automatic Control*, vol. 64, no. 8, pp. 3239–3252, 2019.

[4] Y. Wang, Y. Lei, T. Bian, and Z. Guan, "Distributed control of nonlinear multi-agent systems with unknown and nonidentical control directions via event-triggered communication," *IEEE Transactions on Cybernetics*, 2019.

[5] H. Shen, S. Huo, J. Cao, and T. Huang, "Generalized state estimation for markovian coupled networks under round-robin protocol and redundant channels," *IEEE Transactions on Cybernetics*, vol. 49, no. 4, pp. 1292–1301, 2019.

[6] H. Shen, T. Wang, J. Cao, G. Lu, Y. Song, and T. Huang, "Nonfragile dissipative synchronization for markovian memristive neural networks: a gain-scheduled control scheme," *IEEE Transactions on Neural Networks and Learning Systems*, vol. 30, no. 6, pp. 1841–1853, 2019.

[7] Y. Tang, H. Gao, W. Zhang, and J. Kurths, "Leader-following consensus of a class of stochastic delayed multi-agent systems with partial mixed impulses," *Automatica*, vol. 53, pp. 346–354, 2015.

[8] W. Zhang, Q.-L. Han, Y. Tang, and Y. Liu, "Sampled-data control for a class of linear time-varying systems," *Automatica*, vol. 103, pp. 126–134, 2019.

[9] J. Wang, D. Wang, H. Wu, and T. Huang, "Finite-time passivity and synchronization of complex dynamical networks with state and derivative coupling," *IEEE Transactions on Cybernetics*, 2019.

[10] J. Wang, X. Zhang, H. Wu, T. Huang, and Q. Wang, "Finite-time passivity of adaptive coupled neural networks with undirected and directed topologies," *IEEE Transactions on Cybernetics*, 2018.

[11] Z. Tang, J. H. Park, Y. Wang, and J. Feng, "Parameters variation-based synchronization on derivative coupled Lur'e networks," *IEEE Transactions on Systems, Man, and Cybernetics: Systems*, 2019.

[12] Z. Tang, J. H. Park, Y. Wang, and J. Feng, "Distributed impulsive quasi-synchronization of Lur'e networks with proportional delay," *IEEE Transactions on Cybernetics*, vol. 49, no. 8, pp. 3105–3115, 2019.

[13] M. Dai, J. Xia, H. Xia, and H. Shen, "Event-triggered passive synchronization for Markov jump neural networks subject to randomly occurring gain variations," *Neurocomputing*, vol. 331, pp. 403–411, 2019.

[14] J. Wang, L. Shen, J. Xia, Z. Wang, and X. Chen, "Asynchronous dissipative filtering for nonlinear jumping systems subject to fading channels," *Journal of the Franklin Institute*, vol. 357, no. 1, pp. 589–605, 2020.

[15] J. Wang, T. Ru, J. Xia, Y. Wei, and Z. Wang, "Finite-time synchronization for complex dynamic networks with semi-Markov switching topologies: an H∞ event-triggered control scheme," *Applied Mathematics and Computation*, vol. 356, no. 1, pp. 235–251, 2019.

[16] A. Polyakov, "Nonlinear feedback design for fixed-time stabilization of linear control systems," *IEEE Transactions on Automatic Control*, vol. 57, no. 8, pp. 2106–2110, 2012.

[17] G. Mei, X. Wu, D. Ning, and J.-A. Lu, "Finite-time stabilization of complex dynamical networks via optimal control," *Complexity*, vol. 21, no. S1, pp. 417–425, 2016.

[18] D. Zhang, Y. Shen, and J. Mei, "Finite-time synchronization of multi-layer nonlinear coupled complex networks via intermittent feedback control," *Neurocomputing*, vol. 225, pp. 129–138, 2017.

[19] B. Zhang and Y. Jia, "Fixed-time consensus protocols for multi-agent systems with linear and nonlinear state measurements," *Nonlinear Dynamics*, vol. 82, no. 4, pp. 1683–1690, 2015.

[20] Y. Xu, W. Zhou, J. A. Fang, C. Xie, and D. Tong, "Finite-time synchronization of the complex dynamical network with non-derivative and derivative coupling," *Neurocomputing*, vol. 173, pp. 1356–1361, 2016.

[21] Z. Tang, J. H. Park, and H. Shen, "Finite-time cluster synchronization of Lur'e networks: a nonsmooth approach," *IEEE Transactions on Systems, Man, and Cybernetics: Systems*, vol. 48, no. 8, pp. 1213–1224, 2018.

[22] X. Yang, J. Lam, D. W. C. Ho, and Z. Feng, "Fixed-time synchronization of complex networks with impulsive effects via nonchattering control," *IEEE Transactions on Automatic Control*, vol. 62, no. 11, pp. 5511–5521, 2017.

[23] Y. Xu, X. Wu, N. Li, L. Liu, C. Xie, and C. Li, "Fixed-time synchronization of complex networks with a simpler non-chattering controller," *IEEE Transactions on Circuits and Systems II: Express Briefs*, 2019.

[24] S. Mobayen and J. Ma, "Robust finite-time composite nonlinear feedback control for synchronization of uncertain chaotic systems with nonlinearity and time-delay," *Chaos, Solitons & Fractals*, vol. 114, pp. 46–54, 2018.

[25] R. Wei, J. Cao, and A. Alsaedi, "Finite-time and fixed-time synchronization analysis of inertial memristive neural networks with time-varying delays," *Cognitive Neurodynamics*, vol. 12, no. 1, pp. 121–134, 2018.

[26] G. Hardy, J. Littlewood, and G. Polya, *Inequalities*, Cambridge University Press, Cambridge, UK, 1952.

[27] W. Zhou, Y. Xu, H. Lu, and L. Pan, "On dynamics analysis of a new chaotic attractor," *Physics Letters A*, vol. 372, no. 36, pp. 5773–5777, 2008.

Hindawi
Discrete Dynamics in Nature and Society
Volume 2020, Article ID 3436461, 8 pages
https://doi.org/10.1155/2020/3436461

Research Article

H_∞ Filter Design for Networked Control Systems: A Markovian Jump System Approach

WanRu Wang,[1,2] **LianKun Sun**,[1,2] **and HongRu Gu**[1]

[1]*School of Computer Science and Technology Engineering, Tiangong University, Tianjin 300387, China*
[2]*Tianjin Key Laboratory of Autonomous Intelligence Technology and Systems, Tianjin 300387, China*

Correspondence should be addressed to WanRu Wang; tjpuwwr@126.com

Received 8 February 2020; Accepted 9 March 2020; Published 8 April 2020

Guest Editor: Hao Shen

This paper puts forward a method to design the H_∞ filter for networked control systems (NCSs) with time delay and data packet loss. Based on the properties of Markovian jump system, the packet loss is treated as a constant probability independent and identically distributed Bernoulli random process. Thus, the stochastic stability condition can be acquired for the filtering error system, which meets an H_∞ performance index level γ. It is shown that, by introducing a special structure of the relaxation matrix, a linear representation of the filter meeting an H_∞ performance index level for NCSs with time delay and packet loss can be obtained, which uses linear matrix inequalities (LMIs). Finally, numerical simulation examples demonstrate the effectiveness of the proposed method.

1. Introduction

As a new generation of control systems, NCSs [1–10] have attracted more and more researchers' attention because of their extensive application. Compared with the traditional control system, NCSs have some advantages, such as easy wiring, installation, maintenance, expansion, reliability, and flexibility, so that resource sharing is achieved in such systems. However, the network also brought some new problems, in which time delay and packet dropout are two main aspects, which will not only make a negative impact on system but also may even lead to the instability of system. Recently, the problem of NCSs with time delay and packet dropout phenomenon has become a hot topic in the control field [11–13].

The Markovian jump system (MJS) refers to a stochastic system with multiple model states and the system transitions between modes in accordance with the properties of the Markov chain due to the multimode transition characteristics of the Markovian jump system in the actual engineering. It can be used to simulate many systems with abrupt characteristics, such as manufacturing systems and fault-tolerant systems [14–24]. In [25], the exponential L_2–L_∞ filter problem of the linear system is explored, and the system has both distributed delay, Markovian jump parameter, and norm bounded parameter uncertainty. In [26], the H_∞ filtering design about a continuous MJS in distributed sampled-data asynchronous is involved; in addition, the system's mode jumping instants and filter are asynchronous. In [27], the design of a sampled system H_∞ filter is studied. However, many conclusions only consider time delay or packet loss separately, which is not very consistent with the actual situation of network application. In addition, the H_∞ filter design of NCSs with time delay and packet dropout has not yet been considered widely.

Based on this, this paper studies the stability of networked control systems considering both time delay and packet loss. Although the analysis process is more complicated than considering time delay or packet loss alone, however the conclusion is more general and universal, and then the existence conditions of system filters are given. The effectiveness of the proposed method is verified by simulation, and the relevant conclusions are more practical. In Section 2, NCSs with time delay are present by a Markov model. The two probabilities of packet dropout in the Bernoulli random process is designed. In Section 3,

according to Lyapunov's stability theorem, the H_∞ performance of system is proven. In Section 4, a H_∞ filter for NCSs with time delay and packet loss is designed. In Section 5, numerical simulation examples are given to verify the result of this paper. In Section 6, we make a conclusion.

Notation: here are some of the symbols in the paper. The superscript "T" means the matrix transposition, and R^{n_x} shows the n_x-dimensional Euclidean space. I denotes the unit matrix of adaptive dimension, and 0 refers to the zero matrix of adaptive dimension. $P > 0$ indicates P is real symmetric and positive matrix, and the notation stands for the norm of matrix $\|A\|$ that is defined according to $\|A\| = \sqrt{\mathrm{tr}(A^T A)}$, where "tr" denotes the trace operator. $\|\cdot\|_2$ indicates the usual Euclidean vector norm. Prob $\{\cdot\}$ stands for the occurrence probability of the event "$\cdot$". $E\{x\}$ and $E\{x \mid y\}$ represent the expectation of event x and the expectation of x conditional on y, respectively.

2. Problem Formulation

First, consider the following kind of discrete-time linear systems [28] with time delay as

$$\begin{cases} x(k+1) = A(r(k))x(k) + \mathrm{B}(r(k))w(k), \\ z(k) = L(r(k))x(k) + D(r(k))w(k), \\ y(k) = C(r(k))x(k). \end{cases} \tag{1}$$

where $x(k) \in R^n$ refers to the state vector in the plant; $w(k) \in R^h$ belongs to $l_2[0, \infty)$, which indicates the measured output; $z(k) \in R^m$ shows the estimating intended signal; and $A(r(k))$ indicates system parameters depend on $r(k)$. $B(r(k))$, $C(r(k))$, $D(r(k))$, and $L(r(k))$ have a similar situation. $R(k)$ is assumed to a discrete Markov chain, and the values of it are in a finite set $h \triangleq \{1, \ldots, N\}$ with a transition probabilities matrix $\overline{\wedge} = (\pi_{\mathrm{ij}})$; set $\overline{r}_k = i$ and $\overline{r}_{k+1} = j$, such that system mode variable $r(k)$ satisfies $P_r(\overline{r}_{k+1} = j \mid \overline{r}_k = i) = \pi_{ij}$, where $\pi_{ij} \geq 0$ and $\sum_{j=1}^{N} \pi_{ij} = 1$; h has N Markov modes, and for $\overline{r}_k = i$, $A(r(k))$ are denoted by A_i with appropriate dimensions. B_i, C_i, D_i, and L_i also have the same situation. $\beta \in R$ shows a Bernoulli-distributed sequence with relationship as follows:

$$\begin{cases} P_{\mathrm{rob}}\{\beta = 1\} = E\{\beta\} \triangleq \overline{\beta}, \\ P_{\mathrm{rob}}\{\beta = 0\} = 1 - E\{\beta\} \triangleq 1 - \overline{\beta}. \end{cases} \tag{2}$$

After calculations, another important expectation can be shown as follows:

$$\mathrm{var}\left\{E(\beta - \overline{\beta})^2\right\} = (1 - \overline{\beta})\overline{\beta} = \sigma. \tag{3}$$

Remark 1. For network packet loss, both Bernoulli distribution and Poisson distribution have been considered. According to the network protocols adopted in actual systems, such as industrial Ethernet and profibus, it is more practical to model network packet loss with Bernoulli distribution in this paper.

Mathematical model description of filtering is in the following formula:

$$\begin{cases} \widehat{x}(k+1) = A_{fi}\widehat{x}(k) + B_{fi}\widehat{y}(k), \\ \widehat{z}(k) = C_{fi}\widehat{x}(k) + D_{fi}\widehat{y}(k), \\ \widehat{y}(k) = \beta y(k) + (1-\beta)y(k+1), \end{cases} \tag{4}$$

where $\widehat{x}(k) \in R^n$ and $\widehat{y}(k) \in R^m$ are the state vector of filter mode estimator and $\widehat{z}(k) \in R^p$ indicates the output vector of the estimator. $A_{f\,i}$, $B_{f\,i}$, $C_{f\,i}$, and $D_{f\,i}$ are real matrices to be determined with compatible dimensions. Combining (4) and (1), a filter error system with Markov chain can be shown as

$$\begin{cases} \widetilde{x}(k+1) = \widetilde{A}_i\widetilde{x}(k) + \widetilde{A}_i\widetilde{x}(k-1) + \widetilde{B}_i\omega(k) \\ \widetilde{z}(k) = \widetilde{C}_i\widetilde{x}(k) + \widehat{C}_i\widetilde{x}(k-1) + \widetilde{D}_i\omega(k) \end{cases}, \tag{5}$$

where

$$\begin{aligned} \widetilde{A}_i &= \widetilde{A}_{1i} + (\beta - \overline{\beta})\widetilde{A}_{2i} = \begin{bmatrix} A_i & 0 \\ \beta B_{fi}C_i & A_{fi} \end{bmatrix} = \begin{bmatrix} A_i & 0 \\ \overline{\beta} B_{fi}C_i & A_{fi} \end{bmatrix} \\ &\quad + (\beta - \overline{\beta})\begin{bmatrix} 0 & 0 \\ B_{fi}C_i & 0 \end{bmatrix}, \\ \widehat{A}_i &= \widehat{A}_{1i} - (\beta - \overline{\beta})\widehat{A}_{2i} = \begin{bmatrix} 0 & 0 \\ (1-\beta)B_{fi}C_i & 0 \end{bmatrix} \\ &= \begin{bmatrix} 0 & 0 \\ (1-\overline{\beta})B_{fi}C_i & 0 \end{bmatrix} - (\beta - \overline{\beta})\begin{bmatrix} 0 & 0 \\ B_{fi}C_i & 0 \end{bmatrix}, \\ \widetilde{C}_i &= \widetilde{C}_{1i} - (\beta - \overline{\beta})\widetilde{C}_{2i} = \left[L_i - \beta D_{fi}C_i - C_{fi}\right] \\ &= \left[L_i - \overline{\beta} D_{fi}C_i - C_{fi}\right] - (\beta - \overline{\beta})\left[D_{fi}C_i \;\; 0\right], \\ \widehat{C}_i &= \widehat{C}_{1i} - (\beta - \overline{\beta})\widehat{C}_{2i} = \left[-(1-\beta)D_{fi}C_i \;\; 0\right] \\ &= \left[-(1-\overline{\beta})D_{fi}C_i \;\; 0\right] + (\beta - \overline{\beta})\left[D_{fi}C_i \;\; 0\right], \\ \widetilde{B}_i &= \begin{bmatrix} B_i \\ 0 \end{bmatrix}, \\ \widetilde{D}_i &= D_i. \end{aligned} \tag{6}$$

Obviously, a filter error system (5) is a Markovian jump system with packet loss. We will use some important definitions in the following for essential later steps.

Definition 1 (see [29]). A filter error system (5) is stochastically stable when $\omega(k) = 0$. There $x_0 \in R$ and $r_0 \in l$, and the following inequality exists:

$$E\left\{\sum_{k=0}^{\infty} \|\widetilde{x}(k)\| \,\middle|\, \widetilde{x}_0, r_0\right\} < \infty. \tag{7}$$

Definition 2 (see [29]). Give a scalar $\gamma > 0$, assume that system (5) is stochastically stable, and (5) also can meet an H_∞ performance index level γ under zero conditions for all nonzero $\omega(k) \in L_2[0, \infty)$ if it satisfies

$$E\left\{\sum_{k=0}^{\infty} \|\widetilde{z}(k)\|^2\right\} < \gamma^2 \|\omega(k)\|^2. \tag{8}$$

3. Main Results and Proofs

Based on the previous known conditions, a stochastically stable condition meets an H_∞ performance index level γ for NCSs with the development of time delay and packet loss.

Theorem 1. *If there exists symmetric matrices P_i and $R_i > 0$, consider NCSs with filter in (5); when $\omega(k) = 0$, system (5) will be stochastically stable such that*

$$\begin{bmatrix} \overline{Q}_i - P_i & * & * & * \\ 0 & -Q_i & * & * \\ \widetilde{A}_{1i} & \widehat{A}_{1i} & -\widetilde{P}_i^{-1} & * \\ \delta\widetilde{A}_{2i} & \delta\widehat{A}_{2i} & 0 & -\delta\widetilde{P}_i^{-1} \end{bmatrix} < 0, \tag{9}$$

where $\overline{Q}_i \triangleq \sum_{j=1}^{N} \pi_{ij} Q_j$ and $\overline{P}_i \triangleq \sum_{j=1}^{N} \pi_{ij} P_j$.

Proof. Consider a Lyapunov functional candidate as follows:

$$V(k) = \widetilde{x}^T(k) P_i \widetilde{x}(k) + \widetilde{x}^T(k-1) Q_i \widetilde{x}(k-1), \tag{10}$$

and next

$$\begin{aligned} E\{\Delta V(k)\} &= E\left\{\widetilde{x}^T(k+1) P_i \widetilde{x}(k+1)\right\} + \widetilde{x}^T(k)\overline{Q}_i\widetilde{x}(k) \\ &\quad - \widetilde{x}^T(k) P_i \widetilde{x}(k) - \widetilde{x}^T(k-1) Q_i \widetilde{x}(k-1) \\ &= E\Big\{\Big[\widetilde{x}^T(k)\widetilde{A}_{1i}^T + (\beta-\overline{\beta})\widetilde{x}^T(k)\widetilde{A}_{2i}^T + \widetilde{x}^T(k-1)\widetilde{A}_{1i}^T \\ &\quad - (\beta-\overline{\beta})\widetilde{x}^T(k-1)\widehat{A}_{2i}^T\Big]^T P_i \big[\widetilde{A}_{1i}\widetilde{x}(k) + (\beta-\overline{\beta})\widetilde{A}_{2i}\widetilde{x}(k) \\ &\quad + \widehat{A}_{1i}\widetilde{x}(k-1) - (\beta-\overline{\beta})\widehat{A}_{2i}\widetilde{x}(k-1)\big]\Big\} \\ &\quad + \widetilde{x}^T(k)\overline{Q}_i\widetilde{x}(k) - \widetilde{x}^T(k) P_i \widetilde{x}(k) \\ &\quad - \widetilde{x}^T(k-1) Q_i \widetilde{x}(k-1) \\ &= \eta^T(k)\widetilde{\wedge}\,\eta(k), \end{aligned} \tag{11}$$

where $\eta(k) = \begin{bmatrix} \widetilde{x}(k)^T & \widetilde{x}(k-1)^T \end{bmatrix}^T$ and

$$\widetilde{\Lambda} = \begin{bmatrix} \widetilde{A}_{1i}^T \widetilde{P}_i \widetilde{A}_{1i} + \delta\widetilde{A}_{2i}^T \widetilde{P}_i \widetilde{A}_{2i} + \widetilde{Q}_i - P_i & \widetilde{A}_{1i}^T \overline{P}_i \widehat{A}_{1i} - \delta\widetilde{A}_{2i}^T \overline{P}_i \widehat{A}_{2i} \\ \widehat{A}_{1i}^T \overline{P}_i \widetilde{A}_{1i} - \delta\widehat{A}_{2i}^T \overline{P}_i \widetilde{A}_{2i} & \widehat{A}_{1i}^T \overline{P}_i \widehat{A}_{1i} + \delta\widehat{A}_{2i}^T \overline{P}_i \widehat{A}_{2i} - Q_i \end{bmatrix}. \tag{12}$$

Applying Schur complement theorem to the above $\widetilde{\Lambda}$,

$$\Lambda = \begin{bmatrix} \overline{Q}_i - P_i & * & * & * \\ 0 & -Q_i & * & * \\ \widetilde{A}_{1i} & \widehat{A}_{1i} & -\widetilde{P}_i^{-1} & * \\ \delta\widetilde{A}_{2i} & -\delta\widehat{A}_{2i} & 0 & -\delta\widetilde{P}_i^{-1} \end{bmatrix}. \tag{13}$$

From Theorem 3, we can get

$$\begin{aligned} E\{\Delta V(k)\} < 0 \Rightarrow E\{V(\widetilde{x}(k+1), r(k+1)) \mid \widetilde{x}(k), r(k+1)\} \\ - V(\widetilde{x}(k), r(k)) \\ \le -\lambda_{\min}(-\Lambda) \le -\varepsilon\widetilde{x}^T(k)\widetilde{x}(k), \end{aligned} \tag{14}$$

where $\lambda_{\min}$ (-Λ) indicates the minimum value of the eigenvalue for -Λ and $\varepsilon = \inf\{\lambda_{\min}(-\Lambda)\}$ is the lower bound of $\lambda_{\min}$ (-Λ); for any $M \ge 1$, we can obtain

$$\begin{aligned} &E\{V(\widetilde{x}(M+1), r(M+1))\} - E\{V(\widetilde{x}(0), r(0))\} \\ &\le -\varepsilon \sum_{k=0}^{M} E\left\{\widetilde{x}^T(k)\widetilde{x}(k)\right\}. \end{aligned} \tag{15}$$

Thus, we can get

$$\sum_{k=0}^{M} E\left\{\widetilde{x}^T(k)\widetilde{x}(k)\right\} \le \frac{1}{\varepsilon} E\{V(\widetilde{x}(0), r(0))\} < \infty. \tag{16}$$

As a result, it can be proved that system (5) will be stochastically stable. The proof is completed. □

Theorem 2. *For NCSs (5), give a scalar $\gamma > 0$. For all $\omega(k) \neq 0$, if there are symmetric matrices P_i, $R_i > 0$ satisfied the following matrix inequalities, and the system (5) will be stochastically stable, which meets the H_∞ norm performance level γ:*

$$\begin{bmatrix} \overline{Q}_i - P_i & * & * & * & * & * & * \\ 0 & -Q_i & * & * & * & * & * \\ 0 & 0 & -\gamma^2 I & * & * & * & * \\ \widetilde{A}_{1i} & \widehat{A}_{1i} & \widetilde{B}_i & -\widetilde{P}_i^{-1} & * & * & * \\ \delta\widetilde{A}_{2i} & -\delta\widehat{A}_{2i} & 0 & 0 & -\delta\widetilde{P}_i^{-1} & * & * \\ \widetilde{C}_{1i} & \widehat{C}_{1i} & \widetilde{D}_i & 0 & 0 & -I & * \\ \delta\widetilde{C}_{2i} & -\delta\widehat{C}_{2i} & \delta\widetilde{D}_i & 0 & 0 & 0 & -\delta I \end{bmatrix} < 0. \tag{17}$$

Proof. When $\omega(k) \neq 0$ is similar to Theorem 3 proof process, we obtain the following equation:

$$E\{\Delta V(k)\} + E\left\{\widetilde{z}^T(k)\widetilde{z}(k)\right\} - \gamma^2 E\left\{\omega^T(k)\omega(k)\right\} = \widetilde{\eta}^T \wedge_1 \widetilde{\eta}, \tag{18}$$

where $\widetilde{\eta} = \left(\widetilde{x}^T(k) \;\; \widetilde{x}^T(k-1) \;\; \omega^T(k)\right)^T$,

$$\Lambda_1 = \begin{bmatrix} \Lambda_{11} & \Lambda_{12} & \widetilde{A}_{1i}^T \overline{P}_i \widetilde{B}_i + \widetilde{C}_{1i}^T \widetilde{D}_i \\ \Lambda_{21} & \Lambda_{13} & \widehat{A}_{1i}^T \overline{P}_i \widetilde{B}_i + \widehat{C}_{1i}^T \widetilde{D}_i \\ \widetilde{B}_i^T \overline{P}_i \widetilde{A}_{1i} + \widetilde{D}_i^T \widetilde{C}_{1i} & \widetilde{B}_i^T \overline{P}_i \widehat{A}_{1i} + \widetilde{D}_i^T \widehat{C}_{1i} & \widetilde{B}_i^T \overline{P}_i \widetilde{B}_i + \widetilde{D}_i^T \widetilde{D}_i \end{bmatrix}, \tag{19}$$

in which

$$\begin{aligned}
\Lambda_{11} &= \widetilde{A}_{1i}^T\overline{P}_i\widetilde{A}_{1i} + \delta\widetilde{A}_{2i}^T\overline{P}_i\widetilde{A}_{2i} + \overline{Q}_i - P_i + \widetilde{C}_{1i}^T\widetilde{C}_{1i} + \delta\widetilde{C}_{2i}^T\widetilde{C}_{2i},\\
\Lambda_{21} &= A_{1i}^T\overline{P}_i\widetilde{A}_{1i} - \delta\widehat{A}_{2i}^T\overline{P}_i\widetilde{A}_{2i} + \widehat{C}_{1i}^T\widetilde{C}_{1i} - \delta\widehat{C}_{2i}^T\widetilde{C}_{2i},\\
\Lambda_{12} &= \widetilde{A}_{1i}^T\overline{P}_i\widehat{A}_{1i} - \delta\widetilde{A}_{2i}^T\overline{P}_i\widehat{A}_{2i} + \widetilde{C}_{1i}^T\widehat{C}_{1i} - \delta\widetilde{C}_{2i}^T\widehat{C}_{2i},\\
\Lambda_{11} &= \widehat{A}_{1i}^T\overline{P}_i\widehat{A}_{1i} + \delta\widehat{A}_{2i}^T\overline{P}_i\widehat{A}_{2i} - \overline{Q}_i + \widehat{C}_{1i}^T\widehat{C}_{1i} + \delta\widehat{C}_{2i}^T\widehat{C}_{2i}.
\end{aligned} \tag{20}$$

By Schur complement, (19) is equivalent to the following formula:

$$\begin{bmatrix}
\overline{Q}_i - P_i & * & * & * & * & * & *\\
0 & -Q_i & * & * & * & * & *\\
0 & 0 & -\gamma^2 I & * & * & * & *\\
\widetilde{A}_{1i} & \widehat{A}_{1i} & \widetilde{B}_i & -\widetilde{P}_i^{-1} & * & * & *\\
\delta\widetilde{A}_{2i} & -\delta\widehat{A}_{2i} & 0 & 0 & -\delta\widetilde{P}_i^{-1} & * & *\\
\widetilde{C}_{1i} & \widehat{C}_{1i} & \widetilde{D}_i & 0 & 0 & -I & *\\
\delta\widetilde{C}_{2i} & -\delta\widehat{C}_{2i} & \delta\widetilde{D}_i & 0 & 0 & 0 & -\delta I
\end{bmatrix} < 0, \tag{21}$$

where $\overline{\eta}^T\Lambda\overline{\eta} < 0$, and it can obtain that

$$\begin{aligned}
&E\{\Delta V(k)\} + E\left\{\widetilde{z}^T(k)\widetilde{z}(k)\right\} - \gamma^2 E\left\{\omega^T(k)\omega(k)\right\} < 0,\\
&\sum_{k=0}^{\infty} E\left\{\|\widetilde{z}(k)\|^2\right\} < \gamma^2 E\left\{\|\omega(k)\|^2\right\} + E\{V(0)\} - E\{V(\infty)\},
\end{aligned} \tag{22}$$

initial conditions $V(0) = 0$ and $E\{V(\infty)\} \geq 0$; system (5) meets H_∞ norm performance level γ, and it can clearly see that

$$E\left\{\sum_{k=0}^{\infty}\|\widetilde{z}(k)\|^2\right\} < \gamma^2\|\omega(k)\|^2. \tag{23}$$

The proof is over. □

4. Filter Design

Here, we will go to solve the system filter.

Theorem 3. *Consider NCSs (5) with a scalar $\gamma > 0$. If symmetric matrix $P_{1i} > 0$, $P_{3i} > 0$, $Q_{1i} > 0$, $Q_{3i} > 0$, $X_i > 0$, and $Y_i > 0$ and P_{2i}, Q_{2i}, Z_i, A_{Fi}, B_{Fi}, C_{Fi}, and D_{Fi} satisfied the following matrix inequalities, then*

$$\begin{bmatrix}
\psi_{11} & * & * & * & * & *\\
0 & \psi_{22} & * & * & * & *\\
0 & 0 & -\gamma^2 I & * & * & *\\
\psi_{41} & \psi_{42} & \psi_{43} & \psi_{44} & * & *\\
\psi_{51} & \psi_{52} & 0 & 0 & \psi_{55} & *\\
\psi_{61} & \psi_{62} & \psi_{63} & 0 & 0 & \psi_{66}
\end{bmatrix} < 0, \tag{24}$$

in which

$$\begin{aligned}
\psi_{11} &= \begin{bmatrix} \overline{Q}_{1i} - P_{1i} & * \\ \overline{Q}_{2i} - P_{2i} & \overline{Q}_{3i} - P_{3i} \end{bmatrix},\\
\psi_{22} &= \begin{bmatrix} -Q_{1i} & * \\ -Q_{2i} & -Q_{3i} \end{bmatrix},\\
\psi_{41} &= \begin{bmatrix} X_i^T A_i + \overline{\beta}B_{Fi}C_{Fi} & A_{Fi} \\ Z_i^T A_i + \overline{\beta}B_{Fi}C_{Fi} & A_{Fi} \end{bmatrix},\\
\psi_{42} &= \begin{bmatrix} (1-\overline{\beta})B_{Fi}C_{Fi} & 0 \\ (1-\overline{\beta})B_{Fi}C_{Fi} & 0 \end{bmatrix},\\
\psi_{43} &= \begin{bmatrix} X_i B_i \\ Z_i B_i \end{bmatrix},\\
\psi_{44} &= \begin{bmatrix} P_{1i} - X_i^T - X_i & * \\ P_{2i} - Y_i^T - Z_i & P_{3i} - Y_i^T - Y_i \end{bmatrix},\\
\psi_{51} &= \begin{bmatrix} \delta B_{Fi}C_{Fi} & 0 \\ \delta B_{Fi}C_{Fi} & 0 \end{bmatrix},\\
\psi_{52} &= \begin{bmatrix} -\delta B_{Fi}C_{Fi} & 0 \\ -\delta B_{Fi}C_{Fi} & 0 \end{bmatrix},\\
\psi_{61} &= \begin{bmatrix} L_i - \overline{\beta}D_{Fi}C_{Fi} & -C_{Fi} \\ \delta D_{Fi}C_{Fi} & 0 \end{bmatrix},\\
\psi_{55} &= \begin{bmatrix} \delta P_{1i} - \delta X_i^T - \delta X_i & * \\ \delta P_{2i} - \delta Y_i^T - \delta Z_i & \delta P_{3i} - \delta Y_i^T - \delta Y_i \end{bmatrix},\\
\psi_{62} &= \begin{bmatrix} -(1-\overline{\beta})D_{Fi}C_{Fi} & 0 \\ -\delta D_{Fi}C_{Fi} & 0 \end{bmatrix},\\
\psi_{63} &= \begin{bmatrix} D_{Fi} \\ 0 \end{bmatrix},\\
\psi_{66} &= \begin{bmatrix} -I & * \\ 0 & -\delta I \end{bmatrix}.
\end{aligned} \tag{25}$$

System (5) meets H_∞ norm performance level γ, which is stochastically stable. Then, the filter which is achieved by the desired γ is calculated by $A_{fi} = Y_i^{-1}A_{Fi}$, $B_{fi} = Y_i^{-1}B_{Fi}$, $C_{fi} = C_{Fi}$, and $D_{fi} = D_{Fi}$.

Proof. Slack matrix approach can be used for (17) by setting

$$\begin{aligned}
P_i &= \begin{bmatrix} P_{1i} & P_{2i} \\ * & P_{3i} \end{bmatrix},\\
Q_i &= \begin{bmatrix} Q_{1i} & Q_{2i} \\ * & Q_{3i} \end{bmatrix},\\
R_i &= \begin{bmatrix} X_i & Z_i \\ Y_i & Y_i \end{bmatrix} > 0.
\end{aligned} \tag{26}$$

Then, we have following equation using (26):

$$
\begin{aligned}
\overline{Q}_i - P_i &= \begin{bmatrix} \overline{Q}_{1i} - P_{1i} & * \\ \overline{Q}_{2i} - P_{2i} & \overline{Q}_{3i} - P_{3i} \end{bmatrix}, \\
R_i^T \widehat{A}_{1i} &= \begin{bmatrix} (1-\overline{\beta}) Y_i B_{fi} C_i & 0 \\ (1-\overline{\beta}) Y_i B_{fi} C_i & 0 \end{bmatrix}, \\
R_i^T \widehat{A}_{1i} &= \begin{bmatrix} Y_i B_{fi} C_i & 0 \\ Y_i B_{fi} C_i & 0 \end{bmatrix}, \\
R_i^T \widetilde{A}_{1i} &= \begin{bmatrix} X_i^T A_i + \overline{\beta} Y_i B_{fi} C_i & Y_i A_{fi} \\ Z_i^T A_i + \overline{\beta} Y_i B_{fi} C_i & Y_i A_{fi} \end{bmatrix}, \\
R_i^T \widetilde{B}_{1i} &= \begin{bmatrix} X_i^T B_i \\ Z_i^T B_i \end{bmatrix}, \\
\overline{P}_i - R_i^T - R_i &= \begin{bmatrix} \overline{P}_{1i} - R_i^T - R_i & * \\ \overline{P}_{2i} - R_i^T - R_i & \overline{P}_{3i} - R_i^T - R_i \end{bmatrix}, \\
R_i^T \widetilde{A}_{1i} &= \begin{bmatrix} Y_i B_{fi} C_i & 0 \\ Y_i B_{fi} C_i & 0 \end{bmatrix}.
\end{aligned} \tag{27}
$$

According to equations in (17) and (27), we can get

$$
\begin{bmatrix}
\overline{Q}_{1i} - P_{1i} & * & * & * & * \\
\overline{Q}_{2i} - P_{2i} & \overline{Q}_{3i} - P_{3i} & * & * & * \\
0 & 0 & -Q_{1i} & * & * \\
0 & 0 & -Q_{2i} & -Q_{3i} & * \\
0 & 0 & 0 & 0 & -\gamma^2 I \\
X_i^T A_i + \overline{\beta} Y_i B_{fi} C_i & Y_i A_{fi} & (1-\overline{\beta}) Y_i B_{fi} C_{fi} & 0 & X_i B_i \\
Z_i^T A_i + \overline{\beta} Y_i B_{fi} C_i & Y_i A_{fi} & (1-\overline{\beta}) Y_i B_{fi} C_{fi} & 0 & Z_i B_i \\
\delta Y_i B_{fi} C_{fi} & 0 & -\delta Y_i B_{fi} C_{fi} & 0 & 0 \\
\delta Y_i B_{fi} C_{fi} & 0 & -\delta Y_i B_{fi} C_{fi} & 0 & 0 \\
L_i - \overline{\beta} D_{fi} C_{fi} & -C_{Fi} & -(1-\overline{\beta}) D_{fi} C_{fi} & 0 & D_{fi} \\
\delta D_{fi} C_{fi} & 0 & -\delta D_{fi} C_{fi} & 0 & 0
\end{bmatrix}
\tag{28}
$$

$$
\begin{bmatrix}
* & * & * & * & * & * \\
* & * & * & * & * & * \\
* & * & * & * & * & * \\
* & * & * & * & * & * \\
* & * & * & * & * & * \\
P_{1i} - X_i^T - X_i & * & * & * & * & * \\
P_{2i} - Y_i^T - Z_i & P_{3i} - Y_i^T - Y_i & * & * & * & * \\
0 & 0 & \delta P_{1i} - \delta X_i^T - \delta X_i & * & * & * \\
0 & 0 & \delta P_{2i} - \delta Y_i^T - \delta Z_i & \delta P_{3i} - \delta Y_i^T - \delta Y_i & * & * \\
0 & 0 & 0 & 0 & -I & * \\
0 & 0 & 0 & 0 & 0 & -\delta I
\end{bmatrix} < 0.
$$

The proof is over. □

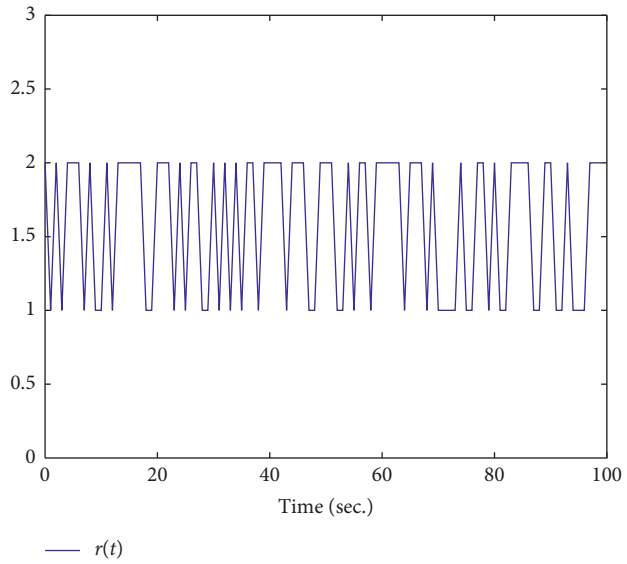

Figure 1: Parameters change of $r(t)$.

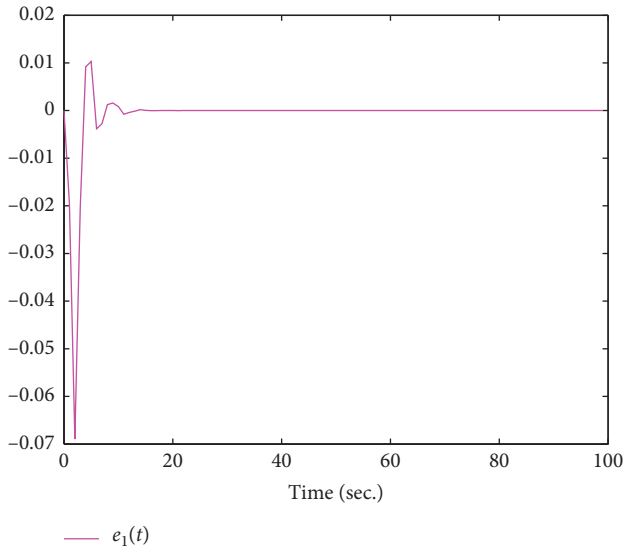

Figure 2: Parameters change of $e_1(t)$.

5. Simulation Result

Consider system (5) with

$$
\begin{aligned}
A_1 &= \begin{bmatrix} -0.2 & -0.405 \\ 0 & -0.55 \end{bmatrix}, \\
A_2 &= \begin{bmatrix} -0.2 & -2.673 \\ 0 & -0.230 \end{bmatrix}, \\
B_1 &= \begin{bmatrix} 0.5 & 0 \\ 0 & 0.5 \end{bmatrix}, \\
B_2 &= \begin{bmatrix} 0.5 & 0 \\ 0 & 0.5 \end{bmatrix}, \\
C_1 &= \begin{bmatrix} 0.4 & -0.4 \end{bmatrix}, \\
C_2 &= \begin{bmatrix} 0.5 & -0.2 \end{bmatrix}, \\
D_1 &= \begin{bmatrix} 0.1 & -0.1 \end{bmatrix}, \\
D_2 &= \begin{bmatrix} 0.1 & -0.1 \end{bmatrix}, \\
L_1 &= \begin{bmatrix} 1 & 0 \end{bmatrix}, \\
L_2 &= \begin{bmatrix} 1 & 0 \end{bmatrix}.
\end{aligned} \tag{29}
$$

Two models in the simulation are set as those data in (29). In the model, the transition probabilities are $\pi_{ij} = \begin{bmatrix} 0.3 & 0.7 \\ 0.4 & 0.6 \end{bmatrix}$, the initial value of $\overline{\beta}$ is 0.5, and the initial condition is set to zero. It is easily observed that the method is feasible, and the system with time delay and packet loss becomes stochastically stable, which meets H_∞ norm performance level γ. Some simulation results are shown in Figures 1–5.

Figure 1 shows the time response of $r(t)$.

Figure 2 is the parameter change of the system error $e_1(t)$. It can be seen from the figure that, with the passage of time, $e_1(t)$ changes from a large fluctuation to a stable state one.

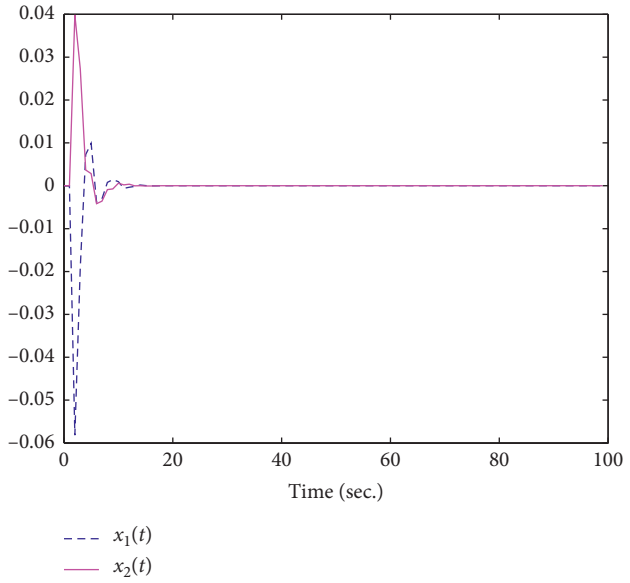

Figure 3: Parameters change of different $x(t)$.

Figure 3 shows the values of $x_1(t)$ and $x_2(t)$. It can be seen from the figure that $x_1(t)$ and $x_2(t)$ remain stable after about 20 seconds.

Figure 4 is the parameter change of the filter state $\widehat{x}_1(t)$ and $\widehat{x}_2(t)$. From the figure, it can be seen that the value of $\widehat{x}_1(t)$ gradually becomes equal to the value of $\widehat{x}_2(t)$ overtime and finally both values remain stable.

Figure 5 is the parameter change of $z_1(t)$ and $\widehat{z}_1(t)$. From the figure, it can be seen that the initial time of $z_1(t)$ fluctuates greatly, and it tends to be consistent with $\widehat{z}_1(t)$ in the end.

Remark 2. As can be seen from the ordinate of the system state diagram of Figure 3 and the filter state diagram of Figure 4, the difference between the two is 100 times, so the

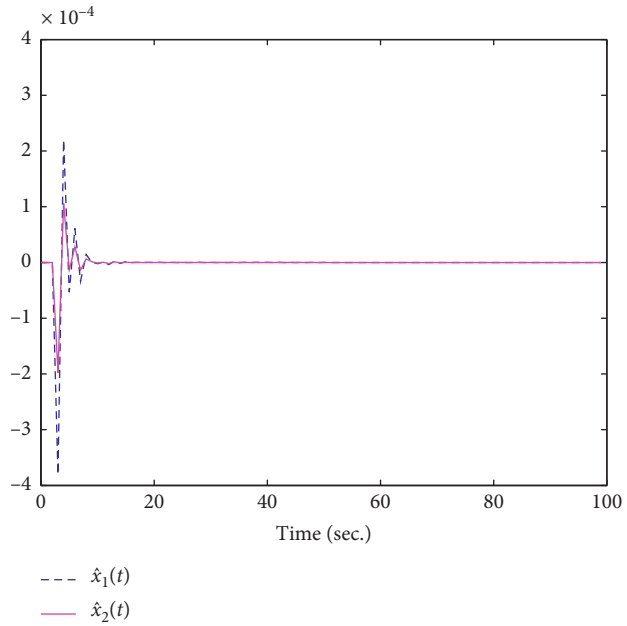

Figure 4: Parameters change of filter parameters.

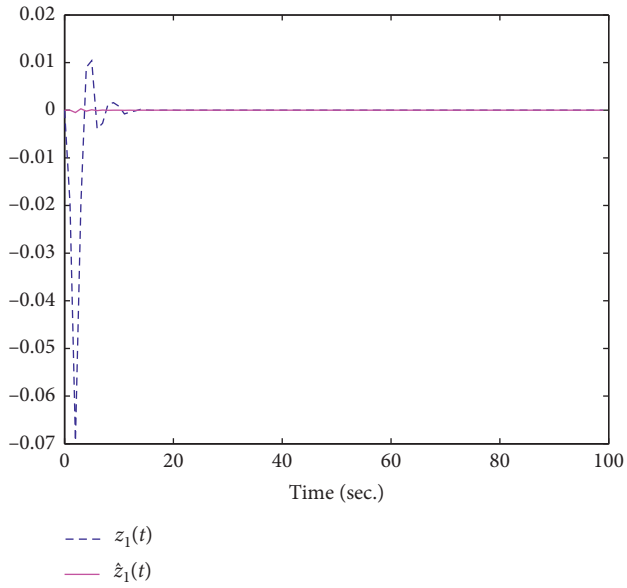

Figure 5: Parameters change of output parameters.

change of $\widehat{z}_1(t)$ appears to be small in Figure 5. This also reflects from one side that the filter designed in this paper has a smaller overshoot and more stable output.

6. Conclusion

This paper has investigated the H_∞ filtering problem about NCSs with time delay and packet dropout phenomenon. Packet dropout is treated as a constant probability independent and identically distributed Bernoulli random process. By the Lyapunov stability theory, system (5) meeting H_∞ norm performance level γ is proven. By introducing a special structure of the relaxation matrix, the solution of filter which meets an H_∞ performance index level of NCSs with time delay and packet dropout is completed. Finally, a simulation result is given to prove the validity of the new design scheme.

Data Availability

The data used to support the findings of this study are included within the article. Because it is a numerical simulation example, readers can get the same results as this article by using the LMI toolbox of Matlab and the theorem given in this article.

Conflicts of Interest

The authors declare that they have no conflicts of interest.

Acknowledgments

This work was supported by the National Natural Science Foundation of China (Grant nos. 61403278 and 61503280).

References

[1] L. Sun and N. Xu, "Stability analysis of Markovian jump system with multi-time-varying disturbances based on improved interactive convex inequality and positive definite condition," *IEEE Access*, vol. 7, pp. 54910–54917, 2019.

[2] H. Zhang, Q. Hong, H. Yan, F. Yang, and G. Guo, "Event-based distributed H_∞ filtering networks of 2-DOF quarter-car suspension systems," *IEEE Transactions on Industrial Informatics*, vol. 13, no. 1, pp. 312–321, 2017.

[3] X. Li, B. Zhang, P. Li, Q. Zhou, and R. Lu, "Finite-horizon H_∞ state estimation for periodic neural networks over fading channels," *IEEE Transactions on Neural Networks and Learning Systems*, pp. 1–11, 2019.

[4] H. Yan, F. Qian, H. Zhang, F. Yang, and G. Guo, "H_∞ fault detection for networked mechanical spring-mass systems with incomplete information," *IEEE Transactions on Industrial Electronics*, vol. 63, no. 9, pp. 5622–5631, 2016.

[5] X.-M. Li, Q. Zhou, P. Li, H. Li, and R. Lu, "Event-triggered consensus control for multi-agent systems against false data injection attacks," *IEEE Transactions on Cybernetics*, pp. 1–11, 2019.

[6] L. Cao, H. Li, G. Dong, and R. Lu, "Event-triggered control for multi-agent systems with sensor faults and input saturation," *IEEE Transactions on Systems, Man and Cybernetics: Systems*, pp. 1–12, 2019.

[7] H. Y. Li, Y. B. Gao, P. Shi, and H.-K. Lam, "Observer-based fault detection for nonlinear systems with sensor fault and limited communication capacity," *IEEE Transactions on Automatic Control*, vol. 61, no. 9, pp. 2745–2751, 2015.

[8] H. C. Yan, Q. Yang, H. Zhang, F. Yang, and X. Zhan, "Distributed H_∞ state estimation for a class of filtering networks with time-varying switching topologies and packet losses," *IEEE Transactions on System, Man, and Cybernetics: Systems*, vol. 48, no. 12, pp. 2047–2057, 2018.

[9] H.-D. Tran, Z.-H. Guan, X.-K. Dang, X.-M. Cheng, and F.-S. Yuan, "A normalized PID controller in networked control systems with varying time delays," *ISA Transactions*, vol. 52, no. 5, pp. 592–599, 2013.

[10] H. Zhang, X. Y. Zheng, H. C. Yan, C. Peng, Z. Wang, and Q. Chen, "Codesign of event-triggered and distributed H_∞ filtering for active semi-vehicle suspension systems," *IEEE Transactions on Mechatronics*, vol. 22, no. 2, pp. 1047–1058, 2017.

[11] Q. X. Zhu, K. H. Lu, and Y. Zhu, "Observer-based feedback control of networked control systems with delays and packet dropouts," *Journal of Dynamic Systems Measurement and Control*, vol. 138, no. 2, pp. 2–11, 2016.

[12] J. Wang, L. Shen, J. W. Xia, Z. Wang, and X. Chen, "Asynchronous dissipative filtering for nonlinear jumping systems subject to fading channels," *Journal of the Franklin Institute*, vol. 357, no. 1, pp. 589–605, 2020.

[13] Q. X. Zhu, K. H. Lu, and Y. Zhu, "H_∞ guaranteed cost control for networked control systems under scheduling policy based on predicted error," *Mathematical Problems in Engineering*, vol. 2014, Article ID 586029, 12 pages, 2014.

[14] H. Y. Li, P. Shi, D. Y. Yao, and L. Wu, "Observer-based adaptive sliding mode control for nonlinear Markovian jump systems," *Automatica*, vol. 64, pp. 133–142, 2016.

[15] G. Nagamani and S. Ramasamy, "Dissipativity and passivity analysis for uncertain discrete-time stochastic Markovian jump neural networks with additive time-varying delays," *Neurocomputing*, vol. 174, pp. 795–805, 2016.

[16] M. C. Dai, J. W. Xia, H. Xia, and H. Shen, "Event-triggered passive synchronization for Markov jump neural networks subject to randomly occurring gain variations," *Neurocomputing*, vol. 331, pp. 403–411, 2019.

[17] L. Shen, X. F. Yang, J. Wang, and J. Xia, "Passive gain-scheduling filtering for jumping linear parameter varying systems with fading channels based on the hidden Markov model," *Proceedings of the Institution of Mechanical Engineers, Part I: Journal of Systems and Control Engineering*, vol. 233, no. 1, pp. 67–79, 2019.

[18] X. Y. Yin, X. Zhang, L. Zhang, C. Wang, M. Al-Yami, and T. Hayat, "H_∞ model approximation for discrete-time Takagi-Sugeno fuzzy systems with Markovian jumping parameters," *Neurocomputing*, vol. 157, pp. 306–314, 2015.

[19] H. Y. Li, H. J. Gao, P. Shi, and X. Zhao, "Fault-tolerant control of Markovian jump stochastic systems via the augmented sliding mode observer approach," *Automatica*, vol. 50, no. 7, pp. 1825–1834, 2014.

[20] M. C. Dai, Z. G. Huang, J. W. Xia, B. Meng, J. Wang, and H. Shen, "Non-fragile extended dissipativity-based state feedback control for 2-D Markov jump delayed systems," *Applied Mathematics and Computation*, vol. 362, Article ID 124571, 2019.

[21] Y. C. Ma, M. H. Chen, and Q. L. Zhang, "Non-fragile static output feedback control for singular TTS fuzzy delay-dependent systems subject to Markovian jump and actuator saturation," *Journal of the Franklin Institute*, vol. 353, no. 11, pp. 2373–2397, 2016.

[22] W. H. Qi and X. W. Gao, "State feedback controller design for singular positive Markovian jump systems with partly known transition rates," *Applied Mathematics Letters*, vol. 46, pp. 111–116, 2015.

[23] L. Qiu, B. Zhang, G. Xu, J. Pan, and F. Yao, "Mixed H_2/H_∞ control of Markovian jump time-delay systems with uncertain transition probabilities," *Information Sciences*, vol. 373, pp. 539–556, 2016.

[24] B. P. Jiang, C. C. Gao, Y. G. Kao, and Z. Liu, "Sliding mode control of Markovian jump systems with incomplete information on time-varying delays and transition rates," *Applied Mathematics and Computation*, vol. 290, pp. 66–79, 2016.

[25] B. Y. Zhang and Y. M. Li, "Exponential L_2–L_∞ filtering for distributed delay systems with Markovian jumping parameters," *Signal Processing*, vol. 93, no. 1, pp. 206–216, 2013.

[26] X. H. Ge and Q. L. Han, "Distributed sampled-data asynchronous H_∞ filtering of Markovian jump linear systems over sensor networks," *Signal Processing*, vol. 127, pp. 86–99, 2016.

[27] G. Mustafa and T. W. Chen, "H_∞ filtering for nonuniformly sampled systems: a Markovian jump systems approach," *Systems & Control Letters*, vol. 60, no. 10, pp. 871–876, 2011.

[28] N. Xu and L. K. Sun, "An improved H_∞ filtering for Markovian jump system with time-varying delay based on finite frequency domain," *Journal of the Franklin Institute*, vol. 356, no. 12, pp. 6724–6740, 2019.

[29] F. W. Li, P. Shi, X. C. Wang, and H. R. Kamiri, "Robust H_∞ filtering for networked control systems with Markovian jumps and packet dropouts," *Modelling, Identification and Control*, vol. 35, no. 3, pp. 159–168, 2014.